ISSN 0288-4534
CODEN: KONAE7

KONA Powder and Particle Journal

No.28 (2010)

Published by Hosokawa Powder Technology Foundation

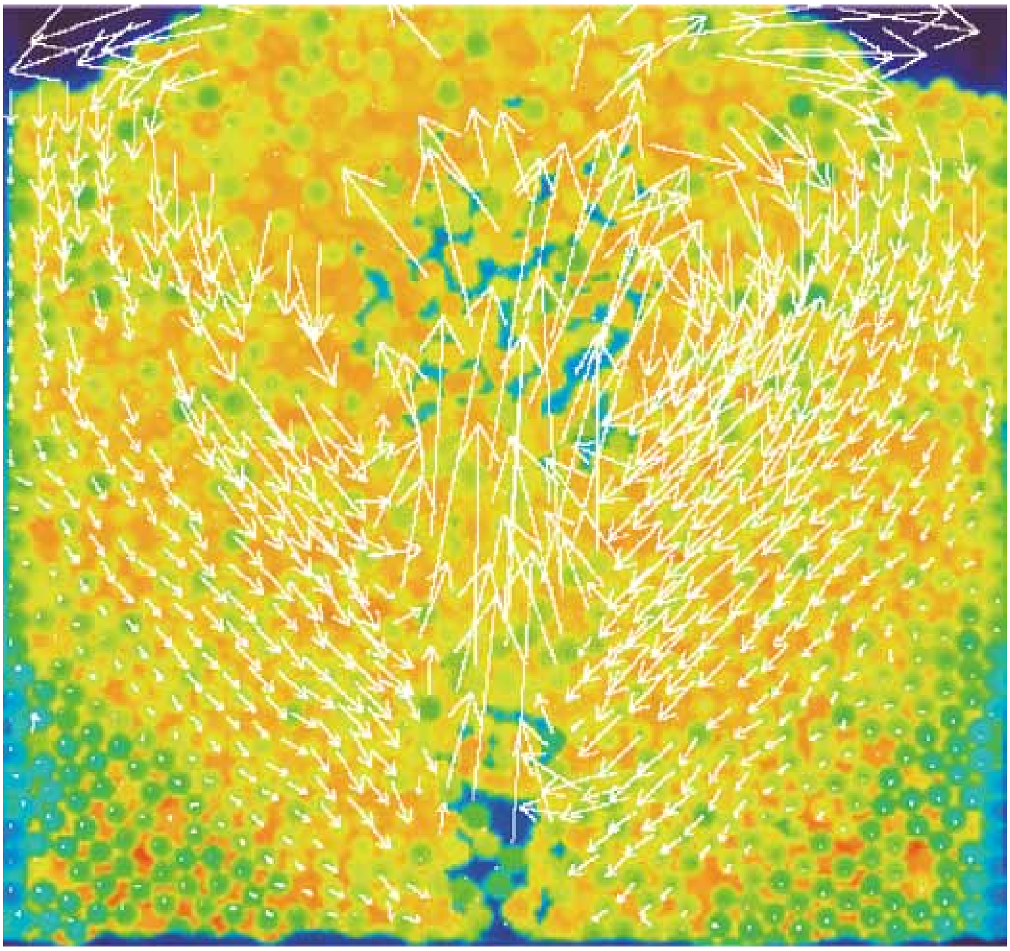

available online – www.kona.or.jp

KONA Powder and Particle Journal

http://www.kona.or.jp

KONA is a refereed scientific journal that publishes articles on powder and particle sciences and technology. KONA has been published annually since 1983 in Japan. KONA is distributed to researchers, members of the scientific community, universities and research libraries throughout the world.

About the Cover of Journal “KONA”

The Chinese character “粉” is pronounced “KONA” in Japanese, and means “Powder”. The hand written “粉” is after the late Mr. Eiichi Hosokawa, founder of the Hosokawa Micron Corporation.

Headquarters of Hosokawa Micron Corporation

Editorial Board
Y. Tsuji — Editor-in-Chief (Professor Emeritus of Osaka Univ., JAPAN)

Asia / Oceania Editorial Board
H. Emi (Professor Emeritus of Kanazawa Univ., JAPAN)
Y. Fukumori (Kobe Gakuin Univ., JAPAN)
J. Hidaka (Doshisha Univ., JAPAN)
K. Higashitani (Kyoto Univ., JAPAN)
Y. Kang (Chungnam National Univ., KOREA)
Y. Kousaka (Professor Emeritus of Osaka Prefecture Univ., JAPAN)
J. Li (Chinese Academy of Science)
H. Masuda (Professor Emeritus of Kyoto Univ., JAPAN)
M. Naito (Osaka Univ., JAPAN)
K. Nogi (Osaka Univ., JAPAN)
Pradip (Tata Research Development and Design Centre)
M. Rhodes (Monash Univ., AUSTRALIA)
M. Takahashi (Nagoya Institute of Technology, JAPAN)
W. Tanthapanichakoon (National Science and Technology Development Agency, THAILAND)
T. Yokoyama (Hosokawa Powder Technology Research Institute, JAPAN)
Secretariat
H. Yamashita (Hosokawa Powder Technology Foundation, JAPAN)

Europe / Africa Editorial Board
M. Ghadiri Chairman (Univ. of Leeds, UNITED KINGDOM)
B. Biscans (Univ. de Toulouse, FRANCE)
N.Z. Lyakhov (Institute of Solid State Chemistry, RUSSIA)
J. Marijnissen (Univ. of Delft, NETHERLANDS)
W. Peukert (Univ. Erlangen, GERMANY)
S.E. Pratsinis (ETH Züich, SWITZERLAND)
Secretariat
P. Krubeck (Hosokawa Alpine AG, GERMANY)
J. Stein (Hosokawa Alpine AG, GERMANY)

American Editorial Board
B.M. Moudgil Chairman (Univ. of Florida., U.S.A.)
D.W. Fuerstenau Vice Chairman (Univ. of California, U.S.A.)
F. Concha (Univ. of Concepció, CHILE)
R. Flagan (California Institute of Technology, U.S.A.)
A.I. Hickey (Univ. of North Carolina, U.S.A.)
R. Hogg (Pennsylvania State Univ., U.S.A.)
V.A. Marple (Univ. of Minnesota, USA)
S.B. Savage (McGill Univ., CANADA)
Secretariat
C.C. Huang (Hosokawa Micron International INC, U.S.A.)

■Publication Office
Hosokawa Powder Technology Foundation
Shodai- Tajika 1-9, Hirakata, Osaka, 573-1132 Japan
e-mail : info@kona.or.jp

KONA Powder and Particie Journal No. 28 (2010)

CONTENTS

<Review Papers>

<Original Research Papers >

< Information Articles >

The Letter from the Editor

Mr. Masuo Hosokawa

Yutaka Tsuji

Mr. Masuo Hosokawa, Chairman of Hosokawa Micron Corp. and the president of Hosokawa Powder Technology Foundation, passed away on March 31st, 2010. He was 85 years old. Many people in powder process industry know him as the man who has brought up the Hosokawa Micron Group as a world-leading company. He was a charismatic leader. He was admired with a feeling of awe by everybody who knows him. He attracted attention of the business circle for his activities of M & A (Mergers and Acquisition). In public of Japan he was known as an owner of many racehorses. I have always had an impression that he was quite different from many company presidents. He valued science and technology as a base supporting his company. His belief was that the growth of his company would be difficult without the progress of powder technology and science. He expressed his gratitude to this academic field not by talk but by action. Many years before the Hosokawa group became a big company, he was contributing much to the development and promotion of powder technology and science. In 1957 he launched a journal "The Micromeritics", which is an annual publication, named "Funsai" in Japanese. The 1957 is such a year when Japan entered an age of high economic growth. At that time the name of his company was not "Hosokawa Micron Corp." but "Hosokawa Iron Works, Ltd." . He was in early 30s and a young managing director. After taking over the presidency from his father, he steered the company toward its globalization. The contents of the first issue of "The Micromeritics" were introductions of technology developed in Hosokawa, but from the second issue "The Micromeritics" came up with academic aspects presenting original papers and reviews by researchers besides the information of the company. Hosokawa Iron Works held the first Symposium of Powder Technology in 1968 under his leadership to promote powder technology and science. The Party of Powder Technology (Japan) was organized around that time as a group planning the symposium. The Party of Powder Technology (Japan) changed its name to the Council of Powder Technology later. The Council is formed by university professors. The Micromeritics journal and the Symposium of Powder Technology have been continued without interruption up to the present. Publishing the journal for 54 years and holding the symposium for 43 years are enough to admire Hosokawa Micron's contribution to academics. What surprised many companies and researchers in Japan and other countries about Hosokawa Micron was that this company issued an English journal named "KONA" in 1983. Those days it was hard to imagine that a small Japanese company of powder machinery published an academic journal in English. At first, the purpose of KONA was to introduce good research papers in Japanese to the world by translating them to English, but later it changed to an international journal publishing papers from all over the world. In 1991, he established the Hosokawa Powder Technology Foundation and became the president of the Foundation. The basic fund was from Mr. Hosokawa. The foundation activities include providing research grants, holding the symposium and publishing KONA Powder and Particle Journal. Nearly 20 years have gone by since the start of the foundation and the total of grantees reaches a big number.

All these activities of Hosokawa Micron Corp. have been done under his strong leadership. Numerous services he rendered during his life time are great and immeasurable. With grateful appreciation for his services, I offer this token of my deepest sympathy.

Comment of the Cover Photograph

Simultaneous measurement of particle motion and temperature in two-dimensional fluidized bed with heat transfer

Takuya Tsuji, Takuya Miyauchi, Satoshi Oh and Toshitsugu Tanaka
Department of Mechanical Engineering,
Osaka University

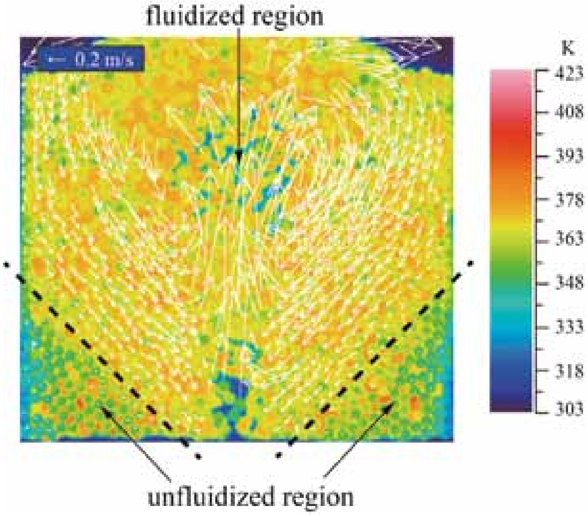

Gas-fuidized beds are widely used in industrial processes concerned with heat transfers. Complex interactions between particles, gas flows and bounded walls induce the formation of characteristic spontaneous flow structures that give large influence on the dispersion and mixing characteristics of particles and heat transfers. For the better understandings of heat transfers in fluidized beds and further improvement of numerical models, it is important to know the relations between the behavior of spontaneous flow structures, the motion of individual particles and heat transfers in detail.

The figure shows a result of simultaneous measurement of particle velocity and temperature distributions in a two-dimensional fluidized bed under a spouting condition. A coupling technique between Particle Tracking Velocimetry (PTV) and Infrared Thermography (IT) is developed. In the present case, a gas flow at room temperature is injected to the vessel filled with spherical aluminium particles elevated to 423 K initially. By the present technique, particle velocity and temperature can be observed in the individual particle-level. The particle layer is divided into fluidized and unfluidized regions and a typical circulating flow pattern is observed in the fluidized region. In the unfluidized region, the motion of particles is not active and the temperature is lower than that in the fluidized region due to the contact with the front wall for a long time.

Surface Analytical Techniques in Solid-State Particle Characterization for Predicting Performance in Dry Powder Inhalers[†]

Xiao Wu, Xiaojian Li, and Heidi M. Mansour*
University of Kentucky College of Pharmacy
Department of Pharmaceutical Sciences-Drug Development Division[1]

Abstract

The pulmonary route is of interest for both effective local therapy for respiratory and lung diseases, such as asthma, chronic obstructive pulmonary disease and cystic fibrosis, and systemic administration of drugs, such as proteins and peptides. Dry powder inhalers (DPIs) are devices through which a dry powder formulation of drug is delivered via the pulmonary route. The DPIs are highly efficient but complicated systems, the performance of which relies on many aspects, including aerodynamic diameter of the powder formulation, particle density, bulk density, surface morphology and composition, particle shape, interparticulate cohesive forces between drug particles and interparticulate adhesive forces between drug and carrier particles. Among them, surface morphology of both drug particles and carrier particles within the formulation is a very important factor in determining the interparticulate contact area and forces, aerosolization efficiency and subsequent lung deposition. Techniques that have been applied to study surface properties of solid-state particles in DPIs include atomic force microscopy, micro- and nanothermal analysis, inverse gas chromatography and X-ray photoelectron spectroscopy. This paper reviews different aspects of DPIs, with emphasis on their surface properties and influence on aerosol performance, and the techniques that are utilized to examine their surface properties.

Keywords: pulmonary drug delivery, inhalation aerosols, surface chemistry, interparticulate forces, particle engineering, pharmaceutical powders

1. Pharmaceutical Solids

1.1 Overview

The solid-state[1, 2] is the most common state in marketed pharmaceutical products. The final solid state dosage form includes the active pharmaceutical ingredient (API) and excipients. One of the main advantages of the solid state relative to the liquid state is higher physical and chemical stability due to slower degradation kinetics. Thereby, a longer pharmaceutical shelf-life can be achieved. Pharmaceutical compounds in the solid-state can exist as crystalline[3-5] and amorphous[6-9] forms.

1.2 The Crystalline state & polymorphism

In crystalline materials, structural units are repeated in a regular manner and form a well-defined lattice. In other words, crystalline materials possess both short-range and long-range molecular order. The crystalline forms include polymorphs[10, 11] and pseudopolymorphs[12]. Polymorphism[13, 14] describes the ability of the crystalline substance to exhibit different lattice structures and/or molecular conformations, without undergoing changes in its chemical composition. The pseudopolymorph refers to crystalline hydrates and solvates[10, 15, 16], which incorporate bound water molecules (hydrates) or bound organic solvent molecules (solvates) in the crystal structure. Depending on the solid phase of an API, properties such as morphology, density, stability, melting point, solubility and color can be different. These differences may, in turn, have significant influence on the API's physical and chemical stability, bioavailability[17] and processability[18], including powder flowability[19, 20]

[†] Accepted: July 27th, 2010

[1] 789 South Limestone St., Lexington, KY 40536-0596, USA

* Corresponding Author
Telephone: (859) 257-1571
E-mail heidi.mansour@uky.edu

and compressability[21]. Typically, the thermodynamically stable crystalline form is preferred since the risk of solid-state transformations (ie. solid-state phase transitions) during process and storage is minimized.

Thermodynamically over time, the less stable solid form possesses a higher Gibbs free energy, and hence, will convert to the more stable form which has a lower Gibbs free energy. Hence, solid-state phase transitions are of great importance in pharmaceutical material science. A phase transition can arise through melting, in solution, and solution-mediated, solid-solid transition. Molten transition takes place when a compound is heated and subsequently cooled after melting. A new solid phase can be obtained through solvent evaporation after being suspended or dissolved in a solvent. Solution-mediated phase transition has three steps: 1). dissolution of the metastable form; 2). nucleation as a more stable form; and 3). crystal growth of the stable phase. The solid-solid phase transition circumvents the transient liquid or vapor phase. The solid-solid transition can be categorized into monotropic and enantiotropic systems, in the case of polymorphic pairs. In a monotropic system, one polymorph is stable and the transition is irreversible. However, in an enantiotropic system, the transition is reversible and each polymorph is stable within a certain temperature range. Solid-state phase transformations[22-25] include polymorphic interconversions, dehydration or desolvation processes, and order-disorder transformations[26]. Furthermore, solid-phase transitions can be either thermodynamically or kinetically controlled processes.

In crystalline pharmaceutical powders, a crystalline particle has a number of crystal faces[27]. Each crystal face possesses unique surface properties. Typical crystal faces and Miller indices are shown in **Fig. 1**. Various faces of the L-Lysine monohydrochloride dihydrate (LH) crystals have different surface free energies which relates to crystal habit and orientation[28]. Therefore, understanding the surface energetics[29] of a particular crystalline face is of importance in pharmaceutical formulation, processing, and therapeutic delivery. For instance, surfaces energetics of a particular crystal face influences the nature of chemical interactions with excipients in the formulation, as well as with other particles.

1.3 The Amorphous state & other metastable states

Unlike crystalline compounds, which have orientational and positional long-range molecular order in all three dimensions of space, the amorphous state shows no long-range molecular packing ie. lacks long-range molecular order. Since, the amorphous state is a mesophase/metastable phase (ie. not a thermodynamically stable phase), physicochemical properties such as higher solubility, higher bioavailability, higher molecular mobility (ie. more disordered with higher entropy), higher chemical and physical degradation kinetics, and less stability over pharmaceutically relevant time scales are observed. Pharmaceutical development of amorphous form is being conducted in recent years to gain higher solubility[30] because of a higher molecular mobility, although lower physical and chemical stability is associated with it. The strategy of rationally designing the amorphous state into a pharmaceutical product can be utilized to overcome low bioavailability of poorly water-soluble crystalline drug candidates[6, 9, 31, 32] which is increasingly more common with newer and promising drug candidates. The amorphous form can be generated intentionally or unintentionally by many common pharmaceutical processing methods, including milling[33-35], quench-cooling[36], spray-drying[37-42], freeze-drying[9, 43, 44] and compression[9, 32].

The amorphous phase often originates on the surfaces of particles during various types of pharmaceutical processing procedures. The oxygen gas and water vapor adsorption on these disordered regions (having a higher molecular mobility) occurs initially on the surface of particles (ie. adsorption) resulting in acceleration in oxidation and hydrolysis reactions

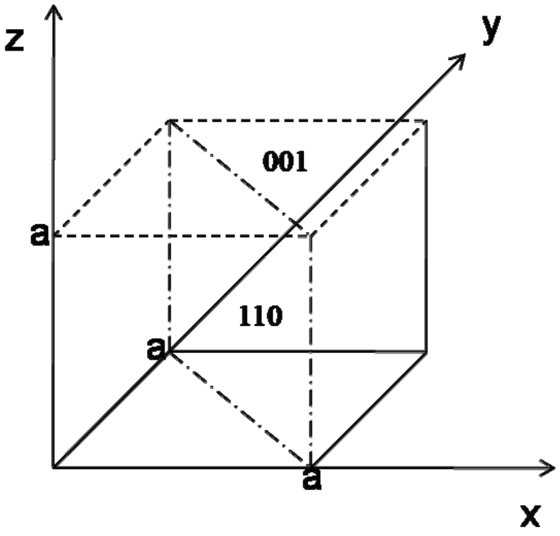

Fig. 1 Illustration of the miller indices of crystal faces of a cubic crystal. The "short dash" (—) plane (001) meets the x, y and z axes at infinity, infinity and a, respectively. The "long dash dotted" (—. — . —) plane (110) meets the x, y and z axes at a, a and infinity, respectively.

that then propagates below the surface into the bulk region (ie. absorption). Furthermore, the relatively higher molecular mobility of compound is further increased, where absorbed water acts as a plasticizer. Consequently, the physical and chemical stability45) over pharmaceutical timescales for the powder becomes compromised.

The thermodynamic tendency for metastable phases existing on the surface of particles in the solid-state to readily take up small amounts of water vapor molecules in the environment is the basis on which quantification of very small amounts (1% or less) of these metastable phases can be carried out using gravimetric water vapor sorption. Gravimetric vapor sorption (GVS), also sometimes called dynamic vapor sorption (DVS), is a powerful and highly quantitative analytical interfacial technique used in pharmaceutical solid-state development, including inhalation aerosols. Moreover, vapor-induced solid-state phase transitions (eg. disorder-to-order phase transition, recrystallization, liquid crystallization, etc.) can be systematically examined and quantified. It is of particular utility in the characterization and performance prediction of particles intended for inhalation aerosol delivery, as often particle size reduction methods (eg. micronization) induce minute but significant amounts of metastable surface phases that can impact aerosol powder dispersion and particle behavior in the high relative humidity of the lungs (> 90%), as well as overall stability of the aerosol formulation product.

In addition to the amorphous form, other mesophases/metastable phases46, 47) are important in the solid-state phase behavior of pharmaceuticals and phase transitions induced by pharmaceutical processing techniques. Based on the type of molecular mobility and directional molecular order along one or two dimensions, a mesophase can be classified into liquid crystal48) (with positional and if applicable conformational mobility), plastic crystal (with orientational mobility)49-51), and condis crystal (with conformational mobility)52).

Therefore, it is important to be able to determine that the desired form chosen for a pharmaceutical formulation is not contaminated with other solid-state forms that have varying bioavailability and stability. Based on this, it is essential to determine the effects of processing and storage conditions on the API, which may induce solid-state phase transitions and polymorphic transformations caused by mechanical (milling, compression) and thermal stresses or interactions with formulation ingredients. Hence, solid-state transformations have to be closely monitored and trace amount of contaminating polymorphs or non-crystalline metastable forms (eg. amorphous) should be detected to ensure safety, quality and efficacy of the pharmaceutical product53).

Finally, the presence of partially ordered/disordered phases are influential in affecting performance of particles constituting powders intended for aerosol inhalation, both *in vitro* and *in vivo*23, 26, 54, 55). These partially ordered/disordered phases may process-induced or rationally designed into the particle for improving aerosol performance56-58) and therapeutic properties (ie. enhanced solubility and bioavailability). These phases include nanocrystals59-61) (non-amorphous state lacking long-range order), liquid crystals, plastic crystals, and amorphous phases. There is much interest in dry powder inhaler (DPI) performance prediction based on the static and dynamic properties of the powder, as a manifestation of the solid-state phases described above. Recently, novel insight and predictive correlations between DPI particle surface properties and DPI aerosol performance have been reported62-65).

2. Dry Powder Inhalers (DPIs)

2.1. Definition of DPIs

In medical therapy, inhaled and aerosolized medications have been used for the treatment respiratory tract diseases, such as asthma and chronic obstructive pulmonary disease, for many decades66).

Based on the physical states of dispersed-phase and continuous medium, inhaled drug delivery systems can be divided into three principle categories67): pressurized metered-dose inhalers (pMDIs), dry powder inhalers (DPIs), and nebulizers68). Within each class further differentiation is based on metering, means of dispersion, or design69). In nebulizers, the drug is dissolved or suspended in a polar liquid, usually water. Because of their large dimensions (including pump, tubing and possibly ventilating air supply), nebulizers are not convenient to use. They are usually used in hospital or ambulatory care settings, and the aerosol is delivered continuously over an extended period of time. pMDIs are bolus drug delivery devices that contain solid drug, suspended or dissolved in a nonpolar volatile propellant. Dry powder inhalers are devices through which a dry powder formulation of drug is delivered for local or systemic effect via the pulmonary route. Lactose carrier-based DPI formulations are comprised of coarse non-respirable carrier particles of α-lactose monohydrate (FDA-approved) physically mixed with jet-milled drug that is in the respirable size range[62, 63, 70-72]. Advanced particle engineering design techniques have enabled the formulation of lactose carrier-free DPI formulations[73].

2.2. Advantages of a dry powder inhaler

The development of DPIs has been motivated by the desire for alternatives to pMDIs, In 1987, the Montreal protocol called for signatory countries to phase out the production of CFC propellants in medical products, in order to stop depletion of the ozone layer[74].

In addition to being propellant free, DPIs are very portable, patient friendly, easy to use and do not require spacers[73]. Because a pMDI is pressurized, it emits the dose at high velocity, probably causing premature deposition in the oropharynx[75, 76]. Despite use of spacers, incorrect use of pMDIs is still a prevalent problem[77]. Thus, pMDIs require careful coordination of actuation and inhalation. Contrastingly, DPIs with passive devices are activated by the patient's respiratory airflow. They require little or no coordination of actuation and inhalation and can achieve better lung delivery[78, 79].

Since DPIs are comprised of particles in the solid-state (ie. powders)[73], they possess higher stability relative to the liquid state[80] and compared with pMDI formulations containing propellant and cosolvents[81]. Summary of the advantages and disadvantages of dry powder inhalers is shown in **Table 1**.

2.3. Drugs incorporated in DPIs

There are several factors which should be taken into consideration in the development of a dry powder aerosol delivery system, including drug powder production, aerosol performance and delivery device.

Among them, the desired site of deposition should be the starting point for every DPI development. When local effects are desired, receptor densities may be indicative for the preferred site of drug deposition, while when systemic absorption is desired, differences in membrane permeability and clearing mechanisms may be decisive. The majority of pulmonary drugs on the market are short-acting and long-acting ß agonists, corticosteroids, and anti-cholinergic agents. Bronchodilators (ß$_2$-agonists) in asthma and COPD, such as salbutamol and formoterol, interact with ß$_2$-adrenoceptors, which are located on a variety of cells, including smooth muscle and epithelial cells. The concentration of ß-receptors throughout the lungs varies. Most of them are located in the alveoli[82-85]. Inhalation steroids are the cornerstone in asthma therapy and their molecular action occurs at intracellular glucocorticoid receptors, which are located through out the airways and alveoli[86, 87]. Anti-cholinergic agents target muscarinic receptors, which are moderately distributed throughout the airways and periphery[82, 88].

2.4. Powder production process

The first step of DPIs manufacture is to produce bulk drug preparations by crystallization from solution, filtration and drying. Subsequently, to create particles in the respirable size range (< 5 μm in diameter), the drug particle size must be reduced. The conventional size-reduction technique is milling[89-92], which is simple, cheap and easy to scale up. There are many different mills, three main types of which used in active pharmaceutical ingredient manufacture are fluid-energy mills, high-peripheral-speed

Table 1 Summary of advantages and disadvantages of dry powder inhalers.

Advantages	Disadvantages
Different dose forms (single unite dose, multi-unit dose and multiple dose)	Moderate to high respiratory flow required
Formulation stability	Deposition efficiency dependent on patient's respiratory airflow
No propellant, environmental sustainability	May cause high pharyngeal deposition
Small, portable and quick to use	Not all medications available
Breath-actuated, little or no patient coordination required	
Short treatment time	
Spacers not required and dose counters incorporated in most newer designs	

mills, and the ball mill. The shortcoming of milling is its poor control over the particle crystallinity, shape, size and size distribution.

Other techniques for production of stable micron-sized particles involve spray drying[93-95] and supercritical fluid technology[96-98]. In spray drying, the feed solution is supplied at room temperature and pumped to the nozzle where it is atomized by the nozzle gas. The atomized solution is then dried by preheated drying gas in a special chamber to remove water moisture from the system, thus forming dry particles. These prepared particles are collected with a cyclone separation device[99, 100]. Compared with milling, spray-drying offers more flexibility and the possibility of morphology control in addition to size control[101, 102]; however, spray dried particles are mostly amorphous[103].

The basic feature of the supercritical fluid process is the controlled crystallization of drugs from dispersion in supercritical fluids, carbon dioxide. This method has demonstrated a wide range of application in producing pulmonary inhalable formulations[104-106]. Supercritical fluid technology can be divided into several classes. The most important two are supercritical anti-solvent precipitation (SAS)[107, 108] and supercritical fluid extraction of emulsions (SFEE)[109, 110]. The fundamental mechanism of SAS is based on rapid precipitation when a drug solution is brought into contact with a supercritical CO_2. SFEE is based on extraction of the organic phase in oil-in-water or multiple emulsions using supercritical CO_2[109, 110]. Because most of the drugs (e.g., asthma drugs) are not soluble in CO_2, SAS processes provide an easy and excellent way to produce dry powder inhalation formulations. SFEE can provide uniform crystalline drug particles, composite particles containing polymeric materials and the drugs[109, 110]. For the formulator, it is important to consider the effect of each technique on the drug when choosing a suitable one to produce the desired results.

2.5. Interparticulate forces and strategies to improve aerosol performance

Micron-sized particle (< 5 µm) produced by high-energy operations such as milling usually have large surface areas and surface energies, which cause poor flow and a high tendency to aggregate[111]. These interparticulate cohesive forces include mechanical interlocking due to surface asperities, capillary forces from the presence of water, electrostatics arising from the insulating nature of the material, and van der Waals forces from the fundamental electromagnetic nature of matter[92, 112]. One way to add in particle separation is to agglomerate micron-sized drug particles with larger "carrier" particles of the excipients[113]. Excipients can reduce drug cohesiveness by occupying the high-energy sites of the drug particles, consequently improving handling, dispensing, and metering of the drug. According to the FDA guidance for dry powder inhaler drug products, α-lactose monohydrate is the only approved sugar that can be used as a larger carrier particle in dry powder inhalation aerosol products to fluidize and disperse the respiratory drug while itself not being delivered to the lung. Lactose is highly crystalline and has the smooth surfaces and satisfactory flow properties desirable for a DPI carrier particle. The disadvantage of lactose is that it is a reducing sugar, which may lead to chemical instability particularly in formulations containing protein and peptides[114]. Other sugars, such as mannitol and glucose have been shown to be feasible alternatives to lactose[115].

Except for blends using fine carriers and ternary components, several other methods can be used to improve the performance of dry powder aerosol delivery systems:

- Low aerodynamic diameters (e.g., small physical size)
- Low particle density (e.g., porous particles)[116]
- Low bulk density (loose particle packing to reduce particle contacts)[117]
- Rough surface (to increase air drag force and reduce particle interaction)[118-120]
- Surface composition (to reduce surface energy)
- Shape (e.g., elongated particles)

The basic principle of the above methods is to overcome the cohesive forces between drug particles. Moreover, to generate an aerosol containing drug particles in the aerodynamic size range of 1 – 5 µm and deliver the drug particles to the target area for deposition, the drug particles must be detached from the carrier crystals in adhesive mixtures or nucleus agglomerates by shear forces during an adequate inhalation. Coates et al. analyzed computationally and experimentally the influence of airflow rate of a DPI on particle dispersion and throat deposition. An optimal inhaler performance was found at a respiratory airflow rate of 65 liters/min[121].

2.6. Device design of a dry powder inhaler

From the design viewpoint, the primary components of a dry powder inhaler are the same for all types of devices on the market as well as those in development. They consist of a powder formulation, a dose mechanism, a powder de-agglomeration principle, and the inhaler's mouthpiece. The dose mechanism is applied to measure a single drug dose. The powder de-agglomeration principle is used to dispense the powder into the inhaled air stream. In some devices, secondary inhaler parts may be applied for different purposes, such as safety, ease of handling, signaling to the patient and moisture protection of the drug formulation. The de-agglomeration principle is one of the most important parts of the inhaler, as to a large extent it determines the de-agglomeration efficiency and thereby the lung deposition of the drug. The dry powder formulation is also a critical component of a DPI[122, 123]. Most formulations are sensitive to moisture during manufacturing, storage, and usage, which may affect the ultimate delivery of 1 to 5 micron-sized, stable, and reproducible drug aerosols. Therefore, new packaging technologies, including multidose blister packs, the use of nonirritating excipients, and improved device designs have made DPIs more acceptable[124].

3. Surface Properties of Powder Formulations and Surface Analytical Techniques

For pharmaceutical solid systems, the surface of the primary active pharmaceutical ingredient and associated excipient particles is crucial during manufacturing, as it affects not only the handling characteristics such as powder flowability and compressibility but also the product performance such as wettability, hardness, and dissolution rates[125-127]. For dry powder inhalation aerosols, surface morphology (corrugated or smooth surface) of both drug particles and carrier particles within the formulation directly influence the interparticulate contact area, interparticulate forces, aerosolization efficiency and subsequent lung deposition[120, 128, 129]. Surface properties of dry powders can be exploited for DPI formulation design by creating or selecting drug particles and carrier particles with specific morphology[130, 131]. Drug particles, with a higher degree of surface rugosity are reported in lower powder cohesion and consequently increased dispersibility of powder particles[120]. Conversely, high degrees of surface roughness may also promote mechanical interlocking between particles, influencing the powder flow and dispersion[132]. Hence, it is important to choose an optimal value considering both advantages and disadvantages. Surface morphology, together with particle size and shape, determines surface area, which in turn determines the contact area and interparticulate forces between particles. Corrugated particles have more surface area than smooth particles that occupy the same volume. Therefore, ideally, surface properties, including surface morphology, contact area and interparticulate forces, should be adjusted to a level that provides enough adhesion between drug and carrier to obtain a stable formulation, and also allows easy separation upon inhalation. Techniques that have been applied to study surface properties of solid-state particles in dry powder inhalers include atomic force microscopy, micro- and nanothermal analysis, inverse gas chromatography, and X-ray photoelectron spectroscopy. They are summarized in **Table 2** and described in the following sections.

Table 2 Summary of surface analytical techniques as well as parameters accessible by them.

Surface analytical techniques	Applications
Atomic force microscopy (AFM)	Microscopic analytical technique. Characterizes surface structure, morphology, adhesive forces, interparticulate interaction between drug and drug particles, and drug and carrier particles.
Micro- and nanothermal Analysis (MTA/NanoTA)	Highly localized (micrometer or sub-micrometer scale) thermal analytical technique. Measures the composition, morphology, and transition of inhalation powder particles. Distinguishes between the drug substance and excipients in solid dispersion. Evaluates heterogeneity of multicomponent systems and provides three-dimensional information.
Inverse gas chromatography (IGC)	Chromatographic analytical technique. Elucidates a wide range of physicochemical properties of the solid, including surface energy, heats of sorption, adsorption isotherms, glass transition temperatures, solubility parameters, energetic heterogeneity profiles, diffusion coefficients and particular functional groups on the surface of solid materials.
X-ray photoelectron spectroscopy (XPS)	Quantitative spectroscopic technique. Measures surface elemental composition of a dry powder inhalation aerosol, empirical formula, chemical state and electronic state of the elements that exist within a material.

3.1. Atomic force microscopy (AFM)

Atomic force microscopy is a technique employed to analyze and characterize the surface structure, morphology and forces of materials at the nanoscopic and atomic level[133-136].

One of the important components of AFM is a micro-fabricated cantilever whose deflection is usually recorded by laser reflection when it interacts with a moving substrate. Direct measurement of force can be achieved by ramping the tip vertically in z axis direction, towards and away from a sample. When the tip approaches, makes contact with, and is removed from a surface, the relative deflection of the cantilever produces a force-distance curve. The change in hysteresis in cantilever deflection during approach and retraction is related to the magnitude and type of forces acting between the two surfaces[137, 138]. A schematic representation of principle of AFM is shown in **Fig. 2**.

Based on its capability to measure morphological properties of materials, AFM is used to predict the aerosolization performance of micron-sized particles for inhalation. As stated above, the force required to aerosolize an adhered drug particle is directly proportional to the sum of the surface energies of the contiguous surfaces, and inversely proportional to the projected contact area. The two most common approaches to improve the aerosolization efficiency in these systems are to reduce the surface free energy of the contacting surfaces or modify the particle shape to limit contact area. Producing drug particles with rough surfaces can reduce surface free energy and particle adhesive forces. Spray drying process has demonstrated the potential to prepare physically stable drug powders with modified surface morphology, presumably due to the differences in initial feed concentration and solvent evaporation rate[118, 120, 139-141]. To clarify this, in one study, a series of spherical model drug particles of bovine serum albumin (BSA) was prepared with different degrees of surface corrugation by spray drying process[142]. The relationship between the morphology of the prepared particles, adhesion and aerosolization efficiency was investigated quantitatively using AFM imaging and colloid probe measurements. The results confirmed that as the degree of corrugation increased, particle adhesion was reduced which, resulted in a concomitant increase in fine particle fraction FPF and better aerosolization performance.

AFM has also been identified as a tool capable of measuring the interactions between individual particulates and substrates at specific environmental conditions, such as temperature and relative humidity (RH). Capillary interaction due to the water vapor is one of the primary interparticulate forces in dry powder delivery systems. Young et al. investigated into the effect of humidity on drug-drug interactions using the AFM with an attached custom-built perfusion apparatus[143]. Salbutamol sulfate drug particulates were chosen as a model system and mounted on V-shaped AFM cantilevers using a novel micromanipulation technique. Force-distance curves obtained from the measurements between cantilever drug probes and model compacts of salbutamol sulfate were integrated to determine separation energies as a function of RH (15-75%). Significant increases in the median separation energies were observed as humidity was increased, most likely attributed to stronger capillary interaction at higher humidity. This study also shows the potential of AFM as a rapid preformulation tool to quantify the separation energies between micronized drug particles.

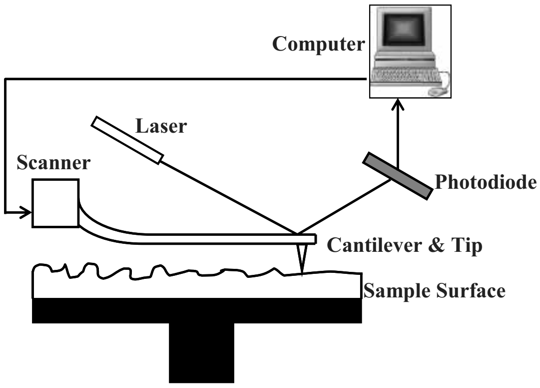

Fig. 2 A schematic representation of general principle of atomic force microscope.

In addition to the characterization of the surface morphology and interparticulate interactions between drug and carrier particles, the AFM provides opportunity to assess the interaction between inhaled drug particles and the internal surfaces of the deep lung, that is to say the interaction between micronized drug particles and pulmonary surfactant. In one study, the force of adhesion between micronized budesonide particles and simulated pulmonary surfactant (PS) monolayers (Survanta® monolayers) were visualized and quantified by the combination of AFM with a Langumir-Blodgett (LB) approach[144]. The results indicated that budesonide is hydrophobic and Survanta® films at increasing surface pressure exhibit a rising hydrophobic character. AFM revealed that PS properties were governed by applied surface pressure and that the degree of interaction of budesonide was greater at higher surface pressure, where packing of the lipid film was increased; consistent with the point of exhalation. The increasing hydrophobicity of the PS film, on increased pressure, was believed to be the primary reason for increased interaction with the hydrophobic budesonide, which correlates well with the accepted inhaler technique.

Besides, AFM has been used to observe and monitor the crystallization of lactose and the effect of mechanical processing on the powder surface. The cohesive-adhesive balance (CAB) approach to colloid probe AFM has been employed to measure the interfacial force balance between an active pharmaceutical ingredient and substrate surfaces[145, 146] and determine the influence of micronized budesonide crystal habit on the prediction of dry powder inhalation formulation performance[147]. Tapping mode AFM effectively images crystals of various organic compounds, including drugs (cimetidine[148] and felodipine[149]), and the adhesional properties of carrier-particle[130, 145, 150-152].

3.2. Micro- and nanothermal analysis

Micro- and nanothermal analysis is an emerging localized thermal analysis technique which in essence involves the replacement of the tip of a conventional atomic force microscope with a thermal probe, thereby allowing site-specific characterization[153-158]. It overcomes the disadvantage of conventional bulk thermal measurement techniques, such as differential scanning calorimetry (DSC) and modulated temperature DSC (MTDSC). DSC and MTDSC only provide results representing the sum of all the constituents in the specimen and no information on the size, shape or spatial distribution of constituents within a multicomponent system. The principle of micro- and nanothermal analysis is based on performing highly localized material property characterization on a micrometer to a sub-micrometer scale on a sample subjected to a controlled temperature programme using a heated tip.

Like an AFM, the major component of a micro- and nanothermal system is a cantilever with an integrated tip that is used to scan the surface, its position being controlled in the x, y and z directions by means of a piezoelectric scanner. Laser light is used to measure the bending degree of the cantilever, and thereby the normal force acting between the tip and sample. Instead of standard AFM tips, the instrument uses a thermal probe. Two popular thermal probes are Wollaston wire based probes (platinum/rhodium core surrounded by a silver sheath) and silicon-based nanoprobe. Wollaston wire based probes are approximately 1 μm, although the use of thinner wires[159] or the addition of diamond tips[160] has achieved a resolution around 100 nm. Silicon-based nanoprobe with a miniature heater has a topographic spatial resolution of around 5 nm and thermal property measurement resolution of up to 20 nm[161].

Micro- and nanothermal techniques allow the investigation of the composition, morphology and transition of inhalation powder particles[162, 163]. It is able to distinguish between the drug substance and excipients in solid dispersions. This technique also allows the study of sample surface as well as analysis of the distribution of materials below the surface of the material by having the probe penetrate the sample surface. Consequently, materials can be characterized in a spatially resolved manner, especially in terms of providing three-dimensional information.

The manufacturing of dry powder inhalers involves the micronization of the drug and mixing with an inert carrier such as lactose in order to facilitate adequate drug penetration into the lungs. The surface properties of both components are crucial to subsequent performance. Since the amorphous material is thermodynamically unstable in terms of recrystallization and may also be more susceptible to chemical degradation, the generation of even small quantities of amorphous material may have a profound effect if the material is located extensively on the powder surface. Therefore, the quantification and mapping of amorphous materials in otherwise crystalline samples has become a major concern. Dai et al. has described a case study using nanothermal analysis for a reliable identification of partially amorphous surface[153]. The authors prepared compressed tablets of amorphous and crystalline lactose and used thermomechanical analysis (L-TMA) performed by using micro- and nanothermal analysis in addition to single point variable temperature pull-off force measurements for mapping amorphous and crystalline lactose at a nano-scale. L-TMA was shown to be able to differentiate the amorphous and crystalline forms of lactose via measurement of the thermal events associated with them. Pull-off force measurement showed that amorphous lactose has higher adhesion than crystalline, even at temperatures below glass transition temperature (T_g), and this kind of adhesion increased on approaching the T_g.

Nanothermal analysis (nano-TA) has also been utilized to characterize nano- and micro-scale heterogeneity in the solid-state properties of drug-polymer formulations[164]. Zhang et al. demonstrated that the morphology of a nano-dispersed pharmaceutical system containing carbamazepine (CBZ) and hydroxypropyl methyl cellulose (HPMC) at a 50/50 polymer/drug ratio was mapped and determined by using nano-TA probes[164]. High resolution image obtained from AFM tapping mode showed a structure with an occluded phase, and the continuous matrix corresponded to HPMC while the bright occluded phase was attributed to the presence of CBZ nano-crystals, approximately 50 nm in size. The phase image contrast observed confirmed the presence of heterogeneity.

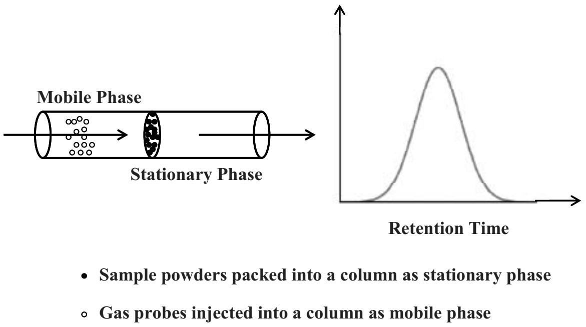

Fig. 3 Inverse gas chromatography uses injection of a probe gas to analyze the characteristics of solid sample packed into a standard column.

3.3. Inverse gas chromatography (IGC)

IGC is a physical characterization technique that has been used for the measurement of the surface properties of a wide range of solid materials, including pharmaceutical powders, nanomaterials, polymers and coatings.

The concept of IGC is rather simple; taking a standard gas chromatography (GC) experiment and inverting the roles of the stationary (solid) and mobile (gas or vapor) phases. In GC, a standard column is used to separate and characterize several gases and/or vapors. With IGC, the unknown surface is the powder that is packed into a column and the known materials are the vapor probes that are injected into the column (**Fig. 3**). The retention time of the probe molecule is then measured by traditional GC detectors, such as flame ionization detector and thermal conductivity detector. Measuring how the retention time changes as a function of probe molecule chemistry, probe molecule size, probe molecule concentration, column temperature, or carrier gas flow rate can elucidate a wide range of physicochemical properties of the solid.

Parameters accessible by IGC include heats of sorption, adsorption isotherms, glass transition temperatures[165], solubility parameters[166], and particularly surface energy of solids[167-169]. Many publications have shown potential for IGC use in batch to batch variability[170], the influence of milling on the surface free energy[171, 172], differences of surface free energy for two isomers[28], the influence of humidity on surface free energy of different powders and drug-carrier interactions for dry powder formulations[173, 174].

The surface energetics of two supercritical CO_2-processed and two commercial reference samples of salmeterol xinafoate (SX), a selective long-acting β_2-adrenergic bronchodilator used clinically for asthma prophylaxis, have been characterized by IGC at infinite dilution[175, 176]. The results showed that the metastable SX-II polymorph possessed a higher surface free energy, higher surface entropy, and a more polar surface than the stable SX-I polymorph.

IGC can give information on the relative exposure of particular functional groups on the surface of solid materials, due to electron acceptor and donor properties[177]. Grimsey et al. have demonstrated that the acidic and basic parameters of saccharides determined by IGC reflected the concentration of hydroxyl groups exposed on their surface[178]. Furthermore, IGC can be used to determine the functional groups on the surface of solid materials at various relative humidities, to explore the extent of the interaction between the surface and water[179, 180]. Sunkersett et al. have demonstrated that the specific energies of adsorption of polar probes for paracetamol and carbamazepine changed as RH was raised and the particular interaction sites of water molecules on the surface have been identified using a combination of IGC and molecular modeling[173].

Summarily, IGC appears to be of particular utility for DPI formulation work, as it requires only small samples for analysis, and it is nondestructive, fast and information rich. A more comprehensive review of this technique has been published elsewhere[169, 181-183].

3.4. X-ray photoelectron spectroscopy (XPS)

As a quantitative spectroscopic technique, X-ray photoelectron spectroscopy measures the elemental composition, empirical formula, chemical state and electronic state of the elements within a material. Briefly, powder samples are irradiated by an X-ray beam, which induces the ejection of electrons from the atoms. The kinetic energies of the photoelectrons are analyzed and their binding energies are determined. Since the binding energies of electrons in the atom of origin are characteristic for the elements in a certain chemical environment, XPS provides an elemental analysis and further information on functional groups, including the atomic compositions of a sample, the chemical state of a certain element, the electronic structure and band structure. In many cases, chemical shifts can be used to draw direct conclusions on the local coordination in a system and the electronic change upon adsorption.

One example of the application of this technology in the characterization of surface composition of a dry powder inhalation aerosol is given here. The surface composition of a dry powder aerosols prepared by spray-drying was analyzed by XPS[184]. The powder aerosols were made of albumin, dipalmitoylphosphatidylcholine (DPPC) and a protein stabilizer (lactose, trehalose or mannitol). The powders exited a SpinhalerTM inhaler as particle aggregates. XPS results revealed a large surface excess with DPPC relative to albumin under certain spray-drying conditions and self-organized in a gel phase in the particle. Furthermore, no sugar or mannitol crystals were detected by X-ray diffraction and water sorption isotherms showed that albumin/sugar/DPPC combinations were not prone to crystallization upon exposure to moisture. The surface enrichment of DPPC and the avoidance of crystallization offer a physical environment favorable to protein stability.

Conclusion

The fundamental understanding of rational DPI formulation and aerosol dispersion performance is rooted in fundamental principles in the basic science disciplines of solid-state physics, physical chemistry, surface chemistry, micromeritics, powder technology, and aerosol science. This paper describes the important features of DPIs and the techniques used to examine the surface properties of the particles comprising a DPI formulation. Surface analytical techniques such as AFM, MTA/NanoTA, IGC, XPS, and GVS can provide very useful and unique surface parameters, including surface composition, morphology, structure, energetics, phase behavior, and interparticulate forces. The fundamental data acquired from these surface analytical techniques can greatly facilitate an in-depth and rigorous understanding of the powder formulation at the level of particle interfaces (ie. the solid-solid interface, the solid-liquid interface, and/or the solid-air interface) existing in dry powder inhalation aerosol formulations. These interfaces give rise to the interfacial interactions acting between particles and consequently greatly influence the aerosol dispersion performance of particles in the solid-state. A fundamental understanding, as such, can provide unique predictive insight into rationally designing particles in the solid-state that are intended for use in DPIs having optimal surface properties to provide optimal aerosol dispersion performance for a given DPI formulation. Furthermore, a given DPI formulation can be rationally tailored at the particle surface level to increase its aerosol dispersion performance.

References

1) York, P. (1983): Solid-state Properties of Powders in the Formulation and Processing of Solid Dosage Forms, Int. J. Pharm., 14. pp.1-28.
2) Cui, Y. (2007): A Material Science Perspective of Pharmaceutical Solids, Int. J. Pharm., 339. pp.3-18.
3) Clas, S.D. (2003): The Importance of Characterizing the Crystal Form of the Drug Substance during Drug Development, Curr. Opin. Drug Discov. Devel., 6. pp.550-560.
4) Datta, S. and Grant, D.J. (2004): Crystal Structures of Drugs: Advances in Determination, Prediction and Engineering, Nat. Rev. Drug Discov., 3. pp.42-57.
5) Vippagunta, S.R., Brittain, H.G. and Grant, D.J. (2001): Crystalline Solids, Adv. Drug Deliv. Rev., 48. pp.3-26.
6) Hancock, B.C. and Zografi, G. (1997): Characteristics and Significance of the Amorphous State in Pharmaceutical Systems, J. Pharm. Sci., 86. pp.1-12.
7) Hilden, L.R. and Morris, K.R. (2004): Physics of Amorphous Solids, J. Pharm. Sci., 93. pp.3-12.
8) Kaushal, A.M., Gupta, P. and Bansal, A.K. (2004): Amorphous Drug Delivery Systems: Molecular Aspects, Design, and Performance, Crit. Rev. Ther. Drug Carrier Syst., 21. pp.133-193.
9) Yu, L. (2001): Amorphous Pharmaceutical Solids: Preparation, Characterization and Stabilization, Adv. Drug Deliv. Rev., 48. pp.27-42.
10) Rodriguez-Spong, B., Price, C.P., Jayasankar, A., Matzger, A.J. and Rodriguez-Hornedo, N. (2004): General Principles of Pharmaceutical Solid Polymorphism: A Supramolecular Perspective, Adv. Drug Deliv. Rev., 56. pp.241-274.
11) Singhal, D. and Curatolo, W. (2004): Drug Polymorphism and Dosage Form Design: A Practical Perspective, Adv. Drug Deliv. Rev., 56. pp.335-347.
12) Giron, D., Goldbronn, C., Mutz, M., Pfeffer, S., Piechon, P. and Schwab, P. (2002): Solid State Characterizations of Pharmaceutical Hydrates, J. Therm. Anal. Calorim., 68. pp.453-465.
13) Bouche, R. and Draguet-Brughmans, M. (1977): Polymorphism of Organic Drug Substances, J. Pharm. Belg., 32. pp.23-51.
14) Li, H., Kiang, Y.H. and Jona, J. (2009): Multiple Approaches to Pharmaceutical Polymorphism Investigation–A Case Study, Eur. J. Pharm. Sci., 38. pp.426-432.
15) Byrn, S.R. (1982): “Solid State Chemistry of Drugs”,

Academic Press, New York.
16) Hilfiker, R. (2006): "Polymorphism in the Pharmaceutical Industry", Wiley-VCH, Weinheim.
17) Haleblian, J. and McCrone, W. (1969): Pharmaceutical Applications of Polymorphism, J. Pharm. Sci., 58. pp.911-929.
18) Ghebremeskel, A.N., Vemavarapu, C. and Lodaya, M. (2007): Use of Surfactants as Plasticizers in Preparing Solid Dispersions of Poorly Soluble API: Selection of Polymer-surfactant Combinations Using Solubility Parameters and Testing the Processability, Int. J. Pharm., 328. pp.119-129.
19) Genina, N., Raikkonen, H., Ehlers, H., Heinamaki, J., Veski, P. and Yliruusi, J. (2010): Thin-coating as an Alternative Approach to Improve Flow Properties of Ibuprofen Powder, Int. J. Pharm., 387. pp.65-70.
20) Lee, Y.S., Poynter, R., Podczeck, F. and Newton, J.M. (2000): Development of a Dual Approach to Assess Powder Flow from Avalanching Behavior, AAPS PharmSci.Tech., 1. Article 21.
21) Builders, P.F., Ibekwe, N., Okpako, L.C., Attama, A.A. and Kunle, O.O. (2009): Preparation and Characterization of Mucinated Cellulose Microparticles for Therapeutic and Drug Delivery Purposes, Eur. J. Pharm. Biopharm., 72. pp.34-41.
22) Taylor, M.K., Ginsburg, J., Hickey, A. and Gheyas, F. (2000): Composite Method to Quantify Powder Flow as a Screening Method in Early Tablet or Capsule Formulation Development, AAPS PharmSci.Tech., 1. Article 18.
23) Hickey, A.J., Jackson, G.V. and Fildes, F.J. (1988): Preparation and Characterization of Disodium Fluorescein Powders in Association with Lauric and Capric Acids, J. Pharm. Sci., 77. pp.804-809.
24) Taylor, L.S. and Zografi, G. (1998): The Quantitative Analysis of Crystallinity Using FT-Raman Spectroscopy, Pharm. Res., 15. pp.755-761.
25) Newman, A.W. and Byrn, S.R. (2003): Solid-state Analysis of the Active Pharmaceutical Ingredient in Drug Products, Drug Discov. Today, 8. pp.898-905.
26) Hickey, A.J., Mansour, H.M., Telko, M.J., Xu, Z., Smyth, H.D., Mulder, T., McLean, R., Langridge, J. and Papadopoulos, D. (2007): Physical Characterization of Component Particles Included in Dry Powder Inhalers. I. Strategy Review and Static Characteristics, J. Pharm. Sci., 96. pp.1282-1301.
27) Strom, C.S. (1975): Indexing of Crystal Faces on Sem Photographs, Acta Crystallographica Section A, 31. pp.S216-S216.
28) Rebanta Bandyopadhyay and David J. W. Grant (2000): Influence of Crystal Habit on the Surface Free Energy and Interparticulate Bonding of L-Lysine Monohydrochloride Dihydrate, Pharm. Dev. Technol., 5. pp.27-37.
29) Muster, T.H. and Prestidge, C.A. (2002): Face Specific Surface Properties of Pharmaceutical Crystals, J. Pharm. Sci., 91. pp.1432-1444.
30) Hancock, B.C. and Parks, M. (2000): What Is the True Solubility Advantage for Amorphous Pharmaceuticals?, Pharm. Res., 17. pp.397-404.
31) Dannenfelser, R.M., He, H., Joshi, Y., Bateman, S. and Serajuddin, A.T. (2004): Development of Clinical Dosage Forms for a Poorly Water Soluble Drug I: Application of Polyethylene Glycol-polysorbate 80 Solid Dispersion Carrier System, J. Pharm. Sci., 93. pp.1165-1175.
32) Craig, D.Q., Royall, P.G., Kett, V.L. and Hopton, M.L. (1999): The Relevance of the Amorphous State to Pharmaceutical Dosage Forms: Glassy Drugs and Freeze Dried Systems, Int. J. Pharm., 179. pp.179-207.
33) Gupta, M.K., Vanwert, A. and Bogner, R.H. (2003): Formation of Physically Stable Amorphous Drugs by Milling with Neusilin, J. Pharm. Sci., 92. pp.536-551.
34) Sharma, P., Denny, W.A. and Garg, S. (2009): Effect of Wet Milling Process on the Solid State of Indomethacin and Simvastatin, Int. J. Pharm., 380. pp.40-48.
35) Willart, J.F. and Descamps, M. (2008): Solid State Amorphization of Pharmaceuticals, Mol. Pharm., 5. pp.905-920.
36) Patterson, J.E., James, M.B., Forster, A.H., Lancaster, R.W., Butler, J.M. and Rades, T. (2005): The Influence of Thermal and Mechanical Preparative Techniques on the Amorphous State of Four Poorly Soluble Compounds, J. Pharm. Sci., 94. pp.1998-2012.
37) Gupta, P. and Bansal, A.K. (2005): Spray Drying for Generation of a Ternary Amorphous System of Celecoxib, PVP, and Meglumine, Pharm. Dev. Technol., 10. pp.273-281.
38) Healy, A.M., McDonald, B.F., Tajber, L. and Corrigan, O.I. (2008): Characterisation of Excipient-free Nanoporous Microparticles (NPMPs) of Bendroflumethiazide, Eur. J. Pharm. Biopharm., 69. pp.1182-1186.
39) Horvat, M., Mestrovic, E., Danilovski, A. and Craig, D.Q. (2005): An Investigation into the Thermal Behaviour of a Model Drug Mixture with Amorphous Trehalose, Int. J. Pharm., 294. pp.1-10.
40) Kim, J.S., Kim, M.S., Park, H.J., Jin, S.J., Lee, S. and Hwang, S.J. (2008): Physicochemical Properties and Oral Bioavailability of Amorphous Atorvastatin Hemicalcium Using Spray-drying and SAS Process, Int. J. Pharm., 359. pp.211-219.
41) Learoyd, T.P., Burrows, J.L., French, E. and Seville, P.C. (2008): Chitosan-based Spray-dried Respirable Powders for Sustained Delivery of Terbutaline Sulfate, Eur. J. Pharm. Biopharm., 68. pp.224-234.
42) Takeuchi, H., Nagira, S., Yamamoto, H. and Kawashima, Y. (2005): Solid Dispersion Particles of Amorphous Indomethacin with Fine Porous Silica Particles by Using Spray-drying Method, Int. J. Pharm., 293. pp.155-164.
43) Bhattacharya, S. and Suryanarayanan, R. (2009): Local Mobility in Amorphous Pharmaceuticals--Characterization and Implications on Stability, J. Pharm. Sci., 98. pp.2935-2953.
44) Liu, J. (2006): Physical Characterization of Pharmaceutical Formulations in Frozen and Freeze-dried Solid States: Techniques and Applications in Freeze-drying

Development, Pharm. Dev. Technol., 11. pp.3-28.

45) Xiang, T.X. and Anderson, B.D. (2004): A Molecular Dynamics Simulation of Reactant Mobility in an Amorphous Formulation of a Peptide in Poly(vinylpyrrolidone), J. Pharm. Sci., 93. pp.855-876.

46) Bonacucina, G., Palmieri, G.F. and Craig, D.Q. (2005): Rheological and Dielectric Characterization of Monoolein/water Mesophases in the Presence of a Peptide Drug, J. Pharm. Sci., 94. pp.2452-2462.

47) Efrat, R., Shalev, D.E., Hoffman, R.E., Aserin, A. and Garti, N. (2008): Effect of Sodium Diclofenac Loads on Mesophase Components and Structure, Langmuir, 24. pp.7590-7595.

48) Stevenson, C.L., Bennett, D.B. and Lechuga-Ballesteros, D. (2005): Pharmaceutical Liquid Crystals: The Relevance of Partially Ordered Systems, J. Pharm. Sci., 94. pp.1861-1880.

49) Descamps, M., Correia, N.T., Derollez, P., Danede, F. and Capet, F. (2005): Plastic and Glassy Crystal States of Caffeine, J. Phys. Chem. B, 109. pp.16092-16098.

50) Rey, R. (2008): Orientational Order and Rotational Relaxation in the Plastic Crystal Phase of Tetrahedral Molecules, J. Phys. Chem. B, 112. pp.344-357.

51) Singh, L.P. and Murthy, S.S. (2009): Dielectric and Calorimetric Investigation of an Unusual Two-component Plastic Crystal: Cyclohexanol-neopentylglycol, Phys. Chem. Chem. Phys., 11. pp.5110-5118.

52) Grebowicz, J., Cheng, S.Z.D. and Wunderlich, B. (1986): Kinetics of Transitions Involving Condis Crystals, J. POLYM. SCI. POL. PHYS., 24. pp.675-685.

53) Heinz, A., Strachan, C.J., Gordon, K.C. and Rades, T. (2009): Analysis of Solid-state Transformations of Pharmaceutical Compounds Using Vibrational Spectroscopy, J. Pharm. Pharmacol., 61. pp.971-988.

54) Bell, J.H., Hartley, P.S. and Cox, J.S. (1971): Dry Powder Aerosols. I. A New Powder Inhalation Device, J. Pharm. Sci., 60. pp.1559-1564.

55) Telko, M.J. and Hickey, A.J. (2005): Dry Powder Inhaler Formulation, Respir. Care, 50. pp.1209-1227.

56) Andya, J.D., Maa, Y.F., Costantino, H.R., Nguyen, P.A., Dasovich, N., Sweeney, T.D., Hsu, C.C. and Shire, S.J. (1999): The Effect of Formulation Excipients on Protein Stability and Aerosol Performance of Spray-dried Powders of a Recombinant Humanized Anti-IgE Monoclonal Antibody, Pharm. Res., 16. pp.350-358.

57) Clarke, M.J., Tobyn, M.J. and Staniforth, J.N. (2000): Physicochemical Factors Governing the Performance of Nedocromil Sodium as a Dry Powder Aerosol, J. Pharm. Sci., 89. pp.1160-1169.

58) Costantino, H.R., Andya, J.D., Nguyen, P.A., Dasovich, N., Sweeney, T.D., Shire, S.J., Hsu, C.C. and Maa, Y.F. (1998): Effect of Mannitol Crystallization on the Stability and Aerosol Performance of a Spray-dried Pharmaceutical Protein, Recombinant Humanized Anti-IgE Monoclonal Antibody, J. Pharm. Sci., 87. pp.1406-1411.

59) Junghanns, J.U. and Muller, R.H. (2008): Nanocrystal Technology, Drug Delivery and Clinical Applications, Int. J. Nanomedicine, 3. pp.295-309.

60) Merisko-Liversidge, E., Liversidge, G.G. and Cooper, E.R. (2003): Nanosizing: A Formulation Approach for Poorly-water-soluble Compounds, Eur. J. Pharm. Sci., 18. pp.113-120.

61) Merisko-Liversidge, E., Sarpotdar, P., Bruno, J., Hajj, S., Wei, L., Peltier, N., Rake, J., Shaw, J.M., Pugh, S., Polin, L., Jones, J., Corbett, T., Cooper, E. and Liversidge, G.G. (1996): Formulation and Antitumor Activity Evaluation of Nanocrystalline Suspensions of Poorly Soluble Anticancer Drugs, Pharm. Res., 13. pp.272-278.

62) Xu, Z., Mansour, H.M., Mulder, T., McLean, R., Langridge, J. and Hickey, A.J. (2010): Dry powder aerosols generated by standardized entrainment tubes from drug blends with lactose monohydrate: 1. albuterol sulfate and disodium cromoglycate, J. Pharm. Sci., 99. pp.3398-3414.

63) Xu, Z., Mansour, H.M., Mulder, T., McLean, R., Langridge, J. and Hickey, A.J. (2010): Dry powder aerosols generated by standardized entrainment tubes from drug blends with lactose monohydrate: 2. Ipratropium bromide monohydrate and fluticasone propionate, J. Pharm. Sci., 99. pp.3415-3429.

64) Xu, Z., Mansour, H.M., Mulder, T., McLean, R., Langridge, J. and Hickey, A.J. (2010): Heterogeneous particle deaggregation and its implication for therapeutic aerosol performance, J. Pharm. Sci., 99. pp.3442-3461.

65) Mansour, H.M., Xu, Z. and Hickey, A.J. (2010): Dry powder aerosols generated by standardized entrainment tubes from alternative sugar blends: 3. Trehalose dihydrate and D-mannitol carriers, J. Pharm. Sci., 99. pp.3430-3441.

66) Atkins, P.J. (2005): Dry Powder Inhalers: an Overview, Respir. Care, 50. pp.1304-1312; discussion 1312.

67) Hickey, A.J. and Mansour, H.M., *Chapter 5: Delivery of Drugs by the Pulmonary Route*, in *Modern Pharmaceutics*, A.T. Florence and J. Siepmann, Editors. 2009, Taylor and Francis, Inc: New York. p. 191-219.

68) Geller, D.E. (2005): Comparing clinical features of the nebulizer, metered-dose inhaler, and dry powder inhaler, Respir Care, 50. pp.1313-1321; discussion 1321-2.

69) Kleinstreuer, C., Zhang, Z. and Donohue, J.F. (2008): Targeted Drug-Aerosol Delivery in the Human Respiratory System, Annu. Rev. Biomed. Eng., 10. pp.195-220.

70) Xu, Z., Mansour, H.M., Mulder, T., McLean, R., Langridge, J. and Hickey, A.J., *Comparative Dispersion Study of Dry Powder Aerosols of Albuterol Sulfate/Lactose Monohydrate and Cromolyn Sodium/Lactose Monohydrate Delivered by Standardized Entrainment Tubes*, in *Respiratory Drug Delivery XI*, R.N. Dalby, et al., Editors. 2008, Davis Healthcare International Publishing, LLC: Scotsdale, Arizona. p. 897-900.

71) Young, P.M., Kwok, P., Adi, H., Chan, H.K. and Traini, D. (2009): Lactose composite carriers for respiratory delivery, Pharm Res, 26. pp.802-810.

72) Hickey, A.J., Mansour, H.M., Telko, M.J., Xu, Z.,

Smyth, H.D.C., Mulder, T., McLean, R., Langridge, J. and Papadopoulous, D. (2007): Physical Characterization of Component Particles included in Dry Powder Inhalers: II. Dynamic Characteristics, J Pharm Sci, 96. pp.1302-1319.

73) Hickey, A.J. and Mansour, H.M., Chapter 43: *Formulation Challenges of Powders for the Delivery of Small Molecular Weight Molecules as Aerosols.*, in *Modified-Release Drug Delivery Technology*, M.J. Rathbone, et al., Editors. 2008, Informa Healthcare: New York. p. 573-602.

74) Montreal protocol 1987. Montreal protocol on substances that deplete the ozone layers, 1987.

75) Newman, S.P. and Clarke, S.W. (1993): Bronchodilator Delivery from Gentlehaler, a New Low-Velocity Pressurized Aerosol Inhaler, Chest, 103. pp.1442-1446.

76) Ganderton, D. (1997): General Factors Influencing Drug Delivery to the Lung, Respir. Med., 91 Suppl A. pp.13-16.

77) Newman, S.P. and Newhouse, M.T. (1996): Effect of Add-on Devices for Aerosol Drug Delivery: Deposition Studies and Clinical Aspects, J. Aerosol Med., 9. pp.55-70.

78) Borgstrom, L., Derom, E., Stahl, E., Wahlin-Boll, E. and Pauwels, R. (1996): The Inhalation Device Influences Lung Deposition and Bronchodilating Effect of Terbutaline, Am. J. Respir. Crit. Care Med., 153. pp.1636-1640.

79) Telko, M.J. and Hickey, A.J. (2005): Dry Powder Inhaler Formulation, Respir. Care, 50. pp.1209-1227.

80) Ashurst, I.I., Malton, A., Prime, D. and Sumby, B. (2000): Latest Advances in the Development of Dry Powder Inhalers, Pharm. Sci. Technolo. Today, 3. pp.246-256.

81) Norwood, D.L., Prime, D., Downey, B.P., Creasey, J., Sethi, S.K. and Haywood, P. (1995): Analysis of Polycyclic Aromatic Hydrocarbons in Metered Dose Inhaler Drug Formulations by Isotope Dilution Gas Chromatography/Mass Spectrometry, J. Pharm. Biomed. Anal., 13. pp.293-304.

82) Howarth, P.H. (1997): What is the Nature of Asthma and Where are the Therapeutic Targets?, Respir. Med., 91 Suppl A. pp.2-8.

83) Carstairs, J.R., Nimmo, A.J. and Barnes, P.J. (1985): Autoradiographic Visualization of Beta-Adrenoceptor Subtypes in Human Lung, Am. Rev. Respir. Dis., 132. pp.541-547.

84) Barnes, P.J., Basbaum, C.B., Nadel, J.A. and Roberts, J.M. (1982): Localization of Beta-Adrenoreceptors in Mammalian Lung by Light Microscopic Autoradiography, Nature, 299. pp.444-447.

85) Labiris, N.R. and Dolovich, M.B. (2003): Pulmonary Drug Delivery. Part I: Physiological Factors Affecting Therapeutic Effectiveness of Aerosolized Medications, Br. J. Clin. Pharmacol., 56. pp.588-599.

86) Pedersen, S. and O'Byrne, P. (1997): A Comparison of the Efficacy and Safety of Inhaled Corticosteroids in Asthma, Allergy, 52. pp.1-34.

87) Leach, C.L., Davidson, P.J. and Boudreau, R.J. (1998): Improved Airway Targeting with the CFC-Free HFA-Beclomethasone Metered-Dose Inhaler Compared with CFC-Beclomethasone, Eur. Respir. J., 12. pp.1346-1353.

88) Barnes, P.J., Basbaum, C.B. and Nadel, J.A. (1983): Autoradiographic Localization of Autonomic Receptors in Airway Smooth Muscle. Marked Differences between Large and Small Airways, Am. Rev. Respir. Dis., 127. pp.758-762.

89) Irngartinger, M., Camuglia, V., Damm, M., Goede, J. and Frijlink, H.W. (2004): Pulmonary Delivery of Therapeutic Peptides via Dry Powder Inhalation: Effects of Micronisation and Manufacturing, Eur. J. Pharm. Biopharm., 58. pp.7-14.

90) Steckel, H., Markefka, P., teWierik, H. and Kammelar, R. (2006): Effect of Milling and Sieving on Functionality of Dry Powder Inhalation Products, Int. J. Pharm., 309. pp.51-59.

91) Rasenack, N. and Muller, B.W. (2004): Micron-Size Drug Particles: Common and Novel Micronization Techniques, Pharm. Dev. Technol., 9. pp.1-13.

92) Dunbar, C.H.A., Hickey, A.J. and Holzner, P. (1998): Dispersion and Characterization of Pharmaceutical Dry Powder Aerosols, KONA Powder Part., 16. pp.7-45.

93) Mosen, K., Backstrom, K., Thalberg, K., Schaefer, T., Kristensen, H.G. and Axelsson, A. (2004): Particle Formation and Capture during Spray Drying of Inhalable Particles, Pharm. Dev. Technol., 9. pp.409-417.

94) Seville, P.C., Li, H.Y. and Learoyd, T.P. (2007): Spray-Dried Powders for Pulmonary Drug Delivery, Crit. Rev. Ther. Drug Carrier Syst., 24. pp.307-360.

95) Weers, J.G., Tarara, T.E. and Clark, A.R. (2007): Design of Fine Particles for Pulmonary Drug Delivery, Expert Opin. Drug Deliv., 4. pp.297-313.

96) Tom, J.W. and Debenedetti, P.G. (1991): Particle formation with supercritical fluids--a review, J Aerosol Sci, 22. pp.555-584.

97) Chow, A.H., Tong, H.H., Chattopadhyay, P. and Shekunov, B.Y. (2007): Particle Engineering for Pulmonary Drug Delivery, Pharm. Res., 24. pp.411-437.

98) Mansour, H.M., Rhee, Y.S. and Wu, X. (2009): Nanomedicine in Pulmonary Delivery, Int. J. Nanomedicine, 4. pp.299-319.

99) Ozeki, T., Beppu, S., Mizoe, T., Takashima, Y., Yuasa, H. and Okada, H. (2006): Preparation of Polymeric Submicron Particle-Containing Microparticles Using a 4-Fluid Nozzle Spray Drier, Pharm. Res., 23. pp.177-183.

100) Elversson, J. and Millqvist-Fureby, A. (2005): Particle Size and Density in Spray Drying-Effects of Carbohydrate Properties, J. Pharm. Sci., 94. pp.2049-2060.

101) White, S., Bennett, D.B., Cheu, S., Conley, P.W., Guzek, D.B., Gray, S., Howard, J., Malcolmson, R., Parker, J.M., Roberts, P., Sadrzadeh, N., Schumacher, J.D., Seshadri, S., Sluggett, G.W., Stevenson, C.L. and Harper, N.J. (2005): EXUBERA: Pharmaceutical De-

velopment of a Novel Product for Pulmonary Delivery of Insulin, Diabetes Technol. Ther., 7. pp.896-906.
102) Gilani, K., Najafabadi, A.R., Barghi, M. and Rafiee-Tehrani, M. (2005): The Effect of Water to Ethanol Feed Ratio on Physical Properties and Aerosolization Behavior of Spray Dried Cromolyn Sodium Particles, J. Pharm. Sci., 94. pp.1048-1059.
103) Vidgren, M.T., Vidgren, P.A. and Paronen, T.P. (1987): Comparison of Physical and Inhalation Properties of Spray-Dried and Mechanically Micronized Disodium Cromoglycate, Int. J. Pharm., 35. pp.139-144.
104) Chattopadhyay, P., Shekunov, B.Y., Yim, D., Cipolla, D., Boyd, B. and Farr, S. (2007): Production of Solid Lipid Nanoparticle Suspensions Using Supercritical Fluid Extraction of Emulsions (SFEE) for Pulmonary Delivery Using the AERx System, Adv. Drug Deliv. Rev., 59. pp.444-453.
105) Tom, J.W. and Debenedetti, P.G. (1991): Particle Formation with Supercritical Fluids--a Review, J. Aerosol Sci., 22. pp.555-584.
106) Rehman, M., Shekunov, B.Y., York, P., Lechuga-Ballesteros, D., Miller, D.P., Tan, T. and Colthorpe, P. (2004): Optimisation of Powders for Pulmonary Delivery Using Supercritical Fluid Technology, Eur. J. Pharm. Sci., 22. pp.1-17.
107) Steckel, H., Thies, J. and Muller, B.W. (1997): Micronizing of Steroids for Pulmonary Delivery by Supercritical Carbon Dioxide, Int. J. Pharm., 152. pp.99-110.
108) Steckel, H. and Muller, B.W. (1998): Metered-Dose Inhaler Formulation of Fluticasone-17-Propionate Micronized with Supercritical Carbon Dioxide Using the Alternative Propellant HFA-227, Int. J. Pharm., 173. pp.25-33.
109) Shekunov, B.Y., Chattopadhyay, P., Seitzinger, J. and Huff, R. (2006): Nanoparticles of Poorly Water-Soluble Drugs Prepared by Supercritical Fluid Extraction of Emulsions, Pharm. Res., 23. pp.196-204.
110) Chattopadhyay, P., Huff, R. and Shekunov, B.Y. (2006): Drug Encapsulation Using Supercritical Fluid Extraction of Emulsions, J. Pharm. Sci., 95. pp.667-679.
111) Rasenack, N. and Muller, B.W. (2004): Micron-Size Drug Particles: Common and Novel Micronization Techniques, Pharm. Dev. Technol., 9. pp.1-13.
112) Concessio, N.M. and Hickey, A.J. (1994): Assessment of Micronized Powders Dispersed as Aerosols, Pharm. Tech., 18. pp.88-98.
113) Newman, S.P. and Busse, W.W. (2002): Evolution of Dry Powder Inhaler Design, Formulation, and Performance, Respir. Med., 96. pp.293-304.
114) Steckel, H. and Bolzen, N. (2004): Alternative Sugars as Potential Carriers for Dry Powder Inhalations, Int. J. Pharm., 270. pp.297-306.
115) Harjunen, P., Lankinen, T., Salonen, H., Lehto, V.P. and Jarvinen, K. (2003): Effects of Carriers and Storage of Formulation on the Lung Deposition of a Hydrophobic and Hydrophilic Drug from a DPI, Int. J. Pharm., 263. pp.151-163.
116) Vanbever, R., Mintzes, J.D., Wang, J., Nice, J., Chen, D., Batycky, R., Langer, R. and Edwards, D.A. (1999): Formulation and Physical Characterization of Large Porous Particles for Inhalation, Pharm. Res., 16. pp.1735-1742.
117) Steckel, H. and Brandes, H.G. (2004): A Novel Spray-Drying Technique to Produce Low Density Particles for Pulmonary Delivery, Int. J. Pharm., 278. pp.187-195.
118) Chew, N.Y. and Chan, H.K. (2001): Use of Solid Corrugated Particles to Enhance Powder Aerosol Performance, Pharm. Res., 18. pp.1570-1577.
119) Maa, Y.F., Costantino, H.R., Nguyen, P.A. and Hsu, C.C. (1997): The Effect of Operating and Formulation Variables on the Morphology of Spray-Dried Protein Particles, Pharm. Dev. Technol., 2. pp.213-223.
120) Chew, N.Y., Tang, P., Chan, H.K. and Raper, J.A. (2005): How Much Particle Surface Corrugation is Sufficient to Improve Aerosol Performance of Powders?, Pharm. Res., 22. pp.148-152.
121) Coates, M.S., Chan, H.K., Fletcher, D.F. and Raper, J.A. (2005): Influence of Air Flow on the Performance of a Dry Powder Inhaler Using Computational and Experimental Analyses, Pharm. Res., 22. pp.1445-1453.
122) Chan, H.K. (2006): Dry Powder Aerosol Delivery Systems: Current and Future Research Directions, J. Aerosol Med., 19. pp.21-27.
123) Edwards, D.A. and Dunbar, C. (2002): Bioengineering of Therapeutic Aerosols, Annu. Rev. Biomed. Eng., 4. pp.93-107.
124) Dolovich, M.B., Ahrens, R.C., Hess, D.R., Anderson, P., Dhand, R., Rau, J.L., Smaldone, G.C. and Guyatt, G. (2005): Device Selection and Outcomes of Aerosol Therapy: Evidence-Based Guidelines: American College of Chest Physicians/American College of Asthma, Allergy, and Immunology, Chest, 127. pp.335-371.
125) Heng, J.Y., Bismarck, A., Lee, A.F., Wilson, K. and Williams, D.R. (2006): Anisotropic Surface Energetics and Wettability of Macroscopic Form I Paracetamol Crystals, Langmuir, 22. pp.2760-2769.
126) Eaton, P., Estarlich, F.F., Ewen, R.J., Nevell, T.G., Smith, J.R. and Tsibouklis, J. (2002): Combined Nanoindentation and Adhesion Force Mapping Using the Atomic Force Microscope: Investigations of a Filled Polysiloxane Coating, Langmuir, 18. pp.10011-10015.
127) El-Sabawi, D., Price, R., Edge, S. and Young, P.M. (2006): Novel Temperature Controlled Surface Dissolution of Excipient Particles for Carrier Based Dry Powder Inhaler Formulations, Drug Dev. Ind. Pharm., 32. pp.243-251.
128) Traini, D., Young, P.M., Jones, M., Edge, S. and Price, R. (2006): Comparative Study of Erythritol and Lactose Monohydrate as Carriers for Inhalation: Atomic Force Microscopy and in Vitro Correlation, Eur. J. Pharm. Sci., 27. pp.243-251.
129) Zeng, X.M., Martin, A.P., Marriott, C. and Pritchard, J. (2000): The Influence of Carrier Morphology on Drug Delivery by Dry Powder Inhalers, Int. J. Pharm., 200. pp.93-106.

130) Young, P.M., Cocconi, D., Colombo, P., Bettini, R., Price, R., Steele, D.F. and Tobyn, M.J. (2002): Characterization of a Surface Modified Dry Powder Inhalation Carrier Prepared by "Particle Smoothing", J. Pharm. Pharmacol., 54. pp.1339-1344.
131) Fults, K.A., Miller, I.F. and Hickey, A.J. (1997): Effect of Particle Morphology on Emitted Dose of Fatty Acid-Treated Disodium Cromoglycate Powder Aerosols, Pharm. Dev. Technol., 2. pp.67-79.
132) Heng, P.W. and Staniforth, J.N. (1988): The Effect of Moisture on the Cohesive Properties of Microcrystalline Celluloses, J. Pharm. Pharmacol., 40. pp.360-362.
133) Bunker, M.J., Davies, M.C., Chen, X., James, M.B. and Roberts, C.J. (2006): Single Particle Friction on Blister Packaging Materials Used in Dry Powder Inhalers, Eur. J. Pharm. Sci., 29. pp.405-413.
134) Traini, D., Young, P.M., Rogueda, P. and Price, R. (2006): Investigation into the Influence of Polymeric Stabilizing Excipients on Inter-particulate Forces in Pressurised Metered Dose Inhalers, Int. J. Pharm., 320. pp.58-63.
135) Eve, J.K., Patel, N., Luk, S.Y., Ebbens, S.J. and Roberts, C.J. (2002): A Study of Single Drug Particle Adhesion Interactions Using Atomic Force Microscopy, Int. J. Pharm., 238. pp.17-27.
136) Berard, V., Lesniewska, E., Andres, C., Pertuy, D., Laroche, C. and Pourcelot, Y. (2002): Affinity Scale between a Carrier and a Drug in DPI Studied by Atomic Force Microscopy, Int. J. Pharm., 247. pp.127-137.
137) Heinz, W.F. and Hoh, J.H. (1999): Spatially Resolved Force Spectroscopy of Biological Surfaces Using the Atomic Force Microscope, Trends Biotechnol., 17. pp.143-150.
138) Binnig, G., Quate, C.F. and Gerber, C. (1986): Atomic Force Microscope, Phys. Rev. Lett., 56. pp.930-933.
139) Duddu, S.P., Sisk, S.A., Walter, Y.H., Tarara, T.E., Trimble, K.R., Clark, A.R., Eldon, M.A., Elton, R.C., Pickford, M., Hirst, P.H., Newman, S.P. and Weers, J.G. (2002): Improved Lung Delivery from a Passive Dry Powder Inhaler Using an Engineered PulmoSphere Powder, Pharm. Res., 19. pp.689-695.
140) Dellamary, L.A., Tarara, T.E., Smith, D.J., Woelk, C.H., Adractas, A., Costello, M.L., Gill, H. and Weers, J.G. (2000): Hollow Porous Particles in Metered Dose Inhalers, Pharm. Res., 17. pp.168-174.
141) Edwards, D.A., Hanes, J., Caponetti, G., Hrkach, J., Ben-Jebria, A., Eskew, M.L., Mintzes, J., Deaver, D., Lotan, N. and Langer, R. (1997): Large Porous Particles for Pulmonary Drug Delivery, Science, 276. pp.1868-1871.
142) Adi, S., Adi, H., Tang, P., Traini, D., Chan, H.K. and Young, P.M. (2008): Micro-Particle Corrugation, Adhesion and Inhalation Aerosol Efficiency, Eur. J. Pharm. Sci., 35. pp.12-18.
143) Young, P.M., Price, R., Tobyn, M.J., Buttrum, M. and Dey, F. (2003): Investigation into the Effect of Humidity on Drug-Drug Interactions Using the Atomic Force Microscope, J. Pharm. Sci., 92. pp.815-822.
144) Davies, M.J., Brindley, A., Chen, X., Doughty, S.W., Marlow, M. and Roberts, C.J. (2009): A Quantitative Assessment of Inhaled Drug Particle-Pulmonary Surfactant Interaction by Atomic Force Microscopy, Colloids Surf. B Biointerfaces, 73. pp.97-102.
145) Begat, P., Morton, D.A., Staniforth, J.N. and Price, R. (2004): The Cohesive-Adhesive Balances in Dry Powder Inhaler Formulations I: Direct Quantification by Atomic Force Microscopy, Pharm. Res., 21. pp.1591-1597.
146) Hooton, J.C., Jones, M.D. and Price, R. (2006): Predicting the Behavior of Novel Sugar Carriers for Dry Powder Inhaler Formulations via the Use of a Cohesive-Adhesive Force Balance Approach, J. Pharm. Sci., 95. pp.1288-1297.
147) Hooton, J.C., Jones, M.D., Harris, H., Shur, J. and Price, R. (2008): The Influence of Crystal Habit on the Prediction of Dry Powder Inhalation Formulation Performance Using the Cohesive-Adhesive Force Balance Approach, Drug Dev. Ind. Pharm., 34. pp.974-983.
148) Danesh, A., Chen, X., Davies, M.C., Roberts, C.J., Sanders, G.H. and Tendler, S.J. (2000): Polymorphic Discrimination Using Atomic Force Microscopy: Distinguishing between Two Polymorphs of the Drug Cimetidine, Langmuir, 16. pp.866-870.
149) Trojak, A., Kocevar, K., Musevic, I. and Srcic, S. (2001): Investigation of the Felodipine Glassy State by Atomic Force Microscopy, Int. J. Pharm., 218. pp.145-151.
150) Hooton, J.C., German, C.S., Allen, S., Davies, M.C., Roberts, C.J., Tendler, S.J. and Williams, P. (2003): Characterization of Particle-Interactions by Atomic Force Microscopy: Effect of Contact Area, Pharm. Res., 20. pp.508-514.
151) Louey, M.D. and Stewart, P.J. (2002): Particle Interactions Involved in Aerosol Dispersion of Ternary Interactive Mixtures, Pharm. Res., 19. pp.1524-1531.
152) Louey, M.D., Mulvaney, P. and Stewart, P.J. (2001): Characterisation of Adhesional Properties of Lactose Carriers Using Atomic Force Microscopy, J. Pharm. Biomed. Anal., 25. pp.559-567.
153) Dai, X., Reading, M. and Craig, D.Q. (2009): Mapping Amorphous Material on a Partially Crystalline Surface: Nanothermal Analysis for Simultaneous Characterisation and Imaging of Lactose Compacts, J. Pharm. Sci., 98. pp.1499-1510.
154) Harding, L., King, W.P., Dai, X., Craig, D.Q. and Reading, M. (2007): Nanoscale Characterisation and Imaging of Partially Amorphous Materials Using Local Thermomechanical Analysis and Heated Tip AFM, Pharm. Res., 24. pp.2048-2054.
155) Nelson, B.A. and King, W.P. (2007): Measuring Material Softening with Nanoscale Spatial Resolution Using Heated Silicon Probes, Rev. Sci. Instrum., 78. p023702.
156) Ye, J., Reading, M., Gotzen, N. and Van Assche, G. (2007): Scanning Thermal Probe Microscopy: Nanothermal Analysis with Raman Microscopy, Microsc. Anal., 21. pp.S5-S8.

157) Reading, M., Price, D.M., Grandy, D.B., Smith, R.M., Bozec, L., Conroy, M., Hammiche, A. and Pollock, H.M. (2001): Micro-Thermal Analysis of Polymers : Current Capabilities and Future Prospects, Macromol. Symp., 167. pp.45-62.

158) Tsukruk, V.V., Gorbunov, V.V. and Fuchigami, N. (2002): Microthermal Analysis of Polymeric Materials, Thermochim. Acta, 395. pp.151-158.

159) Pollock, H.M. and Hammiche, A. (2001): Micro-Thermal Analysis: Techniques and Applications, J. Phys. D: Appl. Phys., 34. pp.R23-R53.

160) Brown, E., Hao, L., Cox, D.C. and Gallop, J.C. (2008): Scanning Thermal Microscopy Probe Capable of Simultaneous Electrical Imaging and the Addition of a Diamond Tip, J. Phys.: Confer. Ser., 100. p052012.

161) Sedman, V.L., Allen, S., Chen, X., Roberts, C.J. and Tendler, S.J. (2009): Thermomechanical Manipulation of Aromatic Peptide Nanotubes, Langmuir, 25. pp.7256-7259.

162) Murphy, J.R., Andrews, C.S. and Craig, D.Q. (2003): Characterization of the Thermal Properties of Powder Particles Using Microthermal Analysis, Pharm. Res., 20. pp.500-507.

163) Wu, J., Reading, M. and Craig, D.Q. (2008): Application of Calorimetry, Sub-Ambient Atomic Force Microscopy and Dynamic Mechanical Analysis to the Study of Frozen Aqueous Trehalose Solutions, Pharm. Res., 25. pp.1396-1404.

164) Zhang, J., Bunker, M., Chen, X., Parker, A.P., Patel, N. and Roberts, C.J. (2009): Nanoscale Thermal Analysis of Pharmaceutical Solid Dispersions, Int. J. Pharm., 380. pp.170-173.

165) Buckton, G., Ambarkhane, A. and Pincott, K. (2004): The Use of Inverse Phase Gas Chromatography to Study the Glass Transition Temperature of a Powder Surface, Pharm. Res., 21. pp.1554-1557.

166) Tong, H.H., Shekunov, B.Y., York, P. and Chow, A.H. (2006): Predicting the Aerosol Performance of Dry Powder Inhalation Formulations by Interparticulate Interaction Analysis Using Inverse Gas Chromatography, J. Pharm. Sci., 95. pp.228-233.

167) Columbano, A., Buckton, G. and Wikeley, P. (2003): Characterisation of Surface Modified Salbutamol Sulphate-Alkylpolyglycoside Microparticles Prepared by Spray Drying, Int. J. Pharm., 253. pp.61-70.

168) Newell, H.E. and Buckton, G. (2004): Inverse Gas Chromatography: Investigating Whether the Technique Preferentially Probes High Energy Sites for Mixtures of Crystalline and Amorphous Lactose, Pharm. Res., 21. pp.1440-1444.

169) Buckton, G. and Gill, H. (2007): The Importance of Surface Energetics of Powders for Drug Delivery and the Establishment of Inverse Gas Chromatography, Adv. Drug Deliv. Rev., 59. pp.1474-1479.

170) Ticehurst, M.D., York, P., Rowe, R.C. and Dwivwdi, S.K. (1994): Determination of the Surface Properties of Two Batches of Salbutamol Sulphate by Inverse Gas Chromatography, Int. J. Pharm., 111. pp.241-249.

171) York, P., Ticehurst, M.D., Osborn, J.C., Roberts, R.J. and Rowe, R.C. (1998): Characterisation of the Surface Energetics of Milled dl-Propranolol Hydrochloride Using Inverse Gas Chromatography and Molecular Modelling, Int. J. Pharm., 174. pp.179-186.

172) Feeley, J.C., York, P., Sumby, B.S. and Dicks, H. (1998): Determination of Surface Properties and Flow Characteristics of Salbutamol Sulphate, before and after Micronisation, Int. J. Pharm., 172. pp.89-96.

173) Sunkersett, M.R., Grimsey, I.M., Doughty, S.W., Osborn, J.C., York, P. and Rowe, R.C. (2001): The Changes in Surface Energetics with Relative Humidity of Carbamazepine and Paracetamol as Measured by Inverse Gas Chromatography, Eur. J. Pharm. Sci., 13. pp.219-225.

174) Newell, H.E., Buckton, G., Butler, D.A., Thielmann, F. and Williams, D.R. (2001): The Use of Inverse Phase Gas Chromatography to Study the Change of Surface Energy of Amorphous Lactose as a Function of Relative Humidity and the Processes of Collapse and Crystallisation, Int. J. Pharm., 217. pp.45-56.

175) Tong, H.H., Shekunov, B.Y., York, P. and Chow, A.H. (2001): Characterization of Two Polymorphs of Salmeterol Xinafoate Crystallized from Supercritical Fluids, Pharm. Res., 18. pp.852-858.

176) Tong, H.H., Shekunov, B.Y., York, P. and Chow, A.H. (2002): Influence of Polymorphism on the Surface Energetics of Salmeterol Xinafoate Crystallized from Supercritical Fluids, Pharm. Res., 19. pp.640-648.

177) Ohta, M. and Buckton, G. (2004): The Use of Inverse Gas Chromatography to Assess the Acid-Base Contributions to Surface Energies of Cefditoren Pivoxil and Methacrylate Copolymers and Possible Links to Instability, Int. J. Pharm., 272. pp.121-128.

178) Grimsey, I.M., Feeley, J.C. and York, P. (2002): Analysis of the Surface Energy of Pharmaceutical Powders by Inverse Gas Chromatography, J. Pharm. Sci., 91. pp.571-583.

179) Ohta, M. and Buckton, G. (2004): Determination of the Changes in Surface Energetics of Cefditoren Pivoxil as a Consequence of Processing Induced Disorder and Equilibration to Different Relative Humidities, Int. J. Pharm., 269. pp.81-88.

180) Ambarkhane, A.V., Pincott, K. and Buckton, G. (2005): The Use of Inverse Gas Chromatography and Gravimetric Vapour Sorption to Study Transitions in Amorphous Lactose, Int. J. Pharm., 294. pp.129-135.

181) Voelkel, A., Strzemiecka, B., Adamska, K. and Milczewska, K. (2009): Inverse Gas Chromatography as a Source of Physiochemical Data, J. Chromatogr. A, 1216. pp.1551-1566.

182) Charmas, B. and Leboda, R. (2000): Effect of Surface Heterogeneity on Adsorption on Solid Surfaces. Application of Inverse Gas Chromatography in the Studies of Energetic Heterogeneity of Adsorbents, J. Chromatogr. A, 886. pp.133-152.

183) Thielmann, F. (2004): Introduction into the Characterisation of Porous Materials by Inverse Gas Chromatography, J. Chromatogr. A., 1037. pp.115-123.

184) Bosquillon, C., Rouxhet, P.G., Ahimou, F., Simon, D., Culot, C., Preat, V. and Vanbever, R. (2004): Aerosolization Properties, Surface Composition and Physical State of Spray-Dried Protein Powders, J. Control. Release, 99. pp.357-367.

Author's short biography

Xiao Wu

Dr. Xiao Wu, Ph.D., is currently a Postdoctoral Research Scholar in Pharmaceutical Sciences at University of Kentucky College of Pharmacy. She received her B.S. in Pharmacy from Peking University, China in 2003 and her Ph.D. in Pharmacy and Pharmacology from the University of Bath, United Kingdom in 2008. Her Ph.D. work was in transdermal drug delivery, with an emphasis on various strategies utilizing nano-scaled delivery systems to retard cutaneous absorption of agents that should primarily act on the skin surface or to enhance skin transport of dermal and systemic therapeutics. Her current research in Dr. Heidi Mansour's group at the University of Kentucky College of Pharmacy focuses on the rational design and development of advanced dry powder inhalation aerosols containing multifunctional microparticles and nanoparticles in the solid-state for the treatment and prevention of lung transplant rejection by targeted pulmonary delivery.

Xiaojian Li

Xiaojian Li, M.S. is a graduate student in the Division of Drug Development, Department of Pharmaceutical Sciences at University of Kentucky College of Pharmacy in Lexington, KY, USA. He received his B.S. degree in Pharmaceutical Sciences from Zhejiang University City College, China in 2005 and M.S. degree in Division of Industrial Pharmacy, Department of Pharmaceutical Sciences from University of Toledo in Toledo, Ohio, USA in 2008. His M.S. research focused on physicochemical characterization of amorphous and crystalline pharmaceutical drugs. His Ph.D. thesis project is on the rational design and advanced development of dry powder inhalation microparticulate and nanoparticulate aerosols for the treatment of Cystic Fibrosis by targeted pulmonary delivery.

Heidi M. Mansour

Dr. Heidi M. Mansour, Ph.D., R.Ph. is Assistant Professor of Pharmaceutics and Pharmaceutical Technology in the Drug Development Division at the University of Kentucky College of Pharmacy and Faculty Associate in the University of Kentucky Center for Membrane Sciences,. She currently holds Faculty appointments and Graduate Faculty appointments in the College of Pharmacy at the University of Kentucky and University of North Carolina-Chapel Hill and in the NSF IGERT and NSF REU research training programs joint with the University of Kentucky College of Engineering. Prior to her faculty appointment at the University of Kentucky College of Pharmacy, she was an Instructor (both in the Graduate and Pharm.D. Programs) and a Postdoctoral Fellow and Scholar at the University of North Carolina at Chapel Hill, School of Pharmacy, in the Division of Molecular Pharmaceutics, receiving the 2007 UNC-Chapel Hill Postdoctoral Award for Research Excellence from the Office of the Vice-Chancellor. She earned a B.S. degree in Pharmacy with Honors & High Distinction, PhD in Pharmaceutical Sciences with a PhD Major in Drug Delivery/Pharmaceutics (School of Pharmacy) and a PhD Minor in Advanced Physical & Biophysical Chemistry (Dept of Chemistry), all from the University of Wisconsin-Madison.

More information can be found on her websites:
http://pharmacy.mc.uky.edu/faculty/HeidiMansour.php
http://myprofile.cos.com/surfchemlungmed

Luminescent and Magnetic Nanoparticulates as Biomarkers†

Amit Singh[1], **Parvesh Sharma**[2], **Scott Brown**[2] **and Brij Moudgil**[1, 2*]
Department of Materials Science and Engineering[1]
Particle Engineering Research Center[2]
University of Florida,

Abstract

Non invasive imaging modalities such as computed x-ray tomography, ultrasound, magnetic resonance imaging and positron emission tomography are used clinically for diagnostic medical applications. Contrast agents are frequently used for providing better spatial resolution with higher sensitivities. In recent years, advances in the field of nanotechnology have further fueled the research and development of contrast agents and introduced nanoplatforms to obtain sensitive imagery and detect changes at cellular and molecular level. Nanoparticles such as fluorescent silica, quantum dots, iron oxides, magnetically and optically labeled liposomes, dendrimer's are routinely employed in research investigations. A rising trend in this area is the development and use of multimodal contrast agents which enable multiple imaging modalities using a single entity and offer the possibility of improved diagnostics, preclinical research and therapeutic monitoring. This review paper focuses on the synthesis and application of optical and magnetic nanoparticulate probes and their integration into single multimodal nanoparticulate entities.

Keywords: Nanoparticles, multimodal, multifunctional, MRI, magnetofluorescent, magnetic, fluorescent

1. Introduction

Since early developments in x-ray imaging, medicine has become more and more reliant on bioimaging for the diagnosis of disease, the identification of physiological abnormalities, and the selection of therapeutic interventions. Modern medicine has been transformed by robust imaging modalities such as optical and magnetic resonance imaging (MRI) and continues to evolve with the ever changing technology landscape. These imaging methodologies and their corresponding contrast agents have made profound contributions to human health; a feature that is being further augmented with the advent of engineered nanotechnology based contrast agents.

The potential of X-rays for medical imaging was realized soon after their discovery by William Rontgen in 1895. The advancement of X-rays based imaging techniques was continued for next several decades and resulted in the development of computed tomography (CT), an indispensible tool for medical imaging. During this period other imaging techniques *eg* MRI and Nuclear imaging (PET, SPECT) based on different physical principles have been developed. These imaging modalities have been employed clinically and in research to visualize the anatomical structures and to obtained information about the physiological function of various tissues and organs. Over the past decade, the research in bioimaging has become focused on the visualization of cellular and molecular activities in real time for an intact organism. However, no single imaging modality has the sensitivity and resolution to allow the direct observation of these processes at that level. Each imaging modality has its own unique strengths and weaknesses (**Table 1**). For instance CT provides high resolution but uses potentially harmful ionizing radiation and offers poor soft tissue contrast. MRI provides excellent soft tissue contrast but suffers form low sensitivity. Nuclear imaging has high sensi-

---

† Accepted: July 27th, 2010

[1] Gainesville, Florida, USA 32611
[2] Gainesville, Florida, USA 32611
* Corresponding Author
PO Box 116135 205 Particle Science and Technology Building
Phone: 352-846-1194; Fax: 352-846-1196
E-mail: bmoudgil@perc.ufl.edu

Table 1 Comparison of commonly used imaging modalities for small animal imaging (Reprinted, with permission, from Reference [98])

Techniques	Labels	Signal Measured	Strengths	Weaknesses	Cost	Through-put	Sensitivity (moles of label detected)	Resolution
PET	Radiolabeled molecules	Positron from radionuclides	Highly sensitive	Can detect only one radionuclide, requires radioactivity	High	Low	10^{-15}	1-2 mm
SPECT	Radiolabeled molecules	γ -rays	Can distinguish between radionuclides, so more processes can be imaged at once	requires radioactivity	High	Low	10^{-14}	1-2 mm
CT	None	X-rays	Fast cross-sectional images	Poor resolution of soft tissues	High	Low	10^{-6}	50 µm
MRI	Can use isotope labeled molecular tracers	Alterations in magnetic fields	Harmless, high resolution of soft tissues	Can not follow many labels	High	Low	10^{-9}-10^{-6}	50 µm
Optical	Genetically engineered proteins and bioluminescent and fluorescently labeled probes	Light, particularly in the infrared	Easy, non-damaging technique readily adapted to study specific molecular events	Poor depth penetration	Low	High	10^{-12}	1-2mm
Photo-acoustic	Probes that absorb light and create sound signals	Sound	Better depth resolution than light	Information processing and machines still being optimized	Low	High	10^{-12}	50 µm
Ultrasound	Microbubbles, which can be combined with targeted contrast agents	Sound	Quick, harmless	Poor image contrast, works poorly in air-containing organs	Low	High	10^{-8}	50 µm

tivity but provides limited anatomical information. In the recent past attempts have been made to integrate imaging modalities synergistically to enable better diagnosis and help plan for effective therapeutic strategies. For example, by combining CT with MRI detailed information about both soft and dense tissue can be obtained. Combination of MRI and optical imaging provides the high resolution (spatial and temporal) and deep tissue penetration of MRI and the sensitivity of optical imaging probes.

Contrast agents are frequently used in various imaging modalities to improve the signal to noise ratio and provide better spatial resolution and/or higher sensitivities. In recent years, advances in the field of nanotechnology have introduced novel nanoplatforms to obtain sensitive imagery and detect changes at cellular and molecular level. Nanoparticles such as fluorescent dye doped silica, quantum dots, iron oxides, magnetically and optically labeled liposomes, dendrimers are routinely employed in research investigations. Incorporation of contrast agent in nanoparticles can lead to improved stability and sensitivity of the encapsulated imaging agents. Further, multimodal contrast agents, or the incorporation of multiple types of contrast agents into a single nanomaterial, may offer improvements in patient care and at the same time can reduce costs and enhance safety by limiting the number of contrast agent administrations required for imaging purposes.

This review focuses on the synthesis and application of optical and magnetic nanoparticulate probes and various challenges faced by researchers for their integration into single multimodal nanoparticulate entities. In general, nanoparticles based probes should possess following properties

1) High sensitivity for their administration at ultra low concentrations
2) Chemical and physical stability in the biological environment
3) Amenable to surface functionalization for easy conjugation with targeting moieties
4) High dispersibility in biological environment
5) Stealth properties to avoid uptake by reticuloendothelial system (size, shape and surface modification)
6) Elimination from the body after achieving de-

sired task (Biodegradibility, biocompatibility, clearance)

The first part of the review briefly describes the existing optical and MR probes and provides rationale for developing multimodal nanoparticles based probes. This is followed by the main focus of the review on developing multimodal probes and their categorization based on their physical construction.

2. Optical Imaging

The most distinguishing aspect of optical imaging is its non-invasive nature and extremely high sensitivity. The wavelength dependent interactions of light generate contrast in an image by means of various mechanisms based on differences in absorption, scattering and fluorescence between sample and background. In recent years, invivo fluorescence imaging has emerged as an important technique for bioimaging due to the extensive research on fluorophores that enables non-invasive study of a large number of cellular processes.

A large variety of flurophores are currently being used for the imaging of biological systems. The criteria for selecting flurophores include solvent solubility, high quantum efficiency, absorbance cross-section (combined with quantum yield to determine brightness) and degree of photobleaching and chemical stability in biological medium. In addition dyes should have minimal chemical and phototoxicity to cells. Different types of endogenous and exogenous fluorophores and their specific properties are discussed below.

2.1. Endogenous fluorophores

Some of the most commonly used endogenous fluorophores are Flavins, Lipofuscin, Elastin and collagen. Detailed information about their properties including excitation and emission wavelengths is given elsewhere1). Green fluorescent protein (GFP) is another example of endogenous flurophore. Due to its unique properties, such as high stability, negligible toxicity, high quantum yield, and intrinsic fluorescence, GFP has become a versatile non-invasive fluorescent marker for a wide range of biological applications. At low concentrations of GFP its fluorescence signal is significantly affected by autofluorescence of other endogenous flurophores present in the system and consequentially imaging contrast diminishes. Various methods for eliminating autofluorescene are systematically and critically reviewed by Billinton et al1).

2.2. Exogeneous fluorophores

Biological structures which do not possess autofluoroscence e.g. DNA and lipids, are generally labeled with exogeneous fluorophores. These exogenous flurophores based on their specificity and sensitivity can be used to image a specific site, a particular cell, or an organelle inside a cell. Some examples of exogenous flurophores are Alexa Fluor dyes, Cyanine dyes, Fluoroscien, Rhodamine and Texas red dyes. For bioimaging applications organic flurophores are used more frequently due to their high quantum efficiency, high absorptivity, nontoxic behavior and availability in wide range of excitation and emission wavelengths.

The resolution and penetration depth of optical imaging, particularly in tissues, is limited by the high light scattering, autofluorescence, and high absorption by most relevant tissue chromophores, deoxy- and oxyhemoglobin (HbO_2), hemoglobin, myoglobin and other heme proteins in the visible region of electromagnetic spectrum. Depending on the wavelength of emission light, different penetration depths are achieved. For example UV-VIS spectral range photons are strongly absorbed within the first few micrometers to a millimeter of tissue thickness while near-infrared (NIR) light of 650 to 900 nm achieves the highest tissue penetration (up to centimeter depth) due to minimal absorbency of the surface tissue in this spectral region. In addition autofluorescence effects are minimized when the excitation wavelength is in NIR range. Thus in order to eliminate autofluoroscence effects and reduce scattering, NIR dyes are currently being used as optical probes for bioimaging (**table 2**). Common problems associated with NIR dyes are related to their biological, environmental and photochemical stability. These dyes tend to form aggregates in water, often causing self-quenching of fluorescence. Also, these dyes are more prone to photobleaching compared to dyes that have their emission spectrum in visible region2).

2.3. Dye doped silica nanoparticles

Amorphous silica nanoparticles have been extensively used to encapsulate dyes in order to enhance their stability and brightness for in vitro and in vivo applications3,4). Silica is an optically transparent material and allows emission and excitation light to pass through it without any alteration. Silica is water dispersible, resistant to microbial attack and practically nontoxic at the dose levels required for diagnostic and therapeutic purposes5). Silica particles are also resistant to swelling which allows their synthesis in a

Table 2 Commonly used and commercially available near-infrared dyes, their excitation and emission maxima and their extinction coefficient

NIR Dyes	Excitation Wavelength (nm)	Emission Wavelength (nm)	Extinction Coefficient ($M^{-1}cm^{-1}$)
Cy7 Bis NHS Ester	750	780	200,000
Cy 5.5	675	694	250,000
Cy 5	646	664	250,000
IRDye800RS	770	786	300,000
IRDye800DX	680	687	210,000
IRDye800CW	778	794	300,000
Alexa Fluor APC Conjugate	650	775	165,000-230,000
Indocyanine Green	780	810	100,000

wide selection of solvents without altering the porosity and minimizing the leaching of dye[6]. These chemically stable and highly fluorescent optical probes improve detection sensitivity and provide enhanced contrast when used for bioimaging.

In addition, for targeted delivery of the nanoparticles several biomolecules such as proteins, peptides, antibodies, oligonucleotides can be easily conjugated to the surface of silica using silane based chemistry[3,7,8] (**Fig. 1**). Both inorganic as well as organic dyes can be incorporated in the silica matrix either by covalent linkage to the silica (silane precursor), which prevents leakage from the matrix or simply by encapsulation (physical entrapment).

2.3.1. Synthesis

2.3.1.1. Sol-gel synthesis of silica nanoparticles

Sol-gel based method for synthesizing monodisperse silica nanoparticles was first developed by Stöber[9]. This method has been widely used for synthesizing spherical, monodisperse and electrostatically stabilized silica particles in the range from tens of nanometers to submicron regime. In this method hydrolysis and condensation reactions of alkoxysilane compounds [tetraethylortosilicate (TEOS) and tetramethylortosilicate (TMOS)] are performed in ethanol solution in the presence of water and ammonia which is used as a catalyst[9]. Commonly used organic flurophores are hydrophobic in nature and hence there incorporation in hydrophilic silica matrix is achieved by modification of either dye or silica itself. For example, fluorescein isothicynate (FITC) dye can be chemically modified with an amine containing silane agent (e.g. APTS, aminopropyltriethoxy silane) and then this conjugated dye is allowed to hydrolyze and condense to form FITC conjugated silica particles[10]. It is shown that using modified Stöber' s method organic fluorophores can be covalently incorporated in to silica matrix by coupling them with reactive organosilicates[11].

2.3.1.2. Microemulsion synthesis of silica nanoparticles

Another approach for synthesizing dye-doped silica particles is by using oil-in-water (o/w) or water-in-oil (w/o) microemulsions. Particles down to a size of 15 nm can be synthesized by using this method[12]. W/o microemulsions consist of an oil (continuous phase) and water (as surfactant coated nanosize droplets). These water droplets serve as nano-reactors and their collision, coalescence and de-coalescence causes nucleation and growth of silica particles inside the confined volume of nanoreactor[13-15] (**Fig. 1**). This elegant synthesis approach facilitates the size-tuning of silica particles by varying the water to surfactant molar ratio and the dynamic properties of the microemulsion system[14-16]. W/o emulsion mediated sol gel synthesis is currently used for the synthesis of organic as well as inorganic dye-doped silica nanoparticles[3,12].

Dye doped silica nanoparticles are currently being used for a range of biological diagnostics and studies involving DNA[17] antibodies[18], and cells[19]. Zhao et al.[20] have developed a bioassay for precise and accurate determination of a single bacteria (Escherichia coli) cell using antibody-conjugated fluorescent (RuBpy dye doped) silica nanoparticles. Highly fluorescent dye doped silica particles were also used for the ultrasensitive detection of gene products down to subfemtomolar concentrations[17]

2.4. Quantum Dots

Owing to their small size (in most cases less than 10nm) and unique tunable optical features, QDs are widely being used in place of organic dyes for imaging applications in biological systems. Some of the unique features of QDs include- bandgap energy

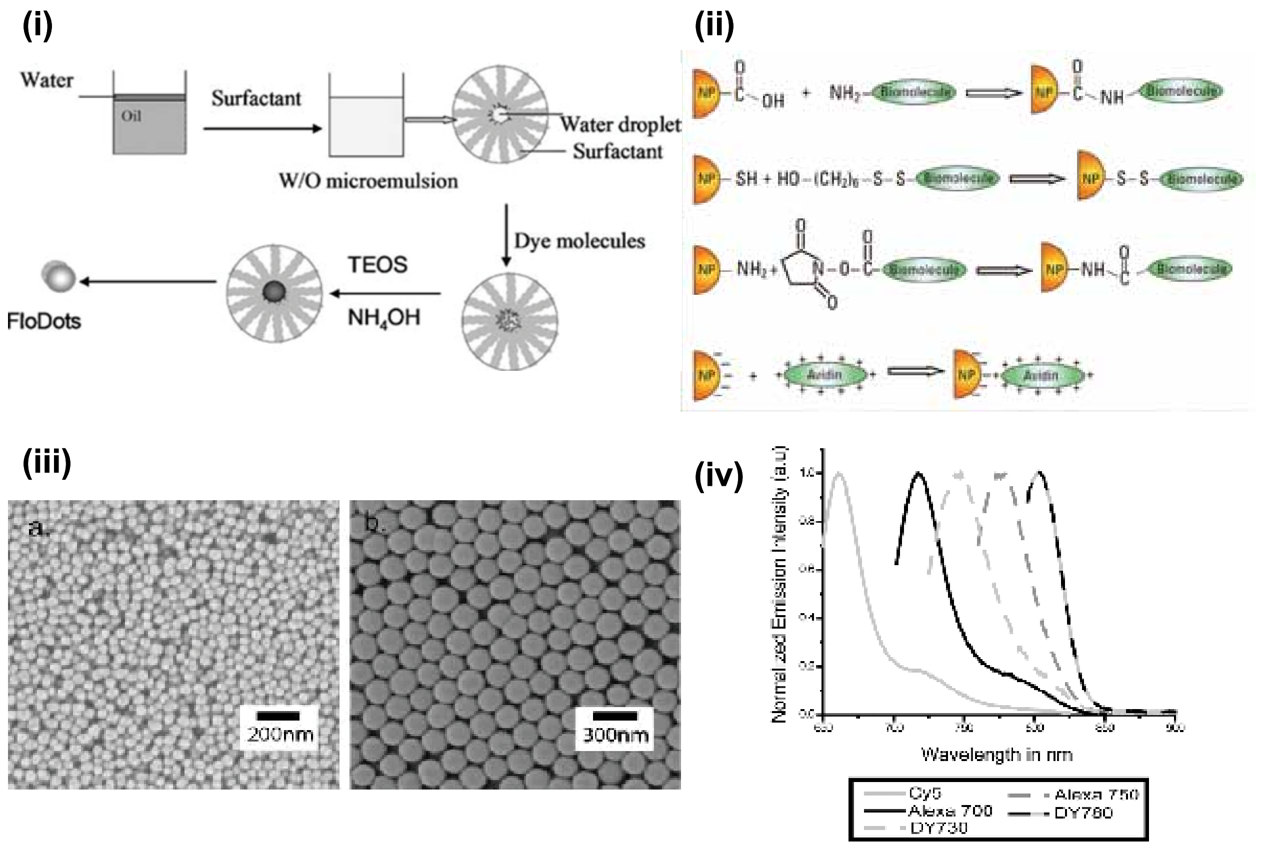

Fig. 1 (i) Schematic representation of microemulsion process commonly used for the synthesis of silica nanoparticles[3]. (ii) surface functionalization methods for silica nanoparticles[4] (iii) TEM images of monodisperse dye doped silica nanoparticles[149] (iv) Typical fluorescence spectra for dye doped silica nanoparticles[150]. (Reprinted, with permission, from Reference [3, 4, 149, 150])

dependence on size, broad excitation spectra, narrow emission spectra, high quantum yield, large separation between excitation spectra and emission spectra and high photostability. The broad excitation spectra permit use of a single excitation source to excite QDs of different colors while narrow emission spectra reduce overlap of emission and excitation spectra. The large Stoke's shift enables the collection of whole spectra by detector and therefore improves sensitivity of detection.

2.4.1. Synthesis

Initially top down lithographic techniques were employed for the synthesis of QDs e.g. first QDs were fabricated from GaAs/AlGaAs quantum well structures by using deep etching technique. However, even currently available lithographic techniques require significant improvement in producing feature sizes for routinely fabrication of QDs. With the feature size limitation on lithographic approaches another technique based on colloidal methods came in to existence in early 1980s when Henglin[21] and Rossetti[22] synthesized CdS QDs by mixing cadmium and sulfide salts in an aqueous buffer.

For the synthesis of highly crystalline and monodisperse organometallic QDs a simple method was introduced by Murray et al[23]. This method is based on producing temporally discrete homogenous nucleation by rapid injection of organometallic reagents into a hot coordinating solvent. Organometallic CdSe QDs of size ranging from 1.1-11.5 nm were produced by this method. After achieving nucleation final size of QDs was controlled by changing the growth temperature[23,24]. Photo-oxidation of QDs is generally prevented by capping them with a protective coating which minimizes the interaction with environmental oxygen and limits photobleaching. In general, the shell should be a wide band gap material and structurally similar to the core (QD) material. For example encapsulation of CdSe (QD) core by ZnS shell (ZnS has larger bandgap energy compared to CdSe) reduces the photochemical bleaching and drastically increases its quantum yield[25].

The well studied and most commonly used CdS QDs were synthesized using a novel one step solid state reaction between $CdCl_2.2.5H_2O$ and $Na_2S.9H_2O$

by Wang et al[26]. The average size of the particles formed was 5 nm. It was hypothesized that nonionic surfactant, C18EO10, used in this synthesis forms a shell surrounding the CdS particles which helped in preventing aggregation by steric hindrance and by absorbing heat of the reaction during grinding process.

In another approach using reverse micelle technique CdS QDs were synthesized by mixing two w/o emulsions viz. $Cd(ClO_4)_2$ in water/Heptane/AOT(surfactant) and Na2S in water/Heptane/AOT (surfactant)[27]. In this work water to surfactant ratio was kept constant ($[H_2O]/[AOT]=6$) and CdS particles of mean size 6 nm were synthesized. However, the size of QDs can easily be controlled by changing the amount of water in the emulsion e.g. particles of the size 1 nm were obtained when water to surfactant ratio of 1 was used and the particle size was increased to 5 nm when water to surfactant ratio was changed to 10[28].

QDs synthesized using organometallic reagents described above are hydrophobic due to surface capping with coordinating surfactants. In order to use QDs for biological applications it is necessary to make them polar or water dispersible. Several coating methods have been developed for efficiently dispersing these particles in water such as by encapsulation in phospholipid micelles[29], derivatization of surface using mercaptoacetic acid[30], ligand exchange, adsorption of amphiphilic molecules/polymers or coating them with silica[31]. The hydrophilic coating process can be selected to introduce organic functional groups such as COOH and NH2 for conjugation to biorecognition molecules such as proteins, oligonucleotides, antibodies, peptides etc[24]. Due to the success of hydrophilic surface treatment and conjugation to biorecognition molecules, QDs were readily adopted for bioimaging applications. Some of the main application areas include nucleic acid detection[32-35], immunoassays[36-38], cell tracking, tumor targeting and fluorescence resonance energy transfer (FRET) sensing[39-42]. However, toxicity of QDs remains a concern for invivo applications[43,44].

3. Magnetic Resonance Imaging (MRI)

MRI, primarily used for clinical imaging, is a noninvasive imaging method which provides information about physiological and pathological alteration of living tissues inside the body. MRI uses nuclear magnetic resonance (NMR) signals, generated by hydrogen nuclei located in different physiological environments, to generate contrast in tissue imaging. When a specimen consisting of hydrogen nuclei is placed in an external homogeneous magnetic field, their magnetic moment vectors align themselves either parallel or antiparallel to the direction of magnetic field. Upon application of radio frequency (RF) pulse at the appropriate resonant frequency the net magnetization of hydrogen nuclei changes. When the RF pulse stops and the nuclei spins relax back to their equilibrium state, electromagnetic signals are produced (**Fig. 2**). These signals depend on time required for a paramagnetic substance to become magnetic (T1, longitudinal relaxation time) and on how long these nuclei remain precess (rotating) in phase following the RF pulse (T2, transverse relaxation time). In other words T1 represents dissipation of energy from excited state to surrounding lattice and T2 represents the loss of phase coherence of the precessing nulei spins. T2* is also an important parameter, which is same as T2, but also contains local heterogeneities in the magnetic field. These signals are used to construct three dimension images of the body. Areas with faster T1 relaxation appear brighter in T1 weighted MRI, while area with faster T2 relaxation looks darker in T2 weighted MRI. The inverse of relaxation time is referred to as relaxation rate.

Contrast agents (CA) are frequently employed in clinical MRI to improve the sensitivity and/or specificity of the process and provide much more accurate diagnosis in many applications such as cancer detection, inflammation and angiography. The ability of a CA to generate contrast is characterized by its “relaxivity” value, which is defined as the ratio of change in the relaxation rate (of water protons) to the concentration of CA. The CAs accumulate in targeted region (by conjugating to antibodies or peptides), and manipulate relaxation times (T_1 and T_2) so that these subregions appear darker or brighter. On the basis of their magnetic properties contrast agents can broadly be classified as paramagnetic CA and superparamagnetic CA.

3.1. Paramagnetic CA

Paramagnetic materials possess magnetic dipole moment even in the absence of external magnetic field but due to their random orientation the net magnetic moment remains zero. In presence of external magnetic field these materials have positive magnetic susceptibility and can be used as MRI contrast agents. Gadolinium (Gd) chelates are the most commonly used paramagnetic CA in MRI. Gd CA shorten T1 more compared to T2, improve signal

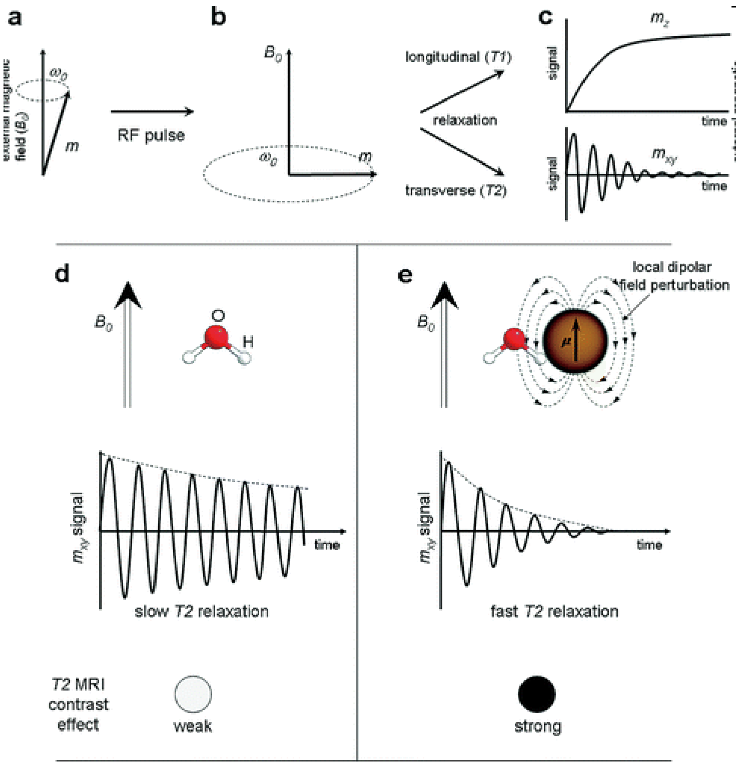

Fig. 2 Illustration of the magnetic resonance (MR) principle and the role of magnetic nanoparticles as a contrast agent: (a) net magnetic spins (*m*) of water protons precess with a Larmor frequency (ω_0); (b) upon application of a RF pulse, *m* begins precessing perpendicular to B0; (c) *m* relaxes back to its original equilibrium states through longitudinal (T1, *mz*) and transverse in-planar (T2, m_{xy}) modes; (d) for in-planar (T2) relaxation mode without magnetic nanoparticle, water protons have a relatively slow relaxation time with a weak MR contrast effect; (e) in the presence of magnetic nanoparticles, protons inside the local dipolar field perturbation area around the nanoparticle relax faster with a strong MRI signal, which produces strong MR contrast effects. (Reprinted, with permission, from Reference [151]), Copyright American Chemical Society.

in T1 weighted images and generate bright contrast. For this reason Gd CA are sometime referred to as positive CA. Since Gd is highly toxic in its ionic form and causes disruption of Ca^{2+}-required signaling, it is used in a complexed form with different kinds of ligands. These ligands not only form thermodynamically and kinetically stable chelates but also increase the relaxation rates of the protons. Commonly used chelating ligands for contrast enhancement include derivatives of polyaminocarboxylic acids such as DTPA (diethylenetriamineentaacetic acid), macrocyclic Gd chelates such as DOTA (1,4,7,10-tetraazacyclododecane-1,4,7,10-tetraacetic acid).

Paramagnetic CA increase the relaxation rate through interactions between the electron spins of the paramagnetic center and the proton nuclei. These CAs influences both outer coordination sphere (long range interactions) and inner coordination sphere protons relaxivity (short range interactions). For the CA of same size and composition the outer sphere interaction does not vary significantly. However, the effect on protons relaxivity related to inner coordination sphere is substantially high. Hence the relaxivity of paramagnetic agents is generally enhanced by tuning the various parameters, such as rotational correlation time Tr (tumbling time of CA in water), water proton residence time TM (exchange rate of single inner coordinated water molecule with the bulk water) and electron spin relaxation time Te, related to inner sphere interaction[45].

Relaxivity of the protons associated with inner sphere can be increased by increasing the tumbling time of CA which can be achieved by increasing the effective size of the CA either by using polymer or dendrimer scaffold[46-53] or by conjugating them with slowly tumbling macromolecules[54]. Relaxivity can also be increased by decreasing the TM which depends on the coordination number, charge and geometry of the paramagnetic CA. For increasing the relaxation rate of Gd, complexes bearing hydrophobic moities were designed and with the aid of the hydrophobic groups, human serum albumin (HSA) proteins were conjugated to Gd. In presence of HSA higher relaxation rates were achieved[55]. In another studies Polyamidoamine (PAMAM) based dendrimers of different generations were used to form multiple Gd labeled PAMAM chelates[56].

3.2. Superparamagnetic contrast agents: iron oxide nanoparticles

Superparamagnetic iron oxide nanoparticles (SPION) are the only clinically used nanoparticles based CA for MRI. Owing to their small size (5-20 nm) these particles can be considered as fully magnetized magnetic monodomain and exhibit superparamagnetic properties. SPIONs are characterized based on their hydrodynamic diameter. Oral-SPIO has size in the range from 300 nm to 3500 nm. Standard SPIO (SSPIO) have size between 60-150 nm, Ultrasmall-SPIO (USPIO) are in the range from 5-40 nm and monocrystalline iron-oxide nanoparticles (MION) which is a subset of USPIO has size from 10 -30 nm. The core of SPION particles is composed of ferrites (magnetite Fe_3O_4 and/or maghemite γ-Fe_2O_3). Magnetite (Fe_3O_4) and maghemite (γ-Fe_2O_3) both are being used as CA for MRI however magnetite is preferred due to its superior magnetic properties. For biological applications iron oxide nanoparticles should have homogeneous composition and narrow particle size distribution. The most common method for synthesizing these nanoparticles is by the co-precipitation of iron salts with a base in an oxygen free environment. Large amount of particles can be synthesized using this method however; control on particle size remains a concern with this method. Monodisperse and homogenous iron oxide nanoparticles have been synthesized using various methods and are reviewed in details elsewhere[57].

Particles synthesized by above methods are hydrophobic in nature and thus unsuitable for applications in aqueous biological environments. Several hydrophilic coatings encompassing organic and inorganic materials have been used to render these particles water soluble (**Table 3**). For biological applications polymer coatings are preferred as they not only provide the steric stabilization to the particles but also offer additional functional groups for further bioconjugations.

4. Multimodal Magnetofluorescent Particles

The desirable physical and chemical properties of contrast agents needed for bimodal optical and magnetic imaging can be combined in a single nanoparticle. In the following section three different types of commonly used magnetic and fluorescent (magnetofluorescent) particles and various synthesis approaches used for their integration in to a single nanoconstructs are described.

4.1. Luminescent core -magnetic shell

Multimodal magnetic and fluorescent particles have been synthesized by first synthesizing a fluorescent core and then attaching a magnetic component on its surface. The fluorescent core consist of either dye doped silica or semiconducting QDs. The magnetic shell was constructed by attaching either Gd or iron oxide nanoparticles on the surface of core particles.

4.1.1. Dye doped silica particles coated with magnetic shell

In this construct first a fluorescent dye doped silica particle is synthesized and then it is coated with either paramagnetic chelated Gd shell or iron oxide nanoparticles to make it MR active. Santra et al[58] have reported the synthesis of monodisperse (~100nm) Rubpy dye doped silica nanoparticles coated with Gd-TSPETE silane. These particles were synthesized in AOT/heptane/water microemulsion. The MR and optical contrast generating ability of these nanoparticles was demonstrated in phantom and in *in vitro* experiments. The high relaxivity values of the Gd chelated silica nanoparticles as compared to the Gd-chelates was explained on the basis of (a) decrease in the tumbling rate of silica nanoparticles and (b) high Gd loading per nanoparticle. Santra et. al. have shown presence of nearly 16,000 Gd atoms per nanoparticle58. Additionally the presence of Gd on the surface of nanoparticles also permits a rapid water exchange of the inner coordination sphere water with the bulk. The Gd chelation to ligands on the surface of smaller (40nm) silica nanoparticles was improved by using higher coordinating ligands e.g. mono (Gd DTTA) and bis (Gd DTPA) silylated gadolinium chelates[59].

Lee et al[60] have developed 30 nm "core-satellite" particles by attaching 9 nm water soluble iron oxide (WSIO) nanoparticles on the surface of rhodamine dye doped silica particles (**Fig. 3**). Maleimide groups, incorporated on the surface of silica, were reacted with thiol groups of WSIO particles using well known sulfo maleimide chemistry. The hybrid silica-WSIO particles were ~45nm in size with an average of 10 WSIO particles per silica particle. Synergistic magnetism of multiple WSIO satellites surrounding the silica particles caused 3.4 fold increase in T2 relaxivity. Furthermore, it was reported that the fluo-

Table 3 Commonly used molecules for the surface functionalization of iron oxide nanoparticles for biological applications

Organic Materials		
Type	Example	References
Surfactant / Small Molecules	(Citric, Gluconic, carboxylic, phosphonic) Acids	66,99,100
	Polyethylene glycol nonylphenyl ether	101
	silanes	102-104
Polymers	Dextran	105-109
	Starch	110
	Gelatin	111
	Chitosan	112,113
	Polyethyleneglycol	104,114-121
	Polyvinylalcohol	122-125
Biological Molecules	Aptamers	126,127
	Peptides	76-78,81,128,129
	Proteins	74,106,130-132
	Antibodies	133-136
Inorganic Materials		
Metal Oxides	Titanium, Zirconium, Aluminum	137-139
Precious Metals	Gold	140-144
Ceramic	Silica	93,145-148

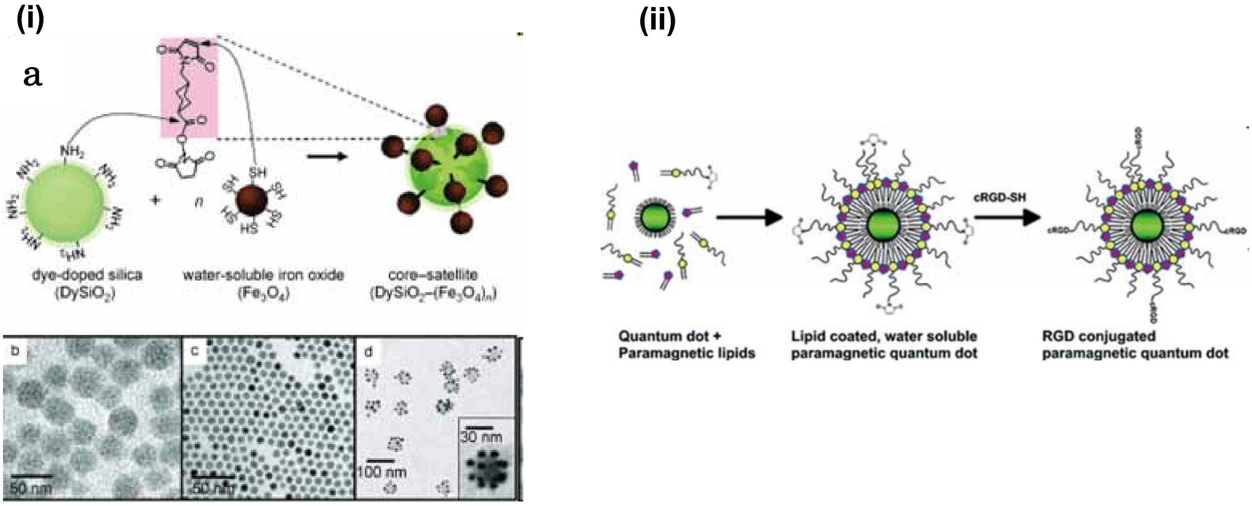

Fig. 3 (i) a) Schematic diagram for the synthesis of core-satellite $DySiO_2$-$(Fe_3O_4)n$ nanoparticles. b-d) TEM images of b) rhodamine-doped silica ($DySiO_2$), c) iron oxide (Fe_3O_4), and d) core-satellite $DySiO_2$-$(Fe_3O_4)n$ nanoparticles. (ii) Schematic representation of quantum dots coated with paramagnetic lipids. (Reprinted, with permission, from Reference〔60, 62〕), Copyright American Chemical Society.

rescence intensity of these particles increased by 1.7 times due to the core-satellite structure.

Fe_3O_4 nanoparticles have been assembled on dye-doped mesoporous silica nanoparticles (MSNs) as multifunctional nanoparticles for bimodal imaging and drug delivery. MR contrast was significantly enhanced due to the synergistic magnetism of iron oxide nanoparticle assembly[61][61]. For the synthesis of these particles 3-aminopropyl triethoxy silane (APTS) modified dye (Rhodamine isothiocyanate or Fluorescein isothiocyanate) was co-condensed during the synthesis of mesoporous silica nanoparticles using Cetyl trimethylammonium bromide templates. The surface of MSN was functionalized with amine groups by refluxing with APTS in ethanol. 2-bromo-2-methylpropionic acid (BMPA) functionalized Fe_3O_4 nanoparticles were coated on amine-functionalized MSN by direct nucleophilic substitution between the terminal bromine groups of BMPA and the amine groups of MSN.

4.1.2. Quantum dots coated with magnetic shell

Mulder et al.[62] have reported the first example of paramagnetic quantum dots (pQDs) that can be utilized for MR and optical imaging. These high quality CdSe/ZnS core/shell pQDs were synthesized by hot solvent method and coated with PEGylated phospholipids and paramagnetic lipids to make them water dispersible. PEG chains forms a hydrophilic coating at the surface and enhances the half life time significantly for invivo applications. The Qdots were bioconjugated to cyclic RGD peptides for targeting angeogenic blood vessel and tumors overexpressing $\alpha v \beta 3$ integrin (**Fig. 3**). In another report these pQDs upon conjugation with annexin A5 were used for the detection of apoptosis by targeting phosphatidylserine (PS) in T lymphoma cell lines. PS translocates from the inner to the outer leaflet of the cellular membrane in dying cells for triggering phagocytosis[63)].

Annexin A5 functionalized quantum dots with improved MR sensitivity were reported by Prinzen et al.[64)]. MR sensitivity of these particles was enhanced by increasing the number of Gd per particle using a lysine based biotinylated construct (AnxA5-Qd-Gd-wedge) designed to incorporate up to eight Gd-DTPA complexes. This wedge shaped construct was attached to the streptavidin coated QDs by utilizing biotin-avidin affinity. The MR activity (r1) of AnxA5-Qd-Gd-wedge particles was increased significantly compared to that of streptavidin coated QDs coupled to unmodified biotinylated AnxA5 (AnxA5-Qd-Gd). The higher MRI signal intensity (T1-weighted imaging) of AnxA5-Qd-Gd-wedge particles was further demonstrated in cultured Jurkat cells and human whole-blood clot system. The optical imaging capabilities of AnxA5-Qd-Gd-wedge particles were tested to discriminate between living and dying Jurkat cells and for the visualization of labeled human blood clots using two-photon laser scanning microscopy. The feasibility of these nanoparticles as a target-specific bimodal imaging probe for cell death in the vascular wall was demonstrated *ex vivo* by MR and fluorescence imaging of injured murine carotid artery.

In another approach using microemulsions Yang and coworkers[65)] have reported synthesis of Gd doped CdS:Mn/ZnS/SiO2 QDs (size ~20nm). The CdS:Mn/ZnS QDs (~3nm) were first coated with a 4-7 nm thick layer of silica and then were conjugated to Gd using a metal chelating carboxyl silane coupling agent (n-(trimethoxysilylpropyl)ethyldiamine triacetic acid trisodium salt, TSPETE). The presence of Gd at the outer surface of the particles resulted in the significantly higher relaxivity values when compared with commercially available contrast agents (Omniscan and Prohance).

4.2. Magnetic core luminescent shell

This class of particles consists of a magnetic core that is modified with a fluorescent moiety. Direct conjugation of a fluorophore with a magnetic core results in the quenching of its fluorescence. Based on the various strategies used by researchers to overcome this problem, this section is divided into following subsections:

4.2.1. Fluorophore labeling of magnetic particles using molecular spacers

Using a sufficiently long molecular linker between magnetic core and fluorophore minimizes the quenching effect. The simplest strategy adopted for this purpose was to use the functional groups of stabilizing agents already present on iron oxide nanoparticle surface. Sahoo et al.[66)] have used carboxylic acid groups of citrate stabilized magnetic nanoparticles for their conjugation with rhodamine 110 using EDC coupling. In another approach large excess of 2,3-dimercaptosuccinic acid (DMSA) was used to make Fe_3O_4 nanoparticles water dispersible during there phase transfer from toluene to DMSO[67)]. Thiol groups available on DMSA were used to attach FITC labeled Herceptin as the targeting antibody for in vitro and ex vivo optical detection and in vivo MRI for HER2/*neu* receptor overexpressed from breast cancer cells[68)]. In an attempt to make magnetofluorescent particles that could potentially be used for photodynamic therapy, Gu et al have conjugated porphyrin derivative with Fe_3O_4 nanoparticles. Porphyrin is traditionally used for photodynamic therapy and has fluorescence in the visible range. Catechol chemistry was used for linkage of porphyrin with magnetic particles to avoid quenching of its fluorescence[69)]. In another study a negatively charged carboxylic acid containing porphyrin was electrostatically attached to amine containing polyhedral silsesquioxane coated Fe_3O_4 nanoparticles[70)].

4.2.2. Fluorescently iabeled polymer coated magnetic particles

Iron oxide nanoparticles are coated with various polymeric moieties such as dextran, PEG, polyelectrolytes to render them water dispersible and available for various bioconjugations. Dextran (a branched polysaccharide) has been used widely to coat iron oxide nanoparticles for biological applications. Dextran forms hydrogen bonds with iron oxide surface and is susceptible for detachment. To solve this problem Weissleder and coworkers cross-linked the dextran on the surface of magnetic nanoparticles by using epichlorohydrin to form cross-linked iron oxide (CLIO) nanoparticle[71,72]. These particles were reacted with ammonia to yield amine groups on the surface for their further chemical modifications. CLIO nanoparticles were conjugated with various organic fluorescent dyes such as FITC, Cy3.5, Cy5.5, and Alexa-488 to yield contrast agent for both MR and optical imaging. Josephson et al.[71] have reacted CLIO particles with N-succinimidyl 3-(2-pyridyldithio)propionate (SPDP) in phosphate buffer to yield pyridyldisulphide group on the particle surface. These groups were reacted with FITC labeled membrane translocating signal peptide (HIV-Tat) through a disulfide exchange reaction. These HIV-Tat modified particles were internalized into lymphocytes over 100-fold more efficiently than unmodified particles. Similar particles were radiolabeled with 111In by reacting the dextran coating with DTPA bisanhydride. CLIO-Tat particles showed high uptake efficiency into hematopoietic and neural progenitor cells as verified by flow cytometry and nuclear accumulation[73]. Further it was shown that upon intravenous injection of CLIO-Tat labeled CD^{34+} cells into immunodeficient mice, 4% of CD^{34+} cells homed to bone marrow per gram of tissue. The author suggested that localization and retrieval of cell populations in vivo could enable detailed analysis of specific stem cell and organ interactions, critical for the advancement of stem cell-based therapies.

Bioconjugation of fluorescent CLIO nanoparticles has been carried out extensively to synthesize targeted probes towards phosphatidylserine[74,75], vascular adhesion molecule-1 (VCAM-1)[76], mucin-1[77], $\alpha v \beta 3$ integrins[78] and lymphocytes[71]. Some other applications of fluorescent CLIO nanoparticles include monitoring in changes in tumor volume caused by treatment with a chemotherapeutic agent[79] and design of smart probes whose position can be located by MR imaging while their luminescence can be activated through cleavage of dye molecule by a specific enzyme[80].

For targeting most common and lethal brain tumor cells, gliomas, a magnetofluorescent probe was developed by Veiseh et al[81]. This probe was synthesized by coating Fe_3O_4 nanoparticles with amine terminated PEG silane polymer. The amine groups on the surface of iron oxide particles were used to covalently bind a NIR dye (Cy 5.5) for optical imaging and sulfhydryl-modified chlorotoxin for specific targeting of 9 L gliomas cells. The preferential uptake of these multimodal probes was demonstrated invitro by both MR and optical imaging.

Magnetic and luminescent nanocomposites were also synthesized by multilayer deposition of CdTe QDs and polyelectrolytes on Fe_3O_4 nanoparticles. Two oppositely charged polyelectrolytes polyallylamine hydrochloride (positively charged) and poly sodium styrene sulfonate (negatively charged) were deposited alternatively on the surface of iron oxide nanoparticles until the desired thickness of polymer coating was obtained. The outermost positively charged polyelectrolyte layer was then coated with negatively charged CdTe QDs to incorporate the OI modality in the nanoconstruct. By using this construct it was demonstrated that photoluminescence intensity of the construct increases with the increase in number of polyelectrolytes layers and remained constant after 21 layers of polyelectrolytes[82].

Polymer coated γ-Fe_2O_3 superparamagnetic nanoparticles were coated with dimercapto-succinimid acid (DMSA) to stabilize and functionalize the ferrofluid with both SH and carboxyl acid groups in the ratio 3:20. Trioctylphosphine oxide (TOPO) capped CdSe/ZnS QDs were coupled to magnetic particles using thiol chemistry in 10:5:1 mixture of chloroform/methanol/water. The resulting particles had approximately 3 times lower quantum yield compared to the bare quantum dots in chloroform. This relatively lower quantum yield was attributed to the quenching effect from magnetic core and closely packed structure of quantum dots. These water dispersible nanocomposites were functionalized with anticyclone E using EDC coupling for the detection and separation of breast cancer specific marker cycline E expressing cells in serum[83].

4.2.3. Fluorescently labeled lipid coated magnetic particles

Biocompatible amphiphilic lipid molecules have been used for the stabilization and further conjugation of nanoparticles. Becker et al.[84] have synthesized oleate lipid bilayer coated Fe_3O_4 nanoparticles. These particles were further functionalized with biotin in order to attach streptavidin-FITC conjugate. It was shown invitro that these nanoparticles localized in the lysosomal compartment of the HeLa cells through a receptor-mediated uptake mechanism. Van Tilborg et al.[63] have used Annexin A5 functionalized lipid-coated Fe_3O_4 nanoparticles for the detection of apoptosis in Jurkat cells.

Nitin et al.[85] have synthesized PEG-modified phospholipid micelle coated superparamagnetic iron oxide nanoparticles (mMIONs) for intracellular molecular probes for MRI based deep tissue imaging. Iron oxide nanoparticles were synthesized with reverse micelle technique to achieve efficient control on the size of nanoparticles. These monodispersed particles were coated with PEG-phospholipid micelles to render them water dispersible and biocompatible. The amine groups available on the surface of micelles were used for attaching Texas Red dye molecules for OI and FTAT peptide for targeting.

4.2.4. Fluorescent inorganic shell coated magnetic particles

Fluorescent dyes exposed to harsh biological environment suffer from photobleaching. This problem was solved by the incorporation of these dye molecules into an optically transparent biocompatible matrix of silica. Silica provides a mechanically and chemically stable, biocompatible, and optically transparent coating that can be used for further functionalization of particles using well developed silica chemistry.

Lu et al.[86] have described the synthesis of fluorescent silica coated superparamagnetic iron oxide nanoparticles. Commercially available ferrofluid (EMG 304, size 5-15 nm) and magnetite particles synthesized using wet chemical method were coated with silica utilizing base catalyzed hydrolysis and condensation of TEOS. The thickness of silica coating was controlled in the range from 2-100 nm by varying the concentration of TEOS used in the reaction. In addition fluorescent dyes such as 7-(dimethylamino)-4-methylcoumarin-3-isothiocyanate and tetramethylrhodaine-5-isothiocyanate were covalently incorporated in the silica shell. These nanocomposites form chain like structures in presence of an external magnetic field as demonstrated by fluorescence microscopy. In another approach Lin et al.[87] have synthesized tumbler like magnetofluorescent particles for cell tracking and drug delivery applications. These multifunctional particles were synthesized by adding organic dye and silica coated Fe_3O_4 nanoparticles during the synthesis of mesoporous silica nanoparticles.

The application of magnetic core and fluorescent shell particles for targeted diagnostics and therapy was demonstrated by Levy et al.[88]. Fe_2O_3 particles were coated with a thin layer of silica using sodium silicate. A two photon dye (1-Methyl-4-(E)-2-. ethenyl) pyridinium iodide or ASPI) that absorbs two photons at 800 nm and emits a photon at 580 nm was encapsulated inside the silica shell. The surface of these nanocomposites was functionalized with a luteinizing-hormone-releasing-hormone (LH-RH) for specific targeting and selective lysing of KB cells in a dc magnetic field.

Kim et al.[89] have synthesized magnetofluorescent Co/CdSe core shell nanoparticles by controlled deposition of CdSe shell onto preformed cobolt core. Cobolt nanoparticles were synthesized by thermal decomposition of octacarbonyldicobalt in solution in the presence of coordinating ligand trioctylphosphane oxide (TOPO). The low quantum yield (2-3%) of similar type of core shell (Fe_3O_4-CdSe) nanoparticles was improved to 10-15% by the deposition of ZnS shell on CdSe. The increase in quantum yield was attributed to decrease in the number of defects in the CdSe shell.

Gu et al.[69] have described a one pot synthesis of sub 10 nm CdS-FePt hetrodimer nanoparticle that has both fluorescent and superparamagnetic properties. Similar construct (CdSe-Fe_3O_4) was synthesized by Gao et al.[90] for intracellular manipulation of magnetofluorescent Fe_3O_4 – CdSe nanoparticles using magnetic force generated by a small magnet. Several other groups have synthesized similar hetrodimer nanoparticles that could potentially be used for bioimaging applications [91,92].

4.3. Magnetic probes embedded inside organic/inorganic matrix

4.3.1. Iron oxide inside silica matrix

Yi et al.[93] have encapsulated both Fe_2O_3 nanoparticles and QDs inside a silica matrix using reverse micelles of Igepal CO-520/cyclohexane/water microemulsion. It was observed that co-encapsulation of these particles in silica matrix resulted in decrease of quantum yield from 11.4% to 1.1% for CdSe QDs and from 14.5% to 4.8% for ZnS-capped CdSe QDs. Further, SiO_2 coated Fe_2O_3 particles showed higher magnetization compared to the particles in which Fe_2O_3 and QDs were co-encapsulated.

Magnetic mesoporous silica nanoparticles covalently bonded with near-infrared (NIR) luminescent lanthanide complexes were synthesized by a two step method. Firstly, Fe_3O_4 nanoparticles were embedded in the mesoporous silica nanoparticles during their synthesis by surfactant templated method. Secondly, lanthanide complexes were introduced into the nanocomposites via a ligand exchange reaction[94].

4.3.2. Gadolinium inside silica matrix

Accessibility of the paramagnetic center to water molecules is an important parameter for the design of highly efficient nanoparticulate based MR contrast agents[59]. Mesoporous silica nanoparticles provide an ideal platform for the development of MR enhancing contrast agents due to their highly porous structure. Reiter and coworkers have incorporated a large payload of Gd chelates in mesoporous silica nanoparticles for the synthesis of highly efficient MR contrast agent (MSN-Gd particles). Mesoporous silica nanoparticles were coated with a mixture of rhodamine B-aminopropyl-triethoxysilane and Gd-Si-DTTA complex by refluxing the particles in toluene. The relaxivity values obtained for MSN-Gd are much larger than that of solid silica nanoparticles that are coated with multilayers of the Gd-DTPA derivative. The enhanced MR relaxivity of MNS-Gd was attributed to the ready access of water molecules through the nanochannels of the MSN?Gd particles[95]. Using similar approach Gd incorporated mesoporous silica nanorods were developed for use as both T_1 and T_2 contrast agent[96].

Hsiao et al.[97] have synthesized FITC and Gd incorporated fluorescent (Gd-Dye@MSN) T1 contrast agent for human stem cell tracking applications. Gd based contrast agents produce bright positive contrast that is desirable for distinguishing cells in tissues that have low intrinsic MR signal. These particles were synthesized by co-condensing a chelating ligand N-1-(3-trimethoxysilylpropyl)-N-2-(DTPA) phenyl thiourea (DTPA-ph-NCS-APTMS) and N-1-(3-trimethoxysilylpropyl)-N-fluoresceyl thiourea (FITC-APTS) with TEOS during the synthesis of mesoporous silica nanoparticles using CTAB as structure guiding templates. These particles were stirred in a methanolic solution of gadolinium chloride hexahydrate in order to load Gd3+ at the chelating sites. Invitro cellular uptake studies were performed with Gd-Dye@MSN particles using flow cytometry and MRI. Further, Gd-Dye@MSN labeled hMSCs cells implanted into the basal ganglions of nude mice were visualized using MR imaging.

5. Concluding Remarks

Multimodal nanoparticles can provide far more comprehensive and complementary information ranging from tissue structure to biological processes at molecular levels. Although multimodal nanoparticles for simultaneous MR and OI are still at an early stage of development, they offer multiple advantages for clinical diagnostics. *In vivo* optical imaging using NIR probes is a latest trend in small animal imaging for monitoring the progression of disease and therapy. The recent development of new NIR optical probes with high quantum yield and high photostability are expected to significantly enhance imaging sensitivity. Incorporation of therapeutic moieties within multimodal nanoparticles can be employed for image guided therapies. The ultimate goal is to develop nanoparticles for early stage diagnostics and treatment of diseases. Ability to monitor changes in organ/tissue in response to therapy will eventually enable selection of optimum strategy with minimal side effects, reduced patient discomfort and better prognosis. However, our limited knowledge on the targeted delivery and long term biocompatibility of these particles still remain a challenge that needs to be addressed.

6. Acknowledgements

The authors acknowledge the financial support of the Particle Engineering Research Center (PERC) at the University of Florida and the NSF-NIRT Grant EEC-0506560. Any opinions, findings, and conclusions or recommendations expressed in this material are those of the author(s) and do not necessarily reflect those of the National Science Foundation.

References

1) Billinton, N. and Knight, A. W. (2001): *Analytical Biochemistry,* 291, 175.

2) Prasad, P. N. (2003): *Introduction to Biophotonics*; Wiley-Interscience,.

3) Yao, G., Wang, L., Wu, Y. R., Smith, J., Xu, J. S., Zhao, W. J., Lee, E. J. and Tan, W. H. (2006): *Analytical And Bioanalytical Chemistry*, 385, 518.

4) Wang, L., Wang, K. M., Santra, S., Zhao, X. J., Hilliard, L. R., Smith, J. E., Wu, J. R. and Tan, W. H. (2006): *Analytical Chemistry*, 78, 646.

5) Chang, J. S., Chang, K. L. B., Hwang, D. F., Kong, Z. L. (2007): *Environmental Science & Technology*, 41, 2064.

6) Santra, S., Wang, K. M., Tapec, R. and Tan, W. H. (2001): *Journal Of Biomedical Optics, 6,* 160.

7) Yan, J. L., Estevez, M. C., Smith, J. E., Wang, K. M., He, X. X., Wang, L. and Tan, W. H. (2007): *Nano Today, 2,* 44.

8) Murcia, M. and Naumann, C. (2006): *Biofunctionalization of Nanomaterials*; 1 ed.; Wiley-VCH,.

9) Stober, W., Fink, A. and Bohn, E. (1968): *Journal Of Colloid And Interface Science, 26*, 62.

10) Santra, S., Yang, H., Dutta, D., Stanley, J. T., Holloway, P. H., Tan, W. H., Moudgil, B. M. and Mericle, R. A. (2004): *Chemical Communications,* 2810.

11) Vanblaaderen, A. and Vrij, A. (1993): *Journal Of Colloid And Interface Science,* 156, 1.

12) Bagwe, R. P., Yang, C. Y., Hilliard, L. R. and Tan, W. H. (2004): *Langmuir, 20*, 8336.

13) Finnie, K. S., Bartlett, J. R., Barbe, C. J. A. and Kong, L. G. (2007): *Langmuir, 23*, 3017.

14) Arriagada, F. J. and Osseo-Asare, K. (1999): *Journal Of*

Colloid And Interface Science, 211, 210.

15) Arriagada, F. J. and Osseo-Asare, K. (1999): *Colloids And Surfaces A-Physicochemical And Engineering Aspects, 154,* 311.

16) Yao, L., Xu, G. Y., Dou, W. L. and Bai, Y. (2008): *Colloids And Surfaces A-Physicochemical And Engineering Aspects, 316,* 8.

17) Zhao, X. J., Tapec-Dytioco, R. and Tan, W. H. (2003): *Journal Of The American Chemical Society, 125,* 11474.

18) Yang, H. H., Qu, H. Y., Lin, P., Li, S. H., Ding, M. T. and Xu, J. G. (2003): *Analyst, 128,* 462.

19) He, X. X., Duan, J. H., Wang, K. M., Tan, W. H., Lin, X. and He, C. M. (2004): *Journal Of Nanoscience And Nanotechnology, 4*, 585.

20) Zhao, X. J., Hilliard, L. R., Mechery, S. J., Wang, Y. P., Bagwe, R. P., Jin, S. G. and Tan, W. H. (2004): *Proceedings Of The National Academy Of Sciences Of The United States Of America, 101,* 15027.

21) Henglein, A. (1982): *Journal Of Physical Chemistry, 86,* 2291.

22) Rossetti, R., Nakahara, S. and Brus, L. E. (1983): *Journal Of Chemical Physics, 79,* 1086.

23) *Murray, C. B., Norris, D. J. and Bawendi, M. G. (1993): Journal Of The American Chemical Society, 115,* 8706.

24) Klostranec, J. M. and Chan, W. C. W. (2006): *Advanced Materials, 18,* 1953.

25) Hines, M. A. and Guyot-Sionnest, P. (1996): *Journal Of Physical Chemistry, 100,* 468.

26) Wang, W. Z., Liu, Z. H., Zheng, C. L., Xu, C. K., Liu, Y. K. and Wang, G. H. (2003): *Materials Letters, 57,* 2755.

27) Tsuruoka, T.,Akamatsu, K. and Nawafune, H. (2004): *Langmuir, 20,* 11169.

28) Nakanishi, T., Ohtani, B. and Uosaki, K. (1998): *Journal Of Physical Chemistry B, 102,* 1571.

29) Dubertret, B., Skourides, P., Norris, D. J., Noireaux, V., Brivanlou, A. H. and Libchaber, A. (2002): *Science, 298,* 1759.

30) Chan, W. C. W. and Nie, S. M. (1998): *Science, 281,* 2016.

31) Yang, H. S., Holloway, P. H. and Santra, S. (2004): *Journal Of Chemical Physics, 121,* 7421.

32) Gerion, D., Parak, W. J., Williams, S. C., Zanchet, D., Micheel, C. M. and Alivisatos, A. P. (2002): *Journal Of The American Chemical Society, 124,* 7070.

33) Gerion, D., Chen, F. Q., Kannan, B., Fu, A. H., Parak, W. J., Chen, D. J., Majumdar, A. and Alivisatos, A. P. (2003): *Analytical Chemistry, 75,* 4766.

34) Shepard, J. R. E. (2006): *Analytical Chemistry, 78,* 2478.

35) Liang, R. Q., Li, W., Li, Y., Tan, C. Y., Li, J. X., Jin, Y. X. and Ruan, K. C. (2005): *Nucleic Acids Research, 33.*

36) Goldman, E. R., Anderson, G. P., Tran, P. T., Mattoussi, H., Charles, P. T. and Mauro, J. M. (2002): *Analytical Chemistry, 74,* 841.

37) Goldman, E. R., Balighian, E. D., Mattoussi, H., Kuno, M. K., Mauro, J. M., Tran, P. T. and Anderson, G. P. (2002): *Journal Of The American Chemical Society, 124,* 6378.

38) Goldman, E. R., Clapp, A. R., Anderson, G. P., Uyeda, H. T., Mauro, J. M., Medintz, I. L. and Mattoussi, H. (2004): *Analytical Chemistry, 76,* 684.

39) Goldman, E. R., Medintz, I. L., Whitley, J. L., Hayhurst, A., Clapp, A. R., Uyeda, H. T., Deschamps, J. R., Lassman, M. E. and Mattoussi, H. (2005): *Journal Of The American Chemical Society, 127,* 6744.

40) Medintz, I. L.,Clapp, A. R., Mattoussi, H., Goldman, E. R., Fisher, B. and Mauro, J. M. (2003): *Nature Materials, 2,* 630.

41) Medintz, I. L., Goldman, E. R., Lassman, M. E. and Mauro, J. M. (2003): *Bioconjugate Chemistry, 14,* 909.

42) Levy, M.,Cater, S. F. and Ellington, A. D. (2005): *Chembiochem, 6,* 2163.

43) Biju, V., Mundayoor, S., Omkumar, R. V., Anas, A. and Ishikawa, M. (2010): *Biotechnology Advances, 28,* 199.

44) Rzigalinski, B. A. and Strobl, J. S. (2009): *Toxicology And Applied Pharmacology, 238,* 280.

45) Reichert, D. E., Hancock, R. D. and Welch, M. J. (1996): *Inorganic Chemistry, 35,* 7013.

46) Querol, M. and Bogdanov, A. (2006): *Journal Of Magnetic Resonance Imaging, 24,* 971.

47) Toth, E., Pubanz, D., Vauthey, S., Helm, L. and Merbach, A. E. (1996): *Chemistry-A European Journal, 2,* 1607.

48) Wang, S. C., Wikstrom, M. G., White, D. L., Klaveness, J., Holtz, E., Rongved, P., Moseley, M. E. and Brasch, R. C. (1990): *Radiology, 175,* 483.

49) Kornguth, S., Anderson, M., Turski, P., Sorenson, J., Robins, H. I., Cohen, J., Rappe, A. and Markley, J. (1990): *American Journal Of Neuroradiology, 11,* 313.

50) Vanhecke, P., Marchal, G., Bosmans, H., Johannik, K., Jiang, Y., Vogler, H., Vanongeval, C., Baert, A. L. and Speck, U. (1991): *Magnetic Resonance Imaging, 9,* 313.

51) Marchal, G., Bosmans, H., Vanhecke, P., Speck, U., Aerts, P., Vanhoenacker, P. and Baert, A. L. (1990): *American Journal Of Roentgenology, 155,* 407.

52) Curtet, C., Maton, F., Havet, T., Slinkin, M., Mishra, A., Chatal, J. F. and Muller, R. N. (1998): *Investigative Radiology, 33,* 752.

53) Dong, Q., Hurst, D. R., Weinmann, H. J., Chenevert, T. L., Londy, F. J. and Prince, M. R. (1998): *Investigative Radiology, 33,* 699.

54) Caravan, P., Cloutier, N. J., Greenfield, M. T., McDermid, S. A., Dunham, S. U., Bulte, J. W. M., Amedio, J. C., Looby, R. J., Supkowski, R. M., Horrocks, W. D., McMurry, T. J. and Lauffer, R. B. (2002): *Journal Of The American Chemical Society, 124,* 3152.

55) Lauffer, R. B. (1991): *Magnetic Resonance In Medicine, 22,* 339.

56) Kobayashi, H., Sato, N., Kawamoto, S., Saga, T., Hiraga, A., Haque, T. L., Ishimori, T., Konishi, J., Togashi, K. and Brechbiel, M. W. (2001): *Bioconjugate Chemistry, 12,* 100.

57) Laurent, S., Forge, D., Port, M., Roch, A., Robic, C., Elst, L. V. and Muller, R. N. (2008): *Chemical Reviews,*

108, 2064.
58) Santra, S., Bagwe, R. P., Dutta, D., Stanley, J. T., Walter, G. A., Tan, W., Moudgil, B. M. and Mericle, R. A. (2005): *Advanced Materials, 17,* 2165.
59) Rieter, W. J., Kim, J. S., Taylor, K. M. L., An, H. Y., Lin, W. L., Tarrant, T. and Lin, W. B. (2007): *Angewandte Chemie-International Edition, 46,* 3680.
60) Lee, J. H., Jun, Y. W., Yeon, S. I., Shin, J. S. and Cheon, J. (2006): *Angewandte Chemie-International Edition, 45,* 8160.
61) Josephson, L., Perez, J. M. and Weissleder, R. (2001): *Angewandte Chemie-International Edition, 40,* 3204.
62) Mulder, W. J. M., Koole, R., Brandwijk, R. J., Storm, G., Chin, P. T. K., Strijkers, G. J., Donega, C. D., Nicolay, K. and Griffioen, A. W. (2006): *Nano Letters, 6,* 1.
63) van Tilborg, G. A. F., Mulder, W. J. M., Chin, P. T. K., Storm, G., Reutelingsperger, C. P., Nicolay, K. and Strijkers, G. J. (2006): *Bioconjugate Chemistry, 17,* 865.
64) Prinzen, L., Miserus, R., Dirksen, A., Hackeng, T. M., Deckers, N., Bitsch, N. J., Megens, R. T. A., Douma, K., Heemskerk, J. W., Kooi, M. E., Frederik, P. M., Slaaf, D. W., van Zandvoort, M., Reutelingsperger, C. P. M. (2007): *Nano Letters, 7,* 93.
65) Yang, H. S., Santra, S., Walter, G. A. and Holloway, P. H. (2006): *Advanced Materials, 18,* 2890.
66) Sahoo, Y., Goodarzi, A., Swihart, M. T., Ohulchanskyy, T. Y., Kaur, N., Furlani, E. P. and Prasad, P. N. (2005): *Journal Of Physical Chemistry B, 109,* 3879.
67) Jun, Y. W., Huh, Y. M., Choi, J. S., Lee, J. H., Song, H. T., Kim, S., Yoon, S., Kim, K. S., Shin, J. S., Suh, J. S and Cheon, J. (2005): *Journal Of The American Chemical Society, 127,* 5732.
68) Huh, Y. M., Jun, Y. W., Song, H. T., Kim, S., Choi, J. S., Lee, J. H., Yoon, S., Kim, K. S., Shin, J. S., Suh, J. S.and Cheon, J. (2005): *Journal Of The American Chemical Society, 127,* 12387.
69) Gu, H. W., Xu, K. M., Yang, Z. M., Chang, C. K. and Xu, B. (2005): *Chemical Communications,* 4270.
70) Corr, S. A., O' Byrne, A., Gun'ko, Y. K., Ghosh, S., Brougham, D. F., Mitchell, S., Volkov, Y. and Prina-Mello, A. (2006): *Chemical Communications,* 4474.
71) Josephson, L., Tung, C. H., Moore, A. and Weissleder, R. (1999): *Bioconjugate Chemistry, 10,* 186.
72) Shen, T., Weissleder, R., Papisov, M., Bogdanov, A.and Brady, T. J. (1993): *Magnetic Resonance In Medicine, 29,* 599.
73) Lewin, M., Carlesso, N., Tung, C. H., Tang, X. W., Cory, D., Scadden, D. T., Weissleder, R. (2000): *Nature Biotechnology, 18,* 410.
74) Schellenberger, E. A., Sosnovik, D., Weissleder, R. and Josephson, L. (2004): *Bioconjugate Chemistry, 15,* 1062.
75) Quinti, L., Weissleder, R. and Tung, C. H. (2006): *Nano Letters, 6,* 488.
76) Kelly, K. A., Allport, J. R., Tsourkas, A., Shinde-Patil, V. R., Josephson, L. and Weissleder, R. (2005): *Circulation Research, 96,* 327.
77) Moore, A., Medarova, Z., Potthast, A. and Dai, G. P. (2004): *Cancer Research, 64,* 1821.
78) Montet, X., Montet-Abou, K., Reynolds, F., Weissleder, R. and Josephson, L. (2006): *Neoplasia, 8,* 214.
79) Medarova, Z., Pham, W., Kim, Y., Dai, G. P. and Moore, A. (2006): *International Journal Of Cancer, 118,* 2796.
80) Josephson, L., Kircher, M. F., Mahmood, U., Tang, Y. and Weissleder, R. (2002): *Bioconjugate Chemistry, 13,* 554.
81) Veiseh, O., Sun, C., Gunn, J., Kohler, N., Gabikian, P., Lee, D., Bhattarai, N., Ellenbogen, R., Sze, R., Hallahan, A., Olson, J. and Zhang, M. Q. (2005): *Nano Letters, 5,* 1003.
82) Hong, X., Li, J., Wang, M. J., Xu, J. J., Guo, W., Li, J. H., Bai, Y. B. and Li, T. J. (2004): *Chemistry Of Materials, 16,* 4022.
83) Wang, D. S., He, J. B., Rosenzweig, N. and Rosenzweig, Z. (2004): *Nano Letters, 4,* 409.
84) Becker, C., Hodenius, M., Blendinger, G., Sechi, A., Hieronymus, T., Muller-Schulte, D., Schmitz-Rode, T. and Zenke, M. (2007): *Journal Of Magnetism And Magnetic Materials, 311,* 234.
85) Nitin, N., LaConte, L. E. W., Zurkiya, O., Hu, X. and Bao, G. (2004): *Journal Of Biological Inorganic Chemistry, 9,* 706.
86) Lu, C. W., Hung, Y., Hsiao, J. K., Yao, M., Chung, T. H., Lin, Y. S., Wu, S. H., Hsu, S. C., Liu, H. M., Mou, C. Y., Yang, C. S., Huang, D. M. and Chen, Y. C. (2007): *Nano Letters, 7,* 149.
87) Lin, Y. S., Wu, S. H., Hung, Y., Chou, Y. H., Chang, C., Lin, M. L., Tsai, C. P. and Mou, C. Y. (2006): *Chemistry Of Materials, 18,* 5170.
88) Levy, L., Sahoo, Y., Kim, K. S., Bergey, E. J. and Prasad, P. N. (2002): *Chemistry Of Materials, 14,* 3715.
89) Kim, H., Achermann, M., Balet, L. P., Hollingsworth, J. A. and Klimov, V. I. (2005): *Journal Of The American Chemical Society, 127,* 544.
90) Gao, J. H., Zhang, W., Huang, P. B., Zhang, B., Zhang, X. X., Xu, B. (2008): *Journal Of The American Chemical Society, 130,* 3710.
91) Deka, S., Falqui, A., Bertoni, G., Sangregorio, C., Poneti, G., Morello, G., De Giorgi, M., Giannini, C., Cingolani, R., Manna, L. and Cozzoli, P. D. (2009): *Journal Of The American Chemical Society, 131,* 12817.
92) Kwon, K. W. and Shim, M. (2005): *Journal Of The American Chemical Society, 127,* 10269.
93) Yi, D. K., Selvan, S. T., Lee, S. S., Papaefthymiou, G. C., Kundaliya, D. and Ying, J. Y. (2005): *Journal Of The American Chemical Society, 127,* 4990.
94) Feng, J., Song, S. Y., Deng, R. P., Fan, W. Q. and Zhang, H. J. (2010): *Langmuir, 26,* 3596.
95) Taylor, K. M. L., Kim, J. S., Rieter, W. J., An, H., Lin, W. L. and Lin, W. B. (2008): *Journal Of The American Chemical Society, 130,* 2154.
96) Tsai, C. P., Hung, Y., Chou, Y. H., Huang, D. M., Hsiao, J. K., Chang, C., Chen, Y. C., Mou, C. Y. (2008): *Small, 4,* 186.
97) Hsiao, J. K., Tsai, C. P., Chung, T. H., Hung, Y., Yao, M., Liu, H. M., Mou, C. Y., Yang, C. S., Chen, Y. C. and

Huang, D. M. (2008): *Small, 4,* 1445.
98) Baker, M. (2010): *Nature, 463,* 977.
99) Morais, P. C., Oliveira, A. C., Tronconi, A. L., Goetze, T. and Buske, N. (2003): *Ieee Transactions On Magnetics, 39,* 2654.
100) Sahoo, Y., Pizem, H., Fried, T., Golodnitsky, D., Burstein, L., Sukenik, C. N. and Markovich, G. (2001): *Langmuir, 17,* 7907.
101) Xia, H. B., Yi, J. B., Foo, P. S. and Liu, B. H. (2007): *Chemistry Of Materials, 19,* 4087.
102) Lee, H., Yu, M. K., Park, S., Moon, S., Min, J. J., Jeong, Y. Y., Kang, H. W. and Jon, S. (2007): *Journal Of The American Chemical Society, 129,* 12739.
103) De Palma, R., Peeters, S., Van Bael, M. J., Van den Rul, H., Bonroy, K., Laureyn, W., Mullens, J., Borghs, G. and Maes, G. (2007): *Chemistry Of Materials, 19,* 1821.
104) Kohler, N., Fryxell, G. E. and Zhang, M. Q. (2004): *Journal Of The American Chemical Society, 126,* 7206.
105) Berry, C. C. and Curtis, A. S. G. (2003): *Journal Of Physics D-Applied Physics, 36,* R198.
106) Berry, C. C., Wells, S., Charles, S. and Curtis, A. S. G. (2003): *Biomaterials, 24,* 4551.
107) Mikhaylova, M., Kim, D. K., Bobrysheva, N., Osmolowsky, M., Semenov, V., Tsakalakos, T. and Muhammed, M. (2004): *Langmuir, 20,* 2472.
108) Lee, K. M., Kim, S. G., Kim, W. S. and Kim, S. S. (2002): *Korean Journal Of Chemical Engineering,* 19, 480.
109) Gamarra, L. F., Brito, G. E. S., Pontuschka, W. M., Amaro, E., Parma, A. H. C. and Goya, G. F. (2005): *Journal Of Magnetism And Magnetic Materials, 289,* 439.
110) Kim, D. K., Mikhaylova, M., Wang, F. H., Kehr, J., Bjelke, B., Zhang, Y. and Tsakalakos, T., Muhammed, M. (2003): *Chemistry Of Materials, 15,* 4343.
111) Olsen, D., Yang, C. L., Bodo, M., Chang, R., Leigh, S., Baez, J., Carmichael, D., Perala, M., Hamalainen, E. R., Jarvinen, M. and Polarek, J. (2003): *Advanced Drug Delivery Reviews, 55,* 1547.
112) Khor, E. and Lim, L. Y. (2003): Biomaterials, 24, 2339.
113) Li, G. Y., Huang, K. L., Jiang, Y. R., Ding, P. and Yang, D. L. (2008): *Biochemical Engineering Journal, 40,* 408.
114) Hong, R., Fischer, N. O., Emrick, T. and Rotello, V. M. (2005): *Chemistry Of Materials, 17,* 4617.
115) Peng, S., Wang, C., Xie, J. and Sun, S. H. (2006): *Journal Of The American Chemical Society, 128,* 10676.
116) Latham, A. H. and Williams, M. E. (2006): *Langmuir, 22,* 4319.
117) Xie, J., Xu, C. J., Xu, Z. C., Hou, Y. L., Young, K. L., Wang, S. X., Pourmond, N. and Sun, S. H. (2006): *Chemistry Of Materials, 18,* 5401.
118) Nasongkla, N., Bey, E., Ren, J. M., Ai, H., Khemtong, C., Guthi, J. S., Chin, S. F., Sherry, A. D., Boothman, D. A. and Gao, J. M. (2006): *Nano Letters, 6,* 2427.
119) Kim, D. K., Zhang, Y., Kehr, J., Klason, T., Bjelke, B. and Muhammed, M. (2001): *Journal Of Magnetism And Magnetic Materials, 225,* 256.
120) Tamaura, Y., Takahashi, K., Kodera, Y., Saito, Y. and Inada, Y. (1986): *Biotechnology Letters, 8,* 877.
121) Gupta, A. K. and Curtis, A. S. G. (2004): *Journal Of Materials Science-Materials In Medicine, 15,* 493.
122) Shan, G. B., Xing, J. M., Luo, M. F., Liu, H. Z. and Chen, J. Y. (2003): *Biotechnology Letters, 25,* 1977.
123) Yokoi, H. and Kantoh, T. (1993): *Bulletin Of The Chemical Society Of Japan, 66,* 1536.
124) Sairam, M., Naidu, B. V. K., Nataraj, S. K., Sreedhar, B. and Aminabhavi, T. M. (2006): *Journal Of Membrane Science, 283,* 65.
125) Neuberger, T., Schopf, B., Hofmann, H., Hofmann, M. and von Rechenberg, B. (2005): *Journal Of Magnetism And Magnetic Materials, 293,* 483.
126) Wang, A. Z., Bagalkot, V., Vasilliou, C. C., Gu, F., Alexis, F., Zhang, L., Shaikh, M., Yuet, K., Cima, M. J., Langer, R., Kantoff, P. W., Bander, N. H., Jon, S. Y.and Farokhzad, O. C. (2008): *Chemmedchem, 3,* 1311.
127) Yigit, M. V., Mazumdar, D., Lu, Y. (2008): *Bioconjugate Chemistry, 19,* 412.
128) Zhao, M., Beauregard, D. A., Loizou, L., Davletov, B. and Brindle, K. M. (2001): *Nature Medicine, 7,* 1241.
129) Sun, C., Fang, C., Stephen, Z., Veiseh, O., Hansen, S., Lee, D., Ellenbogen, R. G., Olson, J. and Zhang, M. Q. (2008): *Nanomedicine, 3,* 495.
130) Schellenberger, E. A., Hogemann, D., Josephson, L. and Weissleder, R. (2002): *Academic Radiology, 9,* S310.
131) Leuschner, C., Kumar, C., Hansel, W., Soboyejo, W., Zhou, J. K. and Hormes, J. (2006): *Breast Cancer Research And Treatment, 99,* 163.
132) Kresse, M., Wagner, S., Pfefferer, D., Lawaczeck, R., Elste, V. and Semmler, W. (1998): *Magnetic Resonance In Medicine, 40,* 236.
133) Toma, A., Otsuji, E., Kuriu, Y., Okamoto, K., Ichikawa, D., Hagiwara, A., Ito, H., Nishimura, T. and Yamagishi, H. (2005): *British Journal Of Cancer, 93,* 131.
134) Funovics, M. A., Kapeller, B., Hoeller, C., Su, H. S., Kunstfeld, R., Puig, S. and Macfelda, K. (2004): *Magnetic Resonance Imaging, 22,* 843.
135) Sakamoto, J. H., Smith, B. R., Xie, B., Rokhlin, S. I., Lee, S. C. and Ferrari, M. (2005): *Technology In Cancer Research & Treatment, 4,* 627.
136) Cirstoiu-Hapca, A., Bossy-Nobs, L., Buchegger, F., Gurny, R. and Delie, F. (2007): *International Journal Of Pharmaceutics, 331,* 190.
137) Chen, C. T. and Chen, Y. C. (2005): *Analytical Chemistry, 77,* 5912.
138) Lo, C. Y., Chen, W. Y., Chen, C. T. and Chen, Y. C. (2007): *Journal Of Proteome Research,* 6, 887.
139) Chen, C. T., Chen, W. Y., Tsai, P. J., Chien, K. Y., Yu, J. S. and Chen, Y. C. (2007): *Journal Of Proteome Research, 6,* 316.
140) Lin, J., Zhou, W. L., Kumbhar, A., Wiemann, J., Fang, J. Y., Carpenter, E. E. and O'Connor, C. J. (2001): *Journal Of Solid State Chemistry, 159,* 26.
141) Lyon, J. L., Fleming, D. A., Stone, M. B., Schiffer, P. and Williams, M. E. (2004): *Nano Letters, 4,* 719.

142) Kim, J., Park, S., Lee, J. E., Jin, S. M., Lee, J. H., Lee, I. S., Yang, I., Kim, J. S., Kim, S. K., Cho, M. H. and Hyeon, T. (2006): *Angewandte Chemie-International Edition, 45,* 7754.

143) Carpenter, E. E. (2001): *Journal Of Magnetism And Magnetic Materials, 225,* 17.

144) Zhou, W. L., Carpenter, E. E., Lin, J., Kumbhar, A., Sims, J. and O'Connor, C. J. (2001): *European Physical Journal D, 16,* 289.

145) Yi, D. K., Lee, S. S., Papaefthymiou, G. C. and Ying, J. Y. (2006): *Chemistry Of Materials, 18,* 614.

146) Ulman, A. (1996): *Chemical Reviews, 96,* 1533.

147) Mulvaney, P., Liz-Marzan, L. M., Giersig, M. and Ung, T. (2000): *Journal Of Materials Chemistry, 10,* 1259.

148) Tartaj, P., Gonzalez-Carreno, T. and Serna, C. J. (2002): *Langmuir, 18,* 4556.

149) Burns, A., Ow, H. and Wiesner, U. (2006): *Chemical Society Reviews, 35,* 1028.

150) Herz, E., Ow, H., Bonner, D., Burns, A. and Wiesner, U. (2009): *Journal Of Materials Chemistry, 19,* 6341.

151) Cheon, J. and Lee, J. H. (2008): *Accounts Of Chemical Research, 41,* 1630.

Author's short biography

Amit Singh

Amit Singh is a PhD student in the department of Materials Science and Engineering at the University of Florida. In 2005, he joined the PhD program and is currently conducting research in the field of cancer nanotechnology for his dissertation. He can be reached at asingh@perc.ufl.edu.

Parvesh Sharma

Parvesh Sharma received his B.Sc. and M.Sc. in Chemistry from St. Stephen's College, Delhi University. He completed his PhD in area of analytical coordination Chemistry from Department of Chemistry, Delhi University in 1998. He joined Chemistry Faculty, St. Stephen's College, Delhi University and taught for 7 years. He is currently working as Postdoc Associate in Particle Engineering Research Center at the University of Florida, Gainesville, USA. His areas of interests include development of engineered particulates as contrast agents for medicinal and agricultural applications; non- invasive imaging; multimodal-multifunctional nanoparticles; drug delivery and targeting; effects and fate of nanoparticles in biological systems and environment; applications of surfactant science in industrial processes.

Scott Brown

Scott Brown is a Research Scientist at the Particle Engineering Research Center at the University of Florida. He received his BS in Chemical Engineering in 2002 from the University of Florida. He later earned his MS and PhD from the same institution in Materials Science & Engineering in 2004 and 2007, respectively. His research interests include the design and synthesis of multifunctional engineered nanoparticulate systems for biological and energy applications, cell based therapies, cell adhesion & mechanotransduction, tribology in particulate and biological systems, interfacial phenomena, nanotoxicology, thin films, and electrostatic interactions in powder systems.

Brij Moudgil

Brij Moudgil is a Distinguished Professor of Materials Science and Engineering at the University of Florida where he currently holds the Alumni Chair in Materials Science and is also the Director of the Particle Engineering Research Center. He served as the president of the Society for Mining, Metallurgy, and Exploration (SME) for the year 2006-2007. His research interests are in polymer and surfactant adsorption, dispersion and aggregation of fine particles, nanotoxicity, multifunctional nanoparticles for bioimaging, diagnosis, and therapy, nanoparticulate processing and separation technology for enhanced performance in mineral, chemical, microelectronics, pharmaceutics, advanced materials, and resource recovery & waste disposal applications. He received his B.E degree in Metallurgical Engineering from the Indian Institute of Science, Bangalore, India and his M.S and Eng. Sc.D degrees in Mineral Engineering from the Columbia University. In 2002 he was elected as a member of the U.S National Academy of Engineering for his contributions to mineral processing and professional leadership in the particle community. He can be reached at bmoudgil@perc.ufl.edu.

Nanoparticles: Characteristics, Mechanisms and Modulation of Biotoxicity[†]

P.Somasundaran[*], X. Fang, S. Ponnurangam and B. Li
Langmuir Center for Colloids and Interfaces,
Columbia University[1]

Abstract

Particulates of 1 to 100 nanometers size are being increasingly used for a variety of clinical and commercial purposes due to their large surface-to-volume ratio and unique physico-chemical, mechanical and electronic properties. While utilizing them for their beneficial functions, it has become vital to heed recent alerts on their toxic biological effects in order that benign systems might be developed. In this paper we review emerging mechanisms of nanotoxicity and possible means for remediation. Challenges in monitoring, characterizing and remediation of nanoparticles are also presented.

Keywords: nanoparticles, bacteria, nano-bio interface, nanotoxicity, particle characterization

Introduction

A revolution in materials technology that is changing the way we live is shadowed by a toxic storm rising on the horizon. Indeed the use of nanoparticles in industrial, health and personal care areas is increasing exponentially owing to their special and often novel mechanical, electronic and chemical properties. Examples include fluorescent quantum dots as markers in biological imaging, gold and carbon nanoparticles as controlled drug and nutrient delivery vehicles in medicine and agriculture, metal nanoparticles as fuel cell components, oxide particles as UV filters in cosmetic and personal care products and pigments and lubricants in commodities. Furthermore, inorganic functionalized nanoparticles are used to produce UV resistant and flame retardant plastics for automotive and aviation industries and metallic ones are used as viscosity modifiers for lubricants and controlling the dielectric properties of electronic coatings.

Alarmingly, metal oxide and magnetic nanoparticles are increasingly used without adequate knowledge and precaution in areas such as cosmetics to produce brighter pigmentation and UV protection and in medicine for chemotherapy as well as NMR contrast enhancers. While developing new consumer applications of nanosized materials, potential long-term adverse effects on living species must be considered. Also, as the safety of nanomaterials marketed during past decades does not appear to be adequately addressed, methods are needed to determine the cytotoxicological safety of current and future nanomaterials under different scenarios, particularly since cell cytoskeletons and genetic material have been definitely shown to be damaged in the presence of nanoparticles[1,3,4]. It should be noted that even when direct effects on humans are not recognized, some recent reports suggest that nanoparticles suspended in wash water can work their way into organisms with potentially serious health effects to humans through the food chain. Clearly, there is a dire need for a full understanding of the mechanisms by which nanoparticles bio-accumulate, intrude the skin barrier, as well as interact with biomacromolecules, such as proteins and DNA. It also suggests caution regarding the exposure of human beings during the manufacture, transport and handling of nanoparticles.

Nano-bio interfaces

Nano-bio interfaces are the most complex and the least understood interfacial systems. The behavior

---

[†] Accepted: July 27th, 2010
[1] New York, USA, 10027
[*] Corresponding author
E-mail: ps24@columbia.edu

of this interface is dependent on properties of the nanoparticles, the biophase (protein, cell membranes, endocytic vesicles or organelles), the medium and most importantly any changes in them due to mutual effects within the interfacial region. Those nanoparticle characteristics which predominantly govern the surface behavior include the chemical composition and the resultant solubility, surface charge, semi-conductivity, size, shape, surface curvature, crystallinity as well as porosity, surface heterogeneity, roughness, surface functionalization with charged groups, peptides or polymers [5-7] (**Fig. 1**). Indeed, it is the combined effect of the nanoparticle properties in the suspending medium as well as the interactive biological components that describe the nano-bio interface[2] (**Fig. 2**). Properties of the biosubstrate vary depending on the biomolecular moieties and their sequence in the molecule, molecular weight, the configuration of the macromolecule and membranes or cells comprising them. Many of these properties are in turn dependent upon medium properties such as ionic strength, pH, polarity and temperature[8] . The above characteristics govern other important interfacial processes such as adsorption of ions, surfactants, polymers and proteins as well as aggregation/dispersion and solubility of particles[9,10] . These processes are controlled by forces at the nano-bio interface that operate at the whole range of length scales.[10,11] These forces determine the dispersion of nanoparticles which in turn is controlled, in

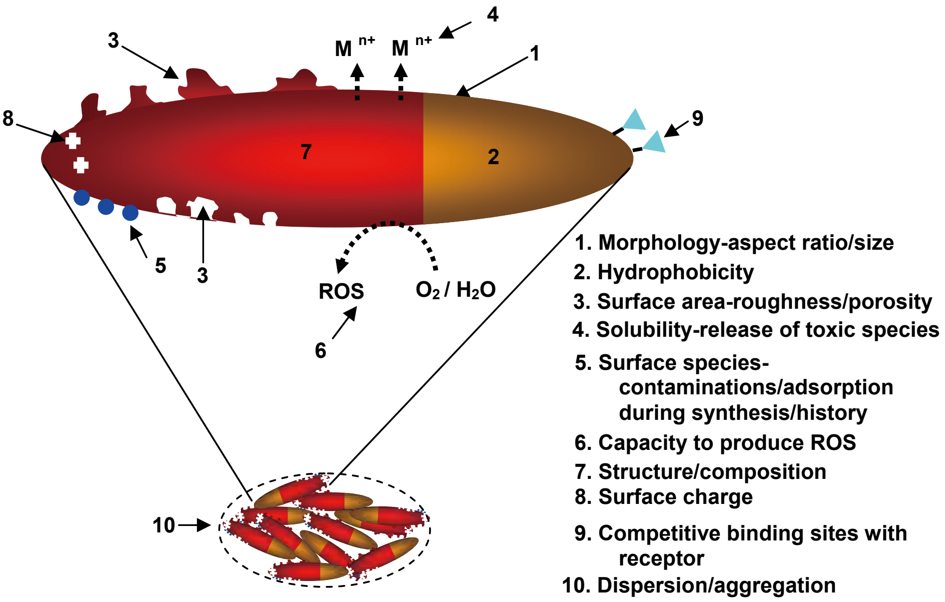

Fig. 1 The properties of nanoparticles related with nanotoxicity.

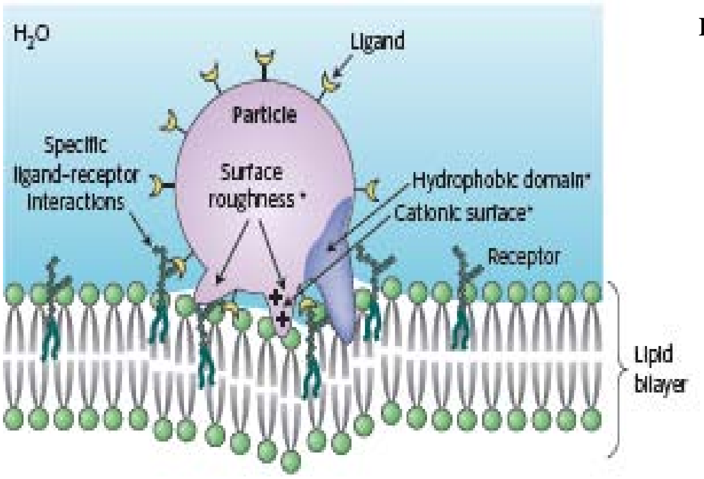

Fig. 2 Representation of receptor mediated uptake. This is a specific biological mechanism for particles interacting with the surface membrane and undergoing cellular uptake. The intrinsic nanoparticle characteristics that promote surface binding (roughness, hydrophobicity, cationic charge) generally lead to nonspecific binding forces (marked by asterisks) that promote cellular uptake. In contrast, specific receptor– ligand interactions generally lead to endocytic uptake. A combination of nonspecific binding forces on the surface of spiked particles can lead to direct penetration of the surface membrane without the need to involve endocytic compartments.[2]

addition to the size, by their charge, hydration and surface polymeric groups [6,12-20]. It has been found recently that the nanoparticles with different surface properties and aggregation behavior can cause different responses to the culture medium, which in turn can lead to different degrees of toxicity.[21,22] The toxic effects of inorganic nanoparticles on biological cells have attracted increasing attention of researchers in recent times[3,16,23-26] Reported negative biological effects include the production of intracellular reactive oxygen species (ROS) and related oxidative stress[6], DNA lesions, denaturation, and even particle wrapping by the surface membrane.[27,28] As in the case of engineered composite nanoparticles, cytotoxicity of polymeric nanogels can also be driven by surface and morphological heterogeneous effects.[2]. It is to be noted that the entire nano-bio interface is a dynamic system where many short and long term interactions occur simultaneously as well as sequentially.

The characterization of the nanoparticle/liquid interface is possibly the primary challenge when trying to understand the nano-bio interface. While characterization often assumes steady-state behavior to assess the overall behavior of the suspension by monitoring such properties as iso-electric point, size and average aggregate size, these assumptions have to be adjusted when considering the nano-bio interface. Moreover, methods used to monitor relevant properties of large particles under static conditions are most often not valid for nanoparticles. Also many of these methods do not report special inhomogeneities that can result from spatial localization of ionic groups, proteins and lipids as well as imperfections and contaminants on the surface of particles and the cell membranes. The nano-bio interface is highly dynamic and undergoes continuous changes as a result of nanoparticles dissolution and resulting cellular response. While it may take some time to develop substantive investigative methods to explore this interface at the usual level of sophistication in colloid chemistry, it is worthwhile exploring the nano-bio interface through novel imaging techniques and biological approaches.

Fundamental and complex forces at the nano-bio interface

The forces between particles are typically classified into long range and short range forces. The former forces arise from usually attractive van der Waals forces and repulsive or attractive electrostatic interactions, whereas, the latter arise from steric, depletion and hydration interactions. Even though the forces that control interactions between cells and nanoparticles are similar to the forces between two larger colloidal particles, the cellular response and the resulting mutual effects on nanoparticles and the cells render traditional surface chemical methods unreliable. One such phenomenon that is important for inorganic and other hydrophilic or "water loving" nanoparticles is hydration. If water is attracted to nanoparticles more strongly than nanoparticles to each other, hydration can interfere with the aggregation of nanoparticles.[15] Another major variable is the dynamic effect due to the morphologically and chemically compliant nature of the membrane[29]. In addition, inter-particle interactions can be affected by the chemical heterogeneity of the nanoparticles.[30] Also, it is important to note that multiple particles could form rafts that may exhibit markedly different properties than single particles. In addition, as in the case of flotation of mineral particles by air bubbles, possible roll over of the particle on the cell surface has to be recognized. On the other hand, nanoparticles are not passive. Upon interaction with the cell components, they can change (dissolve/grow, aggregate/disperse, or even experience phase transformation). This generates a time-dependent and dynamic nano-bio interface.[31,32] Other complexities such as endocytosis of the nanoparticles and specific receptor-ligand interactions make these interactions difficult to predict by theoretical considerations.

Challenges and Solutions to the Monitoring Nanoparticle systems

Nano-toxicology is an emerging scientific discipline aimed towards studying the impact of nanotechnology on human health[33] as a growing number of consumer products contain engineered nano-particles. One need that must be addressed in this regard is the development and selection of accurate methods for monitoring nano-particles of various products, many being dispersions containing mixtures of not only different nano-sized particles, but also particles of much larger size.

Monitoring the presence of nano-particles in dispersions with broad particle size distributions is difficult because their effect could be masked by the presence of larger particles or the aggregates of the nano-particles themselves. While there are some methods for measuring systems containing only nano-particles, there are no well established techniques for monitoring nano-particles in the presence of larger ones. Development of such methods is imperative for reliable investigation of nano-particles in natural and engineered systems. The first logical step in this regard is an investigation of currently available techniques. To make the study reliable, it is necessary that the same set of nano-particles is studied. Hence we measured different samples with acoustic spectroscopy and TEM, since these techniques have been reported to be well suited for characterizing nano-particles with rather narrow size distributions[34-38]. Acoustic techniques can handle concentrated systems (>1% vol), which can not usually be dealt with by most other techniques[39]. Suspensions of 5%wt ZnO particles were prepared by ultrasonicating samples from different manufacturers in the presence of hexametaphosphate. The acoustic measurement yielded a median value of 200 nm to 700 nm for the size of these powders. Independent TEM photographs confirmed the trend of size variation from sample to sample. Importantly, the acoustic measurement indicated that all of these dispersions contain different amounts of nano-particles, even though they were specified by the manufacturers as nano-powders rather than large particles. **Table 1** presents the averaged content of nano-particles for each ZnO sample. Precision of this measurement, defined as the ratio of the "absolute average deviations" to the "average content" , varied significantly from sample to sample.

Toxicity due to the portion of particles on the Nano levels

Although there is some controversy about the toxicity of nanoparticles, there is by and large enough evidence of their adverse effects. As a noteworthy example, Oberdorster et al. have reported that 36 nm carbon nanoparticles can translocate to the brain via the olfactory nerve upon inhalation in rats.[40] In their investigation, rats exposed to the nanoparticles for six hours exhibited increasing accumulation of nanoparticles within the olfactory bulb even seven days after exposure. Oberdorster has also shown that 36 nm carbon particles have a significant potency to induce inflammatory lung injury.[41] Lam et al. also demonstrated that carbon nanotubes could cause lung granulomas in mice.[42] Other studies showed that titanium dioxide (TiO_2) particles smaller than 20 nm can cause inflammatory reactions in both animals and humans.[43] Gutwein[44] et al. have reported a dramatic decrease in the growth rate for cells exposed to alumina particles for only 2 hours. **Table 2** summarizes reported works on cytotoxicity of various nanoparticles and the mechanisms of toxicity along with potentially useful design methods. As of today, most of the research on nanotoxicity has been on the eukaryotic cells.

We have recently investigated cytotoxicity of ZnO, CeO_2, and anatase TiO_2 nanoparticles on Nitrosomonas europaea cultures.[2,21,45,46] Nitrosomonas europaea (N. europaea) is a microbe whose growth relies on the oxidation of ammonia to nitrite.[47] Therefore, it is used in general for waste water treatment. The presence of nanoparticles could possibly damage the activity of the Nitrosomonas europaea cells, leading to their poor performance in the treatment of industrial and sewage waste of oxidizing ammonia to nitrate. Nitrosomonas europaea in chemostat state were cultured in the presence of ZnO, CeO_2 and anatase TiO_2 nanoparticles at concentrations of 20 ppm and 200 ppm for 4 hours. The cells were collected for further characterization using TEM. **Fig. 3** shows the transmission electron microscopic images of the particles

Table 1 Median particle size and percentage of the nano particles (<100nm) in various ZnO samples at 5%wt stabilized at pH 10 with hexametaphosphate. (median sizes of the particles were provided by manufacturers)[50]

POWDER, Manufacturer	Median size, (μ m)	Acoustic cumulative % of nano-particles, <100 nm	TEM cumulative % of nano-particles, <100 nm
Zinc oxide, 99.5+% by Acros Organics	0.27 ± 0.01	11.0 ± 1.4	61.3
Zinc oxide, reagent ACS by Acros Organics	0.43 ± 0.02	7.0 ± 0.5	14.8
Z50-500 USP powder packaged by Fisher Scientific	0.56 ± 0.02	2.7 ± 0.4	31.0
Z52-500 USP powder packaged by Fisher Scientific	0.66 ± 0.04	1.9 ± 0.4	17.5
S80249 by Fisher Scientific	0.40	6.1 ± 0.2	28.3
Zinc oxide ACS reagent grade by MO Biomedicals, LLC	0.35 ± 0.02	8.2 ± 2.1	23.4
Zinc oxide Polystormor™ by Mallinckrodt Chemicals	0.223 ± 0.009	19.6 ± 1.8	85.9
Zinc oxide Nanopowder by American Elements	0.631 ± 0.1	4.7 ± 2.5	34.2

Table 2 Potential mechanisms/routes of adverse effects of nanoparticles and possible ways of mitigation (adapted from Ref. 2)

Nanomaterials	Possible mechanisms/routes of toxicity	Suggested mitigation strategies
	Organic Nanomaterials	
MWCNT, and SWCNT[51-54]	Frustrated phagocytosis: cell wall disruption and enzymes release, generation of ROS, and inflammation due to aggregation of CNT	Surface functionalization with anti-oxidants, complete purification to eliminate residual metal ions; coating with polymer matrix to prevent release of toxic metal ions; surface functionalization.
Fullerenes[42]	Generation of ROS and resulting oxidative stress	
Cationic Polymer nanospheres and Dendrimers[24,55,56]	Endosomal cellular uptake	Modulation of cationic charge density and increasing specific cellular interaction through functionalization with appropriate receptors
	Metals	
Gold nanoparticles[57,58]	Denaturing of protein	Coating of nanoparticles with amphipathic agents to modulate charge, size, dispersion and hydrophobicity
Silver nanoparticles[59]	generation of ROS, Alteration of transport through membrane	Capping agents to prevent release of Ag^+ ions
	Metals Oxides	
TiO_2[27,60,61]	Oxidative stress due to generation of ROS and photoactivity; cell death and fibrillation due to interference in macrophage cell membrane functions	Capping NMs with ; coating with anti-oxidants (ascorbate, glutathione, alpha-tocopherol (vitamin E)), enzymatic scavengers of activated oxygen such as superoxide dismutase, surfactants, polymers or complexing ligands; Control of redox properties; Surface passivation
ZnO[25,62]	High dissolution of ZnO nanoparticles under physiological condition and release of toxic cations.	
Al_2O_3[63,64]	Induce proinflammatory response	
SiO_2[65-67]	Protein denaturation; oxidative stress due to ROS generation	
CeO_2[25]	Inducing protein aggregation	
	Other Nanoparticles	
Co/Ni ferrite Nanoparticles, magnetic metallic nanoparticles[68]	Low cell viability due to the release of toxic cations	Encapsulation with polymer, Capping with phosphonic and hydroxamic acids; positively charged tetraheptylammonium (for Ni nanoparticles)
CdSe[69]	High cell mortality due to easy dissolution and release of ions	

tested in this work. The median size of the elliptical shaped TiO_2 particles are ~25 nm and 200 nm. The elliptically shaped ZnO particles had a median size of ~30 nm. CeO_2 particles are needle-shaped with an average dimension of ~60 nm in length and 20 nm in width. The surface areas from the BET measurement for 25 nm anatase TiO_2, anatase 200 nm TiO_2, ZnO and CeO_2 particles were 117.7 m^2/g, 9.2 m^2/g, 42.1 m^2/g, and 93.8 m^2/g, respectively. In addition to TEM, a Beckman Optima XL-1 analytical ultracentrifuge with scanning optics in an interference system was employed to investigate the complex distribution in solution by monitoring sedimentation velocity.[48]

The morphological changes of bacteria are illustrated in Figure 4a-h. The intercellular particle accumulation was found for cells treated with all three types of nanoparticles except for the 200 nm anatase TiO_2. 25 nm anatase TiO_2 produced changes in the morphology of the elliptical N. Europaea (**Fig. 4a**) to an irregular and distorted form (**Fig. 4b**). Most of the cells that remained in their elliptical shapes contained a cavity. Those cells that are distorted still kept their cytosolic compositions. Hardly any dividing cells were observed in the cells with particles. Also, it was difficult to visualize the clear multilayered cell membranes under nanoparticles stress, especially when 200 ppm of nanoparticles were added (**Fig. 4c**). At the same loading concentration smaller particles distorted the cells more than the larger particles. Cells in the media with 200 nm particles remained more spherical in shape with their membrane largely unperturbed (**Fig4. d**) than the ones in media with 25 nm particles. At similar total surface area, 200 ppm 200 nm anatase TiO_2 nanoparticles show less damage to cell shape as compared to 20 ppm 25 nm anatase TiO_2 NPs. However, empty vacuoles were observed inside the cells for all the sizes. The size effect has also been studied on eukaryotic cells. It has been found that for the same type of particles, larger size creates less damage in general. The cells show little morphological distortion in shape under the stress of ZnO nanoparticles (**Fig. 4e**) as compared

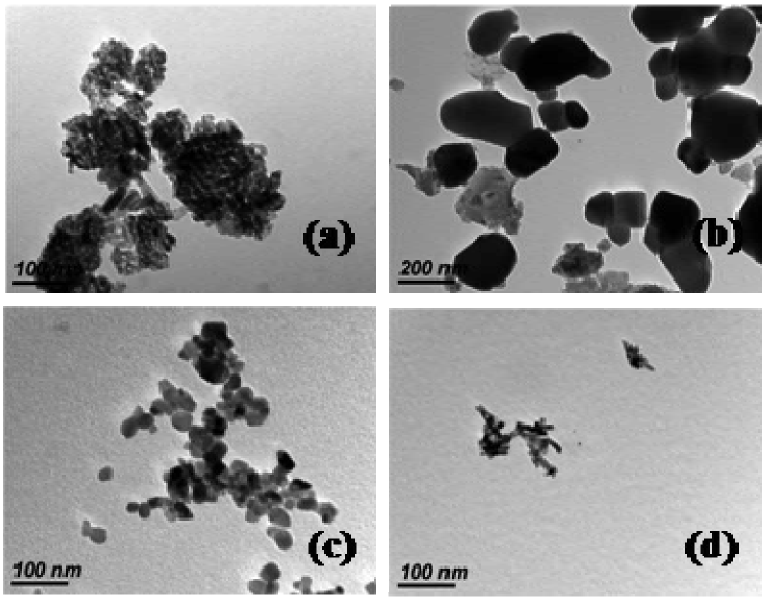

Fig. 3 Transmission electron microscopy images of a) 25nm Anatase TiO_2, b) 200nm Anatase TiO_2, c) ZnO, and d) CeO_2 particles studied in this research.

with cells cultured in media with 25 nm anatase TiO_2 particles. However, most of the inner leaflet of the membrane wrapped the interior cell structures and separated from the rest of outer membrane bilayer compartments. The outer cell membrane bilayers become indistinguishable too. No broken membrane debris was observed in the fixed cell sample. Neither were empty cavities/vacuoles seen in the cell. On the other hand, a few dark spots can be observed having entered the cells and gathered within the center of the cells. Similar morphological responses were found for CeO_2 treated N. Europaea (**Fig. 4f**). No particles were observed to intrude the cell, although some can be observed to adhere to the outer membrane leaflet along their longitudinal needle axis (**Fig. 4g**). Much significant damage was observed in cells that were close to CeO_2 aggregates, which display large cavities and bubbles in them (**Fig. 4h**). The cell walls/membranes, however, remain undamaged. Considering the fact that during TEM sample preparation heavy particles as well as cells precipitate first due to centrifugation, it can be assumed that the cells near the CeO_2 aggregates would be heavier and show more damage with vacuoles than the cells far away from them.

The stresses exerted by the same type of nanoparticles on eukaryotic cells have been reported by us recently.[25] It has been concluded that ZnO particles induce cytotoxicity by dissolution of Zn^{2+} ions as well as the uptake of ZnO particle remnants. The nano-ZnO exposure on cells could increase the membrane permeability via Na^+ and K^+ fluxes through cells and ionic homeostasis disturbance based on rat tests.[49] Since the *N. Europaea* has a cell wall and multilayered membrane bilayer shell, it would be very unlikely that the uptake is via endosomal ways. Moreover, a close contact between cells and particles is also prevented by the electrostatic interaction since both are negatively charged. As from previous references on eukaryotic cells, TiO_2 nanoparticles would be toxic under UV energy in the cells.[23] The CeO_2 particles, on the other hand, have been reported to be safe and can protect the cells against secondary oxidative stress stimulus.[25] Our results of stress exerted by the anatase TiO_2 and CeO_2 nanoparticles on the prokaryotic N. Europaea, however, showed observations of toxicity. From the morphological observation, all particles were observed to have caused damage irrespective of their sizes and charges. The shrinkage of the inner cell membrane near the cell wall and the release of cytosolic compartments indicate possible high osmotic pressure in and out of the cell membrane under the stress of nanoparticles. TiO_2 cause cell membrane dissociation even when possible UV-radiation was screened to some degree under dark culturing conditions. It is also seen from the TEM images that there are many fibrous structures surrounding the cells, which can be considered to result from shedding of the cell walls or membrane compartments. Since the charges on the cell-complex shifted to the positive side and the original zeta potential for the particles is negative, we propose

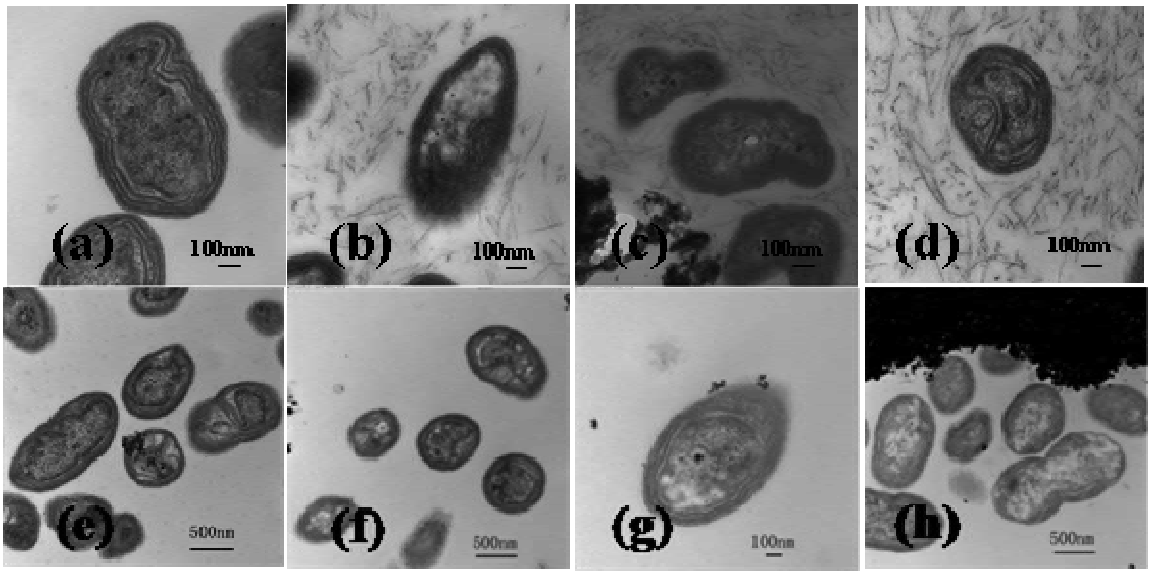

Fig. 4 *N. Europaea* cells grown in media containing a) control (no anatase TiO_2 nanoparticles (Nanoparticles)), b) 20ppm of 25nm anatase TiO_2 Nanoparticles, c) 200ppm of 25nm anatase TiO_2 Nanoparticles, d) 200ppm of 200nm anatase TiO_2 Nanoparticles for 4 hours, e) 20ppm of ZnO Nanoparticles, f) 20ppm CeO_2 Nanoparticles for 4 hours, g) 20ppm CeO_2 Nanoparticles, showing the particle align themselves longitudinally on the cell wall, h) 20ppm CeO_2 Nanoparticles, the cells close to the particle aggregates shows more cavities in them.1)

that only some positive ionic species from the media get adsorbed onto the cell walls. This statement is validated by the results from three separate analytical ultracentrifuge measurements in **Fig. 5**, which shows in general that when under nanoparticles' stress, the cells become heavier than the control and thus sediment faster. Cells in 200 ppm TiO_2 (and CeO_2) nanoparticles media have a sedimentation peak position close to that of the cells with lower NP loading, while an apparent right-shift is seen between the 200 ppm and 20 ppm peak positions of cells in ZnO nanoparticles media (**Fig. 5b**). This is not unexpected considering the lower dissolution of the TiO_2 (and CeO_2) nanoparticles as compared with ZnO nanoparticles. These results correlated well with the light scattering and zeta potential data.

Toward the production of environmental benign particles

The above discussion raises the following questions in order to produce safe nanoparticles:

- How do nanoparticles enter cells, and how can this phenomenon as well as subsequent interactions with cell components be controlled?
- What is the hierarchy in morphological, structural, and electronic properties of nanoparticles that govern their penetration into cells?
- What are the mechanisms of generation of reactive oxygen species (ROS) upon nanoparticle-cell interaction?
- How can particle size and surface functionalization control each of these processes?
- How does the heterogeneity of the nanoparticles make further complications in the mysterious nano/bio interface regions?

In summary, is it possible to tune out nanotoxicity?

Tackling the above questions requires us to develop a new paradigm that will enable a full understanding of nanoparticle-cell membrane and nanoparticle-media interactions while taking account of the environment-dependent acid-base, redox, electronic, aggregation, and wettability properties of nanoparticles. As stated earlier, the entire nano-biointerface is a dynamic system where many simultaneous and sequential short and long term interactions play different roles at different time and place. The effects have been suggested to be controlled by characteristics of nanoparticles such as hydrophobicity, surface roughness/porosity, solubility-release of toxic species, surface species-contaminations/adsorption during synthesis/history, capacity to produce ROS, structure/composition, surface charge, binding sites competitive for receptor, dispersion/aggregation. Based on the current observation/understandings gained with regard to bio-nano interfaces, the following strategies are proposed towards the production of greener nanoparticles:

1) Promotion of aggregation of nanoparticles using

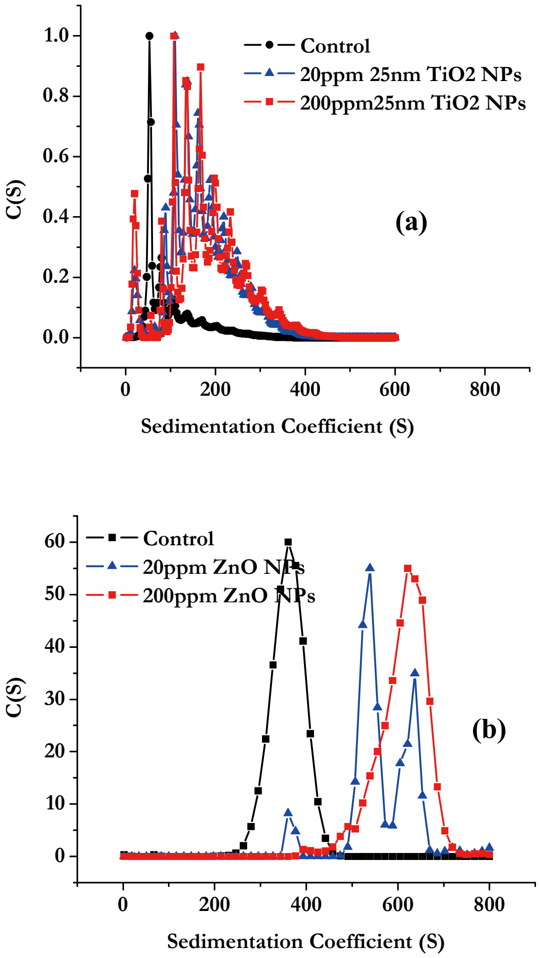

Fig. 5 The analytical ultracentrifuge result on *N. Europaea* cells grown in media loaded with 0ppm, 20ppm and 200ppm of a) 25nm anatase TiO_2 Nanoparticles. b) ZnO Nanoparticles. Cells under the stress of NPs have larger sedimentation coefficient than the control.[1)]

preferably natural reagents. Our results with both fibroblast and the *N. Europaea* research have shown that particles of the same materials but larger sizes cause less damage to cells. Therefore, aggregation of particles particularly by natural biomacromolecules, soils, or even small living creatures should increase the safety of particles (**Fig. 6a**).

2) Modification of the nanoparticles with biocompatible coatings to prevent their catalysis of various reactions with water and other surrounding organic materials. On the other hand, the large production of free radicals can also react and degrade organics in matrix, especially bio-macromolecules such as DNA. To solve the problem, Lee et al.59 have modified the titania nanoparticles with multi-component polymer coatings (**Fig. 6b**). The inner-most layer is antioxidants (Oligomeric Proanthocyanidins) to capture free radicals generated by titania particles under UV irradiation. Then, a layer of anionic polymers is coated onto the particle surface, which can provide negative charges to the surface of titania particles with attendant decreased possibility for contact or penetration of particles into cell membranes. To protect the integrity of whole particles with coating layers, the outermost layer is fully covered with hydrophilically modified polysiloxane. The hydrophilicity of the particles could facilitate the dispersion in the aqueous media, maximizing the efficiency of sequestering hazardous radicals. Such a chemical and physical grafting approach remarkably reduces the photocatalytic degradation and enables highly effective screening against the UV radiation.

3) Mixing with benign particles. Nanoparticles, when mixed with biocompatible particles or species are likely to be less toxic but still effective for enhancing mechanical as well as electronic properties.

Conclusions

Past work shows that nanoparticles can potentially cross the cell membranes and stress biological cells.

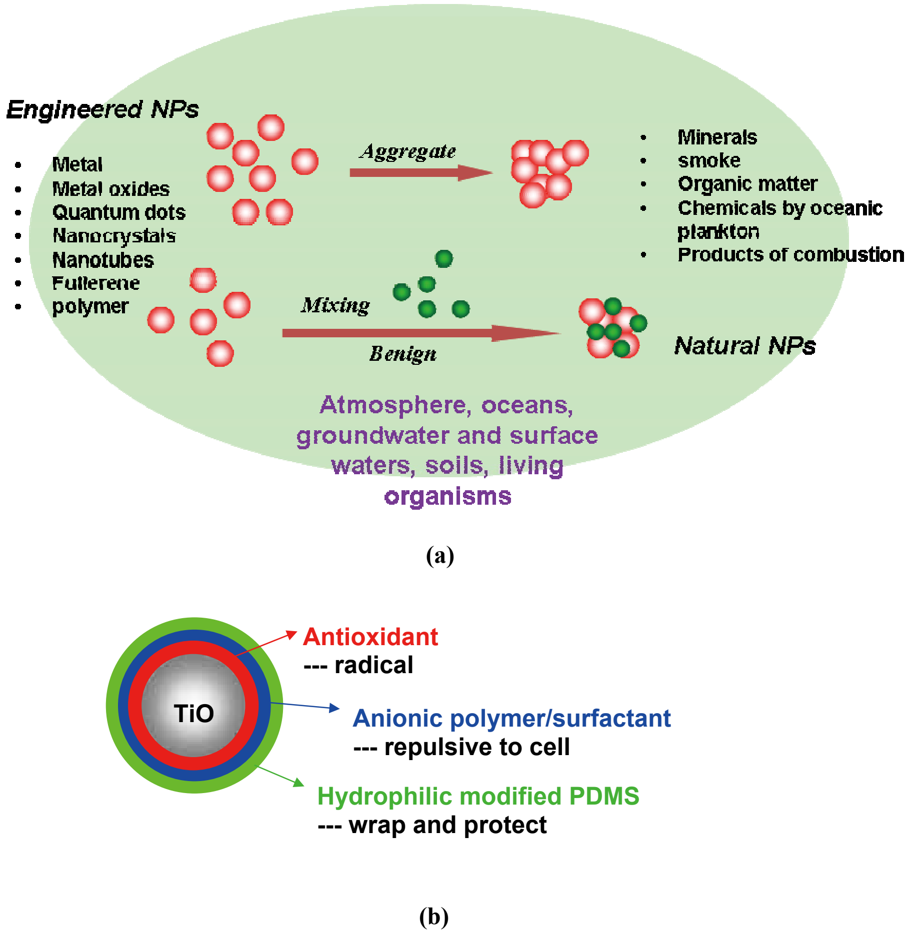

Fig. 6 Schematic drawing of a) the aggregation strategy, and b) the surface modification strategy for greener nanoparticles by coating.

The presence of the particles has been shown to be responsible for the abnormal actin filaments and extracellular matrix behaviors in dermal fibroblasts, which in turn decreases cell growth and proliferation. When possible toxicity effects of 25 nm and 200 nm anatase TiO_2 nanoparticles on waste water treatment N. Europaea bacteria were probed, cells were found to be distorted with membrane damage. CeO_2 and ZnO nanoparticles affect cell morphologies, too. Possible means for mitigating toxicity include aggregation, surface modulation with multiple polymer coatings, biocompatible functionalization and mixing with benign particles.

It is clear from an examination of the work done with nanoparticles thus far that there is dire need to develop methods to monitor, characterize and tame, so to speak, nanoparticles so that we may fully reap the benefits of nanotechnology for producing better technological and medical products for a long happy life and a healthier planet.

Acknowledgements: This material is based upon work supported by the National Science Foundation and the Environmental Protection Agency under Cooperative Agreement Number EF 0830117. Any opinions, findings, and conclusions or recommendations expressed in this material are those of the author(s) and do not necessarily reflect the views of the National Science Foundation or the Environmental Protection Agency. This work has not been subjected to EPA review and no official endorsement should be inferred.

References

1) Fang, X. H., Yu, R., Li, B. Q., Sonasundaran, P. and Chandran, K. (2010): Journal of Colloid and Interface Science, 348, 329.
2) Nel, A. E., Madler, L., Velegol, D., Xia, T., Hoek, E. M. V., Somasundaran, P., Klaessig, F., Castranova, V. and Thompson, M. (2009): Nature Materials, 8, 543.

3) Xia, T., Li, N.and Nel, A. E. (2009): Annual Review of Public Health, 30, 137.
4) Pernodet, N., Fang, X. H., Sun, Y., Bakhtina, A., Ramakrishnan, A., Sokolov, J., Ulman, A. and Rafailovich, M. (2006): Small, 2, 766.
5) Gratton, S. E. A., Ropp, P. A., Pohlhaus, P. D., Luft, J. C., Madden, V. J., Napier, M. E. and DeSimone, J. M. (2008): Proceedings of the National Academy of Sciences of the United States of America, 105, 11613.
6) Nel, A., Xia, T., Madler, L. and Li, N. . (2006): Science, 311, 622.
7) Vertegel, A. A., Siegel, R. W. and Dordick, J. S. (2004): Langmuir, 20, 6800.
8) Sigmund, W., Pyrigiotakis, G. and Daga, A. (2005)
9) Gilbert, B., Huang, F., Zhang, H. Z., Waychunas, G. A. and Banfield, J. F. (2004): Science, 305, 651.
10) Israelachvili, J. N. (1991): Intermolecular Surface Forces, Academic Publishers: London,
11) Velegol, D. (2007): Journal of Nanophotonics, 1, 25.
12) Noohom, W., Jack, K. S., Martin, D. and Trau, M. (2009): Biomedical Materials, 4.
13) Mistry, A. S., Cheng, S. H., Yeh, T., Christenson, E., Jansen, J. A. and Mikos, A. G. (2009): Journal of Biomedical Materials Research Part A, 89A, 68.
14) Kothapalli, C. R. and Ramamurthi, A. (2009): Acta Biomaterialia, 5, 541.
15) Depan, D., Kumar, A. P. and Singh, R. P. (2009): Acta Biomaterialia, 5, 93.
16) Seil, J. T. and Webster, T. J. (2008): International Journal of Nanomedicine, 3, 523.
17) Erisken, C., Kalyon, D. M. and Wang, H. J. (2008): Biomaterials, 29, 4065.
18) Crouzier, T., Nimmagadda, A., Nollert, M. U. and McFerridge, P. S. (2008): Langmuir, 24, 13173.
19) Bi, S. X., Wei, X. Y., Li, N. and Lei, Z. L. (2008): Materials Letters, 62, 2963.
20) Somasundaran, P., Mehta, S. C., Rhein, L. and Chakraborty, S. (2007): Mrs Bulletin, 32, 779.
21) Mahmoudi, M., Shokrgozar, M. A., Simchi, A., Imani, M., Milani, A. S., Stroeve, P., Vali, H., Hafeli, U. O. and Bonakdar, S. (2009): Journal of Physical Chemistry C, 113, 2322.
22) Mahmoudi, M., Simchi, A., Imani, M., Milani, A. S. and Stroeve, P. (2009): Nanotechnology, 20, 8.
23) Pan, Z., Lee, W., Slutsky, L., Clark, R. A. F., Pernodet, N. and Rafailovich, M. H. (2009): Small, 5, 511.
24) Xia, T., Kovochich, M., Liong, M., Zink, J. I. and Nel, A. E. (2008): Acs Nano, 2, 85.
25) Xia, T., Kovochich, M., Liong, M., Madler, L., Gilbert, B., Shi, H. B., Yeh, J. I., Zink, J. I. and Nel, A. E. (2008): Acs Nano, 2, 2121.
26) Nel, A., Xia, T., Madler, L. and Li, N. (2006): Science, 311, 622.
27) Karlsson, H. L., Cronholm, P., Gustafsson, J. and Moller, L. (2008): Chemical Research in Toxicology, 21, 1726.
28) Mahmoudi, M., Simchi, A., Vali, H., Imani, M., Shokrgozar, M. A., Azadmanesh, K. and Azari, F. (2009): Advanced Engineering Materials, 11, B243.
29) Dagastine, R. R., Manica, R., Carnie, S. L., Chan, D. Y. C., Stevens, G. W. and Grieser, F. (2006): Science, 313, 210.
30) Velegol, D. and Thwar, P. K. (2001): Langmuir, 17, 7687.
31) Baca, H. K., Ashley, C., Carnes, E., Lopez, D., Flemming, J., Dunphy, D., Singh, S., Chen, Z., Liu, N. G., Fan, H. Y., Lopez, G. P., Brozik, S. M., Werner-Washburne, M. Brinker, C. J. (2006): Science, 313, 337.
32) Baca, H. K., Carnes, E., Singh, S., Ashley, C., Lopez, D. and Brinker, C. (2007): J. Accounts of Chemical Research, 40, 836.
33) Behra, R. and Krug, H. (2008): Nature Nanotechnology, 3, 253.
34) Gaydardzhiev, S. and Ay, P. (2006): Journal of Dispersion Science and Technology, 27, 413.
35) Stenger, F., Mende, S., Schwedes, J. and Peukert, W. (2005): Chemical Engineering Science, 60, 4557.
36) Sun, Y. P., Li, X. Q., Cao, J. S., Zhang, W. X. and Wang, H. P. (2006): Advances in Colloid and Interface Science, 120, 47.
37) Sun, Y. P., Li, X. Q., Zhang, W. X. and Wang, H. P. (2007): Colloids and Surfaces a-Physicochemical and Engineering Aspects, 308, 60.
38) Wilhelm, P., Stephan, D. (2006): Journal of Colloid and Interface Science, 293, 88.
39) Dukhin, A. S., Goetz, P. J., Fang, X. H. and Somasundaran, P. : Journal of Colloid and Interface Science, 342, 18.
40) Oberdorster, G., Ferin, J. and Lehnert, B. E. (1994): Environmental Health Perspectives, 102, 173.
41) Oberdorster, G., Sharp, Z., Atudorei, V., Elder, A., Gelein, R., Kreyling, W. and Cox, C. (2004): Inhalation Toxicology, 16, 437.
42) Lam, C. W., James, J. T., McCluskey, R. and Hunter, R. L. (2004): Toxicological Sciences, 77, 126.
43) Lindenschmidt, R. C., Driscoll, K. E., Perkins, M. A., Higgins, J. M., Maurer, J. K. and Belfiore, K. A. (1990): Toxicology and Applied Pharmacology, 102, 268.
44) Gutwein, L. G. and Webster, T. J. (2004): Biomaterials, 25, 4175.
45) Cedervall, T., Lynch, I., Lindman, S., Berggard, T., Thulin, E., Nilsson, H., Dawson, K. A. and Linse, S. (2007): Proceedings of the National Academy of Sciences of the United States of America, 104, 2050.
46) fang, X. H., Yu, R., Li, B. Q., Sonasundaran, P. and Chandran, K. (2010): Journal of Colloid and Interface Science.
47) Chain, P., Lamerdin, J., Larimer, F., Regala, W., Lao, V., Land, M., Hauser, L., Hooper, A., Klotz, M., Norton, J., Sayavedra-Soto, L., Arciero, D., Hommes, N., Whittaker, M. and Arp, D. (2003): Journal of Bacteriology, 185, 6496.
48) Schuck, P. (2000): Biophysical Journal, 78, 1606.
49) Zhao, J., L. Xu, T. Zhang, G. Ren, and Z. Yang. (2009): NeuroToxicology, 30, 220.
50) Dukhin, A. S., Goetz, P. J., Fang, X. H. and Somasun-

daran, P. (2010): Journal of Colloid and Interface Science, 342, 18.
51) Peng, J., Qu, X. X., Wei, G. S., Li, J. Q. and Qiao, J. L. (2004): Carbon, 42, 2741.
52) Monthioux, M., Smith, B. W., Burteaux, B., Claye, A., Fischer, J. E. and Luzzi, D. E. (2001): Carbon, 39, 1251.
53) Magrez, A., Kasas, S., Salicio, V., Pasquier, N., Seo, J. W., Celio, M., Catsicas, S., Schwaller, B. and Forro, L. (2006): Nano Letters, 6, 1121.
54) Ding, L. H., Stilwell, J., Zhang, T. T., Elboudwarej, O., Jiang, H. J., Selegue, J. P., Cooke, P. A., Gray, J. W. and Chen, F. Q. F. (2005): Nano Letters, 5, 2448.
55) Tansey, W., Ke, S., Cao, X. Y., Pasuelo, M. J., Wallace, S. and Li, C. (2004): Journal of Controlled Release, 94, 39.
56) Hong, S. P., Bielinska, A. U., Mecke, A., Keszler, B., Beals, J. L., Shi, X. Y., Balogh, L., Orr, B. G., Baker, J. R. and Holl, M. M. B. (2004): Bioconjugate Chemistry, 15, 774.
57) Khan, J. A., Pillai, B., Das, T. K., Singh, Y. and Maiti, S. (2007): Chembiochem, 8, 1237.
58) Hauck, T. S., Ghazani, A. A. and Chan, W. C. W. (2008): Small, 4, 153.
59) Navarro, E., Baun, A., Behra, R., Hartmann, N. B., Filser, J., Miao, A. J., Quigg, A., Santschi, P. H. and Sigg, L. (2008): Ecotoxicology, 17, 372.
60) Vevers, W. F. and Jha, A. N. (2008): Ecotoxicology, 17, 410.
61) Lee, W. A., Pernodet, N., Li, B. Q., Lin, C. H., Hatchwell, E. and Rafailovich, M. H. (2007): Chemical Communications, 4815.
62) Hanley, C., Layne, J., Punnoose, A., Reddy, K. M., Coombs, I., Coombs, A., eris, K. and Wingett, D. (2008): Nanotechnology, 19, 10.
63) Oesterling, E., Chopra, N., Gavalas, V., Arzuaga, X., Lim, E. J., Sultana, R., Butterfield, D. A., Bachas, L. and Hennig, B. (2008): Toxicology Letters, 178, 160.
64) Dey, S., Bakthavatchalu, V., Tseng, M. T., Wu, P., Florence, R. L., Grulke, E. A., Yokel, R. A., Dhar, S. K., Yang, H. S., Chen, Y. M. and Clair, D. K. S. (2008): Carcinogenesis, 29, 1920.
65) Slowing, I., Trewyn, B. G. and Lin, V. S. Y. (2006): Journal of the American Chemical ociety, 128, 14792.
66) Fujiwara, K., Suematsu, H., Kiyomiya, E., Aoki, M., Sato, M. and Moritoki, N. (2008): Journal of Environmental Science and Health Part a-Toxic/Hazardous Substances & Environmental Engineering, 43, 1167.
67) Brown, S. C., Kamal, M., Nasreen, N., Baumuratov, A., Sharma, P., Antony, V. B. and Moudgil, B. M. (2007): Advanced Powder Technology, 18, 69.
68) Guo, D. D., Wu, C. H., Li, X. M., Jiang, H., Wang, X. M. and Chen, B. A. (2008): Journal of Nanoscience and Nanotechnology, 8, 2301.
69) Kirchner, C., Liedl, T., Kudera, S., Pellegrino, T., Javier, A. M., Gaub, H. E., Stolzle, S., Fertig, N. and Parak, W. J. (2005): Nano Letters, 5, 331.

Author's short biography

Professor Somasundaran

Professor Somasundaran got his PhD from the University of California, Berkeley. He is the La von Duddleson Krumb Professor at Columbia University School of Engineering and Applied Science, the Director of the Langmuir Center for Colloids & Interfaces and the founding director of the National Science Foundation Industry/University Cooperative Research Center for Particulate and Surfactant Systems. He is a member of the U.S. National Academy of Engineering, the highest professional distinction conferred upon an engineer, and the equivalent national academies in China, India, Russia and the Balkans and winner of many awards including Richards Award, Ellis Island Medal of Honor, Gaudin Award, Taggart Award and the AIME Education Award etc. and the title of Padma Shri from the Indian Government. His research interests are surface and colloid chemistry, polymer, surfactant and protein adsorption, flocculation/dispersion and biosurface phenomena, molecular interactions at surfaces using advanced spectroscopy, environmental engineering（waste treatment）.

Xiaohua Fang

Dr. Xiaohua Fang is a research associate in the Earth and Environmental Engineering department at Columbia University. She received her doctoral degree in the department of Materials Science and Engineering from the State University of New York at Stony Brook. Her research interests span from soft condensed matter to colloids and interfaces sciences, including the various liquid-vapor interfaces, liquid-liquid interfaces, liquid-solid interfaces as well as the nano-bio interfaces.

Sathish Ponnurangam

Mr. Sathish Ponnurangam is a chemical engineer and currently is a PhD candidate in the Earth and environmental engineering at Columbia University. His interests include surface and colloids chemistry, ab-initio and molecular modeling of surfaces and surfactant adsorption, reagents chemistry in mineral processing and personal care industries, structure properties relationships of metal oxides nanoparticles having applications in alternative energy, environmental remediation and biomedical engineering and application of polymeric nanogel particles for delivery in tissue engineering applications.

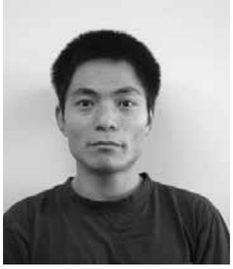

Bingquan Li

Dr. Bingquan Li got both his bachelor and master degrees in polymer and composites from Beihang University（formerly known as Beijing University of Aeronautics and Astronautics）in China. He received a PhD degree in material science from State University of New York at Stony Brook in 2006. Currently he works as a Postdoctoral research scientist in the Langmuir Center for Colloids and Interfaces at Columbia University. His interests include: polymer physics, biomaterials, nanomaterials, colloid and surface chemistry.

Fabrication and Electrochemical Characteristics of $LiFePO_4$ Powders for Lithium-Ion Batteries[†]

Ozan Toprakci, Hatice A.K. Toprakci, Liwen Ji, and Xiangwu Zhang[*]
Fiber and Polymer Science Program,
Department of Textile Engineering, Chemistry and Science,
North Carolina State University[1]

Abstract

Novel powder fabrication technologies provide opportunities to develop high-performance, low-cost cathode materials for rechargeable lithium-ion batteries. Among various energy storage technologies, rechargeable lithium-ion batteries have been considered as effective solution to the increasing need for high-energy density electrochemical power sources. Rechargeable lithium-ion batteries offer energy densities 2 - 3 times and power densities 5 - 6 times higher than conventional Ni-Cd and Ni-MH batteries, and as a result, they weigh less and take less space for a given energy delivery. However, the use of lithium-ion batteries in many large applications such as electric vehicles and storage devices for future power grids is hindered by the poor thermal stability, relatively high toxicity, and high cost of lithium cobalt oxide ($LiCoO_2$) powders, which are currently used as the cathode material in commercial lithium-ion batteries. Recently, lithium iron phosphate ($LiFePO_4$) powders have become a favorable cathode material for lithium-ion batteries because of their low cost, high discharge potential (around 3.4 V versus Li/Li$^+$), large specific capacity (170 mAh/g), good thermal stability, and high abundance with the environmentally benign and safe nature. As a result, there is a huge demand for the production of high-performance $LiFePO_4$ powders. However, $LiFePO_4$ also has its own limitation such as low conductivity (~10^{-9} S/cm), which results in poor rate capability. This can be addressed by modifying the powder structure using novel fabrication technologies. This paper presents an overview of recent advances in the fabrication of high-performance $LiFePO_4$ powders for lithium-ion batteries. The $LiFePO_4$ powder fabrication methods covered include: solid-state synthesis, mechanochemical activation, carbothermal reduction, microwave heating, hydrothermal synthesis, sol-gel synthesis, spray pyrolysis, co-precipitation, microemulsion drying, and others. The impacts of these fabrication methods on the structure and performance of $LiFePO_4$ powders are discussed. In addition, the improvement of the conductivity of $LiFePO_4$ powders through novel powder technologies is addressed.

Keywords: powder fabrication, $LiFePO_4$ powder, cathode, lithium-ion battery, energy storage

1. Introduction

Lithium is an alkali metal with silver-white appearance, soft handle, low density (0.534 g/cm^3), large specific capacity (3860 Ah/kg), high electrochemical potential, high electro-negativity, and high energy density[1, 2]. As an alkali metal, lithium is highly reactive, and hence it is found in nature as compounds that can be used for different applications, such as pharmacology, aerospace, construction, and energy storage.

Rechargeable lithium-ion batteries, which are based on lithium chemistry and were first commercialized by Sony in 1992[3], are of importance as new generation power sources because they are lighter and have higher energy density, lower self discharge, no memory effect, prolonged service-life, larger number of charge/discharge cycles, better environmental friendliness, and higher safety when compared to

---

[†] Accepted: July 27th, 2010

[1] Raleigh, NC, 27695-8301, USA

[*] Corresponding author
Fiber and Polymer Science Program, Department of Textile Engineering, Chemistry and Science, North Carolina State University
E-mail address: xiangwu_zhang@ncsu.edu

many other battery systems. Hence, lithium-ion batteries are being widely used for portable electronics from digital cameras to notebooks and music players to cell phones. They are also potential systems for large-scale applications, such as electric vehicles and storage devices for future power grids, if they can be produced with lower cost, smaller sizes, lighter weights, and higher energy storage capacities.

A standard lithium-ion battery consists of anode, cathode and electrolyte, as shown in **Fig. 1**. When the battery is charged, lithium ions deintercalate from the cathode and intercalate into the anode through the electrolyte; while on the discharging process, lithium ions deintercalate from the anode and intercalate into the cathode. During charge/discharge cycles, electrons flow between the anode and the cathode, enabling the conversion of chemical energy and also the storage of electrochemical energy within the battery. Therefore, the performance of rechargeable lithium-ion batteries strongly depends on the active materials employed in both anodes and cathodes for lithium storage.

The common materials for anodes are carbon, lithium-alloying metals, graphite varieties (such as modified natural graphite or kish graphite), and carbon nanotubes/nanofibers. The most used cathode material is $LiCoO_2$, which is currently being used in commercial lithium-ion batteries found in portable electronic devices such as laptops and cell phones. However, the high cost, poor thermal stability at elevated temperatures and high toxicity of $LiCoO_2$ make it an unsuitable material for larger-scale applications. Therefore, battery manufacturers have turned to find other alternative materials to replace $LiCoO_2$, and examples of such materials include layered lithium nickel oxide ($LiNiO_2$), lithium manganese spinels ($LiMn_2O_4$), vanadium oxides (LiV_3O_8), and olivines ($LiMPO_4$, M = Fe, Co, Mn or Ni)4).

Among various alternative cathode materials, lithium iron phosphate ($LiFePO_4$), which was discovered by Goodenough in 19975), is gaining significant attention because of its relatively low cost, high discharge potential (very flat voltage curve around 3.4 V versus Li/Li^+), large specific capacity (170 mAh/g), good thermal stability, excellent cycling performance, and high abundance with the environmentally benign and safe nature. However, $LiFePO_4$ also has its own limitation such as low conductivity ($\sim 10^{-9}$ S/cm), which leads to high impedance and low rate capability for batteries using that material5). Approaches to solve that problem include but not limited to: doping $LiFePO_4$ with supervalent cations that enhance the material conductivity at the crystal level6, 7), coating $LiFePO_4$ with conductive materials such as carbons from organic precursors8, 9), and decreasing the particle size of $LiFePO_4$ in order to make the diffusion path of lithium shorter10, 11). These approaches can be realized by using novel fabrication technologies.

This paper presents an overview of recent advances in the fabrication of high-performance $LiFePO_4$ powders for lithium-ion batteries. The $LiFePO_4$ powder fabrication methods covered include: solid-state synthesis, mechanochemical activation, carbothermal reduction, microwave heating, hydrothermal synthesis, sol-gel synthesis, spray pyrolysis, co-precipitation, microemulsion drying, and others. The impacts of these fabrication methods on the structure and performance of $LiFePO_4$ powders are discussed. In addition, the improvement of the conductivity of $LiFePO_4$ powders through novel powder technologies is addressed.

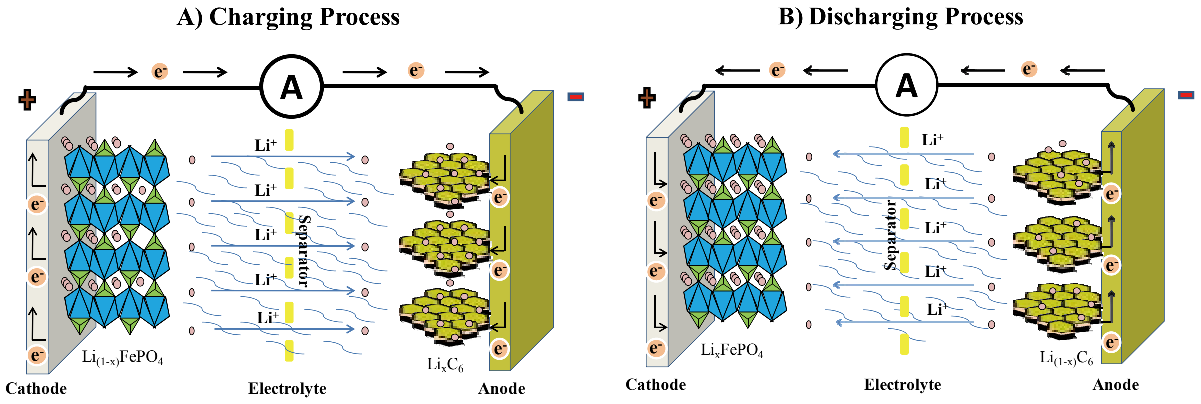

Fig.1 Charging (A) and discharging (B) processes of a typical lithium-ion battery.

2. Crystalline Structure of $LiFePO_4$

$LiFePO_4$ has an ordered olivine structure with a Pnma space group, in which P atoms (PO_4) reside within tetrahedral 4c sites, and Fe and Li cations (FeO_6 and LiO_6) reside within octahedral 4c and 4a sites, respectively, as shown in **Fig. 2**. Oxygen atoms show slightly distorted hexagonal close packed arrangement[3, 5]. FeO_6 is a corner shared octahedron and PO_4 is an edge-shared tetrahedron, and they form the zigzag skeleton by sharing oxygen and Li ions locate in the octahedral channels. The FeO_6 octahedra are connected through the corners in the bc plane and LiO_6 grows as a linear chain along the b axis and a PO_4 tetrahedral shares the edges with one FeO_6 and two LiO_6. The PO_4 tetrahedral structure is the reason for the good phase stability during lithium deintercalation[3, 5, 12-15].

$LiFePO_4$ powders can be prepared by both solid-state and solution-based methods. Solid-state techniques are carried out at high temperatures without any solvent addition. On the other hand, solution-based methods are based on reactions that take place with the presence of appropriate solvent systems.

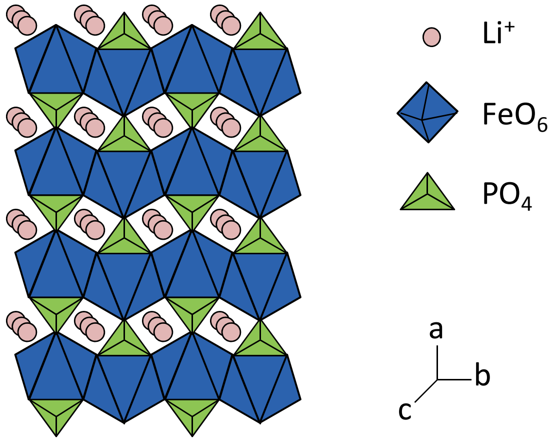

Fig. 2 Crystal structure of $LiFePO_4$.

3. Solid-State Methods for $LiFePO_4$ Powders

Solid-state synthesis, mechanochemical activation, carbothermal reduction and microwave heating are based on solid-state chemistry and are the most common solid-state methods for preparing $LiFePO_4$ powders. **Fig. 3** shows typical routes used in these solid-state methods. Solid state methods are of importance in terms of obtaining ordered crystal structure in a simple way at elevated temperatures.

3.1. Solid-State synthesis

Solid-state synthesis is a technique used to produce chemical structures by reactions carried out at extreme conditions, such as high temperature and pressure, without any solvent. This method is generally used for the mass production of unique, advanced structures, such as special ceramics, scintillation crystals, and piezoelectrics. $LiFePO_4$ powders can be fabricated using the solid-state synthesis method and **Table 1** shows typical precursors used in this method and the particle size and discharge capacity of the resultant $LiFePO_4$ powders. The most commonly used precursors are Li_2CO_3 or $LiOH \cdot H_2O$ for Li, $FeC_2O_4 \cdot 2H_2O$ or $Fe(C_2O_4)_2$ for Fe, and $NH_4H_2PO_4$ for P, respectively[16-20]. However, other precursors can also be used. For example, Wang *et al.*[21] used LiF to replace $LiOH \cdot H_2O$ and Li_2CO_3 and obtained $LiFePO_4$ powders with an average particle diameter of around 500 nm. These $LiFePO_4$ powders have good electrochemical performance, but the release of HF gas, a

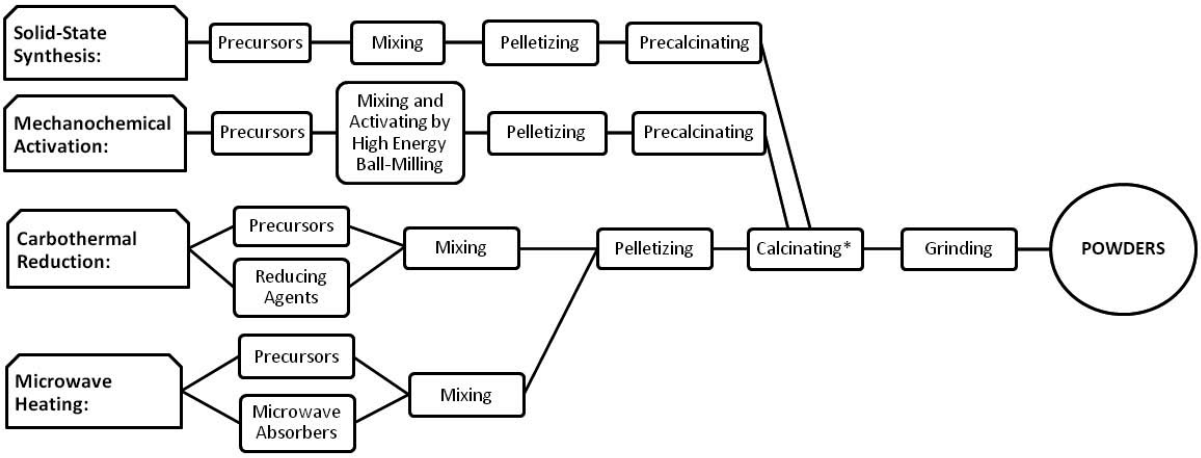

Fig. 3 Typical routes for producing $LiFePO_4$ powders using solid-state methods.

Table 1 Precursors used in the solid-state synthesis method, and particle size and electrochemical performance of the resultant $LiFePO_4$ powders

Li Precursor	Fe Precursor	P Precursor	Metal Dopant	Molar Ratio	Carbon Source	Product	Particle Size (nm)	Discharge Capacity (mAh/g)	Ref
Li_2CO_3	$Fe(CH_3\ CO_2)_2$	$NH_4H_2PO_4$		1:1:1		$LiFePO_4$	<30	162 (C/10)	16
Li_2CO_3	$FeC_2O_4{\cdot}2H_2O$	$NH_4H_2PO_4$		1:1:1		$LiFePO_4$		92	17
Li_2CO_3	$FeC_2O_4{\cdot}2H_2O$	$NH_4H_2PO_4$		1:1:1	Polyvinyl alcohol	$LiFePO_4/C$	200-300	156 (C/10)	18
Li_2CO_3	$FeC_2O_4{\cdot}2H_2O$	$NH_4H_2PO_4$		1.03:1:1	Malonic acid	$LiFePO_4/C$	100-200	149 (C/5)	19
Li_2CO_3	$FePO_4(H_2O)_2$			1:1	Cellulose acetate/sucrose	$LiFePO_4/C$	200-300	160 (C/4)	20
LiF	$FeC_2O_4{\cdot}2H_2O$	$NH_4H_2PO_4$		1:1:1		$LiFePO_4$	500	151 (C/15)	21
Li_2CO_3	$FeC_2O_4{\cdot}2H_2O$	$NH_4H_2PO_4$		1.03:1:1	Malonic acid	$LiFePO_4/C$	188	161 (C/10)	22
Li_2CO_3	FeC_2O_4	$(NH_4)_2HPO_4$				$LiFePO_4$			23
LiF	$FeC_2O_4{\cdot}2H_2O$	$NH_4H_2PO_4$		1:1:1		$LiFePO_4$	300-600	149 (C/5)	24
Li_2CO_3	$FeC_2O_4{\cdot}2H_2O$	$NH_4H_2PO_4$		1:1:1		$LiFePO_4$	1,000	111 (C/8)	25
Li_2CO_3	$Fe(C_2O_4)_2$	$NH_4H_2PO_4$	$MnCO_3$	0.5:y:1:1-y		$LiFe_yMn_{1-y}PO_4$		160 (C/2)	26
Li_2CO_3	$FeC_2O_4{\cdot}2H_2O$	$NH_4H_2PO_4$		1:0.97:1		$LiFePO_4/Fe_2P$			27
Li_2CO_3	$FeC_2O_4{\cdot}2H_2O$	$NH_4H_2PO_4$		1:1:1		$LiFePO_4$			28
Li_2CO_3	$FeC_2O_4{\cdot}2H_2O$	$(NH_4)_2HPO_4$		1:1:1	Chitosan gel	$LiFePO_4/C$		90 (C/5)	29
$LiOH{\cdot}2H_2O$	$FeC_2O_4{\cdot}2H_2O$	$NH_4H_2PO_4$		1:1:1	Glucose, Carbon gel	$LiFePO_4/C$	500	163 (C/10)	30
$LiOH{\cdot}H_2O$	$FePO_4{\cdot}4H_2O$			1:1	Polypropylene	$LiFePO_4$			31
$LiOH{\cdot}H_2O$	$FeC_2O_4{\cdot}2H_2O$	$NH_4H_2PO_4$	Nb_2O_5	0.99:1:1:0.01	Polypropylene	$Li_{0.99}FeNb_{0.01}PO_4$			31
Li_2CO_3	$FeSO_4$	$(NH_4)_2HPO_4$				$LiFePO_4$			32
$LiOH{\cdot}H_2O$	$FeC_2O_4{\cdot}2H_2O$	$(NH_4)_2HPO_4$		3:1:1		$LiFePO_4$		115 (C/2)	33

byproduct of reaction, should be appropriately managed during powder production.

The solid-state synthesis of $LiFePO_4$ powders typically starts with the mixing of precursors by ball-milling or other techniques (**Fig. 3**). For example, Fey *et al.*[22] prepared $LiFePO_4/C$ powder by ball milling of mixed precursors for 3, 12 and 18 hours, followed by heat treatment at 600℃. An 18 hour ball-milling time was found to produce $LiFePO_4$ powders that have an average particle size of 188 nm and a good discharge capacity of 161 mAh/g at C/10 with good cycling performance. In addition to ball milling, precursors can also be mixed by generating dispersion in a solvent such as acetone, followed by solvent evaporation[16, 18-20, 23, 24].

Mixed precursors can be pelletized and then calcined using one-step heat treatment. For example, Li *et al.*[25] prepared $LiFePO_4$ powders by one-step heat treatment under vacuum at 700℃ for 10 h. The resultant $LiFePO_4$ powders have a particle size of 1 μm with a few aggregations, and the discharge capacity is around 111 mAh/g. Although one-step heat treatment is convenient[18], prepared mixtures are more often heat treated in two steps. The first step (precalcination) is carried out at 250 − 350℃, which is designed for the decomposition of the precursors and expelling of the gases. The second step is the final calcination of powders, which occur at relatively high temperatures (400 − 800℃). The calcination temperature has an important effect on the structure, particle size (particle growth), and discharge capacity of $LiFePO_4$ powders. For example, Yamada *et al.*[16] synthesized $LiFeO_4$ powders by solid-state synthesis at different temperatures and found that the highest discharge capacity of 162 mAh/g was obtained by calcining the homogeneously mixed precursors at 500 − 600℃. Takahashi *et al.*[33] also fabricated $LiFePO_4$ powders by solid-state synthesis and found that the optimum calcination temperature for achieving the highest discharge capacity was 675℃. In addition to the calcination temperature, it is also important to control the calcination atmosphere for avoiding oxidized byproducts, such as Fe_2O_3 and $Li_0Fe_2(PO_4)_3$[16, 18, 23, 24]. Atmospheres that can be used include inert (Ar), slightly reductive ($Ar\text{-}H_2$), reductive ($H_2\text{-}N_2$ or N_2)[16, 18, 23-28], and vacuum conditions[25].

One limitation of pure $LiFePO_4$ powders is their low electrical conductivity, which results in poor rate capability. In solid-state synthesis, the conductivity of $LiFePO_4$ powders can be improved by introducing conductive carbon, which can be obtained by directly adding a carbon source into the precursors. Yun *et al.*[18] prepared $LiFePO_4/C$ powders by solid-state synthesis using polyvinyl alcohol (PVA) as a carbon source. The presence of PVA prevents the particle growth during calcination because the polymer decomposes around the same temperature of $LiFePO_4$ formation. As a result, these $LiFePO_4/C$ powders have small particle sizes ranging from 200 to 300 nm. The maximum capacity achieved in that work was 156 mAh/g, but the cycling performance was poor.

The performance of $LiFePO_4/C$ powders can be improved by using other carbon sources to replace PVA. Fey *et al.*[19] used malonic acid as a carbon source, and the resultant $LiFePO_4/C$ powders (100 – 200 nm) have a discharge capacity 149 mAh/g at C/5 and a good cycling performance. In addition to malonic acid, other carbon sources that have been studied include but not limited to chitosan, glucose, cellulose acetate, and sucrose[20, 29, 30].

In addition to carbon, metal dopants can be added in solid-state synthesis to adjust the structure and performance of $LiFePO_4$ powders. Mi *et al.*[31] used Nb_2O_5 as a metal dopant to form Nb-doped $Li_{0.99}Nb_{0.01}FePO_4$ powders by solid state synthesis. $MnCO_3$ has also been used as a metal dopant to produce $LiFe_yMn_{1-y}PO_4$ powders with enhanced conductivity.

Solid-state synthesis is of importance in terms of obtaining unique structures; however, reactions take place in a solid phase, which requires high temperature, high energy, long processing time, repeated grinding, and special atmosphere. As a result, the product cost of solid-state synthesis is relatively high.

3.2. Mechanochemical activation

Mechanochemical activation is one of the most common methods for preparing metal and alloy powders, and is mainly based on increasing the chemical reactivity of the mixtures by high-energy ball milling. The main reasons for the enhancement of reactivity can be given as: the formation of free valences on the outermost layer of the material and the increase in the surface area where reactions take place. Mechanochemical activation enables the preparation of powders with relatively low particle size and high surface area. However, mechanochemical activation also has some drawbacks, such as higher impurity stemmed from the milling medium and the rise of temperature during the high-energy milling process[34]. For the synthesis of $LiFePO_4$ powders, the temperature rise during high-energy ball milling may contribute to the decomposition of precursors, but is not sufficient for the formation of $LiFePO_4$ crystalline structure[34-36]. Therefore, mechanochemical activation is generally used as a preparation step prior to the classical solid-state synthesis, and the aim is to have the smallest possible particle size to drive the reactions at lower temperatures. Franger *et al.*[23] compared different synthesis methods and found that $LiFePO_4$ powders prepared by the mechanochemical activation have pure, uniform, and well-crystallized structure, and present higher specific capacity (150 mAh/g at C/5) than those prepared by conventional solid-state synthesis.

Table 2 shows typical precursors used in the mechanochemical activation method and the particle size and electrochemical performance of the resultant $LiFePO_4$ powders. As shown in **Fig. 3**, typical procedure starts with activating mixed precursors using high-energy ball-milling for 3 – 15 hours, depending on the desired particle size, in air[37] or in an inert atmosphere[38]. Mechanochemically activated mixtures are then pelletized and calcined at elevated temperatures at 600 – 900℃ in appropriate atmosphere such as 95% Ar + 5% H_2[37], N_2[38], or vacuum[39] for 0.5 – 10 hours[37-39].

To improve the electrical conductivity of $LiFePO_4$ powders, carbon materials, such as graphite, carbon black, and acetylene black, can be added to the mixtures during high-energy ball milling[37]. As reported by Shin *et al.*[37], among these three carbon materials, graphite gave the highest conductivity with the highest stability and capacity (141 mAh/g at C/10) because of its low charge transfer resistance and low ion migration resistance. The dispersion of carbon in $LiFePO_4/C$ composite powders is important. Porcher *et al.*[40] investigated the effect of surfactants on the dispersion of carbon black in the $LiFePO_4/C$ powders, which were produced by using mechanochemical activation. In their work, three different types of surfactants (anionic, non-ionic, and cationic) were added during the electrode preparation process. It was found that non-ionic surfactant (Triton X-100) led to more homogeneous carbon dispersion and the resultant $LiFePO_4/C$ powders have better electrochemical performance than those prepared using ionic surfactants.

In addition to carbon, Fe_2P can be used to modify the conductivity of $LiFePO_4$ powders. Kim *et al.*[39] produced pure $LiFePO_4$ and $LiFePO_4/Fe_2P$ powders by mechanochemical activation, followed by calcination at 900℃ for different time intervals under 10^{-6} Torr pressure. Pure $LiFePO_4$ showed a discharge capacity of 162 mAh/g and good capacity retention. As reported, Fe_2P had an important effect on the conductivity of the powders, especially at higher concentrations; however, lower capacity values were obtained mainly because of the increase in particle size and decrease in surface area. Maximum initial discharge capacity obtained was 113 mAh/g for $LiFePO_4/Fe_2P$ powders (Fe_2P : 8 wt. %).

Table 2 Precursors used in the mechanochemical activation method, and particle size and electrochemical performance of the resultant $LiFePO_4$ powders

Li Precursor	Fe Precursor	P Precursor	Carbon Source	Molar Ratio	Product	Particle Size (nm)	Discharge Capacity (mAh/g)	Ref
Li_3PO_4	$Fe_3(PO_4)_2 \cdot 5H_2O$		Sucrose	1:1	$LiFePO_4/C$		150 (C/5)	23
Li_2CO_3	$FeC_2O_4 \cdot 2H_2O$	$(NH_4)_2HPO_4$	Graphite	1:1:1	$LiFePO_4/C$	100-300	141 (C/10)	37
Li_2CO_3	$FeC_2O_4 \cdot 2H_2O$	$(NH_4)_2HPO_4$	Acetylene black	1:1:1	$LiFePO_4/C$	60-115	152 (C/10)	38
Li_2CO_3	$FeC_2O_4 \cdot 2H_2O$	$(NH_4)_2HPO_4$	Acetylene black	1:1:1	$LiFePO_4/C$	65-90	166 (C/10)	38
$LiOH \cdot H_2O$	Fe_2O_3	$(NH_4)_2HPO_4$	Acetylene black	1:0.5:1	$LiFePO_4/Fe_2P$	100-1,000	113-122 (C/5)	39
$LiOH \cdot H_2O$	Fe_2O_3	$(NH_4)_2HPO_4$		1:0.5:1	$LiFePO_4$	100-1,000	162 (C/20)	39
Li_3PO_4	$FeSO_4 \cdot 7H_2O$	Na_3PO_4	Sucrose	1.05:3:2	$LiFePO_4/C$		140 (C/10)	40
Li_3PO_4	$FeSO_4 \cdot 7H_2O$	BPO_4	Sucrose	1:3:2	$LiFePO_4/C$		160 (C/10)	41
$LiOH \cdot H_2O$	$FeC_2O_4 \cdot 2H_2O$	$(NH_4)_2HPO_4$		1:1:1	$LiFePO_4$	100-2,000	115 (C/10)	42
$LiOH \cdot H_2O$	$FeC_2O_4 \cdot 2H_2O$	$(NH_4)_2HPO_4$	Carbon black	1:1:1	$LiFePO_4/C$	100-1,000	140 (C/10)	42
Li_2CO_3	$FeC_2O_4 \cdot 2H_2O$	$NH_4H_2PO_4$		1:1:1	$LiFePO_4$		110-120 (C/10)	43
$LiOH \cdot H_2O$	Fe_2O_3	$(NH_4)_2HPO_4$	Acetylene black	1:0.5:1	$LiFePO_4$	100-2,000	140 (C/20)	44
Li_3PO_4	$FeSO_4 \cdot 7H_2O$	BPO_4	Sucrose	1:1:1	$LiFePO_4/C$		110 (C/10)	45

The particle sizes of $LiFePO_4$ and $LiFePO_4/C$ powders prepared by mechanochemical activation are typically in the range of 60 – 300 nm[37, 38]. In addition to conventional mechanochemical activation, modified methods can be designed to further reduce the particle size. Kim *et al.*[38] prepared $LiFePO_4/C$ powders by mixing the precursors with distilled water for 7 hours, evaporating the water, high-energy ball milling for 15 h under Ar atmosphere, powder pressing in order to obtain pellets, and thermal processing at 600 ℃ for 10 h under N_2 atmosphere. Using this modified mechanochemical activation method, the particle size of the resultant $LiFePO_4/C$ powders reduced from 60 – 115 nm to 65 – 90 nm. As a result, the modified method gave better and more uniform carbon coating, larger specific surface area, and higher electronic conductivity. The discharge capacity for $LiFePO_4/C$ powders obtained by the modified method is 166 mAh/g at C/10 and 154 mAh/g at C/2, respectively.

3.3. Carbothermal reduction

In both conventional solid-state synthesis and mechanochemical activation methods, Fe(II) compounds are used as the Fe precursor for $LiFePO_4$ powders. However, it is often challenging to prevent the oxidation of unstable Fe(II), which tends to form Fe(III) as the impurity during the $LiFePO_4$ formation. Recently, carbothermal reduction is gaining attention because it allows the direct use of Fe(III) compounds as Fe precursor. In general, Fe(III) compounds are relatively cheap, readily available, and chemically stable when compared with Fe(II) compounds.

Carbothermal reduction is a high-temperature reduction reaction, which utilizes a carbon source as the reducing agent. Carbon black, graphite, and pyrolyzed organic chemicals are commonly used reducing agents. Carbothermal reduction is a highly endothermic reaction, and hence the critical energy, which is given to the synthesis environment, must be high enough to drive the reaction. In addition, since solid carbon is used as the reducing agent, it is important to keep all precursors/reactants in good contact with each other throughout the reaction. The mechanism and reaction rate are closely related with the particle sizes of precursors and reducing agents, mixing conditions, diffusion rates, gas concentration, and impurities in the environment[46-48]. Properties of the resultant powders depend on the processing conditions such as temperature, pressure, precursors, and reducing agents.

When used to produce $LiFePO_4$ powders, the carbothermal reduction method is excellent for the reduction of Fe(III), stabilization of Fe(II), control of particle morphology, and enhancement of electrical conductivity by coating $LiFePO_4$ with residual carbon. Studies show that, compared with other solid-state methods, carbothermal reduction is an energy efficient approach to produce $LiFePO_4$ powders with fine, uniform particle morphology and high capacity[3, 48-50]. **Table 3** shows the precursors used in the carbothermal reduction method, and the particle size and discharge capacity of the resultant $LiFePO_4$ powders. Typical procedure includes two major steps: mixing stoichiometric amounts of precursors and reducing agents by ball milling for 2 – 4 hours, and calcining (generally without precalcination) the mixtures at a temperature between 550 and 850℃ for 8 – 10 hours in an inert atmosphere, such as N_2 or Ar (**Fig. 3**). During the calcination process, two main carbon oxidation reactions occur to reduce Fe(III) to Fe(II)[48]

Table 3 Precursors used in the carbothermal reduction method, and particle size and electrochemical performance of the resultant $LiFePO_4$ powders

Li Precursor	Fe Precursor	P Precursor	Metal Dopant	Reducing Agent and Carbon Source	Molar Ratio	Product	Particle Size (nm)	Discharge Capacity (mAh/g)	Ref
LiH_2PO_4	Fe_2O_3		$Mg(OH)_2$	Carbon	1:0.45:0.1	$LiFe_{0.9}Mg_{0.1}PO_4$	100, 000	151 (C/20)	48
Li_2CO_3	$FeSO_4 \cdot 7H_2O$	$NH_4H_2PO_4$		Carbon	1:2:2	$LiFePO_4$/C	100-300	156 (C/10)	49
Li_2CO_3	$FePO_4 \cdot 4H_2O$			Acetylene black	1:2	$LiFePO_4$/C	1,000-3,000	133 (C/10)	51
Li_2CO_3	Fe_2O_3	$NH_4H_2PO_4$		Glucose, Carbon black	1:1:1	$LiFePO_4$/C	300-1,000	159 (C/10)	52
Li_2CO_3	$FePO_4$			Glucose	0.5:1	$LiFePO_4$/C	2,490	151 (C/5)	53
Li_2CO_3	Fe_2O_3	$(NH_4)_2HPO_4$		Ferric citrate	1:1:1	$LiFePO_4$/C		135 (C/10)	54
LiH_2PO_4	Fe_2O_3			Glucose	2:1	$LiFePO_4$/C	1,330	154 (C/5)	55
$LiOH \cdot H_2O$	$Fe(NO_3)_3$	$NH_4H_2PO_4$		$C_3H_8O_2$:H_2O, Sucrose	1:1:1	$LiFePO_4/(C+Fe_2P)$	36	157 (C/10)	56
Li_2CO_3	$Fe(NO_3)_3 \cdot 9H_2O$	$NH_4H_2PO_4$		Citric acid	1:1:1	$LiFePO_4$/C		150 (C/10)	57
LiH_2PO_4	$Fe(NO_3)_3 \cdot 9H_2O$			Polycarboxylic acid, Polyhydric alcohol	1:1	$LiFePO_4$/C		134 (C/100)	58

$$\mathrm{C + O_2 \rightarrow CO_2} \qquad (T < 650^\circ\mathrm{C}) \tag{1}$$

$$\mathrm{2C + O_2 \rightarrow 2CO} \qquad (T > 650^\circ\mathrm{C}) \tag{2}$$

Both the volume and entropy changes in Reaction (1) are negligible and the reaction produces less reductive atmosphere. However, Reaction (2) occurs at temperatures higher than 650℃, which results in a stronger reducing condition than Reaction (1), and the volume and entropy increases are significant[48].

In carbothermal reduction, processing conditions, especially calcination temperature, are of great importance for the morphological and electrochemical performance of the resultant powders. Mi *et al.*[50] synthesized $LiFePO_4$/C powders by using $FePO_4$ as the Fe precursor and polypropylene as the reducing agent and carbon source. Calcination was carried out at 650℃ for 10 h under N_2 atmosphere without any pre-calcination step. The pyrolysis of polypropylene during the calcination ensured the reduction of Fe(III) to Fe(II). The resultant $LiFePO_4$/C powders have homogeneous carbon coating with particle sizes ranging from 100 to 300 nm. Initial discharge capacity was 160 mAh/g (C/10) at 30℃ . Liu *et al.*[51] synthesized $LiFePO_4$/C powders by the carbothermal reduction method using different calcination temperatures. The best calcination temperature was reported as 750℃, which produced powders with an initial discharge capacity of 133 mAh/g at C/10 and capacity retention of 96% after 20 cycles. Liu *et al.*[52] used cheap Fe_2O_3 as the Fe source and carbon black and glucose as the reducing agent and carbon source. The effects of calcination temperature on the particle size and electrochemical performance of $LiFePO_4$/C powders were investigated. When the precursors were treated with glucose at 700℃ for 8 h, the best performance was obtained: the capacity was 159 mAh/g at C/10 and the cycling fading was 2.2% at the end of 30 cycles. It was also found that the use of high concentration carbon source not only decreased the particle size but also enhanced the cycle life.

The distribution of particle size can also be controlled during the carbothermal reduction. Wang *et al.*[53] synthesized $LiFePO_4$/C powders by using $FePO_4$ as the iron source and glucose as the reducing agent and carbon source. $LiFePO_4$/C powders with uniform particle size distribution were obtained when the precursors were calcined at 650℃ for 9 h. The discharge capacities of these powders are 151 mAh/g at C/5 rate and 144 mAh/g at 1C rate, respectively. Zhong *et al.*[54] prepared high tab-density $LiFePO_4$/C powders by the carbothermal reduction method using Fe_2O_3 and ferric citrate as the Fe (III) source with an equimolar ratio. It was found that the resultant $LiFePO_4$/C powders consisted of nanometer-sized and micrometer-sized particles, and showed tri-modal particle size distribution with good discharge capacity (135 mAh/g at C/10). In these powders, the small particles filled the free space between the bigger particles, and led to high tap density (1.4 g/cm^3).

In addition to particle size and its distribution, the processing conditions also influence the crystallization degree of $LiFePO_4$ powders. One important contribution of high crystallization degree is that it can suppress the dissolution of $LiFePO_4$ during cycling and leads to improved cycling behavior[55]. Therefore, in order to obtain good electrochemical performance, it is important to determine the optimum crystallization degree. Zhi *et al.*[55] studied the effect of calcination temperature on the crystallinity degree and electrochemical performance of $LiFePO_4$/C powders obtained by carbothermal reduction. It was found that the powders calcined at lower temperatures have lower degree of crystallization with nano-sized structure, which leads to higher electrochemical activity and larger initial discharge capacity. But, they showed unsatisfactory cycling performance because of their metastable structures.

To obtain optimized powder structure and performance, modified carbothermal reduction methods were also developed. Liu *et al.*[56] designed a modified process by introducing amorphous gel precursor into conventional carbothermal reduction, and they obtained $LiFePO_4/(C+Fe_2P)$ and $LiFePO_4/C$ composite powders. While $LiFePO_4/C$ showed a discharge capacity of 146 mAh/g, $LiFePO_4/(C+Fe_2P)$ has a higher capacity of 157 mAh/g, which was attributed to the enhanced conductivity caused by Fe_2P in the structure. Yu *et al.*[57] prepared $LiFePO_4/C$ powders by combining carbothermal reduction with spray drying and used different carbon sources (such as carbon black, sucrose, citric acid and polyethylene glycol (PEG)) as the reducing agents. As reported, the best electrochemical performance was obtained from citric acid-added powders, which were calcined at 539℃. It was also found that 453℃ was the crystallization temperature of $Li_3Fe_2(PO_4)_3$, 539℃ was the transform temperature from $Li_3Fe_2(PO_4)_3$ to $LiFePO_4$, 840℃ was the formation temperature of $LiFePO_4/C$ with an excess of Fe_2P impurity phase, and 938℃ was the decomposition temperature of $LiFePO_4/C$. Recently, Zhu *et al.*[49] synthesized $LiFePO_4$ powders from $FeSO_47H_2O$ and $NH_4H_2PO_4$ by combining the carbothermal reduction and aqueous precipitation methods. The resultant $LiFePO_4/C$ powders showed capacities ranging from 95 – 156 mAh/g at C/10, depending on the processing conditions.

3.4. Microwave heating

Microwave heating is another easy and useful method for producing $LiFePO_4$ powders[59-63]. Unlike other solid-state methods, microwave heating is a molecular level heating process, which allows volumetric heating of the material by the absorption of microwave energy. In microwave heating, the heat is generated directly inside the material and is caused by the change of polarization that is activated by the motion of electric charges. Heating rate is controlled by the power of the microwave and heat dissipation occurs through the surface of the material.

Major advantages of microwave heating include good controllability, uniform and selective heating, short processing time (2 – 20 min), reduced energy consumption, and low cost. In addition, microwave heating is a low temperature process with good repeatability and no reductive gas is required for the synthesis of $LiFePO_4$ powders[59-66]. Higuschi *et al.*[59] used the microwave heating method to obtain $LiFePO_4$ powders with an initial discharge capacity of around 125 mAh/g at 60℃ with low capacity loss. Guo *et al.*[67] compared $LiFePO_4$ powders synthesized by microwave heating and solid-state synthesis methods. It was found that microwave-processed $LiFePO_4$ powders have smaller particle size, more uniform size distribution, smoother surface morphology, and higher discharge capacity.

In microwaving processing, a microwave absorber is often added to ensure effective heat generation (**Fig. 3**). **Table 4** shows typical precursors, microwave absorbers, and processing time used in the microwave heating methods. Carbon is the most used microwave absorber because it is low cost, produces rapid heating, and is capable of forming reductive atmosphere, which protects Fe(II) and prevents Fe(III) based impurities. As a result, when carbon is used as the microwave absorber, the formation of $LiFePO_4$ powders can be directly carried out in air, which significantly lowers the production cost[60, 64]. In addition, the use of carbon can help to reduce the particle size and improves the electrical conductivity of $LiFePO_4$ powders[68]. Wang *et al.*[61] used active carbon as a microwave absorber to synthesize nano-sized $LiFePO_4$ powders, which have a particle size of 40 – 50 nm and discharge capacity of around 112 mAh/g at C/2. Although carbon is the most used microwave absorber, other materials can be used to enhance the heat generation efficiency, such as Fe[59], glucose[69], and yeast cells[69].

The microwave heating time is of importance for controlling the particle size and electrochemical performance of the powders. Typically, longer microwave heating time causes larger particle size, lower Li diffusion coefficient, and consequently more capacity loss[60]. In addition to increased particle size, some impurities such as Fe_2P can be observed with prolonged heating time[70]. It was found that the amount of Fe_2P in $LiFePO_4$ powders is directly proportional to the heating time, and above a critical amount of Fe_2P, $LiFePO_4$ tends to change into an insulating phase, $Li_4P_2O_7$. However, when the heating time is too short, incomplete crystalline structure can form contaminates in the resultant $LiFePO_4$ powders, which in turn decreases the charge and discharge capacities[66]. Park *et al.*[60] synthesized $LiFePO_4$ using the microwave heating method, and found that a heating time of 4 min is sufficient and can produce $LiFePO_4$ powders that have a specific capacity of 151 mAh/g at C/10 with stable cycling behavior.

Like most other methods, $LiFePO_4$ powders pro-

Table 4 Precursors, microwave absorbers, power, and time used in the microwave heating method, and particle size and electrochemical performance of the resultant $LiFePO_4$ powders

Li Precursor	Fe Precursor	P Precursor	Microwave Absorber	Power (W)	Time (min)	Carbon Source	Molar Ratio	Product	Particle Size (nm)	Discharge Capacity (mAh/g)	Ref
Li_2CO_3	$Fe(CH_3COO)_2$	$NH_4H_2PO_4$		500	5-20		1:1:1	$LiFePO_4$		95 (C/11)	59
Li_2CO_3	$Fe(CH_3CHOHCOO)_2 \cdot 2H_2O$	$NH_4H_2PO_4$	Iron Powder	500	5-20		1:1:1	$LiFePO_4$		100 (C/11)	59
LiOH	$(NH_4)_2Fe(SO_4)_2 \cdot 6H_2O$	H_3PO_4	Activated Carbon	650	4	Carbon black	1:1:1	$LiFePO_4$	1,000	151 (C/10)	60
CH_3COOLi	$FeC_2O_4 \cdot 2H_2O$	$NH_4H_2PO_4$	Activated Carbon	850	A few	Citric acid	1:1:1	$LiFePO_4$	40-50	112 (C/2)	61
Li_3PO_4	$FeSO_4 \cdot 7H_2O$	H_3PO_4	Carbon	300	A few	Glucose	1:1:1	$LiFePO_4/C$	100	117 (C/10)	62
LiOH	$Fe(CH_3COO)_2$	H_3PO_4		600	5		1:1:1	$LiFePO_4$	40 ± 6	135 (C/15)	63
LiOH	$Fe(CH_3COO)_2$	H_3PO_4		600	5	Poly(3,4-ethylenedioxythiophene)	1:1:1	$LiFePO_4/C$	40 ± 6	166 (C/15)	63
$CH_3COOLi \cdot 2H_2O$	$FeSO_4 \cdot 7H_2O$	H_3PO_4	Carbon Black	400	18	Polyethylene glycol	1:1:1	$LiFePO_4/C$	132 - 465	147 (C/10)	66
$LiOH \cdot H_2O$	$FePO_4 \cdot 4H_2O$		Graphite	700	4	Glucose	1:1	$LiFePO_4/C$	160 - 600	150 (C/10)	67
Li_3PO_4	$Fe_3(PO_4)_2 \cdot 8H_2O$		Activated Carbon	750	2-5	Acetylene black	1:1	$LiFePO_4/C$	≤640	161 (C/10)	68
Li_2CO_3	$FePO_4 \cdot 4H_2O$			1000	1.33	Glucose	1:1	$LiFePO_4/C$	50 - 100	162 (C/10)	69
Li_3PO_4	$Fe_3(PO_4)_2 \cdot 8H_2O$			750	2	Acetylene black	1:1	$LiFePO_4/C$		165 (C/50)	70
LiOH	$Fe(CH_3COO)_2$	H_3PO_4		600	5	MWCNT	1:1:1	$LiFePO_4$/MWCNT	40 ± 6	161 (C/10)	71
LiOH	$Fe(CH_3COO)_2$	H_3PO_4		600	5		1:1:1	$LiFePO_4$	40 ± 6	147 (C/10)	71
Li_3PO_4	$C_6H_5FeO_7$	H_3PO_4		300				$LiFePO_4/C$			73
$CH_3COOLi \cdot 2H_2O$	$FeSO_4 \cdot 7H_2O$	Na_2HPO_4	Activated carbon, Yeast cells	650	A few	Yeast cells	1:1:1	$LiFePO_4/C$	35-100	147 (C/10)	74
Li_2CO_3	$FeSO_4 \cdot 7H_2O$	$(NH_4)_2HPO_4$	Carbon Black	300	10	Carbon black,	0.3:1:1	$LiFePO_4/C$			75

duced by microwave heating typically have spherical shape. However, other unique particle structure can be obtained using the microwave heating method. For example, Muraliganth *et al.*[71] synthesized $LiFePO_4$ nanorods (width: 25 – 40 nm; length: 0.1 – 1 μm) using microwave heating. These nanorods were mixed with multi-walled carbon nanotubes (MWCNTs) to improve the conductivity, which resulted in a high discharge capacity of around 161 mAh/g at C/10 with good cyclic performance. Zhou *et al.*[74] synthesized mesoporous $LiFePO_4$ powders by using yeast cells as a template for the porous structure. During the formation of $LiFePO_4$, yeast cells not only connected metal ions chemically but also acted as a reducing agent because of their microwave absorbency. These mesoporous $LiFePO_4/C$ powders have specific capacity of 147 mAh/g at C/10 and good cycle performance. Jegal *et al.*[72] also synthesized mesoporous $LiFePO_4$ spheres, which consisted of smaller particles with average thickness of 2 – 30 nm. The mesoporous structure gave short lithium diffusion length during charge/discharge.

In most cases, traditional continuous microwaves are used to produce $LiFePO_4$ powders. However, other microwave patterns can also be used. For example, Zou *et al.*[69] used intermittent microwave and obtained $LiFePO_4/C$ powders with small particle size, ranging from 50 to 100 nm. The powders have enhanced conductivity and improved capacity (162 mAh/g at C/10).

Microwave heating can also be combined with other methods to produce $LiFePO_4$ powders with controlled structure and performance. Methods that have been combined with microwave heating include: solid-state synthesis[59, 66], mechanochemical activation[68], sol-gel synthesis[66, 73], hydrothermal synthesis[72], solvothermal[71], and co-precipitation[65, 74]. For example, Song *et al.*[68] combined microwave heating (2 – 5 min) with mechanochemical activation (30 min) to obtain $LiFePO_4/C$ powders. The mechanochemical activation decreased the process temperature and led to a uniform distribution of carbon. The average particle size of the resultant $LiFePO_4/C$ powders was ≤ 0.64 μm and the discharge capacity was 161 mAh/g at C/10 with a stable capacity retention. Li *et al.*[75] synthesized $LiFePO_4/C$ powders by combining microwave heating with the co-precipitation method. During the synthesis, beer yeast, a nontoxic, environmentally-friendly, and low cost biosurfactant, was used as a carbon source to increase the material conductivity. Li *et al.*[65] also reported the synthesis of $LiFePO_4$ powders by incorporating the solid state synthesis and microwave heating methods, and these powders have a high specific capacity of around 156 mAh/g at C/20. Zhang *et al.*[66] synthesized $LiFePO_4$/C powders by the combination of sol-gel synthesis and microwave heating, and achieved initial specific capacity of 147 mAh/g at C/10 and good cycling performance.

4. Solution-Based Methods for $LiFePO_4$ Powders

Although solid-state methods are simple to use, they are typically time and energy consuming techniques and often lead to large particle size, low purity, and relatively poor electrochemical performance. Therefore, solution-based methods are of increasing importance since they often result in smaller and more uniform particle size, higher purity, more homogeneous carbon coating, and higher electrochemical capacity. Hydrothermal synthesis, sol-gel synthesis, spray pyrolysis, co-precipitation, and microemulsion drying are common solution-based methods used for the preparation of $LiFePO_4$ powders. General production routes are shown schematically in **Fig. 4**.

4.1. Hydrothermal synthesis

Hydrothermal synthesis is a chemical process that occurs in an aqueous solution of mixed precursors above the boiling temperature of water. In hydrothermal synthesis, it is possible to avoid the calcinations step and obtain pure $LiFePO_4$ powders directly from the heated solution. However, if the carbon coating is desired, it is necessary to carry out the calcination step at higher temperatures. During hydrothermal synthesis, heated water accelerates the diffusion of particles and the crystal growth is relatively fast. Hydrothermal synthesis is typically carried out in a closed system called autoclave and there are less environmental concerns than many other powder production technologies. Therefore, hydrothermal synthesis is a simple, clean, and relatively low-cost method that can be used to produce powders with high uniformity and purity[76-78]. Currently, hydrothermal synthesis has been widely used for the synthesis of oxides, silicates, and some specific compounds with unique characteristics.

Hydrothermal synthesis was first used by Yang *et al.*[79,80] to prepare $LiFePO_4$ powders. As shown in **Fig. 4**, standard hydrothermal synthesis starts with the mixing of precursors with the exact stoichiometric ratio in an aqueous solution. After the homogeneous mixing of the precursors, the solution is treated in an autoclave at a temperature above 100℃, generally between 120 – 220℃ for 5 – 10 h. $LiFePO_4$ powders can then be obtained by drying the slurries or participates[7, 79-85]. $LiFePO_4$ powders produced by hydrothermal synthesis are typically low cost, high purity, and have small grain size and large surface area. In addition, the presence of high-temperature water hinders the oxidation of Fe(II) to Fe(III). **Table 5** shows precursors that have been used in the hydrothermal synthesis of $LiFePO_4$ powders.

Like many other methods, carbon sources can be added to the hydrothermally obtained $LiFePO_4$ powders to enhance the conductivity. However, in this case, an additional heat-treatment (or calcination) step should be carried out at elevated temperatures such as 400 – 750℃ for 0.5 – 12 h under N_2 or argon atmosphere in order to carbonize the carbon source[79, 83-86]. Carbon sources used include sugar,

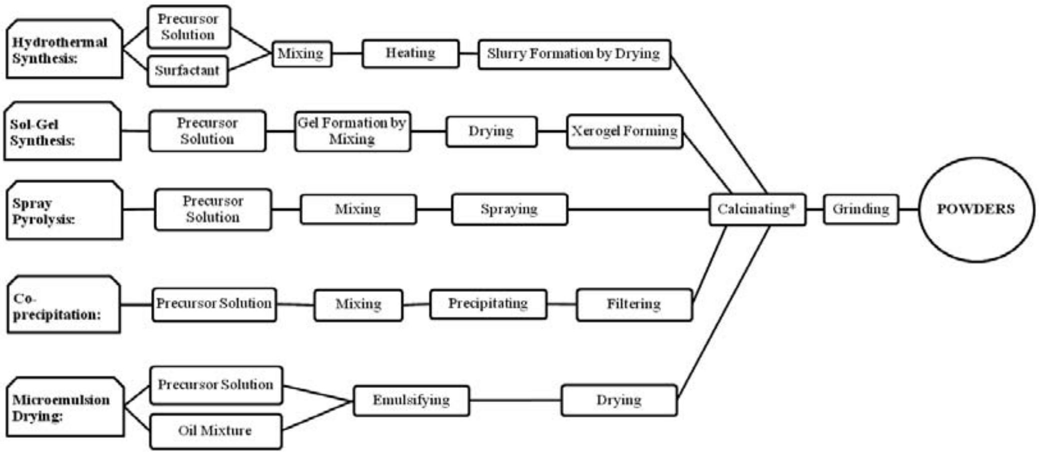

Fig. 4 Typical routes for producing $LiFePO_4$ powders using solution-based methods.

Table 5 Precursors used in the hydrothermal synthesis method, and particle size and electrochemical performance of the resultant $LiFePO_4$ powders

Li Precursor	Fe Precursor	P Precursor	Metal Dopant	Carbon Source	Molar Ratio	Product	Particle Size (nm)	Discharge Capacity (mA/g)	Ref
CH_3COOLi	$FeC_2O_4{\cdot}2H_2O$	$NH_4H_2PO_4$	Iron wire	Sugar	1:1:1	$LiFePO_4/C$		136 (1C)	7
$LiOH{\cdot}H_2O$	$(NH_4)_2Fe(SO_4)_2$	H_3PO_4		Ascorbic acid	3:1:1	$LiFePO_4$		160	17
Li_3PO_4	$Fe_3(PO_4)_2{\cdot}5H_2O$			Sucrose		$LiFePO_4/C$	1,000	140 (C/10)	23
Li_3PO_4	$FeSO_4{\cdot}7H_2O$	Na_3PO_4		Sucrose (5wt.%)	1:1:1	$LiFePO_4/C$		160 (C/20)	45
LiOH	$FeSO_4$	H_3PO_4		Sucrose	3:1:1	$LiFePO_4/C$	3,000	100 (0.14C)	79
CH_3COOLi	$FePO_4{\cdot}2H_2O$			Carbon gel	1.2:1	$LiFePO_4/C$		148 (C/2)	80
LiOH	$FeSO_4{\cdot}7H_2O$	H_3PO_4		Sucrose , Ascorbic acid, CNT	3:1:1	$LiFePO_4/C$	3,000-5,000	145 (0.3C)	81
$LiOH{\cdot}H_2O$	$FeSO_4{\cdot}7H_2O$	H_3PO_4		Ascorbic acid, sugar	3:1:1	$LiFePO_4/C$	1,000-3,000	90 (0.15C)	82
$LiOH{\cdot}H_2O$	$FeSO_4{\cdot}7H_2O$	$(NH_4)_3PO_4{\cdot}3H_2O$		Ascorbic acid	2.5:1:1	$LiFePO_4$	100-200	167 (C/10)	83
LiOH	$FeSO_4{\cdot}7H_2O$	H_3PO_4		CTAB ($C_{19}H_{42}BrN$)	3:1:1	$LiFePO_4/C$	50	135 (C/10)	84
LiOH	$FeSO_4{\cdot}7H_2O$	H_3PO_4		CTAB ($C_{19}H_{42}BrN$)	3:1:1	$LiFePO_4/C$	20-30	145 (C/10)	85
$LiOH{\cdot}H_2O$	$FeSO_4{\cdot}7H_2O$	H_3PO_4	$MgSO_4{\cdot}7H_2O$	Glucose	3:0.98:1:0.02	$LiMg_{0.02}Fe_{0.98}PO_4$	500-1,000	144 (C/5)	86
$LiOH{\cdot}H_2O$	$FeSO_4{\cdot}7H_2O$	H_3PO_4		Ascorbic acid, Carbon black (3, 5, 10w%)	3:1:1	$LiFePO_4/C$	100-200	128 (C/10)	87
$LiOH{\cdot}H_2O$	$FeSO_4{\cdot}7H_2O$	H_3PO_4		Ascorbic acid w/ CNT	3:1:1	$LiFePO_4/C$	3,000-5,000	153 (0.15C)	88
$LiOH{\cdot}H_2O$	$FeSO_4$	H_3PO_4		Hydrazine	3:1:1	$LiFePO_4/C$	3,000-5,000	80 (0.15C)	88
$LiOH{\cdot}H_2O$	$FeSO_4{\cdot}7H_2O$	H_3PO_4		MWCNTs	3:1:1	$LiFePO_4$/MWCNTs		160 (0.3C)	89
$LiOH{\cdot}H_2O$	$FeSO_4{\cdot}7H_2O$	H_3PO_4		Citric acid	3:1:1	$LiFePO_4/C$	200-500		90
LiOH	$FeSO_4{\cdot}7H_2O$	H_3PO_4			3:1:1	$LiFePO_4$			91
LiOH	$FeSO_4{\cdot}7H_2O$	H_3PO_4			3:1:1	$LiFePO_4$	1,000-2,000		92
Li_3PO_4	$FeSO_4{\cdot}7H_2O$	H_3PO_4			1:3:2	$LiFePO_4$	3,000-10,000		93
Li_3PO_4	$FeSO_4{\cdot}7H_2O$			Sucrose	1:1	$LiFePO_4/C$	100	140 (C/10)	93
$LiOH{\cdot}H_2O$	$(NH_4)_2Fe(SO_4)_2{\cdot}6H_2O$	H_3PO_4			3.75:1:1	$LiFePO_4$		90 (C/100)	94

L-ascorbic acid, carbon, MWCNTs, and organic surfactant cetyl trimethyl ammonium bromide (CTAB), which not only increase the conductivity but also act as the reducing agent to prevent the oxidation of Fe(II) during calcination[79, 81-84, 86-88]. Chen *et al.*[82, 88] studied the effect of different carbon sources, such as hydrazine, ascorbic acid, sugar, carbon black, and MWCNTs, and found that ascorbic acid gave $LiFePO_4/C$ powders with the highest discharge capacity of 153 mAh/g at 0.15C. In addition, Xu *et al.*[89] prepared MWCNT-coated $LiFePO_4$ by hydrothermal synthesis, followed by calcination. These $LiFePO_4$-MWCNT (5 wt.%) powders showed an initial discharge capacity of 160 mAh/g at 0.3C, and the capacity fading was only 0.4% after 50 cycles. However, the agglomeration of MWCNT particles was observed at higher MWCNT concentrations. In addition to carbon, metal can be doped into $LiFePO_4$ powders to improve the conductivity. For example, Ou *et al.*[86] synthesized Mg-doped $Li_{0.08}Mg_{0.02}FePO_4$ by hydrothermal synthesis at 180℃ for 6 h, followed by calcination at 750℃ for 6 h.

During hydrothermal synthesis, organic surfactants are often used to improve the dispersion of precursors and increase the specific surface area of final products. Meligrana *et al.*[84] prepared $LiFePO_4$ powders by hydrothermal synthesis and investigated the effect of organic surfactants on the morphological and electrochemical properties of $LiFePO_4$ powders. It was found that the pyrolysis of surfactants increased the material conductivity and generated a reductive environment for avoiding the oxidation of Fe(II) to Fe(III). As a result, the cycling performance and discharge capacity increased noticeably after the addition of surfactants. Zhang *et al.*[90] also prepared monodispersed and well-crystallized $LiFePO_4$ powders by the hydrothermal synthesis of Fe(II)-citric acid complex precursors at 180℃ and the application of isopropanol as a surfactant. It was found that the powder morphology was significantly influenced by the volume ratio of isopropanol to water. Monodispersed short rod-like $LiFePO_4$ crystals were obtained when equal volume isopropanol and water were used, and the particle size was in the range of 200 – 500 nm. However, when isopropanol was absent, column-like $LiFePO_4$ particles were obtained, and the particle size was in the range of 800 – 1100 nm.

Water temperature is one of the most important parameters for the hydrothermal synthesis process because reaction rate, ionization degree, particle size and crystalline structure of $LiFePO_4$ powders are all temperature dependent. Chen *et al.*[81] investigated the effect of water temperature on the structure and performance of $LiFePO_4$ powders. It was found that the water temperature is directly related with the crystal structure and must be above 170℃ to produce correct lattice parameters. With a water temperature of above 170℃, they obtained $LiFePO_4$ powders with a discharge capacity of 145 mAh/g, which did not decay even after 50 cycles. Jin *et al.*[83] also synthesized $LiFePO_4$ powders by hydrothermal synthesis at 150, 170 and 200℃ for 10 h, followed by an additional calcination step. $LiFePO_4$ powders hydrothermally synthesized at 170℃ and calcined at 500℃ have the highest discharge capacity of 167 mAh/g at C/10. This value is one of the highest capacities reported for $LiFePO_4$ powders in the literature. The average particle size of these $LiFePO_4$ powders was in the range of 100 – 200 nm. Although the water temperature is typically above 170℃, there is report on obtaining $LiFePO_4$ powders using a temperature below 170℃. For example, Jin *et al.*[87] synthesized $LiFePO_4$ powders by hydrothermal synthesis at 150℃. These $LiFePO_4$ powders were assembled into cells with solid polymer electrolyte, which showed higher discharge capacity when compared with $LiFePO_4$ cells using liquid electrolyte.

In addition to the water temperature, the flow rate of water and the concentrations of precursors have significant influence on the structure and electrochemical properties of $LiFePO_4$ powders. Xu *et al.*[91] prepared $LiFePO_4$ powders at different water flow rates and precursor concentrations. It was found that high flow rates led to more uniform particles and higher precursor concentrations resulted in larger particle size.

Recently, supercritical hydrothermal synthesis was developed to produce $LiFePO_4$ powders. Lee *et al.*[92] carried out the $LiFePO_4$ synthesis under sub and supercritical water at different temperatures, pH values, and reaction times. It was found that neutral or slightly basic pH was required for the successful synthesis of $LiFePO_4$ powders. Supercritical water gave smaller particle size ranged in the submicron scale and lower reactant concentration led to better particle size distribution. In addition, the heating time should be short in order to prevent the growth and agglomeration of particles. In a similar study, the same authors obtained $LiFePO_4$ powders by supercritical water with a capacity of 140 mAh/g at C/10, which is higher than that achieved by the subcritical approach[93].

So far, most $LiFePO_4$ powders were produced using the batch hydrothermal synthesis approach. However, a continuous hydrothermal synthesis route can be used for the mass production of $LiFePO_4$ powders[91]. Aimable *et al.*[94] prepared $LiFePO_4$ powders by continuous hydrothermal synthesis and investigated the effects of heating temperature and time on the morphological and electrochemical properties of $LiFePO_4$ powders. It was found that, with increase in temperature from subcritical to supercritical water conditions and increase in time from 6 to 12 s, well-crystalline and impurity-free $LiFePO_4$ powders were produced. Although the discharge capacities of these $LiFePO_4$ powders were only 90 mAh/g at C/100 and 75 mAh/g at C/10, it can be improved with a carbon coating.

4.2. Sol-Gel synthesis

Sol-gel synthesis is a low temperature, wet chemical approach, which is often used for the preparation of metal oxides or other specific compositions. Standard sol-gel synthesis involves the formation of a sol, *i.e.*, a stable colloidal suspension of solid particles in a solvent, and the gelation of the sol to form a gel consisting of interconnected rigid skeleton with pores made of colloidal particles. The properties of the gel are determined by the particle size and cross-linking ratio[95-98]. The gel can then be dried to form xerogel, which shows reduced volume[95-98]. To obtain the final powder products, all liquids need to be removed from the surface of pores by a heat treatment carried out at elevated temperatures, which also reduces the number and connectivity of pores, known as densification[97, 98]. Reaction parameters, such as temperature, time, pH, precursor, solvent, concentration, and viscosity, etc., are of importance for the formation and ultimate morphology (particle size and shape, pore size, and porosity) of the obtained powders. In sol-gel synthesis, the surfaces of the powder products are controlled from the beginning of reactions. In addition, sol-gel synthesis is low cost and does not require high processing temperature, and powders produced by this method have the advantages of precise stoichiometry control, high purity, uniform structure, and very small size.

Sol-gel synthesis has become an important means to prepare $LiFePO_4$ powders[99, 100]. Dominko *et al.*[101] compared $LiFePO_4$ powders prepared by sol-gel and solid-state synthesis methods. Powders prepared by sol-gel synthesis have more micropores and higher capacity (150 mAh/g at C/10) than those by solid-state synthesis (130 mAh/g at C/10). Hsu *et al.*[102] also used the sol-gel synthesis method to prepare $Li_{0.99}Al_{0.01}FePO_4$ powders, and they found that the sol-gel synthesis gave powders with higher conductivity when compared with the solid-state route. The resultant specific capacity was about 150 mAh/g at C/40 rate.

As shown in **Fig. 4**, during the sol-gel synthesis of $LiFePO_4$ powders, precursor solutions are mixed to form sols, which are vigorously stirred at 60 – 80℃ for 12 – 24 h in order to obtain wet gel[103, 104]. After the gelation, wet gel is dried in a vacuum or in argon atmosphere at 80℃ for 12 h in order to produce xerogel[103, 104]. Finally, xerogel is calcined either in one or two steps at 500 – 900℃ for 3 – 30 h to produce $LiFePO_4$ powders[102-105]. In general, a slow heating rate during calcination causes rougher and relatively less porous structure. On the other hand, with a high heating rate, more porous structure can be obtained, which also affects the electrochemical properties of $LiFePO_4$ powders[101].

Different precursors and solvents have been used in sol-gel synthesis to produce $LiFePO_4$ powders (**Table 6**). The type of solvent is extremely important for the control of powder structure. Water is the most used solvent, but organic solvent can also be used in sol-gel synthesis[105-106]. For example, Yang *et al.*[105] synthesized $LiFePO_4$ powders by sol-gel synthesis and used ethylene glycol as a solvent. These $LiFePO_4$ powders have a specific capacity of 165 mAh/g at C/100 and 150 mAh/g at both C/5 and 2C, which is the indication of good rate capacity. Li *et al.*[107] used ethanol-based sol-gel synthesis method, which took relatively shorter synthesis time when compared with water-based sol-gel synthesis.

$LiFePO_4$ powders obtained by sol-gel synthesis often have pores in the range of 30 – 200 nm. For example, Dominko *et al.*[103] synthesized porous $LiFePO_4/C$ powders, which have pore size between 60 and 90 nm and initial capacities of 160, 140 and 120 mAh/g at C/20, C/2 and 5C, respectively. During the formation of porous $LiFePO_4$ powders, the agglomeration tendency can be reduced noticeably by using surfactants[108]. Choi *et al.*[108] prepared porous $LiFePO_4$ powder with a narrow particle size distribution (100 – 300 nm) by employing lauric acid as a surfactant and achieved discharge capacities of 123, 157 and 170 mAh/g at 10C, 1C and C/10, respectively. The presence of pores not only increases the specific surface area but also shortens the transportation pathway of lithium inside the material. The porous structure is useful especially if the pores are covered by an electrical conductor[102-105, 108].

The most common approach to create an electrically conducting coating on the pore surface is by directly adding a carbon source during sol-gel synthesis[103, 109, 110]. The carbon source not only improves the electrical conductivity of $LiFePO_4$ powders, but also contributes to the formation of the porous structure through the degradation and pyrolysis processes. In addition, the presence of carbon source enhances the uniform growth of $LiFePO_4$ particles with relatively small sizes by decreasing the aggregation tendency[102, 105, 109]. The thickness of the carbon layer can be as low as 1 – 2 nm in the form of amorphous carbon or graphene-rich phase[104, 109, 110]. Sucrose and citric acid are the most commonly used carbon sources for the sol-gel method[103, 104, 110]. Kim *et al.*[104] used sucrose and citric acid as the carbon sources to synthesize porous $LiFePO_4/C$ powders, in which the pore surfaces are covered by a graphine-rich carbon layer of 2 – 4 nm thick. It was found that these porous $LiFePO_4/C$ powders showed high discharge capacities of 153 and 94 mAh/g at C/10 and 5C, respectively, which are probably caused by the large surface areas of the porous structures. In addition to sucrose and citric acid, other carbon sources can be used. For example, Li *et al.*[107] used PEG and D-fructose as the carbon source and obtained porous $LiFePO_4/C$ powders with the highest specific capacities of 130.9 and 157.7 mAh/g at 1C and C/5, respectively. One advantage of the sol-gel synthesis method is the relatively easy control of carbon coating thickness. Dominko *et al.*[110] synthesized $LiFePO_4/C$ powders with different carbon layer thicknesses ranging from 1 to 10 nm, which are among the lowest values in the literature. These $LiFePO_4/C$ powders have high discharge capacity of 150 mAh/g at C/5.

In addition to carbon coating, metal dopants can also be added to modify the structure and electrochemical performance of $LiFePO_4$ powders. Wang *et al.*[111] doped Mg, Zr, and Ti metals into the crystal structure of $LiFePO_4$ powders and they found that the Ti doping led to the highest discharge capacity, which is around 160 mAh/g at C/8. Lee *et al.*[112] also prepared sulfur-doped $LiFePO_{3.98}S_{0.03}$ powders by sol-gel synthesis in order to enhance the performance of the $Li/LiFePO_4$ cells at high temperatures. They obtained good discharge capacities of around 155 mAh/g at all temperatures because of the improved stability caused by the substitution of O^{2-} with S^{2-}.

4.3. Spray pyrolysis

Spray pyrolysis is an important method for the preparation of ultrafine powders[119, 120], and it is based on the generation of droplets in a continuous way from a solution containing precursor colloidal particles. Droplets can be generated by using different techniques, such as ultrasonic transduction[121] and

Table 6 Precursors used in the sol-gel synthesis method, and particle size and electrochemical performance of the resultant $LiFePO_4$ powders

Li Precursor	Fe Precursor	P Precursor	Metal Dopant	Solvent	Carbon Source	Molar Ratio	Product	Pore* or Particle Size (nm)	Discharge Capacity (mAh/g)	Ref
$LiOH{\cdot}H_2O$	$Fe(NO_3)_3{\cdot}9H_2O$	H_3PO_4		Methanol	Ascorbic acid	1:1:1	$LiFePO_4/C$	100, 000	80 (C/5)	14
Li_3PO_4	$FeC_6H_5O_7{\cdot}nH_2O$	H_3PO_4		Deionized water		1:3:2	$LiFePO_4$		117	17
Li_3PO_4	$C_6H_5FeO_7$	H_3PO_4		Deionized water		1:3:2	Porous $LiFePO_4/C$	*90	150 (C/10)	101
$LiNO_3$	Iron powder	$NH_4H_2PO_4$	$Al(NO_3)_2{\cdot}6H_2O$	Deionized water	Citric acid	0.99:1:1:0.01	$Li_{0.99}Al_{0.01}FePO_4/C$	50	150 (C/40)	102
Li_3PO_4	$C_6H_5FeO_7$	H_3PO_4		Deionized water	Citric acid	1:3:2	Porous $LiFePO_4/C$	*60-90	160 (C /20)	103
$LiCO_3$	$FeC_2O_4{\cdot}2H_2O$	$NH_4H_2PO_4$		Deionized water	Citric acid	1:1:1	Porous $LiFePO_4/C$	*9.1	128 (C/10)	104
$LiCO_3$	$FeC_2O_4{\cdot}2H_2O$	$NH_4H_2PO_4$		Deionized water	Sucrose	1:1:1	Porous $LiFePO_4/C$	*6.1	153 (C/10)	104
$Li(COOCH_3){\cdot}2H_2O$	$Fe(COOCH_3)_2$	H_3PO_4		Ethylene glycol	Ethylene glycol	1:1:1	$LiFePO_4/C$	200-300	165 (C/100)	105
$LiNO_3$	$FeC_2O_4{\cdot}2H_2O$	$NH_4H_2PO_4$		Deionized water	Ethylene glycol	1:1:1	$LiFePO_4/C$		155 (C/10)	106
$LiCl{\cdot}H_2O$	$FeCl_2{\cdot}4H_2O$	H_3PO_4		Ethanol		1:1:1	$LiFePO_4$		116 (C/5)	107
$LiCl{\cdot}H_2O$	$FeCl_2{\cdot}4H_2O$	H_3PO_4		Ethanol	PEG, 1-hexadecanol	1:1:1	Porous $LiFePO_4/C$		145 (C/5)	107
$LiCl{\cdot}H_2O$	$FeCl_2{\cdot}4H_2O$	H_3PO_4		Ethanol	PEG, D-fructose	1:1:1	Porous $LiFePO_4/C$		157.7 (C/5)	107
$LiCl{\cdot}H_2O$	$FeCl_2{\cdot}4H_2O$	H_3PO_4		Ethanol	PEG, Cinnamic acid	1:1:1	Porous $LiFePO_4/C$	100-200	137 (C/5)	107
$Li(COOCH_3){\cdot}2H_2O$	$FeCl_2.4H_2O$	P_2O_5		Ethanol	Lauric acid	1:1:1	$LiFePO_4$	100-300	170 (C/10)	108
$Li(COOCH_3){\cdot}2H_2O$	$FeCl_2.4H_2O$	P_2O_5		Ethanol		1:1:1	$LiFePO_4$	500-3,000	146 (C/10)	108
Li_3PO_4	$C_6H_5FeO_7$	H_3PO_4		Deionized water		1:3:2	Porous $LiFePO_4/C$	500-20,000	140 (C/2)	109
Li_3PO_4	$C_6H_5FeO_7$	H_3PO_4		Deionized water	Hydroxy ethyl cellulose	1:3:2	Porous $LiFePO_4/C$		150 (C/5)	110
$LiOH{\cdot}H_2O$	$FeC_2O_4{\cdot}2H_2O$	$NH_4H_2PO_4$		Deionized water	Polyacrylic acid, Citric acid	1:1:1	$LiFePO_4$		160-165(C/8)	111
$LiOH{\cdot}H_2O$	$FeC_2O_4{\cdot}2H_2O$	$NH_4H_2PO_4$	$Mg(CH_3CO_2)_2{\cdot}4H_2O$	Deionized water	Polyacrylic acid, Citric acid	1:0.99:1:0.01	$LiMg_{0.01}Fe_{0.99}PO_4$		160-165(C/8)	111
$LiOH{\cdot}H_2O$	$FeC_2O_4{\cdot}2H_2O$	$NH_4H_2PO_4$	$Zr(OC_2H_5)_4$	Deionized water	Polyacrylic acid, Citric acid	1:0.99:1:0.01	$LiZr_{0.01}Fe_{0.99}PO_4$		160-165(C/8)	111
$LiOH{\cdot}H_2O$	$FeC_2O_4{\cdot}2H_2O$	$NH_4H_2PO_4$	$Ti(OCH_3)_4$	Deionized water	Polyacrylic acid, Citric acid	1:0.99:1:0.01	$LiTi_{0.01}Fe_{0.99}PO_4$		160-165(C/8)	111
Li_3PO_4	$C_6H_5FeO_7$	H_3PO_4		Deionized water	Citric acid	1:3:2	Porous $LiFePO_4/C$	*50	120 (1C)	113
$LiCO_3$	$Fe(NO_3)_3{\cdot}9H_2O$	$NH_4H_2PO_4$		Deionized water	Ascorbic acid	1:1:1	$LiFePO_4$			114
$LiOH{\cdot}H_2O$	$Fe(NO_3)_3{\cdot}9H_2O$	H_3PO_4		Deionized water		1:1:1	$LiFePO_4$			114
$Li(COOCH_3){\cdot}2H_2O$	$Fe(COOCH_3)_2$	H_3PO_4		DMF		1:1:1	$LiFePO_4$			114
$Li(COOCH_3){\cdot}2H_2O$	$Fe(COOCH_3)_2$	H_3PO_4		DMF		1.05:1:1	$LiFePO_4$	5,000	145 (C/2)	115
$Li(COOCH_3){\cdot}2H_2O$	$Fe(COOCH_3)_2$	H_3PO_4		Ethylene glycol	Functionalized CNF by HNO_3	1:1:1	$LiFePO_4/CNF$	200	120 (C/2)	116
$Li(COOCH_3){\cdot}2H_2O$	$Fe(COOCH_3)_2$	H_3PO_4		Ethylene glycol		1:1:1	$LiFePO_4/C$	500-1,000	110 (C/2)	116
$LiOH{\cdot}H_2O$	$Fe(NO_3)_3{\cdot}9H_2O$	H_3PO_4		Deionized water	Ascorbic acid	1:1:1	$LiFePO_4/C$	350	165 (3C)	117
$LiOH{\cdot}H_2O$	$Fe(NO_3)_3{\cdot}9H_2O$	H_3PO_4		Deionized water	Ascorbic acid	1:1:1	$LiFePO_4/C$		110 (C/5)	118
$LiOH{\cdot}H_2O$	$Fe(NO_3)_3{\cdot}9H_2O$	H_3PO_4	Metal powder (Co, Ag)	Deionized water	Ascorbic acid	1:1:1	$LiFePO_4/C$		140 (C/5)	118

peristaltic pump[122)]. In spray pyrolysis, the generation of droplets is a key step because the droplets act as the nucleation centers and eventually evolve to well-crystallized, dense, and pure particles. Powders produced by this method have small particle size (< 1 μm), narrow size distribution (1 – 2 μm), large surface area, and high purity[121-126, 128, 129)]. All these properties are desirable for achieving high electrochemical performance for $LiFePO_4$ powders, and hence spray pyrolysis method is becoming an important alternative approach for producing $LiFePO_4$ powders[122-124)]. **Table 7** shows the precursors used in the spray

Table 7 Pecursors used in the spray pyrolysis method, and particle size and electrochemical performance of the resultant $LiFePO_4$ powders

Li Precursor	Fe Precursor	P Precursor	Metal Dopant	Solvent	Carbon Source	Molar Ratio	Product	Particle Size (nm)	Discharge Capacity (mAh/g)	Ref
$LiNO_3$	$FeSO_4$	H_3PO_4		Deionized water	Sucrose		$LiFePO_4/C$			32
$LiNO_3$	$Fe(NO_3)_3{\cdot}9H_2O$	H_3PO_4	$Mg(NO_3)_2{\cdot}6H_2O$	Deionized water	White sugar 40 wt%	1:0.9:1:0.1	$LiFe_{0.9}Mg_{0.1}PO_4/C$	1,000-2,000	132 (C/10)	121
Li_2CO_3	$FeC_2O_4{\cdot}2H_2O$	$NH_4H_2PO_4$	$Mg(C_2H_3O_2)_2{\cdot}4H_2O$	Deionized water		1-x:1:1:x	$Li_{1-x}FeMg_xPO_4$	1,000-2,000		122
$LiNO_3$	$Fe(NO_3)_3{\cdot}9H_2O$	H_3PO_4		Deionized water	Ascorbic acid, white sugar	1:1:1	$LiFePO_4/C$	1,000-2,000	124 (C/10)	124
$LiCO_3$	$FeC_2O_4{\cdot}2H_2O$	$NH_4H_2PO_4$		Deionized water (HNO_3)	Sucrose ($C_{12}H_{22}O_{11}$)		$LiFePO_4/C$	300		125
$Li(HCOO){\cdot}H_2O$	$FeCl_2{\cdot}4H_2O$	H_3PO_4		Deionized water (HCl)		1:1:1	$LiFePO_4$		100 (C/10)	126
$Li(HCOO){\cdot}H_2O$	$FeCl_2{\cdot}4H_2O$	H_3PO_4		Deionized water (HCl)	Citric acid	1:1:1	$LiFePO_4/C$	1,000-3,000	140 (C/10)	126
$Li(HCOO){\cdot}H_2O$	$FeCl_2{\cdot}4H_2O$	H_3PO_4		Deionized water (HCl)	Acetylene black	1:1:1	$LiFePO_4/C$	58	163 (C/10)	128
$Li(HCOO){\cdot}H_2O$	$FeCl_2{\cdot}4H_2O$	H_3PO_4		Deionized water (HCl)	Acetylene black	1:1:1	$LiFePO_4/C$	300-1,000	158 (C/10)	129

pyrolysis method and the particle size and discharge capacity of the resultant $LiFePO_4$ powders.

The spray pyrolysis of $LiFePO_4$ powders typically starts with the pumping (or spraying) of a solution of mixed precursors into a pyrolysis furnace (around 400 – 600℃) in the droplet form by a carrier gas **(Fig. 4)**[122-125]. Collected precursor powders are then calcined at temperatures around 700 – 800℃. Jugovic *et al.*[32] compared $LiFePO_4$ powders prepared by solid state synthesis and spray pyrolysis, and found that $LiFePO_4$ powders by spray pyrolysis have smaller particle size and present spherical morphology without agglomeration. However, powders by solid-state synthesis are formed of larger and nonspherical particles with apparent agglomeration. In addition, powders prepared by solid-state synthesis show well crystallized structure as single-phase phospho-olivines, whereas those prepared by spray pyrolysis have olivine phase with small portion of other phases such as lithium carbon and iron carbon, which lead to higher electrical conductivity.

Like many other methods, carbon sources can be added during spray pyrolysis, and the resultant $LiFePO_4/C$ powders not only have higher electrical conductivity, but also have smaller particle size, which increases the specific surface area of the powders[124, 126]. Bewlay *et al.*[125] used sucrose as a carbon source to prepare $LiFePO_4/C$ powders, which had an average diameter of 300 nm and showed a conductivity from 10^{-7} to 10^{-1} S/cm, depending on the amount of the carbon source added in the precursor solution. Konarova *et al.*[126] also prepared $LiFePO_4$ and $LiFePO_4/C$ powders by the spray pyrolysis method. While $LiFePO_4$ powders had low discharge capacity of around 100 mAh/g at C/10, $LiFePO_4/C$ powders showed 140 mAh/g at C/10 and 84 mAh/g at 5C, respectively, with small capacity fading during cycling. Ju *et al.*[123] also reported fine, spherical $LiFePO_4/C$ powders with charge capacities between 108 – 136 mAh/g, depending on the size and amount of the carbon. Capacities and cycling performance of $LiFePO_4/C$ powders are reported to be improved by preparing nano-sized particles. It must be noted that, when a carbon source is added, the carbon content in the final $LiFePO_4/C$ product needs to be carefully controlled because, if the carbon content is too high, the discharge capacity may decrease due to either reduced $LiFePO_4$ content[127] or dominant barrier behavior of the thick carbon layer[126, 110]. Yang *et al.*[124] prepared non-agglomerated, smooth $LiFePO_4/C$ powders with carbon evenly distributed. When the carbon content is 15 %, the $LiFePO_4/C$ powders have the highest discharge capacity of 124 mAh/g at C/10.

Metal dopants have also been used in the spray pyrolysis method to improve the performance of $LiFePO_4$ powders. For example, Teng *et al.*[121, 124] synthesized Mg-doped $LiFePO_4/C$ powders, which have an average particle size between 1 and 2 μm and a conductivity 10^4 times greater than that of pure $LiFePO_4$. These powders have a capacity of 132 mAh/g at C/10 and exhibit lower capacity decay when compared with undoped $LiFePO_4/C$ powders. Wang *et al.*[122] also prepared Mg-doped $LiFePO_4$ powders using spray pyrolysis and achieved 10^4 times higher conductivity than pure $LiFePO_4$ powders.

The spray pyrolysis method can also be combined with wet or dry ball-milling techniques in order to increase the specific surface area and discharge capacity of the resultant $LiFePO_4$ powders[128, 129]. Konarova *et al.*[128] produced $LiFePO_4$ powders with average diameter less than 100 nm by the combination of spray pyrolysis and wet ball-milling. These powders have discharge capacities of 163 mAh/g at C/10 and 100 mAh/g at 10C, respectively. The same authors also reported the preparation of $LiFePO_4$/C powders with diameters ranging from 300 to 1000 nm by the combination of spray pyrolysis and planetary ball-milling, and achieved a discharge capacity of 158 mAh/g at C/10[129].

4.4. Co-Precipitation

Co-precipitation is another solution-based method, which is easy to control and can lead to well-crystallized powders with high purity and small particle size. In that method, lithium and phosphate compounds in mixed precursor solutions are co-precipitated by controlling the pH values. The co-precipitated slurries are then filtered, washed, and dried under N_2 atmosphere. During that process, dried precursors may form amorphous $LiFePO_4$. Crystalline $LiFePO_4$ powders are obtained by carrying out the calcination at 500 – 800℃ for 12h under N_2 or argon flow[130, 131]. The typical synthesis route for the co-precipitation method is shown in **Fig. 4** and precursors used in this method are shown in **Table 8.** Depending on the precursors and other processing conditions, the particle sizes of the synthesized $LiFePO_4$ powders can range from 100 nm to several microns[130-133]. For example, Zheng *et al.*[131] prepared pure crystalline $LiFePO_4$ powders by calcining an amorphous co-precipitated $LiFePO_4$ at 500℃. These powders have a homogenously distributed particle size ranging from 100 and 200 nm, and their discharge capacity is 166 mAh/g at C/10. In addition to particle size, the particle morphology can also be controlled using the co-precipitation method. Arnold *et al.*[130] prepared flat, rhombus-shaped $LiFePO_4$ powders in the submicron range by an aqueous co-precipitation method. These pure and well-crystallized $LiFePO_4$ powders have a high discharge capacity of 160 mAh/g at C/20.

The structure and performance of $LiFePO_4$ powders can be improved by introducing carbon source or metal dopant into the co-precipitation process. For example, Ding *et al.*[132] prepared $LiFePO_4$/graphene composite powders by directly adding graphene during co-precipitation, and observed the restacking of graphene sheets because the van der Waals forces during synthesis caused a decrease in surface area of graphene. The resultant $LiFePO_4$/graphene powders have an average particle size of around 100 nm and a discharge capacity of 160 mAh/g at C/5 rate. Li *et al.*[133] prepared spherical shaped, sub-micron sized Ti-doped $LiFePO_4$ powders by the co-precipitation method. $Ti(SO_4)_2$ was used as the titanium dopant. It was found that 3%-Ti-doped powders exhibited a good discharge capacity of 150 mAh/g at C/10 with good cycling performance.

Co-precipitation can also be combined with other methods to produced $LiFePO_4$ powders with controlled structures and performance. Chang *et al.*[134] prepared high-density $LiFePO_4$/C powders by the solid-state synthesis of $FePO_4$ (1.56 g/cm^3), which was obtained by using the co-precipitation method supported with high-pressure filtering and two-step drying at 80℃ . The tap-density of the obtained $LiFePO_4$/C powders was 1.80 g/cm^3 when the carbon content was 7 wt.%. The initial volumetric and gravimetric discharge capacities were 300.6 mAh/cm^3 and 167 mAh/g, respectively, at C/10.

4.5. Microemulsion drying

$LiFePO_4$ powders can also be prepared by the drying of microemulsion solutions[135-137], which are thermodyamically stable liquid mixtures consisting of water, oil, and emulsifying agent that stabilizes the microemulsions[135-138]. During the microemulsion drying process, microemulsions act as microreactors for the synthesis of $LiFePO_4$ powders. The type and property of the microemulsions are depended on the amount of oil and water, type and amount of emulsifying agent, and process temperature, etc[139-142]. As shown in **Fig. 4**, the microemulsion drying process of $LiFePO_4$ powders starts with the preperation of aqueous precursor solutions based on the stoichiometric ratios. The aqueous phase is mixed intensively with an oily phase consisting of hydrocarbons such as Kerosene[135-138]. The obtained microemulsions are dried between 300 and 400℃, during which extensive weight loss can be observed due to the evaporation of water and pyrolysis of organic hydrocarbons. It was reported that little amount of crystalline olivine $LiFePO_4$ starts to form during drying. However, in most cases, dried microemulsions need to be calcined at 650 – 850℃ under argon flow for 12 h. The optimum calcination temperature is reported to be around 750 ℃[136, 137]. Higher calcination temperature might result in increased particle size[136]. The microemulsion drying process is of importance for $LiFePO_4$ synthesis

Table 8 Precursors used in the co-precipitation and microemulsion drying methods, and particle size and electrochemical performance of the resultant $LiFePO_4$ powders

Method	Li Precursor	Fe Precursor	P Precursor	Solvent	Carbon Source	Molar Ratio	Product	Particle Size (nm)	Discharge Capacity (mAh/g)	Ref
Co-precipitation	LiOH	Ferrous ions	H_3PO_4	Deionized water			$LiFePO_4$			23
Co-precipitation	Li_3PO_4	$Fe_3(PO_4)_2 \cdot 5H_2O$		Deionized water		1:1	$LiFePO_4$	<1,000	160 (C/20)	130
Co-precipitation	Li_2CO_3	$FeSO_4 \cdot 7H_2O$	H_3PO_4	Deionized water	$C_2O_4H_2 \cdot 2H_2O$	1:1:1	$LiFePO_4$	100-200	166 (C/10)	131
Co-precipitation	LiOH	$(NH_4)_2Fe(SO_4)_2 \cdot 6H_2O$	$NH_4H_2PO_4$	Deionized water	Natural graphite		$LiFePO_4$/ graphene	100	160 (C/5)	132
Co-precipitation	Li_2CO_3	$Fe(NO_3)_3 \cdot 9H_2O$	H_3PO_4	Deionized water	Glucose	1:1:1	$LiFePO_4$/C	2,000-4,000	167 (C/10)	134
Emulsion-Drying	$LiNO_3$	$Fe(NO_3)_3 \cdot 9H_2O$	$(NH_4)_2HPO_4$	Deionized water	Carbon Bl (40%)	1:1:1	$LiFePO_4$/C	1,000	133 (C/8.5)	136
Emulsion-Drying	$LiNO_3$	$Fe(NO_3)_3 \cdot 9H_2O$	$(NH_4)_2HPO_4$	Deionized water		1:1:1	$LiFePO_4$	1,000	121 (C/8.5)	136
Emulsion-Drying	$LiNO_3$	$Fe(NO_3)_3 \cdot 9H_2O$	$(NH_4)_2HPO_4$	Deionized water	Karosene:Tween85	1:1:1	$LiFePO_4$/C	<1,000	125(C/8.5)	137
Emulsion-Drying	LiOH	$(NH_4)_2Fe(SO_4)_2$	H_3PO_4	Octane, Butyl alcohol	Sugar	3:1:1	$LiFePO_4$/C	90	163 (C/10)	143

because the formation of pure, fine powders is facilitated by the atomic scale, homogeneous distrubution of reactants in microemulsions from the beginning[135-137].

During microemulsion drying, the partcile growth is directly restricted by the size of the droplets in the emulsions. As a result, the particle size and morphology are affected by many factors such as solution concentration, droplet size, stirring power, and surfactant. Particle sizes and discharge capcities of $LiFePO_4$ powders produced by microemulsion drying are shown in **Table 8**. Myung *et al.*[137] used the microemulsion drying method (drying at 300℃ and calcination at 750℃) to prepare $LiFePO_4$/C powders, which have an average particle size of 1 μm. Good discharge capacity (around 125 mAh/g at C/8.5 and 25℃) and good electrical conductivity (10^{-4} S/cm) were obtained for the $LiFePO_4$/C powders due to the atomic level mixing of precursors and carbon source. Smaller particle size can be obtained using the microemulsion drying method. For example, Xu *et al.*[143] prepared $LiFePO_4$/C powders by using CTAB and PEG in emulsions to control the particle size and using sugar as the carbon source. $LiFePO_4$/C powders calcined at 600℃ exhibited 90 nm average particle size and very good discharge capacity of 163 mAh/g at C/10. Cho *et al.*[136] prepared pristine $LiFePO_4$ and $LiFePO_4$/C powders using the same method. Discharge capacities of 121 and 133 mAh/g at C/8.5 with excellent cycle stability were obtained for $LiFePO_4$ and $LiFePO_4$/C powders, respectively.

5. Other Methods

There are other methods that can be used to produce $LiFePO_4$ powders in addition to the previously mentioned approaches. Among these methods, template synthesis[117], polyol process[11], in-situ polymerization restriction method[144] and solid-state synthesis with controlled off-stoichiometry[145] stand out because they lead to $LiFePO_4$ powders with desired structure and fast charge/discharge behavior. In addition, a molten salt synthesis method was used to accelerate the crystallization process and help form spherical powders with increased tap density[146]. Other methods that have been used to produce $LiFePO_4$ powders include ceramic granulation[148], freeze-drying[148], sonochemical synthesis[135, 32], and rheological synthesis[149].

Recently, a few research groups are working on synthesizing $LiFePO_4$ films that have comparable electrochemical performance to powders. For example, LiFePO4[150-153] thin films with different thicknesses, such as 35 nm[152], 50 nm[150], and 300 nm[151, 153], have been produced by using pulsed laser deposition method. Another method to produce $LiFePO_4$ thin films is radio frequency magnetron sputtering, which can be used to obtain submicron size film thickness[154].

6. Conclusion

A good cathode material for lithium-ion batteries should have large capacity, good cycling performance, high stability, low toxicity, and high purity, and it should be easily produced and affordable. In order to obtain these features, small particle size, narrow size distribution, uniform morphology, optimum crystallinity degree, high specific surface area, minimum defects and agglomeration, and homogeneous carbon coating or metal doping are required for the practical application of $LiFePO_4$ powders in lithium-ion batteries. Methods described in this review were designed to obtain $LiFePO_4$ powders with desirable structures and high electrochemical performance. However, it is often challenging to obtain all the desired properties. Typically, solid state methods are of importance in terms of obtaining ordered crystal structure, but they require higher treatment temperature and longer process time, which may lead to larger particle size and lower electrochemical capacity. On the other hand, solution-based methods give high purity, small particle size, uniform size distribution, and hence relatively higher electrochemical capacity, but additional solvent cost and environmental issues are major disadvantages of these methods. Many solid-state and solution-based methods are good candidates for the mass production of $LiFePO_4$ powders at industrial scale; however, the cost, productivity, reproducibility and complexity of these methods should be taken into consideration.

Acknowledgements

The authors acknowledge the financial support from National Textile Center (ITA-08-07400), ERC Program of National Science Foundation under Award Number EEC-08212121, ACS Petroleum Research Fund (47863-G10), and Advanced Space Technologies Research & Engineering Center.

References

1) Balbuena, P. B. and Wang, Y., (2004): "Lithium-Ion Batteries: Solid-Electrolyte Interphase" , Imperial College Press, London, U.K.
2) Vincent, C. A., (2000): Lithium batteries: A 50-year perspective, Solid State Ionics, No.134(1-2), 1959-2009, pp.314-331.
3) Cheruvally, G., (2008): "Lithium Iron Phosphate: A Promising Cathode-Active Material for Lithium Secondary Batteries" , Trans Tech Publications Ltd, Stafa-Zuerich, Switzerland.
4) Shukla, A. K. and Prem Kumar,T., (2008): Materials for next-generation lithium batteries, Current Science, No.94(3), pp.314-331.
5) Padhi, A.K., Nanjundaswamy, K.S. and Goodenough, J. B., (1997): Phospho-olivines as Positive-Electrode Materials for Rechargeable Lithium Batteries, Journal of Electrochemical Society, No.144, pp.1188-1194.
6) Chung, S. Y., Bloking, J. T. and Chiang, Y. M., (2002): Electronically conductive phospho-olivines as lithium storage electrodes, Nature Materials, No.1, pp.123-128.
7) Yang, S., Song, Y., Ngala, K., Zavalij, P. Y. and Whittingham, M. S., (2003): Performance of $LiFePO_4$ as lithium battery cathode and comparison with manganese and vanadium oxides, Journal of Power Sources, No.119-121, pp.239-246.
8) Ravet, N. C. Y., Magnan, J. F., Besner, S., Gauthier, M. and Armand, M., (2001): Electroactivity of natural and synthetic triphylite, Journal of Power Sources, No.97(8), pp.503-507.
9) Herle, P. S., Ellis, B., Coombs, N. and Nazar, L. F., (2004): Nano-network electronic conduction in iron and nickel olivine phosphates, Nature Materials, No.3, pp.7-152.
10) Delacourt, C., Poizot, P., Levasseur, S. and Masquelier, C., (2006): Size effects on carbon-free $LiFePO_4$ powders, Electrochemical and Solid State Letters, No.9, pp.A352-A355.
11) Kim, D. H. and Kim, J. (2006): Synthesis of $LiFePO_4$ nanoparticles in polyol medium and their electrochemical properties, Electrochemical and Solid State Letters, No.9, pp.A439-A442.
12) Andersson, A.S. and Thomas, J.O., (2001): The source of first-cycle capacity loss in $LiFePO_4$, Journal of Power Sources, No.97-98, pp.498-502.
13) Wang, G. X., Bewlay, S., Needham, S. A., Liu, H. K., Liu, R. S., Drozd, V. A., Lee, J.-F. and Chen, J. M., (2006): Synthesis and Characterization of $LiFePO_4$ and LiTi0.01Fe0.99PO4 Cathode Materials, Journal of The Electrochemical Society, No.153(1), pp.A25-A31.
14) Ruffo, R., Huggins, R.A., Mari, C.M., Piana, M. and Weppner, W., (2005): Phosphate Materials for Cathodes in Lithium Ion Secondary Batteries, Ionics, No.11, pp.213-219.
15) Yao, J., Konstantinov, K., Wang, G. X. and Liu, H. K., (2007): Electrochemical and magnetic characterization of $LiFePO_4$ and $Li_{0.95}Mg_{0.05}FePO_4$ cathode materials, Journal of Solid State Electrochemistry, No.11, pp.177-185.
16) Yamada, A., Chung, S.C. and Hinokuma, K., (2001): Optimized $LiFePO_4$ for lithium battery cathodes, Journal of The Electrochemical Society, No.148, pp.A224-A229.
17) Koltypin, M., Aurbach, D., Nazar, L. and Ellis, B., (2007): More on the performance of $LiFePO_4$ electrodes — The effect of synthesis route, solution composition, aging, and temperature, Journal of Power Sources, No.174, pp.1241-1250.
18) Yun, N.J., Ha, H.-W., Jeong, K.H., Park, H.-Y. and Kim, K., (2006): Synthesis and electrochemical properties of olivine-type $LiFePO_4$/C composite cathode material prepared from a poly(vinyl alcohol)-containing precursor, Journal of Power Sources No.160, pp.1361-1368.
19) Fey, G.T.K. and Lu, T.L., (2008): Morphological characterization of $LiFePO_4$/C composite cathode materials synthesized via a carboxylic acid route, Journal of Power Sources, No.178, pp.807-814.
20) Zaghib, K., Ravet, N., Gauthier, M., Gendron, F., Mauger, A., Goodenough, J.B. and Julien, C.M., (2006): Optimized electrochemical performance of $LiFePO_4$ at 60℃ with purity controlled by SQUID magnetometry, Journal of Power Sources, No.163, pp. 560-566.
21) Wang, D., Li, H., Wang, Z., Wu, X., Sun, Y., Huang, X. and Chen, L.,(2004): New solid-state synthesis routine and mechanism for $LiFePO_4$ using LiF as lithium precursor, Journal of Solid State Chemistry, No.177, pp.4582-4587.

22) Fey, G.T.K., Chen, Y.G. and Kao, H.M., (2009): Electrochemical properties of $LiFePO_4$ prepared via ball-milling, Journal of Power Sources, No.189, pp.169-178.

23) Franger, S., Le Cras, F., Bourbon, C. and Rouault, H., (2003): Comparison between different $LiFePO_4$ synthesis routes and their influence on its physico-chemical properties, Journal of Power Sources No.119-121, pp.252-257.

24) Wang, D., Wu, X., Wang, Yh. and Chen, L., (2005): Cracking causing cyclic instability of $LiFePO_4$ cathode material, Journal of Power Sources No.140, pp.125-128.

25) Li, M., Xie, K., Li, D. and Pan Y., (2005): Synthesis of $LiFePO_4$ by one-step annealing under the vacuum condition, Journal of Materials Science, No.40, pp.2639-2641.

26) Yamada, A., Hosoya, M., Chung, S.Ch., Kudo, Y., Hinokuma, K., Liu, K.-Y. and Nishi, Y., (2003): Olivine-type cathodes: Achievements and problems, Journal of Power Sources 119-121, pp.232-238.

27) Ojczyk, W., Marzec, J., Swierczek, K., Zajac, W., Molenda, M., Dziembaj, R. and Molenda, J., (2007): Studies of selected synthesis procedures of the conducting $LiFePO_4$-based composite cathode materials for Li-ion batteries, Journal of Power Sources, No.173, pp.700-706.

28) Zhou, F., Kang, K., Maxisch, T., Ceder, G. and Morgan, D., (2004): The electronic structure and band gap of $LiFePO_4$ and $LiMnPO_4$, Solid State Communications, No.132, pp.181-186.

29) Hong, K.S., Yu, S. M., Ha, M. G., Ahn, C. W., Hong, T. E., Jin, J. S., Kim, H. G., Jeong, E. D., Kim, Y.S., Kim, H.J., Doh, C.H., Yang, H.S. and Jung, H., (2009): Preparation of $LiFePO_4$ Using Chitosan and its Cathodic Properties, Bulletin of the Korean Chemical Society, No.30(8), pp.1719-1723.

30) Lai, C., Xu, Q., Ge, H., Zhou, G. and Xie, J., (2008): Improved electrochemical performance of $LiFePO_4$/C for lithium-ion batteries with two kinds of carbon sources, Solid State Ionics, No.179, pp.1736-1739.

31) Mi, C.H., Zhang, X.G. and Li H.L., (2007): Electrochemical behaviors of solid $LiFePO_4$ and $Li_{0.99}Nb_{0.01}FePO_4$ in Li_2SO_4 aqueous electrolyte, Journal of Electroanalytical Chemistry, No.602, pp.245-254.

32) Jugović, D., Cvjetićanin, N., Mitrić, M., Mentus S. and Uskokovic, D., (2007): Comparison between different $LiFePO_4$ synthesis routes, Materials Science Forum, No.555, pp.225-230.

33) Takahashi, M., Tobishima, Sh., Takei, K. and Sakurai, Y., (2001): Characterization of $LiFePO_4$ as the cathode material for rechargeable lithium batteries, Journal of Power Sources No.97-98, pp.508-511.

34) Rahaman, M. N., (2003): "Ceramic processing and sintering" , 2nd ed., Marcel Dekker, Inc., New York, U.S.A.

35) Morales, J., Trócoli, R., Castellon, E. R., Franger, S. and Pena, J. S., (2009): Effect of C and Au additives produced by simple coaters on the surface and the electrochemical properties of nanosized $LiFePO_4$, Journal of Electroanalytical Chemistry, No.631, pp.29-35.

36) Kim, H. S., Cho, B. W. and Cho, W. I., (2004): Cycling performance of $LiFePO_4$ cathode material for lithium secondary batteries, Journal of Power Sources, No.132, pp.235-239.

37) Shin, H. Ch., Cho, W. I., and Jang, H., (2006): Electrochemical properties of carbon-coated $LiFePO_4$ cathode using graphite, carbon black, and acetylene black, Electrochimica Acta, No.52, pp.1472-1476.

38) Kim, J. K., Cheruvally, G., Ahn, J. H., Hwang G. Ch., and Choi, J. B., (2008): Electrochemical properties of carbon-coated $LiFePO_4$ synthesized by a modified mechanical activation process, Journal of Physics and Chemistry of Solids, No.69, pp.2371-2377.

39) Kim, Ch. W., Park, J. S. and Lee, K. S., (2006): Effect of Fe_2P on the electron conductivity and electrochemical performance of $LiFePO_4$ synthesized by mechanical alloying using Fe^{3+} raw material, Journal of Power Sources, No.163, pp.144-150.

40) Porcher, W., Lestriez, B., Jouanneau, S. and Guyomard D., (2010): Optimizing the surfactant for the aqueous processing of $LiFePO_4$ composite electrodes, Journal of Power Sources, Article in Press, doi:10.1016/j.jpowsour.2009.11.088.

41) Franger, S., Benoit, C., Bourbon, C. and Le Cras, F., (2006): Chemistry and electrochemistry of composite $LiFePO_4$ materials for secondary lithium batteries, Journal of Physics and Chemistry of Solids, No.67, pp.1338-1342.

42) Kwon, S.J., Kim, C.W., Jeong, W.T. and Lee, K.S., (2004): Synthesis and electrochemical properties of olivine $LiFePO_4$ as a cathode material prepared by mechanical alloying, Journal of Power Sources, No.137, pp.93-99.

43) Kosova, N. and Devyatkina, E., (2004): On mechanochemical preparation of materials with enhanced characteristics for lithium batteries, Solid State Ionics, No.172, pp.181-184.

44) Kim, C.W., Lee, M.H., Jeong, W.T. and Lee, K.S., (2005): Synthesis of olivine $LiFePO_4$ cathode materials by mechanical alloying using iron(III) raw material, Journal of Power Sources, No.146, pp.534-538.

45) Franger, S., Le Cras, F., Bourbon, C. and Rouault, H., (2002): $LiFePO_4$ Synthesis Routes for Enhanced Electrochemical Performance, Electrochemical and Solid-State Letters, No.5(10), pp.A231-A233.

46) Weimer, A. W., (1997): "Carbide, nitride, and boride materials synthesis and processing" , Chapman & Hall, London, U.K.

47) Schubert, U. and Hüsing N., (2005): "Synthesis of inorganic materials", 2nd ed., Wiley-VCH Verlag GmbH & Co., Weinheim, Germany.

48) Barker, J., Saidi, M. Y. and Swoyer, J. L., (2003): Lithium iron(II) phospho-olivines prepared by a novel carbothermal reduction method, Electrochemical Solid-State Letters, No.6, pp.A53-A55.

49) Zhu, B. Q., Li, X. H., Wang, Yh. X. and Guo, H. J., (2006): Novel synthesis of $LiFePO_4$ by aqueous precipitation and carbothermal reduction, Materials Chemistry and Physics, No.98, pp.373-376.

50) Mi, C. H., Cao, G. S. and Zhao, X. B., (2005): Low-cost, one-step process for synthesis of carbon-coated $LiFePO_4$ cathode, Materials Letters, No.59, pp.127-130.

51) Liu, H., Zhang, P., Li, G. C., Wu, Q., and Wu, Y. P., (2008): $LiFePO_4/C$ composites from carbothermal reduction method, Journal of Solid State Electrochemistry, No.12, pp.1011-1015.

52) Liu, H. P., Wang, Z. X., Li, X. H., Guo, H. J., Peng, W. J., Zhang, Y. H. and Hu, Q. Y., (2008): Synthesis and electrochemical properties of olivine $LiFePO_4$ prepared by a carbothermal reduction method, Journal of Power Sources, No.184, pp.469-472.

53) Wang, L., Liang, G. C., Ou, X. Q., Zhi, X. K., Zhang, J. P. and Cui, J. Y., (2009): Effect of synthesis temperature on the properties of $LiFePO_4/C$ composites prepared by carbothermal reduction, Journal of Power Sources, No.189, pp.423-428.

54) Zhong, M. E. and Zhou, Z.T., (2010): Preparation of high tap-density $LiFePO_4/C$ composite cathode materials by carbothermal reduction method using two kinds of Fe^{3+} precursors, Materials Chemistry and Physics, No.119, pp.428-431.

55) Zhi, X., Liang, G., Wang, L., Ou, X., Zhang, J. and Cui, J., (2008): The cycling performance of $LiFePO_4/C$ cathode materials, Journal of Power Sources, No.189(1), pp.779-782.

56) Liu, H., Xie, J. and Wang, K., (2008): Synthesis and characterization of $LiFePO_4/(C+Fe_2P)$ composite cathodes, Solid State Ionics, No.179, pp.1768-1771.

57) Yu, F., Zhang, J., Yang, Y. and Song, G., (2009): Reaction mechanism and electrochemical performance of $LiFePO_4/C$ cathode materials synthesized by carbothermal method, Electrochimica Acta, No.54, pp.7389-7395.

58) Delacourt, C., Laffont, L., Bouchet, R., Wurm, C., Leriche, J.B., Morcrette, M., Tarascon, J.-M. and Masquelier, C., (2008): Toward Understanding of Electrical Limitations (Electronic, Ionic) in $LiMPO_4$ (M = Fe, Mn) Electrode Materials, Journal of The Electrochemical Society, No.152(5), pp.A913-A921.

59) Higuchi, M., Katayama, K., Azuma, Y., Yukawa, M. and Suhara, M., (2003): Synthesis of $LiFePO_4$ cathode material by microwave processing, Journal of Power Sources, No.119-121, pp.258-261.

60) Park, K. S., Son, J. T., Chung, H. T., Kim, S. J., Kim, C. H., Lee, C. H. and Kim, H. G., (2003): Synthesis of $LiFePO_4$ by co-precipitation and microwave heating, Electrochemistry Communications, No.5, pp.839-842.

61) Wang, L., Huang, Y., Jiang R. and Jia, D., (2007): Preparation and characterization of nano-sized $LiFePO_4$ by low heating solid-state coordination method and microwave heating, Electrochimica Acta, No.52, pp.6778-6783.

62) Beninati, S., Damen, L., Mastragostino, M., (2008): MW-assisted synthesis of $LiFePO_4$ for high power applications, Journal of Power Sources, No.180, pp.875-879.

63) Murugan, A. V., Muraliganth, T. and Manthiram, A., (2008): Rapid microwave-solvothermal synthesis of phospho-olivine nanorods and their coating with a mixed conducting polymer for lithium ion batteries, Electrochemistry Communications, No.10, pp.903-906.

64) Bykov, Y. V., Rybakov, K. I. and Semenov, V. E., (2001): High-temperature microwave processing of materials, Journal of Physics D: Applied Physics, No.34, pp.R55-R75.

65) Li, W., J. Ying, Wan, C., Jiang, C., Gao, J. and Tang, C., (2007): Preparation and characterization of $LiFePO_4$ from $NH_4FePO_4 \cdot H_2O$ under different microwave heating conditions, Journal of Solid State Electrochemistry, No.11(6), pp.799-803.

66) Zhang, Y., Feng, H., X. Wu, L. Wang, A. Zhang, T. Xia, H. Dong and M. Liu, (2009): One-step microwave synthesis and characterization of carbon-modified nanocrystalline $LiFePO_4$, Electrochimica Acta, No.54(11), pp.3206-3210.

67) Guo, X. F., Zhan, H., Zhou, Y. H., (2009): Rapid synthesis of $LiFePO_4/C$ composite by microwave method, Solid State Ionics, No.180, pp.386-391.

68) Song, M. S., Kang, Y. M., Kim, J. H., Kim, H. S., Kim, D. Y., Kwon H. S. and Lee, J. Y., (2007): Simple and fast synthesis of $LiFePO_4$-C composite for lithium rechargeable batteries by ball-milling and microwave heating, Journal of Power Sources, No.166(1), pp.260-265.

69) Zou, H., Zhang, G. and Shen, P. K., (2009): Intermittent microwave heating synthesized high performance spherical $LiFePO_4/C$ for Li-ion batteries, Materials Research Bulletin, Article in Press, doi:10.1016/j.materresbull.2009.09.031.

70) Song, M. S., Kang, Y. M., Kim, Y. I., Park, K. S.and Kwon, H. S., (2009): Nature of Insulating-Phase Transition and Degradation of Structure and Electrochemical Reactivity in an Olivine-Structured Material, $LiFePO_4$, Inorganic Chemistry, No.48(17), pp.8271-8275.

71) Muraliganth, T., Murugan, A. V. and Manthiram, A., (2008): Nanoscale networking of $LiFePO_4$ nanorods synthesized by a microwave-solvothermal route with carbon nanotubes for lithium ion batteries, Journal of Materials Chemistry, No.18(46), pp.5661-5668.

72) Jegal, J.P. and Kim, K.B. (2008): Preparation of Vanadium Oxide Nano Particles by Microwave Synthesis for Electrochemical Capacitor Application, 213th ECS Meeting, Abstract #34, Phoenix, Arizona, U.S.A.

73) Beninati, S., Damen, L. and Mastragostino, M., (2009): Fast sol-gel synthesis of $LiFePO_4/C$ for high power lithium-ion batteries for hybrid electric vehicle application, Journal of Power Sources, No.194, pp.1094-1098.

74) Zhou, W.,?He, W., Li, Z.,?Zhao, H. and?Yan, S., (2009): Biosynthesis and electrochemical characteristics of $LiFePO_4/C$ by microwave processing, Journal of Solid

State Electrochemistry, No.13(12), pp.1819-1823.

75) Li, P., He, W., Zhao H. and Wang, S., (2009): Biomimetic synthesis and characterization of the positive electrode material $LiFePO_4$, Journal of Alloys and Compounds, No.471(1-2), pp.536-538.

76) Wold, A. and Dwight, K., (1993): "Solid state chemistry: synthesis, structure, and properties of selected oxides and sulfides", Chapman & Hall Inc., New York, U.S.A.

77) Avvakumov, E. G., Senna, M. and Kosova, N., (2001): "Soft mechanochemical synthesis: a basis for new chemical Technologies", Kluwer Academic Publishers, New York, U.S.A.

78) Somiya, S. and Roy, R., (2000): Hydrothermal synthesis of fine oxide powders, Bulletin of Materials Science, No.23(6), pp.453-460.

79) Yang, S., Zavalij, P. Y. and Whittingham, M. S., (2001): Hydrothermal synthesis of lithium iron phosphate cathodes, Electrochemistry Communications, No.3, pp.505-508.

80) Yang, S., Song, Y., Zavalij, P. Y. and Whittingham, M. S., (2002): Reactivity, stability and electrochemical behavior of lithium iron phosphates, Electrochemistry Communications, No.4, pp.239-244.

81) Chen, J. and Whittingham, M. S., (2006): Hydrothermal synthesis of lithium iron phosphate, Electrochemistry Communications, No.8, pp.855-858.

82) Chen, J., Wang, S. and Whittingham, M. S., (2007): Hydrothermal synthesis of cathode materials, Journal of Power Sources, No.174, pp.442-448.

83) Jin, B. and Gu, H. B., (2008): Preparation and characterization of $LiFePO_4$ cathode materials by hydrothermal method, Solid State Ionics, No.178, pp.1907-1914.

84) Meligrana, G., Gerbaldi, C., Tuel, A., Bodoardo, S. and Penazzi, N., (2006): Hydrothermal synthesis of high surface $LiFePO_4$ powders as cathode for Li-ion cells, Journal of Power Sources, No.160, pp. 516-522.

85) Bodoardo, S., Gerbaldi, C., Meligrana, G., Tuel, A., Enzo S. and Penazzi, N., (2009): Optimization of some parameters for preparation of nanostructured $LiFePO_4/C$ cathode, Ionics, No.15, pp.19-26.

86) Ou, X., Liang, G., Wang, L., Xu, Sh. and Zhao, X., (2008): Effects of magnesium doping on electronic conductivity and electrochemical properties of $LiFePO_4$ prepared via hydrothermal route, Journal of Power Sources, No.184, pp.543-547.

87) Jin, E. M., Jin, B., Jun, D. K., Park, K. H., Gu, H. B. and Kim K. W., (2008): A study on the electrochemical characteristics of $LiFePO_4$ cathode for lithium polymer batteries by hydrothermal method, Journal of Power Sources, No.178, pp.801-806.

88) Chen, J., Vacchio, M. J., Wang, S., Chernova, N., Zavalij, P. Y. and Whittingham, M. S., (2008): The hydrothermal synthesis and characterization of olivines and related compounds for electrochemical applications, Solid State Ionics, No.178, pp.1676-1693.

89) Xu, J., Chen, G. and Li, X., (2009): Electrochemical performance of $LiFePO_4$ cathode material coated with multi-wall carbon nanotubes, Materials Chemistry and Physics, No.118, pp.9-11.

90) Zhang, C., Huang, X., Yin, Y., Dai, J. and Zhu, Z., (2009): Hydrothermal synthesis of monodispersed $LiFePO_4$ cathode materials in alcohol-water mixed solutions, Ceramics International, No.35, pp.2979-2982.

91) Xu, Ch., Lee, J. and Teja, A. S., (2008): Continuous hydrothermal synthesis of lithium iron phosphate particles in subcritical and supercritical water, The Journal of Supercritical Fluids, No.44, pp.92-97.

92) Lee, J. and Teja, A. S., (2005): Characteristics of lithium iron phosphate ($LiFePO_4$) particles synthesized in subcritical and supercritical water, The Journal of Supercritical Fluids, No.35, pp.83-90.

93) Lee, J. and Teja, A. S., (2006): Synthesis of $LiFePO_4$ micro and nanoparticles in supercritical water, Materials Letters, No.60, pp.2105-2109.

94) Aimable, A., Aymes, D., Bernard, F. and Le Cras, F., (2009): Characteristics of $LiFePO_4$ obtained through a one step continuous hydrothermal synthesis process working in supercritical water, Solid State Ionics, No.180, pp.861-866.

95) Sangeeta, D. and LaGraff, J. R., (2005): "Inorganic materials chemistry desk reference" , CRC Press, 2nd ed., Florida, U.S.A.

96) Bergna, H. E. and Roberts, W.O., (2006): "Colloidal silica: fundamentals and applications" , CRC Press, 2nd ed., Florida, U.S.A.

97) Brinker, C. J. and Scherer, G. W., (1990): "Sol-gel science: the physics and chemistry of sol-gel processing" , Academic Press Inc., San Diego, CA, U.S.A.

98) Hench, L. L. and West, J. K., (1990): The Sol-Gel process, Chemical Reviews, No.90, pp.33-72.

99) Rana, K., Sil, A. and Ray, S., (2009): Synthesis of ribbon type carbon nanostructure using $LiFePO_4$ catalyst and their electrochemical performance, Materials Research Bulletin, No.44, pp.2155-2159.

100) Arumugam, D., Kalaignan, G.P. and Manisankar, P., (2009): Synthesis and electrochemical characterizations of nano-crystalline $LiFePO_4$ and Mg-doped $LiFePO_4$ cathode materials for rechargeable lithium-ion batteries, Journal of Solid State Electrochemistry, No.13, pp.301-307.

101) Dominko, R., Goupil, J. M., Bele, M., Gaberscek, M., Remskar, M., Hanzel, D .and Jamnik, J. (2005): Impact of $LiFePO_4/C$ Composites Porosity on Their Electrochemical Performance, Journal of The Electrochemical Society, No.152(5), pp.A858-A863.

102) Hsu, K. F., Tsay, S. Y. and Hwang, B. J., (2005): Physical and electrochemical properties of $LiFePO_4$/carbon composite synthesized at various pyrolysis periods, Journal of Power Sources, No.146, pp.529-533.

103) Dominko, R., Bele, M., Gaberscek, M., Remskar, M., Hanzel, D., Goupil, J. M., Pejovnik, S. and Jamnik, J., (2006): Porous olivine composites synthesized by sol-gel technique, Journal of Power Sources, No.153, pp.274-280.

104) Kim, J. K., Choi, J. W., Chauhan, G. S., Ahn, J. H.,

Hwang, G. Ch., Choi, J. B., and Ahn, H. J., (2008): Enhancement of electrochemical performance of lithium iron phosphate by controlled sol-gel synthesis, Electrochimica Acta, No.53, pp.8258-8264.

105) Yang, J. and Xu, J. J., (2004): Nonaqueous Sol-Gel Synthesis of High-Performance $LiFePO_4$, Electrochemical and Solid-State Letters, No.7, pp.A515-A518.

106) Lin, Y., Gao, M. X., Zhu, D., Liu, Y. F. and Pan, H. G., (2008): Effects of carbon coating and iron phosphides on the electrochemical properties of $LiFePO_4$/C, Journal of Power Sources, No.184, pp.444-448.

107) Li, X., Wang, W., Shi, C., Wang, H. and Xing, Y., (2009): Structural and electrochemical characterization of $LiFePO_4$/C prepared by a sol-gel route with long- and short-chain carbon sources, Journal of Solid State Electrochemistry, No.13, pp.921-926.

108) Choi, D. and Kumta, P. N., (2007): Surfactant based sol-gel approach to nanostructured $LiFePO_4$ for high rate Li-ion batteries, Journal of Power Sources, No.163, pp.1064-1069.

109) Dominko, R., Bele, M., Goupil, J. M., Gaberscek, M., Hanzel, D., Arcon, I. and Jamnik, J., (2007): Wired porous cathode materials: A novel concept for synthesis of $LiFePO_4$, Chemistry of Materials, No.19, pp.2960-2969.

110) Dominko, R., Bele, M., Gaberscek, M., Remskar, M., Hanzel, D., Pejovnik, S. and Jamnik, J., (2005): Impact of the Carbon Coating Thickness on the Electrochemical Performance of $LiFePO_4$/C Composites, Journal of The Electrochemical Society, No.152(3), pp.A607-A610.

111) Wang, G.X., Bewlay, S., Yao, J., Ahn, J.H., Dou, S.X. and Liu, H.K., (2004): Characterization of $LiM_xFe_{1-x}PO_4$ (M=Mg, Zr, Ti) Cathode Materials Prepared by the Sol-Gel Method, Electrochemical and Solid State Letters, No.7(12), pp.A503-A506.

112) Lee, S. B., Cho, S.H., Aravindan, V., Kim, H.S. and Lee, Y.S., (2009): Improved Cycle Performance of Sulfur-Doped $LiFePO_4$, Bulletin of the Korean Chemical Society, No.30(10), pp.2223-2226.

113) Gaberscek, M., Dominko, R., Bele, M., Remskar, M. and Jamnik, J., (2006): Mass and charge transport in hierarchically organized storage materials. Example: Porous active materials with nanocoated walls of pores, Solid State Ionics, No.177, pp.3015-3022.

114) Salah, A., Mauger, A., Julien, C.M. and Gendron, F., (2006): Nano-sized impurity phases in relation to the mode of preparation of $LiFePO_4$, Materials Science and Engineering B, No.129, pp.232-244.

115) Iltchev, N., Chen, Y., Okada, Sh. and Yamaki, J., (2003): $LiFePO_4$ storage at room and elevated temperatures, Journal of Power Sources, No.119-121, pp.749-754.

116) Bhuvaneswari, M.S., Bramnik, N.N., Ensling, D., Ehrenberg, H. and Jaegermann, W., (2008): Synthesis and characterization of Carbon Nano Fiber/$LiFePO_4$ composites for Li-ion batteries, Journal of Power Sources, No.180, pp.553-560.

117) Sides, C.R., Croce, F., Young, V.Y., Martin, C.R. and Scorsati, B., (2005): A high rate, Nanocomposite $LiFePO_4$/Carbon cathode, Electrochemical and Solid-State Letters, No.8(9), pp.A484-A487.

118) Croce, F., Epifanio, A.D., Hassoun, J., Deptula, A., Olczac, T. and Scorsati, B., (2002): A novel concept for the synthesis of an improved $LiFePO_4$ lithium battery cathode, Electrochemical and Solid-State Letters, No.5(3), pp.A47-A50.

119) Lee, S.J., (2002): "Spray combustion synthesis process for the preparations of nano-sized ultrafine ceramic powders" , Ph.D. thesis in materials science and engineering, Kyungnam University, South Korea.

120) Lee, J. H., Jung, K. Y., and Park, S.B., (1999): Modification of titania particles by ultrasonic spray pyrolysis of colloid, Journal of Materials Science, No.34, pp.4089-4093.

121) Teng, T. H., Yang, M. R., Wu, Sh. H. and Chiang, Y. P., (2007): Electrochemical properties of $LiFe_{0.9}Mg_{0.1}PO_4$ / carbon cathode materials prepared by ultrasonic spray pyrolysis, Solid State Communications, No.142, pp.389-392.

122) Wang, G. X., Bewlay, S. L. Konstantinov, K., Liu, H. K., Dou, S. X. and Ahn, J. H., (2004): Physical and electrochemical properties of doped lithium iron phosphate electrodes, Electrochimica Acta, No.50, pp.443-447.

123) Ju, S. H. and Kang, Y. C., (2008): $LiFePO_4$/C cathode powders prepared by spray pyrolysis from the colloidal spray solution containing nano-sized carbon black, Materials Chemistry and Physics, No.107, pp.328-333.

124) Yang, M. R., Teng, T. H. and Wu, Sh. H., (2006): $LiFePO_4$/carbon cathode materials prepared by ultrasonic spray pyrolysis, Journal of Power Sources, No.159, pp.307-311.

125) Bewlay, S. L., Konstantinov, K., Wang, G.X., Dou, S. X., and Liu H. K., (2004): Conductivity improvements to spray-produced $LiFePO_4$ by addition of a carbon source, Materials Letters, No.58, pp.1788-1791.

126) Konarova, M. and Taniguchi, I., (2008): Preparation of $LiFePO_4$/C composite powders by ultrasonic spray pyrolysis followed by heat treatment and their electrochemical properties, Materials Research Bulletin, No.43, pp.3305-3317.

127) Zhang, S. S., Allen, J. L., Xu, K. and Jow, T. R., (2005): Optimization of reaction condition for solid-state synthesis of $LiFePO_4$-C composite cathodes, Journal of Power Sources, No.147, pp.234-240.

128) Konarova, M. and Taniguchi I., (2009): Physical and electrochemical properties of $LiFePO_4$ nanoparticles synthesized by a combination of spray pyrolysis with wet ball-milling, Journal of Power Sources, No.194, pp.1029-1035.

129) Konarova, M. and Taniguchi, I., (2009): Preparation of carbon coated $LiFePO_4$ by a combination of spray pyrolysis with planetary ball-milling followed by heat treatment and their electrochemical properties, Powder Technology, No.191, pp.111-116.

130) Arnold, G., Garche, J., Hemmer, R., Strobele, S., Vo-

gler, C. and Wohlfahrt-Mehrens, M., (2003): $LiFePO_4$ with enhanced performance synthesized by a novel synthetic route, Journal of Power Sources, No.119-121, pp. 247-251.

131) Zheng, J. Ch., Li, X. H., Wang, Zh. X., Guo, H. J. and Zhou, Sh. Y., (2008): $LiFePO_4$ with enhanced performance synthesized by a novel synthetic route, Journal of Power Sources, No.184, pp. 574-577.

132) Ding, Y., Jiang, Y., Xu, F., Yin, J., Ren, H., Zhuo, Q., Long, Z. and Zhang, P., (2010): Preparation of nano-structured $LiFePO_4$/graphene composites by co-precipitation method, Electrochemistry Communications, No.12, pp.10-13.

133) Li, L., Li, X., Wang, Z., Wu, L., Zheng, J. and Guo, H., (2009): Stable cycle-life properties of Ti-doped $LiFePO_4$ compounds synthesized by co-precipitation and normal temperature reduction method, Journal of Physics and Chemistry of Solids, No.70, pp.238-242.

134) Chang, Z.R., Lv, H.J., Tang, H.W., Li, H.J., Yuan, X.Z. and Wang, H., (2009): Synthesis and characterization of high-density $LiFePO_2$/C composites as cathode materials for lithium-ion batteries, Electrochimica Acta, No.54, pp.4595-4599.

135) Jugović , D., Mitrić , M., Cvjetić anin, N., Jančar, B., Mentus, S. and Uskoković , D., (2008): Synthesis and characterization of $LiFePO_4$/C composite obtained by sonochemical method, Solid State Ionics, No.179, pp. 415-419.

136) Cho, T.H. and Chung, H.T., (2004): Synthesis of olivine-type $LiFePO_4$ by emulsion-drying method, Journal of Power Sources, No.133, pp. 272-276.

137) Myung, S.T., Komaba, Sh., Hirosaki, N., Yashiro, H. and Kumagai, N., (2004): Emulsion drying synthesis of olivine $LiFePO_4$/C composite and its electrochemical properties as lithium intercalation material, Electrochimica Acta, No.49, pp. 4213-4222.

138) Myung, S.T. and Chung, H.T., (1999): Preparation and characterization of $LiMn_2O_4$ powders by the emulsion drying method, Journal of Power Sources, No.84, pp.32-38.

139) Myung, S.T., Kumagai, N., Komaba, S. and Chung, H.T., (2000): Preparation and electrochemical characterization of $LiCoO_2$ by the emulsion drying method, Journal of Applied Electrochemistry, No.30, pp.1081-1085.

140) Miller, J.S. and Drillon, M., (2002): "Magnetism: Molecules to Materials III, Nanosized magnetic materials", WILEY-VCH Verlag GmbH, Germany.

141) Solans, C. and Kunieda, H. (1997): "Industrial applications of microemulsions" , Marcel Dekker Inc., New York, U.S.A.

142) Gotoh, K., Masuda, H. and Higashitani, K., (1997): "Powder technology handbook" , 2nd ed., Marcel Dekker Inc., New York, U.S.A.

143) Xu, Zh., Xu, L., Lai, Q. and Ji, X., (2007): Microemulsion synthesis of $LiFePO_4$/C and its electrochemical properties as cathode materials for lithium-ion cells, Materials Chemistry and Physics, No.105, pp.80-85.

144) Wang, Y., Wang, Y. and Hosono, E., (2008): The Design of a $LiFePO_4$/Carbon Nanocomposite With a Core-Shell Structure and Its Synthesis by an In Situ Polymerization Restriction Method, Angewandte Chemie, No.47(39), pp.7461-7465.

145) Kang, B. and Ceder, G., (2009): Battery materials for ultrafast charging and discharging, Nature, No.458, pp.190-193.

146) Ni, J. F., Zhou, H. H., Chen, J. T. and Zhang, X. X., (2007): Molten salt synthesis and electrochemical properties of spherical $LiFePO_4$ particles, Materials Letters, No.61(4-5), pp.1260-1264.

147) Luo, S., Tang, Z., Lu, J. and Z. Zhang, (2008): Electrochemical properties of carbon-mixed $LiFePO_4$ cathode material synthesized by the ceramic granulation method, Ceramics International, No.34, pp.1349-1351.

148) Palomares, V., Goni, A., Gil de Muro, I., De Meatza, I., Bengoechea, M., Miguel O. and Rojo, T., (2007): New freeze-drying method for $LiFePO_4$ synthesis, Journal of Power Sources, No.171, pp.879-885.

149) Liu, H. and Tang, D., (2008): The low cost synthesis of nanoparticles $LiFePO_4$/C composite for lithium rechargeable batteries, Solid State Ionics, No.179, pp.1897-1901.

150) Iriyama, Y., Yokoyama, M., Yada, C., Jeong, S.K., Yamada, I., Abe, T., Inaba, M., and Ogumia, Z., (2004): Preparation of $LiFePO_4$ Thin Films by Pulsed Laser Deposition and Their Electrochemical Properties, Electrochemical and Solid-State Letters, No.7(10), pp.A340-A342.

151) Sauvage, F., Baudrin, E., Morcrette, M. and Tarascon, J. M., (2004): Pulsed Laser Deposition and Electrochemical Properties of $LiFePO_4$ Thin Films, Electrochemical and Solid-State Letters, No.7(1), pp.A15-A18.

152) Sun, J., Tang, K., Yu, X., Li, H. and Huang, X., (2009): Needle-like $LiFePO_4$ thin films prepared by an off-axis pulsed laser deposition technique, Thin Solid Films, No.517(8), pp.2618-2622.

153) Palomares, V., Ruiz de Larramendi, I., Alonso, J., Bengoechea, M., Goni, A., Miguel, O. and Rojo, T., (2009): $LiFePO_4$ thin films grown by pulsed laser deposition: Effect of the substrate on the film structure and morphology, Applied Surface Science, Article in Press, doi:10.1016/j.apsusc.2009.10.105.

154) Xie, J., Imanishi, N., Zhang, T., Hirano, A., Takeda, Y. and Yamamoto, O., (2009): Li-ion diffusion kinetics in $LiFePO_4$ thin film prepared by radio frequency magnetron sputtering, Electrochimica Acta, No.54, pp.4631-4637.

Author’s short biography

Ozan Toprakci

Mr. Ozan Toprakci is currently a Ph.D. student in the Fiber and Polymer Science Program, Department of Textile Engineering, Chemistry and Science, at North Carolina State University. His research interests focus on electrospinning and the design of nanofiber-based cathode materials for Li-ion batteries and energy applications in textiles.

Hatice A.K. Toprakci

Mrs. Hatice A.K. Toprakci is currently a Ph.D. student in the Fiber and Polymer Science Program, Department of Textile Engineering, Chemistry and Science, at North Carolina State University. Her research interests focus on plasma modification of textile materials, conducting polymer nanocomposites, piezoresistive composites, electrospinning, and Li-ion batteries.

Liwen Ji

Dr. Liwen Ji is currently a Post-Doctoral Research Associate at Lawrance Berkeley National Labratory in California. He earned a Ph.D. from the Fiber and Polymer Science Program at North Carolina State University in 2009. His research interests include the synthesis of inorganic nanostructures, electrospinning, and nanofiber-based anode materials for Li-ion batteries.

Xiangwu Zhang

Dr. Xiangwu Zhang is an Assistant Professor in Textile Engineering, Chemistry, and Science Department at North Carolina State University. He received his B.S. in Polymer Materials and Engineering in 1997 and Ph.D. in Materials Science and Engineering in 2001, both from Zhejiang University. He joined the Center for Electrochemical Systems and Hydrogen Research at Texas A&M University as a postdoctoral associate under the supervision of Professor A. John Appleby in 2001. During 2002 - 2006, he was a postdoctoral associate under the supervision of Professor Peter S. Fedkiw in the Department of Chemical and Biomolecular Engineering at North Carolina State University. He joined the faculty in the Department of Textile Engineering, Chemistry, and Science at North Carolina State University in 2006. Zhang's current research interests focus on nanostructured and multifunctional polymer, composite, and fiber materials with an emphasis on practical applications: i) energy storage and conversion, and ii) chemical and biological protection. His research encompasses both fundamental materials studies such as synthesis and physical characterization, as well as system design and fabrication.

Forming and Microstructure Control of Ceramics by Electrophoretic Deposition (EPD)†

Yoshio Sakka*and Tetsuo Uchikoshi
National Institute for Materials Science[1]

Abstract

Electrophoretic deposition (EPD) is one of the colloidal processes during in ceramic production and has gained significant interest because of the high versatility of its use with different materials including nanoparticles and its cost-effectiveness requiring simple equipment. Of the major parameters for ceramic processing involving the EPD, preparation of the suspensions and application methods of electric fields are particularly important factors that affect the microstructure. At the beginning of this review, we introduce the fundamental aspects of the EPD processing. We then focus on the following four points: (1) the stability of the $Pb(Zr,Ti)O_2$ */ethonol suspension by the addition of phosphate esters and its influence on the subsequent EPD process, (2) the stability of a* TiO_2*/(2-propanal + 2.4 − pentanedione) suspension, which is a suspension without dispersants, (3) the film performance of the pulsed direct current EPD using an aqueous suspension, and (4) the laminated textured ceramics by EPD in a strong magnetic field.*

Keywords: electrophoretic deposition, colloidal stability, pulsed DC, textured ceramics, magnetic field

1. Introduction

Electrophoretic deposition (EPD) is the process of forming deposited layers of particles on substrates. In this process material, particles such as ceramics are electrically charged and dispersed in a liquid medium. When an electric field is applied to the suspension, the charged particles migrate toward the electrode with the opposite charge and the particles are then deposited onto the substrates. This EPD technique is receiving attention as a convenient method of producing relatively uniform deposition films of particles within a short time interval and at low cost[1-7]. Electrically conductive materials such as metals and graphite are generally used as substrates and as electrodes. Although the mechanism of the particle deposition has not been completely elucidated, it is generally believed that particles migrate toward the oppositely charged electrode under the effect of an electric field; when they reach the surface of the substrate, the repulsive potential between the particles is reduced, and the particles coagulate because of van der Waals attraction and are deposited on the substrate.

Of the major parameters for ceramic processing involving the EPD, preparation of the suspensions and application methods of the electric fields are particularly important factors that affect the microstructure[8-12]. In this review, after introduction to the EPD processing, we focus on the following four points: (1) the stability of the ceramic particle /ethonal suspension by the addition of phosphate esters and its influence on the subsequent EPD process, (2) the stability of the ceramic particle/(2-propanal + 2.4-pentanedione) suspension, which is a suspension without dispersants, (3) the film performance of the pulsed direct current EPD using an aqueous suspension, and (4) the laminated textured ceramics by EPD in a strong magnetic field.

2. Electrophoretic Process as Consolidation and Formation Technology for Particles

The electrophoretic process, as a colloidal process, can easily accommodate denser green bodies as compared to dry processes. **Fig. 1** shows a comparison

---

† Accepted: August 30th, 2010

[1] 1-2-1, Sengen, Tsukuba, Ibaraki 305-0047, Japan

* Corresponding author
TEL:81-29-859-2461, FAX: 81-29-859-2401
E-mail: SAKKA.Yoshio@nims.go.jp

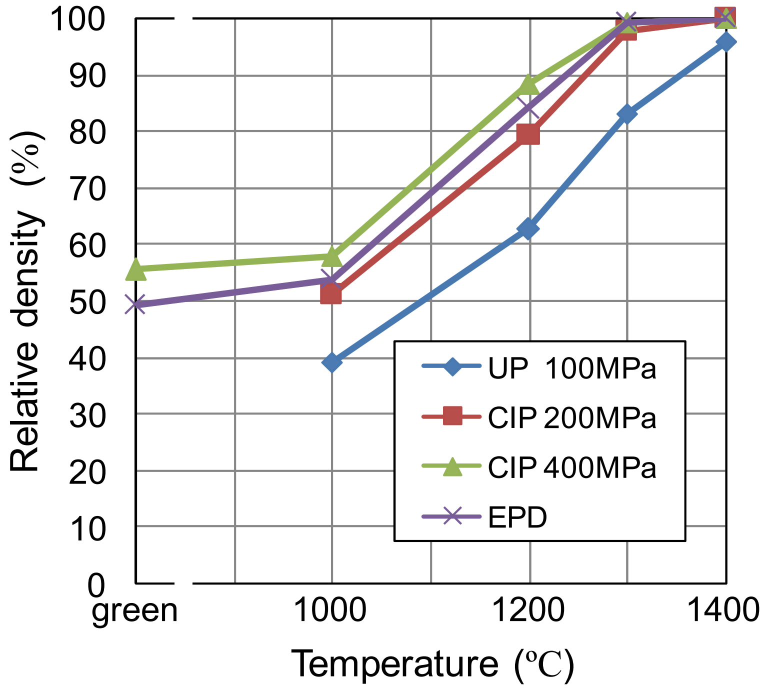

Fig. 1 Difference in sintering density of zirconia nanoparticles depending on preparation methods.

of the sintering behavior in air of the following samples: (1) zirconia (3YTZ) nanoparticle green body formed by uniaxial pressing (UP) at 100 MPa, (2) zirconia nanoparticle green body formed by UP at 100 MPa and subsequent cold isostatic pressing (CIP) at 200 or 400 MPa, and (3) zirconia nanoparticle green body formed by EPD. The green body formed by EPD exhibited a degree of sintering comparable to or better than the degree of sintering of the green body formed by CIP at 200 MPa

In the casting method such as slip casting in which a solvent moves through the pore channels consolidated by the particles, the channel size becomes narrower and the casting rate declines as the particle size decreases[13,14]. However, during the electrophoretic process in which particles themselves move, the deposition rate does not depend on the particle size and is extremely fast. Based on this point, EPD is a suitable method for consolidating nanoparticles. As compared with tape casting, EPD is also suitable for the production of thickness-controlled laminates with good adherence between the layers.[15] Therefore, recently EPD has recently been applied in many fields, such as dielectric films[16-19], electrochromic films[20], lithium batteries[21], fiber-reinforced composites[22], solid oxide fuel cell laminates [23-26], phosphor films[27,28], etc.

A significant advantage of using electric fields is that the charged particles in solution do not directly migrate to the electrodes the shortest distance away, but rather migrate along the electric potential gradient in a space filled with solution and then deposit. **Fig. 2** shows a schematic representation of the electric field lines and migration of particles between two cylindrical electrodes. Unlike during vapor deposition and sputtering, particles migrating between the electrodes along the electric field lines can reach the backside of the electrodes, and thus, relatively uniform deposition layers can be easily formed on substrates with curved or uneven surfaces. Therefore, by three-dimensionally controlling the polarity and spatial position of the electrodes and electric field potential, particles can be led to a specific location on a substrate and deposited there.[29] Such particle assembling by precise control of the electric fields is considered a great advantage of the electrophoretic process. **Fig. 3** shows an example of a deposition pattern formed with zirconia (3Y-SZ) nanoparticles on a conducting polymer (polypyrrole; PPy) pattern electrode formed on silica glass.[30, 31]

Attention is being focused on a process of producing ceramics onto which the contours and patterns of the substrates are transferred. In this process, by using the capability of EPD to produce dense green bodies, as shown in **Fig. 1**, and to form deposition layers on substrates with curved or uneven surfaces, particles are deposited on a substrate that has been previously processed into the desired form or

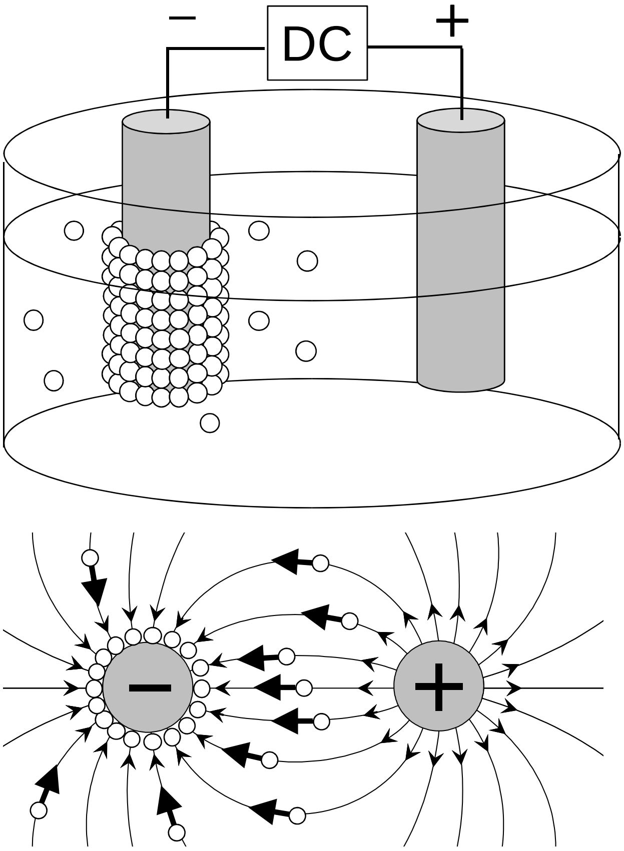

Fig. 2 Electric field lines and migration of particles between two cylindrical electrodes.

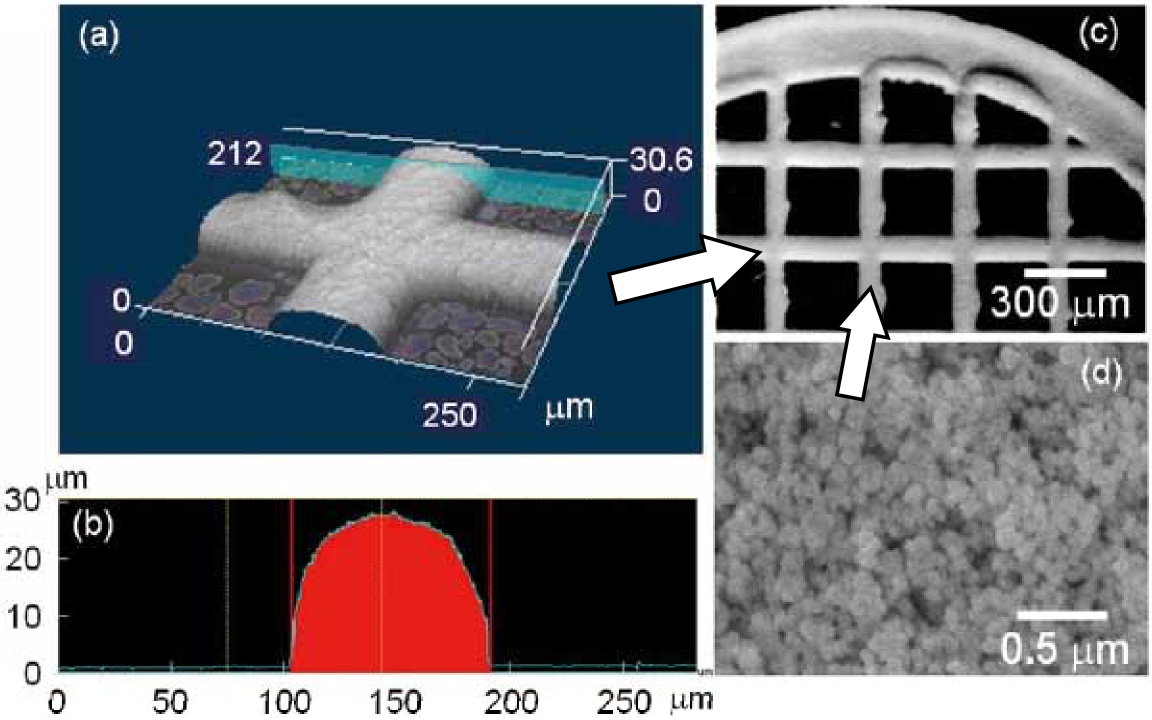

Fig. 3 Zirconia particle deposition layer on a polypyrrole (PPy) pattern electrode. (a), (b): cross section by 3D laser microscope, (c) stereoscopic microscope image, and (d) SEM image of deposited particles.

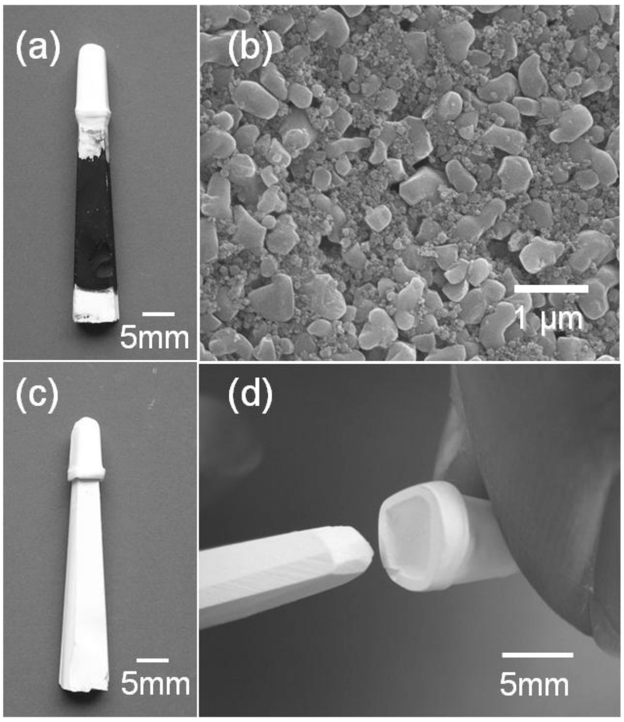

Fig. 4 Alumina deposition layer formed onto the ceramic substrate coated with conducting polymer: (a) appearance before sintering, (b) surface of deposition layer before sintering, and (c) and (d) appearance after sintering.

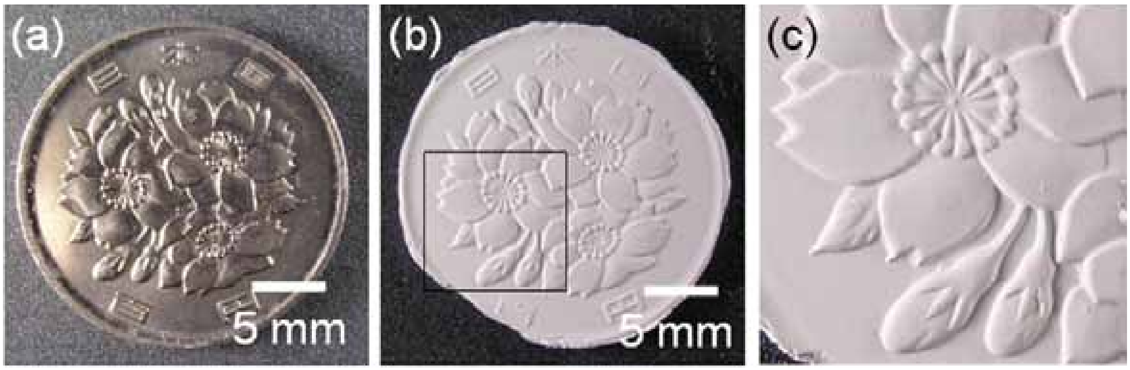

Fig. 5 Free-standing alumina film (after sintering) onto which the pattern of a 100-yen coin was copied.

impressed with complex patterns in advance. The obtained deposition layer and the substrate, which is also the electrode, are then sintered together. **Fig. 4** shows a cap-like sintered body that is an example of such products. Bimodal alumina powders (particle size: 0.6 μm + 30 nm) are deposited by the EPD on a ceramic substrate coated with PPy, and the deposited layer and the coated substrate are then dried and sintered together in air. Because the PPy layers are then decomposed during sintering in air, the use of ceramic substrates that have been previously processed into the desired shape in advance produces ceramic sintered bodies to which the shape of the substrates are clearly transferred. **Fig. 5** shows an example of a free-standing alumina films with the surface pattern of a coin produced by this method. An elaborate pattern has been accurately copied onto the film.[31)]

Fig. 6 shows a schematic representation of the migration and deposition of particles and ions in a suspension in an electric field. Particles having an electric double layer migrate in a medium. When they reach the substrate, they gradually lose the electric double layer; subsequently, they coagulate and are deposited on the substrate. During this process, the particles are pressed onto the substrate due to the effect of the electric field. Because the cohesive power becomes weak if the repulsive potential does not significantly decrease, only low-density green

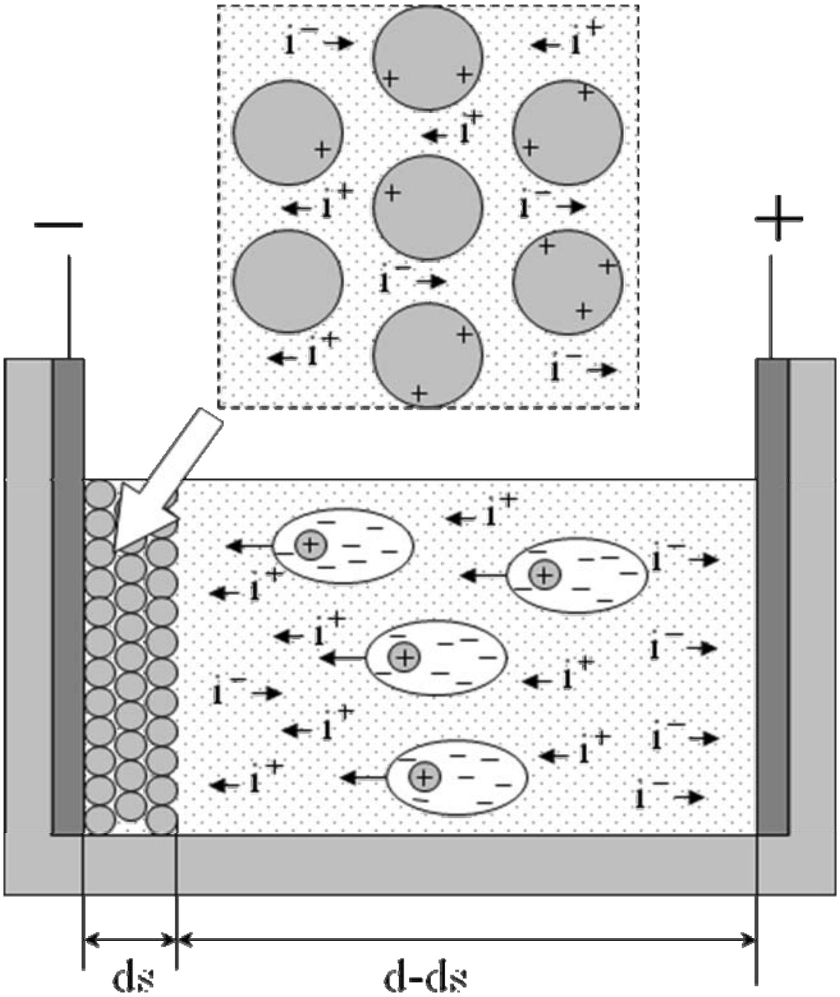

Fig. 6 Migration and deposition of particles and ions in suspension.

bodies may be obtained or particles may slip off the substrate when the electricity is turned off. According to Hamaker's mass balance law, the weight of particles deposited by the electrophoretic process W (g) can be expressed by the following equation:[32)]

$$\frac{dW}{dt} = f\mu CES \tag{1}$$

where t is the deposition time (s), μ is the electrophoretic mobility ($m^2V^{-1}s^{-1}$), E is the electric potential gradient (V/m), C is the amount of the solid phase in the suspension (g/m^3), S is the electrode area (m^2), and f is the adhesion probability of particles reaching the substrate ($0 \leqq f \leqq 1$). The electric potential gradient E varies during the particle deposition, and the following equation holds between the current in the circuit I (A) and the electric conductivity Λ (S/m):

$$E = \frac{I}{S\Lambda} \tag{2}$$

The potential applied to the circuit V_a decreases due to potential drops at the anode and cathode, and also by any ohmic loss in the suspension and the solidified layer. Therefore, the following equation holds among them:

$$V_a = \Delta\phi_{anode} + IR_{sus}(d - d_s) + IR_s d_s + \Delta\phi_{cathode} \tag{3}$$

where $\Delta\Phi_{anode}$ and $\Delta\Phi_{cathode}$ are the potential drops at the anode and cathode, respectively; R_{sus} and R_s are the values of the apparent resistance (Ω/m) of the suspension and solidified layer, respectively; d is the distance between the electrodes; and d_s is the thickness of the solidified layer. When the electrophoretic process is performed in a constant voltage mode, the decrease in the current of the circuit with time indirectly indicates the IR-drop, that is, the progress of the particle deposition. In the constant current mode, the increase in voltage with time indicates the progress of the particle deposition.

3. Suspensions Suitable for EPD

Difficulties in the EPD process can be classified into the following four categories: particles do not deposit; layers do not thicken; the quality of layers is poor; and the layers crack. These are mostly caused by problems with the method used for preparing the suspensions. Generally, suspensions suitable for the EPD process require the following:

- The particle surfaces are charged. (If the particles are not charged, they do not migrate by the applied electric field.)
- Particles are well dispersed. (Coagulated suspensions result in low-density deposited bodies.)
- Suspensions contain excess ions. (Ions other than the charged particles lower the transport number of the particles. Compression of the electric double layer reduces the stability of the slurry.)
- Particles have a high adhesion ability. (Binders can be added as necessary.)

Normal colloidal processes often involve aqueous solvents because of their lower cost and environmental load, and ease in controlling dispersion and coagulation[33-40]. Although aqueous solvents can be used in the electrophoretic process, non-aqueous solvents are often selected because aqueous solvents evolve gases, which cause the formation of pores in deposited bodies due to the electrolysis of water. As stated above, the electrophoretic process requires particles that have surfaces charged in a liquid. In a few cases, stable suspensions with high zeta potentials can be prepared by simply adding particles to the solvents and stirring. However, in general, to positively or negatively charge particles, a proper amount of acid, base, or polyelectrolytes having functional groups such as amino groups and carboxylic groups on the side chains must be added to a solution to which powders are added.

Ceramic particles in solution usually adsorb hydroxyl groups on their surfaces. When an acid or base is added to the solution, the hydroxyl groups on the surfaces are protonated or deprotonated, as shown in the following formulas. Thus, the particle surfaces are charged positively or negatively.

$$(\mathrm{M-OH})+\mathrm{H}^{+}\leftrightarrow(\mathrm{M\text{-}OH_2})^{+} \quad \text{(acidic condition)} \quad (4)$$

$$(\mathrm{M-OH})+\mathrm{OH}^{-}\leftrightarrow(\mathrm{M\text{-}O})^{-}+\mathrm{H_2O} \quad \text{(basic condition)} \quad (5)$$

Polyelectrolytes are adsorbed onto the particle surfaces, and the side chains of the polyelectrolytes are positively or negatively charged according to the functional group. Consequently, the particle surfaces modified by the polyelectrolytes can be considered to have positive or negative charges corresponding to the functional group. While acid, base, and polyelectrolytes have the advantage of producing positive or negative charges (which are necessary to electrophoresis) to the particle surfaces, they are disadvantageous because the unadsorbed ions compress the electric double layers; in this case, the dispersiveness of the suspensions becomes worse if they are added in excess. Furthermore, excess free ions become the majority charge carriers in solution and the transport number of the charged particles significantly drops. Therefore, special care must be taken not to add excess ions because this may prevent particle deposition and thickening of the layers even though the EPD is conducted for a long time. Cationic, anionic, or nonionic polymers are ofen used as binders. Because the excess addition of binders also causes the poor deposition of particles, a decrease in the layer density, and lack of uniformity of layers, the optimum amount of binders must be determined by adding them in small increments and carefully observing the results.

3.1. Preparation of suspensions using acidic phosphoesters

Phosphate esters are formed by dehydration condensation between phosphoric acid ($\mathrm{O{=}P(OH)_3}$) and an alcohol (ROH), and all or part of the three hydrogen atoms in the phosphoric acid are substituted by organic groups R. Phosphate esters having one, two, and three substituents are called monophosphate esters, dishosphate esters, and triphosphate esters, respectively. Of these, the monophosphate esters and dishosphate esters are also called acidic phosphate esters because they easily lose protons due to the dissociation of the O-H bond of the hydroxyl groups bounded to the phosphorus; conseqyently, they act as relatively strong acids even in organic solvents[30, 31].

$$\mathrm{O{=}P(OR)(OH)_2} \leftrightarrow \mathrm{O{=}P(OR)(OH)O^{-}+H^{+}} \leftrightarrow \mathrm{O{=}P(OR)O^{2-}+2H^{+}} \quad (6)$$

$$\mathrm{O{=}P(OR)_2OH} \leftrightarrow \mathrm{O{=}P(OR)_2O^{-}+H^{+}} \quad (7)$$

In suspensions to which acidic phosphate esters are added, dissociated protons $\mathrm{H^+}$ in organic solvents are adsorbed onto the particle surfaces to produce the positive charges. When the adsorbed amount of protons becomes saturated and the concentration of protons in the solution becomes excessive, the degree of dissociation declines and an excessive increase in the ionic strength of the solution can be avoided.

Fig. 7 shows the relationship between the amount of butyl acid phosphate (JP-504; Johoku Chemical

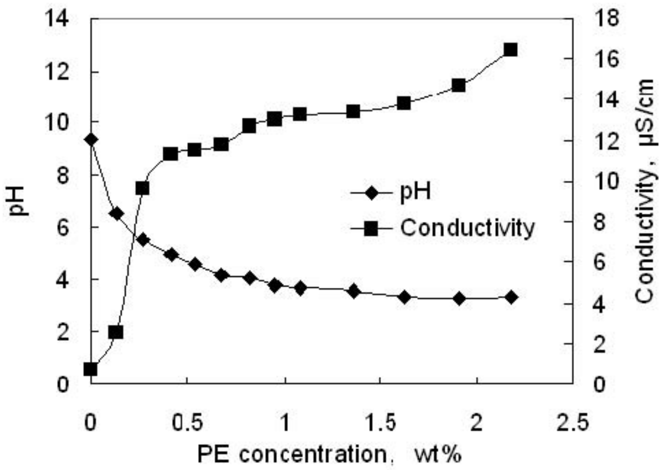

Fig. 7 Relationship between the amount of added phosphoester and the pH and electric conductivity of PZT suspension (left).

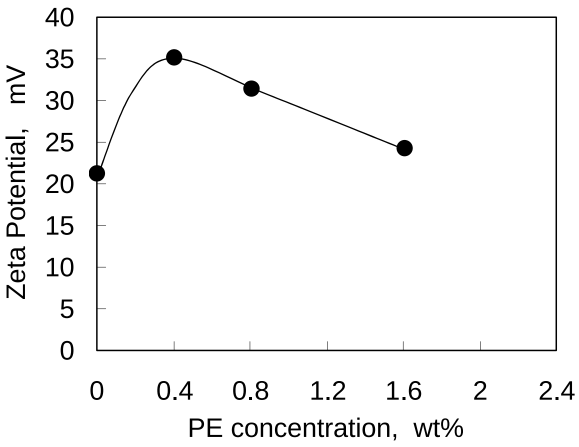

Fig. 8 Relationship between zeta potential of PZT and the amount of added phosphoester (right).

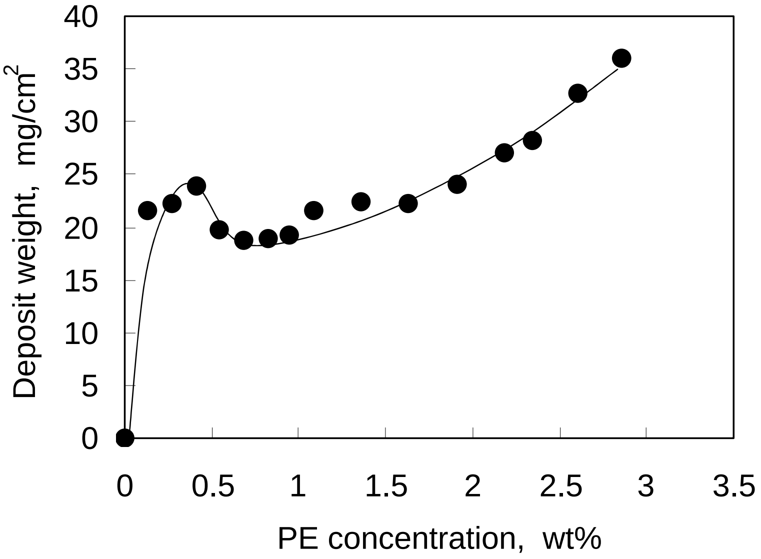

Fig. 9 Relationship between the weight of PZT particles deposited by EPD and the amount of added phosphoester (100 V, 4-min energizing).

Co., Ltd.) added and the pH and electric conductivity of a suspension of PZT (average particle size: 93 nm; Sakai Chemical Industry Co., Ltd.)28). At first, the pH and electric conductivity significantly change with the addition of the phosphate ester, but the changes slow down when the added amount reaches about 0.4wt%. The zeta potential at this level is shown in **Fig. 8**. It represents the zeta potential that reaches a peak when the added amount reaches about 0.4wt%. A comparison showed that the adsorption equilibrium can be easily determined by monitoring the changes the pH and electric conductivity of the slurry when adding the phosphate esters. **Fig. 9** shows the relationship between the deposited weight of the PZT particles on a 304 stainless steel substrate and the amount of added phosphate ester (Experimental conditions: concentration, 1.3 vol; applied voltage, 100 V; area of a substrate, $4cm^2$; and energized time, 4min). The deposited weight of the particles reaches a local maximum at 0.4wt% of the amount of added phosphate ester and then decreases once, but increases again with the addition of excess phosphate ester. When the slurry to which the added phosphate ester in excess was used in an experiment, the adhesiveness of the particles to the stainles steel substrate was so strong that the deposited layers could not be easily wiped off with a Kimwipe®wipe paper. This may be because phosphate esters have the effect of enhancing the affinity to metals. A dense PZT ceramics was obtained after sintering at 1250℃ and the following properties were observed; the remanent polarization, Pr, was 38mC/cm^2; and the coercive field, Ec, was 20kV/cm. No influence of residual phosphorous impurities (0.41wt% of phosphate ester addition) was observed[28].

3.2 Preparation of binder-free suspensions

If binders are added to the suspensions, in some cases they must be removed during the subsequent heating or sintering process. Although a normal binder-removal treatment usually involves heating at 773 K or higher, the heat treatment must be avoided in some cases. For example, in the case of photoelectrodes for dye-sensitized solar cells (DSSCs), which are formed by the deposition of titania (anatase) onto transparent indium tin oxide (ITO) transparent electrodes, the heat treatment temperature is restricted to 673 K or less to prevent a drastic drop in the electric conductivity of the ITO. Such cases require binder-free suspensions having a good stability and adherence [41, 42].

A mixed solvent system of 2,4-pentanedione (acetylacetone) and 2-propanol is a dispersion medium that allows control of the particle dispersion by simply varying the mixing ratio. **Fig. 10** shows the appearances of suspensions having various solvent mixing ratios, in which titania nanoparticles (TiO_2, average particle size: 30 nm; NanoTek) were dispersed using an ultrasonic homogenizer. The solutions stood for two weeks after the dispersion. The figure indicates that the suspensions become stable when the suspensions contain 20 to 50 vol% of 2-propanol. **Fig. 11** shows the relationship between the electrophoretic mobility of these nanoparticles the mixed solvents of 2,4-pentanedione and 2-propanol, and the mixing ratio of the solvents. The electrophoretic mobility shows the highest value at the mixing ratio of 50:50, suggesting that the surface charges of titania reach a peak at that ratio. The amount of protons generated by the keto−enol tautomerism of 2,4-pentanedione (represented in the following equation) and the amount of protons adsorbed onto the titania particles was balanced [43].

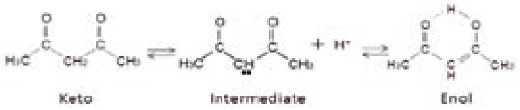

(8)

Measurement of the electric conductivity demonstrated that there are a few excess ions when the ratio of 2-propanol is lower than the mixing ratio of 50:50, and excess ions in the solution increase when the ratio of 2-propanol becomes higher. **Fig. 12** is an example of a uniform titania nanoparticle membrane formed on an ITO substrate using a suspension prepared with a solvent whose mixing ratio is 50:50. Even though binders were not added to the suspension, this membrane did not detach from the substrate even after heat treatment at 673 K, and it had a good adherence.

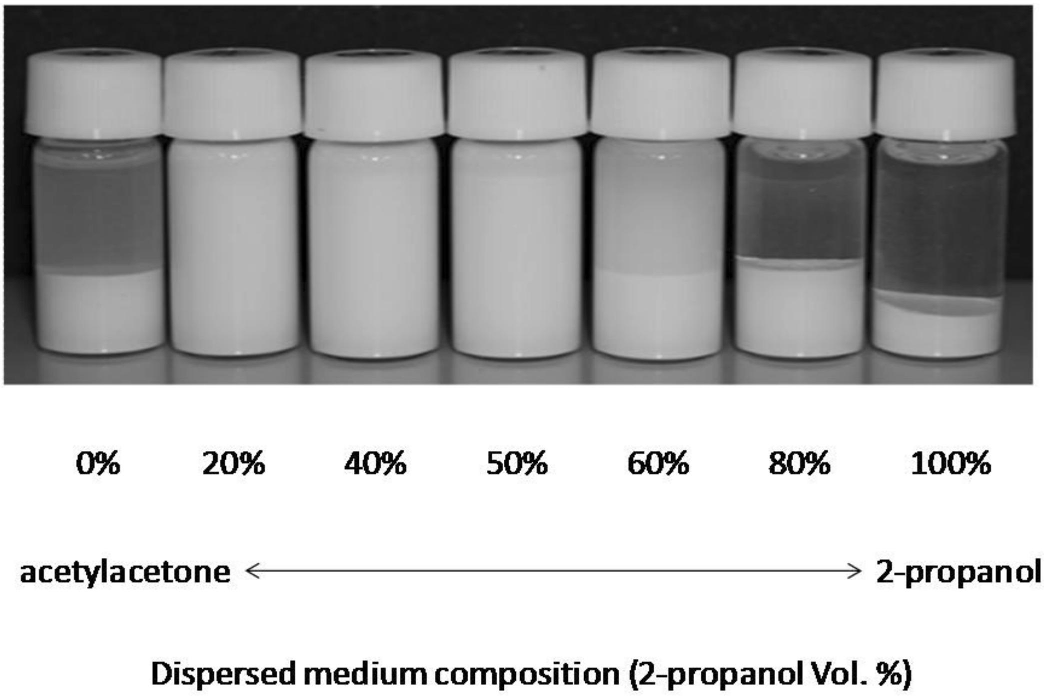

Fig. 10 Sedimentation test for dispersiveness of titania nanoparticles in a mixed solvent system of 2,4-pentanedione and 2-propanol (after two weeks).

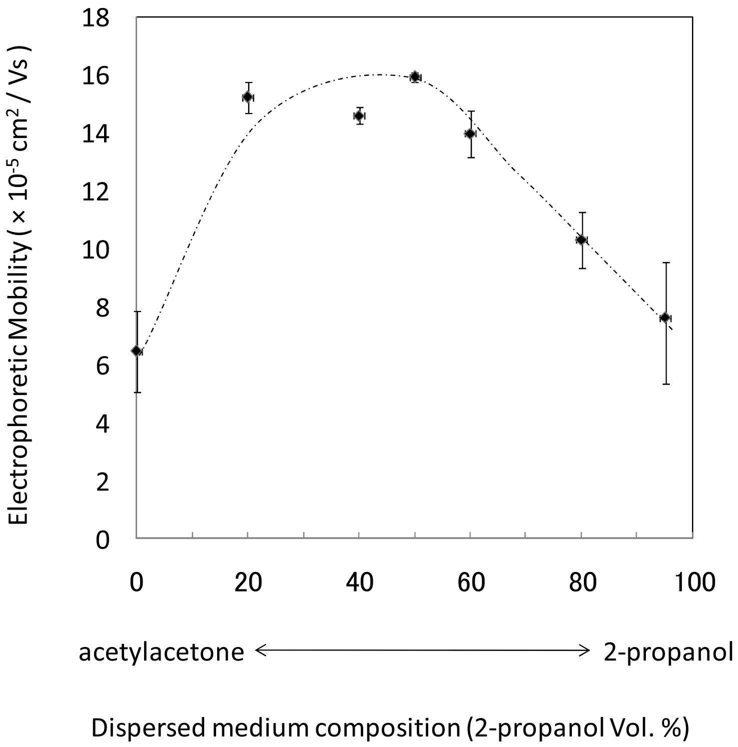

Fig. 11 Electrophoretic mobility of titania nanoparticles and the mixing ratio of 2,4-pentanedione and 2-propanol.

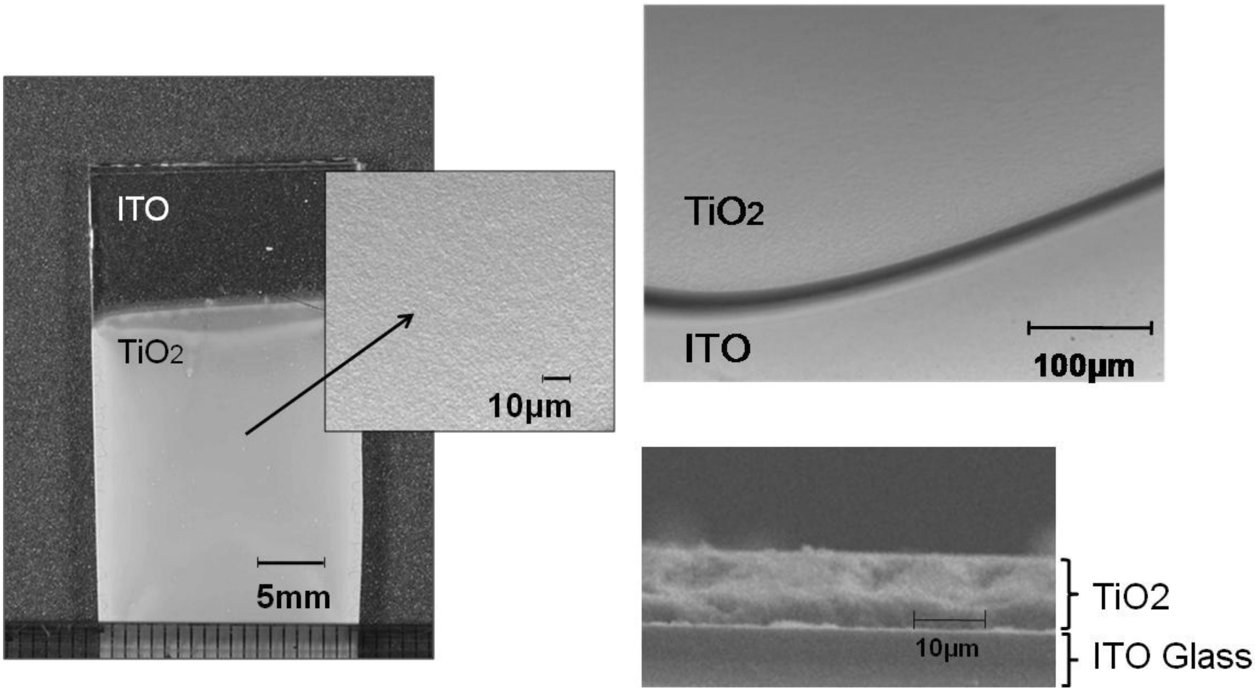

Fig. 12 Appearance and cross section of titania membrane formed on ITO glass (sintered at 673 K for 2 h).

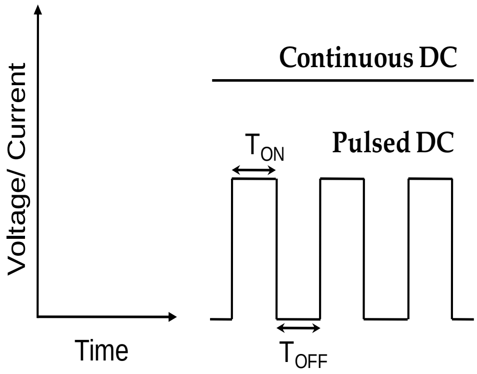

Fig. 13 Waveforms of modulated electric fields used in this study (left).

4. Use of Modulated Electric Fields

Although normal EPD processes involve a continuous direct current (DC), microstructure control of the deposited layers by using modulated electric fields such as pulsed DC electric fields [44-47] and asymmetric alternating current (AC) electric fields [48] has recently been receiving attention. This study investigated the influence of applying of a square wave and a continuous wave, as shown in **Fig. 13**, on deposited layers using a Source Meter (Model 2611; Keithley Instruments). **Fig. 14** shows the deposited layers formed from an aqueous suspension (pH 4.5) of alumina (AKP-50, average particle size: 0.2 μm; Sumitomo Chemical Co., Ltd.) on SUS316L cathode substrates by applying a square-wave current having 20 V/0 V of ON/OFF voltages and the same pulse width of the ON/OFF time for 3 min in total [44]. While a continuous current without a pulse caused formation of an unlimited number of bubbles on the surface of the deposited layers due to the electrolysis of water, the formation of bubbles was inhibited as the pulse frequency increased. The formation of bubbles was completely inhibited at a certain pulse frequency and a smooth deposited layer was obtained. When the pulse frequency was further increased, the particles did not deposit. In other words, the optimum values of the pulse frequency were within a certain range. When an increasing voltage was applied, the optimum values shifted to higher frequencies and the suitable range became narrower. The same results were obtained in a constant-current condition.

Fig. 15 shows the conditions where good-quality deposited layers having no bubbles were obtained when applying DC pulses in the constant-current mode. Alternatively, when particles negatively charged by the addition of the anionic dispersants were deposited onto the anode, the formation of bubbles could be inhibited by optimizing the pulse frequency. Although this mechanism is still under study, it is believed that the evolution of hydrogen due to the dissociation of water ($H_2O \rightarrow H^+ + OH^-$) is prevented under the conditions depicted in the diagonally shaded area of **Fig. 15** by fast switching between ON and OFF. Thus, particles continue to migrate during the OFF time due to an inertial force, and reach the substrate, resulting in formation of deposited layers having no bubbles. This suggests that the use of modulated electric fields may become more important in order to convert conventional nonaqueous-solvent processes to aqueous-solvent processes that have a lower environmental load [46),49)].

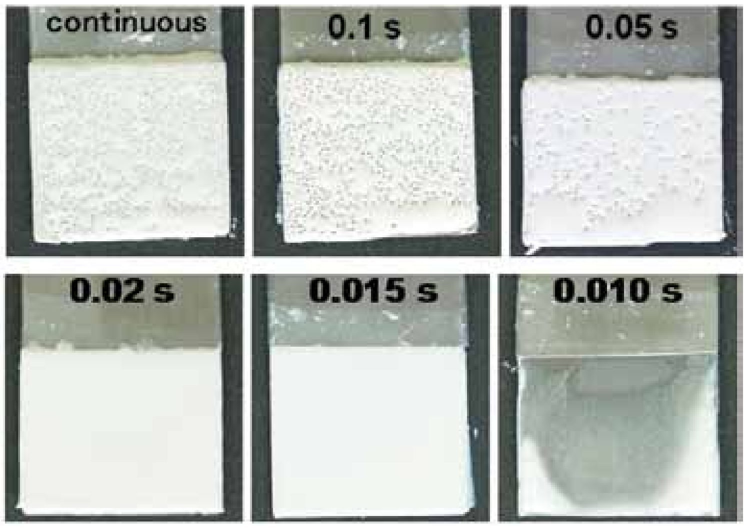

Fig. 14 Relationship between pulse width and deposited layers formed by pulsed DC EPD from an aqueous suspension of alumina on an SUS substrate (ON/OFF voltage = 20 V/0 V, 3 min in total) (right).

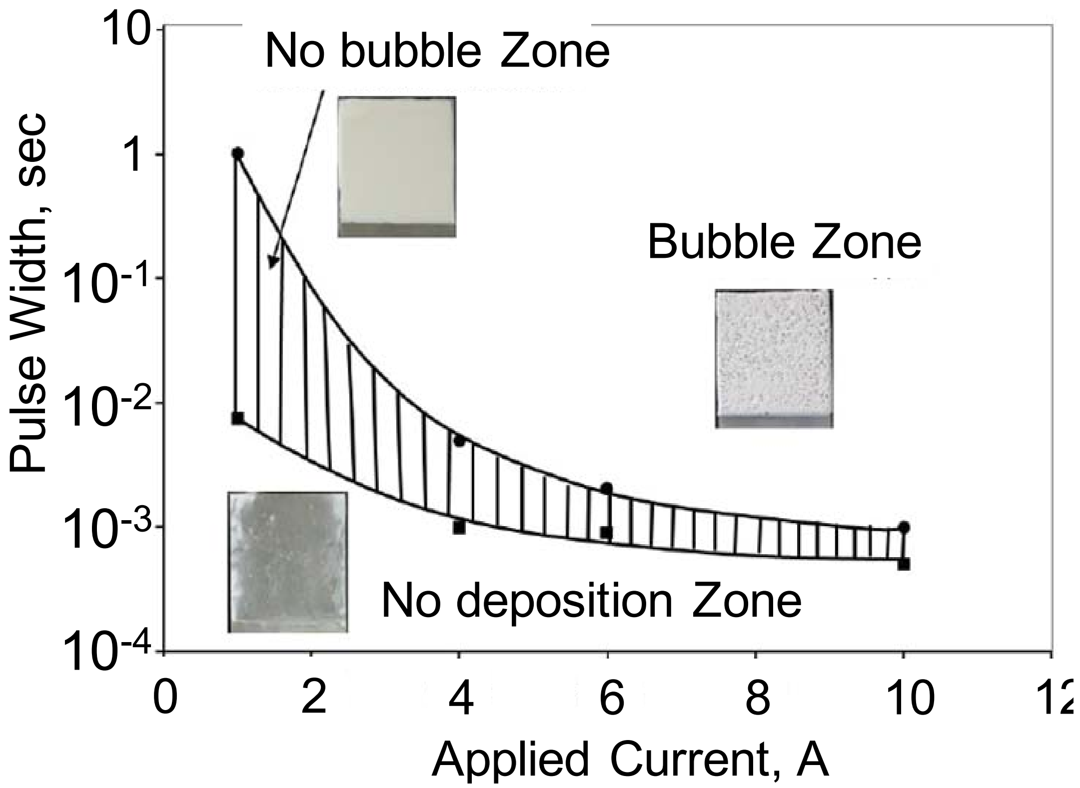

Fig. 15 Relationships between applied current and pulse width in pulsed DC EPD (in constant-current mode) and the quality of the membrane.

5. Textured Ceramics

The controlled development of a texture is one of the ways for effectively improving various properties[50-52]. Textured ceramics have been produced by a variety of techniques; such as tape casting, hot forging and templated or seeded grain growth. [50] Recently, we have demonstrated that the crystal orientation of feeble magnetic materials such as alumina can be controlled by colloidal processing in a high magnetic field. [52-54]

The principle of the process is that a crystal with an anisotropic magnetic susceptibility will rotate to an angle minimizing the system energy when placed in a magnetic field. The magnetic torque T attributed to the interaction between the anisotropic susceptibility and a magnetic field is estimated by **Eq. (9)** [52].

$$T = -\Delta\chi V B^2 \sin 2\theta / 2\mu_0 \tag{9}$$

where $\Delta\chi$, $(= |\chi_{a,b} - \chi_c|)$ is the anisotropy of the magnetic susceptibilities which are measured for the a,b-axis ($\chi_{a,b}$) and c-axis (χ_c), V is the volume of the materials, B is the applied magnetic field, θ is the angle between the easy magnetization axis in a crystal and imposed magnetic field direction, and μ_0 is the permeability in a vacuum. This magnetic torque is the driving force for the magnetic alignment.

To obtain the oriented materials with feeble magnetic susceptibilities, the following conditions are necessary: [52] 1) the crystal structure should be non-cubic in order to apply the anisotropic magnetic susceptibilities, 2) the particle should be a single crystal and well dispersed, 3) the viscosity of the suspension should be low enough to rotate the particles with a low energy, and 4) grain growth is necessary to obtain a highly oriented structure especially when a spherical particle is used. We have fabricated many kinds of oriented ceramics by the slip casting in a high magnetic field followed by sintering, such as Al_2O_3, TiO_2, ZnO, AlN, SiC, Si_3N_4, etc., [52-64] their composites, [60,65] and multi-component ceramics by reaction sintering [66]. However, when we use whisker or plate-like particles, special attention is necessary due to the effect of gravity energy[67,68] that is the highest energy in the colloidal dispersion system[69]. The effect also strongly depends on the easy magnetization angle, which has been described elsewhere.[68]

We have demonstrated that EPD in a high magnetic field is an excellent method to fabricate thick crystalline textured ceramic bodies.[70-78] The direction of the electric field relative to the magnetic field (the angle between the vector E and B) was altered (0, 45, 90°) to control the dominant crystal faces as is shown in **Fig. 16**.

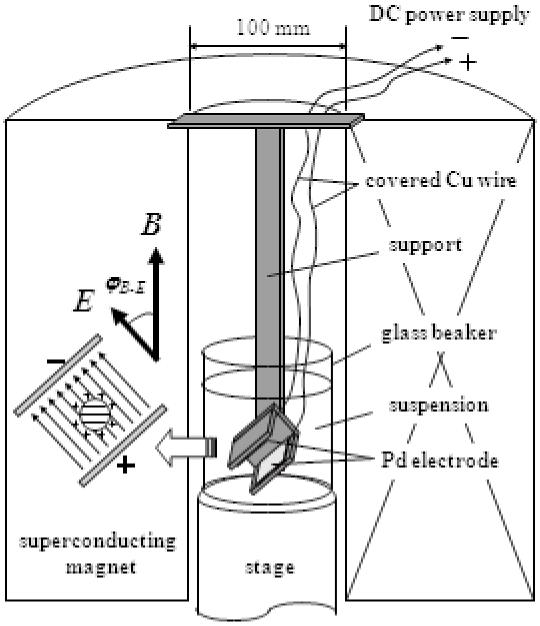

Fig. 16 Schematic of EPD in a strong magnetic field.

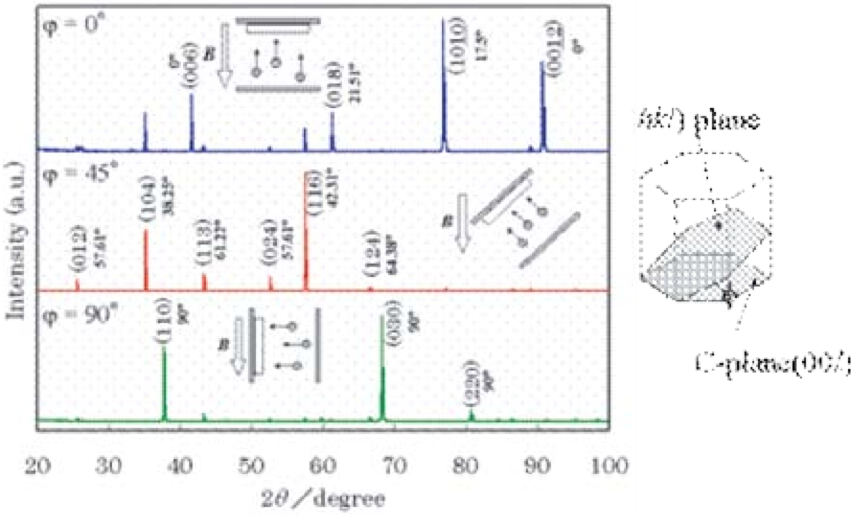

Fig. 17 Changes in the XRD patterns of the top planes with the angle between the direction of B and E.

Fig. 17 shows the variation in the XRD patterns of the top planes with the angle between the directions of B and E, where the α-alumina (particle size of 0.2µm) was deposited in 10 T followed by sintering at 1873 K. The Φ_{hkl} of the appeared peaks are also shown in the figure. When the E is parallel to B (ϕ_{B-E}=0°)), the diffraction peaks of the planes at low interplanar angles (Φ_{hkl} is close to 0°) are predominant. When the Φ_{hkl} is changed to 45°, the dominant diffraction peaks change to the planes of the intermediate interplanar angles (ϕ_{B-E} is close to 45°). When E is perpendicular to B (ϕ_{B-E} =90°)), the dominant diffraction peaks changed to the planes of high interplanar angles (Φ_{hkl} is close to 90°). These results clearly show that the dominant crystal faces can be controlled by varying the angle of E and B.

Fig. 18 shows an example of textured laminated alumina prepared by EPD in a high magnetic field. Here, the cross-sectional microstructure was prepared by alternately changing ϕ_{B-E}=0° / 90° layer by layer. It is seen that the microstructure well-reflects the change in ϕ_{B-E} during the deposition [73].

The combination of the orientation and lamination is one of the possible ways of the tailoring the micro-

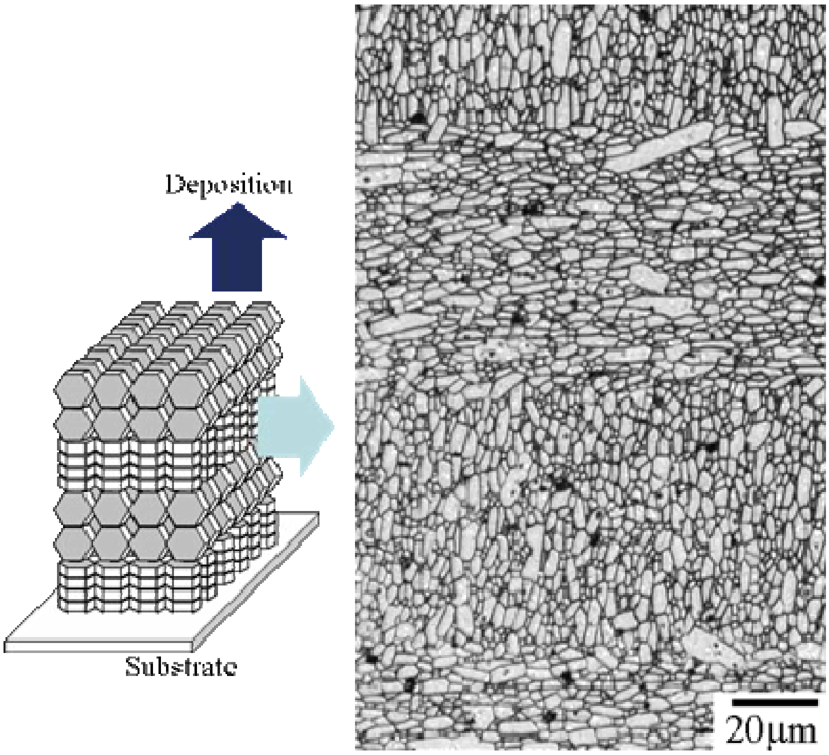

Fig. 18 Schematic illustration and the cross-sectional microstructure of a crystalline-textured alumina/alumina laminated composite prepared by electrophoretic deposition in a strong magnetic field (12 T), in which the direction of the electric current relative to the magnetic field is alternately changed from 0° to 90° , layer by layer.

structure for the improvement of the mechanical, dielectric, and thermo-electric properties, etc.[74-76]

6. Summary

Recently EPD has received a significant amount of attention for fabricating highly structured controlled ceramics resulting in advanced ceramics. The process is a simple, easy to use and cost-eefective method of deposition. Here, the preparation of suspensions suitable for EPS is very important. In this review we have introduced our recent results; (1) the stable Pb(Zr,Ti)O_2 /ethanol suspension is prepared by the addition of phosphate esters and a good film is fabricated by the subsequent EPD process, (2) the stable TiO_2/(2-propanol +2.4-pentanedione acetylacetone) suspension is prepared without dispersants and a good film is also fabricated by the subsequent EPD process , (3) a film without voids is prepared by the appropriate tpulsed DC EPD using an aqueous suspension, and (4) the laminated textured ceramics is fabricated by the EPD in a strong magnetic field. These techniques are expected to be applicable for various fields.

Acknowledgments

We wish to thank Dr. T. S. Suzuki, Dr. F.Q. Tang and Dr. L. Besra for their great contributions of this work. This work was supported by the Budget for the Grant-in Aid for Scientific Research from the Ministry of Education, Culture, Sports, Science and Technology.

References

1) Sarkar, P. and Nicholson, P. S. (1996): Electrophoretic deposition (EPD): Mechanisms, kinetics, and application to ceramics, J. Am. Ceram. Soc., 79, pp. 1987-1996.
2) Boccaccini, A. R. (2006): J. Ceram. Soc. Jpn., 114, pp.1-14.
3) Van der Biest and Vandeperre L. J. (1999): Annual Rev. Mater. Sci. 29, pp.327-352.
4) Zhitomirsky I. (2002): Cathodic electrophoretic deposition of ceramics and organoceramic materials-fundamental aspects, Adv. Colloid Interface Sci. 97, pp. 279-317.
5) Besra L. and Liu M. (2007): A review of fundamentals and spplications of electrophoretic despotion (EPD), Prog. Mater. Sci., 52, pp. 1-61.

6) Ferrari, B. and Moreno, R. (2010): EPD kinetics: A review, J. Europ. Ceram. Soc., 30, pp. 1069-1078.

7) Corni, I., Ryan, M.P. and Boccaccini, A. R. (2008): Electrophoretic deposition: From traditional ceramics to nanotechnology, J. Europ. Ceram. Soc., 28, pp. 1353-1367.

8) Lange F. F. (1989):Powder Processing Science and technology for Increased Reliability, J. Am. Ceram. Soc., 72, pp.3-15.

9) Sakka, Y. (2006): Fabrication of highly microstructure controlled ceramics by novel colloidal processing, J. Ceram. Soc. Jpn., 114, pp.371-376.

10) Tang, F. Q., Uchikoshi, T., Ozawa K, and Sakka, Y. (2006): Effect of polyethylenimine on the dispersion and electrophoretic deposition of nano-sized titania aqueous suspensions, J. Europ. Ceram. Soc., 26, pp. 1555-1560.

11) Zhu, X. W. , Uchikoshi, T., Suzuki, T.S. and Sakka, Y. (2007): Effect of polyethylenimine on hydrolysis and dispersion properties of aqueous Si3N4 suspensions, J. Am. Ceram. Soc., 90, pp.797-804 .

12) Iijima M. and Kamiya H. (2009): Surface Modification for Improving the Stability of Nanoparticles in Liquid Media, KONA, No. 27, pp. 119-129.

13) Uchikoshi, T. Sakka, Y. Ozawa, K. and Hiraga, K. (1998): Pressure Filtration and Sintering of Fine Zirconia Powder, J. Europ. Ceram. Soc., 18, pp.669-674.

14) Hirata, Y. and Tanaka,Y. (2008): Pressure filtration model of ceramic nanoparticles, J. Am. Ceram. Soc., 91, pp. 819-824 .

15) Uchikoshi, T., Hatton, B. D., Sakka, Y. and Nicholson, P. S. (2002): Electrical Conductivity of a 3Y-TZP/Alumina Laminate Composite Synthesized by Electrophoretic Deposition, J. Ceram. Soc. Jpn., 110, pp.959-962.

16) Abe, N. Hoshino, M., Kitamura, N., Ichiryu, A. and Idemoto, Y. (2010): Preparation and estimation of Ba0.9Sr0.1TiO3 dielectric films by EPD method with fine powder slurry, J. Ceram. Soc. Jpn., 118, pp. 374-379.

17) Jeong, S. J., Kim, M. S., Kim, I.S . and Cho, K. H. (2010): Electric properties of $0.2Pb(Mg_{1/3}Nb_{2/3})O_3$-$0.8Pb(Zr_{0.475}Ti_{0.52}5)O_3$ thick film fabricated by electrophoresis deposition, J. Ceram. Soc. Jpn., 118, pp. 283-290.

18) Wanga, J.Q. and Kuwabara, M. (2008): Electrophoretic deposition of BaTiO3 films on a Si substrate coated with conducting polyaniline layers, J. Europ. Ceram. Soc., 28, pp. 101-108.

19) Doungdaw, S., Uchikoshi, T., Noguchi, Y., Eamchotchawalit and Sakka, Y. (2005): Electrophoretic deposition of lead zirconate titanate (PZT) powder from ethanol suspension prepared with phosphate ester, Sci. Technol. Adv. Mater., 6, pp. 927-932.

20) Khoo, E., Lee, P. S. and Ma, J. (2010): Electrophoretic deposition (EPD) of WO_3 nanorods for electrochromic application, J. Europ. Ceram. Soc., 30, pp. 1139-1144.

21) Ferrari, B., Moreno, R., Hernan, L., Melero, M., Morales, J. and Caballero, A. (2007): EPD of thick films for their application in lithium batteries, J. Europ. Ceram. Soc., 27, pp. 3823-3827.

22) Yoshida, K. (2010): Development of silicon carbide fiber-reinforced silicon carbide matrix composites with high performance based on interfacial and microstructure control, J. Ceram. Soc. Jpn., 118, pp. 82-90.

23) Matsuda, A., Kambayashi, T., Daiko, Y., Muto, H. and Sakai, M. (2010): Electrophoretic deposition of surface-modified titanate nanosheets via layer-by-layer assembly and deposited film properties, J. Europ. Ceram. Soc., 30, pp. 1151-1158.

24) Santillan, M. J., Caneiro, A. Quaranta, N. and Boccaccini, A. R. (2010): Electrophoretic deposition of $La_{0.6}Sr_{0.4}Co_{0.8}Fe_{0.2}O_3$-delta cathodes on $Ce_{0.9}Gd_{0.1}O_{1.95}$ substrates for intermediate temperature solid oxide fuel cell (IT-SOFC), J. Europ. Ceram. Soc., 30, pp. 1125-1132.

25) Bozza, F,. Polini, R. and Traversa, E. (2009): Electrophoretic Deposition of Dense $La_{0.8}Sr_{0.2}Ga_{0.8}Mg_{0.115}Co_{0.085}O_3$-delta Electrolyte Films from Single-Phase Powders for Intermediate Temperature Solid Oxide Fuel Cells, J. Am. Ceram. Soc., 92, pp.1999-2004.

26) Suzuki, H.T., Uchikoshi, T,. Kayashi, K., Suzuki, T.S., Sugiyama, T., Furuya, K., Matsuda, M ., Sakka, Y. and Munakata, F. (2009): Fabrication of GDC/LSGM/GDC tri-layers on polypyrrole-coated NiO-YSZ by electrophoretic deposition for anode-supported SOFC, J. Ceram. Soc. Jpn., 117, pp. 1246-1248.

27) Kitabatake, T., Uchikoshi, T., Munakata, F., Sakka, Y. and Hirosaki, N. (2010): Emission color tuning of laminated and mixed SiAlON phosphor films by electrophoretic deposition, J. Ceram. Soc. Jpn., 118, pp. 1-4.

28) Kitabatake, T., Uchikoshi, T., Munakata, F., Sakka, Y. and Hirosaki, N. (2009): lectrophoretic deposition of Eu2+ doped Ca-alpha-SiAlON phosphor particles for packaging of flat pseudo-white light emitting devices, J. Ceram. Soc. Jpn., 117, pp. 740-743.

29) Hamagami, J., Hasegawa, K. and Kanamura, K.(2006): Micropattern of colloidal crystal by using electrophoretic deposition process with three-electrode system, Key Eng. Mater., 320, pp. 171-174.

30) Uchikoshi, T., Furumi, S., Shirahata, N., Suzuki, T. S. and Sakka, Y. (2006): Electrophoretic deposition of alumina on conductive polymer-coated ceramic substrates, J. Ceram. Soc. Jpn., 114, pp. 55-58 .

31) Uchikoshi, T., Furumi, S., Shirahata, N., Suzuki, T. S. and Sakka, Y. (2008): Conductive polymer coating on nonconductive ceramic substrates for use in the electrophoretic deposition process, J. Am. Ceram. Soc., 91, pp. 1674-1677.

32) Put, S., Vleugels, J. and Van der Biest, O. (2003): Acta Mater., 51, pp. 6303-6317.

33) Ferrari, B. and Moreno, R. (1996): The conductivity of aqueous Al2O3 slips for electrophoretic deposition, Mater. Letter., 28, pp.353-355.

34) Ferrari, B. and Moreno, R. (1997): Electrophoretic deposition of aqueous alumina, J. Europ. Ceram. Soc.,

17, pp.549-556.

35) Hirata,Y. , Nishimoto, A. and Ishihara, Y. (1991): J. Ceram. Soc. Jpn., 99, pp.108.

36) Fisher, R., Fisher, E., De Portu, D. and Roncari, E. (1995): Preparation of ceramic micro-laminate by electrophoresis in aqueous system, J. Mater. Sci. Lett., 14, pp. 25-27.

37) Uchikoshi, T., Ozawa, K., Hatton, B. D., Okuyama, H. and Sakka, Y. (2001): Dense, bubble-free ceramic deposits from aqueous suspensions by electrophoretic deposition, J. Mater. Res., 16, pp. 321-324.

38) Tang, F. Q., Sakka, Y. and Uchikoshi, T. (2003): Electrophoretic deposition of aqueous nano-sized zinc oxide suspensions on a zinc electrode, Mater. Res. Bull., 38, pp. 207-212.

39) Tang, F. Q., Uchikoshi, T. and Sakka, Y. (2002): Electrophoretic deposition behavior of aqueous nanosized zinc oxide suspensions, J. Am. Ceram. Soc., 85, pp. 2161-2165.

40) Tang, F. Q., Uchikoshi, T. and Sakka, Y. (2002): Electrophoretic deposition of aqueous nano-gamma-Al_2O_3 suspensions, Mater. Res. Bull., 37, pp. 653-660.

41) Kawakita, M., Uchikoshi, T., Kawakita, J. and Sakka, Y. (2009): Preparation of Crystalline-Oriented Titania Photoelectrodes on ITO Glasses from a 2-Propanol-2,4-Pentanedione Solvent by Electrophoretic Deposition in a Strong Magnetic Field, J. Am. Ceram. Soc., 92, pp.984-989.

42) Kawakita, M., Kawakita, J., Uchikoshi, T. and Sakka, Y. (2009): Photoanode characteristics of dye-sensitized solar cell containing TiO2 layers with different crystalline orientations, J. Mater. Res., 24, pp.1417-1421.

43) Yamashita, K., Nagai, M. and Umakoshi, M. (1997): Fabrication of green films of single and multi-component ceramic composites by electrophoretic deposition technique, J. Mater. Sci., 32, pp.6661-4.

44) Besra, L., Uchikoshi, T., Suzuki, T. S. and Sakka, Y. (2008): Bubble-Free Aqueous Electrophoretic Deposition (EPD) by Pulse-Potential Application, J. Am. Ceram. Soc., 91, pp.3154-3159.

45) Besra, L., Uchikoshi, T., Suzuki, T. S. and Sakka, Y. (2010): Experimental verification of pH localization mechanism of particle consolidation at the electrode/solution interface and its application to pulsed DC electrophoretic deposition (EPD), J. Europ. Ceram. Soc., 30, pp. 1187-1193.

46) Besra, L., Uchikoshi, T., Suzuki, T. S. and Sakka, Y. (2009): Application of constant current pulse to suppress bubble incorporation and control deposit morphology during aqueous electrophoretic deposition (EPD), J. Europ. Ceram. Soc., 29, pp. 1837-1845.

47) Naim, M. Kuwata, M., Kamiya, H. and Lenggoro, I.W. (2009): Deposition of TiO_2 nanoparticles in surfactant-containing aqueous suspension by a pulsed DC charging-mode electrophoresis, J. Ceram. Soc,. Jpn., 117, pp.127-132.

48) Neirinck, B., Fransauer, J., Van der Biest, O. and Vlengels, J. (2009): Electrchem. Comm., 11, pp.57-60

49) Mishra, M., Bhattacharjee, S., Besra, L., Sharma, H.S., Uchikoshi, T. and Sakka, Y. (2010): Effect of pH localization on microstructure evolution of deposits during aqueous electrophoretic deposition (EPD), J. Europ. Ceram. Soc., 30, pp. 2467-2473.

50) Messing, G. L., Trolier-McKinstry, S., Sabolsky, E. M., Duran, C., Kwon, S., Brahmaroutu, B., Park, P., Yilmaz, H., Rehrig, P. W., Eitel, K. B., Suvaci, E., Seabaugh, M. and Oh, K. S.(2004): Critical Rev. Solid State Mater. Sci., Vol. 29, pp. 45-96.

51) Zhu, X.W. and Sakka, Y. (2008): Textured silicon nitride: processing and anisotropic properties, Sci. Technol. Adv. Mater., 9, 033001.

52) Sakka, Y. and Suzuki, T. S. (2005): Textured development of feeble magnetic ceramics by colloidal processing under high magnetic field, J. Ceram. Soc. Jpn., 113, pp. 26-36.

53) Suzuki, T. S., Sakka, Y. and Kitazawa, K., (2001): Orientation Amplification of Colloidally Filtrated Alumina in a Strong Magnetic Field by Sintering , Adv. Eng. Mater. , 3, pp. 490-492.

54) Suzuki, T. S. and Sakka, Y. (2005): Preparation of oriented bulk 5 wt% Y2O3-AlN ceramics by slip casting in a high magnetic field and sintering, Scripta Mater., 52, pp. 583-586.

55) Zhu, X. W., Suzuki, T. S., Uchikoshi, T., Nishimura, T. and Sakka, Y. (2006): Texture development in Si3N4 ceramics by magnetic field alignment during slip casting, J. Ceram. Soc. Jpn., 114, pp.1093-1096.

56) Zhu, X. W., Suzuki, T. S., Uchikoshi, T, and Sakka, Y. (2007): Texturing Ca-alpha-sialon via strong magnetic field alignment, J. Ceram. Soc. Jpn., 115, pp. 701-705.

57) Zhu, X.,W. Suzuki, T. S., Uchikoshi, T. and Sakka, Y. (2008): Highly texturing beta-sialon via strong magnetic field alignment, J. Am. Ceram. Soc., 91, pp. 620-623.

58) Suzuki, T. S., Uchikoshi, T. and Sakka, Y. (2007): Fabrication of textured alpha-SiC using colloidal processing and a strong magnetic field, Mater. Trans., 48, pp. 2883-2887.

59) Tsuda, K. and Sakka, Y. (2009): Simultaneous alignment and micropatterning of carbon nanotubes using modulated magnetic field, Sci. Technol. Adv. Mater., 10, 014603.

60) Yamauchi Y, Sugiyama A, Sawada M, Komatsu. M., Takai, A, Urata, C., Hirota, N ., Sakka, Y. and Kuroda, K. (2008): Magnetically induced orientation of mesochannels inside porous anodic alumina membranes under ultra high magnetic field of 30 T: Confirmation by TEM, J. Ceram. Soc. Jpn., 116, pp.1244-1248.

61) Furumi, S., Uchikoshi, T., Shirahata, N., Suzuki, T.S. and Sakka, Y. (2009): Aqueous Dispersions of Carbon Nanotubes Stabilized by Zirconium Acetate, J. NanoSci. NanoTechnol., 9, pp. 662-665.

62) Makiya, A., Kusano, D., Tanaka, S., Uchida, N., Uematsu, K., Kimura, T. and Kitazawa, K. (2003): Particle oriented bismuth titanate ceramics made in high magnetic field, J. Ceram. Soc. Jpn. 111, pp.702.

63) Tabara, K., Makiya, A., Tanak, S., Uematsu, K. and Doshida, Y.(2007): Particle oriented strontium bismuth titanate ceramics prepared by using high magnetic field and subsequent reaction sintering, J. Ceram. Soc. Jpn., 115, pp. 237-240.
64) Kaga, H., Kinemuchi, Y., Tanaka, S., Makiya, A., Kato, Z., Uematsu, K., and Watari, K.(2006): Fabrication of c-axis oriented Zn0.98Al0.02O by a high-magnetic-field via gelcasting and its thermoelectric properties, J. Ceram. Soc. Jpn., 114, pp.1085-1088.
65) Sakka, Y., Suzuki, T. S. and Uchikoshi, T. (2008): Fabrication and some properties of textured alumina-related compounds by colloidal processing in high-magnetic field and sintering, J. Europ. Ceram. Soc., 28, pp. 935-942 .
66) Sakka, Y., Honda, A., Suzuki, T. S. and Moriyoshi, Y. (2004): Fabrication of Oriented β - Alumina from Porous Bodies by Slip Casting in a High Magnetic Field, Solid State Inonics, 172, pp. 341-344.
67) Sakka, Y., Suzuki, T. S., Tanabe, N., Asai, S. and Kitazawa, K. (2002): Alignment of titania whisker by colloidal filtration in a high magnetic field, Jpn. J. Appl. Phys., 41, pp. L1416-L1418
68) Wu, C. Y.., Li, S. Q., Sassa, K., Sakka, Y., Suzuki, T. S. and Asai,S. (2005): The crystal orientation taking account of gravity force under high magnetic field, ISIJ Inter., 45, pp, 997-1000.
69) Hirata, Y., Nakagama, S. and Ishihara, Y. (1990): J. Mater. Res., Vol. 5, pp. 640-646.
70) Uchikoshi, T., Suzuki, T. S., Okuyama, H. and Sakka, Y. (2003): Electrophoretic deposition of alpha-alumina particles in a strong magnetic field, J. Mater. Res., Vol. 18, pp. 254-256.
71) Uchikoshi, T., Suzuki, T. S., Okuyama, H. and Sakka, Y. (2004): Crystalline-oriented TiO_2 fabricated by the electrophoretic deposition in a strong magnetic field Ceramic Inter., 30, pp1975-1978.
72) Uchikoshi, T., Iimura S., Suzuki, T. S. and Sakka, Y. (2006): Control of crystalline texture in polycrystalline TiO_2 (anatase) by electrophoretic deposition in a strong magnetic field, J. Europ. Ceram. Soc., Vol. 26, pp. 559-563.
73) Suzuki, T. S., Uchikoshi, T., Okuyama, H. and Sakka, Y. (2006): Mechanical properties of textured, multilayered alumina produced using electrophoretic deposition in a strong magnetic field, J. Europ. Ceram. Soc., 26, pp. 661-665.
74) Uchikoshi, T., Suzuki, T. S., Okuyama, H., Sakka, Y. and Nicholson, P. S. (2004): Electrophoretic deposition of alumina suspension in a strong magnetic field, J. Europ. Ceram. Soc., 24, pp. 225-229.
75) Uchikoshi, T., Suzuki, T. S. and Sakka, Y. (2006): Crystalline orientation of alumina ceramics prepared by electrophoretic deposition under a high magnetic field, J. Mater. Sci., 41, pp.8074-8078.
76) Kimura, M., Shiratsuya, K., Ando, A., Suzuki, T. S. and Sakka, Y.(2007): Layer structure of textured $CaBi_4Ti_4O_{15}$ ceramics fabricated by slip casting in high maganetic field, J. Am. Ceram. Soc., 90, pp.1463-1466.
77) Tanaka, S., Tomita, Y., Furushima, R., Shimizu, H., Doshida, Y. and Uemastu, K, (2008): Fabrication of crystal-oriented barium bismuth titanate ceramics in high magnetic field and subsequent reaction sintering, Sci. Technol. Adv. Mater., 10, 01-4602.
78) Horii, S., Ishihara, A., Fukushima, T., Uchikoshi, T., Ogino, H, Suzuki, T. S, Sakka, Y., Shimoyama, J. and Kishio, K. (2009): Magnetic orientation and magnetic anisotropy in paramagnetic layered oxides containing rare-earth ions, Sci. Technol. Adv. Mater., 10, 014604.
79) Hori, S., Kumagai, T., Uchikoshi, T., H. Suzuki, T. S, Sakka, Y., Shimayama, (2007): Improvement of thermoelectric performance in magnetically c-axis-oriented bismuth–based cobaltites, Scripta Mater., 57, pp. 333-336.

Author's short biography

Yoshio Sakka

Yoshio Sakka is a Managing Director of Nano Ceramics Center at National Institute for Materials Science (NIMS), a PI of World Premier International Research Center Initiative（WPI Initiative) for Materials Nanoarchitronics (MANA), NIMS, and Professor of the University of Tsukuba. He received his B.E. in 1978, M.E in 1980, and Ph. D. in 1983 from Kyushu University for his work on cationic diffusion of zirconia solid solution systems. After receiving his Ph.D, he joined National Research Institute for Metals (present NIMS). During 1991-92, he stayed a year in University of Washington. His current interests are to fabricate innovative ceramics that show novel individual property and/or multi-functional properties among electric, dielectric, thermal, optical, chemical and mechanical properties through the development of nanoparticle processing. He is author or coauthors of 14 books, above 400 original referee’ s papers, above 60 review papers, and above 50 patents (including application. By the above establishment, he received many awards, such as Fulrath award from American Ceramic Society (May, 2000), academic achievement from Japanese Ceramic Society (May, 2005), Chinese Ceramic Society Award (Oct., 2005), etc.

Tetsuo Uchikoshi

Dr. Tetsuo Uchikoshi is a chief researcher in the Nano Ceramics Centre at the National Institute for Materials Science (NIMS) and a visiting professor at Kumamoto University. He received a B.S. in metallurgical engineering (1986) and a Ph.D. in materials science (1994) from Waseda University. He Joined the National Research Institute for Metals (NRIM), the predecessor of NIMS. After spending years as a senior researcher and a principal researcher, he has been a chief researcher at NIMS since 2007. In 1997-1998, he visited at McMaster University as a visiting scientist.

Dr. Uchikoshi has authored and co-authored about 180 papers in journals and conference proceedings, 9 books, and holds 8 patents. His main research interests include external field-assisted colloidal process for manufacturing advanced ceramics, such as solid oxide fuel cell, photocatalyst, electric and piezoelectric ceramics, phosphors, and porous materials.

Producing Pharmaceutical Particles via Electrospraying with an Emphasis on Nano and Nano Structured Particles - A Review[†]

C. U. Yurteri*, R.P.A. Hartman, and J.C.M. Marijnissen*
Delft University of Technology[1]

Abstract

Recent advances in nanotechnology offer nano sized or nanostructured pharmaceutical particles, being as small as the size of cells such as receptors or nucleic acids, which can be engineered to provide enhanced efficacy, solubility, or biocompatibility, and to administer at much lower dosages. However, industrial production of these particles is still challenging. Among different techniques, aerosol based ones might be favorable since they are considered as contamination free processes and do not interfere with complex molecules of drugs. We, in this review, consider liquid atomization, where droplet formation is followed by conversion into solid particles. The best candidate is a method, which not only produces mono sized droplets with a diameter smaller than the inside nozzle diameter but also generates small enough start up sizes. Such a method is found in: Electro-Hydrodynamic Atomization (EHDA) or Electrospraying. Electrospraying is now a well practiced technique for producing very fine monodisperse droplets from a liquid under the influence of electrical forces. By controlling the liquid flow rate and the electrostatic potential between the liquid and the counter electrode, droplets within a narrow size range can be generated, while the mean diameter ranges from nanometers up to several micrometers. Besides generating monodisperse droplets, electrosprays are also distinguished by their self dispersing nature due to Coulomb repulsion, the possibility of trajectory control of the produced charged droplets, and the reduced risk of nozzle clogging due to the large size of the orifice compared to the size of the droplets. We will discuss different spraying modes depending on the strength of the electric stresses relative to the surface tension stress on the liquid surface and on the inertia of the liquid leaving the nozzle. However, for the production of monodisperse nanoparticles the so called cone-jet mode will be explained in depth. Scaling laws can be used to estimate the operational conditions for producing nanodroplets of a certain size. Hartman and coworkers refined the scaling laws for EHDA in the Cone-Jet mode using theoretically derived models for the cone, jet, and droplet size. By means of several examples, a generic way to produce nanoparticles, via scaling laws, from a multitude of different precursors will be discussed. Several examples of medicine particles with different properties made by EHDA will be given. Processes based on bipolar coagulation, where oppositely charged carrier particles and nano sized active agents are brought together to form composite drugs, will be discussed. Finally some attention will be given to challenges on out-scaling of EHDA methods for industrial production.

Keywords: EHDA, electrospray, micro droplets, nanoparticles, drug, inhalation

Introduction

During the last several decades, focus on particle technology switched from macro to micro and micro to nano scales due to significant differences in the physical (electrical, optical, magnetic, chemical and mechanical) properties realized in the nano scale.

[†] Accepted: September 23rd, 2010

[1] Delft, 2628 BL, The Netherlands
* Corresponding author C.U. Yurteri
E-mail:c.u.yurteri@tudelft.nl
TEL:+31(15)2784372 FAX:+31(15)2784945

The pharmaceutical industry as well took advantage of this shift in scale, in order to design medications or drug delivery vehicles to provide enhanced efficacy, higher stability, solubility, or biocompatibility and to administer at much lower dosages. Besides the particle size, well defined particle size distributions are useful in the production of numerous industrial products. For example, It is known that pharmaceuticals of distinct and narrow particle size distribution have robust properties with a predictive time release to the body. Micro drug particles may have additional functionalities and therapeutic effects when they are coated with nano particles or attached to various molecules such as proteins, peptides, and DNA. By organizing nano particles in a matrix, intelligent drugs can be built for sustained (controlled) delivery and enhanced efficacy. However, it still remains challenging to produce them on an industrial scale. Many of the medical formulations are prepared and converted into particles from a liquid base. Atomization, disintegration of a bulk liquid in to fine droplets can be achieved by use of several forces. In this paper we will provide a brief summary of atomization techniques and concentrate only on nano or nano structured medical/pharmaceutical particles produced via electrohydrodynamic atomization (EHDA) and provide examples of potential EHDA applications in the medical industry.

Forming particles / powders

Particle generation can be done either via bottom up, i.e. molecular building blocks or top down, i.e. cutting up bigger structures. In the top down way, either bulk solids are broken into small pieces, as in milling, or liquids are disintegrated into fine droplets with suitable methods, as in atomization. A recent publication by Biskos et al. (2008) gives a general overview of production and measurement techniques of nano and micro aerosol particles.

Starting point for generating pharmaceutical particles of well-defined morphology and chemical composition are liquid solutions of a specified chemical composition. Disintegrating these solutions can be achieved by atomization using several techniques and these methods will be briefly discussed in the next section. Droplets formed via atomization are subsequently dried to form solid particles by crystallization. Various techniques can be used to dry pharmaceutical solutions and obtain powders with significantly different powder characteristics. The most common techniques are spray-freeze drying (sublimation), spray drying (evaporation), supercritical fluid drying (precipitation), and spray pyrolosis. Among them the spray drying is the most economical and suitable method for powder production. Spray drying involves atomization, evaporation, and collection. Depending on the primary droplet size and solute concentration of the primary droplets, solid nanoparticles of different diameters can be generated. To produce nanoparticles the initial droplet size should be already fairly small, because otherwise the begin concentration has to be unacceptably low. One should realize that the diameter of the final particle after drying equals the diameter of the initial droplet times the cube root of the volumetric concentration of the non-volatile material (van Erven et al. 2005). For example, to form a nano sized solid particle, a droplet with an initial size of less than 1 micro meter from a solution with or with less than 0.1 weight percent is needed. The choice of atomizer mainly affects the primary droplets size, and size distribution of the spray, which is very important for the uniformity and quality of the dried powder.

Atomizers

Atomizers suitable for aerosol based processes can be categorized depending on the forces applied to breakup the liquid into small airborne droplets (Hinds 1999); i.e. pneumatic, ultrasonic, and electrical. They produce relatively smaller primary droplets (with a size distribution between 1 and 100 μm in diameter), making them suitable for use in aerosol-based applications in nanotechnology (Biskos et al. 2008). However, the relatively low particle concentration of the produced aerosols restricts these methods for applications that require only small amounts of particles

In pneumatic atomizers, the high forces occurring at the air-liquid interface cause the solution to break-up into small liquid droplets which become airborne and are carried away by the air flow. The particles generated by pneumatic atomization are polydisperse (with a geometric standard deviation of the size distribution, σg, of 1.4 or greater). If their size has to be controlled within a narrower range, a classifier has to be employed downstream of the particle generator. In pneumatic atomizers the droplet size not only depends on viscosity, surface tension and density, but also on atomization pressure and orifice size, thus requiring very small orifices and high pressure drops to form very small droplets (Lefebvre 1989).

In ultrasonic atomizers, a solution is broken up to micron-sized droplets by ultrasonically vibrating its air-liquid interface, to create capillary waves. A particle-free air-stream is passed over the solution to take away the generated airborne particles. The diameter of the primary droplets produced is a function of the frequency of vibration and the physical properties of the solution, i.e., surface tension, viscosity and density. Compared to pneumatic atomizers, ultrasonic atomizers can generate relatively monodisperse particles (σ_g of less than 1.2). Although the performance of ultrasonic atomizers remains inherently stable, and although they are suitable for inhalation purposes, coating and spray drying applications, their greatest drawback is low particle number concentration and increasing temperatures at prolonged operations. Ultrasonic atomizers can produce monodispersed bioactive, biocompatible, and biodegradable micro/nano particles appropriate for use in drug delivery systems, or for surface coatings in the implant and electronics industry (Felder et al. 2003, Forde et al. 2006, Freitas et al. 2004, Friend et al. 2008). Ultrasonic atomization is more suitable for low-viscosity liquids and low temperature applications. Recent reviews of ultrasonic droplet formation are provided by Biskos et al. 2008, Barreras et al. 2002, and Yule & Al-Suleimani 1997.

Electrohydrodynamic atomization (EHDA), or electrospraying, is a process where liquid can be disintegrated into uniformly sized droplets under the influence of electrical forces in a very controlled fashion. EHDA comes with plenty of unique advantages in comparison to the conventional systems, one of them being the narrow size distribution. This uniqueness makes it suitable for many industrial and academic applications. Depending on the flow rate and liquid properties, the main droplet size produced ranges from nanometers with production frequencies in the order of 10^9 Hz to hundreds of micrometers with production frequencies of about 10^4 Hz. Besides generating monodisperse droplets, electrosprays are also distinguished by their self dispersing nature due to Coulumbic repulsion, the possibility of trajectory control of the produced charged droplets, and the reduced risk of nozzle clogging due to the large size of the orifice compared to the size of the droplets. EHDA can be operated in many environmental conditions, but mainly in the ambient conditions, thus overcoming possible degradation of drugs under extreme operating conditions. Since EHDA offers many (potential) applications it will be described in more detail.

History of Electrohydrodynamic Atomization (Electrospraying)

The phenomenon of an electric effect on liquid menisci is known since the sixteenth century. William Gilbert reported in 1600 the interaction between a water droplet and a piece of amber held closely to it, leading to a conical shaped droplet. In the beginning of the 20th century Zeleny (1914, 1915, 1917) demonstrated fine droplet formation from a conical shaped meniscus, transformed from a hemispherical meniscus under an electrical stress. In the middle of the same century, theoretical and experimental works followed by Taylor (1964), Vonnegut and Neubauer (1952). It became a subject of thousands of research papers including dissertations (Meesters 1992, Geerse 2003, Hartman 1998, Wilhelm 2004), books (Bailey 1988, Michelson 1990), and special issues are dedicated to review the theory and applications of the electrospray in the Journal of Aerosol Science (issues 25 (1994) and 30 (2000)). Here we provide only highlights, and for details the reader is referred to the early reviews on particle generation via electrospray (Kozhenkov and Fuks 1976, Smith 1986, Grace and Marijnissen 1994) and more recent overviews of electrospray and its applications (Jaworek 2007, de la Mora 2007). The interest in electrospray progressively increased by the Nobel winning work of Fenn on Mass Spectroscopy for detection of macromolecules. Scaling laws for electrospraying of liquids were developed, to predict the characteristic size of the produced droplets on forehand (de la Mora and Loscertales 1994, Gañán-Calvo et al. 1997, Hartman 1999, Chen and Pui 1997). The developed scaling laws refer to the so called cone-jet mode, one of the modes that can be obtained in electrospray, and is of great interest due to its steady operation.

Electrospray modes

In EHDA, where as already mentioned a liquid jet breaks up into droplets under influence of electrical forces, different spraying modes can be obtained depending on the strength of the electric stresses relative to the surface tension stress on the liquid surface and on the kinetic energy of the liquid leaving the nozzle (Zeleny 1914, 1915, 1917, Cloupeau and Prunetfoch 1994, Grace and Marijnissen 1994). For the production of monodisperse nanoparticles the so called cone-jet mode is desirable. In this mode the liquid is typically delivered through a nozzle at a flow rate of the order of μl/hr to ml/hr, and an electric field is applied between the nozzle and a counter electrode. This electric field induces a surface charge in the growing meniscus created at the nozzle. Due to this surface charge and the electric field, an electric stress is created on the liquid-air interface. Depending on the electric field strength and the liquid flow rate, the electric stress can overcome the surface tension stress and transform the shape of the liquid surface to a cone, i.e., the Taylor cone (Taylor 1964). The tangential component of the electric field accelerates the charge carriers at the liquid surface toward the cone apex. These ions collide with liquid molecules, thereby accelerating the surrounding liquid. As a result, a thin liquid jet emerges at the cone apex (Zeleny 1914, 1915, 1917). See **Fig. 1**.

Besides, the aforementioned cone jet mode several other modes exist. As we will only make use of the cone jet mode for the production of nano particles, we will only briefly mention them. Which mode appears depends on the system parameters (flow rate, field strength, liquid properties). The earliest classification is reported by Hayati *et al.* 1987(a and b). The classification mostly used is made by Cloupeau and Prunet-Foch (1994) and based on the spraying geometry. However, there are also classifications based on characteristic time constants (Shiryaeva and Grigorev 1995) and its combination with a geometrical factor, (Jaworek and Krupa 1999), and also based on the emitted currents (Juraschek and Röllgen 1998). The electric field intensity near the tip of the nozzle plays a major role determining the operation mode, with the nozzle dimensions being a critical factor. Based on flow rate and applied potential, starting from zero potential, dripping, and by increasing the potential, fast dripping, intermittent cone jet (**Fig. 2**), cone jet (**Fig. 1** and **6**), and multi jet modes (**Fig. 3**)

Fig. 1 Electrospray in the cone jet mode, with an increasing voltage at a constant flow rate, the meniscus converges to a conical shape at the apex of which a stable continuous jet emerges and breaks into droplets. Ethanol electrospray recorded with a Photron SA-1 high speed camera. Gauge 22 Nozzle (EFD) inner/outer diameter 0.41/0.72 mm diameter ; + 3.3 kV applied potential; 3 cm distance from needle tip to counter electrode; flow rate 1 mL/h.

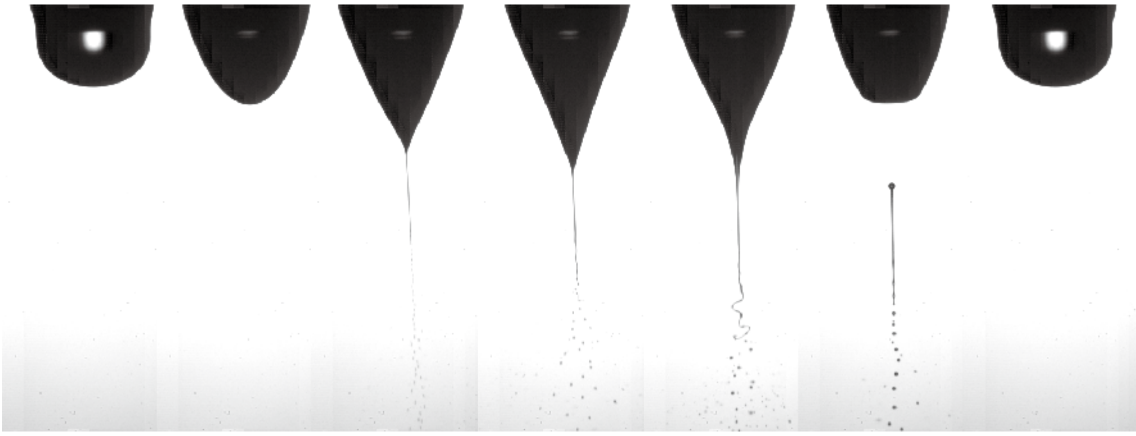

Fig. 2 Electrospray in the intermittent cone jet mode, a cycle starting from a hemispherical meniscus followed by formation of a jet, breaking into droplets, and cone relaxing into the meniscus. Ethanol electrospray recorded with a Photron SA-1 high speed camera. Gauge 22 Nozzle (EFD) inner/outer diameter 0.41/0.72 mm diameter ; + 3 kV applied potential; 3 cm distance from needle tip to counter electrode; flow rate 1 mL/h.

can be realized (Grace and Marijnissen 1994). Micro dripping, simple jet, spindle (**Fig. 4**) and ramified jet modes can also be seen depending on the fluid properties and flow rate. It should be noted that neither for all liquids each mode may occur nor that the modes are always realized in this systematic order. The cone-jet is as aforementioned the most interesting electrospraying mode and its stability makes it useful for various applications; production of particles, printing of bio-molecules, and precision deposition methods. The cone jet mode allows the production of aerosols within a very large range of droplet sizes for a very wide range of liquid properties in terms of conductivity, viscosity and surface tension. The size distribution of the particles produced can be monodisperse, but depending on the experimental conditions, can be bimodal or polydisperse. Due to the excess of surface charge in the liquid cone and jet, the droplets are highly charged.

Scaling of droplet size and current in the cone jet mode

In the past, several attempts have been made to model the cone-jet mode, both analytically and numerically. Various equations have been derived, to estimate the produced main droplet size, and to estimate the electric current through a liquid sprayed

Fig. 3 Electrospray in the multi jet modes, number of jets increases as the potential difference increases, a) multi jet mode, b) rim emission mode. Ethanol electrospray recorded with a Photron SA-1 high speed camera. Gauge 22 Nozzle (EFD) inner/outer diameter 0.41/0.72 mm diameter ; a) + 4 kV and b) 5 kV applied potential; 3 cm distance from needle tip to counter electrode; flow rate 1 mL/h.

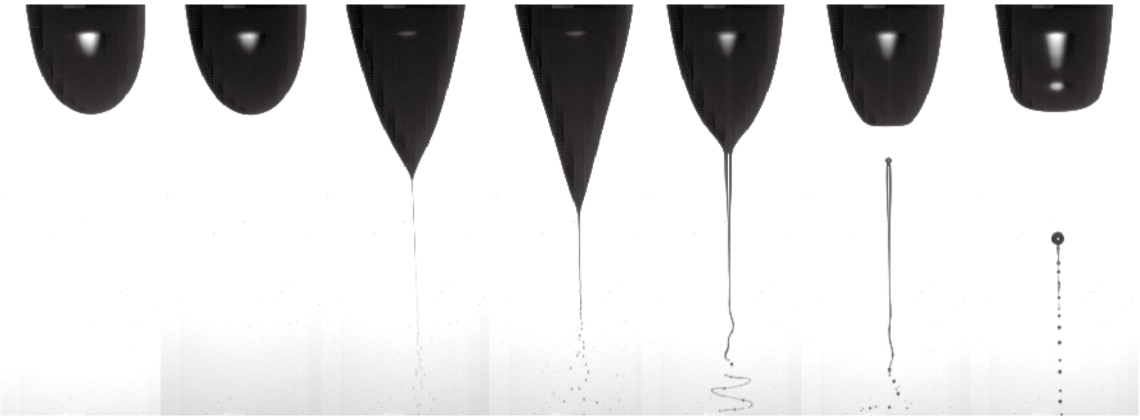

Fig. 4 Electrospray in the spindle mode, a cycle starting with a meniscus followed by formation of a jet, breaking into droplets, ligament breaking from cone, and cone relaxing into meniscus. Ethanol/water (70/30% by volume) electrospray recorded with a Photron SA-1 high speed camera. Gauge 22 Nozzle (EFD) inner/outer diameter 0.41/0.72 mm diameter ; + 3.5 kV applied potential; 3 cm distance from needle tip to counter electrode; flow rate 1 mL/h.

in the Cone-Jet mode as function of liquid properties and flow rate. Combining dimension analysis with experimental results, de la Mora and Loscertales (1994) found relationships for liquids with relatively high conductivities. Also, based on dimensional analysis and experimental results, Gañán-Calvo et al. (1997) found two different relations for the droplet size and current. Highly conductive liquids or highly viscous liquids were found to behave differently from liquids with a low conductivity and a low viscosity. In order to judge, which relation is valid, they introduced the following dimensionless number,

$$\left(\frac{\gamma^3 \varepsilon_0^2}{\mu^3 K^2 Q}\right)^{\frac{1}{3}} \tag{1}$$

where, Q is liquid flow rate [m^3 s^{-1}], K is conductivity [S m^{-1}], ε_0 is electric permittivity of a vacuum [C^2 N^{-1} m^{-2}], γ is surface tension [N m^{-1}], and μ is the absolute viscosity of the liquid [Pa s]. This dimensionless number, viscosity number (VN) as called by Hartman (1998), is formed from multiplication of two dimensionless numbers, the ratio of flow rate to a characteristic flow rate and the viscous dimensionless parameter. The viscous dimensionless parameter is interpreted as the ratio of two characteristic velocities: the characteristic velocity in the liquid bulk and the propagation velocity of a perturbation across the jet by viscous diffusion (Gañán-Calvo et al. 1997). The viscosity number as interpreted by Hartman (1998) represents the ratio of the change in kinetic energy of the liquid jet in the axial direction over the change in viscous stress in the radial direction. If the viscosity is high or the conductivity is high, then this ratio is relatively low. The size of the jet diameter is mainly determined by the liquid flow rate, and the liquid conductivity. The higher the viscosity, and the smaller the jet radius so for higher conductivity, the smaller the difference between the axial liquid velocity in the jet center and this velocity at the jet surface becomes. The radial profile of the axial liquid velocity will then be almost flat. Gañán-Calvo (2004) investigated various scaling laws and data from them with an attempt to unify them, and found that the effect of permittivity is negligible unless polarity is important. Recent summaries of scaling laws for droplet size and current in the cone-jet mode are given by Chen & Pui (2010) and with more emphasis by de la Mora (2007). However some papers contributing to the scaling laws are overlooked in the latter.

Using his physical numerical model Hartman (1999) derived theoretically the following electric current scaling law for Newtonian liquids with a flat radial velocity profile in the jet

$$I^* = b(\gamma K Q)^{0.5} \tag{2}$$

I^* is the electric current for a jet with a flat radial profile of the axial fluid velocity. The difference with the scaling laws of de la Mora and Loscertales (1994) and of Gañán-Calvo et al. (1997) is that the liquid permittivity has completely disappeared from the scaling law. However, as mentioned Gañán-Calvo came in 2004 with comparable conclusions. By using equation (2) and experimental results of Gañán-Calvo et al. (1997) and of Hartman (1999) for "b" a value of approximately 2.17 is found. Yielding, . $I^* = 2.17(\gamma K Q)^{0.5}$

For liquids where the radial velocity profile is not flat Hartman (1998) found

$$I = 0.41 I^* + \frac{0.24 I^{*2}}{E_{z,\max} K Q}\left(A r_{j0.41}^2 + B\right) \tag{3}$$

Where I^* is the current for a flat radial profile of the axial velocity (equation 2) and $E_{z,\max}$, $r_{j0.41}$, A and B are all functions of known parameters. For the derivation of equation 3 and the computation of the different terms see the Appendix.

The value of I/I^* can be found much faster by using **Fig. 5**, representing, I/I^* as a function of the viscosity number. Curve fitting these data composed of experimental values with the least squares method yields $\frac{I^*}{I} = 1 - 0.1 * VN^{0.45}$. For a certain VN, the value I/I^* can be determined graphically or by using the formula. As seen in **Fig. 5**, the points start to scatter around a viscosity number of 10. **Fig. 5** may be safely used till a value of VN of 10.

Scaling laws for the size

Since the initial droplet size is one of the most decisive factors for the end product size, and EHDA quality, an empirical or semi-empirical equation for predicting the droplet size will be very useful. Works of Cloupeau and Prunet-Foch (1994), Rosell-Llompart and de la Mora (1994), Chen and Pui (1997) and Gañán-Calvo et al. (1997) provided earliest semi-empirical models for the mean droplet size. For the droplet size in the cone jet mode, Hartman (1998) also derived scaling laws. The jet break-up mechanism depends on the ratio of the electric normal stress over the surface tension stress. At low values, the jet breaks up due to varicose instabilities. At higher values, the jet starts to whip. The jet break up is now influenced by both varicose and kink instabilities

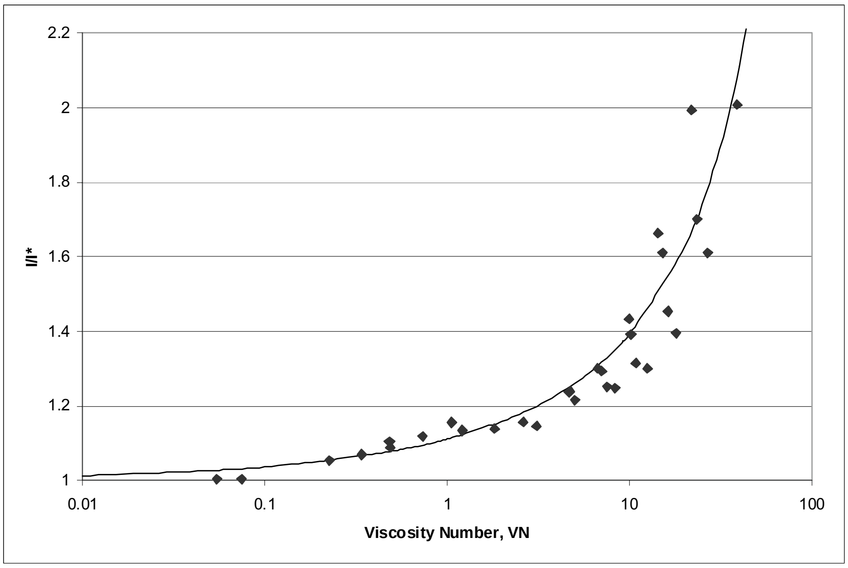

Fig. 5 Viscosity number vs. I/I* - experimental data & curve fit $\frac{I^*}{I} = 1 - 0.1 * VN^{0.45}$

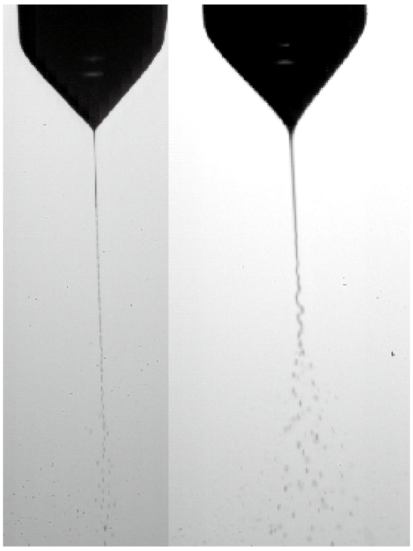

a) b)

Fig. 6 Electrospray in the cone jet mode a) varicose break up and b) whipping jet break up. Ethanol electrospray recorded with a Photron SA-1 high speed camera. Gauge 22 Nozzle (EFD) inner/outer diameter 0.41/0.72 mm diameter ; a) + 3.2 kV, b) 3.3 applied potential; 3 cm distance from needle tip to counter electrode; flow rate 1 mL/h.

(de la Mora and Loscertales 1994; Rosell-Llompart and de la Mora 1994; Tang and Gomez 1994; Hartman et al. 2000). The threshold value of the stress ratio above which the jet starts to whip is not sharply defined but it is around 0.3 (or 0.24 for whipping of the filament). Geerse (2003) also reports that for a stress ratio between 0.2 and 0.3 the jet starts to whip. A smaller stress ratio yields varicose break up, while a higher stress ratio leads to whipping breakup. In the whipping break up mode the size distribution of the main droplets is wider than in the varicose break up mode.

The scaling law for the droplet size in the varicose jet break-up (**Fig. 6-a**) mode as found by Hartman et al. (2000),

$$d_{d,\mathrm{varicose}} = c_d\left(\frac{\rho\,\varepsilon_o Q^4}{I^2}\right)^{\frac{1}{6}} \tag{4}$$

where c_d is a constant, and $d_{d,\mathrm{varicose}}$ means the diameter of the droplet, of which the volume is composed of a primary (main) droplet and, if present, its secondary and satellite droplets. Since the volume of the main droplet is much bigger than the volume of the secondary droplets and satellites, and because the diameter scales to the volume to the power ⅓, $d_{d,\ varicose}$ is close to the primary (main) droplet size. The constant c_d was found to be in the range of 1.76 to 2.05.

Assuming that the radial profile of the axial fluid velocity in the jet is flat, then the current scales according to equation (2) , and relation (4) yields

$$d_{d,\mathrm{varicose}} = \frac{c_d}{b^{1/3}}\left(\frac{\rho\,\varepsilon_o\,Q^3}{\gamma K}\right)^{1/6} \tag{5}$$

Since b and c_d both have values close to 2, by approximating them by 2, giving less than 15% deviation, (5) becomes

$$d_{d,\mathrm{varicose}} = \left(\frac{16\rho\,\varepsilon_o\,Q^3}{\gamma K}\right)^{1/6} \tag{6}$$

For the whipping jet break-up mode (**Fig. 6-b**) Hartman (1998) derived the following the droplet size scaling law:

$$d_{d,whipping} = \left(0.8\frac{288\,\varepsilon_o\,\gamma Q^2}{I^2}\right)^{1/3} \tag{7}$$

where, $d_{d,whipping}$ is the droplet size predicted for a jet that breaks up in the whipping jet break-up mode. Again the droplet size represents a droplet with the total volume of the primary, secondary and satellite droplets. The constant 0.8 was calculated from the measured droplet sizes. However, other measurements of Gomez and Tang (1994), and Gañán-Calvo et al. (1997), indicate that this value can also be 0.49 or 0.64.

As indicated already the threshold between the varicose and whipping breakup is not sharply defined. However, which of the two droplet size scaling laws, equations (7) and (6), should be used, can easily be deduced by calculating both droplet sizes. The equation that yields the smallest droplet size is the appropriate one. This indicates whether the jet is in the varicose mode or in the whipping mode.

Estimation of particle size from a solution

For a spherical droplet, a simple derivation relates the diameter of the (final) solid particle (d_p) after drying to the primary droplet diameter (van Erven et al. 2005) by Equation 8:

$$d_p = \sqrt[3]{f\frac{\rho_{droplet}}{\rho_{particle}}d^3_{droplet}} \qquad [8]$$

where f is the mass fraction of the material in the solution (-), ρ_{droplet} is the density of the solution and ρ_{particle} is the density of the final (product) particle (kg/m^3). This is of course only true if the particle is non porous or not hollow. By choosing the right conditions in concentration, type of solute, solvent, and drying conditions, it is possible to make hollow or porous particles. In this way also the aerodynamic diameter of the particle decreases.

EHDA Configurations

In the preceding sections we have shown that EHDA comes with both empirically and theoretically derived equations, which can be used as predictive tools and can thus help us to produce desired particles, or surface structures in a controlled manner. To achieve this, there exist four major EHDA configurations which have been used and reported in the literature for the production of particles.

The first and the most commonly used basic configuration is known as Needle - plate configuration (see **Fig. 7**). In some cases a ring electrode around the nozzle can be provided, as in **Fig. 8**, (needle - ring extractor - plate) for spray stability and to spray at lower potential differences. This configuration is ideal for direct coating medical substrates such as tablets, individual micro particles, or medical inserts. Droplets in this way can be deposited to form either discrete particles or thin films. In this and other configurations the droplets are produced from an appropriate solution. A solvent is selected to provide appropriate levels of conductivity when the solution is formed or the solution may be doped with conductivity control agents. It is essential to measure the conductivity, and surface tension of the solution. This solution containing the formulation is fed to a nozzle (B) via pumping or a pressure head delivery system (A). The flow rate of the solution is selected to produce the desired primary droplet size. It varies from μl/hr to ml/hr to obtain nano to micron sized droplets. In the needle to plate configuration, the required electrical field is created by applying a voltage between the capillary (B) and a grounded counter electrode or collection substrate (E,F) using a high voltage power supply (C). The distance between the tip of the capillary (B) and the counter electrode (E) is selected to provide enough residence time for drying or reacting for the end product. The set up can be operated at ambient or other conditions.

The first configuration takes advantage of the charge on the particles, however in some applications the charge on the droplets is not desired, such as in using EHDA directly for inhalation purposes or

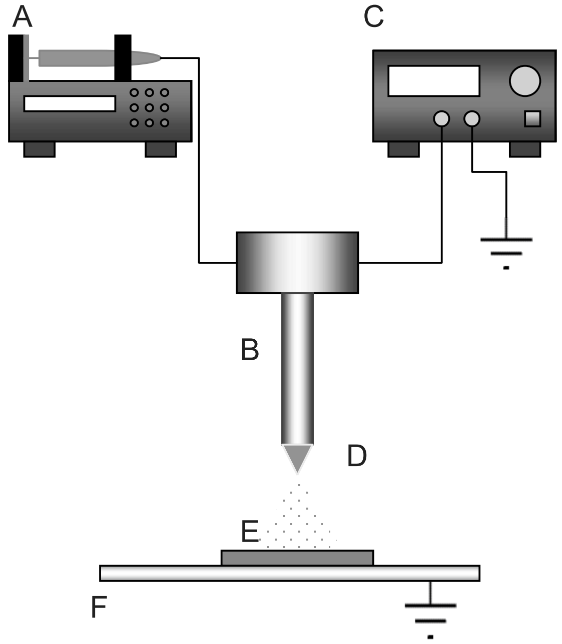

Fig. 7 Schematic of the capillary to plate electrospray set up, A) Syringe pump, B) Nozzle, C) High voltage supply, D) Taylor cone and droplet cloud, E) Collection substrate, F) Earthed support.

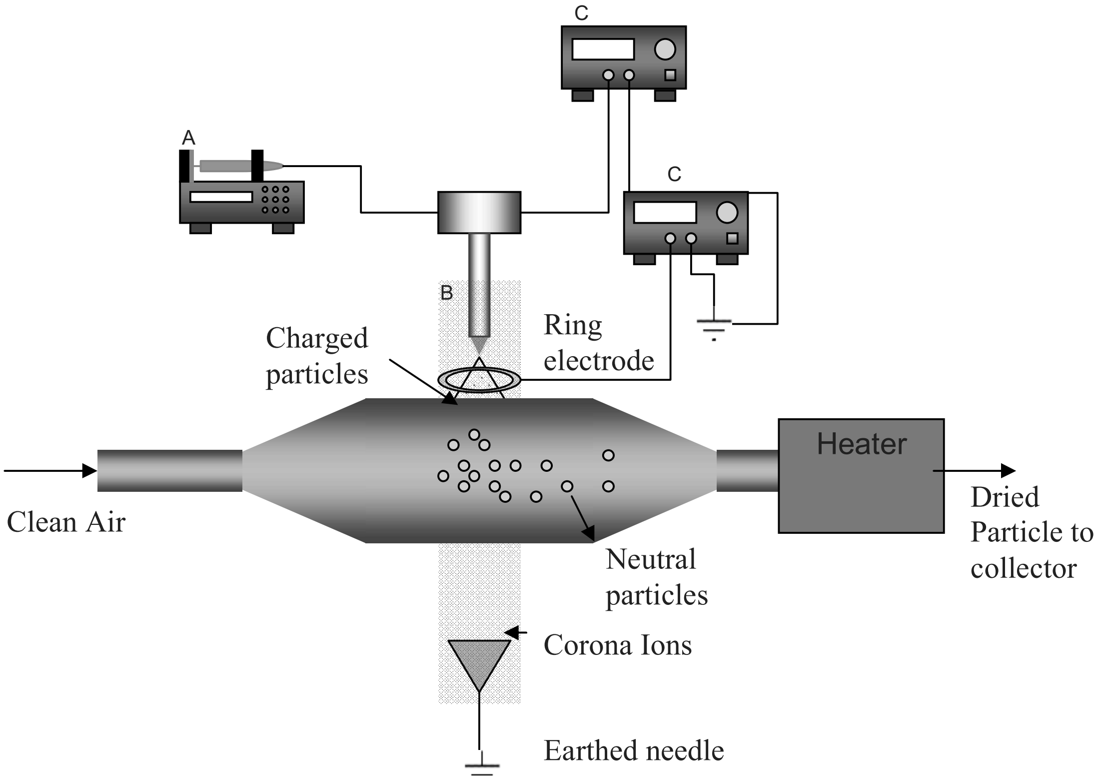

Fig. 8 Aerosol set up to produce particles from electropsray. Droplet genaration and neutralization take place inside a reactor. A drier could be included before particle collection (Adopted from Meesters et al. 1992) A) syringe pump, B) nozzle, C) high voltage supply.

sometimes for powder production. For this purpose, in the second configuration, a setup similar to the first one is enhanced by addition of a charge neutralization mechanism, such as a needle to form oppositely charged ions via corona discharge (Hartman 1998) or a radioactive source (Chen et al. 1995). An air stream carries particles to a collection point or desired location in case of inhalation. A treatment step could also be included, e.g. to induce chemical reactions (Meesters et al. 1992), see **Fig. 8**. In this set up a ring is used as counter electrode. The function of the ring is two fold; to stabilize the atomization at lower voltages, and shield the formation of droplets from destabilization effects of the corona discharge. The ring is connected to a high voltage power supply, but at a lower voltage than the capillary. The distance between the ring and capillary can be adjusted. The potential difference between the nozzle and the ring creates the field to produce the droplets, which will pass through the ring. In this way the droplets are not deposited as in the capillary-plate set up, but are kept airborne. However to prevent them to deposit on the reactor walls, the droplets are discharged by a corona in this case. Another reason to neutralize the droplets is the fact that during drying the volume of the droplet decreases and the surface charge density increases. Once a droplet evaporates to a critical diameter, it will reach the Rayleigh charge limit when the droplets will disintegrate into smaller ones, destroying the control on particle size (Smith et al. 2002). It should be realized that the droplets produced by EHDA carry a high electrical charge in the order of 70% of the Rayleigh limit (Hartman 1998). After the reactor the nanoparticles are collected via a grid or filter.

The third configuration involves use of oppositely charged droplets created by two oppositely charged EHDAs, in the cone-jet mode, see **Fig. 9**. If they are directed towards each other coagulation between the droplets takes place through the electrical attraction between them (Bipolar Coagulation). In this case, droplets of different composition can be mixed and reacted to form composite or new materials (Camelot 1999). The coagulation can also be used just to neutralize the droplets. If the right conditions are chosen, it is also possible to coat one material with another.

The fourth configuration, coaxial EHDA, utilizes two coaxially aligned EHDA nozzles , as seen in **Fig. 10**. This could be the desired configuration to form encapsulated particles in a single step, and when right combinations are found to produce encapsulated particle in the absence of additives (Chang et al. 2009). Each nozzle is fed separately. The central one slightly protrudes to facilitate the coating by the outer liquid. In this way, controlled encapsulation can be done. The spray phenomena are mainly controlled by the properties of the outer liquid (Chen et al. 2000, Loscertales et al. 2002, Chen et al. 2005), which can be as in the case of Chen et al. (2000) very viscous and electrically conductive. However, this configuration is not limited to two coaxially aligned nozzles. Multiple layers can be produced by aligning more nozzles concentrically (Lallave et al. 2007, Kim and Kim 2010)

Medical Applications

Due to its emerging potential in biomedical and pharmaceutical applications, various aspects of EHDA on medicine are recently reviewed by Chen & Pui (2010), Marijnissen et at. (2010), Jaworek (2008), and Ciach (2007). Electrohydrodynamic atomization has been applied to produce thin films, the production of micro and nano sized particles , microencapsulation, implant coating, inhalation therapy, micro reactors via bipolar coagulation for drug powder production, making inorganic nanoparticles via electrospray pyrolysis, electrospray gene transfection and more (Chen & Pui 2010, Marijnissen et al. 2010, Jaworek 2007). The aforementioned scaling laws for the cone jet mode provide a powerful tool to the user to apply electrospray. The different medical and pharmaceutical fields in which electrospray is utilized are described in next sections.

Mass spectrometry

The application of electrospray in the field of mass spectrometry has expanded enormously. In its simplest form, a mass spectrometer(MS) is an instrument that measures the mass-to-charge ratios m/q of ions formed when a sample is ionised by one of a number of different ionisation methods. Electrospray as a method for generating gas-phase ions was introduced in 1968 by Dole et al. His intention was to determine the mass of polystyrene macromolecules. The idea of coupling the electrospray technique to a conventional mass analyser was put forward as early as 1973 by Dole et al., and realised in 1984 by Yamashita and Fenn. Its potential for the analysis of large biomolecules was realised in 1988 by Meng et al.. Today, electrospray MS is used to analyse large biomolecules, such as proteins, nucleic acids, carbohydrates, lipids, and compounds composed of two or

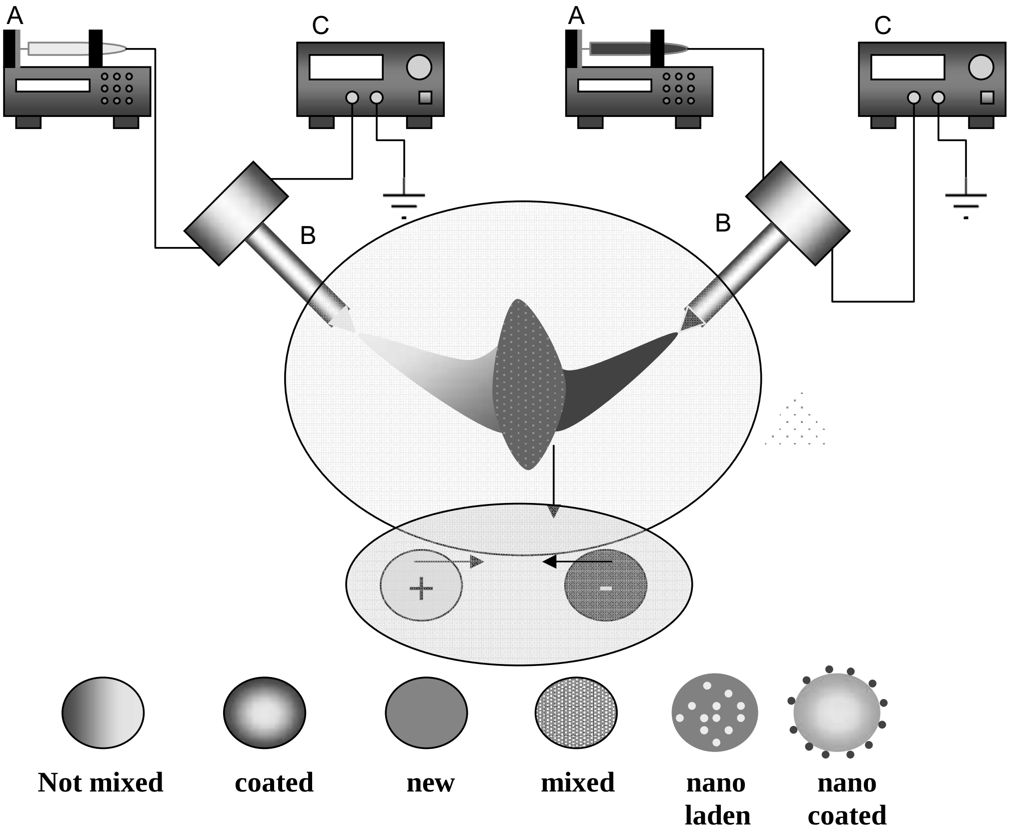

Fig. 9 Schematic of the bipolar coagulation configuration and possibilities for particle production (Adopted from Camelot 1999).

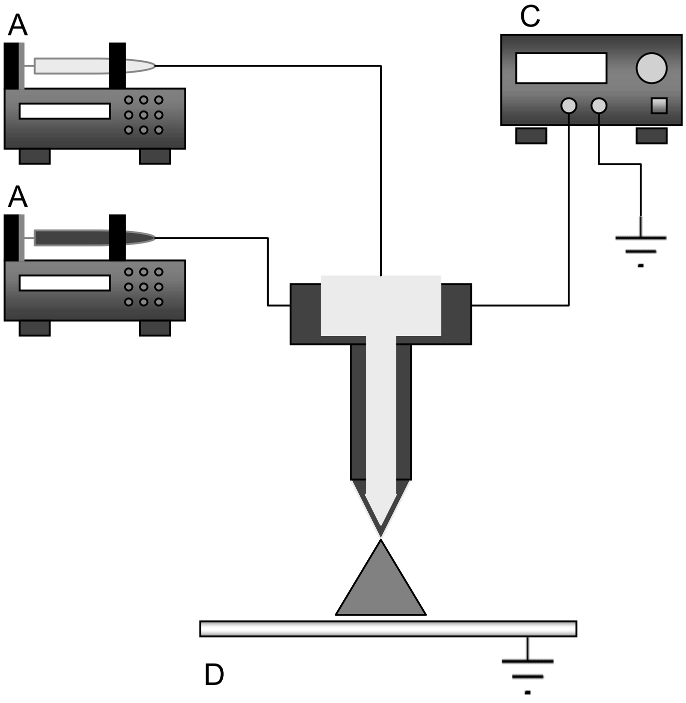

Fig. 10 Dual nozzle (concentric) electrospray set up.

more of these components. Nowadays, the amount of research activities and publications in the field of electrospray MS can hardly be overlooked. Excellent reviews and books dealing with electrospray MS were written by Cole (1997), Kebarle and Tang (1993), Smith et al. (1997) and Dulcks and Juraschek (1999). The work done in Electrospray Ionization obviously proves the fact that the electrospray technique is a soft method to cause no harm to bio-molecules (e.g., DNA, peptides, and proteins), making it a distinct technique to produce pharmaceuticals based on these delicate structures.

Carrier particle and drug particle production

Micro and nano particles produced via the electrohydrodynamic process can be utilized for therapeutic or diagnostic purposes in medicine. Besides in the form of aerosol (inhalation particles), drugs can be delivered efficiently to certain parts of the human body as particles in emulsions or as deposited particles on engineered scaffolds (i.e. tissues, stents, bone anchors...etc.). Considering the unique advantage of the EHDA technique, one can envisage its potential future applications for advanced treating methods and also for diagnostic purposes.

Drug particles with a narrow size distribution have the unique advantage of providing more regular and predictable drug release profiles from batch to batch compared to particles with the same mean size but wider distribution. Electrospraying is an ideal route for the production of such drug particles either in pure or polymer blended form. In this case a drug or a polymer/drug combination dissolved in a suitable solvent is electrosprayed. Several authors have already reported on the production of nanoparticles with narrow size distributions using the EHDA route (de la Mora et al. 1990, Rulison and Flagan 1994, Hull et al. 1997, Gomez et al. 1998, Lenggoro et al. 2000, Ciach et al. 2002, Nakaso et al. 2003, van Erven et al. 2005, Gonzales et al. 2007, Hogan et al. 2007). A recent review on the subject is provided by Jaworek and Sobczyk (2008). If the right solution properties are achieved, EHDA can be seen as a generic way to produce well-defined nanoparticles of various compositions on demand (Marijnissen et al. 2010).

Other examples of processes that use electrospray for the production of powders and drug particles are electrostatic spray pyrolysis (ESP) and bipolar mixing. In electrostatic spray pyrolysis, electrospraying is combined with pyrolysis. The liquid that is used to spray, contains inorganic components that form the powder. Vercoulen et al. (1993) used the technique to produce a powder of SnO_2, which is used as a semi-conductor material or as an additive to alter the electric properties of powders. A precursor solution of $Sn(Ac)_4$ was sprayed into droplets which were dispersed into air and carried through an oven where the droplets were evaporated and the remaining particles pyrolysed. Rulison and Flagan (1994) synthesised high quality yttria powders, composed of dense submicrometer, nanocrystalline oxide particles. This method seems ideal for forming ceramic nano drug delivery vehicles.

As already mentioned, the process of bipolar coagulation (Camelot 1999), where two sprays of oppositely charged droplets are directed towards each other and the coagulation between the droplets takes place through the electrical attraction between them can also be used to produce drug particles, see **Fig. 11**. Bipolar mixing can also be used to coat carrier particles with drug particles, which will be treated in another section. Bipolar coagulation is such a flexible method that one of the solutions can also be selected

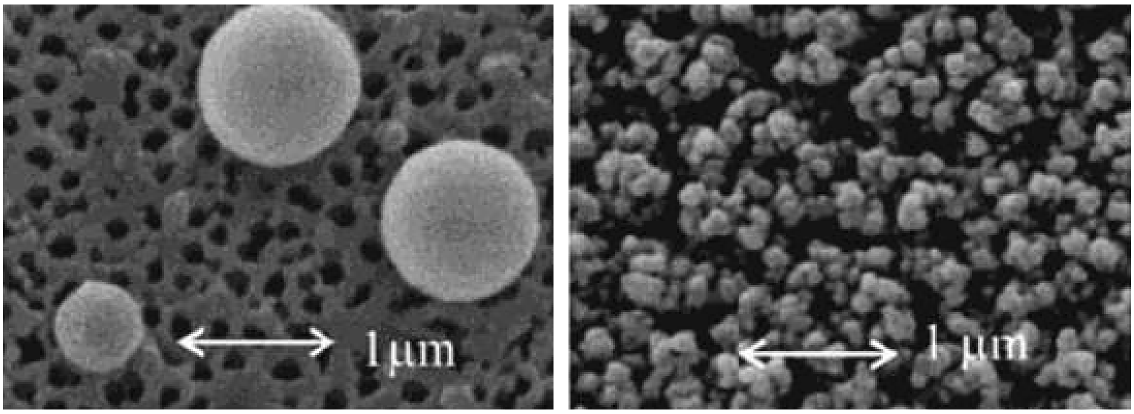

Fig. 11 Micro and nano ZrOx particles produced via bipolar coagulation process (*Camelot et al. 1999*).

to form micro and nano fibers, thus interaction of oppositely charged fibers and droplets could form structured tissues (Park et al. 2008).

Producing Drug particles for Inhalation

Drug delivery by the inhalation route is a non invasive and historically one of the oldest methods to administer drugs and fight several lung diseases such as asthma, emphysema, bronchitis, and chronic obstructive pulmonary diseases. As new types of drugs based on proteins, peptides, and DNA are developed, inhalation routes are considered to be used for insulin delivery, cancer treatment, pain control, and nanotherapeutics (Albert et al. 2007, Kleinstreuer et al. 2008, Heijerman et al. 2009, Siekmeier R. and Scheuch 2008, Shoyele and Slowey 2006, Shoyele and Cawthorne 2006, Sung et al. 2007, Lastow 2007). What makes pulmonary administration in general an advantageous route to deliver therapeutics is the ease of administration, rapid onset because of the area available for permeation to cells and the blood stream, smaller doses administered compared to the oral administration route, and better efficacy to safety ratio compared to systematic delivery. Use of nanoparticles, in addition, could contribute by sustained release in the lung tissue (Sung et al. 2007). However, the success of administration depends greatly on the performance of the delivery device, the size distribution of the delivered particles, the lung state of the patient, and the coordination between device and patient. These aforesaid merits and needs in the pharmaceutical industry have lead into many developments in inhalation devices such as nebulizers, metered dose inhalers, and dry powder inhalers, and a quest for novel delivery devices. Advantages and disadvantages of these devices are discussed in books and reviews such as by Hickey (1996), Gradon and Marijnissen (2003), and Geller (2008). As particles flow from the nose or mouth to the deeper lung regions, they deposit due to the deposition mechanisms of impaction, sedimentation and diffusion. For a good delivery the particle size matters, so an accurate control of the size is vital, and the device should generate drug particles with a predetermined size, ideally an aerodynamic diameter of smaller than 7 micro meters (Hickey 1996, Gradon and Marijnissen 2003). Particles close to the upper limit have a higher probability to get deposited in the mouth, throat and upper airways. Smaller particles have a higher probability to reach the surface of the lower airways and alveoli. Maximum delivery efficiency to the lower airways is achieved with particles either around 20 nm or 2 μm in diameter (Hinds 1999). However, of these particles only about 30 % can efficiently reach the lower airways. The total deposition efficiency even gets lower due to a size distribution associated with the drug particles in a commercially available inhaler and due to obstructions in the patient's lung airways. Conventional inhalers produce polydisperse drug aerosol particles with a mean particle size > 5 mm, which explains the low therapeutic efficiency of the inhaled drugs. In case of dry particle inhalers, powder dispersibility is crucial in view of the fact that such small particles tend to form agglomerates due to cohesive forces leading to variations in the particle size distribution (Weiler et al. 2010). However, a monodisperse drug aerosol with the right size reduces the dose which has to be administred by 80%, providing the same efficacy and reducing the side effects (Zanen et al. 1998, Zanen and Lammers 1999). Besides providing polydisperse aerosols, some inhalers have other disadvantages such as the ones based on ultrasonics which may cause thermal degradation of drug particles (Hickey, 1996). The electrospray technique has the ability of producing monodisperse aerosols with a controlled and predetermined droplet size and therefore it resolves particles size distribution related issues in conventional inhalers and is a perfect technique to produce aerosols for drug inhalation (Geerse and Marijnissen 2003). Using this technique may result in a decrease of the amount of drug administered and so in a decrease of the adverse effects the inhalation drugs have on the body. The first inhaler known using the electrospray technique was patented by Noakes et al. (1989), Tang and Gomez (1994) further developed the electrospray system of Noakes et al. (1989) for the use in an inhaler. The main difference with the system of Noakes et al. (1989) is the flow of CO_2 that is used to isolate the capillary tip from the air. In this way the onset of air discharge is suppressed, which makes it possible to spray liquids with a high surface tension, like water. As mentioned, the size of the droplets may be controlled by changing the conductivity of the liquid. Gomez et al. (1999) disclosed a method to electrospray in the corona assisted cone jet mode. Noakes et al. (2000) then published a description of another EHDA device, which is more suitable for nasal delivery and upper respiratory tract treatment due to charge present on the particles. Ijsebaert et al. (2001) described a EHDA drug atomizer where the droplets are neutralized by corona discharge. Gañán-Calvo (2003) described another device based on coaxial nozzles where formulations in the form of miscible or immiscible liquids, solutions or suspensions can be delivered. His patent application focused on the production of particles but did not incorporate any means of neutralization, which may be preferred to effectively deliver therapeutics to the upper airways. The presence of a controlled charge on the particles in the case of Noakes et al. (2000) and Gañán-Calvo (2003) on the other hand ensures that they will not penetrate beyond the upper airways tract or rapidly deposit on the nasal cavity lining upon inhalation. Of course one should realize that lungs have a clearance mechanism. This should also be considered for drug particle design and administration. Since the clearance mechanisms are size dependent, it is possible to produce particles in determined sizes to avoid these mechanisms. In above mentioned inhaler devices, a patient to device coordination is still necessary. This issue is addressed by Coffee (2005). He claims that, operation with induction charging of the liquid instead of direct charging provided better control of the drop size for liquids which are difficult to EHDA. Though the number of academic efforts to design an EHDA based inhalation device is increasing and there are many patents available, there is still not a commercially viable product in the market even despite the fact that a delivery efficiency of 85% can be achieved Gomez et al. (1999). Chen and Pui (2010) note that the latest attempt was made by the Batelle Memorial Institute for a device named Mystic ™ , which introduction was ceased after early clinical trials.

Medical coatings and Thin film production

Coatings for medical devices serve a numerous of useful purposes. For example, coatings can be used to change device surface properties, to incorporate drug/bioactive or antimicrobial agents for release from the surface of the device, to improve the bio compatibility and reduce the rate of rejection or to provide for cell signaling for better healing. However, in many cases vehicles used for drug administration or medical devices have a complex architecture, such as tissues or stents. In both cases, these devices require fine coatings that closely follow the micro-scale detail of the device. Coatings of this quality are not easily achievable with traditional dip or spray coating, physical or chemical vapor deposition. In addition, the coating materials can be exceedingly expensive if they contain drugs or bioactives and therefore the waste that is generated with these methods renders these processes prohibitive for use in many medical device based applications. On the contrary, electrostatic deposition processing is a highly controllable method that provides coatings that track the detail and architecture of the substrate (van Zomeren et al. 1994). Due to the targeted nature of the electrostatic deposition process, there is very little overspray or waste associated with it. Targeting is the result of the attraction between charged particles and the grounded substrate. The limitation of electrostatic deposition lies in the types of substrate that can be coated using this method. Electrostatic deposition requires that the substrate is conductive. Conductivity allows the substrate to be grounded and thereby attract coating particles. It also provides for the relaxation of the charge on the coating particle, converting it into a micro-current and thereby maintaining the particles on the surface. If the particles are still wet at the deposition then they can spread to form a thin film. In recent years the technique is extensively applied to

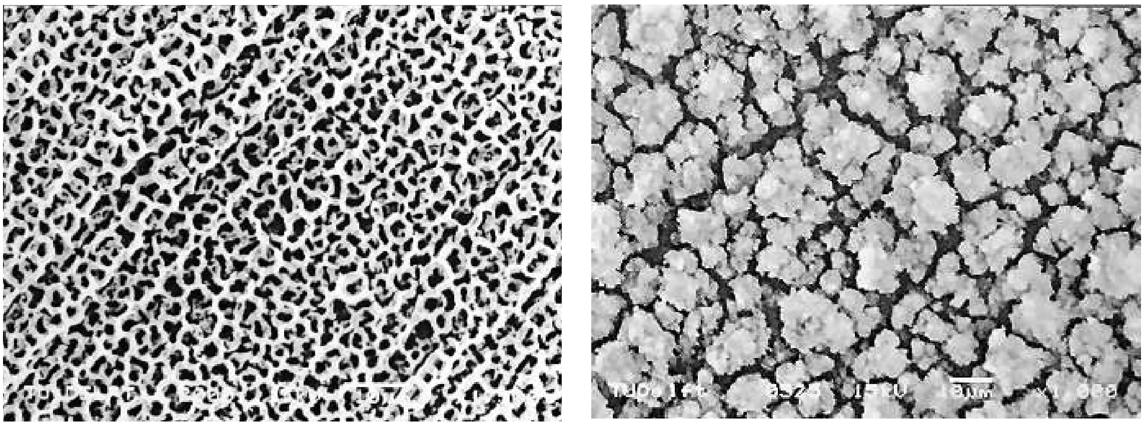

Fig. 12 SEMs of uniform thin layer coatings with different morphologies, calcium phosphate Coatings (Leeuwenburgh 2006b).

deposit a wide range of ceramic thin films with nano structures for bone material on metallic implants, and selective coating of scaffolds, see **Fig. 12** (Leeuwenburgh et al. 2006a, Schacter et al. 2007, Xie et al. 2008). As can be seen from **Fig. 12** micro and nano structures can be formed. Very recently Chen and Pui (2010) reported on a complex way of producing a film by EHDA to study concentration gradients in a layer with a nano scale variation, for cell growth studies.

The minute and accurate flow rate used in EHD atomization makes it usable for dispensing very precise volumes of liquid for automated high throughput chemical and biological analysis. Electric field control (Moerman et al. 2001) and pulsed high voltage (Stachewicz et al. 2009a,b, 2010a,b) are implemented to form short EHDA events and deposit near femto liter samples . Deng et al. (2010) implemented an array of micro nozzles activated by pulses to deposit active liquid suspensions. Pulsed electrosprays are also considered for manipulating single bacteria cells and forming arrays of biological reactors (Kim et al. 2010). One should consider that electrospraying viable bacteria can be used to develop devices for monitoring bioaerosols (Kim et al. 2008).

Tailored particles

Drug particles itself or drug loaded polymer nano and micro particles in general can be produced by a single step of electrospraying (Enayati et al. 2010). Besides the production of medical nanoparticles as such, EHDA (single nozzle or bipolar coagulation) also offers the possibility to produce more complex particles such as slow release and low density particles, which e.g. can be used in inhalation treatment. Although the low density particles suitable for inhalation have been developed for the micron size, the method can be equally used for the production of nanoparticles (Ciach et al. 2002). Low density, i.e. hollow or porous particles can be obtained with the right evaporation conditions and concentration or with coaxial electrospraying (Chang et al. 2010). In reality also other factors play an important role, such as mechanical properties and porosity of the formed solid shell as well as the surface tension of the solution and the presence of surface-active compounds. If we do not choose the composition of the droplets or the conditions of solvent evaporation properly, we can get the wrong particle structure such as small solid particles or remains of collapsed shells.

Electrospraying suspensions of nano particles in a liquid generates a spray of charged droplets that are seeded with nanoparticles, thus offering a solution for dispersing and depositing nanoparticles on a substrate. The charged nature of the nanoparticles is exploited to coat host particles. EHDA yields unipolarly charged suspensions of nanoparticles, while host particles can be charged with opposite polarity by means of tribocharging, corona or inductive charging, or they could have their charge because they are produced by electrospraying with opposite polarity. When these particles are brought into contact in an appropriate way, the mutual electrostatic attraction force between the negative and positive charge will cause a coating to be deposited on the surface. Inter-

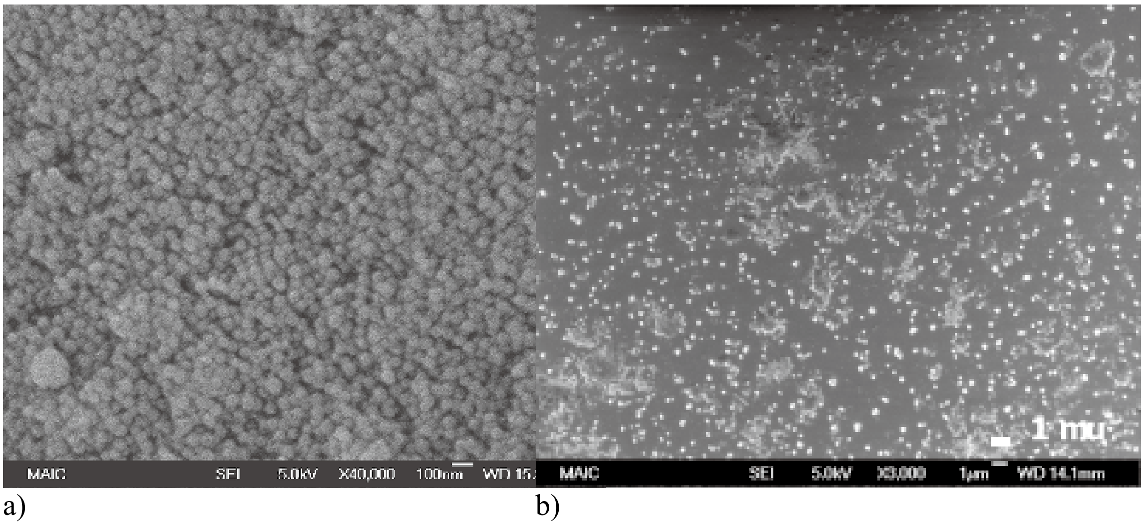

Fig. 13 (a) Stationary coated 165 μm alumina with 65 nm PS particles (Dabkowski et al. 2007) (b) 200 μm glass beads coated with 500 nm PS particles (Coppens 2007).

action can be realized in three ways: nano particles can be embedded in host particles, host particles can be encapsulated with a polymer film containing nano particles , and nano particles can be discretely deposited on the surface of host particles. The coating level can be controlled by changing the interaction time, the concentration of the suspension, and controlling the charge of host particles in the spray, **Fig. 13**. Several possibilities to accomplish mutual interaction of oppositely charged particles in order to deposit electrosprayed or electrospray formed nano particles on micro ones are studied by Dabkowski 2006, Dabkowski et al., 2007, Coppens 2007, van Ommen et al. 2008, and Ellis et al. 2010. Electrospray techniques are also tried for marking proteins with nanoparticles to fabricate biosensors (Mao et al, 2010).

However, it should be noticed that nano particles also come with a potential problem of toxicity. The dispersion of nanoparticles in gaseous phases is needed to investigate the toxicity of nanoparticles through in-vivo and in vitro routes. Electrosprays offers an optimal way of dispersion (Suh et al. 2005) of nanoparticles for toxicity studies.

Non-Spherical particles

Cell–particle interactions are complex. There is evidences that cells sense, identify and respond to particle shape, thus beside spherical particles, non spherical particles such as disk shaped, elongated or filament like morphologies could provide specific benefits (Champion et al. 2007). So for certain medical applications it might be advantageous to consider this effect and produce particles with shapes different from spheres to obtain improved biocompatibility, pharmacokinetics, targeted and sustained drug release (Simone et al. 2008, Muro et al. 2008, Mitragotri 2009 a & b, Decuzzi et al. 2010). Methods for fabricating non-spherical polymeric drug delivery particles are grouped by Champion et al. (2007) under two categories; synthesizing from scratch or modifying a spherical particle. Non spherical shapes from the EHDA process can come under the first category. Depending on the concentration, degree of entanglement, molecular weight of the polymer, solvent and other process conditions it is possible to produce fibres instead of spheres, and asymmetric or elongated particles (Hartman 1998, Almeria et al. 2010), see e.g. **Fig. 14**. Hong et al. 2008 reported that there is a dependence between drug to polymer ratio and particle morphology; and high drug to polymer ratio could lead to wrinkled micro particles. Production of rod or disc like micro particles is also possible using coaxial EHDA (Bhaskar et al. 2010).

Miscellaneous Applications

It is also possible to make emulsions with EHDA, by placing the spraying nozzle in a liquid medium, immiscible with the liquid to be sprayed, with the nozzle on a high potential and a submerged grounded counter electrode. In this case microemulsions, can be made. It is clear that the liquid in which is sprayed (the continuous phase of the emulsion) must have a low conductivity, **Fig. 15**.

Electrospray is used for dispersing hydrophobic compounds such as cholesterol, and demonstrated that when they are dispersed into aqueous solutions, they disperse faster and more efficiently in comparison to bulk mixing (Wu et al. 2009)

Most newly synthesized medicines, such as Taxol, are poorly soluble in water. Because of their poor solubility, a way to increase the solubility is to reduce the size of medicine particles and consequently increase the surface area of the particles, see **Fig. 16**. Chen and Pui (2010) showed that steroid particles of 13 nm diameter can be produced by EHDA.

EHDA is even considered for gene transfixion at the cellular level by Chen et al. (2000) and Wu et al. (2010). Although in this article attention is only given to production in the cone jet mode, other modes such as dripping can be used to generate relatively larger drug loaded particles (Xie and Wang 2007).

Future of EHDA - Out scaling

As shown, Electrospraying enables controlled atomization. Therapeutic aerosols with a narrow size distribution can be generated of a desired size, chemical composition, charge and morphology, hence providing a safe and controlled way of respiratory drug delivery and drug particle production. EHDA can also be used to coat particles or surfaces with medical nanoparticles in a very efficient way. This leads to cost savings in expensive pharmaceutical materials.

However, industrial implementation still suffers from low production rates. In order to generate small sized particles, low flow rates are required. For example, a flow rate of less than 0.1 ml/h for a single nozzle is needed to obtain droplets in the micrometer diameter range. To obtain a desired size is mainly determined by flow rate and conductivity of the liquid as indicated by the scaling laws (**Eq. 6**). For the same droplet size it is impossible to increase the pro-

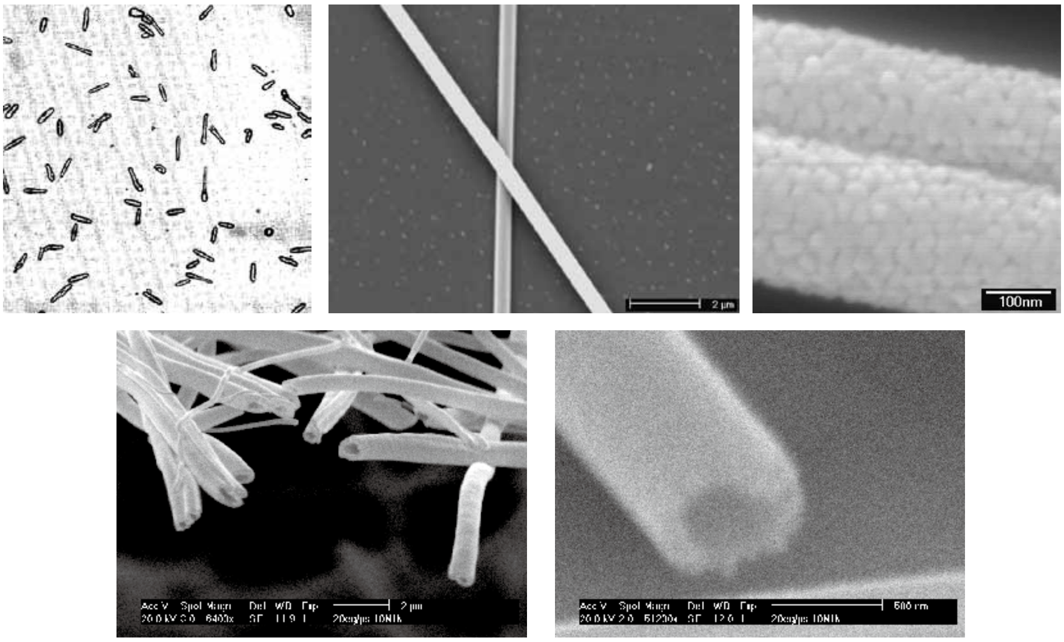

Fig. 14 Different Shapes (a to c first row and d to e second row) (a) Elongated polymer particles, (b) smooth PVP nanofibers, (c)TiO$_2$ nanofibers, (d and e) electrospun nanotubes obtained by co-spinning olive oil / PVP-TiO2 precursor (Marijnissen et al. 2010).

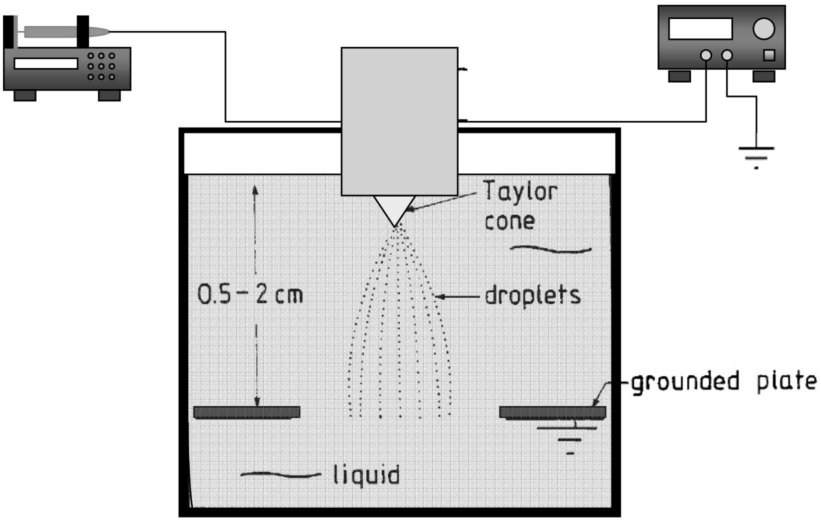

Fig. 15 Schematic Drawing of the set up for producing Emulsions (Adapted from Meesters, 1992).

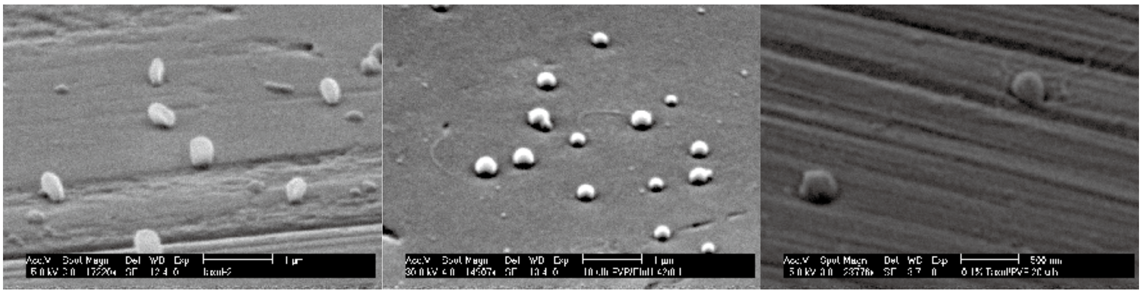

a) b) c)

Fig. 16 (a) Taxol ; 1.0% in EtoH at 22 L/h (21 oC/ 38% RH), 60 sec (spray time), 3 cm (spray to substrate distance), -2.1 kV (High Voltage), (b) PVP ; 0.3% in EtoH at 10 L/h (22 oC/ 47% RH), 60 sec, 3 cm, -2.4 kV, (c) Taxol+PVP ; 0.1% in EtoH at 20 L/h (21 oC/ 64% RH), 120 sec, 3 cm, -2.0 kV. (Marijnissen et al. 2010).

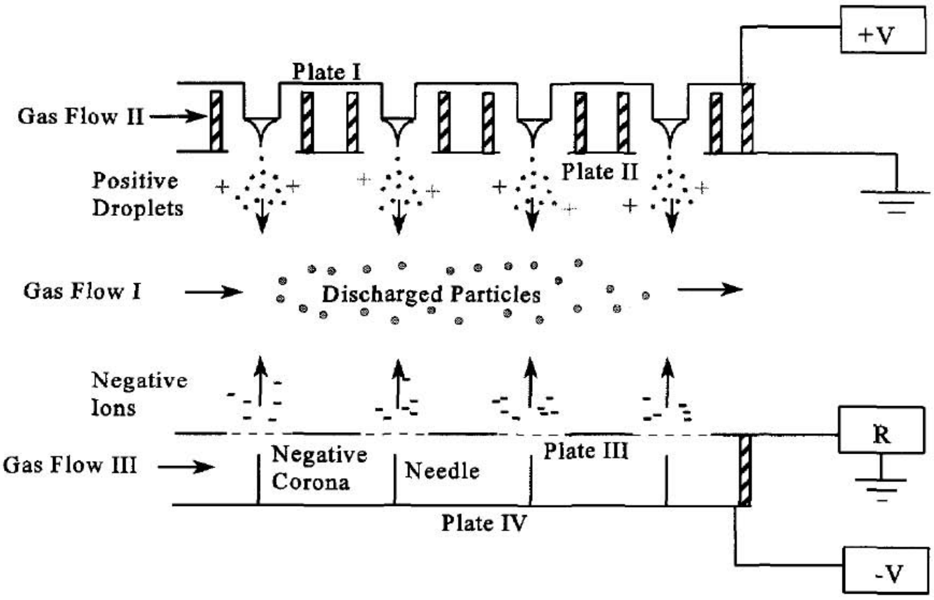

Fig. 17 Schematic of multi nozzle system suggested by Hartman. (Hartman, 1998).

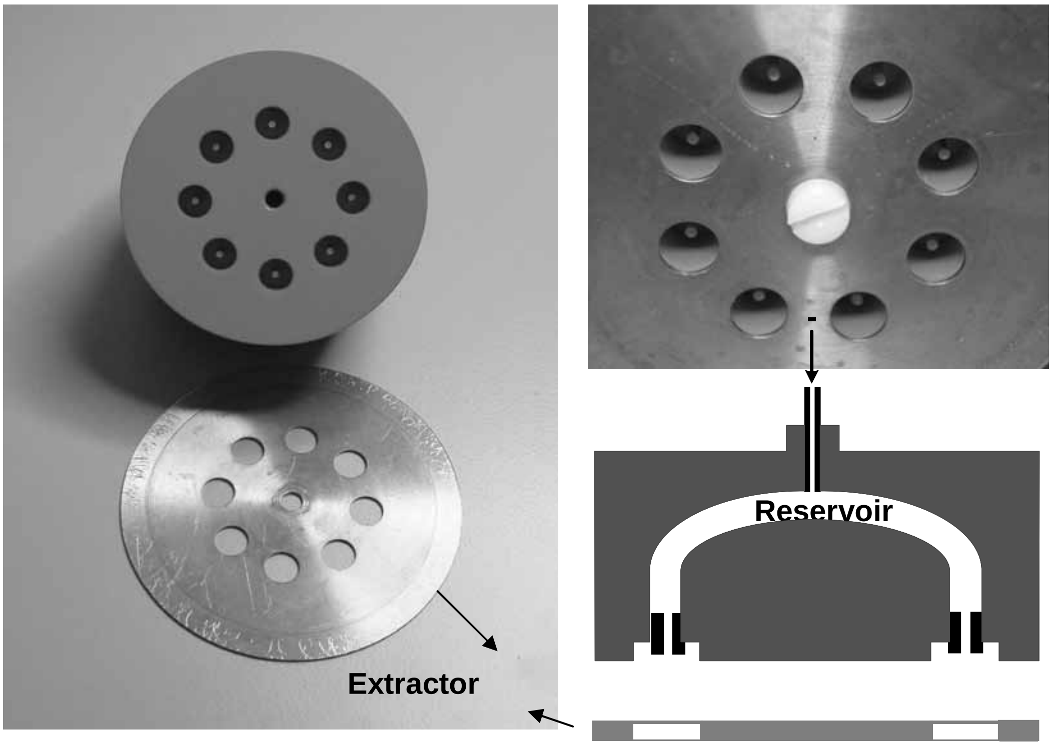

Fig. 18 Schematic of multi nozzle system suggested by Hartman and realized by Arnanthigo (Arnanthigo et al. 2010).

duction rate by increasing the flow rate. Thus an out-scaling rather than up-scaling is needed by means of using multiple sprays.

There are many efforts reported on out-scaling methods including the use of an array of capillaries, an array of holes in combination of non-wetting material, serrations, grooves, multi jet mode operation as summarized by Deng and Gomez (2007), and Deng et al., (2009). Increasing the number of capillary nozzles seems to be a simple and effective way of increasing the number of droplets. However, even in the simplest case of the multi jet mode operation, variation from jet to jet leads droplet size changes from one injection point to another causing a broader droplet size distribution. When the variation of flow rate couples with field intensity variations, operation of the out scaled system becomes unreliable. The design may also be dependent on the nature of the liquid. There is therefore a need for systematic design tools. The challenge is to have at each spraying point a uniform delivery of the liquid and equal field intensities.

Studies of Snarski and Dunn 1991, and Rulison and Flagan 1994 show that the voltage required for the steady cone-jet mode increases with a decrease in distance between the capillary nozzles. As the distance decreases in order to increase the nozzle packing density further issues will arise. Space charge, a dense charged droplet cloud, decreases the field strength at the nozzles, and so may cease the cone jet spraying of one or more nozzles. So for steady spraying a higher voltage setting is needed. So the electric field at the tip of a capillary nozzle is more often influenced by the nearby nozzles' electric field. If the influence between the nozzles is large, also the radial component of the electric force acting on a cone is not negligible and the electric force deforms the cone at the tip of the capillary nozzle leading to no or interrupted droplet break up.

As already discussed the droplets are highly charged and to avoid Rayleigh disintegration, they have to be discharged. More jets result in a higher space charge in the gap between the cones and the counter electrodes. The higher the space charge is, the higher the required potential difference necessary for the formation of the cones. The space charge in the setup could also lead to differences in the electric field at the nozzles. The problem of the electric field can be solved by introducing a ring electrode close to the nozzle just as for a single nozzle. In that case, the electric field is determined by the field between the nozzle and the ring. Neighbouring nozzles have no longer an influence on the field at the nozzle. The problem of space charge can be solved in two ways; collecting the particles immediately after their generation on a conducting surface (counter electrode), or discharging and transporting the particles with a carrier gas flow. **Fig. 17** shows a schematic representation of a multiple nozzle system as suggested by Hartman (1998), in where all the requirements have been fulfilled. Arnanthigo at al. (2010) implemented a circular design satisfying requirements suggested by Hartman (1998) but used a single pump to feed all nozzles, **Fig. 18**. In this configuration no neutralization is included but it can be done by corona discharge or by a radio active source.

Conclusions

Electrospraying is an important technology, and has many applications in the medical and pharmaceutical industry such as in Mass Spectroscopy, production of particles, encapsulation of particles, and thin film formation. Compared with other droplet production and film formation techniques, much smaller droplets with narrower size distribution from relatively large orifices are obtained. It is simple and can be applied in many conditions including the atmospheric ones. Electrospray produces a self dispersing cloud of droplets due to unipolar charge, thus coalescence and so variation in the particle size distribution is minimal. Charge of the droplets offers a good control on the trajectory and targeting, however for certain applications droplets have to be neutralized, which can be done by several means. As seen from the mass spectroscopy application it is even safe for large molecules, i.e. no high shear or thermal stresses are involved. The main factors determining the final product in the production of particles and films are the flow rate, electrical conductivity, surface tension, and concentration. With a right chemistry and processing conditions it is possible to tailor particles with a certain shape and surface morphology. The well established scaling laws can be used as a predictive tool. Many potential uses of electrospraying have been demonstrated in academic settings. However, developments towards higher productivity at industrially acceptable rates are needed.

Acknowledgements

The authors would like to thank L.L.F. Aghostinho and WETSUS, The Netherlands for kindly allowing us to use their high speed camera

References

Albert H. L. Chow, Henry H. Y. Tong, Pratibhash Chattopadhyay, and Boris Y. Shekunov. (2007): Particle Engineering for Pulmonary Drug Delivery, Pharmaceutical Research, Vol. 24, No. 3, March 2007.

Almeria B., Deng W., Fahmy T.A. and Gomez A. (2010): Controlling the morphology of electrospray generated PLGA microparticles for drug delivery, Journal of Colloid and Interface Science, 343, pp.125-133.

Arnanthigo, Y., Yurteri, C., Marijnissen, J. and Schmidt-Ott, A. (2010): 'Improved design of multi-electrospray unit with circular symmetry', in: Meesters, G., Pfeffer, T.V., Hauser-Vollrath, C. (Eds.), Proceedings of the Sixth World Congress on Particle Technology, paper

616.

Bailey, A.G. (1988): "Electrostatic spraying of liquids" , Research Studies Press, Taunton.

Barreras, F., H. Amaveda, et al. (2002): Transient high-frequency ultrasonic water atomization, Experiments in Fluids, 33(3): 405-413.

Bhaskar, S., Pollock, K.M., Yoshida, M. and Lahann, J. (2010): Towards designer microparticles: simultaneous control of anisotropv, shape and size, Small, 6 (3), pp. 404-411.

Biskos G., Vons V., Yurteri C.U. and Schmidt-Ott A. (2008): Generation and Sizing of Particles for Aerosol-Based Nanotechnology, KONA Powder and Particle Journal, No 26. pp.13-35.

Camelot, D.M.A. (1999): "The bipolar coagulation process for powder production", PhD thesis, Delft University of Technology.

Camelot D., Marijnissen J.C.M. and Scarlett B. (1999): Bipolar coagulation process for the production of powders, Industrial and Engineering Chemistry Research, 38 (3), pp. 631-638.

Champion, J.A., Katare, Y.K. and Mitragotri, S. (2007): Particle shape: A new design parameter for micro- and nanoscale drug delivery carriers, Journal of Controlled Release, 121 (1-2), pp.3-9.

Chang, M.-W., Stride, E. and Edirisinghe, M. (2009): A novel process for drug encapsulation using a liquid to vapour phase change material, Soft Matter, 5 (24), pp.5029-5036.

Chang, M.-W., Stride, E. and Edirisinghe, M. (2010): A new method for the preparation of monoporous hollow microspheres, Langmuir, 26 (7), pp.5115-5121.

Chen D. and Pui D.Y.H. (2010): Electrospray and its medical applications in "Nanoparticles in medicine and environment Inhalation and health effects", Marijnissen, J.C.; Gradon, Leon (Eds.), Springer.

Chen, D. and Pui, D.Y.H. (1997): Experimental investigation of scaling laws for electrospraying: dielectric constant effect, Aerosol Sci. Tech., 27(3), pp.367-380.

Chen, D., Pui, D.Y.H., and Kaufman, S. L. (1995): Electrospraying of conducting liquids for monodisperse aerosol generation in the 4 nm to 1.8 μm diameter range, J. Aerosol Sci., 26(6), pp.963-977.

Chen, D.-R., Wendt, C.H. and Pui, D.Y.H. (2000): A novel approach for introducing bio-materials into cells, Journal of Nanoparticle Research, 2 (2), pp.133-139.

Chen, X., Jia, L., Yin, X. and Cheng, J. (2005): Spraying modes in coaxial jet electrospray with outer driving liquid, Physics of Fluids, 17, pp.032101:1-7.

Ciach T., (2007), Application of Electro Hydro Dynamic Atomization in Drug Delivery, A Review, Journal of Drug Delivery Science and Technology, Volume 17, No: 6, pp.367-375.

Ciach, T., Geerse, K. B. and Marijnissen, J. C. M. (Kanuth, P. and Schoonman, J. eds.) (2002): EHDA in Particle Production in "Nanostructured Materials", Kluwer Academic Publisher , Boston.

Cloupeau, M. and Prunet-Foch, B. (1994): Electrohydrodynamic Spraying Functioning Modes: A critical review, J. Aerosol Sci., 25, pp.1021-1036.

Coffee, R.A. (2005): "Dispensing Device", US patent 6880554.

Cole, R.B. (1997): "Electrospmy Ionisation Mass Spectrometry", Wiley, New York.

Coppens, P.F. (2007): "Coating of tribocharged model particles with nanoparticles using EHDA", MS Thesis, Delft University of Technology, Faculty of Applied Sciences, Nanostructured Materials Research Group, Process and Product Engineering Research Group.

Dabkowski, M.F. (2006): "Coating of Particles with Nanoparticles by Means of Electrostatic Forces", MS Thesis, Delft University of Technology, Faculty of Applied Sciences, Nanostructured Materials Research Group, Process and Product Engineering Research Group.

Dabkowski, M.F., van Ommen, J.R., Yurteri, C.U., Hochhaus, G. and, Marijnissen, J.C.M. (2007): 'The coating of particles with nanoparticles by means of electrostatic forces', in: Schreglmann, C., Peukert, W.(Eds.), Partec 2007 - CD proceedings, Nuernberg, Germany, paper S37_2.

de la Mora, J. F. and Loscertales, I. G. (1994): The Current Emitted by Highly Conducting Taylor Cones, J. Fluid Mechanics, 260 , pp.155-184.

De La Mora, J. F., Navascues, J., Fernandez, F. and Rosell-Llompart, J. (1990): Generation of submicron monodisperse aerosols in electrosprays, J. Aerosol Sci., 21 (SUPPL. 1), pp.S673-S676.

de la Mora, J.F. (2007): The fluid dynamics of Taylor Cones, Annual Review of Fluid Mechanics, 39, pp.217-243.

Decuzzi P., Godin B., Tanaka T., Lee S.-Y., Chiappini C., Liu X. and Ferrari M. (2010): Size and shape effects in the biodistribution of intravascularly injected particles, Journal of Controlled Release, 141 (3), pp.320-327.

Deng, W. and Gomez, A. (2007): Influence of space charge on the scale-up of multiplexed electrosprays, J. Aerosol Sci., 38 (10), pp.1062-1078.

Deng, W., Waits, C.M., Morgan, B. and Gomez, A. (2009): Compact multiplexing of monodisperse electrosprays, J. Aerosol Sci., 40 (10), pp.907-918.

Dole M., Cox H.L. and Gieniec, J. (1973): Electrospray Mass Spectroscopy Chapter 7, pp.73-84, in Polymer Molecular Weight Methods, Advances in Chemistry, Vol. 125.

Dole, M., Mack, L.L., Hines, R.L., Chemistry, D.O., Mobley, R.C., Ferguson, L.D. and Alice, M.B. (1968): Molecular beams of macroions, The Journal of Chemical Physics, 49 (5), pp.2240-2249.

Dulcks, T. and Juraschek, R. (1999): Electrospray as an ionisation method for mass spectrometry, J. Aerosol Sci., 30, pp.927-943.

Ellis, N., Yurteri, C.U. and van Ommen, J.R. (2010): Development of a continuous nanoparticle coating with electrospraying, in: Kim, S.D, Kan, Y., Lee, J.K., Seo, Y.C. (Eds.), Fluidization XIII, Engineering Conferences International, New York.

Enayati, M., Ahmad, Z., Stride, E. and Edirisinghe, M. (2010): One-step electrohydrodynamic production of drug-loaded micro- and nanoparticles, Journal of the Royal Society Interface, 7 (45), pp.667-675.

Felder, C. B., M. J. Blanco-Prieto, et al. (2003): Ultrasonic atomization and subsequent polymer desolvation for peptide and protein microencapsulation into biodegradable polyesters, Journal of Microencapsulation 20(5), pp.553-567.

Forde, G., J. Friend, et al. (2006): Straightforward biodegradable nanoparticle generation through megahertz-order ultrasonic atomization, Applied Physics Letters 89(6), art.no.064105.

Freitas, S., H. P. Merkle, et al. (2004): Ultrasonic atomisation into reduced pressure atmosphere - Envisaging aseptic spray-drying for microencapsulation, Journal of Controlled Release, 95(2), pp.185-195.

Friend, J. R., L. Y. Yeo, et al. (2008): Evaporative self-assembly assisted synthesis of polymeric nanoparticles by surface acoustic wave atomization, Nanotechnology 19(14), art.no.145301.

Gañán-Calvo, A. (2003): "Device and Method for Creating Aerosols for Drug Delivery", US patent 6595202.

Gañán-Calvo, A. M., Davila, J. and Barrero, A. (1997): Current and Droplet Size in the Electrospraying of Liquids. Scaling Laws. J. Aerosol Sci., 28 , pp.249-275.

Ganán-Calvo, A.M. (2004): On the general scaling theory for electrospraying, Journal of Fluid Mechanics, 507, pp.203-212.

Geerse, K. B. (2003): "Applications of Electrospray: From People to Plants", PhD thesis, Delft University of Technology.

Geerse, K.B. and Marijnissen J.C.M. (2003) : Electrospray as Means to Produce Monodisperse Drug Particles, pp.75-90, in Gradon, L. and Marijnissen, J. (Editors), "Optimization of Aeorosol Drug Delivery", Kluwer Academic Publishers.

Geller, D.E. (2008): The science of Aerosol Delivery in Cystis Fibrosis, Pediatric Pulmonary 43, S5-S17.

Gilbert W. (1600): "De Magnete".

Gomez, A. and Tang, K. (1994): Charge and fission of droplets in electrostatic sprays. Phys. Fluids., A 6, pp.404-414.

Gomez A., Bingham D., De Juan L. and Tang K. (1998): Production of protein nanoparticles by electrospray drying , J. Aerosol Sci., 29 (5-6), pp.561-574.

Gomez, A., de la Mora, J.F. and Tang, K. (1999): "Electrospray Employing Corona-Assisted Cone-Jet Mode", US patent 5873523.

Gonzalez, D., Nasibulin, A.G., Jiang, H., Queipo, P. and Kauppinen, E.I. (2007): Electrospraying of ferritin solutions for the production of monodisperse iron oxide nanoparticles, Chemical Engineering Communications, 194 (7), pp.901-912.

Grace, J. M. and Marijnissen, J. C. M. (1994): A Review of Liquid Atomization by Electrical Means. J. Aerosol Sci., 25:6 , pp.1005-1019.

Gradon, L. and Marijnissen, J. (Editors) (2003): "Optimization of Aeorosol Drug Delivery", Kluwer Academic Publishers.

Hartman, R. P. A. (1998): " Electrohydrodynamic Atomization in the Cone Jet Mode. From Physical Modeling to Powder Production", PhD thesis, Delft University of Technology.

Hartman, R. P. A., Brunner, D. J., Camelot, D. M. A., Marijnissen, J. C. M. and Scarlett, B. (1999): Electrohydrodynamic Atomization in The Cone-Jet Mode Physical Modeling of The Liquid Cone and Jet. J. Aerosol Sci., 30:7, pp.823-849.

Hartman, R. P. A., Brunner, D. J., Camelot, D. M. A., Marijnissen, J. C. M. and Scarlett, B. (2000): Jet Break-Up in Electrohydrodynamic Atomization in the Cone-Jet Mode. J. Aerosol Sci., 31:(1), pp.65-95.

Hayati, I., Bailey, A. and Tadros, Th.F. (1987b): Investigations into the mechanism of electrohydrodynamic spraying of liquids. II. Mechanism of stable jet formation and electrical forces acting on a liquid cone Journal of Colloid And Interface Science, 117 (1), pp.222-230.

Hayati, I., Bailey, A.I. and Tadros, Th.F. (1987a): Investigations into the mechanisms of electrohydrodynamic spraying of liquids. I. Effect of electric field and the environment on pendant drops and factors affecting the formation of stable jets and atomization Journal of Colloid And Interface Science, 117 (1), pp.205-221.

Heijerman H, Westerman E., Conway S., Touw D. and Doring G. (2009): Inhaled medication and inhalation devices for lung disease in patients with cystic fibrosis: A European Concensus, Journal of Cystic Fibrosis, 8, pp.295-315.

Hickey, A. J., (Editor), (1996): "Inhalation Aerosols: Physical and Biological Basis for Therapy", Informa Healthcare.

Hinds, W. C. (1999): "Aerosol Technology 2nd ed.", John Wiley & Sons, Inc. , New York.

Hogan Jr. C.J., Yun K.M., Chen D.-R., Lenggoro I.W., Biswas P. and Okuyama K. (2007): Controlled size polymer particle production via electrohydrodynamic atomization, Colloids and Surfaces A: Physicochemical and Engineering Aspects, 311 (1-3), pp.67-76.

Hong, Y., Li, Y., Yin, Y., Li, D. and Zou, G. (2008): Electrohydrodynamic atomization of quasi-monodisperse drug-loaded spherical/wrinkled microparticles, Journal of Aerosol Sci., 39 (6), pp.525-536.

Hull, P., Hutchison, J., Salata, O. and Dobson, P. (1997): Synthesis of Nanometerscale Silver Crystallites via A Room-Temperature Electrostatic Spraying Process. Advanced Materials 9:5 , pp.413-417.

Ijsebaert, J.C., Geerse, K.B., Marijnissen, J.C.M., Lammers, J.-W.J. and Zanen, P. (2001): Electro-hydrodynamic atomization of drug solutions for inhalation purposes, Journal of Applied Physiology,91(6), pp.2735-2741.

Jaworek A. (2008): Electrostatic micro- and nanoencapsulation and electroemulsification: A brief review Journal of Microencapsulation, 25 (7), pp.443-468.

Jaworek, A. (2007): Micro- and nanoparticle production by electrospraying, Powder Technology, 176 (1), pp.18-35.

Jaworek, A. and Krupa, A. (1999): Classification of the modes of EHD spraying, J. Aerosol Sci., 30 (7), pp.873-893.

Jaworek, A. and Sobczyk, A.T. (2008): Electrospraying route to nanotechnology: An overview Journal of Electrostatics, 66 (3-4), pp.197-219.

Juraschek, R. and Röllgen, F.W. (1998): Pulsation phenomena during electrospray ionization, International Journal of Mass Spectrometry, 177 (1), pp.1-15.

Kebarle, P and Tang L. (1993): From ions in solution to ions in the gas-phase: The mechanism of electrospray mass-spectrometry. Anal. Chem., 65, pp.972-986.

Kim, K., Kim, W., Hwa Yun, S., Hyun Lee, J., Kim, S. and Lee, B.U. (2008): Use of an electrospray for the generation of bacterial bioaerosols, J. Aerosol Sci., 39 (4), pp.365-372.

Kim, K., Lee, B.U., Hwang, G.B., Lee, J.H. and Kim, S. (2010): Drop-on-demand patterning of bacterial cells using pulsed jet electrospraying, Analytical Chemistry, 82 (5), pp.2109-2112.

Kim, W. and Kim, S.S. (2010): Multishell encapsulation using a triple coaxial electrospray system, Analytical Chemistry, 82 (11), pp.4644-4647.

Kleinstreuer, C., Zhang, Z. and Donohue, J.F. (2008): Targeted drug-aerosol delivery in the human respiratory system, Annual Review of Biomedical Engineering, 10, pp.195-220.

Kozhenkov, V.I. and Fuks, N.A. (1976): Electrohydrodynamic atomization of liquids, Russian Chem. Rev. 45 , pp.1179–1184.

Lallave M., Bedia J., Ruiz-Rosas R., Rodriguez-Mirasol J., Cordero T., Otero J.C., Marquez M. and Loscertales I.G. (2007): Filled and hollow carbon nanofibers by coaxial electrospinning of Alcell lignin without binder polymers, Advanced Materials, 19 (23), pp.4292-4296.

Lastow, O. (2007): “Numerical and Experimental Study of Electrohydrodynamic Atomisation of Aqueous Liquids”, PhD thesis, Brunel University.

Leeuwenburgh, S.C.G, (2006b): “Electrosprayed calcium phosphate coatings for biomedical purposes”, PhD Thesis Radboud University Nijmegen.

Leeuwenburgh, S.C.G., Heine, M.C., Wolke, J.G.C., Pratsinis, S.E., Schoonman, J. and Jansen, J.A. (2006a): Morphology of calcium phosphate coatings for biomedical applications deposited using Electrostatic Spray Deposition Thin Solid Films, 503 (1-2), pp.69-78.

Lefebvre, A.H. (1989): “Atomization and Sprays”, Hemisphere Publishing Company.

Lenggoro, I., Okuyama, K., de la Mora, J. and Tohge, N. (2000): Preparation of ZnS Nanoparticles by Electrospray Pyrolysis, J. Aerosol Sci., 31:(1), pp.121-136.

Loscertales, I.G., Barrero, A., Guerrero, I., Cortijo, R., Marquez, M. and Gañán-Calvo, A.M. (2002): Micro/nano encapsulation via electrified coaxial liquid jets, Science, 295 (5560), pp.1695-1698.

Mao S., Lu G., Yu K., and Chen J. (2010): Protein Viability on Au Nanoparticles during an Electrospray and Electrostatic-Force-Directed Assembly Process, Journal of Nanomaterials, vol. 2010, Article ID 196393, 6 pages,. doi:10.1155/2010/196393.

Marijnissen J.C.M., Yurteri C.U., van Erven J. and Ciach T. (2010): Medicine Nanoparticle production by EHDA in “Nanoparticles in medicine and environment Inhalation and health effects” , Marijnissen, J.C.; Gradon, Leon (Eds.), Springer.

Meesters, G., Vercoulen, P. H. W., Marijnissen, J. C. M. and Scarlett, B. (1992): Generation of Micron-Sized Droplets from the Taylor Cone, J. Aerosol Sci., 23:(1), pp.37-49.

Meesters, G.M.H. (1992): “Mechanisms of droplet formation” , PhD thesis, Delft University of Technology.

Meng, C.K., Mann, M. and Fenn, J.B. (1988): Of protons or proteins - “A beam’s a beam for a’ that.” (O.S. Burns), Zeitschrift für Physik D Atoms, Molecules and Clusters, 10 (2-3), pp.361-368.

Michelson, D. (1990): “Electrostatic atomization”, Bristol, England ; New York, NY, USA, A. Hilger.

Mitragotri S. (2009a): In drug delivery, shape does matter, Pharmaceutical Research, 26 (1), pp.232-234.

Mitragotri S. and Lahann J. (2009b): Physical approaches to biomaterial design, Nature Materials, 8 (1), pp.15-23.

Moerman, R., Frank, J., Marijnissen, J.C.M., Schalkhammer, T.G.M. and Van Dedem, G.W.K. (2001): Miniaturized electrospraying as a technique for the production of microarrays of reproducible micrometer-sized protein spots, Analytical Chemistry,73(10), pp.2183-2189.

Muro S., Garnacho C., Champion J.A., Leferovich J., Gajewski C., Schuchman E.H., Mitragotri S. and Muzykantov V.R. (2008): Control of endothelial targeting and intracellular delivery of therapeutic enzymes by modulating the size and shape of ICAM-1-targeted carriers, Molecular Therapy, 16 (8), pp.1450-1458.

Nakaso, K., Han, B., Ahn, K.H., Choi, M. and Okuyama, K. (2003): Synthesis of non-agglomerated nanoparticles by an electrospray assisted chemical vapor deposition (ES-CVD) method, J. Aerosol Sci., 34 (7), pp.869-881.

Noakes, T. J., Pavey, I. D. Bray, D. and Rowe, R.C. (1989): “Apparatus for producing a spray of droplets of a liquid” , U.S. patent 4829996.

Noakes, T.J., Prendergast, M.J. and Green, M.L., (2000): “Electrostatic Spraying”, US patent 6079634.

Park, C.H., Kim, K.-H., Lee, J.-C. and Lee, J. (2008): In-situ nanofabrication via electrohydrodynamic jetting of countercharged nozzles, Polymer Bulletin, 61 (4), pp.521-528.

Rosell-Llompart, J., Fernández de la and Mora, J. (1994): Generation of monodisperse droplets 0.3 to 4 μm in diameter from electrified cone-jets of highly conducting and viscous liquids, J. Aerosol Sci., 25 (6), pp.1093-1119.

Rulison, A. J. and Flagan, R. C. (1994): Synthesis of Yttria Powders by Electrospray Pyrolysis. J. American Ceramic Society 77, pp.3244-3250.

Schacter, D.M., Shissias R.S., Yurteri C.U. and Escallon

E.C. (2007): "Improved process for coating a medical device", US patent application 2007/0077435.

Shiryaeva, S.O. and Grigor'ev, A.I. (1995): The semiphenomenological classification of the modes of electrostatic dispersion of liquids, Journal of Electrostatics, 34 (1), pp.51-59.

Shoyele, S.A. and Cawthorne, S. (2006): Particle engineering techniques for inhaled biopharmaceuticals, Advanced Drug Delivery Reviews, 58 (9-10), pp.1009-1029.

Shoyele, S.A. and Slowey, A. (2006): Prospects of formulating proteins/peptides as aerosols for pulmonary drug delivery, International Journal of Pharmaceutics, 314 (1), pp.1-8.

Siekmeier, R. and Scheuch, G. (2008): Inhaled insulin - does it become reality? Journal of Physiology and Pharmacology, 59 (SUPPL. 6), pp.81-113.

Simone E.A., Dziubla T.D. and Muzykantov V.R. (2008): Polymeric carriers: Role of geometry in drug delivery, Expert Opinion on Drug Delivery, 5 (12), pp.1283-1300.

Smith, D. P.H. (1986): Electrohydrodynamic Atomization of Liquids, IEEE Transactions on Industry Applications, IA-22 (3), pp.527-535.

Smith, J. N., Flagan, R. C. and Beauchamp, J. L. (2002): Droplet Evaporation and Discharge Dynamics in Electrospray Ionization, J. Physical Chemistry, A 106:42, pp.9957-9967.

Smith, R.D., Bruce, J.A., Wu, Q., and Lei, P. (1997): New mass spectrometric methods for the study of noncovalent associations of biopolymers, Chem. Soc. Rev., 26, pp.191-202.

Snarski, S.R. and Dunn, P.F. (1991): Experiments characterizing the interaction between two sprays of electrically charged liquid droplets, Experiments in Fluids, 11 (4), pp.268-278.

Stachewicz, U., Dijksman, J.F., Burdinski, D., Yurteri, C.U. and Marijnissen, J.C.M. (2009b): Relaxation times in single event electrospraying controlled by nozzle front surface modification, Langmuir,25(4), pp.2540-2549.

Stachewicz, U., Dijksman, J.F., Yurteri, C.U. and Marijnissen, J.C.M. (2010b): Volume of liquid deposited per single event electrospraying controlled by nozzle front surface modification, "Microfluidics and Nanofluidics", q(4-5), pp.635-644.

Stachewicz, U., Yurteri, C.U., Frits Dijksman, J. and Marijnissen, J.C.M. (2010a): Single event electrospraying of water, J. Aerosol Sci., Article in Press.

Stachewicz, U., Yurteri, C.U., Marijnissen, J.C.M. and Dijksman, J.F. (2009a): Stability regime of pulse frequency for single event electrospraying, Applied Physics Letters,95(22),art. no.224105.

Suh, J., Han, B., Okuyama, K. and Choi, M., (2005),:Highly charging of nanoparticles through electrospray of nanoparticle suspension, Journal of Colloid and Interface Science, 287 (1), pp.135-140.

Sung, J.C., Pulliam, B.L. and Edwards, D.A. (2007): Nanoparticles for drug delivery to the lungs, Trends in Biotechnology, 25 (12), pp.563-570.

Tang, K. and Gomez, A. (1994): Generation by electrospray of monodisperse water droplets for targeted drug delivery by inhalation, J. Aerosol Sci., 25, pp.1237-1249.

Taylor, G. I. (1964): Disintegration of Water Drops in An Electric Field, Proc. R. Soc. A280 , pp.383-397.

Van Erven Jan, Moerman Rob, and Marijnissen Jan C. M. (2005): Platinum nanoparticle production by EHDA, Aerosol Science and Technology, vol. 39, no 10, pp.929-934.

van Ommen J.R., Beetstra R., Nijenhuis J., Yurteri C.U. and Marijnissen J.C.M. (2008): Coating of tribocharged host particles with nanoparticles using electrospraying, Particulate Processes in the Pharmaceutical Industry II, San Juan, Puerto Rico, February 3-7,

van Zomeren A.A., Kelder E.M., Marijnissen J.C.M. and Schoonman J. (1994): The production of thin films of LiMn2O4 by electrospraying, J. Aerosol Sci., 25 (6), pp.1229-1235.

Vercoulen P.H.W., Camelot D.M.A., Marijnissen J.C.M., Pratsinis S, and Scarlett B. (1993): 'Sn02 Production by an Electrostatic Spray Pyrolysis Process. In Proc. Intern. Workshop on the Synthesis and Measurement of Ultrajine Particles, Editor Marijnissen J.C.M. and Pratsisnis S. Delft University Press, Delft.

Vercoulen, P.H.W. (1995): "Electrostatic processing of particles. A tool in particle technology",, PhD thesis, Delft University of Technology.

Vonnegut, B. and Neubauer, R.L. (1952): Production of monodisperse liquid particles by electrical atomization, Journal of Colloid Science, 7 (6), pp.616-622.

Weiler, C., Egen, M., Trunk, M. and Langguth, P. (2010): Force control and powder dispersibility of spray dried particles for inhalation, Journal of Pharmaceutical Sciences, 99 (1), pp.303-316.

Wilhelm, O. (2004): "Electrohydrodynamic spraying – Transport, mass and heat transfer of charged droplets and their application to the deposition of thin functional films", PhD thesis, ETH Zurich.

Wu, Y., Chalmers, J.J. and Wyslouzil, B.E. (2009): The use of electrohydrodynamic spraying to disperse hydrophobic compounds in aqueous media', Aerosol Science and Technology, 43 (9), pp.902-910.

Wu, Y., Fei, Z., Lee, L.J. and Wyslouzil, B.E. (2010): Coaxial electrohydrodynamic spraying of plasmid DNA/polyethylenimine (PEI) polyplexes for enhanced nonviral gene delivery, Biotechnology and Bioengineering, 105 (4), pp.834-841.

Xie J., Lim L.K., Phua Y., Hua J. and Wang C.-H. (2006): Electrohydrodynamic atomization for biodegradable polymeric particle production, Journal of Colloid and Interface Science, 302 (1), pp.103-112.

Xie J. and Wang C. (2007): Electrospray in the dripping mode for cell microencapsulation, Journal of Colloid and Interface Science, 312, pp.247–255.

Xie, J., Tan, J.C. and Wang, C.-H. (2008): Biodegradable films developed by electrospray deposition for sustained drug delivery, Journal of Pharmaceutical Sciences, 97 (8), pp.3109-3122.

Yamashita, M. and Fenn, J.B. (1984a): Electrospray ion source. Another variation on the free-jet theme, Journal of Physical Chemistry, 88(20), pp.4451-4459.

Yamashita, M. and Fenn, J.B. (1984b): Negative ion production with the electrospray ion source, Journal of Physical Chemistry, 88(20), pp.4671-4675.

Yule, A. J. and Al-Suleimani Y. (1997): On droplet formation from capillary waves on a vibrating surface, Proceedings of the Royal Society A: Mathematical, Physical and Engineering Sciences, 456, pp.1069-1085.

Zanen, P., Go, L.T. and Lammers, J.-W.J. (1998): The efficacy of a low-dose, monodisperse parasympathicolytic aerosol compared with a standard aerosol from a metered-dose inhaler, European Journal of Clinical Pharmacology, 54(1), pp.27-30.

Zanen, P. and Lammers, J.-W.J. (1999): Reducing adverse effects of inhaled fenoterol through optimization of the aerosol formulation, Journal of Aerosol Medicine: Deposition, Clearance, and Effects in the Lung,12(4), pp.241-247

Zeleny J. (1914): The electrical discharge from liquid points and an hydrostatic method for measuring the electric intensity at their surface, Phys. Rev. 3, pp.69-91.

Zeleny J. (1915): On the condition of instability of liquid drops, with applications to the electrical discharge from liquid points, Proc. Cam. Phil. Soc., 18, pp.71-88.

Zeleny J. (1917): Instability of electrified liquid surfaces, Phys. Rev., 10, pp.1-6.

Appendix

As mentioned in the text, Hartman (1998, 1999) derived theoretically a current scaling law for Newtonian liquids with a flat radial velocity profile in the jet (Equation 2). Gañán-Calvo et al. (1997) pointed out that this radial profile is not always flat in case of a low viscous liquid, or, when the conductivity is low, and the flow rate is high. To address this issue, also theoretically, and assuming that the velocity profile in the jet can be described by a parabolic profile, Hartman derived in his dissertation (Hartman 1998) a current scaling law for Newtonian liquids, with a non-flat radial velocity profile (Equation 3). In these equations, I^* is the current for a flat radial profile, Ez,max is the maximum axial Electric field strength[V m^{-1}] and can be calculated using equation (i),

$$E_{z,\max} = E_{ref}\left(\frac{Q}{Q_{ref}}\right)^{-0.44}\left(\frac{K}{K_{ref}}\right)^{-0.15}\left(\frac{\gamma}{\gamma_{ref}}\right) \quad \text{(i)}$$

where, E_{ref} = 4 10^6 [V m^{-1}], Q_{ref}=1.4 10^{-9} [m^3 s^{-1}], K_{ref}= 69 μS [m^{-1}], and γ_{ref}= 0.048 [N m^{-1}]. $r_{j0.41}$ is the radius of the jet at the position where the conduction current is equal to 41 percent of the total current [m]

$$r_{j0.41} = \left(\frac{0.41 I^*}{\pi E_{z,\max} K}\right)^{\frac{1}{2}} \quad \text{(ii)}$$

$$A = \frac{E_{z,\max}\,\sigma}{2\mu' r_{j,0.41}} \quad \text{(iii)}$$

where σ is the surface charge at $r_{j0.41}$ and defined as

$$\sigma = \frac{0.59 I^* r_{j0.41}}{2Q} \quad \text{(iv)}$$

and, μ' is the effective viscosity.

$$\mu' = \mu + c_{\mu}\,\rho\,\frac{Q}{\pi r_{j0.41}}\,\frac{dr_{j0.41}}{dz} \quad \text{(v)}$$

where, c_{μ} is a constant which equals to 0.635 and

$$B = \frac{Q - 0.5\pi r_{j0.41}^4 A}{\pi r_{j0.41}^2} \quad \text{(vi)}$$

For a complete derivation the reader is referred to the dissertation of R.P.A. Hartman (1998), Go to http://repository tudelft.nl/ and search for Hartman R.P.A.

Author's short biography

Caner U Yurteri

Caner U. Yurteri, born in 1966 in Turkey, a visiting Assistant Professor at Delft University of Technology. He received a B.S. (1987) in Mechanical Engineering from Istanbul Technical University, Turkey. He earned a M.S. (1992) and a PhD (1997) degree in Mechanical Engineering from Case Western Reserve University, U.S.A. He then joined the Chemical Engineering Department of Purdue University as a postdoctoral researcher, the Applied Science Department of the University of Arkansas at Little Rock as a research associate, Terronics Development Corporation as a research scientist, and Particle Engineering Research Center as an assistant scientist respectively. His work extensively involved Laser and Phase Doppler Anemometry and their applications to particle-laden flows. His research interests include particle technology, medical aerosols, electrostatic coating, and electrospraying.

Rob P.A. Hartman

Rob P.A. Hartman is born in 1966 in the Netherlands. He is one of the leading system designers and developers of Jewel Suite, a subsurface modeling software package for the oil industry, at JOA , the Netherlands. He holds a Masters degree in Applied Physics, a designer degree and a Ph.D degree from the Chemical Engineering Department of Delft University of Technology. The subject of his Ph.D thesis was electrohydrodynamic atomization in the cone-jet mode. He has some eighteen years experience in the field of scientific modeling software.

Jan C.M. Marijnissen

Jan C.M. Marijnissen is an Associate Professor and Head of the Aerosol Laboratory at Delft University of Technology, the Netherlands. He is a PERC Visiting Professor at the University of Florida, Gainesville, U.S.A. He holds a Masters degree from Delft University of Technology and a Ph.D. degree from the University of Minnesota, U.S.A. He has some thirty five years experience in the field of Mine Ventilation and Aerosol Technology. He has (co-)authored many articles and several books on Aerosol Technology and is a board member of different scientific associations and journals.

Bio-Inspired Functional Materials Templated From Nature Materials[†]

Di Zhang[1],[*], Wang Zhang[1], Jiajun Gu[1], Shenming Zhu[1], Huilan Su[1], Qinglei, Liu[1], Tongxiang Fan[1], Jian Ding[1] and Qixin Guo[2]
State key lab of metal matrix composites, Shanghai Jiao Tong University[1]
Department of Electrical and Electronic Engineering, Saga University[2]

Abstract

Inspired from nature materials with hierarchical structures, many functional materials are developed based on the templating synthesis method. This review will introduce the way to fabricate novel functional materials based on nature bio-structures with a great diversity of morphologies, in State Key Lab of Metal Matrix Composites, Shanghai Jiao Tong University. We present the idea and methods of obtaining multi-scale porous materials by using wood, agricultural wastes and butterfly wing scales as bio-templates. We change their original components into our desired materials withoriginal morphologies faithfully kept. Properties of the obtained materials are studied in details. Based on these results, we discuss the possibility of using these materials in light control, environment issues, andsolar energy conversion field. This work has great values on the development on structural function materials in the near future.

Keywords: bio-inspired, nature materials, functional materials

1. Introduction

Scientists are always amazed by the nature materials, which are characterized by unique structures and morphologies. Inspired by nature, scientists struggle to fabricate artificial structures with certain functions in a biomimetic way. There has been a great interest in using nature materials with subtle hierarchical structures as nature templates to fabricate biomorphic inorganic materials. In this review, the latest developments in this field done by our group will be discussed. The review is organized into four parts. In the first part, versatile inorganic materials using different wood issues as templates will be discussed. The second part will give an overview on the utilization of agricultural waste to fabricate novel functional materials. The third part will give an intensive review on the latest developments on how to create inorganic materials with unusual structural specialty and complexity using the butterfly wings as the templates. Finally, we will give the summary, expectation and our own perspectives on these active areas.

2. Bio-Inspired Materials Converted From Wood

As a group of the plant, wood is a heterogeneous, hygroscopic, cellular and anisotropic material, composed of fibers of cellulose and hemicellulose held together by lignin. Wood exhibits microstructural features ranging from mm (growth ring patterns) via μm (tracheidal cell patterns, macro- and microfibril cell wall textures) down to nm scale (molecular cellulose fibers and membrane structures of cell walls). Since all the cell walls in the wood link together to form a frame, the body of the wood is then divided into innumerable rooms by this frame. After being heated in high temperature, the mixed biopolymers in the cell walls decomposed into carbon and gases. This gives rise to a porous carbon frame with the morphology derived from its wood template. Our work convinced that the porous carbon wood microstructure has many favorable characteristics such as stable coefficient of friction, good electromagnetic shielding properties, excellent far infrared property and high damping capacity. These outstanding properties of the wood can be attributed to its rational

---

[†] Accepted: October 10, 2010

[1] 800 Dong Chuan Road, Shanghai, 200240 China
[2] 1 Honjo-machi, Saga-city, Saga, 840-8502, Japan
[*] Corresponding author
E-mail:wangzhang@sjtu.edu.cn
TEL:(+86)21-54742476 FAX:(+86)21-62822012

structures.

Generally, wood ceramics are fabricated through three steps: (i) formation of bio-carbon template by pyrolyzing the wood materials; (ii) infiltration of the bio-carbon template with ceramic precursors; (iii) calcination to form ceramics and remove organic materials. Carbides and carbide composites are most reported due to carbonaceous nature of the wood template, but a range of ceramic materials, including oxides, nitrides, and zeolites, were also produced by employing proper precursors and reaction routes. The general schemes for fabricating wood ceramics are illustrated as follows.

2.1 Carbides with wood microstructures

We converted wood carbon frameworks into morph-genetic SiC/C ceramics through methyl organic silicone resin infiltration followed by a high-temperature reaction. The process was investigated and it was revealed that the methyl organic silicone resin was first thermal decomposed into silicon compounds between 400 and 650℃, and then reacted with the carbon preform to form crystalline SiC after 1400℃ sintering [1]. Metal carbides can be synthesized using metal-containing sols as precursors. For example, TiC ceramic was produced by infiltrating tetrabutyl titanate sol into wood template in our group. The sol was first thermally decomposed into TiO_2, and then converted to TiC by reacting with the carbon cellular wall [2,3]. **Fig. 1** are images showing microstructures of several wood species and corresponding TiC wood ceramics prepared by infiltration with Ti-containing sols.

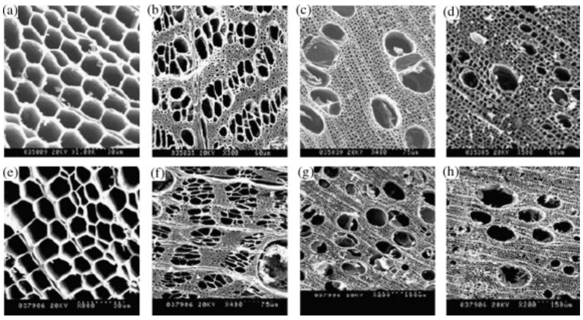

Fig. 1 SEM images of microstructures of TiC wood ceramics converted from wood species: (a) larch, (b) franxinus mandshurica, (c) black walnut, and (d) lauan. (e)?(h) are SEM imges showing corresponding microstructure of original wood tissues of: (e) larch, (f) franxinus mandshurica, (g) black walnut, and (h) lauan.

2.2 Oxides with wood microstructures

In section 2.1, we have studied the wood-templated carbon ceramics, SiC ceramics, Si/SiC/C and SiOC/C composites, metal/carbon composites to preserve wood's structures. Can we remove the carbon inside wood and reserve the wood structure intactly to prepare wood-templated oxide ceramics? Till the beginning of this research, the research both domestic and overseas to this question was still very rare, and the preparation technique of oxide ceramics was not mature and still at an exploratory stage.

There are millions of species of trees all over the world and they all contain unique structures. So by making good use of these natural treasures, different metal oxides with a wide range of pore size can be made. The synthesis scheme proposed here is an example of general and simple approach. It can be expanded to other oxides through changing inorganic precursors. Our team has prepared wood-templated metal oxides (e.g. NiO, ZnO, Co_3O_4), rare earth metal oxide (e.g. Y_2O_3, Ce_2O_3) and composite oxide successfully by the wood-templating method. In other kinds of wood-templated oxides, we also find controllable hierarchical porous structures that will be reported later. The following are several typical examples of our work.

Fig. 2(a) and **(b)** show the cross-sectional morphologies of carbonized Paulownia and Paulownia-templated bulk Fe_2O_3 calcined at 600℃. Vessels of about 50 μm in diameter and fibers of about 10 μm in diameter can be observed in **Fig. 2(a)**. Two kinds of pores can also be found in **Fig. 2(b)** with similar pore size and arrangement as original Paulownia, which illustrates that Fe_2O_3 preserves wood's hierarchical macroporous structures well.

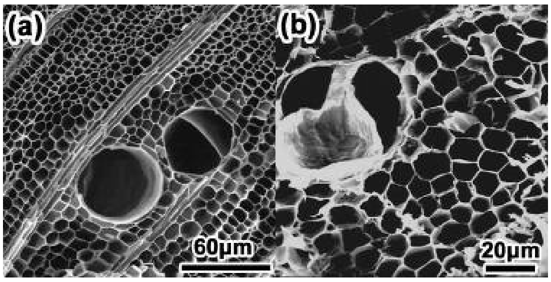

Fig. 2 SEM images of cross section of (a) carbonized Paulownia and (b) Paulownia-templated Fe_2O_3.

The enlarged TEM image of ultrasonic dispersing Fir-templated Fe_2O_3calcined at 600℃ is shown in **Fig. 3(a)**. Whiskered structures can be found in this sample. The SAED (Selected Area Electron Diffraction) of the whisker was inserted in image (a). It illu-

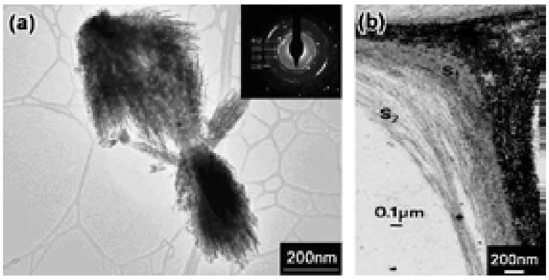

Fig. 3 (a)TEM images of Fir-templated Fe$_2$O^3 powder sample calcined at 600 oC. Insert: selected area electron diffraction (SAED) image; (b) Cellulose microfibrils and lamella of microfibrils of Poplar. (Aslam, Chaudhary, Mulla, Sainkar 1999).

minates the crystalline hematite phase of the Fir-templated Fe$_2$O$_3$. On the other hand, coexistence of the diffraction rings and spots at the SAED photo shows that more than one grain exists in the small diffraction area. In addition, different darkness on the same diffraction ring elucidates the anisotropic diffraction. Image (b) shows the cellulose microfibrils and lamella of microfibrils of Poplar. S1 and S2 are the outer layer and middle layer of the secondary wall. The two layers are composed of microfibrils seen as the whiskered shape in image. S1 has dense microfibrils and S2 has sparse microfibrils. Various woods have similar wood cell composition. The characters of S1 and S2 of Poplar are very like the morphology of Fir-templated Fe$_2$O$_3$ in image (a), which proves that Fe$_2$O$_3$ preserve the microfibrils of wood cell wall and realize the replication in nanometer scale.

Fig. 4(a) and **(b)** show the cross-sectional morphologies of carbonized Pine and Pine-templated bulk NiOcalcined at 600℃. A NiO fiber assembly can be observed in **Fig. 4(b)** along the longitudinal section, which was derived from long and channel-like tracheid cells with the functions of conducting water and supporting in Pine shown in **Fig. 4 (a)**. The pits, through which the Ni-precursor penetrated efficiently, were also preserved by NiO pointed out by arrow in **Fig. 4 (b)**. As can be seen, the original cellular anatomy of Pine template is retained integrally in NiO.

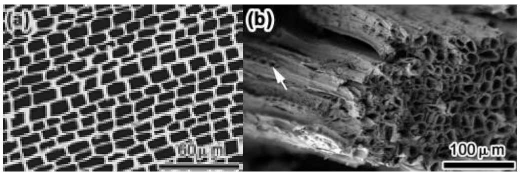

Fig. 4 SEM images of cross section of (a) carbonized Pine and (b) Pine-templated NiO.

Cr$_2$O$_3$ ceramic was synthesized by immersing wood in chromium nitrate solution. These ceramics not only inherited the specific microstructures of the original wood, also possessed a characteristic IR absorption peak, which indicating the potential application in IR absorption devices. Hierarchically porous manganese oxide wood ceramic was also produced using manganese nitrate as the precursor. An overall collapse in IR adsorption spectra was also observed with increasing calcination temperature, related to the effect of nanoscale pore structures [4,5]. Hierarchically porous zinc oxides fabricated from Fir tissues show high sensitivity and selectivity to H$_2$S vapor. Higher porosity and surface area can provide more surface adsorption positions and reacting areas for oxygen and test gases and help gases transfer more quickly, which could lead to the increase of gas response [6].

2.3 Metal/carbon composites with wood microstructures

Not only are the iron oxides, metal/carbon composites prepared from wood templates also been fabricated and characterized. Aluminums alloys are known for their high specific strength, good cast ability, low thermal expansion and high corrosion resistance. The wear rates for the materials increase with increasing the applied load and the test temperature. The carbon-frame in the composites divided the Al alloy into innumerable sections. It can help the Al matrix improve its dry friction behaviors. The coefficient of friction for the materials usually increases with increasing applied load and test temperature. Moreover, during the course of wearing, the coefficient of friction curves for the composites were more smooth and straight than the Al alloy. This demonstrates the more stable friction state for the composites [7-9].

3. Bio-Inspired Materials Converted From Agricultural Wastes

An agricultural establishment produces many types of wastes in its daily operations. Agricultural waste materials particularly those containing cellulose shows potential metal bio-sorption capacity. The basic components of the agricultural waste materials biomass include hemi-cellulose, lignin, extractives, lipids, proteins, simple sugars etc., which is very similar to the wood tissues. To loose the environment pressure and increase the economic value of these wastes, re-using them is a very urgent topic. Studies reveal that various agricultural waste materials such as rice husk, coconut shells, vegetable residues etc. have great potential in electromagnetic wave absorption applications. Here same research details are given as follows.

Rice husk, a by-product of the rice milling industry, accounts for about 20% of the whole rice. With the estimated annual rice production of 500 million tons in developing countries, approximately 100 million tons of rice husk is available annually for utilization in these countries alone. However, the amount of rice husk available is far in excess of any local uses and, thus, has posed disposal problems. In our research, rice husk was chosen to be applied as a template material due to its high porous structure, special components and its local availability at almost no cost. The objectives of this study was to determine selected electromagnetic wave absorption properties of different sorbents made from rice husk by different routes of preparation[10-11].

Fig. 5shows the procedure of nickel-loaded composites preparation. Rice husk were elementarily carbonized at 800℃ . Hereinafter, the product was called black rice husk, the primary components of which were amorphous SiO_2 and carbon. In a sol-gel process, black rice husk was impregnated in nickel nitrate solutions of different concentration chosen as the precursor of nickel for 24 h. This procedure was carried out for the purpose of obtaining higher dispersion of nickel nitrate in black rice husk. Non- and nickel-loaded black rice husk was milled to powders, and then mixed well with 15 wt% phenolic resin powder chosen as a curing agent in a stainless steel vessel. Finally the mixture was molded into disk specimens with 115mm and 6mm in diameter and thickness, respectively. In these molding processes, various pressures (12,16 and 20 MPa) were applied on the mixture for initial 20 min, and then solidification of the mixture was continued free from compression for 12 h. Secondary carbonization was carried out at the temperatures of 800℃, 1200℃ and 1400℃ to yield nickel-loaded carbon matrix composites. The influence of carbonization temperature, molding pressure, nickel loading and the porous structure on the as-synthesized rice husk composites are discussed, which are summarized in **Table 1.**

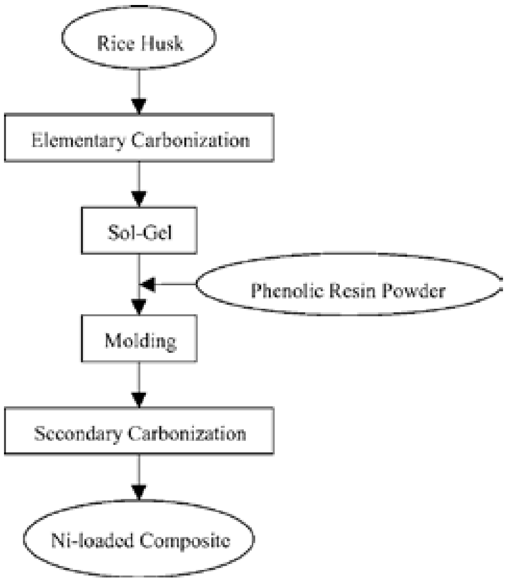

Fig. 5 Procedure of nickel-loaded composites preparation.

The SE of a material is defined as the ratio between the incoming power (Pi) and outgoing powder (Po) of an electromagnetic wave. In general, SE is expressed in decibels (dB). **Table 1** summarizes the electromagnetic SE at 500 MHz, 1 GHz and 1.5 GHz and the conductivity of the composites sintered at 800 ℃ and above at room temperature. It can be seen that the nickel-impregnated samples had significantly higher SE values (at least 10 dB better) than the untreated samples at all sintering temperatures except 800 ℃. Even at 800 ℃ the nickel impregnated sample shows slightly better SE values than the untreated sample at all frequencies tested here. Moreover the SE of the nickel treated samples increases with increasing of the sintering temperature significantly and steadily from 800 ℃ to 1200℃. For the untreated composites, the SE does not seem to increase significantly with the increase of the sintering temperature from 800 ℃ to 1400 ℃ even though the SiO_2 was replaced by SiC at 1400 ℃. The SE values were 47.5 dB, 44.4 dB and 47.7 dB for the samples sintered at 800 ℃ and 51.9 dB, 44.3 dB, 41.8 dB for the samples sintered at 1400 ℃ at 500 MHz, 1 GHz and 1.5 GHz, respectively.

Table 1 Constituents, thickness, SE and electrical conductivity of nickel-impregnated and untreated composites as a function of heat treatment temperature

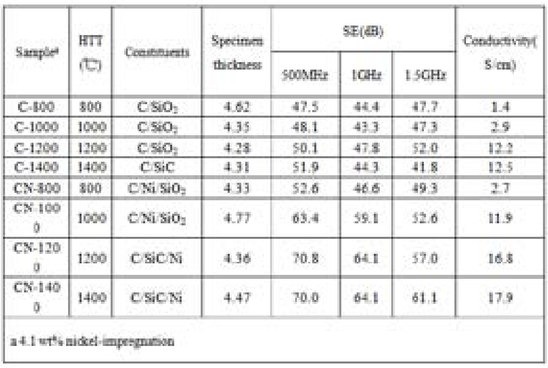

Sample[a]	HTT (℃)	Constituents	Specimen thickness	SE(dB)			Conductivity(S/cm)
				500MHz	1GHz	1.5GHz	
C-800	800	C/SiO_2	4.62	47.5	44.4	47.7	1.4
C-1000	1000	C/SiO_2	4.35	48.1	43.3	47.3	2.9
C-1200	1200	C/SiO_2	4.28	50.1	47.8	52.0	12.2
C-1400	1400	C/SiC	4.31	51.9	44.3	41.8	12.5
CN-800	800	$C/Ni/SiO_2$	4.33	52.6	46.6	49.3	2.7
CN-1000	1000	$C/Ni/SiO_2$	4.77	63.4	59.1	52.6	11.9
CN-1200	1200	C/SiC/Ni	4.36	70.8	64.1	57.0	16.8
CN-1400	1400	C/SiC/Ni	4.47	70.0	64.1	61.1	17.9

a 4.1 wt% nickel-impregnation

More details please refer to our published work,.

Except rice husks, coconut shells were also utilized to enhance the electromagnetic wave absorption properties of the composites. Scanning electron microscopy (SEM) image reveals that both porous carbons and C(Co) nanocomposite are characterized with a hierarchical porous structure. It can be observed from **Fig. 6a** that the C(Co) nanocomposite is constructed with separate carbon tubes with about 10 μm diameter. Little pores with 1–2 μm diameter are distributed uniformly on the walls of the carbon tubes[12].

Porous materials have better impedance match with free space than corresponding solid materials for their low effective permittivity. The electromagnetic waves can easily irradiate into the porous structure, and then dissipate in the composite. Moreover, the porous structure definitely increases interfacial areas throughout the composite, enhances the chance of multi-reflection, and leads to the improved energy loss. In conclusion, porous C(Co) composites exhibit excellent electromagnetic absorption properties, which are attributed to the well impedance match between porous structure and free air, the strong interfacial polarization relaxation loss and Ohmic loss. The porous carbon-based composites have advantages in being light weight and having effective absorption performance and may become attractive candidates for electromagnetic absorption materials.

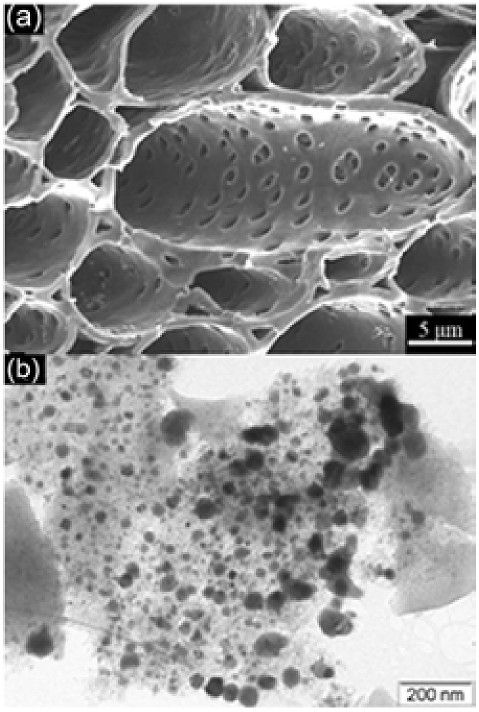

Fig. 6 SEM and TEM images of C(Co) nanocomposites (a. SEM andb.TEM).

4. Bio-Inspired Materials Converted From Dutterfly Wings

Occurred on the earth in Tertiary period 25 million years ago, the butterfly family possesses the largest number of species (about 100 000 species). A butterfly's wing is a uniquely visual exhibition, not only of the aesthetics of nature, but of the machinery of evolution and of inspiration of research. They are made of scales which are quite small and form two or more layers over the wing membrane. Different forms of butterfly microstructures have been categorized based on the nature of structural reflection, scattering and diffraction by H.Ghiradella. To distinguish these species, a main method is to identify the narrow difference of the colors and structures between different wing scales. The scales are of a thin plate-like form, whose typical dimensions are 100 μm in length, 50 μm in width, and about 0.5 μm in thickness, which cover the wing like tiles on a roof or a dense tapestry.

Fabrication the similar hierarchical microstructures shown above in the butterfly wings in lab by using a manmade assembly synthesis rout is an extremely difficult task, since the formation mechanisms are tremendously complex. Therefore, we turned towards naturally occurring photonic structures for inspiration and several nanofabrication techniques have been developed to replicate natural photonic structures in butterfly wings. Chemical synthesis permits the manipulation of matter at the molecular level. Better control of the particle size, shape, and size distribution can be achieved in particle synthesis. To benefit from the advantages of chemical processing, several carefully designed approaches to fabricate butterfly wings replicas have been studied in our group recently. Here, three typical functional butterfly wings replicas with various properties are shown below.

4.1 Optical functional oxides templated from butterfly wings[13]

The beautiful colors exhibited by butterfly wings areusually contributed by two sources: pigments and chitin periodical structures, which are also referred to as “chemical” and “physical” colors, respectively. Physical colors, i.e., structural colors, are essential topics since they can be modulated by the materials’ dielectric coefficients and their internal submicrostructures.Hence, to study the properties of butterfly replica, which are synthesized using different functional materials e.g., Al_2O_3 and ZnOwith natural butterfly as biotemplates, attracted great attention. However, some key features of the structural color, including iridescence, are unfortunately not reported in these works, which questions whether the obtained replica color is an inherited structural one or not.

It is generally believed that an obvious response to the imposed electromagnetic (EM) wave needs a big refractive index (RI) difference between the two materials that compose the photonic crystals (PCs). As compared to the air, the RI of the original chitin, previously reported ZnO, and Al_2O_3 is 1.57, 1.94, and 1.75 at 1.06 μm, respectively. To see what will happen by making the butterfly fossils with some higher RI materials is quite interesting to us. In this letter, we choose ZrO_2 to prepare the butterfly PCs. ZrO_2 has a RI of 2.12 at 1.08 μm, which is at least 9%, 21%, and 35% higher than ZnO, Al_2O_3, and chitin, respectively.

ZrO_2 is a high dielectric constant material with excellent optical properties. It has also been reportedthat ZrO_2 possesses a small thermal expansion coefficient, a very low thermal decomposition temperature, and a well metallic workability in high temperature, which makes it easy to be utilized in present fabrications. The butterfly wings we chose as biotemplate are from *Euploea mulciber* (*Cramer, the family of Danaidae*). The upper surface of its either wing has a prominent large shining metallic blue patch in the whole area. The wings are covered by chitin scales, as thousands of tiny flat platelets lying in rows. All the scales are fixed by peg-and-socked attachments. Scales with the size of about 100 μm in length, 50 μm in width, and 0.5 μm in thickness, form the flat plates overlapping over the membrane like roof tiles when viewed under a microscope.

Intact ZrO_2 replica, which is large in size has been synthesized by using natural butterfly wings as templates. Microstructure characters of original butterfly wing scales are maintained faithfully in this biomorphic ZrO_2. All replicas can reflect iridescent visible lights, which can even be observed by naked eyes, shown in **Fig. 7**. These ZrO_2 fossils with high RI can reflect the visible lights so strongly that the colors can be clearly observed directly even by naked eyes. In addition, iridescent colors can be seen in different observation positions from **Fig. 4b-d**, confirming a good inheritance of the structural colors. Optical microscope investigations indicate that colors reflected by one single scale are different from those done by the overlapped two or even more scales. Colors are not only determined by materials' refractive index, observation angle, and the structure of every single scale, but also by its piled number and modes. With the increase in the number of piled scales, the color is not simply red-shifted or blue-shifted, which is the most direct and powerful evidence for structural colors.

Fig. 8. presents the micrographs of the ZrO_2 replica. Here, **Fig. 8(a)-(c)** are taken using a digital optical microscope at various regions under different magnifications. The system is carefully checked using standard color cards to avoid the color distortion. **Fig. 8(d)** and**(e)**are the field-emission scanning electron microscope images. These scales have clearly identifiable ridges with parallel cross ribs between them, which preserve the original structures well. **Fig. 8(f)** presents an X-ray diffraction (Cu K α) result of the replica, which confirms the as-synthesized products to be ZrO_2. The ZrO_2 fossil presents blue, brown, or red under the investigation of the optical microscope. It should be noted here that colors in the middle of one single scale and in overlapped

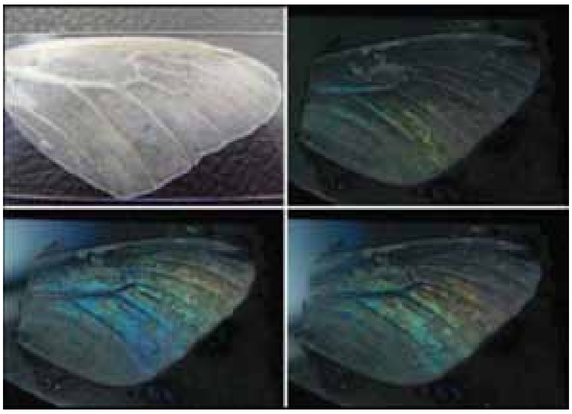

Fig. 7 Photographs of the original faded wing and the ZrO_2 mineralized wing sample. a. The faded wing. b. The ZrO_2 replica in different observation angles.

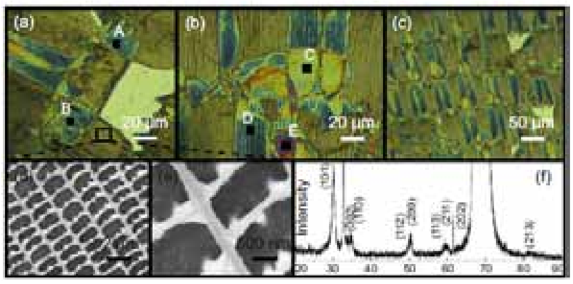

Fig. 8 Images and XRD measurement of the ZrO_2 replica. (a)-(c) Optical microscope images of the ZrO_2 replica. (d)-(e) FESEM images of ZrO_2 replica. (f)XRD result of the as-prepared ZrO_2 replica. The rectangular area in (a) schematically indicates where (d) and (e) are taken from.

edges are different. This property is the same as the original wings and faded ones, but different in colors and clarities, indicating a structural color nature of this phenomenon. Points A–E marked in **Fig. 8(a)** and **(b)** show the optical images of the overlapped area of two or more scales. Colors are determined by the number of overlapped scales. It can be seen that the color is not only simply redshifted or blueshifted with the increase in piled numbers. Instead, the color changed from brown (one single scale), to blue (two piled up, see A, B, D), to yellow (three piled up, see C), and finally to red (four piled up, see E). Because of the length of this letter, more detailed results and analysis will be presented elsewhere.

Reflection measurements were then performed in the visible and near-infrared wavelength regions to reveal the light interaction with the replicated structures. They were taken on UV-visible-near infrared microspectrophotometer. The incident angle is vertical to the surface of the substrate, as shown in the left inset of **Fig. 9a**. **Fig. 9** presents the reflection measurement results, where **Fig. 9a** shows the results from the intact butterfly wing and **Fig. 9b** is the one measured at microareas on the wing scales. The reflectance values of both **Fig. 9a**bare of the same scale. In **Fig. 9a**, the reflectance spectrum of the original butterfly wings is listed for comparison. It shows that the ZrO_2 replica also has a strong reflection peak, though a little lower in intensity than the original butterfly wings. The reflection spectrum of replica shows that there is a strong reflection peak around 650–700 nm, indicating the existence of a photonic band gapin the replicated structure. The reflection peak is redshifted as compared to the wing hybrids a middle state after vacuum annealingand natural butterfly wings. **Fig. 3b** presents the microarea spectrum of the ZrO_2 replica. A and B are the two areas representing two piled up wing scales and their single scale counterpart, respectively. To A, a peak around 350–450 nm confirms the violet to blue colors we viewed directly at points A, B, and D, in **Fig. 8a** and b. To B, a main peak around 600–700 nm explain the brown color we saw at single scale area in **Fig. 8a-c**.

Fig. 9(b) presents the microarea spectrum of the ZrO_2 replica. A and B are the two areas representing two piled up wing scales and their single scale counterpart, respectively. To A, a peak around 35–450 nm confirms the violet to blue colors we viewed directly at points A, B, and D, in **Fig. 8(a)** and **8(b)**. To B, a main peak around 600–700 nm explain the brown color we saw at single scale area in **Fig. 8(a)-(c)**.

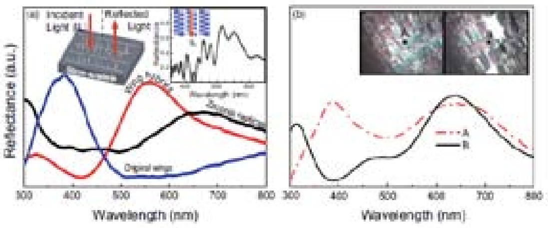

Fig. 9 Reflectance results of butterfly wings and ZrO_2 replicas. (a) Reflectance spectra of original butterfly wings, wing hybrids (soaked wings after vacuum annealing), and ZrO_2 replicas, respectively. Insets show a schematic of the reflection measurement setup and the FDTD simulation results. (b) Reflectance spectra of (a) the overlapped scales and (b) one single scale of ZrO_2 replica. Insets are the opticalimages of the measured scales.

To reconstruct these experimental results, we theoretically calculated the reflection spectrum using a finitedifference time-domain (FDTD) method. The model based on the wing scale we used, as well as the calculated results, is presented in the right inset of **Fig. 9(a)**. The calculated results agree well with the reflection data of B area in **Fig. 9(b)**, which is measured at a single scale simulated directly by our calculation model. It should be noted that the replicas in this work are composed of submicrometer ZrO_2 particles, which can induce additional diffuse reflection because of their granular surfaces. Moreover, the scale replica's surface is not perfectly flat, which may also produce deviations between the experimental and calculated results.

According to these results, we found that with the increase in the RI, a stronger modulation of the periodic submicrostructure to visible EM wave is obtained, giving rise to some phenomena that have not been reported before. Under this RI modulation, the structural color is not sensitive to the layer thickness of the replicaany more. Instead, it can simply be modified by scale-pile numbers, or by collection along various directions, which loosens the preconditions for this replica family to be prepared and broadly applied. Since the reflection peak will shift to long wavelength with the increase in the materials' dielectric constant, colors of the replica, which locate in visible wavelength range, can be further changed or modulated via functional or ferroelectric materials. The present fabrication of large-area and colored replica has great potential applications in display screens, spectroscopes, detectors, and so on. Since there are so many kinds of butterflies with thousands of different microstructures, it is possible to find a suitable structure that meets our demands for certain applications.

4.2 Novel gas sensors inspired from butterfly wings[14)]

By introducing natural butterfly wings as templates, well-organized porous hierarchical SnO_2 replicas with controllable wall thickness were fabricated, on the basis of the control over the impregnants concentration and the immersing time. As far as we know, SnO_2 with the large bandgap (Eg = 3.6 eV, at 300 K), has been themost typical and promising choice for a metal oxides snesors based gas sensor.

The gas sensing properties were evaluated according to the resistance variation under a direct current (dc) voltage of 5 V by using ethanol as the target gas. To avoid structural damage, the samples were cut into small fragments and then mixed with appropriate adhesives to adhere onto a flat alumina substrate, which is attached with two gold electrodes having a gap of about 1 mm. The fittings were then sintered at 500 ℃ for 1 h in air and aged at 350 ℃ for 7 days. Gas sensing experiments were carried out in a gas flow apparatus equipped with an external heating facility. The sample gases used were ethanol diluted in dry air. The gas flow was switched between the sample gas and dry air while the electrical resistance of the SnO_2 sheet was measured continuously on an electrometer.

FESEM images in **Fig. 10** show the well-organized porous hierarchical architecture of the target product SnO_2 and the corresponding natural butterfly wings. They are covered by a large number of overlapping SnO_2 scales and chitin scales (**Fig. 10(a)** and **(e)**), respectively. On each scale (**Fig. 10(b)**, and **(f)**) the parallel-aligned ridges are divided into numerous uniform windows (macropores) by the periodic aligned pillars between them. A higher magnification image (**Fig. 10(c)**, and **(g)**) clearly exhibits that the ridges are stacked stepwise by multi-layers of lamellas, which are supported by a mass of ordered-aligned nano-scaled microribs. The cross sections of scales (**Fig. 10(d)**, and **(h)**) reveal that the pillars are orderly standing on the substrate layers and extend to the top parallel ridges, and thus well-organized macroporous frameworks are produced. In conclusion, the unique architecture of the target product SnO_2 (**Fig. 10(a)–(d)**) is faithfully inherited from that of the natural butterfly wings (**Fig. 10(e)–(h)**) from the nanoto micro-scales, despite some dimensional shrinkage.

More details of SnO_2 scale (**Fig. 12(a)–(c)**) reveal theconnective hollow interiors and thin walls. It is obviousthat the pillars (**Fig. 12(a)**) are indeed fastigiated hollowtubers, and the lamellas (**Fig. 12(b)**) stacked on the ridgesare interconnected tubes with a diameter of about 188 nm.The substrate layer (**Fig. 12(c)**) is piled in two parallel thinlayers. Thus the well-organized hierarchical architecture isactually composed of thin, conformal and continuous wallswith thickness around 32 nm, which provides convincingevidence of the nanocoating process. Energy-

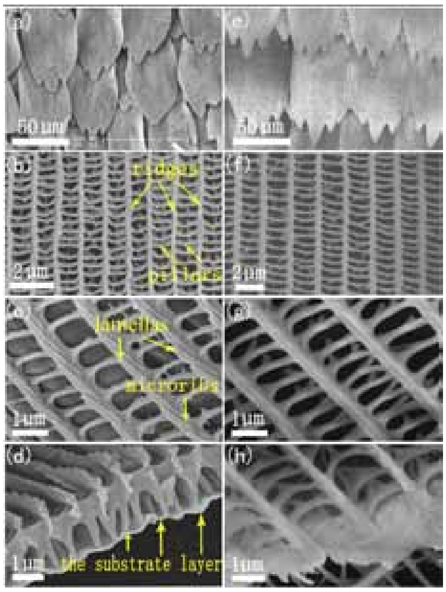

Fig. 11 FESEM images of ((a)–(d)) the target product SnO_2 and ((e)–(h)) the corresponding natural butterfly wings: (a) and (e) well-aligned scales, (b) and (f) part of a single scale, (c) and (g) the detailed structure of the ridges, (d) and (h) the cross section of the scale.

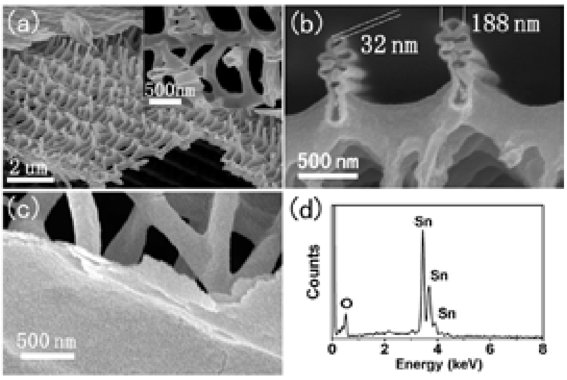

Fig. 12 FESEM images of (a) the inverse side of a single SnO_2 scale with a region of the substrate layer removed, the inset showing the hollow interiors of the pillars, (b) the cross section of the SnO_2 scale, (c) the substrate layer with a double-layered structure; (d) the EDX spectra of the SnO_2 scale.

dispersive xray(EDX) spectroscopy (**Fig. 12(d)**) demonstrates that thewalls are indeed composed of Sn and O elements, which isin accord with the above XRD results.

Transmission electron microscopy (TEM) and highresolution TEM (HRTEM) images (**Fig. 13**) provide further insight into the morphology and microstructure of the biomorphic SnO_2 (the target product). The long dark rows (**Fig. 13(a)**) are the ridges orderly stacked by parallel tubes. The ordered microribs are also clearly seen as parallel dark rods of about 130 nm in diameter on each ridge. Between the ridges are the fastigiated hollow tubers. The top view and the cross section of the ridge in high magnification (**Fig. 13(b)** and **(c)**, respectively) clearly exhibit the hollow interiors with thin walls. The wall thickness is about 31 nm according to the tip of the tube with a diameter of about 183 nm (**Fig. 13(d)**), which is close to the result of FESEM. The higher magnification image (**Fig. 13(e)**) reveals that the well-organized porous hierarchical architecture is actually assembled by the nanocrystallites with an average size of about 7.0 nm, which is in accord with the XRD results. The selected area electron diffraction (SAED) pattern (inset in **Fig. 13(e)**) indicates that the assembled units of the biomorphic SnO_2 are polycrystalline in nature and the diffraction rings are indexed to (110), (101), (200), (211) and (301) planes of rutile SnO_2, respectively. The HRTEM image (**Fig. 13(f)**) reveals the further microstructure of the SnO_2 nanocrystallites. The spacings between two adjacent lattice planes are about 0.3418 and 0.2677 nm, corresponding to (110) and (101) planes of rutile SnO_2.

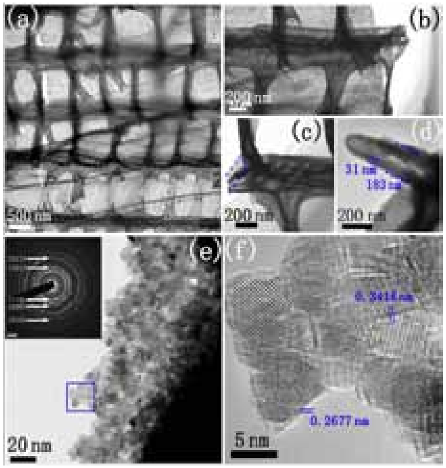

Fig. 13 TEM images of (a) part of single SnO_2 scale, (b) the top view of the ridge, (c) the cross section of the ridge, (d) the tip of the tube, (e) SnO_2 nanoparticles building blocks, inset showing the SAED patterns; (f) the HRTEM image of the rectangular region in (e).

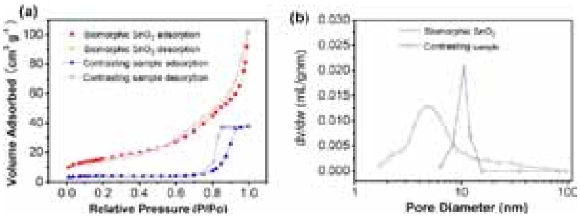

Fig. 14 (a)Nitrogen adsorption–desorption isotherms of the biomorphic SnO_2 and the contrasting sample, (b) the corresponding pore size distribution curves.

The nano-scaled porous structures of the biomorphic SnO_2 and the contrasting sample are characterized by nitrogen adsorption–desorption measurements. The adsorption–desorption isotherms are displayed in **Fig. 14(a)**. The isotherm shape of the biomorphic SnO_2 is typical of an H3-type type- IV isotherm, while that of the contrasting sample is typical of H_2-type type-IV. The presence of a hysteresis loops in the isotherms is associated with the filling and the emptying of mesopores by capillary condensation. The BET (Brunauer–Emmett–Teller) surface areas are calculated to be $514.12 m^2g^{-1}$ for the biomorphic SnO_2 and $14.12\ m^2g^{-1}$ for the contrasting sample. The pore size distributions investigated by the BJH (Barrett–Joyner–Halenda) method are shown in **Fig. 14(b)**, indicating both the two samples are mesoporous structures. The pore size of the biomorphic SnO_2 is distributed from 2 to 50 nm, centered on 4.6 nm, while that of the contrasting sample has a narrow distribution centered on 10.5 nm. Despite of the lower peak value, the biomorphic SnO_2 has much higher pore volume ($0.159\ cm^3g^{-1}$) than that of the contrasting sample ($0.059\ cm^3g^{-1}$). Based on these results, it is obvious that the biomorphic SnO_2, assembled by nanoparticles into the unique porous hierarchical architecture, possesses higher BET surface area and contains more mesopores, which are preponderant for better surface accessibility and more convenient gas transmission.

From the above investigation, the fine porous lightweight skeleton was faithfully inherited from that of natural butterfly wings via the ethanol-assisting sol–gel soakage process followed by a calcination treatment. Rutile SnO_2 nanocrystallites could be assembled to form interconnected tubes, fastigiated hollow tubers, and double-layered substrates, which are further orderly organized into a unique porous hierarchical architecture with connective hollow interiors and thin mesoporous walls. In view of the small grain size and the unique hierarchical architecture, it can be expected that the biomorphic SnO_2 would possess good gas sensing properties. The sensing mechanism could be described as gas surface chemisorption and electron acceptance, resulting in the change of the sensor's resistance. Usually, oxygen molecules from ambient air are adsorbed on the surface of SnO_2 particles to form oxygen ions (O^-, O^{-2} and O^{2-}) by trapping electrons from the conduction band, which gives rise to a high resistance state. Upon exposure to ethanol, the adsorbed oxygen ions (O^-, O^{-2} and O^{2-}) react with the reducing gas to release electrons back into the conduction band, which reduces the resistance. Herein, the gas sensitivity (S) is defined as S = Ra/Rg, where Ra and Rg are the sensor's resistance in air and in ethanol, respectively. The response (rise) or recovery (decay) time is defined as the time needed to reach 90% of the total signal change. The sensing experiments were carried out at 170℃ under an ambient relative humidity of 25%.

The biomorphic porous hierarchy was constructed by a layer of flexural wall that was assembled by SnO_2 nanocrystallites with diameter of around 7.0 nm. The wall thickness was tunable under the control of the impregnants concentration as well as the immersing time. The biomorphic SnO_2 showed good sensing to ethanol and formaldehyde, due to its small nanocrystalline building blocks and unique porous hierarchical architecture. As shown in **Fig. 15**, the real-time sensing response of the sensors to ethanol (at 170℃) and formaldehyde (at 210 ℃), respectively. The responses are reversible with fast response and recovery, and increase with increasing gas concentration. To a fixed gas concentration, the response increases sharply with decreasing wall thickness: $S_{SnO2\text{-}3} < S_{SnO2\text{-}2} < S_{SnO2\text{-}1}$. **Fig. 15(c)** and **(d)** shows the response variation of the sensors exposed to ethanol (at 170 ℃) and formaldehyde (at 210 ℃) at different concentrations, respectively.

Despite the different wall thickness, the as-fabricated biomorphic SnO_2 exhibited the same grain size of about 7.0 nm, well-organized macroporous frameworks, similar BET surface area and pore size distribution. Benefiting from the small grain size effect and the well-organized porous hierarchy facilitating gas diffusion, the biomorphic SnO_2 showed good ethanol and formaldehyde sensing properties. The highest responses to 50 ppm ethanol and formaldehyde are about 49.8 and 30.4, respectively. It is more noticeable that the response of the biomorphic SnO_2 increased with the decreasing wall thickness despite the same grain sizes and similar microstructures. The response dependence should be ascribed to the increasing difficulty of the gas diffusion into inner grains via Knudsen diffusion with the increasing wall thickness, which is similar to that in thin films .

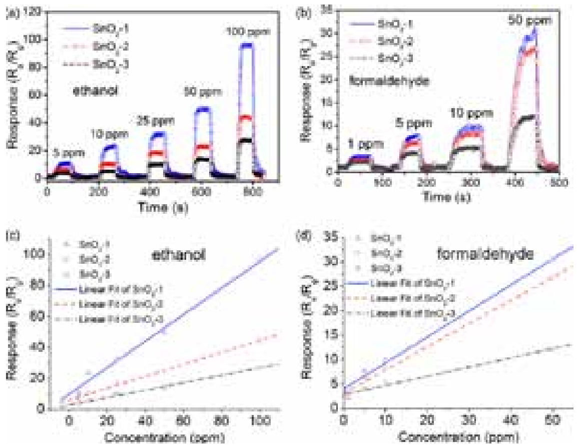

Fig. 15 (a and b) Real-time sensing responses and (c and d) response variations of the sensors to ethanol (170℃) and formaldehyde (210℃) of different concentrations, respectively.

4.2 High light harvest efficiency photoanode derived from butterfly wings[15)]

The discovery that butterfly wings have scales that act as tiny solar collectors has led us to design a more efficient solar cell that could be used for powering homes, businesses, and other applications in the future. In the study, we note that scientists are searching for new materials to improve light-harvesting in so-called dye-sensitized solar cells, also known as Gratzel cells for inventor Michael Gratzel. These cells have the highest light-conversion efficiencies among all solar cells.

We studied a novel photoanode structure inspired by butterfly wing scales with potential application on dye-sensitized solar cell in this paper. Quasi-honeycomb like structure (QHS), shallow concavities structure (SCS), and cross-ribbing structure (CRS) were synthesized onto a fluorine-doped tin-oxide-coated glass substrate using butterfly wings as biotemplates separately, details of the process was shown in **Fig. 16**. The as-synthesized photoanodes are divided into four layers: glass substrates, F:SnO_2 conductive layer, anatase film, and titania film with butterfly wing microstructures.

Papilio paris is a species of beautiful swallowtail butterfly found in South China. Upperside of the wings is black, irrorated with dark green scales, which on the outer portion of the forewing coalesce and form an incomplete post discal narrow band.

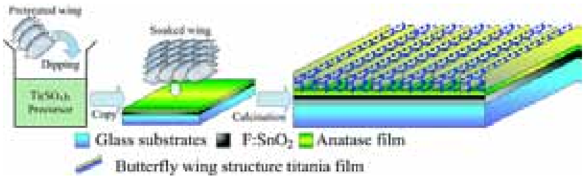

Fig. 16 Schematic Illustrations for the Transition Process of Butterfly Wings onto the FTO Glass Slices: Step 1, Soak the Butterfly Wings in the Titanium Sulfate Precursor; Step 2, Calcine the Soaked Butterfly Wings onto the Prepared Anatase Film on the FTO; Simplified Configuration of the As-Synthesized Quasi-Honeycomb Structure Photoanode Shown on the Right.

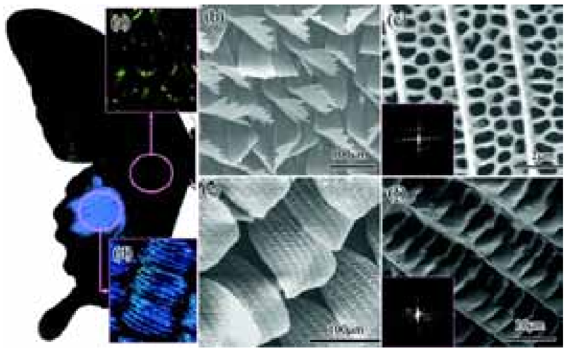

Fig. 17 Nature picture and low-magnification optical microscopy, low-magnification FESEM images and high-resolution FESEM images showing the wing of the blue male (a–c) and black male (d–f). The insets in the lower left-hand (c, f) corner show the two-dimensional, logarithmic Fourier power spectra of square areas selected from the images.

On the hind wing, there is a conspicuous upper discal shining blue patch. The other specie of butterfly used in our work as contrast is Thaumantis diores, the upper wings of which are brown black. A four-level observation methodwas adopted in studying the morphology of butterfly wings. The first level deals with the macroscopic aspect of the butterfly wings, as the left column of **Fig. 17** shows. The second level is the optical microscopy observation level, as images a and d in **Fig. 17** show. **Fig. 1a** shows the area taken from the matte black wings of Paplio paris. The optical image (**Fig. 1d**) is from the shining patch on the hind wings. The outline and color of the scales can be clearly identified in these images. FESEM was used to study the fine structures (the third and fourth level) of the wing scales. For FESEM measurement, all the samples were stuck to microscope stubs with double-sided carbon tape and then coated by a thin, sputtered gold layer to provide a conducting surface and avoid charging effects. It should be noted that previous studies(28) have proven that there is no significant distortion of the scale geometry during this process. The low-magnification images of the scales from blue and black areas on the wings are shown in images b and e in **Fig. 17**. The scale morphologies are totally different, i.e., the blue shining scales (**Fig. 17**e) on the patch presents one layer of scales with rounded endings, the arrangement of which on the wing resembles that of shingles on a roof. By contrast, the matte black scales (**Fig. 17b**) are more elongated and have a deep zigzag ending, composed usually of three to five fingerlike features.

In this paper, we will focus on the fourth level, i.e., the surface and internal hierarchical structures of the scale, because they are responsible for the structural colors of the wings. Medium-magnification FESEM images (images c and f in **Fig. 17**) reveal that the structures of the blue and black scales have more obvious differences in the micron range. The black scales exhibit a complicated network structure called "quasi-honeycomb-like structure" (QHS), whereas the scanning electron micrographs of scales taken from the wings' blue patch regions show that their surfaces comprise a regular two-dimensional array of shallow concavities structure (SCS) of about 5 μm in width and 10 μm in length. These concaves are responsible for the blue coloration of male butterflies according to the similar research doing by P. Vukusic.

The as-synthesized titania photoanode microstructures were shown in **Fig. 18** with corresponding FFT images on the lower left-hand corner. The samples shown in the left column are synthesized in the lower concentration solution, while the right column samples are soaked in higher concentration. The morphology changes greatly, which are shown in the QHS (images a and b in **Fig. 18**). In **Fig. 18b**, the interspaces in the QHS are filled with titania particles, and the surface characters of the quasi-honeycomb structures are covered up. The changes are reflected on the corresponding FFT images, that is the diffuse ring pattern (shown in **Fig. 18a** inset) disappeared in **Fig. 18b** inset. By contrast, the spindle shape FFT from SCS are kept in the titania films, for the concavities are inherited in the titania films integrally, even the continued submicrometer drapes between the longitudinal ridges. The fill factors are nearly the same except the full filled sample (QHS-18 replica). It means that the morphology characteristics are maintained well, which is corroborated by the FFT results shown in **Fig. 18**.

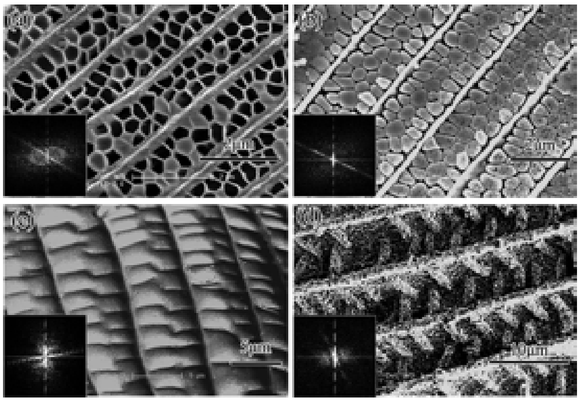

Fig. 18 FESEM images of as-synthesized titania photoanodes templated from butterfly wings with different colors. (a, b) Quasi-beehive structures synthesized in different conditions; (c, d) shallow concavities structures in different conditions.

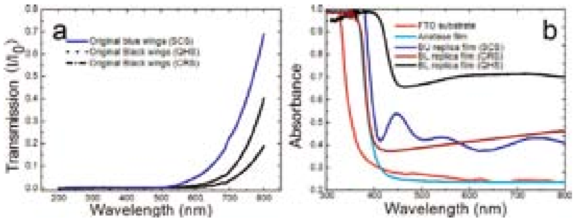

Fig. 19 (a) Transmission spectra of the original butterfly wings: Continuous line (blue), short dash dot line (black wings with cross-ribbing structure), dot line (black wings with quasi-honeycomb structure). (b) The wavelength-dependent absorption (at normal incidence). Different colors represent different samples (cutline shown in the upper right corner).

The transmission spectra measurements in the UV–vis range are shown in **Fig. 19a**. The wing substrate and scales contain nearly the same amounts of pigments, especially the melanin, the differences in the transmission spectra are due to the diversity of the wings microstructures. The blue scales have higher transmissibility in longer wavelength, and the black ones with the CRS take second place, then the QHS ones take the third. According to the absorbance function shown below, $A(\lambda) = 1 - R(\lambda) - T(\lambda)$, with $A(\lambda)$ being the absorbance, $T(\lambda)$ the transmittance, and $R(\lambda)$ the reflectance. For the black wing, reflectance is virtually constant throughout the whole spectral range. The QHS scales will have higher absorptivity than the CRS ones. Previous researchusing scanning photodiode detector has approved this conclusion further both in air and in liquid bromoform. That is because the black scales from Papilio paris clearly comprise a more intricate and densely distributed lattice of cuticle than the scales appearing black in color from Thaumantis diores show. That is why the butterfly wings with QHS has a larger light absorption efficient than normal butterfly wings. Once the light incident to this structure, therefore, is more efficiently scattered than normal strucutures, a larger light absorption can be achieved.

The light harvest efficiency (LHE) of the photoanode was calculated by transmittance (T%) and reflectance (R%) using an integrating sphere (LHE(%) = 100 − R% − T%).(30) This formula was in agreement with the absorbance function given in the previous paragraph. So by comparing the absorbance of the titania replica films, the LHE can be evaluated. After calcination, the absorption spectra of the samples were collected and compared shown in **Fig. 19b**. The absorbance values were converted from reflectance data by instrument based on the Kubelka–Munk theory. The absorption spectrum of the FTO glass substrate (red curve, in **Fig. 19b**) was used as the background absorption in the whole measurements. After coating with a layer of anatase film using doctor blade methods, the curve shifted toward the longer wavelength due to the band-edge absorption of the titania. Three butterfly wing titania replicas with different microstructures (SCS, CRS, QHS) exhibited quite different absorption characteristics. The CRS titania replica film has a higher absorptivity than the normal anatase film in longer wavelength. The blue wings replica shows a lower absorptive peak around 450 nm, and as a result the film appeared a little yellow. It is heart-stirring that the QHS titania replica film has a remarkable increase in the absorption curve. Compared with the normal anatase film and CRS replica, the characteristic band-edge absorption position of the titania film with QHS is red-shifted to nearly 420 nm, because of the scatter and diffuse effect caused by the QHS in the titania replica film. This is similar to what happened in the original butterfly wings. Two main factors could influence the absorption spectra, one is the microstructures of the film, and the other is the remainder composing the film. All the samples were synthesized at the same condition, so the components of the film (TiO_2) would have the same properties, especially the crystal structures.

In conclusion, the butterfly wing scales templating procedure is a facile and economic design for the synthesis of hierarchically periodic microstructure titania photoanode without the need for complicated experimental conditions or equipments, such as photo lithography adopted. The quasi-honeycomb structure titania replica photoanode has a perfect light absorptivity and higher surface area, which give great advantages to the light harvesting efficiency and dye sorption. This structure gives the butterfly ultrablackness wings, so it is convincing that we could obtain potential ultra-absorptivity photoanode adopting the quasi-honeycomb structure. The successfully synthesized butterfly wing microstructure titania photoanode we obtained not only gives us new ideas to DSC researches in technology and theory but also opens a short cut to the photothermal, photocatalyzed, and photosensitized devices research. Also, the fabrication method may be applied to other chitin substrate template and metal oxide systems that could eventually lead to the production of optical, magnetic. or electric devices or components as building blocks for nanoelectronic, magnetic, or photonic integrated systems.

5. Summary

As described in this review, significant developments have been made in Bio-inspired materials using nature materials as templates during the last years. The field continues to grow internationally and contribute to new interdisciplinary areas concerned with the synthesis, self-assembly and processing of organized matter across arrange of length scales. Bio-inspired materials, as the result of learning from nature, will change our life styles and bring us to a higher level of civilization. The fabrication method may be applied to other nature substrate template and inorganic systems that could eventually lead to the production of optical, magnetic. or electric devices or components as building blocks for nanoelectronic, magnetic, or photonic integrated systems.

The authors wish to express their thanks to the financial support ofthe Natural Science Foundation of Shanghai(No.09ZR1414700), Major Fundamental Research Project of the Shanghai Science and Technology Committee (No. 10JC1407600), Sino-French Project of MOST of China (No.2009DFA52410), Sino-Finland International Program of Shanghai (No.09520703400).

References

1) Sun, B.,Fan, T., Zhang, D. and Okabe, T. (2005): Microstructure analysis of morph-genetic SiC/C ceramics from wood,Journal of Advanced Materials,Vol.37, No.4, pp.76-80.

2) Sun, B., Fan, T., Zhang, D. (2002): Porous TiC ceramics derived from wood template. Journal of Porous Materials, Vol. 9, No. 4, pp. 275–277.

3) Sun, B., Fan, T., Zhang, D. and Okabe, T. (2004): The synthesis and microstructure of morph-genetic TiC/C ceramics, Carbon, Volume 42, Issue 1, pp. 177-182.

4) Fan, T., Li, X., Liu, Z., Gu, J., Zhang, D. and Guo, Q. (2006): Microstructure and infrared absorption of biomorphic chromium oxides templated by wood tissues,Journal of The American Ceramic Society, Vol.89, No.11, pp. 3511-3515.

5) Li, X., Fan, T., Liu, Z., Ding, J., Guo, Q. and Zhang, D. (2006): Synthesis and hierarchical pore structure of biomorphic manganese oxide derived from woods, Journal of The European Ceramic Society, Vol.26, No.16, pp.3657-3664.

6) Liu, Z.,Fan, T.,Zhang, D., Gong, X. and Xu, J. (2009): Sensors and Actuators B: Chemical, 136, pp.499-509

7) Wang, T., Fan, T., Zhang, D., Zhang, G. and Xiong, D. (2007): Thermal conductivity and thermal expansions of aluminum/carbon composites based on wood templates, Materials Letters, Vol.61, No.8-9, pp.1849-1854.

8) Wang, T., Fan, T., Zhang, D. and Zhang, G. (2006): Thermal expansions and mechanical properties of Al/C and Al/(SiC+C) composites based on wood templates, Materials Transactions, Vol. 47, No.10, pp. 2576-2581.

9) Wang, T., Fan, T., Zhang, D. and Zhang, G.(2006):The fabrication and wear properties of C/Al and (C plus SiC)/Al composites based on wood template,Materials Letters, Vol.60, No.21-22, pp.2695-2699.

10) Liu, Q., Fan, T. and Zhang,D. (2004): Electromagnetic shielding capacity of carbon matrix composites made from nickel-loaded black rice husk, Journal of Materials Science, Vo.39, No.20,pp.6209 – 6214.

11) Liu, Q., Zhang, D., Fan, T., Gu, J., Miyamoto, Y. and Chen, Z. (2008):Amorphous carbon-matrix composites with interconnected carbon nano-ribbon networks for electromagnetic interference shielding, Carbon, Vol.46, No.3, pp.461-465.

12) Liu, Q.,Fan, T. and Zhang, D. (2008): Electromagnetic wave absorption properties of porous carbon/Co nanocomposites, Applied Physics Letters, Vol.93, No.1,p.013110.

13) Chen, Y., Gu, J., Zhu, S.,Fan, T. and Guo, Q. (2009): Iridescent large-area ZrO photonic crystals using butterfly as templates, Applied Physics Letters,Vol.94, No.5, p.053901.

14) Song, F., Su, H., Han, J.,Zhang, D. and Chen,Z (2009): Fabrication and good ethanol sensing of biomorphic SnO2 with architecture hierarchy of butterfly wings, Nanotechnology, Vol.20, No.49,pp.495-502.

15) Zhang, W., Zhang, D., Fan, TX. (2009): Novel Photoanode Structure Templated from Butterfly Wing Scales, Chemistry of Materials, Vol.21, No.1, pp.33-40.

Author's short biography

Di Zhang

ZHANG Di is a professor of materials science of the "Yangtze River (Changjiang) Scholarship Scheme" invited by Shanghai Jiao Tong University, China. Now he is the vice dean of the School of Materials Science and Engineering, the director of the Institute of Composite Materials and the director of the State Key Laboratory of Metal Matrix Composites of SJTU.

His research fields are process of advanced metal matrix composites, basic and applied research of biomorphic materials. The idea of biomorphic materials he proposed breaks through the traditional thought of composite materials by introducing the perfect structure of nature in the traditional process of materials science. As the exploiter of biomorphic materials, his group has synthesized carbon, oxygen morph-genetic ceramic and its composites, a serial of oxide molecular sieve materials taking advantage of microstructure of animal and plant. Recent three years, his group has published more than 70 papers (Impact Factors of 27 papers are more than 3 and mean IF is 2.558) and he has been invited to talk six times at international conferences.

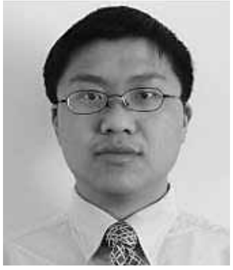

Wang Zhang

ZHANG Wang is a lecturer in Shanghai Jiao Tong University. He belongs to State Key Laboratory of Metal Matrix Composite. His research interests focused on Bio-inspired structural optical function materials.

Jiajun Gu

GU Jiajun is an associate professor in Shanghai Jiao Tong University. He belongs to State Key Laboratory of Metal Matrix Composite. His research interests include nature inspired photonics, morph-genetic electronics, and thermoelectric materials.

Shenmin Zhu

ZHU Shenmin is an associate Prof. in Shanghai Jiao Tong University. She belongs to State Key Laboratory of Metal Matrix Composite. Her research interests include synthesis of morph-genetic materials and porous carbons, and investigation of their applications.

Author’s short biography

Huilan Su

SU Huilan is an associate professor in School of Materials Science and Engineering, Shanghai Jiaotong University. She completed her PhD in Inorganic Chemistry in 2001 from the University of Science and Technology of China under the supervision of Prof. Yi Xie and Prof. Yitai Qian. From 2001 to 2003, she joined Prof. Chunhua Yan's group in the State Key Laboratory of Rare-Earth Materials Chemistry and Applications, Peking University, as a Postdoctoral Research Fellow. Since 2003, she joined the State Key Lab of Metal Matrix Composites, Shanghai Jiao Tong University. Her current research focuses on Bio-inspired Chemistry and Functional nanocomposites.

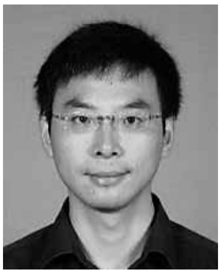

Qinglei Liu

LIU Qinglei is a research associate in Shanghai Jiao Tong University. He belongs to State Key Laboratory of Metal Matrix Composite. His research interests include porous carbons, metal and semiconductor nanoparticles and morph-genetic materials.

Tongxiang Fan

Dr. Tongxiang Fan obtained his PhD degree in material science from Shanghai JiaotongUniversity in 1999. Currently, he is a professor at the School of Materials Science and Engineering, Shanghai Jiaotong University. His research currently includes functional ceramics, bioinspired materials and metal matrix composites.

Jian Ding

DING Jian is an associate professor in Shanghai Jiao Tong University. He belongs to State Key Laboratory of Metal Matrix Composite. His research interests include functional materials and application of synchrotron radiation on materials.

Qixin Guo

Dr. GUO Qixin is a professor of Synchrotron Light Application Center in Saga University, Japan. His research interests include III-V and II-VI compounds, novel functional materials, semiconductor nanostructures, and synchrotron light applications.

Designing With Pores - Synthesis and Applications[†]

J. Luyten, S. Mullens, I. Thijs
Materials Technology, VITO[1]

Abstract

Environment, energy, health and transport issues are dominating our modern daily live. The complex interactions of these problems can only be solved by sustainable processing and the development of improved components. Materials science will play an important role in this new approach. One domain with specific relevance are porous ceramics and metals. It are substrates with pores sizes ranging from vacancies at the atomic level to macro pores with sizes of millimeters. There are plenty of emerging applications for porous components in different industrial sectors. Each application will specify the window of properties of the porous material.

This review is limited to inorganic porous materials which can be synthesized by dry and wet powder processing methods. In order to cope with this large application domain and window of properties, several processing and coating routes and related characterization techniques have been developed. The overview of applications for porous inorganic materials is focused on macro porous components with a designed functional coating. Examples of applications include catalytic supports, diesel particulate filters, molten metal filters, biomedical scaffolds for tissue engineering and ceramic membranes for different separation purposes.

Keywords: Porous materials, processing, applications

1. Introduction

Porous ceramics and metals materials find their applications in a very broad field, each demanding a specific window of properties. Within the last decades, several manufacture and processing routes have been developed, enabling the manufacture of materials with a wide variety of porous architectures, pore size distribution (from a few angstroms to several millimeters), interconnectivity, pore gradients or layers with different pores sizes.

This contribution presents an overview of the different manufacturing routes for porous metallic and ceramic materials produced by powder metallurgical techniques. Their production process and optimization are discussed. The complex 3-dimensional architecture of most porous materials requires a multitude of characterization techniques in order to have a full view on its properties.

The practical use of porous materials and their important role to solve the problems of our modern daily life is illustrated by several examples of applications coming from different industrial sectors.

2. Definitions

Some statements about pore sizes are needed because they are connected to definitions used in specific application sectors. According to the international Union of Pure and Applied Chemistry (IUPAC), pore sizes are classified into three categories, namely micro pores, meso pores and macro pores with pore sizes less than 2 nm, between 2 and 50 nm, and larger than 50nm respectively[1, 2)]. This nomenclature is used in the membrane scientific world. However, biomedical sciences uses micro pores for pore with micrometer diameters. Another example is the definition of ceramic foams as a class of materials comprising large voids (cells), with linear dimen-

---

[†] Accepted: October 12, 2010

[1] Boeretang 200, B-2400 Mol, Belgium
[*] Corresponding author
E-mail: Jan.Luyten@vito.be
TEL:+32 14 335667 FAX:+32 14 321186

sion approximately ranging from 10 μm to 5mm[3, 4]. Therefore careful interpretation of the nomenclature of porous materials as function of the application sector is necessary.

3. Overview of Applications [5-10]

Table 1 classifies the main applications for porous materials as a function of their pore structure.

4. Developing a Porous Component for a Well Determined Application [11-15]

The development of a porous component starts with the pore structure requirements. These include the pore size distribution, the porosity, the nature and shape of the pores (open or closed; spherical, elongated or random), interconnectivity and so on. In addition to these requirements on porous architecture, other demands have to be fulfilled as well for the porous material to be considered for a specific application: mechanical strength, specific surface area, thermal shock resistance, corrosion resistance and so on. All this questions have to be solved by defining the combination of a material and a processing route. In this contribution, as we mentioned, we limit our self to components which can be produced by powder processing. Therefore the macro porous structure will be obtained by different shaping routes followed by conventional thermal treatments as drying, calcining and sintering.

In the case of a functionalized porous material the material is comprised of two or more pore sizes, two or more materials and a mix of manufacturing routes. The functional layer can be realized by various (non-line of sight) coating techniques. For example, inorganic membranes aim at a high performance (i.e. separation factor in combination with a high gas or liquid flux), combined with mechanical, chemical and thermal stability. As such, they are composed of different layers with a gradient in pore sizes and layer thickness. Depending of the elements which has to be separated, the pore sizes goes from 5 - 10 μm to less than 2nm or even dens. The functional layer, i.e. the separation layer, will be obtained by a sol gel coating technique for e.g. nano filtration membranes.

For applications as separation and biomedical porous scaffold for tissue engineering, the interconnectivity of the pores is very important but this is not the case for materials which are used, as isolation, impact material, or kill furniture. The most common diesel particle filter (DPF) material is a honeycomb structure with openings in the range of mm, porous walls with pore sizes ranging from a few microns to ~20 micron, onto which a meso porous wash coat is deposited for the catalytic combustion of the collected soot. Other catalytic supports are zeolite coatings (**Fig. 1**) produced by hydrothermal treatment. With these examples in mind it is clear that the synthesis of functional porous materials can be divided into manufacturing routes to obtain (macro) porous components and in techniques to coat these substrates

Table 1 Classification of applications by the type of pore structure

Pore structure	Application
Micro-and meso porous materials	Desiccant materials
	Sensors and actuators
	Thermal isolation
	Catalyst (support)
	Drug delivery systems, coatings , carriers
Foam- and honeycomb structures	Exhaust gas filter
	Diesel particle filters
	Filters for molten metal
	Porous Electrodes of fuel cells
	Porous Burners
	Catalytic substrates
	Biomedical porous scaffolds for tissue engineering
	Impact and acoustic materials
	Kiln furniture
	Lightweight sandwich structures
Multilayer materials	Ultra filtration membranes
	Nanofiltration membranes
	Gas separation membranes
	Zeolite membranes
	Pervaporation membranes
	Dens membranes (oxygen or proton conductors)

with a porous layer.

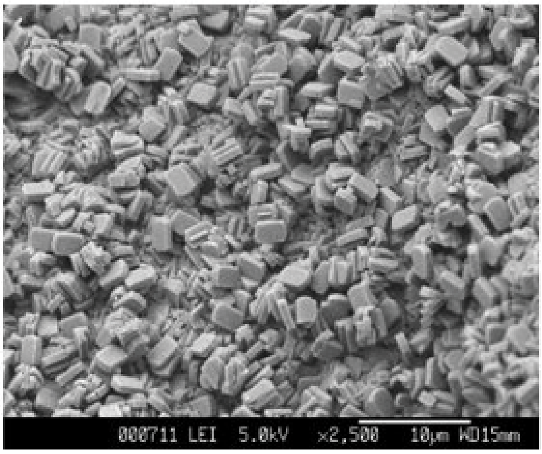

Fig. 1 Zeolite coating on the struts of an Al_2O_3 foam.

5. Synthesis Routes [16-27)]

Table 2 gives such overview of manufacturing routes to produce the macro porous structures and the coating techniques to functionalize their surface.

Table 3 shows a summary of techniques which are conventionally used to determine the pore size distribution, the interconnectivity and the specific surface area of porous materials. Although useful as such, no single technique is able to cover the wide range of characteristics needed to describe the porous material. The complex 3 dimensional architecture of this class of materials necessitate a range of analysis tools to get a view on the structure of the porous network.

These analysis techniques can be classified based on

- the type of pores that are measured (open, closed, or blind pores)
- the pore size range (from 1 nm – millimeters),
- the dimensional determination (2D versus 3D),
- the (non) destructive nature of the measurement, or
- the amount of pores typically taken into account.

Apart from the information on the pore size distribution, other information on the porous architecture can be obtained by the combination of different techniques (shape of pores, pore volume, surface area or strut thickness).

Also some specific application-oriented testing

Table 2 Synthesis techniques for macro substrates and coatings for the functionalization

Manufacture of macroporous support	Coating techniques
Replication of ▪ Polymer (e.g. PU foam) ▪ Natural materials (e.g. wood)	Sol gel ▪ Colloidal ▪ Polymeric
Direct foaming ▪ Preceramic polymers ▪ Gel casting	Wash coat
Use of pore formers	Vapor Deposition ▪ Chemical ▪ Physical
Freeze casting	Precipitation ▪ Hydrothermal ▪ Biomimetic
Extrusion (e.g. honeycombs)	Electroforesis
Gas introduction	Electrodeposition
Hollow building blocks	Plasma coatings ▪ Vacuum ▪ Atmospheric
Additive manufacturing ▪ Selective Laser Melting ▪ Selective Laser Sintering ▪ E-beam melting ▪ Stereolithography ▪ Fused Deposition Modelling ▪ 3D Printing ▪ 3D FD	
Partial sintering ▪ Partial ▪ Large grains	
Connected fiber, rod, other shapes	

Table 3 Characterization techniques for porous materials 28-29)

Main parameter	Analysis tool
Pore size distribution	PPI-method (pore per inch)
	Visiocell
	Image analysis
	Scanning / Transmission Electron microscopy
	Gas adsorption / desorption
	Cutt-off measurements
	Computer Microtomography
	NMR micro-imaging
Interconnectivity	Mercury intrusion porosimetry
	Liquid extrusion
	Capillary flow porometry
	Gas / liquid permeability measurements
Specific Surface Area	Gas adsorption / desorption
	Mercury intrusion porosimetry
	Capillary flow porometry

methods are frequently performed (e.g. cut-off measurements for membrane development). A full description of these characterization techniques is outside the scope of this publication. For more details, reference is made to some review publications.

In addition to the analysis of their pore structure other properties related to their application have also to be tested: mechanical properties, thermal conductivity, dielectric constant, specific surface area, chemical resistance, hardness/wear, tortuosity of the flow path and so on.

6. Designing Porous Materials 30-31)

Recently a new trend towards the design of porous materials with a specific periodic architecture and a highly reproducible porous architecture has emerged. Additive manufacturing routes, already many years used in the shaping of polymeric materials, have been developed to shape metallic and ceramics materials. The class of additive manufacturing routes varies widely with regard to the nature of the starting material (liquid, solid or powder based) and the solidification process (laser induced melting or sintering, e-beam melting). Related to the rapid manufacturing process, also material properties, speed of building, cost, volume, surface finish and complexity of the part varies widely.

The progress of rapid manufacturing techniques for ceramic materials has somewhat been lacking behind. One possibility to overcome this problem is to combine additive manufacturing for the shaping of the ceramic powder with the conventional thermal treatments. One technologies which uses such an approach is 3 Dimensional Fiber Deposition (3DFD). This manufacturing technique enables the production of periodic porous ceramics and metals

3D Fiber Deposition (also called direct-writing or robocasting) comprises the extrusion of a highly viscous paste loaded with metallic or ceramic particles through a thin nozzle. By computer controlled movement in x, y and z-direction, the porous architecture is built layer-by-layer. After sintering, a highly reproducible and periodic porous structure is obtained. The process variables include a.o. the nozzle opening (~fiber thickness), the type of nozzle (~fiber shape), the interfiber distance (~pore size) and the stacking of the layers (~porous architecture, see **Fig. 2**). As such, flow path for either gas or liquids can carefully be controlled and optimized with regard to pressure drop or contact time with the active coating. Moreover, by a patent-pending technology, the microporosity and surface roughness of the fibers can be controlled.

The custom-built equipment for 3DFD consists of a paste reservoir with nozzle, mounted on a CNC machine or on a x, y, z-table. The input for the equipment is a CAD design. This design is sliced (by a customized software) in order to generate the beginning and end positions of each fiber. These positions serve as coordinates for the x,y,z-table.

Typical dimensions of parts are 40 mm by 40 mm and a height of approximately 35 mm, with fiber thickness from 300 μm to 900 μm. Multiple nozzles can be mounted onto the equipment in order to speed the production of similar pieces.

The keys for this type of technology are the composition of the paste that is extruded and the production parameters: a carefull balance between a high viscosity to be able to bridge the underlying gaps, the drying behavior, the speed of deposition and the extrusion force. Both ceramic and metallic parts have

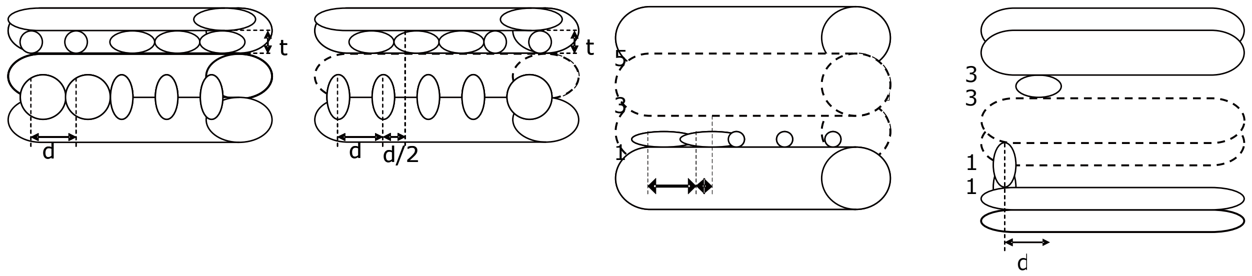

(a) (b) (c) (d)

Fig. 2 Examples of 3DFD stacking designs.

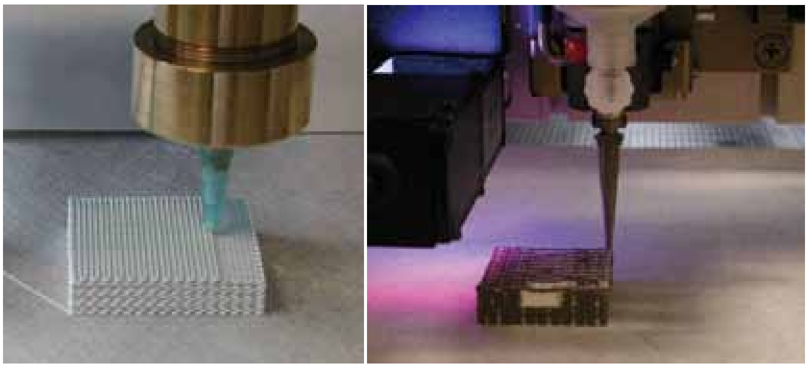

(a) (b)

Fig. 3 Apparatus for three-dimensional fiber deposition using (a) continuous and (b) discontinuous extrusion.

been manufactured (see examples in **Fig. 4**).

7. Some Applications in Detail

7.1. Multilayer ceramic membranes 32-35)

Due to their inherent cost, ceramic membranes will only be used in situations where polymeric cannot meet the requirements: in the case where a high chemical, thermal or mechanical resistance is needed. The optimization of a membrane focuses in the first place on the combination of a high flux and a high separation factor. This can only be obtained by a multilayer component built up by layers with a gradient in pore sizes and layer thickness: in the sense that how smaller the pores how smaller will be the layer (**Fig. 5**).

Tubes, hollow fibers and plates are the most common support shapes. The macro porous substrates with pores of 5 to 10 μm and a porosity of 30 to 50% offer the mechanical strength of the membrane. Mostly, the tubes are produced by extrusion, the hollow fibers by a spinning technique and the plates by pressing or tape casting. By slip casting with powders suspensions with different particles sizes different layer were built up on the macro porous layers till a pore size of about 0.1 to 0.2 μm. A layer with such a pores size can support the thin separation layers which are mostly produced by a sol gel process. A first sol layer(s) is prepared following the colloidal route. After hydrolyses and condensation reactions of the precursor, metal salt or metal-organic precursor with water, a colloidal sol is obtained. After coating, calcining and sintering, a mesoporous layer is obtained. For the polymeric route, the precursors are dissolved in organic solvent -with or without a limit amount of water-. This results in a sol with fractals, and finally with a micro porous (<2nm) top layer. The top layer can also be produced by a hydrothermal treatment as is the case of zeolite membranes. Further surface modifications e. g. by grafting can be performed in function of the specific application e.g. separation of solvents. In a membrane reactor, the catalytic reaction can be enhanced by the separation function of the membrane.

Another category are the dense membranes, the oxygen and proton conductors (**Fig. 6**). Vacancies are here the main transport mechanism of O- or H-ions in elevated temperature ranges. Nevertheless, a membrane with modified surface has a better performance because the total mechanism of transport exists of three steps: the adsorption of O_2 or H_2 at one side of the membrane, the hopping of these


(a) (b) (c)

Fig. 4 Examples of parts built by 3DFD discontinuous extrusion a) cylinder b) a vertebra shape and c) a half sphere.

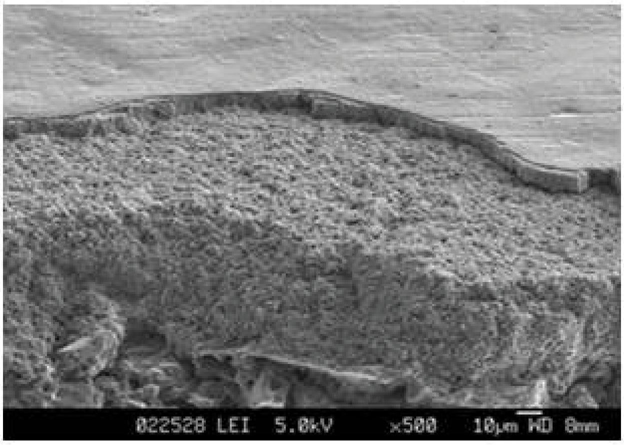

Fig. 5 A multilayer ceramic membrane showing the different layers.

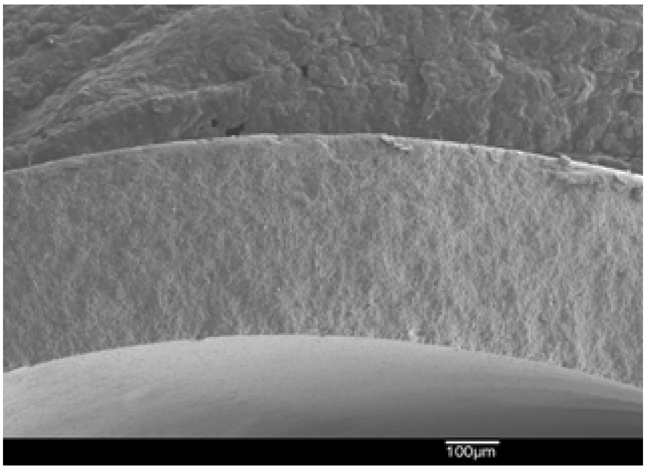

Fig. 6 Dense section of oxygen separation ceramic hollow fiber membrane produced by a spinning technique.

atoms through the dense structure with the help of vacancies and the desorption at the other side of the membrane. Surface modification can be obtained by another structure, by roughness, with a certain micro porosity or by a layer with a catalyst to enhance this adsorption- or desorption step.

7.2 Porous scaffolds for tissue engineering [36-44)]

Although the large regenerative capacity of bone is generally recognized, large bone defects due to trauma or tumors are still a big challenge for surgeons, as no spontaneous healing of the bone occurs. Bone tissue engineering is a new approach to these kind of problems, whereby a porous scaffold is used, onto which stem cells can be seeded, and coated with proteins and other biologically active species.

As the exact biological response of cells in a porous scaffold remains unclear until now, the synthesis of the porous scaffolds is maybe the easiest step in this complex procedure. However, the criteria posed onto a candidate scaffold material is long. First of all, a wide range of biocompatible materials is available. Calcium phosphates (CaP) and bioglasses will be absorbed by the body after some time but they are too brittle to be used as a load bearing material. Metallic materials, mostly Ti and Ti-alloys, offer sufficient mechanical properties, are ductile and the small layer of TiO_2 onto the surface impedes a fast dissolution of metal ions. Mg and its alloys are reported to combine load bearing properties and bio absorbability. Untill now, its high reactivity during synthesis, high corrosion rate and biological interactions need further study before clinical implementation.

For a good integration in the bone structure, the properties of the scaffold (E-modulus, compression strength, porosity, pore sizes, ductility) are to be tuned to the properties of the bone (**Table 4**). The optimal pore size is considered to be in the range of 100 to 500 μm, to allow cell seeding, to stimulate the vascularisation of the scaffold, and the transport of nutrients to the cells and the removal of waste products. Depending on the material and the porosity, the E-modulus and mechanical strength can tuned to avoid stress shielding, a phenomenon which is known to cause implant loosening due to a mismatch in mechanical properties between surrounding bone and implant.

In the case of Ti and Ti alloys, ductility is function of the quantity of the interstitial impurities (O, N, H, and C) of the metal. These impurities can already be present in the powder or are introduced during the processing or the thermal treatments of the component.

Apart from structural and mechanical requirements posed onto the scaffold, its surface should enhance the bioactivity. Cell attachment and the adhesion of a bioactive coating are improved by these microporosity or surface roughness. Examples of porous structures used as biomedical scaffold are given in **Fig. 7** a and b, structures respectively produced by gel casting and by the 3DFD technology.

A further development in scaffold materials are the bioactive coatings. **Fig. 8** shows a CaP coating prepared on a Ti scaffold by a precipitation technique. Such porous CaP structures can be used as drug

Table 4 Some macro porous properties of porous Ti - en Ti- alloys scaffolds

Property	Range
porosity	>65%
Interconnectivity of the pores	>90%
Pore size d	50<d<500 μm
Modulus	<3 GPa
Compression strength	>40 MPa
Ductility	>10%

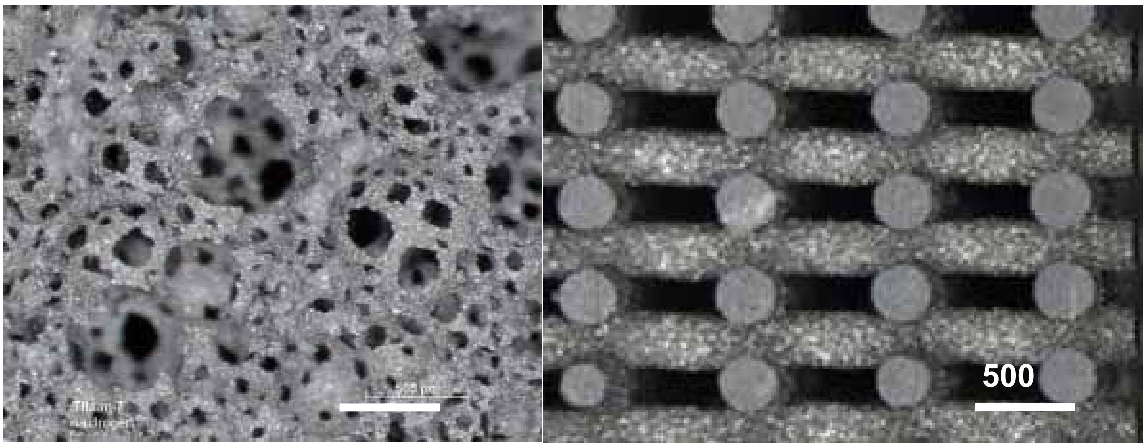

(a) (b)

Fig. 7 Porous architecture of Ti6Al4V scaffold produced by (a) gel casting and (b) 3DFD.

delivery system to overcome bone infections. **Fig. 9** shows the antibiotic release curve of a drug delivery system existing of porous CaP fibers coated with a barrier of poly lactic acid (PLA) coatings with different layer thickness.

7.3 Removal of intermetallic particles for the purification of Aluminum alloys [45-48]

In the framework of a collaborative program on recycling (Growth program of the EC, GIRD-CT-2002-00728), the purification of molten aluminum has been studied. The approach was to capture elements like Fe, Mn, and Si in intermetallic particles, which subsequently have to be removed. One of the different techniques which were used here was filtration. The filtration process is well known for the removal of inclusions from the melt, but due to the formation of rather long intermetallic fiber-like precipitates (**Fig. 10**), clogging of the filter occurred.

Forced filtration (or inverse filtration) was demonstrated as a solution to overcome the clogging on lab scale. After the precipitation of the intermetallics by cooling down the melt to about 600℃, a 40 ppi foam was pressed down through the vessel, compacting the solid intermetallics to the bottom. By repeating this procedure at lower temperatures, by staying at a temperature where liquid and solid phases are present, more intermetallics can be concentrated as a kind of residue at the under part of the crucible. For capturing smaller intermetallic particles an active filter can be a solution. Such filter consists for instance of a foam filter coated with a salt (e.g. NaBr in **Fig. 11 a, b**), which becomes viscous and sticky at the melting temperature of the Al metal.

7.4. Diesel particulate filter (DPF) [49-59]

Another example of a functionalized porous material is DPF. This kind of filters have to remove the carcinogenic soot particles from the outlet of diesel engines. Apart from a high filtration efficiency, other important requirements include a low pressure drop over the filter material (due to the fuel penalty in-

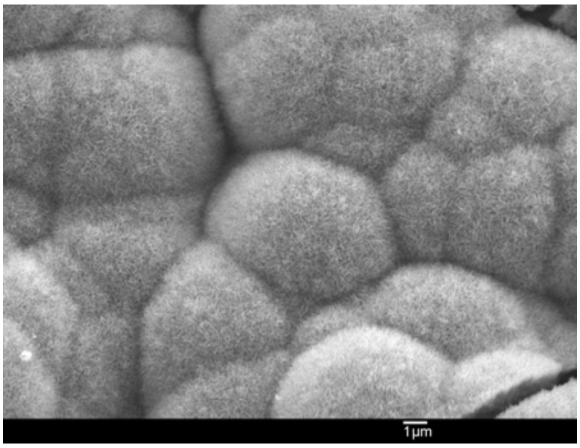

Fig. 8 A porous CaP coating on a Ti-scaffold as drug reservoir.

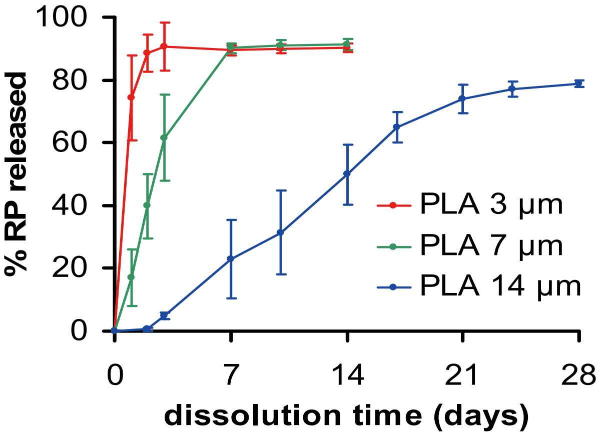

Fig. 9 The release curve of an antibiotic from a porous CaP fiber as a function of time and using PLA coatings with different thicknesses.

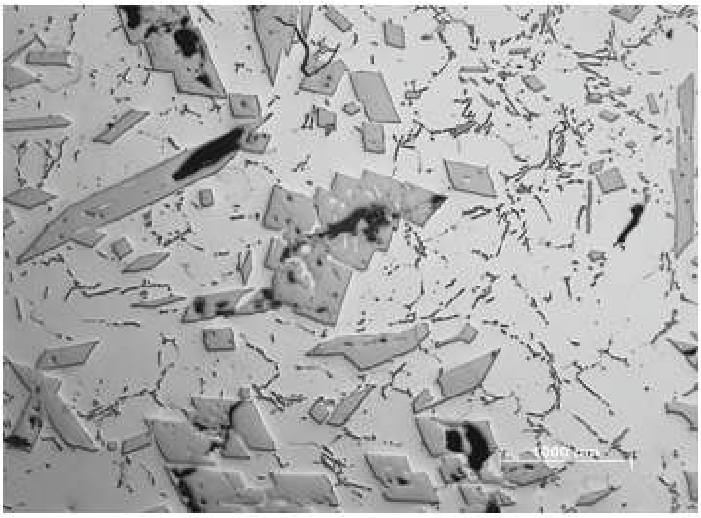

Fig. 10 Metallographic section showing intermetallic needles in Al-Fe-Mn matrix.

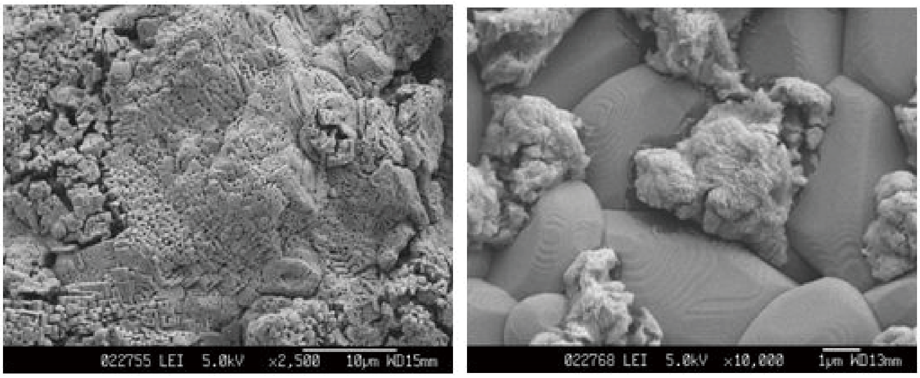

(a) (b)

Fig. 11 NaBr coatings on the struts of an Al_2O_3 foam used in Al purification.

volved) and the material must be able to withstand the temperature shock during the regeneration cyclus.

To design a good filter, a low pressure drop is a prerequisite. Therefore, large pores, high interconnectivity and a high filter surface are important. To combine this high flux with a sufficient separation factor, a thin layer with smaller pores will be needed. Finally, to burn off the soot particles on an economic way, in this case at a relative low temperature, a meso porous catalyst has to be foreseen.

Several porous architectures have been suggested for use as DPF: ceramic or metallic foams, connected fibers or honeycombs (**Fig. 12**). The most of the conventional DPF for cars are based on a honeycomb filter which is obtained by an extrusion process, due to its large filtration capacity and efficiency. The channels with openings in the order of millimeters create the large filtration surface. The thin walls of the honeycomb with pores around 15 μm, the tortuosity of the pore structure and the soot cake formation give the filter an efficiency of more than 99%.

Regeneration of the filter is most commonly performed by the catalytic combustion of the collected soot. Therefore, the honeycomb walls are coated with a wash coat existing of a mesoporous structure with a high specific surface as (e.g. Y-AL_2O_3), containing a few percent of precious metals as Pt and/or Pd.

Of course this filter has to fulfill other requirements as mechanical strength, thermo shock resistance, thermal conductivity, thermal capacity, sufficient high melting point, corrosion resistance, and reasonable price. Because all these requirements could not be fulfilled by one material, different variations are on the market: cordierite, SiC and Al_2TiO_5. A recent variation is the honeycomb structure with an arcicular mullite (developed by Dow Co.) based on a process with a fluor exchange. The development

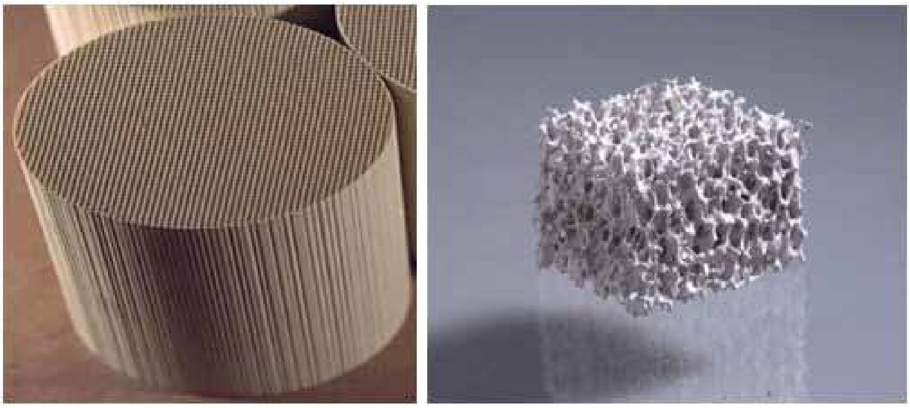
(a) (b)

Fig. 12 Honeycomb wall filter (a) and ceramic foam (b) both used as substrates for a soot filter for diesel engines.

focuses on the mixing of this arcicular mullite structure with common cordierite to improve the other application requirements of a DPF.

8. Summary

This contribution aims to give an overview on the processing and characterization techniques which play a role in the design of inorganic materials for many applications. To illustrate this issue different examples of applications with porous components are discussed in detail. It is clear that porous structures can play a role in solving environment, energy, health and transport issues by their unique combination of porous architecture and materials properties.

Acknowledgement

The authors want to express their appreciation to all the people of the Material Technology group of VITO who has helped in one or another way to realize this research.

References

1) Zhao, G. (2006): Novel porous materials for emerging applications, J. Mater. Chem., 16, pp.623-625.
2) Schaefer, D. (1994): MRS Bulletin, April 1994, p14.
3) Sagio-Woyansky, J., Scott, C. E. and Minnear, W. P. (1992) : Am. Ceram. Soc. Bull., 71, pp. 1674-1682.
4) Colombo, P. (2002): Key Engineering Materials, 206-213, pp.1913-1918.
5) Green, D. and Colombo, P. (2003): Cellular ceramics: intriguing structures, novel properties, and innovative applications, MRS Bulletin, 28, pp.296-300.
6) Scheffler, M. and Colombo, P. (Eds) (2005) : "Cellular ceramics. Structures, manufacturing, properties and applications", Wiley-VCH, Weinheim (Germany).
7) Fain, D. (1994): "Membrane gas separation principles", MRS Bulletin, 4, pp.40-43.
8) Harold, M. et al. (1994): MRS Bulletin, 4, pp.34-39.
9) Burggraaf, A. and Cot, L. (Eds) (1996): " Fundamentals of inorganic membrane science and technology", Elsevier Science & Technology Amsterdam (The Nederlands).
10) Li, Kang (2007): " Ceramic membranes for separation and reaction", John Wiley & Sons, Ltd., Chichester (UK).
11) Ashby, M. (1999): "Materials selection in mechanical design", Butterworth – Heinemann, Oxford (UK).
12) Colombo, P. (2008): "In Praise of pores", Science, 322.
13) Vercauteren, S. et al. (1998): Porous ceramic membranes: preparation, transport properties and applications, J. Porous Materials, 5, pp. 241-258.
14) Van Gestel, T. et al. (2002): Alumina and Titania multilayer membranes for nanofiltration: preparation, characterization and chemical stability, J. Membrane Sc., 207, pp. 73-89.
15) Luyten, J. et al. (2008): Pore architecture for a vast range of applications, Adv. Energy Techn. & Environm., Proc. ICC2, Verona (Italy), pp. 309-317.
16) Gibson, L. and Ashby, M. (1999): "Cellular solids", Cambridge University Press, Cambridge (UK).
17) Banhart, J. (1998): Progr. Mat Sci., 46, pp. 559-632.
18) Studart, A. et al. Gonzenbach, U., Tervoort, E. and Glauckler, L. (2006): J. Am. Ceram. Soc. , 89, pp. 1771-1789.
19) Sepulveda, P. and Binner, J. (1999): J.Eur.Ceram.Soc., 19, pp. 2059-2066.
20) Luyten, J. et al. (2005): Strong ceramic foams from polyurethane templates, , Adv. Appl. Ceram., 104, pp. 4-8.
21) Thijs, I., Luyten, J. and Mullens, S. (2003): J. Am. Ceram. Soc., 87, pp. 170-172.
22) Greil, P., Lifka, T. and Kaindl, A. (1998): J. Eur. Ceram. Soc., 18, pp. 1961-1963.
23) Colombo, P. (2006): Conventional and novel process-

ing methods for cellular ceramic, Phil. Trans. R. Soc. A, , 364, pp. 109-124.

24) Lewis, J. et al. (2006) Direct Ink writing of three-dimensional ceramic structures, J. Am. Ceram. Soc., 2006, 89 [12], pp. 3599-3609.

25) Sigmund, W., Bell, N. and Bergstrom, L. (2000): Novel powder −processing methods for advanced ceramics, J. Am. Ceram. Soc., 83 [7], pp. 1557-??74.

26) Luyten, J. et al. (2009):Different methods to synthesize ceramic foams, J. Eur. Ceram. Soc, 29, pp. 829-832.

27) Buysse, C. et al. (2010): Fabrication and oxygen permeability of gastight, macrovoid-free $Ba_{0.5}$ $Sr_{0.5}$ $Co_{0.8}$ $Fe_{0.2}$ $O_{3-\delta}$ capillaries for high temperature gas separation, J. Membr. Sci., 359, pp. 86-92.

28) Mullens, S., Luyten, J. and Zeschky, J. (2005): In Cellular Ceramics (Eds. M. Scheffler and P. Colombo), Chapter 3, Characterization of structure and morphology, pp. 227-266, Wiley-VCH, Weinheim (Germany).

29) Bhave, R. (1991): “Inorganic membranes, synthesis, characteristics and application.” Ed. Van Nostrand-Rheinhold,, New York (USA).

30) Rombouts, M. et al. (2009): The production of Ti-6Al-4V parts with controlled porous architecture by three-dimensional fiber deposition, Proc. VRAP Conf. (Eds. Taylor& Francis), Leira, Portugal, pp.453-457.

31) Nuyts, P. et al. (2010): The 3D fiber deposition technique for producing porous periodic metals and ceramics, Proceed. ISuP - 2010 conference April 19-21, Bruges (Belgium).

32) Luyten, J. et al. (2000): Processing of multi-layer ceramic nanofiltration membranes, Ceramic transactions, 15, pp. 551-562.

33) Weyten, H. et al. (1997): Dehydrogenation of propane using a packed-bed catalytic membrane reactor, AICE Journal, 43(7), pp. 1819-1827.

34) Luyten, J. et al. (2000): Preparation of $LaSrCoFeCO_{3-\delta}$ membranes, Solid State Ionics, 135, pp. 637-642.

35) Mulder, M. (1996): “Basic principles of membrane technology” , Kluwer Academic Publ. Dordrecht (The Nederlands).

36) Ryan, G., Pandit, A. and Aptsidis, D. (2006): Fabrication methods of porous metals for use in orthopaedic applications, Biomaterials, 27, pp. 2651-2670.

37) Li, J. et al. (2006): Porous Ti6Al4V scaffold directly fabricating by rapid prototyping: preparation and in vitro experiment, Biomaterials, , 27, pp. 1223-1235.

38) Cachinho, S. and Correia, R. (2006): Titanium Scaffolds for osteointegration: mechanical, in vitro and corrosion behavior, J. Mater. Sci. Mater. Med., 19, pp. 2331-2339.

39) Bakker, A. et al. (2008): Quantitative screening of engineered implants in a long bone defect model in rabbits, Tissue Engineering Part C Methods, 14(3), pp. 251-260.

40) Ravelingien, M. et al. (2009): Thermal decomposition of bioactive sodium titanate surfaces, Applied Surface Science, 255, pp. 9539-9542.

41) Impens, S. et al. (2008): Production and Characterization of porous calcium phosphate structures with controllable hydroxyapatite/beta tricalcium phosphate ratios, Adv. Ceram., 108, pp. 494-500.

42) Brar, H. et al. (2009): Magnesium as a biodegradable and bioabsorbable material for medical implants, Biomedical materials and devices, 61(9).

43) Staiger, M. et al. (2006): Magnesium and its alloys as orthopaedic biomaterials: a Review, Biomaterials, 27, pp. 1728-1734.

44) Luyten, J. et al. (2008): Porous scaffold design for bone replacement, Oral Contr. Bioceramics, Biotech. Health Proceed. ICC2, Verona (Italy), pp. 1-6.

45) Pitsch, A. et al. (2005): New experimental approach in the search of intermetallic compounds for Fe, Mn, and Si removal in aluminium recycling, Light Metals 2005, pp. 1191-1195.

46) Instone, S. et al. (2005): Development of molten metal filtration technology for aluminium, Light Metals 2005, pp. 933-938.

47) Le Brun, P. et al. (2007): Removal of intermetallic particles for the purification of aluminum alloys, Light Metals 2007, Ed. Morten Sorlie, TMS 2007, pp. 657-664.

48) Osumi, K. et al. (2000): Development of new filter for the removal of non-metallic inclusions from the molten aluminium, Proc. of the fourth international symposium on Recycling of Metals and engineered materials, TMS 2000.

49) Pyzik, A. and Li, C. (2005): New design of ceramic filter for diesel control applications, Int. J. Appl. Ceram. Technol., 2(6), pp. 440-454.

50) Miyakawa, ??? et al. (2003): Characteristics of Reaction-Bonded Porous Silicon Nitride Honeycomb for DPF Substrate, JSAE Review, 24, pp. 269?276.

51) Alkemade, U. et al. (2006): Engines and exhaust after-treatment systems for future automotive applications, Solid State Ionics, 177(26-32), pp. 2291-2296.

52) Ogunwumi, S. et al. (2005): Aluminium titanate compositions for diesel particulate filters, SAE 2005-01-0583.

53) Adler, J.(2005): Ceramic diesel particulate filters, Int. J. Appl. Ceram. Technol., 2(6), pp. 429-439.

54) Cutler, W. et al. (2000): A new high temperature ceramic material for diesel particulate filter applications, SAE 2000-01-2844.

55) Cutler, W. (2004): Overview for ceramic materials for diesel particulate filter applications, Ceram. Eng. Sci. Proc., 25(3), pp. 421-430.

56) Binner, J. et al. (2004): Gel cast foam diesel particulate filters, Key Engineering Mat., 264-268(1-3), pp. 2231-2234.

57) Görsmann, C. et al. (2005): Catalytic coatings for active and passive diesel particulate filter regeneration, Monatshefte für Chemie, 136, pp. 91-105.

58) Fino, D. (2007): Diesel emission control: catalytic filters for particulate removal, Science & Techn. Adv. Mat., 8, pp. 93-100.

59) Adler, J. (2008): Ceramic Diesel Particulate filters - sta-

tus and trends, Ceramics for Environment., Proceed. ICC2 2008, Verona (Italy), pp. 439-448.

Author's short biography

Jan Luyten

Jan Luyten (born 1951) received his M.S. in metallurgical engineering in 1974 and his Ph.D. in applied sciences in 1979 from the Catholic University of Leuven (KUL, Belgium). After a 1-year post-doc, he worked at Union Miniere (1980), a multinational specialized in mining and refraction ore. From 1981 till 1988, he was a lecturer at the Technical School for Industrial Engineers Groep T in Leuven. In 1988 he joined the Nuclear Research Centre (SCK) in Mol (Belgium), part of which organization was split of in 1991 as the Flemish Institute of Technological Research (VITO). Both at the SCK and now at VITO, he has been working in the field of processing of ceramics, covering areas of chemical sensors and their construction, solid state (mixed) conductors, ceramic membranes, ceramic foams and structural ceramics in general. He is a member of the Belgian, European and American Ceramic Society, and published over 80 articles in the field of ceramic materials and their application. He contributes to conferences, proceedings, and scientific journals both as an author and reviewer. He has participated in several EC-programs.

Steven Mullens

Steven Mullens (born 1972) received his M.S. in quantum chemistry at the Catholic University of Leuven (KUL, Belgium) in 1990, and his Ph.D. in Physical and Inorganic Chemistry at the University of Hassel in 2000 on the determination of sulphur functionalities in elastomer and coals by pyrolysis. Since, he has been working as a researcher at the Flemish Institute of Technological Research on different projects including shaping of ceramic nanocomposites, diesel particulate filters and manufacture of porous calcium phosphate and titanium alloy materials for bone scaffolds. His expertise includes thermal analysis, processing of nanoparticles, formulation of colloidal suspensions and the shaping and characterization of porous materials.

Ivo Thijs

Ivo Thijs (born 1962) is a technician at the Flemish Institute of Technological Research from 1992, highly experienced with ceramic powder handling, suspension preparation and spray drying.

Powder Processing Issues for High Quality Advanced Ceramics[†]

Makio Naito*, Masataro Okumiya, Hiroya Abe and Akira Kondo
Joining and Welding Research Institute, Osaka University[1]
C.C. Huang
Hosokawa Micron Powder Systems[2]

Abstract

In this paper, the effect of powder processing conditions on the fracture strength of advanced ceramics is discussed. Manufacturing processes of silicon nitride ceramics and alumina ceramics are utilized to explain the relationship between powder processing conditions and major fracture origin in the ceramics. The preparation conditions of powder slurry are found affecting the structure and strength of powder granules, which can influence the properties of green compact and thus the quality of sintered ceramics. These phenomena can be investigated by using new characterization tools such as the liquid immersion method and the observation technique using thinned ceramics specimen under the transmission mode. Also, very small amount of coarse particles contained in the powder slurry is found starting the fracture in ceramics by using wet sieve analysis and the observation technique with thinned ceramic specimen. As a result, it is found that the major ceramics fracture is originated from the large pores and coarse particles in powder granules, green compact and sintered ceramics. They can be unintentionally introduced in the manufacturing steps of ceramics, such as powder slurry preparation, spray drying, and forming process of green compact. By making use of these characterization tools, effective processing conditions to eliminate the large pores and coarse particles can be identified for producing high quality advanced ceramics.

Keywords: Powder processing, Sintered ceramics, Green body, Granule, Slurry, Coarse particle, Fracture strength, Fracture origin

1. Introduction

Powder processing technology has been widely used in many industries. However, it needs a lot of know-how to make high quality and low cost products by making use of powder materials. For example, manufacturing process can have a significant influence on the properties of advanced ceramics. For a given production method, a minor change in the powder processing condition can cause a great difference in the ceramic quality. **Fig.1** shows a typical powder granule compaction process used in the ceramic manufacturing [1)] to make sintered ceramics. It indicates that non-uniform structure, such as large pores or coarse particles in the green compact, can become fracture origin [2, 3)], which affects the reliability of sintered ceramics. On the other hand, powder packing structure, such as particle orientation or apparent density distribution in the green compact, also influences the deformation of sintered body; thus leads to its fracture strength and near-net shaping. Therefore, the manufacturing process of green compact before firing is crucial for producing high quality advanced ceramics.

In this paper, the manufacturing process of silicon nitride ceramics and alumina ceramics is used to elucidate the relationship between the powder processing conditions and the fracture origin in the ceramics. For examples, the effects of powder slurry preparation conditions and small amount of coarse particles in the powder slurry on the properties of sintered

---

[†] Accepted: September 8th, 2010
[1] 11-1, Mihogaoka, Ibaraki, Osaka, 567-0047 Japan
[2] 10 Chatham Road, Summit NJ 07901 USA
* Corresponding author
TEL: +81-6-6879-8660, FAX: +81-6-6879-8680
E-mail: m-naito@jwri.osaka-u.ac.jp

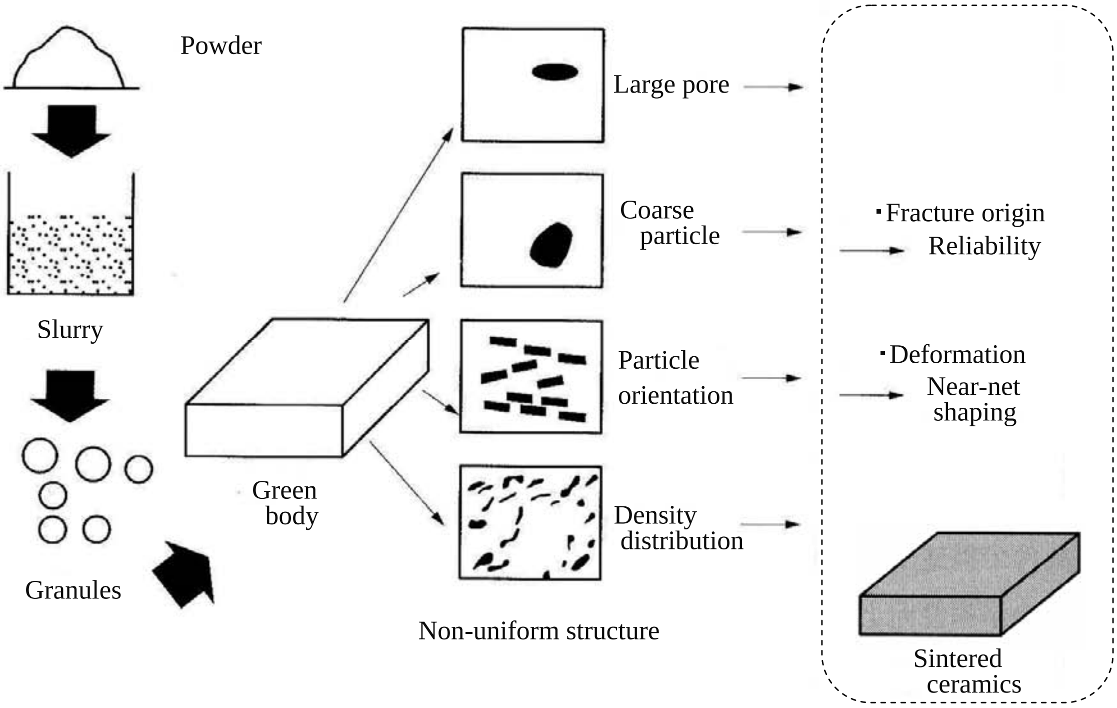

Fig. 1 Powder granule compaction process to make sintered ceramics.

ceramics are discussed. Detailed characterization of powder raw materials, powder slurry, powder granules, green body, and sintered body is found necessary to understand and control ceramic processing conditions and is essential to open the black box of ceramic manufacturing processes.

2. Effect of Powder Processing Conditions on Ceramic Properties

2.1 Powder slurry preparation conditions

Slurry preparation conditions can directly affect the powder granule properties made by spray drying and lead to non-uniform structure of green compact. **Fig.2** shows the fabrication process of silicon nitride ceramics by powder granule compaction [4]. Commercially available silicon nitride, alumina, and yttrium oxide powders were used as the starting materials. Average particle size of each powder measured by X-ray sedimentation was 0.44 μm, 0.33 μm, and 0.29 μm, respectively. Silicon nitride powder (270g) was mixed with alumina (15g) and yttrium oxide (15g) by ball-milling with distilled and deionized water (155g) for 24 hours. Dispersant was not added because the pH of the slurry moved to the basic region (up to 10.5) during mixing, at which silicon nitride could be deflocculated electrostatically due to the reaction of silicon nitride and water. After passing through a sieve (32 μm) to remove undesired large agglomerates or inclusions, the slurry was divided into two groups; one was spray-dried in the as-dispersed state and the other in the flocculated state. For the flocculated one, the pH of the slurry was adjusted to 9.4 by slowly adding a HNO_3-H_2O solution with continuous stirring at room temperature. The slurry was then dried to form powder granules using a spray dryer.

Fig.3 shows a micrograph of the granules prepared from a well-dispersed slurry (pH=10.5, apparent viscosity: 300mPa・s) and that of flocculated slurry (pH=9.4, apparent viscosity 6500mPa・s), respectively 4). They were observed by liquid immersion method [5]. Most of the granules prepared from well-dispersed slurry had distorted spherical shapes and contain dimples, which were also clearly visible in the micrograph taken in the optical transmission mode, as shown in **Fig.3 (a)**. On the contrast, the granules prepared from flocculated slurry were essentially spherical and no dimples as shown in **Fig.3 (b)**. However, when observing the SEM micrographs of theses granules, some dimples shown in **Fig. 3(a)** were apparently absent, because they were placed on the specimen holder with the dimple down. It indicated that conventional characterization tools were insufficient to observe the granule structure as shown in **Fig.3**.

The slurry dispersion state strongly influences the granule structure [6]. Droplets injected into a spray dryer are dried with evaporation of water from the surface. In case of dispersed slurry, water flows from the interior to the surface of a droplet and the particles are carried along with the flow to the area near the surface, leaving behind an internal void, as drying proceeds. It is believed that a partial vacuum is formed in the internal void, leading to the collapse of the granules near the end of the drying cycle. As can be seen in **Fig.3 (a)**, the mechanism results in granule deformation and the formation of a dimple structure on almost all powder granules made from dispersed slurry.

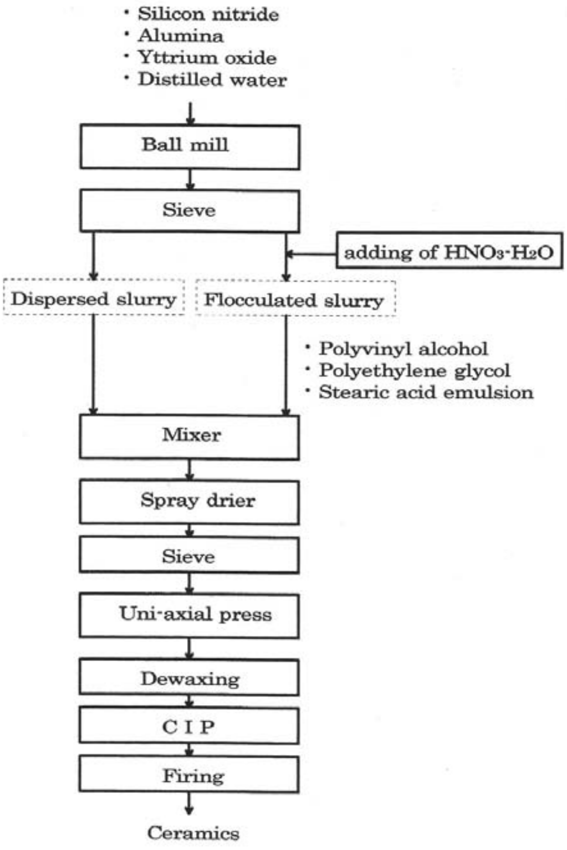

Fig. 2 Fabrication process of silicon nitride ceramics.

On the other hand, droplets made from flocculated slurry are considered to be composed of agglomerates in which primary powder particles are touching each other. Because water can migrate and evaporate easily from the source without distributing the loosely packed structure in and between agglomerates, solid granules are easily formed. As a result, the granules tend to have a spherical shape without dimples as shown in **Fig.3 (b)**.

Fig.4. shows the Weibull distribution curves of the fracture strength of sintered bodies 4). Average strength of sintered body fabricated from flocculated slurry (717MPa) was obviously higher than that from well-dispersed slurry (607MPa), although the calculated Weibull moduli were high for both of them. The fractographical analysis for the fractured specimen clearly indicated that large pore defects were responsible for fracture origins in the silicon nitride ceramics [4]. Such larger pore defects were developed in the ceramics originated from the structure and strength of powder granules. In this case, large pores developed starting at the centers of granules originated from dimples through powder packing during compaction and those at the boundaries caused by incomplete adhesion between granules affected the fracture strength of ceramics. In the experiment, large pore size was apparently larger in the thinned specimen of the sintered ceramics made by well-dispersed slurry. However, such difference cannot be observed by microstructure analysis alone even at higher magnification [7, 8].

Although the structure of powder granules is similar, the fracture strength of the sintered bodies may still be affected by the slurry preparation conditions [9]. **Table 1** indicates the preparing conditions of the

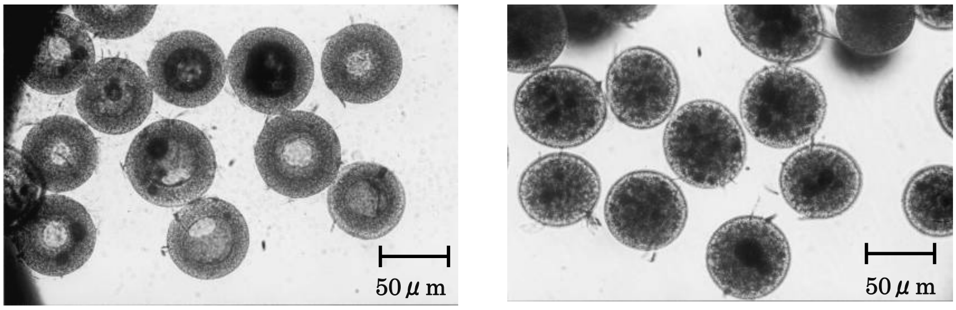

(a)

(b)

Fig. 3 Internal structure of granules observed by liquid immersion method
(a) prepared from well-dispersed slurry ; (b) prepared from flocculated slurry.

three slurries with some difference in apparent viscosity [9]. Alumina powder (AL160-SG4, Showadenko, Japan, average particle size: 0.46 μm) was mixed with 0.2, 0.5, 2.0mass% of polymer dispersant (Ammonium polyacrylate, CELUNA-D305, Chukyoyushi, Japan) and distilled and deionized water for 24h by ball milling. The solid concentration of the slurry was 35 vol%. The pH of slurry with 0.2 mass% dispersant was increased to 10 by adding dilute NH_4OH solution, which also decreased its viscosity to 43mPa･s. The slurries were spray-dried for granulation. The granules were uni-axially pressed at 9.8 MPa, and then isostatically pressed at 176 MPa. The green compact were sintered at 1550 ° C for 2hr in air. As indicated in **Table 1**, three kinds of slurries showed low apparent viscosity; and, the granules made by the slurries had distorted spherical shapes and contained dimples, which were also clearly visible in the micrograph taken under the optical transmission mode, as shown in **Fig.3 (a)**. Also, no big difference was observed in size distribution of granules made from the three slurry preparing conditions, and their average sizes were all about 60 μm.

Table 1 presents the density and fracture toughness of the specimens. The values are almost the same for these ceramics. **Fig.5** shows the strength distribution of the alumina ceramics [9]. However, a significant variation of strength associated with the slurry preparing condition was noted. The average strength is 486, 430 and 363MPa respectively for specimens made from the three slurry preparing conditions.

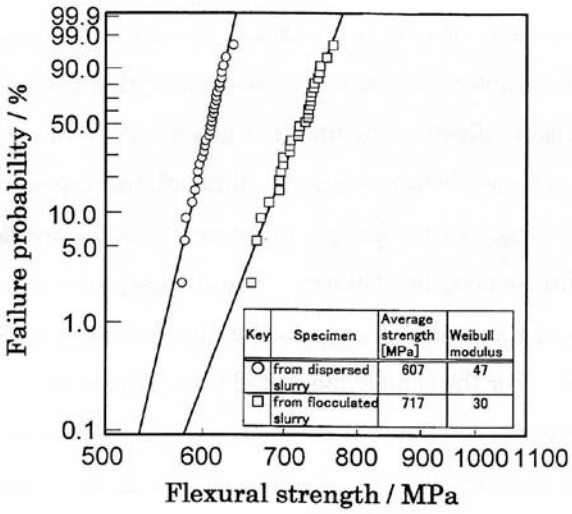

Fig. 4 Weibull distributions of the fracture strength measured for sintered specimens.

Fig.6 shows a comparison of the compressive strength of the granules prepared from the three different slurries [9]. The strength of granules was measured with a micro compression test machine (MCTM-500, Shimadzu Co., Japan) and the compressive strength was calculated by applying the model proposed for the elastic deformation of spherical particle [10,11].

Fig.7 shows the transmission optical micrograph of the thinned ceramics specimens [9]. The dark features are pores in the structures. Clearly, the present ceramics have defects at the center and boundaries of granules. They are developed from the irregularities of packing structure of powder particles in green compact. The pore structure was similar for the three specimens, except for the size of the pores associated with the slurry preparing condition. The relation between the pore number density versus the pore size of the sintered specimens made from the three slurries was measured [9]. The pore number density was defined as the number of pore per unit volume of specimen per unit size interval. The effective volume of specimens under the analysis was about 0.5 mm^3. In this study, relatively large pores were subjected to the analysis. Pores were assumed to have a spherical shape and their sizes were represented by the equivalent diameter.

According to the fracture mechanics, the strength of ceramics σ, can be related to the size of fracture origin, c, by the following equation:

$$K_{IC} = \sigma Y c^{1/2} \quad (1)$$

Where K_{IC} is the fracture toughness and Y is the

Table 1 Slurry preparing conditions and properties of the sintered ceramics

No.	pH	Dispersant Amount [mass%]	Viscosity [mPa･s]	Density [kg/m³]	Fracture Toughness [MPam$^{1/2}$]
#1	10	0.2	43	3.91×10³	3.7
#2	9.1	0.5	22	3.94×10³	3.8
#3	8.1	2.0	54	3.89×10³	3.8

shape factor. As expected from the equation, fracture strength of ceramics should change depending on the size of fracture origin, provided that the fracture toughness and the shape factor are the same. Focusing on large pores, the size as shown in **Fig.7 (b)** is 1.29 times larger than that in the specimen shown in **Fig.7 (a)**. Provided the shape factor is the same, the average strength of the sintered sample made from the slurry of pH 10 is estimated 1.34 times higher than that made from the slurry of pH 8.1. This estimate is in good agreement with the measured strength as shown in **Fig.5.**

The change of the large pore size can be ascribed to the difference in the granule strength as shown in **Fig.6.** In compaction of harder granules, less deformation can occur at a certain compaction pressure and this leaves larger pores in compacts. The size of large pore increases with the granule strength, which was strongly affected by the amounts of dispersant in slurry as shown in **Fig.6.**

The granule strength is influenced by various factors, such as the powder packing structure as well as the amount and distribution of dispersant in granules [12]. In this study, the difference of the granule strength can be ascribed to the latter factor dominantly, since the granule structure was almost similar. It is considered that the amounts of dispersant added, 0.2, 0.5 and 2.0 mass %, are insufficient, a little excess and excess for covering the powder surfaces based on the relation between the amounts of dispersant and the slurry viscosity, respectively. With excessive dispersant, the non-adsorbed dispersant becomes free polymers in the slurry. In spray drying, the free polymers form solid bridges between powder

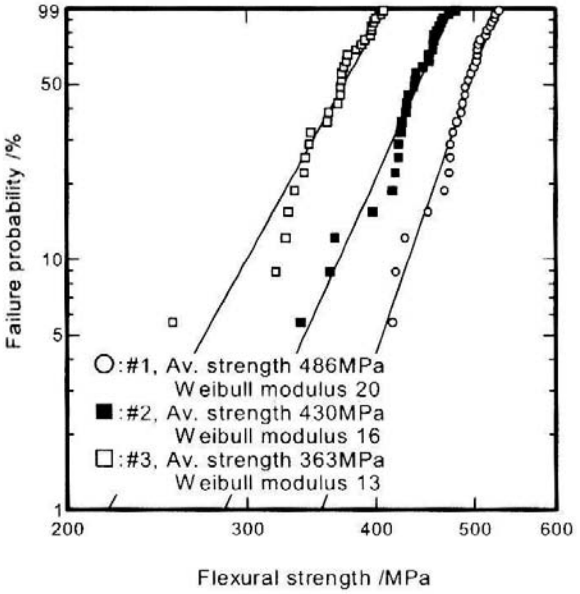

Fig. 5 Strength distribution of the alumina ceramics.

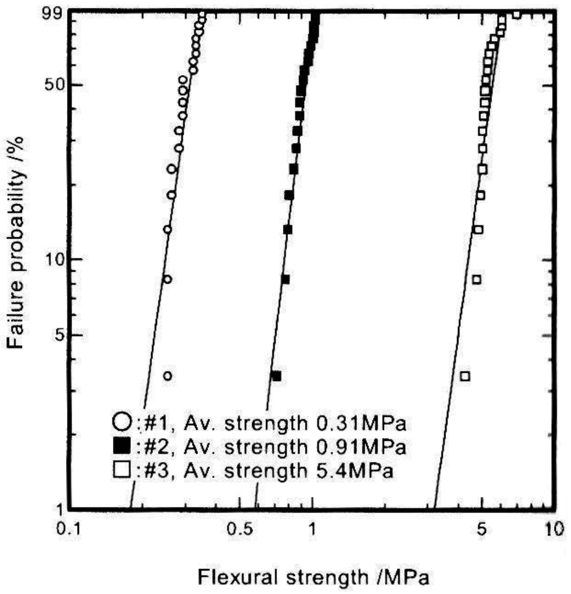

Fig. 6 Compressive strength distribution of alumina granules associated with different slurry preparing conditions.

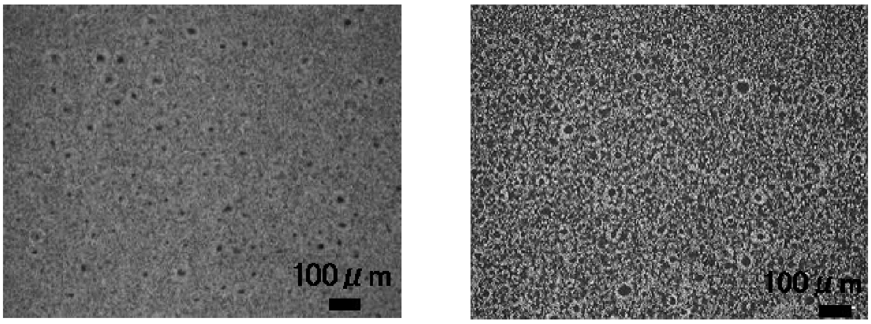

(a)

(b)

Fig. 7 Microstructures of alumina ceramics examined with optical transparent technique,
(a) specimen made from the slurry prepared with #1 condition
(b) specimen made from the slurry prepared with #3 condition

particles, increasing the granule strength considerably. Clearly, polymeric additives have critical effects on the cohesive force between particles and thus on the powder compaction process.

2.2 Coarse particles in powder slurry

The control of particle size distribution of powder is also important in slurry preparation. Powder is processed using mechanical method such as ball milling. Very few numbers of coarse particles can affect the fracture strength of sintered ceramics; therefore, particle size control is very important to achieve high quality advanced ceramics.

A fundamental study was conducted to understand the effect of coarse particles on the fracture strength of ceramics. The specimens were prepared through the procedure as shown in **Fig.8** [13]. Low soda alumina powder (AL-160SG-4, Showa Denko K.K., Japan) was used as raw material. The nominal average particle size was 0.5 μm. The powder was placed in alumina pot mill (SSA-999, Nikkato, Japan, volume 2000ml) with 2kg of alumina balls (SSA-999, Nikkato; diameter 5mm) and 400g of aqueous solution (2 mass%) of dispersant of polyacrylic acid type (CERUNA D-305, Chukyo Yushi, Japan), and mixed for 24h to make a slurry with the solid content 50vol%. The slurry was passed through a mesh (2mm opening) to separate the balls. Weighed slurry was placed in a container and stirred continuously with a stirrer while small amount of coarse particles (0.01-0.1 mass%) was added. The coarse particles for addition were prepared from the unground raw material used in the production of the present fine alumina powder. The coarse particles were classified into three fractions by sieving before being used. Each fraction of coarse particles was added to individual slurry; therefore, three kinds of slurries with coarse particles were prepared. Each slurry was kept stirring for 2h after the coarse particles were added. Finally, each slurry was cast in gypsum molds (100 x 100 x 9mm) to prepare green compacts with coarse particles. After drying, the compact was heated at 1550° C for 2h in an electric furnace to sinter the model ceramics [13].

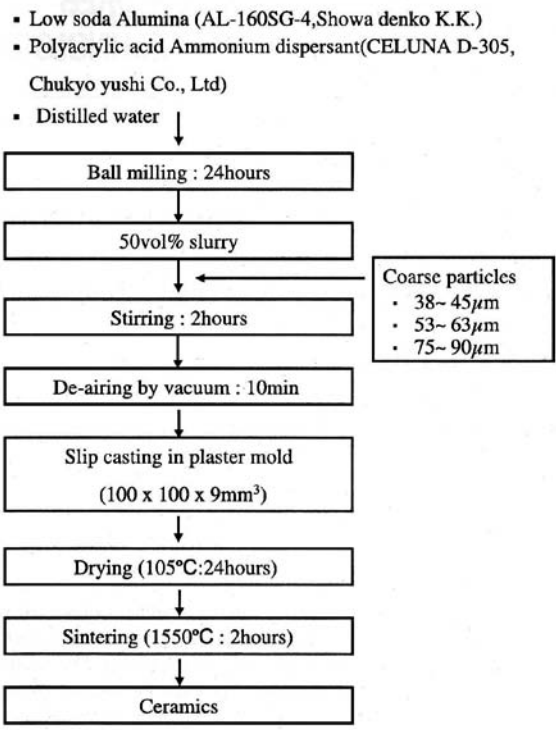

Fig. 8 Fabrication process of alumina ceramics.

In the micrograph, at high magnification, platelet-shape particles form aggregates of porous structure with the size of 10-20 μm [13]. At lower magnification, these aggregates form the coarse aggregates in large scale. In this experiment, such coarse aggregates are referred to as coarse particles. **Table 2** shows the measured densities of green compact and ceramics [13]. The densities were approximately the same for all compacts. The densities of all ceramics were again the same. Clearly, addition of a small amount of coarse particles has no effect on the densities of ceramics.

Fig.9 shows the Weibull plots and the fracture toughness for all specimens[13]. The specimen strength decreased with increasing size of coarse particles added. The Weibull moduli were similar and over 20 for all specimens. All ceramics basically have

Table 2 Densities of green bodies and sintered bodies

Coarse particles size, sieve apertures/μm	Density/10^3 kg m^{-3}	
	Green body	Sintered body
38–45	2.31	3.95
53–63	2.32	3.95
75–90	2.31	3.96

the same fracture toughness. **Fig.10** shows SEM micrographs of representative fracture origins found in this study [13]. The specimen contains coarse particles of the size range 75-90 μm. The fracture origin was noted in the specimen of the lowest strength (370MPa) as seen in **Fig. 10**(a) and **Fig. 10**(b) shows that with the average strength of 406MPa. They were both coarse particles. Lower strength was observed for the specimen containing larger coarse particles. Similar results were obtained for all specimens examined in this study.

Fig.11 shows the IR photomicrographs [14] for the internal structures of ceramics containing the coarse particles of various sizes [13]. The size of coarse particles in the ceramic matrix increased with increasing size of coarse particles added. Again, the sizes of coarse particles are the same as those added in the preparation of specimens [13]. Actually, the estimated values of strength obtained by linear fracture mechanics, assuming that the fracture was always initiated at the coarse particles in the matrix, agreed very well with the measured strength [13]. It means that small amount of coarse particles governs the strength of ceramics. Therefore, carefully preventing the coarse particles is crucial to improve the strength of high quality advanced ceramics.

3. Importance of Powder Characterization Tools

As already explained, small amount of large pores

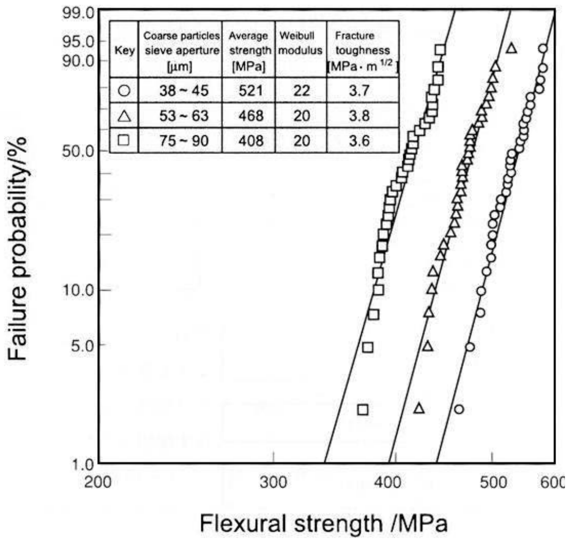

Key	Coarse particles sieve aperture [μm]	Average strength [MPa]	Weibull modulus	Fracture toughness [MPa·m$^{1/2}$]
○	38 ~ 45	521	22	3.7
△	53 ~ 63	468	20	3.8
□	75 ~ 90	408	20	3.6

Fig. 9 Mechanical properties of sintered bodies.

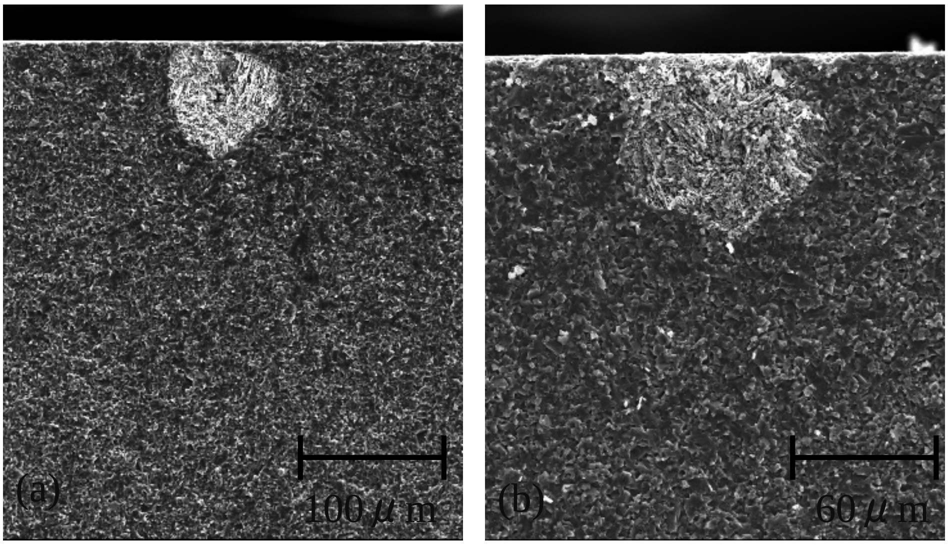

Fig. 10 Examples of fracture origins in alumina ceramics having 75～90 μm coarse particles. (a)370MPa, (b)406MPa.

and coarse particles has large effect on the material properties. Therefore, coarse particles in raw powder materials or in powder slurry must be carefully controlled. This is critical to obtain not only higher quality of advanced ceramics but also other kind of materials such as toner and polishing materials.

However, conventional characterization tools are insufficient to detect such small amount of non-uniform components. For example, **Fig.12** shows the particle size distribution of ground silicon nitride powder by wet ball milling [15]. It was measured by X-ray sedimentation method [16, 17]. The obtained particle size distribution indicates the ground powder has no particles coarser than 45 μm. And, **Fig.13** shows the relationships between average particle size of ground powder and ball-milling time [15]. It shows that average particle size decreases with the milling time, and media ball size has no effect in this case. However, the situation was quite different when using wet sieve to examine the 45 μm oversize mass fraction of the ground powder with ball-milling time [15], as seen in **Fig.14.** Different from **Fig.12**, it shows that coarse particles larger than 45 μm are apparently contained in the ground powder. Media ball size has effect on the change of its mass fraction in the ground powder with milling time. The 10mm sized media ball is the most effective to grind coarse particles. It means the wet sieve analysis would be a reliable method to measure even just a few particles in the ground powder. From **Fig.14**, we can identify the processing conditions to effectively grind very small amount of coarse particles. As a result, the method to measure coarse particles in advanced ceramic powder was developed [18, 19], and it has been already filed as an international standard in advanced ceramics (ISO/TC206). By relating the coarse particle information of raw powder or powder slurry to that of sintered ceramics, we can easily understand how small amount of coarse particles lower the reliability of sintered ceramics thorough its manufacturing process.

Characterization of large pores in powder granules, green compact and sintered ceramics is also very important for producing high quality advanced ceramics [20]. Conventional characterization tools such as SEM or mercury porosimetry are not sufficient to evaluate the small amount of large pores in granules, green compact and sintered ceramics. Liquid immersion method [5] is a very powerful tool to observe the large pores in granules and green compact. And, thinned specimen observation is also very effective for de-

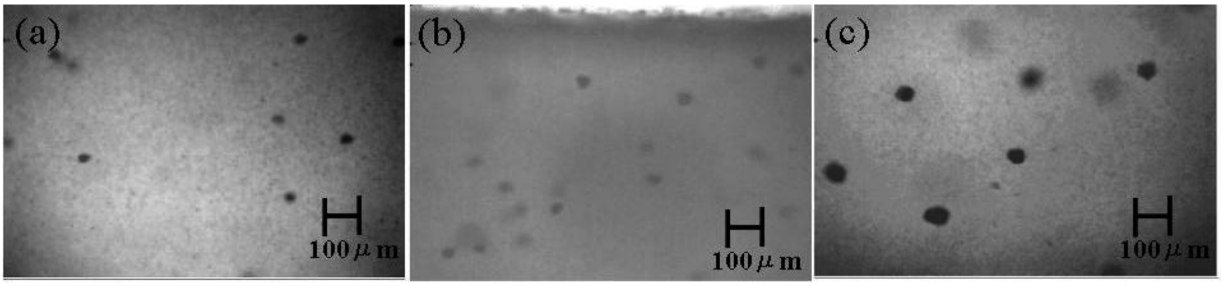

Fig. 11 Mid-infrared micrographs of sintered bodies having coarse particles of (a)38 ~45 μm, (b)53~63 μm,(c)75~90 μm.

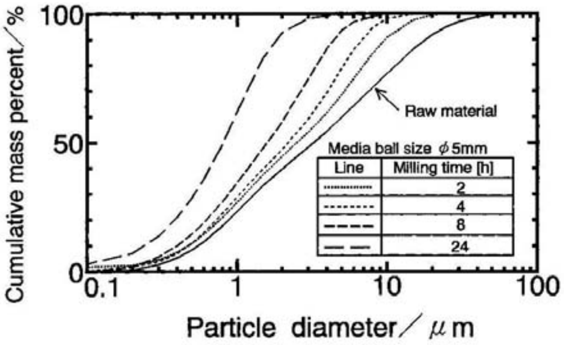

Fig. 12 Particle size distribution of the powder ground with 5mm media balls.

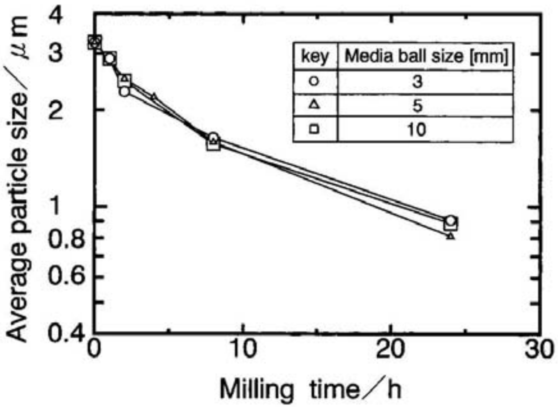

Fig. 13 Relationships between average particle size of ground powder and milling time.

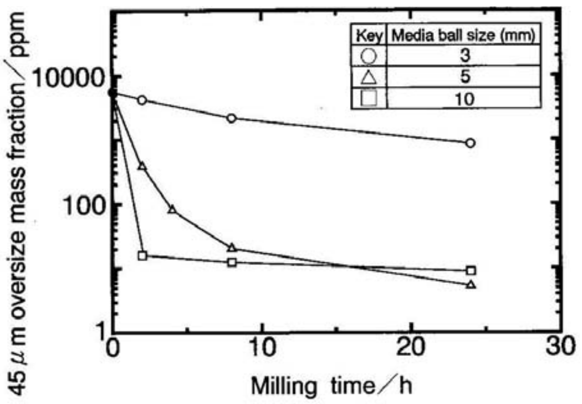

Fig. 14 Change of 45 μm oversize mass fraction of ground powder with milling time.

tecting large pores in sintered ceramics. Effectively using these tools, we can investigate what those processing conditions in the ceramic manufacturing create large pores in sintered ceramics causing product reliability problems. So far, on the microstructure and sintered strength of ceramics, the following issues were clarified using these characterization tools: seasonal variation of microstructure and sintered strength of dry-pressed alumina [21-23], effects of spray drying conditions [8-24], dewaxing procedures [25-27] and granule compaction procedures [28-30] on the fracture origin of sintered ceramics. Of course, these tools are also suitable for other manufacturing processes, such as injection molding process [31], to improve the properties of their ceramic parts.

4. Conclusions

In this paper, the effect of powder processing conditions on the fracture strength of advanced ceramics was clarified. Manufacturing processes of silicon nitride ceramics and alumina ceramics were utilized to explain the relationship between ceramics processing conditions and its major fracture origin. Powder slurry preparing conditions were found creating the large pores in powder granules, green compact and sintered ceramics. These phenomena can be investigated by using new characterization tools such as the liquid immersion method and the observation technique using thinned ceramics specimen under the transmission mode. Also, very small amount of coarse particles contained in the powder slurry is found weakening the strength of ceramics by using wet sieve analysis and the observation technique with thinned ceramic specimen. As a result, it is believed that major fracture origin is caused by the large pores and coarse particles, which are generated in the manufacturing steps of ceramics, such as powder slurry preparation, spray drying, and forming process of green compact. By making use of these characterization tools, effective processing conditions to eliminate the large pores and coarse particles can be identified for producing high quality advanced ceramics.

References

1) Naito, M. and Abe, H. (2004): The Micromeritics, Funsai, No.48, pp.56- 62.

2) Abe, H., Hotta, T., Naito, M., Shinohara, N. and Uematsu, K. (2002): Direct Observation of Detrimental Defects in Ceramics, Am. Ceram. Soc. Bull., Vol.81, No.1, pp.31-34.

3) Abe, H., Naito, M., Hotta, T., Shinohara, N. and Uematsu, K. (2003): Flaw Size Distribution in High-Quality Alumina, J. Am. Ceram. Soc., Vol.86, pp.1019-1021.

4) Naito, M., Hotta, T., Abe, H., Shinohara, N., Okumiya, M. and Uematsu, K. (2000): Optical Characterization of Strength-Limiting Flaws in Silicon Nitride Ceramics Prepared with Different Slurry Flocculation Conditions, British Ceramic Proceedings 61, pp.119-132 , The Institute of Materials.

5) Uematsu, K., Kim, J.-Y., Miyashita, M., Uchida, N. and Saito, K. (1990): Direct observation of internal structure in spray-dried alumina granules, J. Am. Ceram. Soc., Vol.73, pp.2555-2557.

6) Abe, H., Naito, M., Hotta, T., Kamiya, H. and Uematsu, K. (2003): Pore Defects Related to Slurry Character and their Relevance to Strength Distribution in Alumina Cermics, Powder Technology, Vol.134, pp.58-64.

7) Shinohara, N., Okumiya, M., Hotta, T., Nakahira, K., Naito, M. and Uematsu, K. (1999): Formation Mechanisms of Processing Defects and their Relevance to the Strength in Alumina Ceramics made by Powder Compaction Process, J. Mater. Sci., Vol.34, pp.4271-4277.

8) Hotta, T., Nakahira, K., Naito, M., Shinohara, N., Okumiya, M. and Uematsu, K. (1999): Origin of Strength Change in Ceramics Associated with the Alteration of Spray Dryer, J. Material Research, Vol.14, No.7, pp.2974-2979.

9) Abe, H., Hotta, T., Kuroyama, T., Yasutomi, Y., Naito, M., Kamiya, H. and Uematsu, K. (2001): Variation of Microstructure and Fracture Strength of Alumina Ceramics Made From Different Slurry Preparing Condition, Ceramic Processing Science Ⅵ, Ceramic Transactions, Vol.112, pp.809-814, published by Am. Ceram. Soc.

10) Hiramatsu, Y., Oka, Y. and Kiyama, H. (1965): Rapid Determination of Tensile Strength of Rocks with Irregular Test Pieces, Nihon Kogyokai-shi, Vol.81, 1024.

11) Naito, M., Nakahira, K., Hotta, T., Ito, A., Yokoyama, T. and Kamiya, H. (1998): Microscopic Analysis on the

Consolidation Process of Granule Beds, Powder Technology, Vol.95, pp.214-219.

12) Naito, M., Fukuda, Y., Yoshikawa, N., Kamiya, H. and Tsubaki, J. (1997): Optimization of Suspension Characteristics for Shaping Processes, J. European Ceram. Soc., Vol.17, pp.251-257.

13) Hotta, T., Abe, H., Naito, M., Takahashi, M., Uematsu, K. and Kato, Z. (2005): Effect of Coarse Particles on the Strength of Alumina Made by Slip Casting, Powder Technology, Vol.149, pp.106-111.

14) Uematsu, K., Uchida, N., Kato, Z., Tanaka, S., Hotta, T. and Naito, M. (2001): Infrared Microscopy for Examination of Structure in Spray-Dried Granules and Compacts, J. Am. Ceram. Soc., Vol.84, pp.254-256

15) Naito, M., Hotta, T., Hayakawa, O., Shinohara, N. and Uematsu, K. (1998): Ball Milling Conditions of a Very Small Amount of Large Particles in Silicon Nitride Powder, J. Ceram. Soc., Japan, Vol.106, No.8, pp.811-814.

16) Hayakawa, O., Nakahira, K., Naito, M. and Tsubaki, J. (1998): Experimental Analysis on Sample Preparation Conditions for Particle Size Measurement, Powder Technology, Vol.100, pp.61-68.

17) Naito, M., Hayakawa, O., Nakahira, K., Mori, H. and Tsubaki, J. (1998): Effect of Particle Shape on the Particle Size Distribution Measured with the Commercial Equipment, Powder Technology, Vol.100, pp.52-60.

18) Cho, Y-I., Okumiya, M., Naito, M., Rabe, T., Waesche, R., Morrell, R., Ewsuk, K.G. , Hackley, V., Freiman, S. and Uematsu, K. (2002): Characterization of Coarse Particles Contained in Fine Powders at Very Low Concentrations, Ceramic Transactions, Vol.133, pp.71-76, published by Am. Ceram. Soc.

19) Nakahira, K., Hotta, T., Naito, M., Shinohara, N., Cho, Y-I., Katori, S., Emoto, H., Yamada, T., Takahashi, T., Okumiya, M., Kumagai, C. and Uematsu, K. (2003): Characterization of Coarse Particles in Alumina Powders by Wet Sieving Method, J. European Ceram. Soc., Vol.23, pp.1661-1666.

20) Uematsu, K., Zhang, Y., Uchida, N., Hotta, T., Naito, M., Shinohara, N. and Okumiya, M. (1999): Structural Flaw Evaluation in Green Compacts and Ceramics by an Optical Method - For Understanding the Origin of Strength Variation in Ceramics - , Key Engineering Materials, Vols.161-163, pp.145-150

21) Shinohara, N., Okumiya, M., Hotta, T., Nakahira, K., Naito, M. and Uematsu, K. (1999): Effect of Seasons on Density, Strength of Alumina, Am. Ceram. Soc. Bull., Vol.78, No.2, pp.81-84.

22) Shinohara, N., Okumiya, M., Hotta, T., Nakahira, K., Naito, M. and Uematsu, K. (1999): Seasonal Variation of Microstructure and Sintered Strength of Dry-Pressed Alumina, J. Am. Ceram. Soc., Vol.82, No.12, pp.3441-3446.

23) Naito, M., Hotta, T., Abe, H., Shinohara, N., Cho, Y-I., Okumiya, M. and Uematsu, K. (2001): Relevance of the Fracture Strength to Process-Related Defects in Alumina Ceramics, Materials Transactions, The Japan Institute of Metals, Vol.42, pp114-119.

24) Hotta, T., Nakahira, K., Naito, M., Shinohara, N., Okumiya, M. and Uematsu, K. (2001): Origin of the Strength Change of Silicon Nitride Ceramics with the Alteration of Spray Drying Conditions, J. European Ceram. Soc., Vol.21, pp.603-610.

25) Shinohara, N., Katori, S., Okumiya, M., Hotta, T., Nakahira, K., Naito, M., Cho, Y-I. and Uematsu, K. (2002): Effect of Heat Treatment of Alumina Granules on the Compaction Behavior and Properties of Green and Sintered Bodies, J. European Ceram. Soc., Vol.22, pp.2841-2848.

26) Shinohara, N., Okumiya, M., Hotta, T., Nakahira, K., Naito, M. and Uematsu, K. (2000): Variation of the Microstructure and Fracture Strength of Cold Isostatically Pressed Alumina Ceramics with the Alteration of Dewaxing Procedures, J. European Ceram. Soc., Vol.20, pp.843-849.

27) Hotta, T., Abe, H., Fukui, T., Naito, M., Shinohara, N. and Uematsu, K. (2003): Effect of Dewaxing Procedures of Cold Isostatically Pressed Silicon Nitride Ceramics on its Microstructure and Fracture Strength, Advanced Powder Technology, Vol.14, pp.505-517.

28) Abe, H., Hotta, T., Naito, M., Shinohara, N., Okumiya, M., Kamiya, H. and Uematsu, K. (2001): Origin of Strength Variation of Silicon Nitride Ceramics with CIP Condition in a Powder Compaction Process, Powder Technology, Vol.119, pp.194-200.

29) Naito, M., Abe, H., Hotta, T., Shinohara, N. and Uematsu, K. (2002): Fracture Strength Variability of Silicon Nitride Ceramics Made by Powder Compaction, Ceramic Transactions, Vol.133, pp.151-157, published by Am. Ceram. Soc.

30) Abe, H., Sato, K., Naito, M., Nogi, K., Hotta, T., Tatami, J. and Komeya, K. (2005): Effects of granule compaction procedures on defect structure, fracture strength and thermal conductivity of AlN ceramics, Powder Technology, Vol.159, pp.155-160.

31) Shinohara, N., Ohsaka, S., Hotta, T., Abe, H., Naito, M. and Uematsu, K. (2005): Relevance of the internal structures to fracture strength of injection molded and sintered silicon nitride ceramics, Advanced Powder Technology, Vol.16, pp.425-434.

Author's short biography

Makio Naito

Makio Naito received B.S., M.S. and Ph.D. degrees in chemical engineering from Nagoya University, Japan in 1980, 1982 and 1987, respectively. He was with Hosokawa Micron Corp. from 1982 to 1993 and engaged in the R&D of powder processing technology. He joined Japan Fine Ceramics Center (JFCC), Nagoya, Japan in 1993, where he focused on powder characterization and powder processing technology in ceramics manufacturing. He was Vice Director of JFCC from 2000 to 2002, and then became a professor at the Joining and Welding Research Institute (JWRI), Osaka University, Japan in 2002. He continued focusing on important studies on innovative powder and nanoparticle processing to develop advanced materials about energy and environmental issues. He was promoted to be the Director of Smart Processing Research Center, JWRI in 2007, and is also the Vice Director of JWRI from 2009. In addition, he has served as a Director of Hosokawa Micron Corp. from 2005. His publications cover a wide range of studies in the fields related to the advanced materials. He has authored or coauthored more than 500 technical articles, including more than 200 refereed journal articles. He has contributed to 52 books with 13 books as an editor. He has received many awards, and is a Fellow of The American Ceramic Society.

Masataro Okumiya

Masataro Okumiya received B.S., M.S. and PhD. Degrees in material science from University of Tokyo, Japan in 1965, 1967 and 1971, respectively. He was with Asahi Glass Company from 1971 to 1995, and promoted to be a Research Fellow of the company from 1995 to 2000. He joined the Joining and Welding Research Institute (JWRI), Osaka University, as a specially appointed associate professor in 2008.

Hiroya Abe

Hiroya Abe received B.S., M.S. and Ph.D. degrees in electrical engineering from Nagaoka University of Technology, Japan in 1990, 1992 and 1995, respectively. He was with Motorola Japan from 1995 to 1998, and with Japan Fine Ceramics Center (JFCC) from 1998 to 2002. Then, he joined the Joining and Welding Research Institute (JWRI), Osaka University, as an associated professor in 2002. His current research interest is in the development of smart materials and interfaces for functional joining technologies.

Akira Kondo

Akira Kondo received B.S. and M.S. degrees in chemical engineering from Nagoya University, Japan in 1989 and 1991, respectively. He received Ph D. degree in material science from Osaka University in 1999. He was with Hosokawa Micron Corp. from 1991 to 2005, where he engaged in the R&D of powder processing technologies. He became a specially designated researcher at the Joining and Welding Research Institute (JWRI), Osaka University, Japan in 2005, and is engaged in the R&D of powder processing technology for advanced materials.

Author's short biography

C. C. Huang

Dr. C. C. Huang is the Director of Research and Development, Nanoparticle Technology and Micron Products at Hosokawa Micron Powder Systems, which is an operating unit of Hosokawa Micron International Inc., a global supplier of systems and equipment related to material sciences and engineering. He holds an M.S. degree in engineering from Illinois Institute of Technology and a Ph.D. degree in chemical engineering from West Virginia University. He has many years' experiences in industrial R&D, as well as academia, in the field of powder technology and science. Dr. Huang specializes in powder and nanoparticle processing, powder characterization, powder granulation, and fluidization. He has published over 30 articles and 8 patents, chaired several meetings, and continues to be an active member in a number of scientific and engineering societies.

Flow of Non-Homogeneous Particulates in Rotating Drums[†]

Abdel-Zaher M. Abouzeid*
Dept. Mining, Faculty of Engineering, Cairo University[1]
Douglas W. Fuerstenau
Dept. Materials Science and Engineering,
University of California[2]

Abstract

Numerous industries deal with particulate systems such as the cement, ceramics, chemical, metallurgical and pharmaceutical industries. Usually the particulate systems handled in these industries are non-homogeneous, that is, their constituents are heterogeneous in their physical properties such as particle size, density, particle shape, and surface roughness. Handling of these systems during transport and/or manufacturing is usually associated with movements of these particulates at transfer points, being shaken, moving through drums, or sliding over inclined planes, which leads to the particulate mass being energized or disturbed. Disturbing such non-homogeneous systems results in mutual separation of the particulate constituents as a result of differences in their physical properties. The mutual separation is a natural phenomenon called segregation. In some instances, segregation is desired, while in most cases it is detrimental. Segregation in particulate systems takes place as a result of several forces, mainly frictional and gravitational forces, acting on the individual particles inside the system while it is energized. It is well known that the contribution of these forces in controlling the movement of particles are functions of the physical properties of the constituting components of the system. This paper concerns investigation and discussion of the mechanisms of particulate motion and the role of the forces acting during energizing a particulate system, particularly while moving through rotating drums, and their effects on the quality of the final products of non-homogeneous particulate systems.

Keywords: segregation, particulate systems, flow of non-homogeneous particulates, rotating drums, mixing-demixing of particulates, continuous flow of powders

1. Introduction

Particulate systems in most processes consist of various constituents. These constituents may differ in their physical properties such as size, shape, density, surface roughness, etc. Differences in the properties of the constituents are reflected in the behavior of each species when the system is set in motion. In industrial processes, differences in behavior of the various species can affect the quality of the final product

Handling and processing of particulate systems are essential sub-processes in all industries dealing with powders such as cement, chemical, fertilizer, metallurgical and pharmaceutical production. Examples of these operations in mineral processing are size reduction, size enlargement, drying, cooling, induration, calcination, roasting, and clinkering[1-6)]. Processing of these powders is usually accompanied by physical and/or chemical changes. The extent of these changes and the efficiency of these processes are strongly related to the homogeneity (degree of mixedness) of the flowing material. These changes occur whether the process is carried out in batch, continuous, or semi-continuous operations.

It is becoming evident that the role of material flow and transport in product quality and process efficiency is a major one. Several phenomena in the mineral processing and powder technology could not be explained without the consideration of the

---

[†] Accepted: July 27th, 2010
[1] Giza 12613, Egypt
[2] Berkeley, California 94720, USA
* Corresponding Author
abdel.abouzeid@gmail.com
TEL: +20 2 3586 4665
FAX: +20 2 3572 3486

material behavior while being transported, energized (disturbed), or rolled down an inclined plane. Quality control of the product is also manipulated through controlling the powder flow regime.

This paper presents the main mechanisms of particle motion, while moving within a particulate system, while being energized. It also deals with how mixing (homogenizing) and demixing (segregation) actions take place during the relative motion of the powder constituents. Flow of powders in rotating drums will be stressed as an obvious example of powder flow in several industrial processes which deal with powder technology, handling and processing.

1-Mechanisms of Particle Motion within a Particulate System

For simplicity we will limit ourselves to the flow behavior of cohesionless powders, homogeneous and non-homogeneous, in continuous systems, particularly in rotating drums.

1.1 Homogeneous systems: Homogeneous particulate systems are those whose constituents are identical in all their physical properties such as size, density, shape, etc. These are known as ideal systems, but they do not exist in real life[7]. However, for practical purposes, we may obtain systems close enough to ideal systems. Early in the sixties, efforts were made towards isolating the basic mechanisms occurring in particulate mixing operations[8]. To produce a satisfactory mixture the spatial arrangement of particle must be changed, that is, particles must be moved from one place to another within the system. There are four basic mechanisms by which this can be accomplished: a) *diffusion* which is the random motion of individual particles or small aggregates in the space occupied by the mixture under consideration, b) *convection*, where the particles move collectively in groups or clusters, c) *shear*, where clusters of particles are sheared on several planes, and d) *directional flow*, where particles move under a driving force, e.g., head gradient, concentration, etc. Shearing action changes the relative position of the constituent particles and is considered to be a representation of a specific combination of diffusion and convection[9, 10].

Pure diffusion, when it is feasible, is highly effective leading to very intimate mixtures at the individual particle level. However, it is generally an exceedingly slow process[11, 12]. On the other hand, pure convection is much faster but tends to be somewhat less effective in mixing, leading to a final mixture which may still exhibit poor mixedness on a finite scale. This fact suggests that an effective particulate mixing operation can be achieved by an optimum combination of both mechanisms which incorporates both the speed of convection and the effectiveness of diffusion. The directional mixing mechanism leads to the movement of all the species in the system towards a lower potential energy or concentration level[13].

In contrast to liquids and gases, in which diffusion can be regarded as "spontaneous", particulate systems, will only be mixed as a result of mechanical agitation, or some sort of relative motion, which provides circumstances for the particles to change their relative positions collectively of individually. Agitation is provided to the system by shaking, vibration, tumbling, handling, etc.

1.2 Non-homogeneous systems: These are the real particulate systems whose components have different physical properties. When these systems are set in motion, their components tend to sort themselves out into regions rich in one or the other of the system constituents[7, 14]. These systems are said to be "segregated" or "demixed" . Segregation seems to occur whenever there are differences in any of the particle physical properties between the system components[15], such as differences in particle size, shape, density, electrical, magnetic, and surface properties. Size, shape, density and surface roughness are generally recognized to be the most prevalent[16]. In the case of moistened systems, they are strongly affected by the degree of hydrophobicity of the constituents[7].

When particles having different densities are shaken in a container, it is found that the denser particles tend to settle to the bottom of the container[17]. Presumably, because in this way, the total potential energy of the system is lowered. When coarse and fine particles are set in motion, the fine particles tend to segregate to the bottom. In part, this can be explained by a "percolation-biased" diffusion mechanism, whereby the fines can pass through the interstices between large particles with minimum friction. Williams[17, 18] also showed that large particles placed in a bed of smaller particles will, upon vibrating the bed, tend to rise towards the top of the bed, even when their density is greater than that of the finer particles. The explanation offered for this trend is that the large solid particles, which will generally be denser than the loosely packed bed of fine particles, causes a compaction of the bed immediately beneath the coarse particle, consequently, its freedom to move in response to the vibration is restricted to the lateral and upward directions, and the net result is a tendency to rise. These explanations of segregation phenomena are only applicable for certain situations. A generalized theory, regardless of the particular circumstances in which the operation takes place, has not yet been offered to explain the segregation action in particulate systems. Although efforts have been made towards numerical parametric studies[19], quantitative predictions, rate and extent, of the final picture of a segregating system do not exist. Modeling attempts of particulate transverse segregation and scaling up of rotating drums have been exercised but for limited conditions[20, 21].

In the authors' opinion, a generalized theory that can explain the segregation action in moving particulate systems governed by any type of motion (such as tumbling, vibration, shaking, rolling on inclined surfaces, etc.) may be possible by considering the forces acting on the individual particles in a surrounding medium of other particles. The vertical as well as the lateral pressures on the specific particle, calculated from the soil mechanics relationships, and the friction opposing its motion should be considered. A small particle, in a mixture of small and large particles, is affected by its weight and the frictional forces opposing its motion laterally and vertically[22]. For this particle to move in the interstices of the particulate system, it will encounter less friction than a large particle, and hence moves to a deeper location. A heavy particle will be under the influence of its weight and the frictional forces restricting its motion. It is obvious that a heavy particle will experience friction proportional to its weight and size, but the gravitational force pulling it down is relatively larger than that for a light particle. A smooth-surfaced particle in a system where all of its components have the same size and density will experience less frictional forces than any particle of the other constituents[23]. These principal aspects of force analysis on individual particles in a moving particulate system are applicable to any type of particle motion such as handling, heaping, tumbling, shaking, and vibration.

2-Mixing-Demixing Equilibrium

In any blending operation, the mixing and demixing mechanisms will be operational. The participation of each of these two operations will be dictated by the environment and the tendency of each component to segregate out of the system as a result of the differences in their physical properties and the extent of these differences. Since the two operations, mixing and demixing, are acting against each other, an equilibrium level of mixedness will be attained as the final state of the mixture.

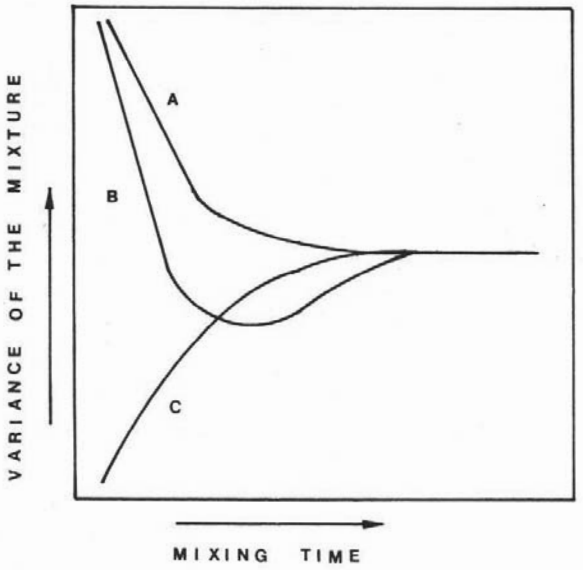

Fig. 1 Schematic progress of mixing-demixing trend at different loading systems of coarse-fine particulates.

If we take a mixture of particles of two different sizes in a container and energize it by shaking or vibrating, mixing and demixing will be going on simultaneously. An equilibrium state between these two processes will be achieved, with a final state where the large particles will be dominating near the top regardless of the start state. The extent of mixedness as a function of time will depend on the way the components are loaded in the container at the beginning. Loading of the two components in the container before energizing it can be: 1) layer loading with fine particles in the bottom and coarse particles on the top, 2) layer loading with coarse particles in the bottom and fine particles on the top, or 3) with the two components being thoroughly mixed. **Fig. 1** shows the schematic progress of mixing and demixing for the three loading conditions[24]. If we think of the variance of the mixture as a function of mixing time to be an indication of the state of mixedeness, line A represents the extent of mixing as a function of mixing time when the initial conditions start with the coarse particles on the top. The degree of mixedness continues increasing (the variance decreasing) smoothly and gradually until it reaches a steady state (equilibrium). This equilibrium state will be such that there is a top region of coarse particles, a bottom region of fine particles, and a middle region of coarse and fine particles with the ratio of coarse to fine particles decreasing downward and a ratio of fine to coarse decreasing upward. When the initial conditions are such that the coarse component is in the bottom, the degree of mixedness follows line B. In this latter case, a state of “overmixing” is observed. The physical meaning of this state is that the two components are crossing each other towards their natural stability at equilibrium, i.e., coarse on the top, fine in the bottom, and a mixed layer in the middle. In these two cases, the mixing mechanism dominates the system in its initial stage, with a decreasing rate as time passes until the rate of mixing is counter balanced by the rate of demixing at the equilibrium level. Line C represents the mixing course of an initially well-mixed system. Under these conditions, the demixing (segregation) mechanism dominates the system in its initial stage. As time passes, the demixing rate decreases as it is counter balanced by the mixing mechanism until the system reaches its equilibrium level. The equilibrium state, obtained after a long time of setting the system in motion, for the three cases, is the same.

3-Analysis of the Continuous Flow in Rotating Drums

Rotary drums are used extensively for particulate processing in several industrial operations[25]. In mineral processing, they are used in comminution, pelletizing, mixing, drying, calcination, and roasting[26]. They are also used in food, chemical, cement, and pharmaceutical industries. The flowing materials in most of these operations are non-homogeneous, i.e., the constituents differ from each other in one or more of their physical properties such as size, density, shape, etc[27]. The Impulse-Response technique is used to follow the behavior of the flowing material inside the rotating drum through monitoring and analyzing the Residence Time Distribution, RTD, of tracers that simulate each of the flowing components[28]. This technique is the most common one used for studying the behavior of particulate flow in such systems[29]. In this technique, a tracer (trace amount) which represents one of the components, and does not disturb the flow, is injected at the entrance of the feed and followed at the exit discharge of the drum. The exit age distribution function, E(t), is analyzed, using the E-curve, in the form of the residence time distribution, RTD, through the C-curve. The E-curve is the number fraction of particulates in the effluent stream with ages between t and t+dt. The C-curve is the concentration of tracer particles in the effluent at dimensionless time, θ. The residence time distribution is used to characterize the flow by calculating the mean residence time, MRT, (τ_T, where T stands for Tracer), of the component as well as the variance of this distribution (σ^2_t) and the standard deviation (σ_t) and the time taken by the tracer to first show up at the exit end of the drum, t_0. Through these parameters, the behavior of the component within the bulk, and the type of flow inside the drum can be characterized[30]. The RTD can be presented as time-dependent, relative concentration of the tracer, C_t/C_0, designated as C(t), versus t in seconds, or as dimensionless distribution, $[C_t/C_0]$ versus t/τ, θ, where C_0 is the initial concentration of the tracer, C_t is the instantaneous tracer concentration in the RTD at time t, τ is the mean residence time, and t is the time at which the sample just came out from the drum discharge end, calculated from the time the tracer was injected into the drum at the inlet end[31, 32].

The foregoing parameters are estimated as follows:

$$\int E(t)\,dt = \int C(t)\,dt = 1 \qquad (1)$$

$$\tau_T = \frac{\int t\,C(t)\,dt}{\int C(t)\,dt} = \int t\,C(t)\,dt \qquad (2)$$

$$\sigma_t^2 = \int (t - \tau)^2\,C(t)\,dt \qquad (3)$$

The dimensionless variance, $\sigma_\theta^2 = \sigma_t^2/\tau^2$ (4)

and the dimensionless time, $\theta = t/\tau$ (5)

The mean residence time can also be estimated from the values of the hold up material in the drum, H, and the material feed rate, F, as follows:

$$\tau_H = H/F \qquad (6)$$

This paper presents, discusses, and analyses the results of an extensive research work, which deals with the flow of non-homogeneous particulate systems flowing in a rotating drum. The systems studied here consist of particulate species different in their size, density, shape and surface roughness. It includes tracers flowing in bulk of different properties, and two major components different in their physical properties flowing simultaneously in the rotating drum. Flow of powders in rotating drums is stressed as an important unit operation step commonly involved in powder technology.

Experimental Technique and Materials

Experimental Set up: The experimental set up

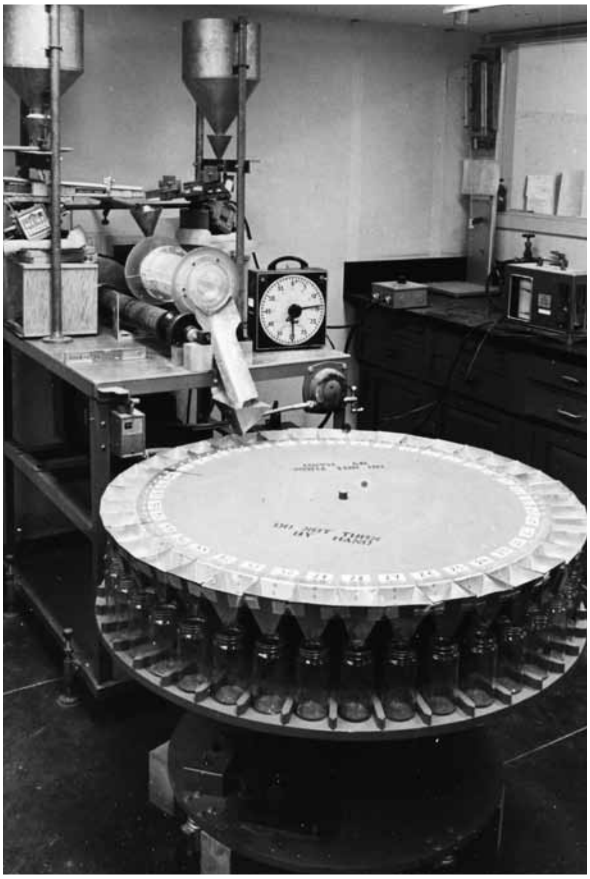

Fig. 2 Experimental set-up (feeding system, rotating drum, and sampling system) for studying the effect of the properties of particulate systems on their flow in a rotating drum.

consists of three main parts; feeding system, rotating drum, and sampling system (**Fig. 2**). The feeding system consists of two parallel lines each of which consists of a bulk material storage bin, a constant head funnel, and a vibratory feeder of the ERIEZ MAGNETICS type model 10 A which is connected to a voltage stabilizer. The particulate material flows from the bottom of the storage bin to the constant head funnel directly underneath. The arrangement of the bin and the funnel is such that regardless of the material level in the bin the material level in the funnel will be constant, and hence the rate of particulate flow from the funnel will be fairly constant (coefficient of variation = 0.031 for 30-second samples). The material flowing from the bottom of the funnel falls directly onto the vibratory feeder, which delivers the material to a feed chute that passes directly to the feed end of the rotating drum. The feed rate is controlled by gates on the vibratory feeder (coarse adjustment) and controlling the amplitude of the vibrator (fine adjustment). The rotating drum, made from a transparent Lucite tube, was 8 cm in diameter and 25 cm in length fitted with two flanges at its two ends, each 20-cm in diameter. The flange at the feed end of the drum has an opening 1.8 cm in diameter, and that at the discharge end has an opening 4.5 cm in diameter. Along the interior surface of the drum (parallel to the longitudinal axis), eight equally-spaced lifter bars of 0.3 cm diameter were mounted. The lifters are needed to insure proper flow of the particulate material in the drum without slipping or surging. The drum is divided longitudinally into two halves such that one half can be replaced by a sampler to split the drum contents into 20 equal samples at the end of the experiment. The drum assembly is rotated by friction on two neoprene rollers (7.5 cm diameter) driven by a Graham variable speed motor. The discharge material from the drum flows into a circular riffler type sampler through an exit chute and a rectangular funnel. The bottom of the rectangular funnel is shaped in the form of an elongated slot of 0.3 cm width and 4.0 cm length to provide sharp cuts between samples. The sampler has 40 equal size buckets under which sample collection bottles are placed. The sampler is rotated by means of a variable speed motor for adjusting the sampler speed, and hence, controlling the sample size (coefficient of variation of sample weight = 0.048 for 30-second samples).

Procedure: The Tracer Impulse-Response technique was used to characterize the material flow inside the drum. Tracers were prepared by taking a fraction of the bulk material, dying it with a food-stuff dye, drying, and screening to obtain the precise size fraction. The tracers are distinguished from the bulk by a different color. A tracer, about one gram, is injected into the feed chute, and the response is obtained by collecting the samples at the discharge end. Samples are collected continuously by the sample riffler until all the tracer, visually, comes out of the drum. The discharged samples are timed, designating the tracer injection time as zero time, t_0. Each sample is spread over a white sheet, and the colored tracer particles counted. The tracer concentration, C_t/C_0, is plotted as a function of the exit time. From this plot, all the required parameters can be calculated. By the end of each experiment, the hold up material inside the drum is sampled and weighed.

Material: The particulate materials used in this investigation, either as bulk or tracer, are:
Dolomite of size fractions 12 × 14, 14 × 20, 20 × 28, 28 × 35, 35 × 48, and 48 × 65 mesh.
Hematite of size fractions 12 × 14, 14 × 20, and 20 × 28 mesh.

Magnetite of size fraction 35 × 48 mesh.
Galena of size fractions 20 × 28 and 35 × 48 mesh.
Glass beads of size fractions 20 × 28 and 35 × 48 mesh.
Copper shot of size fractions 20 × 28 and 35 × 48 mesh.

These species represent differences in particulate properties such as: size, density, shape, and surface roughness.

Results and Discussion

To get a clear picture about the flow of non-homogeneous particulate systems in rotating drums, it may be necessary to start with an example of some homogeneous systems flowing in rotating drums[20]. This way, the contrast in the flow behavior between the two systems, homogeneous and non-homogeneous, becomes obvious. When the flowing material is homogeneous, i.e., very narrow size range with all particles having the same density, shape, and surface roughness, the residence time distribution of the tracer represents perfectly the flow of the bulk inside the rotating drum. Moreover, it seems that the flow characteristics are not affected by the properties of the flowing material whether it is heavy, coarse, fine, regular or irregular shaped as long as it is homogeneous and the drum parameters (speed, diameter, and length) as well as the feed rate are fixed. **Fig. 3** presents the RTD curves for three different materials, of different size fractions, flowing in a rotating drum. There is no noticeable difference in the three RTDs. As a matter of fact, the mean residence times of the three materials range between 165 and 167 seconds with no trend. **Fig. 3** represents the RTD for homogeneous particulate systems where the bulk and tracer in each experiment were the same, both of them were dolomite of the same size fraction, only the tracer was colored with food color, dried, and screened. The RTDs and the mean residence times, MRTs, are almost the same.

Another feature of the flow of the homogeneous materials in the rotating drum is that there is no difference in the value of the bulk mean residence time, τ_H, and the tracer mean residence time, τ_T. **Fig. 4** presents a correlation between τ_H and τ_T, which shows perfect matching between the two parameters even though the values were obtained under a wide range of operating conditions, drum speed, drum size, discharge opening diameter, feed rate, particle size fraction, etc.

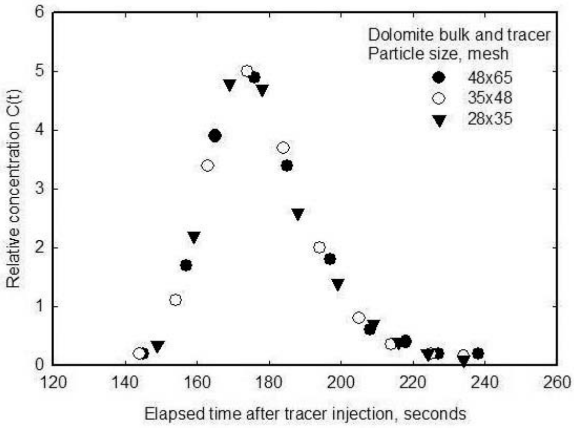

Fig. 3 Residence time distributions for homogeneous particulate systems of different particle sizes.

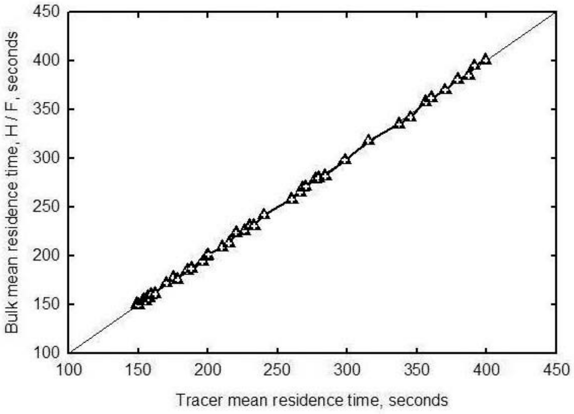

Fig. 4 Comparison between the mean residence times of homogeneous particulate systems flowing in a rotating drum as calculated from the RTD and the H/F relationship.

a) A tracer flowing in a bulk: As we have seen in **Fig. 3**, as long as the tracer and the bulk have the same physical properties, their RTDs under specific operating conditions are almost the same regardless of the size of the flowing particles. In **Fig. 3**, it can be seen that the mean residence time of the tracer and bulk is the same at any operating conditions provided that both of them have the same physical properties and the operating conditions are the same. This means that, under these conditions, particle flow is absolutely random and all the particles are affected equally by the prevailing forces.

Now let us see what happens if the tracer and the bulk have different physical properties. **Fig. 5** presents the RTDs for two dolomite systems; one of them represents the tracer and the bulk of the same size, 35 × 48 mesh, and in the other system the size of the bulk was 35 × 48 mesh with the tracer being 48 × 65 mesh. The mean residence time (MRT) in the first case, homogeneous system, is 162 seconds, where as the MRT in the non-homogeneous system is 177

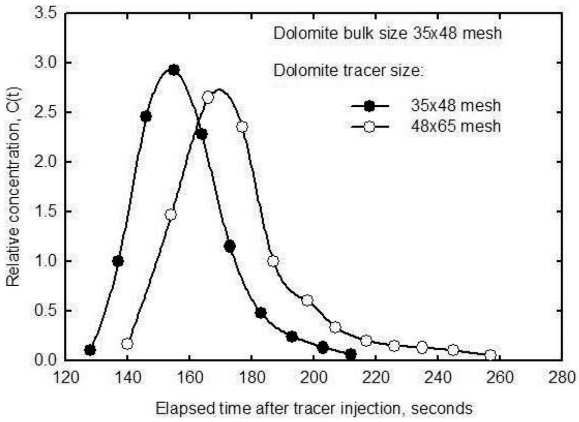

Fig. 5 Residence time distributions for two dolomite particulate systems. In one of them, the tracer and bulk are of the same size, and in the other, the tracer particle size is smaller than that of the bulk.

seconds. This means that the smaller tracer particles were delayed in comparison with flow of the somewhat larger bulk particles. In this latter case, the tracer was radially segregated to the core of the flowing bulk which moves towards the discharge end more slowly than the surface layer (shear zone). Since the discharge of the flowing material from the exit end of the rotating drum is from the shear zone, top layer, the particles in the core, which includes most of the tracer material, take longer time than the average particle in the bulk.

Fig. 6 presents the RTDs for three tracers that differ in their specific gravities, dolomite (sp.gr. = 2.9), magnetite (sp.gr. = 5.2), and galena (sp.gr. = 7.5), flowing in dolomite bulk of the same size as the tracers, namely 35 × 48 mesh. In these systems, the dolomite tracer represents the flow of the bulk. Transport of the denser tracers, magnetite and galena, is retarded because they are segregated radially to the core of the flowing bulk, and hence exited later from the drum than the dolomite tracer. The heavier tracer, galena, is delayed more than the lighter one, magnetite, because it has a greater tendency than magnetite to segregate into the core of the flowing bulk. The MRTs of the three tracers, as calculated from their RTDs, are 156, 185, and 198 seconds for dolomite, magnetite, and galena, respectively. The shape difference between magnetite (irregular) and galena (cubical) may have affected the mean residence time to some extent.

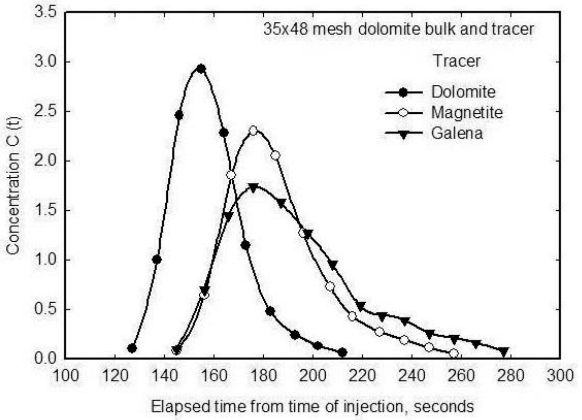

Fig. 6 Residence time distributions for tracers of different densities flowing in dolomite bulk of the same particle size as the tracers.

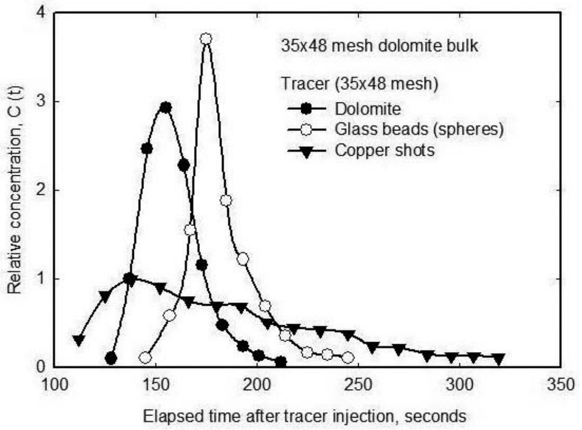

Fig. 7 Residence time distributions of tracers of different physical properties flowing in a dolomite bulk of the same particle size as the tracers.

The combined effect of tracer shape, density, and surface roughness is shown in **Fig. 7**. The bulk and tracers have the same particle size, 35 × 48 mesh. The MRT of dolomite, which represents the bulk material, is 158 seconds, whereas it is 181 and 182 seconds for glass beads and copper shot. Although the specific gravity of the glass beads (sp.gr. = 2.7) is very close to that of dolomite, they differ in the particle shape and surface roughness, so the RTDs and the MRTs are quite different. Because of the spherical shape of the glass beads, they penetrate radially to a lower plane from the surface and probably do not disperse much due to not being totally in the shear zone. They are mainly driven by the driving head of the flowing material towards the discharge end. Since they are slower in motion and not well dispersed, they reach the exit end somewhat late, and a large number of the tracer particles are poured out in a short span of time. This makes the mode of its RTD higher than that of dolomite, with less dispersion and longer MRT compared with the average bulk particles. The copper shot being spherical in shape, having smooth surface, and high density (sp.gr. = 8.9) behave differently. They percolate fast from the top of the moving charge, shear zone, down to the toe, raised up by friction with the rising charge to the top, percolate down to the toe, raised up to the top, and so on facing less friction, having higher momentum, and cutting longer distances radially and axially, i.e., dispersing faster than the average bulk particles. This repeated sequence of motion makes the copper shot in the rotating drum behave as if it were moving in a stirred tank reactor, although it is not thoroughly mixed with the dolomite bulk. Hence, they report earlier than the bulk at the exit and disperse over longer time as shown in **Fig. 7**.

A series of experiments was carried out under fixed operating conditions, using bulk and tracers of the same size, 20 × 28 mesh, but differ from the bulk in their specific gravity. The bulk was dolomite and the tracers were glass beads, dolomite, hematite, galena, and copper shot. The mean residence time for each tracer was calculated and plotted against the relative density, [tracer density] / [bulk density]. **Fig. 8** shows the relation between the MRT of the tracers as a function of the relative density between the tracer and the bulk. The MRT increases as the ratio of the tracer density to bulk density increases as long as both tracer and bulk are natural particles different only in density. Of course this is an indication of segregation. However, when particle shape and surface roughness of the tracer enter into the picture, irregular behavior is observed as can be seen in the case of glass beads and copper shot flowing in dolomite bulk of the same particle size. Interestingly, the MRTs of the two spherical tracers, even though their densities differ widely, tend towards similar values, see **Fig. 7**.

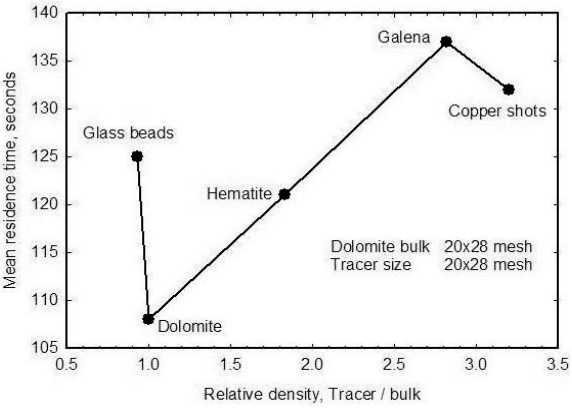

Fig. 8 Mean residence time of different tracers flowing in a dolomite bulk as a function of the relative densities of the tracers and bulk (tracer density/bulk density).

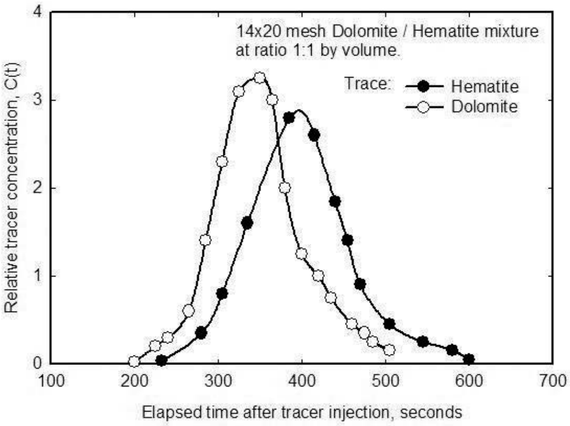

Fig. 9 Residence time distributions of dolomite tracer and hematite tracer when hematite and dolomite are flowing in the rotating drum at 1:1 volume ratio. Bulk components and tracers have the same particle size.

b) Major components flowing simultaneously: When a particulate system is comprised of more than one major component that differ in their physical properties flows continuously through a rotating drum, the same phenomenon, segregation, takes place. Segregation may be observed inside the drum by the naked eye in some cases, and in other cases, although it is happening, additional measurements are needed for confirmation, e.g., sampling of the hold up material inside the drum in the axial direction[31, 33]. To study this, a series of experiments was carried out using hematite and dolomite, 14 × 20 mesh, flowing through the drum at a ratio of 1:1 by volume. **Fig. 9** shows the RTDs of the two components as measured by Impulse-Response technique (following the tracer at the exit end). The main observation that one sees inside the drum is a mixed feed (black hematite particles and white dolomite particles) entering the drum for a short distance beyond the drum inlet, after which only white dolomite is observed on the surface of the flowing charge. Of course what has happened in this case is that, in the first few seconds after entering the drum, the heavy component, hematite, percolates through the flowing bulk to the core of the charge leaving the light component, dolomite, on the surface. Because the particles in the core of the flowing stream progress more slowly towards the exit end than do the surface layers, the heavy component accumulates inside the drum until a steady state is reached at which the feed composition becomes the same as the discharge composition. However, at steady state, the ratio of the hold up of the two components inside the drum becomes different than their ratio in the feed, with the heavy component having higher volume ratio than the light component. This is why in **Fig. 9** the MRT of hematite is longer than that of dolomite, with more dispersion.

In **Fig. 10**, more interesting results are reported. In this series of experiments, the hematite-dolomite

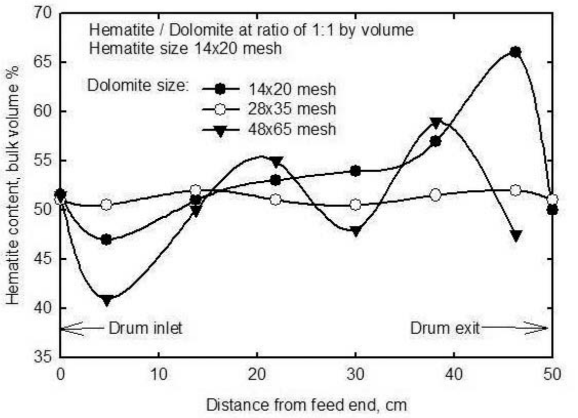

Fig. 10 The axial hold-up of hematite and dolomite systems of different particle sizes flowing at 1:1 volume ratios.

mixture was flowing in the rotating drum at a volume ratio of 1:1. Keeping the particle size of the hematite constant, 14 × 20 mesh, the particle size of the dolomite was varied, 14 × 20, 28 × 35, and 48 × 65 mesh. The differences in physical properties between the mixture constituents in this series were density and particle size. At steady state, when the two components were of the same particle size, the hematite component accumulated inside the drum, occupying a larger volume than its ratio in the feed and in the discharge product, as mentioned earlier. The accumulation of the heavy component was not regular along the drum axis but it was increasing towards the exit end as a result of the convection movement from the inlet to the outlet of the drum. This explains the results presented in **Fig. 9**. When the size of dolomite particles, the lighter component, was smaller than that of the hematite, the heavier component, their volume ratio and their distribution along the drum axis became close to their ratio in the feed and in the discharge. The explanation of this behavior is that each of the two components has a property that favors radial percolation towards the core of the flowing charge: hematite particles are heavy and dolomite particles are small. When the size of the dolomite particles gets smaller than the hematite particles, successive and alternating bands of the coarse hematite and the fine dolomite start to form. These bands, which are less intensive at the inlet end and more intensive at the exit end, cause the discharge to fluctuate, i.e., the volume ratio of the components in the discharge fluctuates with time. This means that the rate of percolation and mobility of the fine dolomite particles are faster than that of the large hematite particles, and when this is combined with the natural perturbation of each species, the bands form.

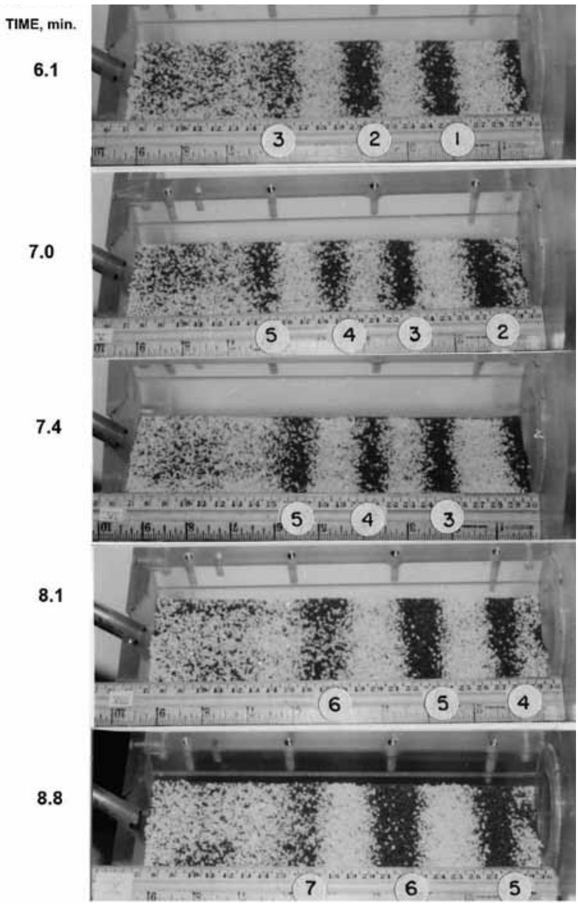

Fig. 11 A series of photographs for the continuous flow of a mixture of two dolomite components of different sizes: coarse of 10 × 14 mesh and fine of 28 × 35 mesh. Band numbers are marked on the drum edge.

These interesting results show that there is a delicate balance among the forces acting on the individual particles within the flowing charge. For example, the forces created as a result of the difference in size and those created as a result of the difference in specific gravity are balanced, in our case, only when dolomite (sp.gr. 2.9 and size 28 × 35 mesh) was flowing in equal volumes with hematite (sp.gr. 5.2 and size 14 × 20 mesh), but not otherwise.

The same banding effect is observed when two dolomite components of different particle sizes, 10 × 14 mesh and 28 × 35 mesh, are flowing through the rotating drum at a volume ratio of 1:1. A series of photographs was taken for this last case, the banded flow, and the bands are numbered and followed. In about 2.7 minutes, four pairs of bands were discharged. **Fig. 11** shows this sequence of bands and how they progress towards the exit end.

Minimizing the Segregation Tendency

Segregation in some non-homogeneous systems is desirable such as in balling drums, screening, particulate separation and cement kilns[33-38]. Because the exit ends of these units are fully opened and the drums are inclined towards the exit end, the hold up material is small (5-10% of the drum volume) and the mean residence time is short. In such cases, segregation takes place radially, and there is no chance for axial segregation. In fact segregation in such systems is essential and should be enhanced for size enlargement of the flowing charge, which is one of the required functions of these systems.

On the other hand, particulate segregation in most operations, carried out in rotating drums, is detrimental to the final product, and hence, should be eliminated or at least minimized. If a material is being roasted in a rotating drum and if there is radial segregation, particles in the segregated core may not have undergone reaction. Among the more common operations are pharmaceutical preparations, food for human and livestock, and all other processes that require homogenization of their constituents. In such cases, mixing aids are used to enhance the convective mechanism, shuffling the material axially and radially, and to minimize effect of the diffusion mechanism. In this paper, the results of two series of experiments that were carried out to minimize segregation of particulate systems flowing continuously through a rotating drum are discussed. The first series was designed to deal with homogenizing, mixing, a tracer flowing in a bulk of different physical properties, and the second series dealt with flowing systems with two major components different in their physical properties flowing at a ratio of 1:1 by volume. Thirty percent of the drum was filled with Lucite balls of diameter 2.54 cm, density 1.2 g/cm^3 and each weighing 10.3 grams, as mixing aids. **Fig. 12** presents the RTDs of various tracers different in their physical properties, density, particle shape, and surface roughness, flowing in dolomite bulk of the same particle size as the tracers, 35×48 mesh. **Fig. 13** shows the RTDs of hematite and dolomite flowing at the ratio of 1:1 by volume in the same drum using the same mixing aids as above. If we compare the RTDs in **Fig. 12** with those reported in **Fig. 7**, we realize that the presence of the mixing aids have almost eliminated the segregation tendency of the tracers flowing within the dolomite bulk regardless of their differences in the physical properties. This is an important finding in particulate mixing in vital processes where the degree of mixedness is critical, such as in mixing drug tracers in a bulk of the carrying material. Comparing the RTDs in **Fig. 9** and the drastic complications inside the drum, **Fig. 10**, with the RTDs in **Fig. 13**, one can appreciate that the complex particulate system of hematite and dolomite flowing in the rotating drum at a volume ratio of 1:1 has been thoroughly mixed by the presence of the mixing aids.

The preceding paragraph shows clearly that minimizing diffusion in particulate systems flowing in rotating drums is the key for minimizing segregation. The diffusion mechanism can be eliminated or minimized, as we have seen, by introducing a means of stirring agent, which enhances shuffling the particulates back and forth, radially and axially within the drum to produce a homogeneous product. Similar effects, if the conditions prevail, may be obtained by moistening the particulate material before being introduced to the mixer[7]. The moisture content will increase the formation of particulate clusters which can be shuffled and sheared with minimum diffusion and maximum dispersion[39]. This effect is quite

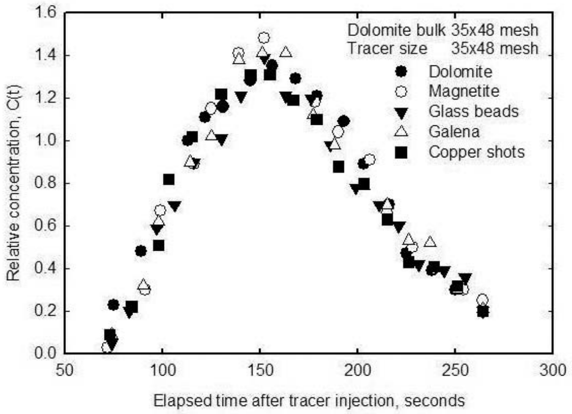

Fig. 12 Residence time distributions for various tracers different in their densities, shape, and surface roughness, flowing in a dolomite bulk of the same size as the tracers in presence of mixing aids.

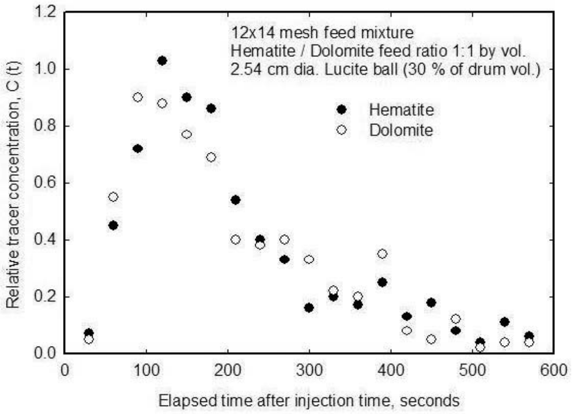

Fig. 13 Residence time distributions of hematite and dolomite flowing at a volume ratio of 1:1 in presence of mixing aids.

similar to that of added mixing aids in producing non-segregated product, which confirms the fact that the key to obtaining a homogeneous product is to eliminate or minimize diffusion of the individual particles within the flowing bulk.

Summary

All non-homogeneous particulate systems suffer mutual separation, segregation, among their constituents whenever these systems are energized, i.e., there is a relative motion among the moving particles. In the case of transporting such systems in rotary drums, the particulates are energized as a result of the drum rotation and the driving material head due to continuous feeding and discharging. This energizing causes relative motion among the particles axially and radially. Because the physical properties (size, density, shape, and/or surface roughness) of particles differ from one component to another, the resultant forces acting on the individual particles (frictional and gravitational forces) will be different from one component to the other. The pass through which particles move within the bulk will differ from one component to the other. The difference in acting forces, coupled with the phenomenon of natural perturbation, lead to regional concentration of one of the components pulling out from the flowing bulk. This is what is called segregation.

Segregation can be axial in nature, forming alternative bands of the flowing components, or radial, forming a core of one component and a shield from the other component.

Segregation may be eliminated or minimized by reducing the motion of single particles within the surrounding bulk, and enhancing the motion of particles in groups, i.e., reducing the diffusion mechanism and encouraging the convective motion (shuffling) associated with shear mechanism. These restrictions can be done by adding mixing aids to the flowing powders in the rotating drums or moistening the flowing material to produce homogeneous products.

REFERENCES

1) Hogg, R., Shoji, K., and Austin, L.G., (1974): Powder Technology, vol. 9, pp. 99-106.
2) Austin, L.G., Luckie, P.T. and Ateya, B.G., (1971): Cement and Concrete Research, vol. 1, pp. 241-248.
3) Karra, V.K. and Fuerstenau, D.W., (1977): International Journal of Mineral Processing, vol. 4, pp. 1-9.
4) Boating, A.A., (2008): Rotary kilns, Butterworth Heinemann, Pub., 368 p.
5) Sheehan, M.E,; Britton, P.F.; Schneider, P.A., (2005): Chemical Engineering Science, Vol. 60, No. 15, pp. 4171-4182.
6) Li, S.Q.; Chi, Y.; Li, I.-D; Yan, J. -H; Cen, K.-F., (2002): Powder Technology, Vol. 126, No. 3, pp. 228-240.
7) Li, H., (2005): Impact of cohesion forces on particle mixing and segregation Ph.D. dissertation, University of Pittsburg.
8) Hogg, R. and Fuerstenau, D.W., (1972): Powder Technology, vol. 6, No. 3, pp. 139-148.
9) Santomaso, A.; Olivi, M.; Canu, P., (2004): Chemical Engineering Science, Vol. 59, No. 16, pp. 3269-3280.
10) Hogg, R.,(2009): KONA Powder and Particle Journal No. 27, pp3-17.
11) Hogg, R., Cahn, D.S. Healy, T.W. and Fuerstenau, D.W., (1966), Chemical Engineering Science, vol. 21, pp. 1025-1037.
12) Hogg, R., (1971): Bulletin of College of Earth Sciences, Penn State University, vol. 40, No. 6, pp. 41-44.
13) Santomaso, A.; Olivi, M.; Canu, P., (2005): Powder Technology, Vol. 152, No. 1-3, pp. 41-51.
14) Shinbrot, T.; Zeggio, M.; Muzzio, F.J., (2001): Powder Technology, Vol. 116, No. 2-3, pp. 224-231.
15) Wegrzyn, M., (2004): Electronic Journal of Polish Agricultural Universities, vol. 7, No.2, 10 p.
16) Ingram, A., Seville, J.P K., Parker, D.J., Fan, X. and Forster, R.G., (2005), Powder Technology, vol. 158, No. 1-3, pp. 76-91.
17) Williams, J. C., (1968/1969): Powder Technology, vol. 2, pp. 13-20.
18) Williams J. C., (1963): Fuel Society Journal, vol. 14, pp. 29-34.
19) Eskin, D. and Kalman, H., (2000): Chemical Engineering and Processing, vol. 39, No. 6, pp. 539-545.
20) van Puyveld, D.R.; Young, B. R.; Wison, M.A.; Shmidt, S.J., (2000): Chmical Engineering Research and Design, Vol. 78, No. 4, pp. 643-650.
21) Ding, Y.L.; Forster, R.N. Seville, J.P.K.; Parker, D.J., (2001): Chemical Engineering Science, Vol. 56, No. 12, pp. 3737-3750.
22) Himmellblau, D.M., and Bischoff, K.B., (1968): Process Analysis and Simulation, Willey, New York.
23) Abouzeid, A.-Z. M. and D.W. Fuerstenau, D.W., (1982): J. Egyptian Society of Engineers, vol. 21, No. 3, pp. 52-60.
24) Abouzeid, A.-Z. M., (1989): Powder Handling and Processing, vol. 1, No. 2, pp. 173-177.
25) Swaroop, S.H.R.; Abouzeid, A.-Z. M., Fuerestenau, D. W., (1981): Powder Technology, Vol. 5, No. 5, pp. 253-260.
26) Boaleng, A.A., (2008): Rotary Kilns, Elsevier publisher, pp. 15-31.
27) Felix, G., Falk, V., and D'Ortona, U.,(2002): Powder Technology, vol. 128, pp. 314-319.
28) Wes, G.W.J., Drinkenburg, A.A.H., and Stemerding, S., (1976): Powder Tecnology, vol. 13, No. 2, pp. 177-184.

29) Abouzeid, A.-Z. M., Mika, T.S., Sastry, K.V.S., Fuerstenau, D.W., (1974): Powder Technology, vol. 10, pp. 273-285.
30) Abouzeid, A.-Z. M., (1973): Transport and mixing behavior of particulate solids through rotary drums, Ph.D. dissertation, University of California, Berkeley, California.
31) Abouzeid, A.-Z. M. and Fuerstenau, D.W., (1985): Powder and Bulk Solids Handling and Processing; Proceedings, Powder Advisory Center, London, pp. 711-721.
32) Venkataraman, K.S. and Fuerstenau, D.W., (1985): Powder and Bulk Solids Handling and Processing; Proceedings, Powder Advisory Center, London, pp. 704-710.
33) Abouzeid, A.-Z. M. and Fuerstenau, D.W., (1979): Powder Technology, vol. 23, pp. 261-269.
34) Sugimoto, M., (1981): Proceedings, International Symposium on Powder Technology, Japan, pp. 726-735.
35) Nakagawa, M., Furuuchi, M., Yamahata, M., and Gotoh, K., (1985): Powder Technology, vol. 44, pp. 195-203.
36) Shinohara, K., (1986), Powder Technology, vol. 48, pp. 151-160.
37) Furuuchi, M., and Nagakawa, M., Suzuki, M. Tsyumine, H., and Gotoh, K., (1978): Powder Technology, vol. 50, pp. 137-146.
38) Furuuchi, M., and Gotoh, K., (1988): Powder Tecnology, vol. 54, pp. 31-40.
39) Abouzeid, A.-Z. M. and Fuerstenau, D.W., (1972): I & EC Process Design & Development, vol.11, pp.296-301.

Author's short biography

Abdel-Zaher M. Abouzeid

Professor Abdel-Zaher M. Abouzeid received his Ph D in Mineral Processing and Extractive Metallurgy from the Department of Materials Science and Mineral Engineering, University of California, Berkeley, California, U S A (UCB) in 1973. He also got an M. S. in Mineral Technology from UCB, M. Sc. and B. Sc. in Mining Engineering from Cairo University, Egypt. Now, he is an Emeritus Professor of Mineral Processing in the Department of Mining, Faculty of Engineering, Cairo University, Egypt. His main fields of interest are Mineral Processing, Powder Technology, Comminution, Transport of materials in mineral processing units, Agglomeration of fine powders, and Environmental protection and preservation. His publications and presentations in the above fields exceed 100 articles. Dr. Abouzeid is a member of several professional organizations in Egypt and abroad.

Douglas W. Fuerstenau

Douglas W. Fuerstenau received his Sc.D. degree in metallurgy (mineral engineering) from MIT. After a period in industry working for Union Carbide Metals Co. and Kaiser Aluminum and Chemical Co., he joined the faculty of the Department of Materials Science and Engineering in the University of California at Berkeley in 1959, where he continues as a Professor in the Graduate School. He has been actively involved over the years in fundamental and applied research on processing minerals and particulate materials, including extensive research on interfacial phenomena in these systems. A member of the National Academy of Engineering since 1976, he was recently recognized as the 2006 recipient of the Particle Technology Forum Lifetime Achievement Award from AIChE.

Simultaneous Measurement of Particle Motion and Temperature in Two-Dimensional Fluidized Bed with Heat Transfer[†]

Takuya Tsuji*, Takuya Miyauchi, Satoshi Oh, Toshitsugu Tanaka
Department of Mechanical Engineering, Osaka University[1]

Abstract

Fluidized beds are widely used in industrial processes concerned with heat transfers. In the present study, a measurement technique based on the coupling between particle tracking velocimetry (PTV) and infrared thermography (IT) measurement is proposed. By using the technique, the motion and the temperature of individual particles and its relations with the characteristic flow structures formed in fluidized beds can be investigated simultaneously without disturbing the flow field. After careful preparations, the technique is applied to a two-dimensional gas-fluidized bed under a spouting condition and the motion and the temperature of individual particles influenced by the bubble occurrence are clearly observed.

Keywords: 2-D Fluidized bed, heat transfer, infrared thermography, particle tracking velocimetry, particle tracking, convection motion

1. Introduction

Fluidized beds are widely used in industrial processes concerned with heat transfer such as combustion, gasification, catalytic reaction and calcination. The heat transfer in fluidized beds is governed by several mechanisms. Solid particles in the beds are fluidized by injected gas flow and the gas goes through the small gaps between particles. When a temperature difference exists between gas and solid phases, the convective heat transfer appears. During a fluidization, dense particles have contacts with surrounding particles, walls and immersed objects such as a heat exchanger pipe. The conductive heat transfer occurs due to the direct contacts between solids. In applications of which operating temperature is high, the radiative heat transfer becomes also important. In actual fluidized bed systems, these elemental heat transfers do not work independently and its behavior is quite complex.

Due to its complexity and measurement difficulties, a numerical simulation model, which predicts the heat transfer phenomena in fluidized beds, has been desired. For the numerical analysis of fluidized beds, Lagrangian-Eulerian models are widely used (e.g., Tsuji et al., 1993; Hoomans et al., 1996 and Xu & Yu, 1997) and the models including heat transfers by several mechanisms are proposed as its extensions (Kaneko et al., 1999; Zhou et al., 2004a, 2004b; Sakurai et al., 2007; Zhao et al., 2009 and Zhou et al., 2009, 2010). Complex interactions between particles, gas flows and walls induce the formation of characteristic spontaneous flow structures such as bubbles in beds. Bubbles are far larger than the particle and have a larger rising velocity. Upward convective motion of particles is induced by the bubbles and the circulation and mixing of the particles are well enhanced in the beds accordingly. Each particle has finite volume and finite heat capacity and they can bring heat by its convective motions. The particle convection does not directly contribute to the heat exchange between two phases, however, as a result of convective motion, particles have contacts with other particles and gas flows that have different temperatures and exchanges heat. The heat transfer in fluidized beds cannot be discussed without the convective motion of individual particles induced by the characteristic spontaneous flow structures.

[†] Accepted: August 10, 2010

[1] 2-1 Yamada-oka Suita, Osaka 565-0871
* Corresponding author
TEL & FAX: 81 6 6879 7317
E-mail : tak@mech.eng.osaka-u.ac.jp

The characteristics of spontaneous flow structures have been one of main topics in the fluidized bed researches (e.g., Kunii & Levenspiel, 1991; Jackson, 2000). It is not our purpose to review all the results in this paper while a large number of theoretical and experimental studies exist. Comparing to that, studies that treat the convective motion of individual particles induced by spontaneous flow structures are relatively limited. Lin et al. (1985) investigated the motion of a particle in a fluidized bed by using a particle tracking facility they developed. A radioactive particle made of ^{46}Sc is used as a tracer. Particle tracking is performed by measuring gamma rays emitted from the tracer particle by using twelve photomultiplier detector tubes. Mostoufi & Chaouki (2001) also performed a particle tracking by using a ^{198}Au radioactive tracer particle. They investigated the diffusivity of particles to know the local mixing characteristics in a fluidized bed. Stein et al. (2000) measured a particle motion in three-dimensional gas fluidized bed by using positron emission particle tracking (PEPT) technique. In the study, a resin particle activated by the ion exchange with irradiated water was used as a tracer. A particle's trajectory in a bubbling fluidized bed was obtained for each run. It is also possible to obtain averaged flow fields by continuing these Lagrangian measurements for a long period. By using PEPT measurement technique, Hoomans et al. (2001) obtained a time-averaged particle velocity distribution for a two-dimensional bubbling gas-fluidized bed and Link et al. (2008) obtained RMS particle velocity distributions in addition to time-averages for a spout-fluid bed. In these measurements, the position of tracer particle cannot be determined in prior to the measurement and the accuracy of measurement depends on the probability of the tracer particle's occurrence at each position. These tracking techniques are non-invesive and provide important data for three-dimensional motion of individual particles. It greatly helps the understanding of convective and mixing motion of particles in the beds. However, by these techniques, it is difficult to track a large number of particles at once. The measurement by using these techniques is still insufficient to investigate the relation between the convective motion of individual particles and the characteristic flow structures such as bubbles of which behaviors are unstable and changing at every moment.

For the heat transfer characteristics of fluidized beds, large numbers of studies have been performed from the applicational point of view. The purpose of these studies is to obtain the heat transfer coefficient, h, of the whole bed and do not go into the detail of relations between heat transfer and flow structures formed inside of the beds (Kunii & Levenspiel, 1991). Studies that measure temperature distributions formed in beds also exist. In these studies, temperature distributions were obtained by inserting the single-point probe such as a thermocouple into a certain position of beds. During a measurement, inserted probes are expected to have convective heat transfers with surrounding gas flows and conductive heat transfers with solids under contact. It is difficult to know the temperature of individual particles by these technique and the studies concerned with the temperature of particles under a fluidization do not exist as much as we know.

For the better understandings of heat transfers in fluidized beds and further improvement of numerical models, it is important to know the relations between spontaneous flow structures, convective motions of individual particles and heat transfers. In the present study, a simultaneous measurement technique based on the coupling between particle tracking velocimetry (PTV) and infrared thermography (IT) measurement is presented. By using the technique, the motion and the temperature of individual particles can be directly observed and its relations with the flow structures formed in beds are investigated without disturbing the flow field.

In section 2, the measurement technique is presented. In section 3 and 4, the technique is applied to a two-dimensional Labo-scale fluidized bed under a spouting condition. In section 5, conclusions of the paper are shown.

2. Measurement Techniques

2. 1 Particle tracking velocimetry (PTV)

PTV is a measurement technique of particle velocity based on the analysis of video images. In principle, the velocity of a particle, $u_b = \Delta x / \Delta t$, is obtained by measuring the displacement of the particle Δx from two sequential images that have an interval Δx PTV is developed mainly in the field of fluid velocity measurement in which tracer particles that have an enough response to a local flow change are tracked. A number of algorithms have been developed to find a particle uniquely from sequential images. In fluidized bed, particles have contacts with other particles and walls very frequently and the direction and the magnitude of particle velocity can change drastically. The majority of PTV algorithms based on the high autocorrelation of tracer particles are not for the measurement in fluidized bed. In the present study, nearest-neighbor method is utilized. In the nearest-neighbor method, the frame rate of camera is adjusted to make the displacement of particle in two sequential images should be less than the particle radius. By enforcing this constraint, a perfect matching of particle image is possible even if a sudden change of particle velocity takes place.

2. 2 Procedure of PTV based on nearest-neighbor method

In this section, the procedure to obtain a particle velocity distribution based on the nearest-neighbor method is shown. We postulate the usage of digital video camera in the following explanation. It is also assumed that the size of pixel is sufficiently small comparing to the size of particle in images.

Due to the device characteristics of camera mainly, noises that can be a source of unphysical velocity vectors are included in original movie images in actual measurements. As the first step, Laplacian and smoothing filters (The Visualization Society of Japan (ed.), 2002) are applied to original images to diminish these noises. In the present PTV measurement, the position of particles at a certain time step is determined by estimating a correlation function between an image at the time step and a standard particle image. As the second step, a particle is chosen from a series of video images and its brightness distribution is stored as a standard particle image. We pay attention to the lighting, however, it is difficult to achieve the uniformity and the brightness distribution of particle image can vary depending on its location in actual. In the present study, three particles existing in different positions are chosen as standard particle images. As the third step, the distributions of correlation function between a video image and the standard particle images are obtained. The fourth step is to find the central coordinate of each particle. The pixels that show the highest correlation is expected to include the center of particles. At this step, a correlation function distribution is not separated for each particle. To find the center pixel of each particle, sub-areas that include one center pixel and surrounding pixels are extracted from a correlation function distribution. In the present study, the extraction is performed by using a threshold method. A group of continuous pixels of which correlation function is larger than 0.85 and is expected to include the particle center and extracted as a sub-area. By searching the pixel, which has the peak value in each pixel sub-area, the center coordinate of each particle is obtained in the pixel-level accuracy. In this study, sub-pixel analysis (The Visualization Society of Japan (ed.), 2002) is also performed and the coordinate of the particle in sub-pixel level accuracy is obtained. In the nearest-neighbor method, the particles having the closest coordinates in two sequential images are the same one because the displacement is restricted to be less than the particle radius. The velocity of a particle is obtained by estimating the displacement Δx in the interval Δt, the temporal-development of particle velocity distribution is obtained by repeating the operation for all sequential images. As we discussed in section 4, it is also possible to obtain the trajectory of particles by using the PTV. The present measurement is purely two-dimensional and only particles of which coordinate is detectable from images are the object of measurement. The tracking of particles is terminated when the overlap of particle images occurs due to its in-depth motions while it is recommenced whenever the detection of particle coordinate can be performed again.

The accuracy of particle displacement measurement is most influential for the overall accuracy of present PTV measurement. The accuracy of displacement measurement of the present measurement system was examined in previous study (Oh et al., 2010). Pre-defined particle displacements were measured by the present PTV along with a CCD laser displacement sensor (LK-G35, Keyence Corporation). From the examination study using a particle with 3.14 mm diameter, we confirmed that the RMS error fraction becomes 100 % at 0.02 mm and 1.27 % at 1.57 mm which corresponds to the particle radius and the maximum displacement allowed in the nearest-neighbor method, respectively.

2.3 Temperature measurement by infrared thermography (IT)

Particle temperature is measured by infrared thermography (IT) technique. An IT camera can detect infrared rays emitted from the surface of objects such as a solid particle. The energy of infrared ray is theoretically related to the temperature of the object surface as

$$W = e\sigma T^4 \quad (1)$$

where W is the infrared energy, e is the emissivity, T is the surface temperature and σ (= 5.67 x 10^{-8} W/$\mathrm{m^2K^4}$) is the Stefan-Boltzmann constant. The emissivity is specific to the material of object and we can estimate the temperature of object by measuring the infrared energy.

If the surface of object is polished, infrared rays from surroundings are reflected on the surface of object and it will lead misinterpretations of temperature. This is also true in-between particles. The infrared rays emitted from particles have reflections on the surface of neighboring particles. This results in multiple reflections of infrared rays on all particles' surface and make the quantitative evaluation of particle temperature difficult (Sakurai et al., 2007). In this study, to reduce the reflection effect on particle surface, all particles are coated with black body paint (THI-1B, TASCO JAPAN) as shown in **Fig. 1**. The catalog value of e for the black body material we introduced is 0.94. From a preliminary study, however, we confirmed that the emissivity varies depending on the temperature as shown in **Fig. 2**. Both PTV and IT are optical measurement techniques and only optically accessible particles are the object of measurement. To enable the observation of particle motion in a fluidized bed, an observation window of container should be made of transparent materials such as glass and acrylic resin. In case of the IT measurement, a special attention should be paid because transmission characteristics of infrared rays change depending on material. In the study, spinel glass ($MgAl_2O_4$) which exhibits good transmission characteristics in the visible light, the near-infrared and the mid-infrared wavelength ranges is utilized for the observation window. The transmission rate of spinel is far better than the other materials while it is not perfect and the decay of infrared energy still exists. Along with the correction for the temperature-dependency of emissivity, the results of temperature measurement appear in this paper are corrected using the following equation.

$$T = 1.0466T_{e=0.94} + 8.0873 \qquad (2)$$

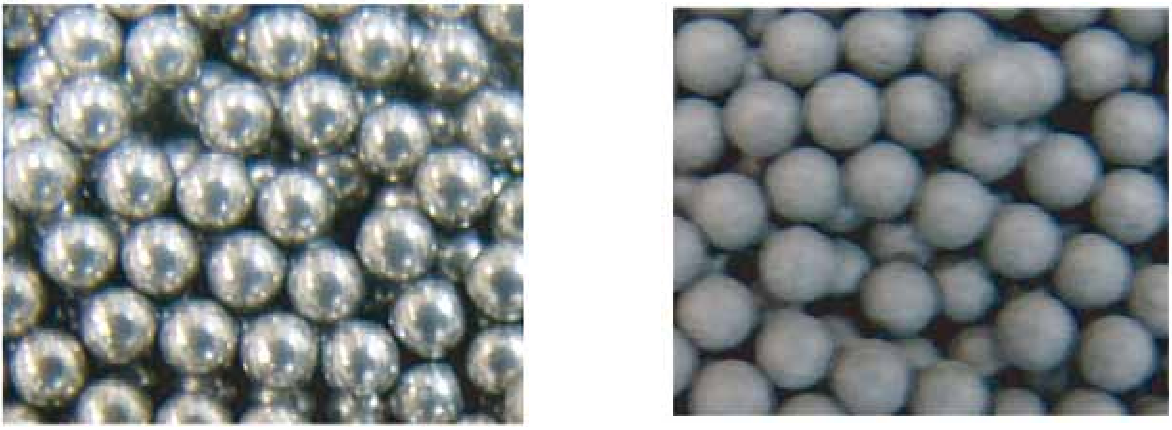

(a) Uncoated Aluminium particle

(b) Coated Aluminium particle

Fig. 1 Coating of particle by black body paint.

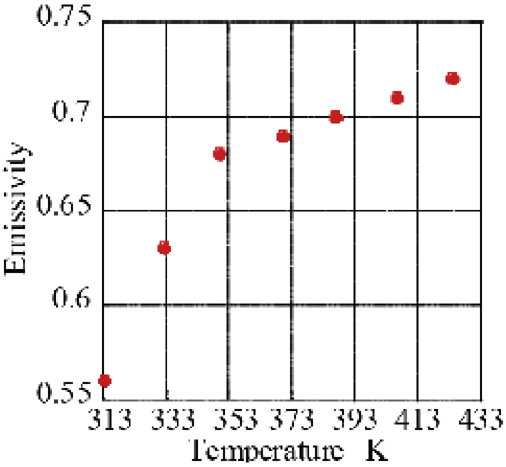

Fig. 2 Temperature dependency of emissivity.

where $T_{e=0.94}$ is the temperature measured by the IT camera introduced in section 3 and T is the corrected temperature. This correction equation is obtained by comparing the results of IT measurement performed through a spinel by keeping $e = 0.94$ and that by a thermocouple.

3. Experimental Setup

The present measurement technique is applied to a Labo-scale fluidized bed under a spouting condition. The experimental setup is shown in **Fig. 3**. This is a specially designed apparatus for the measurement of fluidized bed with heat transfer. The vessel has 400 mm height, 76 mm wide and 21 mm depth. This is a two-dimensional fluidized bed because the depth of the bed is restricted comparing to other dimensions. A slit nozzle with a cross-section 11 mm × 21 mm is installed at the bottom center of the vessel as shown in **Fig. 4**. The observation window is made of spinel. An air flow at 292 K generated by a compressor is injected from the slit nozzle. The flow rate is controlled by the regular and measured by using the laminar flow meter (LEF50-B, Tsukasa Sokken Co., Ltd.). Spherical Aluminium particles with the average diameter of 2.0 mm (Amatsuji steel ball MFG Co., Ltd.) are used. The measurement of temperature distributions existing inside of particles under fluidization is challenging and beyond of our study. It is known that the temperature of a particle is almost uniform if the size of particle is small or the thermal conductivity of the particle is large enough. Biot number, $Bi = hd_p/k_p$, is an index of this assumption where h is the heat transfer coefficient, d_p the particle diameter and k_p the thermal conductivity of the particle. In case of the Aluminium particles we used in the study, $Bi < 0.1$ and the assumption is almost valid. After the coating, particle's average diameter becomes 2.1 mm. Due to the existence of coating layer on the particle's surface, the delay of heat transfer was concerned. In our preliminary study, we confirmed that the effect of coating layer is almost negligible in the present condition. In prior to the measurement, the particles are heated up by using an electric oven (DX400, Yamato Scientific Co., Ltd.). After keeping its temperature to 423 K for 20 min in the oven, the particles are installed into the vessel. Measurements are started as soon as the installation of particles is finished because the particles loose heat due to the temperature difference with the vessel walls and the atmosphere. To perform measurements in a fluidized state, superficial velocity is set to u_f =1.50 m/s while the minimum fluidization velocity, u_{mf}, is 1.09 m/s in the present condition. The initial bed height is set to 55 mm. The effect of radiative heat transfer is small and negligible in the present condition.

Both IT and PTV are measurement techniques based on the analysis of video images and it is preferred to obtain particle motion and its temperature from a series of video images acquired by a single camera. It is not possible to detect infrared rays using a conventional high-speed camera and it is required to perform PTV for IT video images in the present case. As we discussed in section 2.1 and 2.2, however, the constraint exists on the frame rate of video recording in the case of nearest-neighbor method. In this study, two cameras are used simulta-

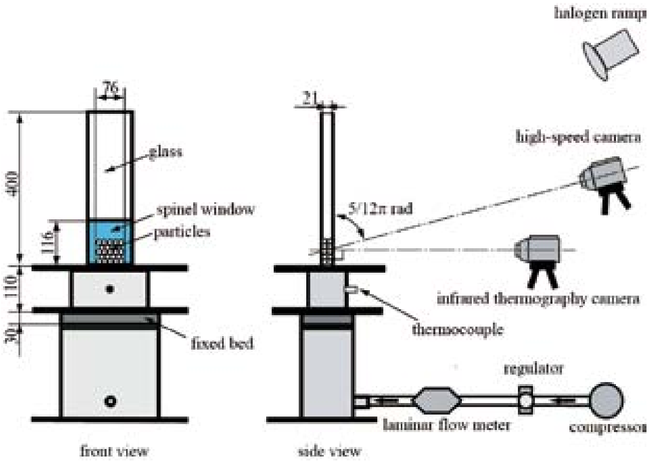

Fig. 3 Experimental setup.

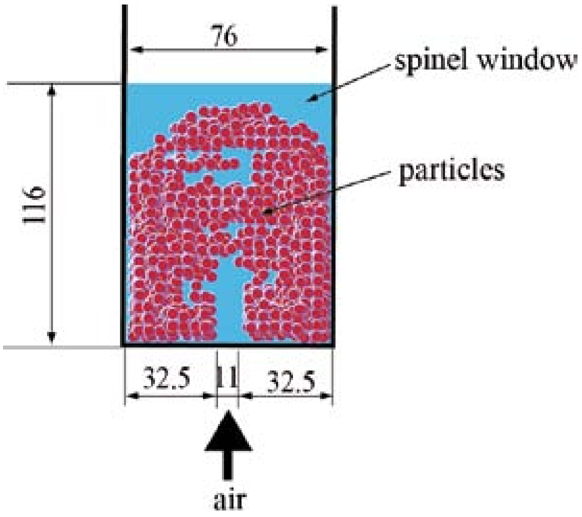

Fig. 4 Spouting condition.

neously because the temporal resolution of currently available IT cameras is not sufficient for the PTV based on the nearest-neighbor method. A high-speed video camera (FASTCAM ultima1024, Photoron, Ltd.) is used for the velocity and trajectory measurements by PTV and an infrared thermography video camera (TVS-8502, NEC Avio Infrared Technologies Co., Ltd.) is for the temperature measurement. Specifications of cameras are shown in **Table 1**. In the measurement, the frame rate of high-speed camera is set to 500 fps to meet the condition of the nearest-neighbor method in the present condition. For the IT camera, it is set to 120 fps, which is the highest frame rate of the camera. In the present setting, the resolutions of high-speed and IT cameras are 0.153 and 0.332 mm/pixel, respectively. The ratios between particle diameter and pixel size in video images, d_p/Δ_{pixel}, become 13.73 in case of the high-speed camera and 6.33 in case of the IT camera.

To avoid the physical interference between two cameras, measurements are performed from different angles as shown in **Fig. 3**. The IT camera is installed in front of the bed as its optical axis is perpendicular to the front wall of the bed. The high-speed camera is installed in an upper position of the IT camera. The angle between its optical axis and the bed wall is $5/12\pi$ rad. Measurements are performed for 8.1 sec after fluidization is started.

4. Results and Discussion

Fig. 5 (a), (b) show the temporal developments of particle motion and temperature just after the fluidization is started ($t-t_0$ = 0.05 to 0.40 sec) and after several seconds is passed (5.95 to 6.30 sec), respectively. t shows the time and t_0 the time when the measurement is started. In the figures, particle velocity distributions obtained by PTV are superimposed on IT images. A typical flow pattern under a spouting condition is observed in **Fig. 5 (a), (b)**. The formation of bubble in the region above the nozzle inlet is clearly confirmed at 0.15 and 0.20 sec in **Fig. 5 (a)** and at 6.05 and 6.10 sec in **Fig. 5 (b).** During the fluidization, the particle layer is divided into fluidized and unfluidized regions as schematically shown in **Fig. 6**. The motion of particles is active in the fluidized region. Bubbles go through the particle layer intermittently and the particles existing in the region above the nozzle inlet are convected upward (0.15 sec in **Fig. 5** (a) and 6.05 sec in **Fig. 5 (b)**). After reaching the region near the free surface of particle layer, their behaviors turn to lateral and downward motions (0.20 sec in **Fig. 5 (a)** and 6.10 sec in **Fig. 5 (b)**). The process is repeated and the intermittent circulation of particle flow is formed in the fluidized region. In contrast, the motion of particles is small in the unfluidized regions existing near lower corners.

We can recognize the temperature of individual particles from **Fig. 5 (a), (b).** As soon as the particles are installed, conductive heat transfers with container walls are started and the temperature of particles contacting with the front wall decreases to 363-373 K when the observation is started. The decrease of temperature is more apparent for the particles contacting with both front and side walls, it becomes

Table 1 Specifications of cameras

camera	**high-speed camera** **(FASTCAM ultima1024, Photoron, Ltd.)**
maximum frame rate	1000 fps
maximum pixels	1024 × 1024
rens	NIKKOR 50 mm, f=1.2 (Nikon Corp.)

camera	**infrared thermography camera** **(TVS-8502, NEC Avio Infrared Technologies Co., Ltd.)**
detector	InSb focal plane array
measurable temperature range	233-1173 K
resolution	less than 0.025 K
accuracy of measurement	± 2 K or ± 2 % of reading, whichever is greater
detectable wave length range	3.5-4.1, 4.5-5.1 μm
maximum frame rate	120 fps
thermal image pixels	256 × 236
rens	standard rens, 30 mm

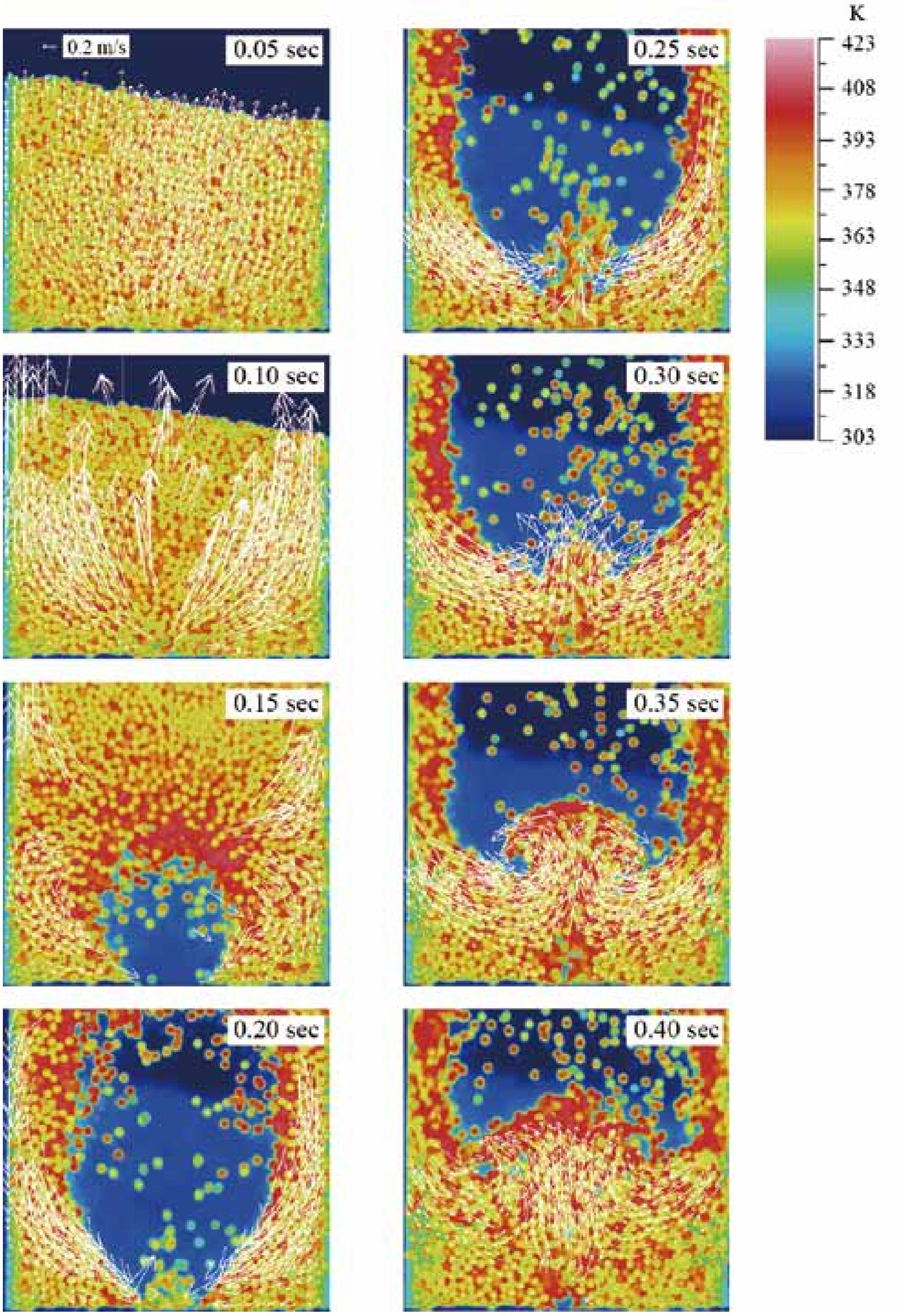

(a) t-t_0= 0.05-0.40 sec

Fig. 5 (a) Temporal development of particle motion and temperature.

under 360 K as observed at 0.05 sec in **Fig. 5 (a).** In the region just above the gas inlet, the relative velocity and relative temperature between gas and particles should be large because a cold air flow is injected into the bed consisted from hot particles. Form the point of view of convective heat transfer, the temperature of particles in the fluidized region should be decreased faster comparing to that in the unfluidized region. **Fig. 5 (a), (b)** give contradicted expressions for us, that is the particle temperature seems higher in the fluidized region and lower in the unfluidized region. The similar tendency is also confirmed in the measurement for a long period shown in **Fig. 7**. It is noted that this is the result from $t-t_0$ =0.05 to 7.05 sec and the motion of each bubble is not captured because it is depicted every 1.00 sec while it is 0.05 sec in **Fig. 5**. From **Fig. 7**, we can confirm the decrease of overall temperature in the bed while the particle

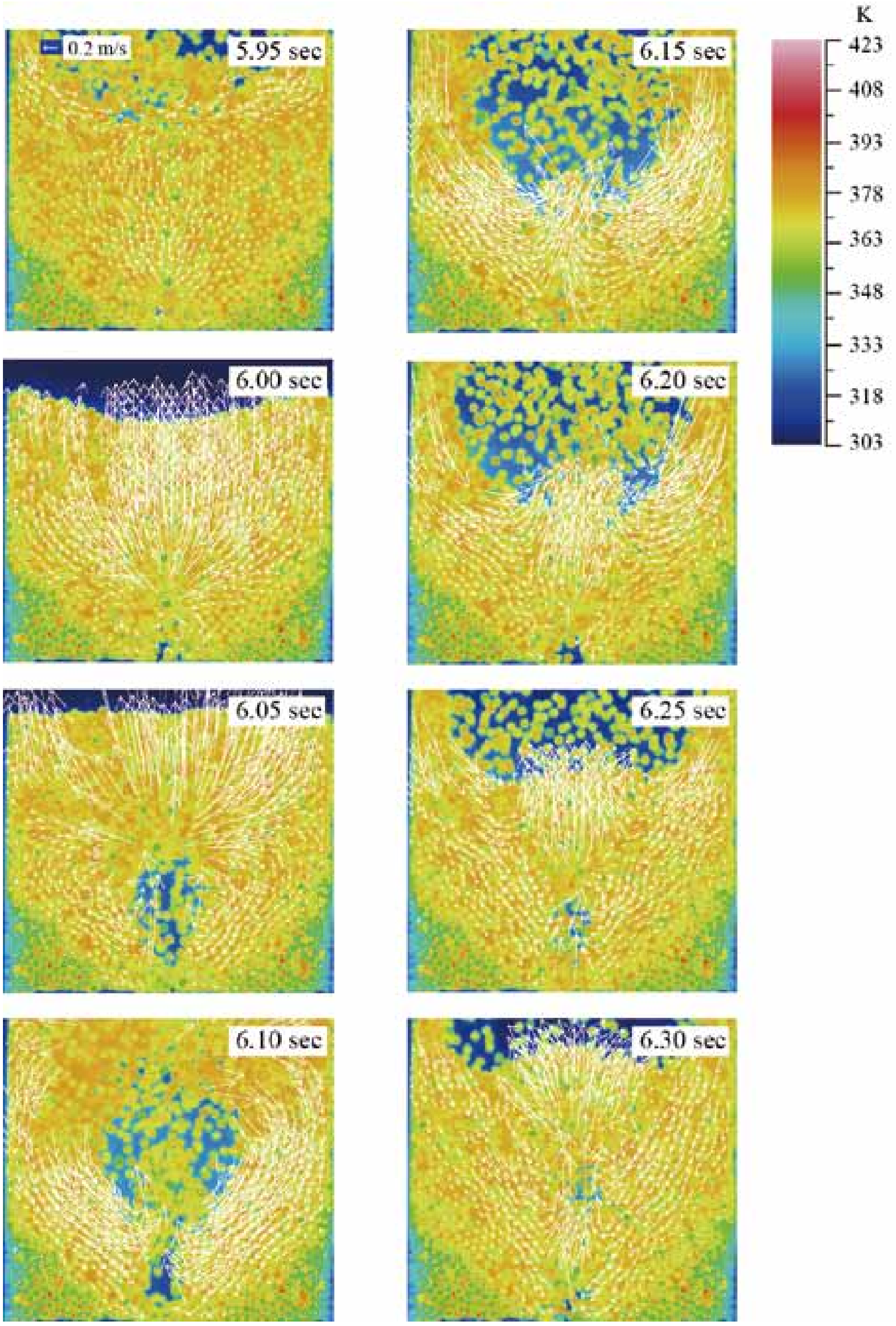

(b) t-t_0= 5.95-6.30 sec

Fig. 5 (b) Temporal development of particle motion and temperature (continued).

temperature seems relatively higher in the fluidized region. We expect this is due to the in-depth motion of particles. The depth of the bed is 21 mm, which is equivalent to 10 d_p of the coated particle, and three-dimensional motions and arrangements of particles are allowed. Before the fluidization, the particles existing internally do not have direct contacts with the container walls and the decreasing of temperature is relatively small. In the fluidized region, the motion of particles is active due to the bubble occurrence and the three-dimensional motion of particles is enhanced. As a result of that, the particles existing in the internal region and keeping higher temperature come out to the front. Comparing to that, the motion of particles existing in the unfluidized region are very small and the particles that keep touching with front and side walls loose more heat.

Fig. 8 shows typical results of particle tracking

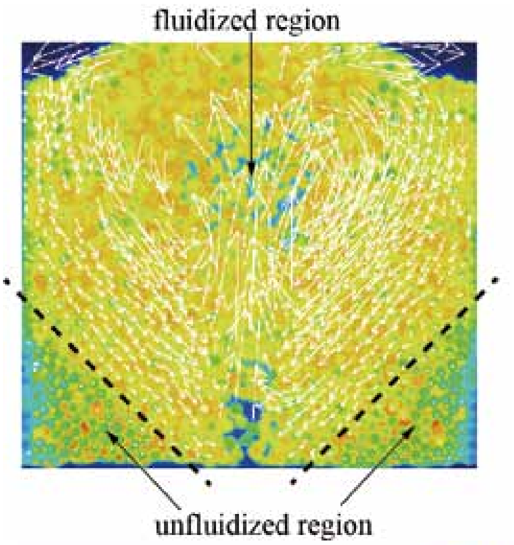

Fig. 6 Fluidized and unfluidized regions. The image is obtained at $t-t_0$=6.9 sec.

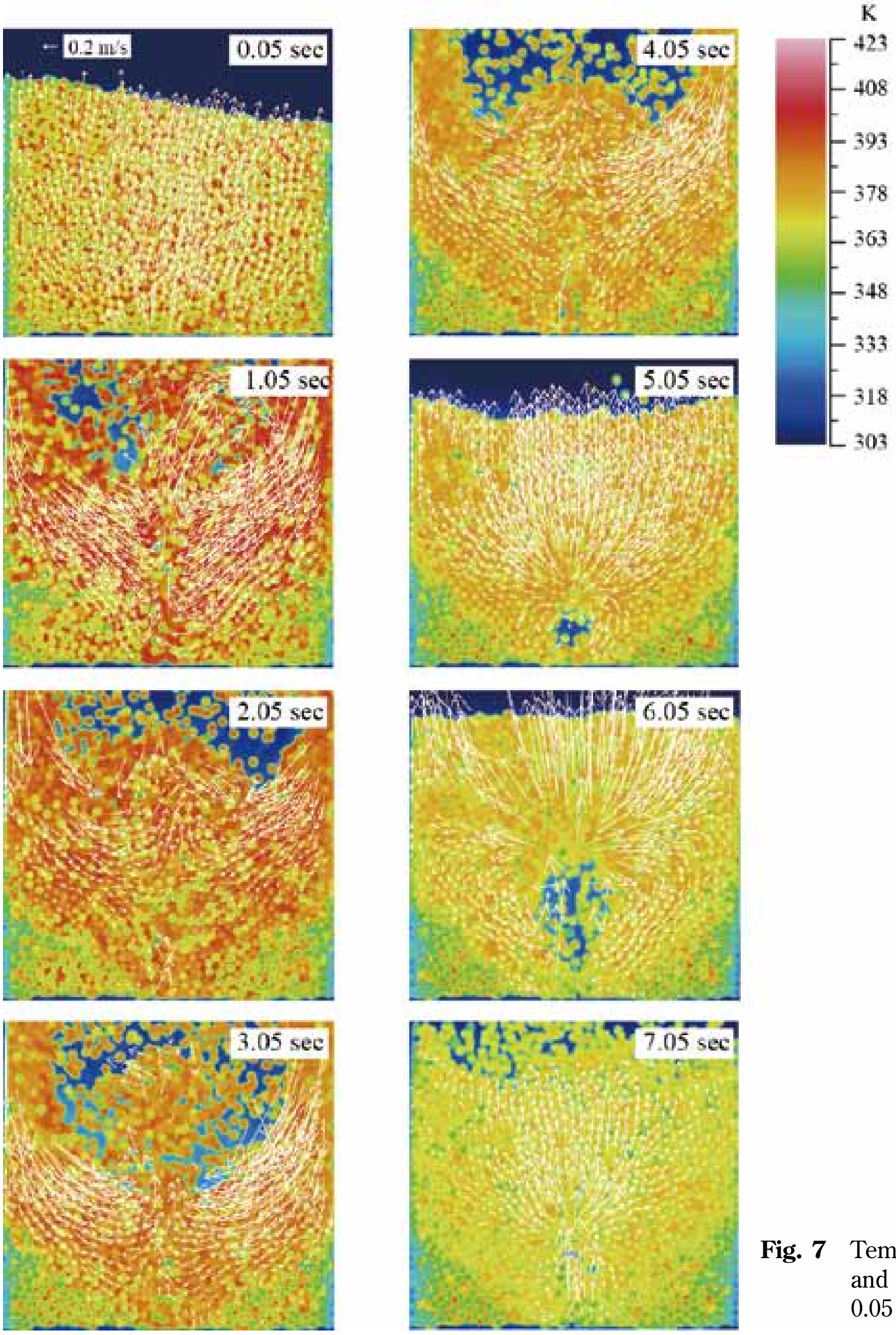

Fig. 7 Temporal development of particle motion and temperature for a long period ($t-t_0$= 0.05 to 7.05 sec).

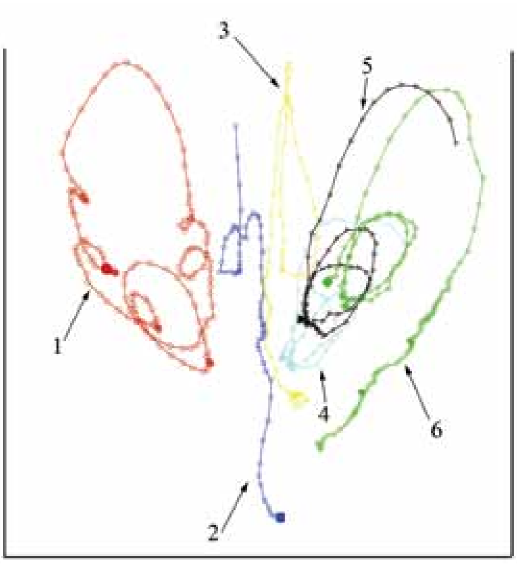

Fig. 8 Trajectories of particles. All tracking are started at $t-t_0$= 3.85 sec. Filled large symbols show the starting points of tracking. Open symbols show the position of particles at every 0.01 sec after the tracking is started.

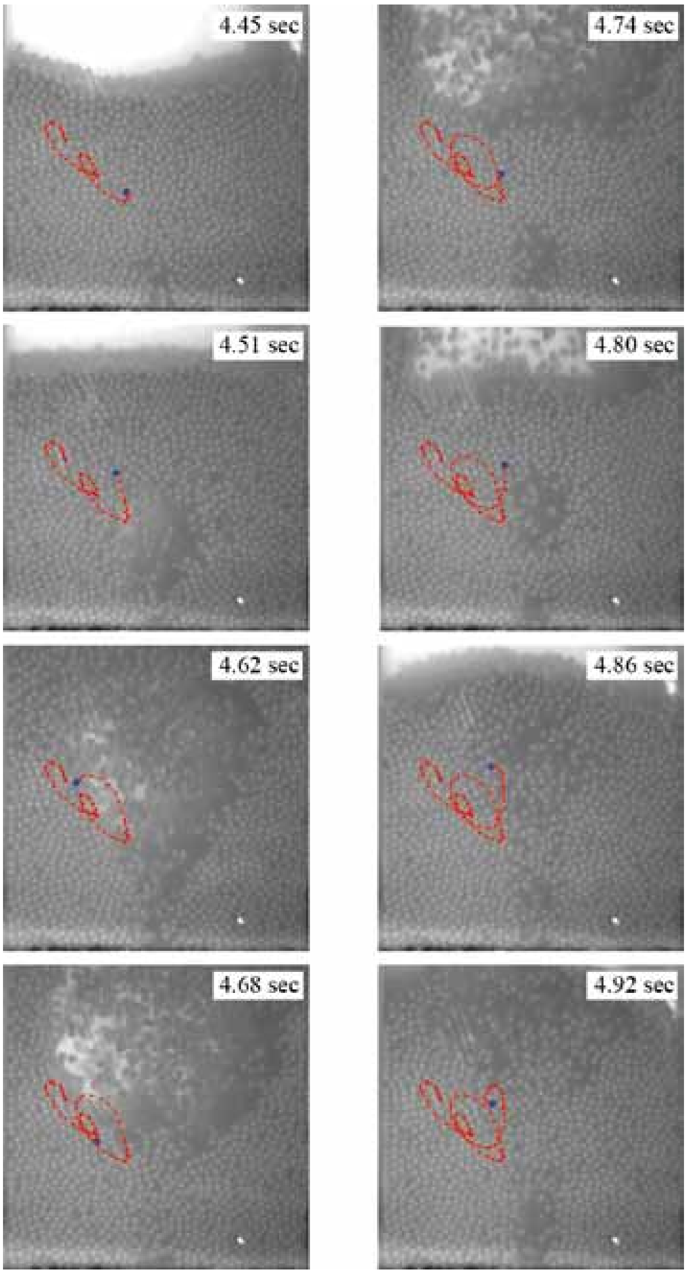

Fig. 9 Trajectory of particle 1 appeared in **Fig. 8** and its relations with characteristic flow structures ($t-t_0$=4.45 to 4.92 sec).

by the PTV, it is possible to track large numbers of particles at the same time. All trajectories shown in **Fig. 8** are from $t-t_0$=3.85 sec. This is a purely two-dimensional measurement and the tracking is terminated when the coordinate of a particle is not detectable due to the overlap of particle images and the length of tracking differs depending on the particles in **Fig. 8**. In the figure, the filled large symbols show the starting positions of tracking and the open symbols show its locations at every 0.01 sec. From **Fig. 8**, we can confirm that the motion of particles differs depending on its initial positions. In general, the particles existing in the regions slightly deviated from the bed center (particle 1, 4, 5 and 6) have circulation patterns. The motion of particles is not steady and the acceleration and the deacceleration of particle are repeated. In the PTV measurement, it is also possible to investigate the relation between the motion of individual particles and the flow structure changing at every moment. **Fig. 9** shows the results of particle tracking along with particle images obtained by the high-speed camera. Only results of particle 1 from $t-t_0$= 4.45 to 4.92 sec are shown here. The particle is convected upward along with a bubble occurrence at $t-t_0$=4.51 and 4.62 sec. The particle’s movement becomes smaller and tends to deposit in the layer at $t-t_0$=4.68 sec while it is reactivated again by the occurrence of next bubble ($t-t_0$=4.74 to 4.86 sec). The process is repeated and we obtained the trajectories shown in **Fig. 8** as a result.

5. Conclusions

A simultaneous measurement technique based on the coupling between particle tracking velocimetry (PTV) and infrared thermography (IT) measurement was presented in the paper. By using the technique, it is possible to obtain the motion and the temperature of particles in fluidized beds. After the careful preparations, the technique was applied to a Labo-scale two-dimensional fluidized bed under a spouting condition and the following conclusions are obtained:

(1) The motion of particle is obtained by PTV based on the correlation of particle images. By using the nearest-neighbor method, it is possible to measure the velocity of particles that have contacts with surrounding particles and walls frequently in fluidized beds. Unlike the techniques such as particle image velocimetry (PIV), the measurement is performed in the particle-level and the motion of individual particles induced by the characteristic flow structure such as bubbles is observable.

(2) It is possible to track a number of particles at once and know the relations between Lagrangian particle motions and flow field at each instance.

(3) Temperature measurement of particles based on the infrared thermography technique is beneficial, however, it is required to pay close attention to its calibration for quantitative measurements.

(4) The combined method between PTV and IT is a unique measurement technique which provides the motion and the temperature of individual particles in fluidized beds simultaneously. It is powerful to have deeper understandings on the heat transfers in fluidized beds.

(5) The flow field is clearly divided into fluidized and unfluidized regions in a two-dimensional fluidized bed under a spouting condition. The motion of particles in the fluidized region is largely influenced by the behavior of bubbles. The temperature of particles in the fluidized region seems relatively higher comparing to that in the unfluidized region due to the three-dimensional active motion of particles in the fluidized region.

For heat transfer problems in fluidized beds, further quantitative studies using the technique developed in the present study will be performed.

Acknowledgement

This study is partially supported by New Energy and Industrial Technology Development Organization (NEDO) and we would like to show our acknowledgements.

References

Hoomans, B. P. B.; Kuipers, J. A. M.; Briels, W. J. and van Swaaij, W. P. M. (1996): Discrete Particle Simulation of Bubble and Slug Formation in a Two-Dimensional Gas-Fluidized Bed, Chemical Engineering Science, Vol.51, pp. 99-108.

Hoomans, B. P. B.; Kuipers, J. A. M.; Salleh, M. A. M.; Stein, M. and Seville J. P. K. (2001): Experimental Validation of Granular Dynamics Simulations of Gas-Fluidised Beds with Homogenous In-Flow Conditions Using Positron Emission Particle Tracking, Powder Technology, Vol.116, pp.166-177.

Jackson, R. (2000): “The Dynamics of Fluidized Particles”, Cambridge University Press, Cambridge, U. K.

Kaneko, Y.; Shiojima, T. and Horio, M. (1999): DEM Simulation of Fluidized Beds for Gas-Phase Olefin Polymerization, Chemical Engineering Science, Vol.54, pp.5809-5821.

Kunii, D. and Levenspiel, O. (1991): “Fluidized Engineering”, 2nd ed., Butterworth-Heinemann, Newton, U. S.

A.

Lin, J. S.; Chen, M. M. and Chao, B. T. (1985): A Novel Radioactive Particle Tracking Facility For Measurement of Solids Motion in Gas-Fluidized Beds, AIChE Journal, Vol.31, pp.465-473.

Link, J. M.; Deen, N. G.; Kuipers, J. A. M.; Fan, X.; Ingram, A.; Parker, D. J.; Wood, J. and Seville, J. P. K. (2008): PEPT and Discrete Particle Simulation Study of Spout-Fluid Bed Regimes, AIChE Journal, Vol.54, pp.1189-1202.

Mostoufi, N. and Chaouki, J. (2001): Local Solid Mixing in Gas-Solid Fluidized Beds, Powder Technology, Vol.114, pp.23-31.

Oh, S.; Yoshikawa, K.; Tsuji, T.; Kawaguchi, T. and Tanaka, T. (2010): Measurement of Velocity Field of Particles in a Two-Dimensional Spouted-Bed by Particle Tracking Velocimetry, Proceedings of 6th World Congress on Particle Technology, CD-ROM VHH1000518.

Sakurai, T.; Minami, T.; Kawaguchi, T.; Tanaka, T.; Tsuji T. and Tsuji, Y. (2007): DEM Simulation and Infrared Thermography Measurement of Fluidized Bed with Heat Transfer, Proceedings of 6th International Conference on Multiphase Flow, CD-ROM No.S2_Fri_A_62.

Stein, M.; Ding Y. L.; Seville, J. P. K.; Parker, D. J. (2000): Solids Motion in Bubbling Gas Fluidised Beds, Chemical Engineering Science, Vol.55, pp.5291-5300.

The Visualization Society of Japan (ed.) (2002) : "Handbook of Particle Image Velocimetry", Morikita Publishing, Tokyo, Japan (In Japanese).

Tsuji, Y.; Kawaguchi, T. and Tanaka, T. (1993): Discrete Particle Simulation of Two-dimensional Fluidized Bed, Powder Technology, Vol.77, pp.79-87.

Xu, B.H. and Yu, A.B. (1997): Numerical Simulation of the Gas-Solid Flow in a Fluidized Bed by Combining Discrete Particle Method with Computational Fluid Dynamics, Chemical Engineering Science, Vol.52, pp.2785-2809.

Zhao, Y.; Jiang, M.; Liu, Y. and Zheng, J. (2009): Particle-Scale Simulation of the Flow and Heat Transfer Behaviors in Fluidized Bed with Immersed Tube, AIChE Journal, Vol.55, pp.3109-3124.

Zhou, H.; Flamant, G. and Gauthier, D. (2004a): DEM-LES of Coal Combustion in Bubbling Fluidized Bed. Part Ⅰ: Gas-Particle Turbulent Flow Structure, Chemical Engineering Science, Vol.59, pp.4193-4203.

Zhou, H.; Flamant, G. and Gauthier, D. (2004b): DEM-LES of Coal Combustion in Bubbling Fluidized Bed. Part Ⅱ: Coal Combustion at the Particle Level, Chemical Engineering Science, Vol.59, pp.4205-4215.

Zhou, Z. Y.; Yu, A. B. and Zulli, P. (2009): Particle Scale Study of Heat Transfer in Packed and Bubbling Fluidized Beds, AIChE Journal, Vol.55, No.4, pp.868-884.

Zhou, Z. Y.; Yu, A. B. and Zulli, P. (2010): A new Computational Method for Studying Heat Transfer in Fluid Bed Reactors, Powder Technology, Vol.197, pp.102-110.

Author's short biography

Takuya Tsuji

Dr. Takuya Tsuji is an associate professor of Mechanical Engineering, Osaka University. He obtained his Ph.D. in Energy Engineering from Kyushu University, Japan and joined the group of Prof. Toshitsugu Tanaka in Osaka University in 2004. From 2009, he is also occupying a position in an industry-academia collaboration laboratory funded by Komatsu Ltd. His research focuses on the dynamics of particle-laden flows and granular flows and he is engaged in numerical modeling / simulation and experimental studies at several different scales.

Takuya Miyauchi

Mr. Takuya Miyauchi graduated from Osaka University in 2010 and now he is a graduate student in Department of Mechanical Engineering, Graduate School of Engineering, Osaka University. He studies particle behaviors in two-dimensional fluidized bed by using Particle Tracking Velocimetry (PTV) technique and Infrared Thermography technique.

Satoshi Oh

Mr. Satoshi Oh graduated from Osaka University in 2009 and now he is a graduate student in Department of Mechanical Engineering, Graduate School of Engineering, Osaka University. He studies particle behaviors in two-dimensional fluidized bed by using Particle Tracking Velocimetry (PTV) technique.

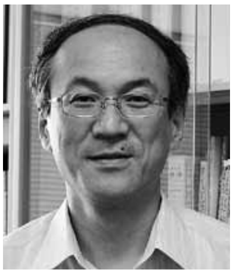

Toshitsugu Tanaka

Dr. Toshitsugu Tanaka graduated from Osaka University in 1982, and from the graduate school of Osaka University in 1984. He received the Ph.D. degree of Engineering from Osaka University in 1994. He became a Research Associate at Osaka University in 1984 and an Associate Professor at Osaka University in 1996. Currently, he is a Professor in the Department of Mechanical Engineering of Osaka University since 2003.

Probing Shear Stress Distribution within Single Particle Scale inside Particulate Packing[†]

S. Joseph Antony[1*] **and David Chapman**[2]
Institute of Particle Science and Engineering, University of Leeds[1]
United Biscuits[2]

Abstract

Studies have been performed to understand the nature of stress distribution within birefringent sensor particles embedded inside a granular bed under axial compression loading. Both the variation of the maximum shear stress and the direction of the major principal stress within single particle scale are analysed with respect to the proximity of particles to the wall boundaries of the compression chamber. The study shows that for an increase in the loading intensity, multiple interactions of contacts result in non-homogeneous distribution of maximum shear stress within sensor particles. The ability of the particles to sustain maximum shear stress depends on how closely these reside with respect to wall boundaries. These results imply that the applicability of present contact interaction laws used in advanced simulation methods such as the Discrete Element Method (DEM) for modelling the mechanical behaviour of micro and nano particulate assemblies could be limited and needs to be revised. This is because DEM modelling is normally based on the assumption that the interaction behaviour of a given particle contact is independent of what happens at its neighbouring contacts. Though further studies are required, the current research is a step towards attaining a clear understanding of the mechanical response of particulate materials under industrial process loading conditions which is rather complex as of now.

Keywords: Particulate mechanics, contact mechanics, inter-particle interaction, powders and grains

1. Introduction

Particulate materials such as powders and grains are assemblies of discrete particles and their mechanical behaviour is different from conventional solid, liquid and gaseous matter [e.g. 1-5]. For example, imagine we fill a container with air, liquid and solid grains. Unlike air, particulate materials do not occupy the whole volume of the container. When we tilt a liquid-filled container, liquid would flow freely. But when we do the same test for a container filled with solid grains, they flow differently - sometimes the flow of the grains may not be initiated until a particular tilt angle is attained. Understanding how contiguous particles interact with each other inside particulate packing under external loading environments is of immense interest for a number of industries who deal with products in powder form. Examples include the geotechnical, mechanical, chemical, food, and mineral engineering sectors. Researchers seek precise information on the internal mechanical behaviour of particulate materials to develop realistic constitutive behaviour of particulate media under mechanical loading.

A fundamental level of understanding of how particle-scale properties affect the bulk behaviour of particulate assemblies under different process loading conditions is not yet well established. As of now, the design of large-scale units such as powder processing equipment used in chemical plants, civil engineering foundations and structures relies on the estimates of the constitutive behaviour of particulate materials mostly based on continuum assumptions. Although continuum-based approaches are mod-

---

[†] Accepted: September 23rd, 2010

[1] LS2 9JT, UK
[2] Harlesden, London, NW10 7NY, UK
[*] Corresponding author
E-mail: S.J.Antony@leeds.ac.uk
TEL: +44 1133 432409 FAX: +44 1133 432405

erately successful in some instances, their general applicability is mostly limited due to their inability in capturing several distinct features of discrete particulate assemblies under mechanical loading. For example, **Fig. 1a** presents a typical photoelastic image of force transmission pathways (commonly referred to as 'force chains')[6,7] inside a sheared granular assembly[6]. **Fig. 1b** shows similar computer-based force networks generated in a sheared discrete assembly using DEM[1]. The thickness of the lines is proportional to the magnitude of normal contact force. It is evident from these pictures that force distribution inside particulate media occurs in a non-homogeneous manner under boundary loading. More details on how the signature of force networks relates to the bulk mechanical strength in discrete assemblies can be found elsewhere[1]. However, we wish to point out that it is entirely possible to find a significant number of non-load-bearing particles residing next to strong force-transmitting contacts inside granular media under mechanical loading. This surprising feature is an inherent characteristic of discrete particulate assemblies under mechanical loading. To the best of our knowledge, it is not yet established that continuum assumptions would be sufficient to capture such phenomena for discrete systems. Over the past two decades, the advancement of other modelling methodologies such as DEM and Molecular Dynamics (MD) have significantly enhanced our understanding of the rather complex mechanical responses of particulate systems under external loading conditions on both single-particle and bulk scales[8]. The studies have revealed how single-particle scale properties such as inter-particle friction [e.g. 2,3,9,10], elastic modulus [e.g. 2,11-13], surface energy [e.g. 14], long range forces [e.g. 15], size distribution and shape of particles [e.g. 16] influence the collective (bulk) mechanical behaviour of particulate assemblies. In spite of the recent advancements of a number of experimental methods such as X-ray Micro Tomography (XMT) [e.g. 17], Nuclear Magnetic Resonance Imaging (NMRI) [e.g. 18] and Positron Emission Particle Tracking (PEPET) [e.g. 19] to characterise the structure of particulate beds, these are mostly limited to obtaining the density and velocity variations of particles (with a moderate degree of success) under external loading conditions. They are not yet established to quantify the distribution of stress profiles within single-particle or bulk scales except for some methods such as indentation [e.g. 20] and Atomic Force Microscopy techniques [e.g. 21], which quantify stresses at best measured on the boundaries of the particles or inter-particle contacts.

DEM has been widely recognised as an efficient route to probe the mechanical properties of discrete particulate assemblies[8]. It provides unparalleled access to probe key internal features of particulate assemblies under external loading environments[1]. However, the method relies strongly on how accurately we prescribe the load-separation relations of particle contacts. Although the current practice is to input this as a function of the net force (/stress) components acting at particle contacts in relation to separation distance between contiguous particles, we have not yet sufficiently understood the implications of ignoring the local distribution of stresses within single particle scale on simulating the micro and nano mechanical properties of particulate assemblies. This

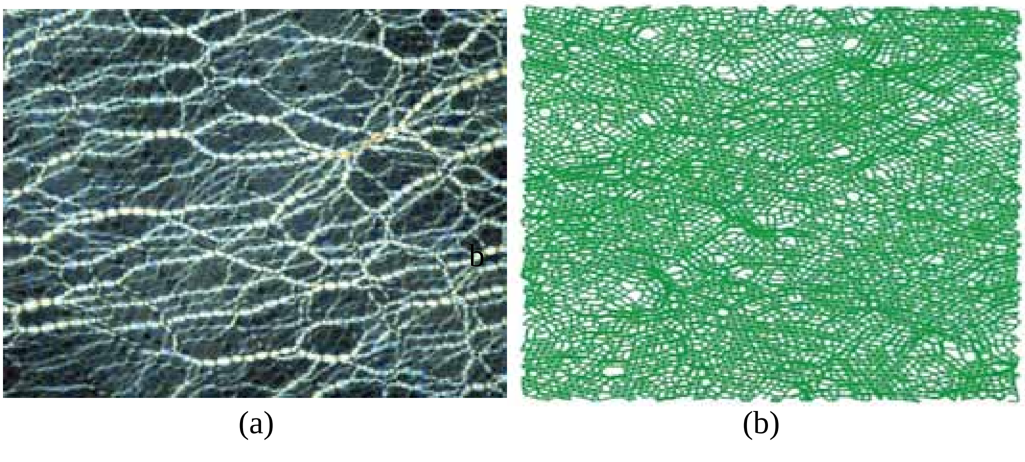

(a) (b)

Fig. 1 (a) Experimentally measured force network of sheared grains using photoelastic stress analysis (courtesy: R. Behringer, details in [6]) (b) Computer based (DEM) force-network generated in a sheared discrete assembly (details in [1]).

gap in knowledge motivated the present work. Here, we study how particles distribute stresses 'within' single-particle scale inside granular media under external mechanical loading, in this case axial compression. The study is based on experimental photonic stress analysis.

2. Background of Photonic Stress Analysis

The theoretical background of photonic stress analysis [e.g. 22] and its application to contact mechanics problems can be found elsewhere [e.g. 23]. However, here we briefly outline its working principle. The theory behind photonic stress analysis is based on the birefringence properties of materials. A ray of light passing through a birefringent material has non-uniform refractive indices. Birefringence only occurs on the application of stress, and the magnitude of the refractive indices at each point is directly related to the state of stress at that point. In the circular polariscope set-up (**Fig. 2**), the model consists of linear polarisers and quarter-wave plates, two each. The first polariser is placed directly in front of the light source to eventually convert the light into circularly polarized light which passes through a birefringent material. When the test material is lightly loaded, the speed differences within the material and phase shift are small. This results in the colour of short wavelength to disappear due to interference. As the load is increased; the interference of the colour cycles and one complete cycling is a fringe order. The light is resolved into two perpendicular components along a fast and slow axis (corresponding to increased and reduced speed of light, respectively), producing polarized light that is separated in time.

The fast and slow axis components are viewed through a second polarizing filter, referred to as an analyser (**Fig. 2**). The speeds of the transmitted light through birefringent materials are directly proportional to the major and minor principal stress components σ_{11} and σ_{22}, respectively. The magnitude of the relative retardation through the difference in reactive indices is given by the stress optic law $R=Ct(\sigma_{11}-\sigma_{22})$, where R is the induced retardation, C the stress optic coefficient, and t the specimen thickness. The difference between major and minor principal stress components can be related to the fringe orders displayed by birefringence materials and hence to the maximum shear stress (τ_{max}) of the material under mechanical loading[9]. It is worth mentioning that by using a plane polariscope set-up, it is possible to visualise the isoclinics, which is the locus of the points along which principal stresses are in the same direction [e.g. 22]. This can be done by eliminating the two quarter-wave plates of the circular polariscope, one each to the front and back of the birefringent model material (**Fig. 2**), and more details of the theoretical background are well documented in the literature [e.g. 22].

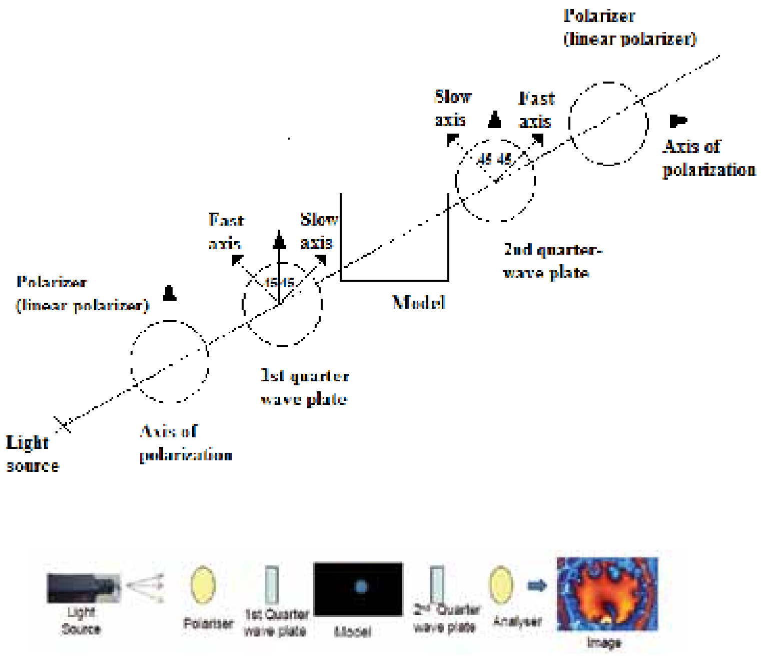

Fig. 2 Illustration of the circular polariscope set up.

3. Experiments

Fig. 3 shows the compression chamber in which an elastic polymer disc (birefringent sensor particle, Young's Modulus-2.9MPa and Poisson's Ratio-0.35) is embedded in the middle of a granular bed comprising uniform-sized, dry, cohesionless Vigna Radiata sphere beads 24) of 4 mm diameter in random packing (initial packing density 0.73 g/cm^3), identical in all assemblies tested here. The non-bias nature of the orientation of particle contacts is verified by performing image analysis on the particle bed to determine the fabric tensor of all the contacts[25], and the deviator component of the fabric tensor was close to zero, thus confirming the random and non-bias nature of the geometry of the initial packing[12]. The particles were filled into the compression chamber (**Fig. 3**) in two stages-at first, up to the bottom level of the required sensor particle position, followed by positioning the sensor particle and then gradually filling to the required height of the granular bed. The size of the inclusion (birefringent particle) was 2.5 times the size of the surrounding beads. This is selected on the basis that if the sensor particle size were of the same size as the beads, it is entirely possible that it might not experience any pressure at all if it were positioned in a weak contact force network[1-3]. The thickness of the sensor particle and surrounding beads was kept identical. The applied loading corresponds to quasi-static axial compression across the width of the bed (**Fig.3**), increased in small increments (P= 1.02, 2.88, 5.33 and 7.3 N).

To analyse how the wall influences the shear stress distribution within the inclusions under mechanical loading, experiments were performed for different cases of the position of inclusion from wall boundaries, represented in terms of λ d (at fixed height from the loading pad as shown in **Fig. 3**), where λ varies between ca. 0-5 and d is the size of the inclusion. We verified that the results are repeatable. Detailed investigation into the fluctuation between repetitions of experiments for a given loading condition showed only minimal differences - the retardation of light between major and minor principal directions at selected tracking positions within inclusions was within about 5% variation among the different test results. Optical images for the distribution of maximum shear stress within the sensor particle were taken and analysed for the magnitude of maximum shear stress distribution and the direction of major principal stress within inclusions for all cases of loading and positions of the inclusion within the granular bed. From the experiments, we observed that the distribution of maximum shear stress within particle scale is non-homogeneous in nature. To quantify this, we scanned the distribution of maximum shear stress along four sections, each passing through the particle centre (**Fig. 4**). Each of the four sections starts from the closest available contact point (contact pane) of $\theta = 0^0$, 45^0, 90^0 and 135^0 position, and ends at the corresponding diametrically opposite point. The distance of the scanning position is normalised by the diameter of the particle and represented as 'Normalised Depth, S (=r/d)' in the plots presented later. In these, the maximum shear stress for a given 'S' is presented as an average value of the data along the four scanning sections (Average τ_{max}).

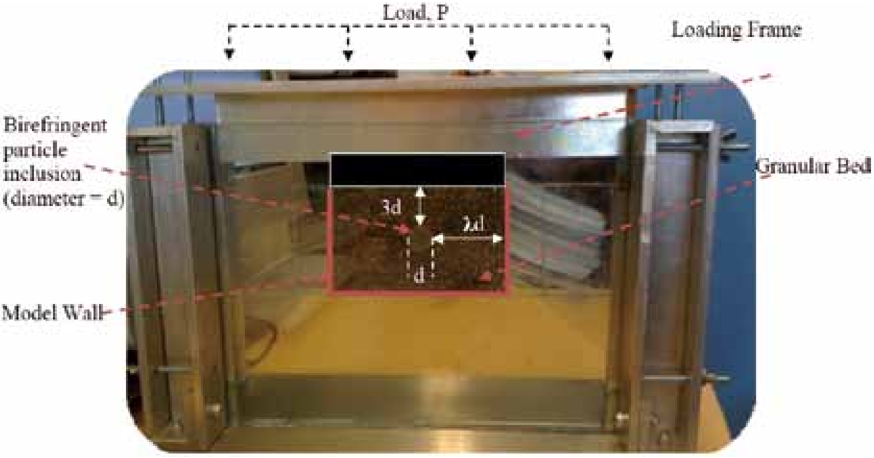

Fig. 3 Experimental loading rig set up.

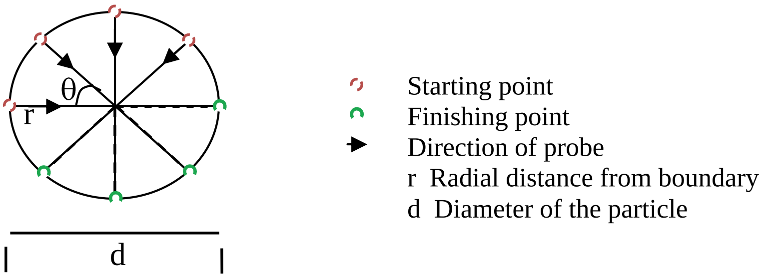

Fig. 4 Schematic representation of probe directions in a birefringent particle.

4. Results and Discussion

Fig. 5 shows the contours of maximum shear stress distribution experienced by the sensor particle for different values of its position with respect to the wall, i.e., λ =0, 1 and 2, while **Fig. 6** presents the same measures for the cases of λ = 2.27 and 4.4 for different load levels. The colour coding of maximum shear stress level is maintained consistently for all the images using a single scale and presented in **Figs. 5, 6** (colour plots are available in the on-line version). The arrows in these plots show the direction of major principal stress in the particles. **Fig. 7** shows the variation of average maximum shear stress (Average τ_{max}) across the sensor particle for the cases of λ =0, 1 and 2, and **Fig. 8** shows these for the cases of λ =2.67 and 4.4. From these results, the following observations can be made:

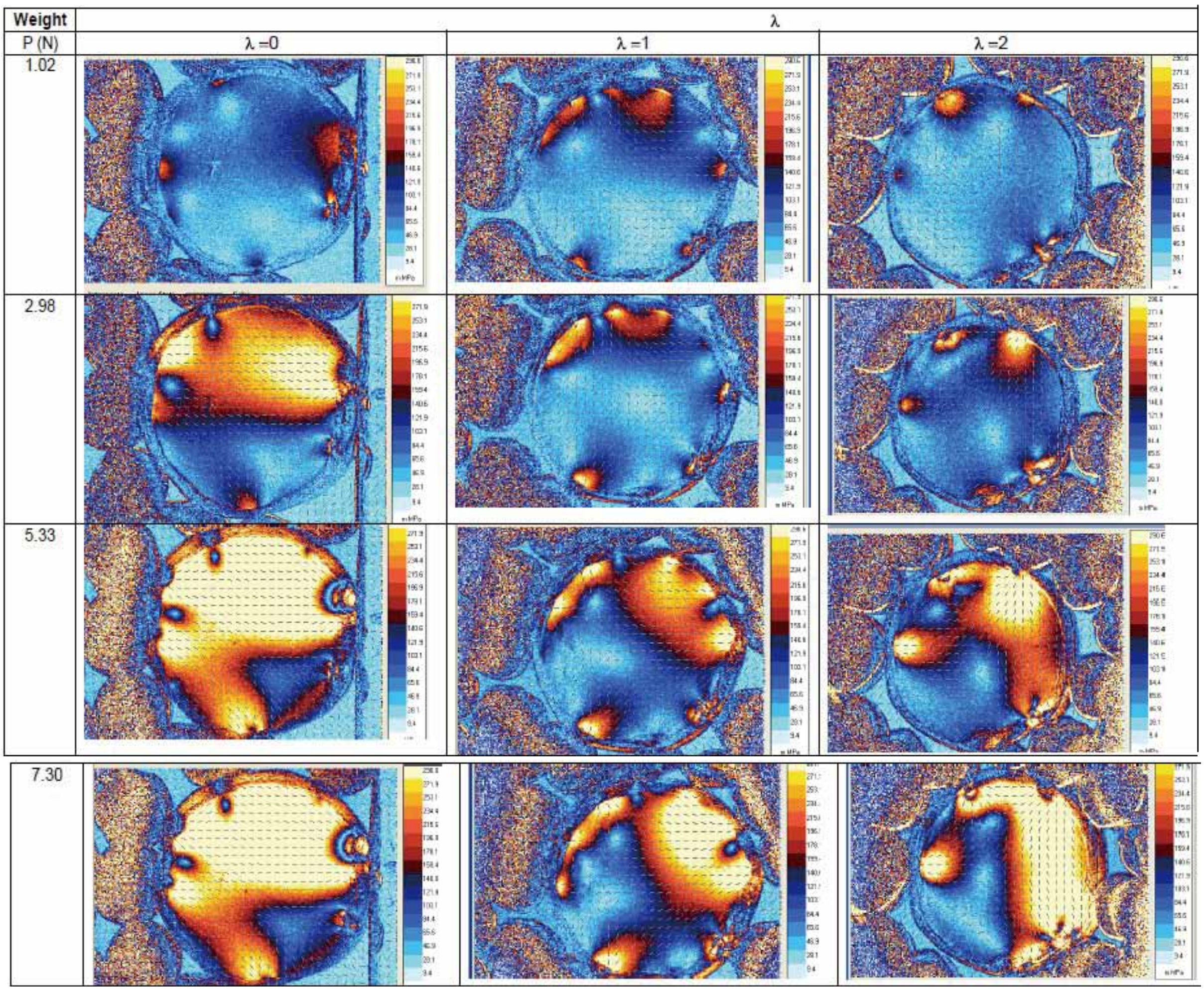

Fig. 5 Photonic images showing contours of maximum shear stress distribution for the cases of λ =0, 1 and 2.

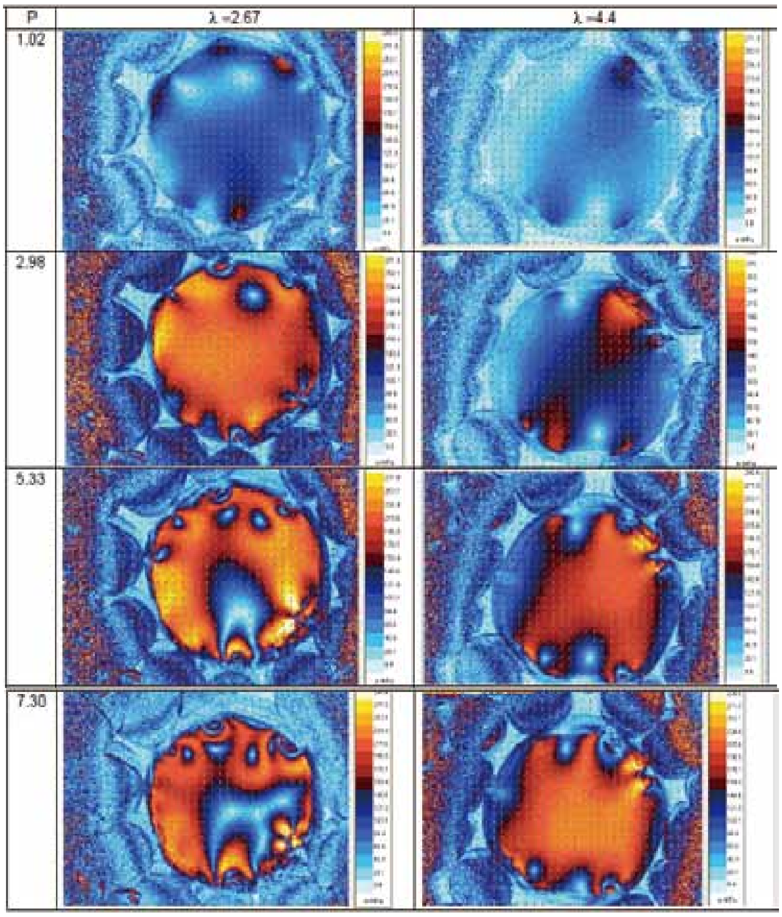

Fig. 6 Photonic images showing contours of maximum shear stress distribution for the cases of λ =2.67 and 4.4.

(i) Maximum shear stress distribution (τ_{max}) within particles occurs in a non-homogeneous manner inside axially compacted granular beds (**Figs. 5, 6**).

(ii) The distribution of τ_{max} in particles is strongly influenced by the proximity of particles with respect to the wall. The particles when positioned next to the wall (λ =0) experience the highest level of maximum shear stress within them (**Fig. 7**).

(iii) In conformance with the results presented above, the direction of major principal stress within particles also depends on the proximity of the particles with respect to the wall boundaries. Indeed, when the particles reside next to the wall, the direction of major principal stress within particles tends to be orthogonal to the direction of axial compression (i.e. strongly anisotropic). However, an increase in the proximity of particles (λ) from the wall causes the level of anisotropy to diminish - for the case of $\lambda \geq 2.67$, the direction of major principal stress in particles is predominantly along the axial direction of compression (**Fig. 5, 6**).

(iv) The distribution of average maximum shear stress within particles presents the maximum value inside the particles (and not at particle-contacts). This suggests that for the systems considered here, shear-induced yielding on a particle scale is most likely to occur inside the particles (**Figs. 7, 8**) rather than at inter-particle contacts. Interestingly, for the case of $\lambda \leq 2.67$, the maximum shear stress attains maximum value at positions relatively closer to the boundaries of the particles than at the centre. However, this could change if the particles are relatively free from wall boundaries as shown in **Fig. 8** - for the case of λ =4.4, the maximum shear stress occurs at the centre section of the particle (**Fig. 8**).

5. Conclusions

To the best of our knowledge, for the first time we have experimentally probed the nature of shear stress distribution ‘within’ single particle scale inside particulate compacts subjected to boundary loading, in this case axial compression. Even under the strongly anisotropic axial compression loading

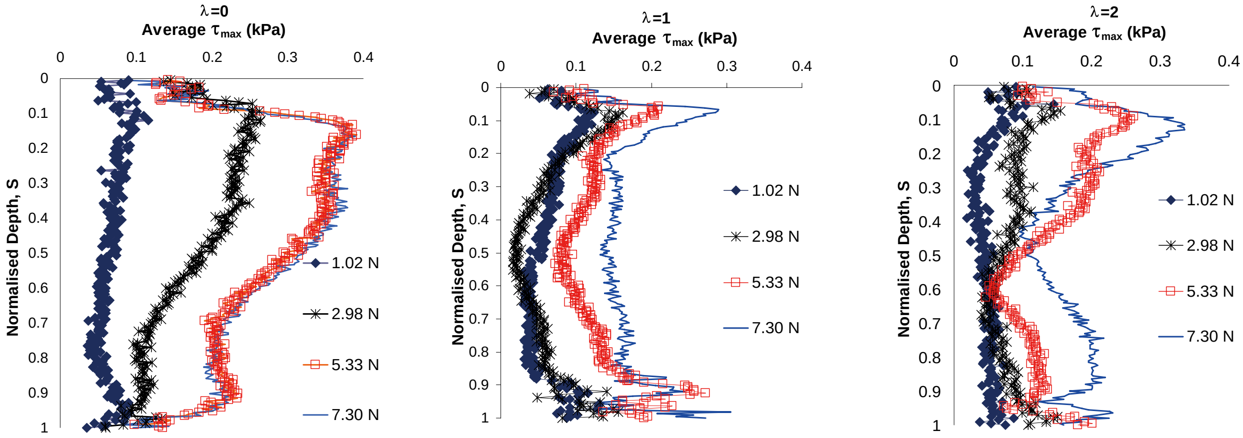

Fig. 7 Variation of average maximum shear stress (τ_{max}) across the particle inclusion for the cases of λ = 0, 1 and 2.

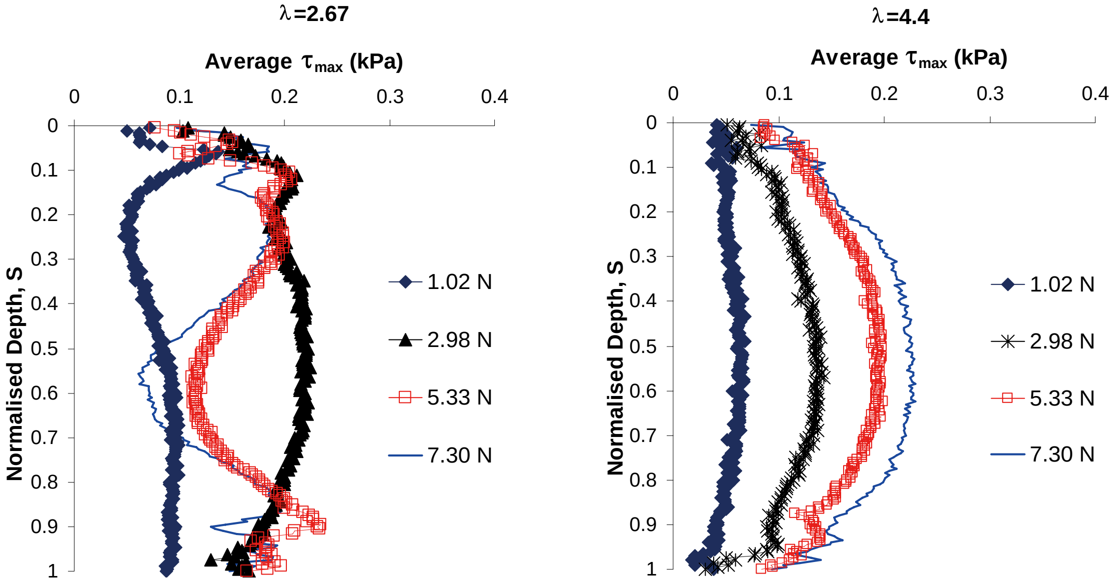

Fig. 8 Variation of average maximum shear stress (τ_{max}) across the particle inclusion for the cases of λ =2.67 and 4.4.

condition, the particles undergo shearing at single-particle level in a non-homogeneous manner. The extent of this behaviour depends on whether the particles reside close to the wall boundaries or relatively far away from the wall boundaries; this cut-off distance, referred to as wall influence zone, is about 3 times the size of the individual beads ($\lambda \leq 2.67$). When the inclusions reside within the wall influence zone, the direction of major principal stress is orthogonal to the direction of axial compression, whereas this tends to align along the direction of the loading when they reside outside the wall influence zone. Hence, even if the material properties of particles and their size are uniform, their mechanical behaviour is position-dependent, an aspect important to consider in the design of functional particulate compacts such as pharmaceutical tablets. Further experimental studies are required to map out the effects of other particle-scale variables such as size effects, shape effects, frictional effects and cohesion of different particle types on the ability of particles to sustain shear stress inside particulate packing. However, the current study is a step forward towards unravelling the rather complex mechanical behaviour of discrete particulate assemblies under industrial process loading conditions in a realistic manner. The results also imply that we need to perhaps revise the constitutive relations employed in the simulations for modelling the mechanical behaviour of particulate systems, for example DEM modelling methodology in which the shear failure criteria of particles are mostly prescribed to occur at inter-particle contacts and independent of the interaction effects of neighbouring contacts [e.g. 26] as well as the variations in the stress quantities between the centre of a given particle and their inter-particle contacts normally neglected at single particle scale. Such simplifications need not be the norm, but could be an exception.

Acknowledgements

The authors gratefully acknowledge METRC, UK and Mr G. Calvert for their support to this work.

References

1) Antony, S. J. (2007): Link between single-particle properties and macroscopic properties in particulate assemblies: role of structures within structures, Philosophical Transactions of the Royal Society of London, Series: A, 365, pp.2879-2891.
2) Antony, S.J. and Kruyt, N.P. (2009): Role of interparticle friction and particle-scale elasticity on shear strength mechanism in three dimensional granular media, Physical Review E, 79, 031308.
3) Antony, S.J. and Sultan, M. (2007): Role of inter-particle forces and inter-particle friction on the bulk friction in charged granular media subjected to shearing, Physical Review E, American Physical Society, 75(1), 031307.
4) Antony, S.J. and Ghadiri, M. (2001): Size Effects in slowly sheared granular media, Journal of Applied Mechanics, American Society of Mechanical Engineers, 68(5), pp.772-775.
5) Antony, S.J. and Kruyt, N.P. (2007): Force, relative displacement and work networks in granular media subjected to quasi-static deformation, Physical Review E, 75, 051308.
6) Zhang, J. , Majmudar, T. and Behringer, R. (2008): Force chains in a two-dimensional granular pure shear experiment, Chaos, 18 , 041107.
7) Drescher, A. and Jong, de J. (1972): Photoelastic verification of a mechanical model for the flow of a granular material, Jl. Mechanics and Physics of Solids, 20, 337-351.
8) Cundall, P.A. and Strack, O.D.L. (1979): A discrete numerical model for granular assemblies, Geotechnique 29(1), pp.47-65.
9) Morgan, J.K. (1999): Numerical simulations of granular shear zones using the distinct element method 2. Effects of particle size distribution and interparticle friction on mechanical behaviour, Jl. Geophysical Research, 104(B2), pp.2721-2732.
10) Sazzad, M. and Islam, M. (2008): Macro and micro mechanical responses of granular material under varying interparticle friction, Jl. Civil Engineering, 36(2), pp.87-96.
11) Thornton, C. (2000): Numerical simulations of deviatoric shear deformation of granular media, Geotechnique, 50, pp.43-53.
12) Thornton, C. and Antony, S.J. (1998): Quasi-static deformation of particulate media, Philosophical Transactions of the Royal Society of London, Series: A, 356(1747), pp.2763-2782.
13) Ning, Z. and Ghadiri, M. (2006): Distinct element analysis of attrition of granular solids under shear deformation, Chemical Engineering Science, 61(18), pp.5991-6001.
14) Quintanilla, M., Castellanos, A. and Valverde, J. (2001): Correlation between bulk stresses and interparticle contact forces in fine powders, Physical Review E, 64, 031301.
15) Moreno-Atanasio, R., Antony, S.J. and Williams, R.A. (2009): Influences of long-range interaction on the structural kinetics and strength of self-assembled nanoparticulate systems, Jl. Particology, 7, pp.106-113.
16) Cleary, P. and Sawley, M. (2002): DEM modelling of industrial granular flows: 3D case studies and the effect of particle shape on hopper discharge, Applied Mathematical Modelling, 26(2), pp.89-111.
17) Fu, X. et al. (2006): Application of X-ray microtomography and image processing to the investigation of a compacted granular system, Particle & Particle Systems Characterization, 23(3-4), pp.229-236.
18) Huan, C., Yang, X. and Candela, D. (2004): NMR experiments on a three-dimensional vibrofluidized granular medium, Physical Review E, 69, 041302.
19) Bridgwater, J., Forrest, S. and Parker, D. (2004): PEPT for agglomeration?, Powder Technology, 140(3), pp.187-193.
20) Arteaga, P.A., Ghadiri, M., Lawson, N.S. and Pollock, H.M. (1993): Use of nano indentation to assess potential attrition of particulate solids, Tribology International, 26(5), pp.305-310.
21) Jones, R. (2004): From single particle AFM studies of adhesion and friction to bulk flow: forging the Links, Granular Matter, 4, pp.191?204.
22) Dally, J.W. and Riley, W.F. (1987): “Experimental stress analysis” , McGraw Hill, Singapore,.
23) Antony, S.J. (1996): “Studies on some soil-structure interaction and contact problems” , PhD thesis, IISC.
24) Unal, H., Isik, E., Izli1, N. and Tekin, Y. (2008): Geometric and mechanical properties of Vigna Radiata.L grain: effect of moisture, Int. Jl. Food Properties, 11, pp.585-599.
25) Satake, M. (1982): In *Deformation and Failure of Granular Materials*, P.A. Vermeer, H.J. Luger, Eds. (Balkema, Rotterdam), pp.63-68.
26) Hosseininia, E. and Mirghasemi, A.A. (2006): Numerical simulation of breakage of two-dimensional polygon-shaped particles using discrete element method. Powder Technology **166**(2), pp.100-112.

Author's short biography

S. Joseph Antony

Dr Antony is a senior lecturer in Chemical Engineering at the Institute of Particle Science and Engineering, University of Leeds. His primary research interest is in the area of Computational and Experimental Particulate Mechanics. He has obtained the prestigious MIT Young Researcher Fellowship Award (2001) for Exemplary Research in Computational Mechanics. One of his recent research works in the area of computational particulate mechanics has been selected as an example of an outstanding achievement in U.K Particle Science & Technology, by the IChemE UK PTSG. He is a member of UK EPSRC College, ASME, and the European Society of Computational Methods in Science and Engineering. He serves in several professional committees, including the ASME Applied Mechanics-Materials Division Joint Committee on Constitutive Equations. His research findings have appeared in several reputed international journals and conference proceedings. He is the lead editor of the book 'Granular Materials: Fundamentals and Applications', published by the Royal Society of Chemistry, London. He has served as a guest editor for Granular Matter. Presently, he serves as an editorial board member of many journals including Journal of Nanotechnology. More details on his academic activities can be viewed through the web link http://www.leeds.ac.uk/speme/antony/CV-SJA.pdf .

David Chapman

Mr. Chapman graduated in Chemical Engineering at the University of Leeds where he undertook many design projects, along with a research project focused on stress analysis in particulate systems. He found this extremely interesting working on his own ideas and theories along with testing currently used simulations against modern-day technologies on a subject not widely acknowledged. Prior to this he studied a science degree at Leeds University which provided him with the analytical and practical skills. Presently he work as a project engineer for United Biscuits, which is a large multi-national company based in London where he is involved in the process control and efficiency of a large scale plant.

The Properties of Cenospheres and the Mechanism of Their Formation During High-Temperature Coal Combustion at Thermal Power Plans[†]

V.B. Fenelonov*, M.S. Mel'gunov, V.N. Parmon
Boreskov Institute of Catalysis, SB RAS.

Abstract

A systematic analysis of the probable scenario of the supramolecular structure (texture) formation of mineral products, formed during the high-temperature combustion of pulverized bituminous coals at thermal power plants (TPP) is provided. The general physico-chemical consideration of the processes that occur at different stages (heating, burning, viscoplastic state in the hot zone, and cooling) during the combustion of bituminous coal makes it possible to allocate the following systematic transformations: coal → char → network structures (including plerospheres)→cenospheres→fly ash..

Keywords: Cenosphere, plerosphere, ash, coal combustion, thermal power plants

1. Introduction

One of the alarming environmental problems that requires an immediate solution is associated with an infinitely increasing amount of ash produced during the burning of coal, oil, and wood and other biomaterials, domestic waste, etc. The ash settling reservoirs of thermal power plants (TPP) have already transformed many tens of hectares of land into lifeless (and constantly growing) deserts. The amount of continuously produced ash is much higher than its consumption, and ash dumps continue to expand[1-5]. The most insidious attendant component of ash that is formed simultaneously with it are aluminosilicate microspheres (**MS**), some of which have an extremely low density (0.3-0.5 g/cc) and are entrained in flue gases together with the superfine fly ash. These **MS** together with the ashes enter ash settling reservoirs, where due to their low density, they accumulate mainly at the external surface, and can be easily carried away by rain and wind. The most dangerous possibility is their entrainment in wind, with which they can be moved over long distances, can ingress the respiratory tracts of humans and animals, and thus promote the development of cardiovascular and respiratory illness [1-5, 6, 7]. In addition, such **MS** can be generated during accidents at nuclear power plants [4], and they were found in the products of volcanic activity [8], etc.

But at the same time, **MS** have several unique properties that provide prospects for their effective use in many up-to-date technologies. This stimulates the necessity to improve the methods of their gathering, the deeper investigation of the properties and mechanisms of their formation, and working out the optimum conditions of utilization [1-5, 9, 10].

There are two main classes of **MS**: really "empty spheres", in which the cavities are filled with gas only, the so-called cenospheres (**CS**), and plerospheres (**PS**) in which the cavities are filled with small mineral particles, foam, spongy or other porous framework. The term *cenosphere*[a] comes from the Greek *kenos* (hollow) + *sphere*, and reflects the most important feature of cenospheres - the presence of a cavity surrounded by a solid or perforated mineral shell. The latter type of microspheres are often called network-structured cenospheres or *plerospheres* - from the Greek *plërës* (filled) + *sphere* (Fisher et al.[11]

[†] Accepted: September 23rd, 2010

[1] 1LS2 9JT, UK
[2] Harlesden, London, NW10 7NY, UK
* Corresponding author
E-mail: S.J.Antony@leeds.ac.uk

[a] The term *cenosphere* was proposed by F.S. Sinnatt at the second international symposium on bituminous coals in 1928, naming both products of coal combustion that quickly pass through a plastic state, followed by curing and formation of hollow spheres.

and Raask[12]).

Both types of **MS** are formed of amorphous glass-like material containing amorphous SiO_2 (~50-65 wt.%), Al_2O_3 (~20-30 wt.%), Fe_2O_3 (~3-8 wt.%), along with Ca, Mg, K, etc., phosphates, sulfates, chlorides, as well as quartz, mullite, etc.[1-5,12]. The specific composition is determined by raw coal and the transformations that occur in the burning chambers of TPPs at 1400-1700° C [2,3,4,12, 14].

Fig. 1 shows the morphology of an **MS**: 1**a** represents cenospheres, 1**b**, 1**c** and 1**e** can be either cenospheres or plerospheres, and 1**d** is a plerosphere (one of possible variants). The images of defective **MS** will be used further to illustrate the mechanisms of their formation. The most typical is **Fig. 1**e, where the **MS** does not have visible defects. Worthy of note is that one cannot distinguish whether it is a cenosphere or plerosphere from the image. At the same time, this picture shows the characteristic aggregation of the **MS** with small particles attached to their surface and the formation of large aggregates of **MS** of comparable or different size. All aggregates are relatively strong, because they are not destroyed during the ultrasonic treatment, usually applied prior to electron-microscopic analysis.

The typical diameter **D_0** of **MS** available for adsorption measurements is 10 ÷ 1000 micrometers, the specific surface area is ~0.1-2 m^2/g. Important for the purpose of this review is the thickness of the wall **t**. The results of SEM studies known from literature and the Web[b] typically give the value of **t/D_0** ≤ 0.1. Corresponding estimations are obtained, as a rule, from studies of partially destroyed **MS** as shown in **Figs. 1a** and 1**d**. A precise study of **MS** was carried out in a recent paper by Ngu et al.[15]. **MS** monolayers were attached to a flat support with epoxy resin. This was followed by a fine polishing step. Several sections of the resulting samples were investigated using modern methods of image analysis. A study of a few hundred samples of various fractional composition (30 μm < **D_0** < 250 μm) was performed. It proves that the values of **t/D_0** vary in a narrow range of 0.025 - 0.105 with the most probable value of **t/D_0** = 0.06, irrespective of the **MS** size. It is essential that these values of **t/D_0** correspond to both cenospheres and plerospheres.

The same study by Ngu et al.[15] gave a numerical ratio between plerospheres and cenospheres. It was shown that this ratio increases with **D_0**, for example, for 45-63 μm the plerosphere fraction is ~6%, ~15% for the 75-90 μm fraction, and rises to ~90% for the greater fraction.

The structure of cenospheres defines their low density (bulk density is 0.3-0.5 g/cc, apparent density δ is 0.6 - 0.7 g/cc), low thermal conductivity (0.1 - 0.2 W/m . K), which is accompanied by high mechanical strength (210-350 kg/cm^2), thermal stability (sintering usually occurs at 1000-1450° C), resistance to acids and general chemical inertness [1- 5,12].

Fly ash comprises 50-90% of the solid products of combustion and usually contains 1-2 wt.% of **MS** of all types (although a higher **MS** content (3.8 wt.%) was also observed [15]). Taking into account that modern TPPs burn millions of tons of coal annually, at the same time they produce thousands of tons of **CS**. According to the results of technical monitoring by Drozhzhin et al.[5], the largest TPPs in Russia produce more than 120 thousand tons of **CS** per year.

A set of unique properties of cenospheres along with their availability opens up the prospects for a wide use as heat insulation of space ships, lightweight building materials, obtained by introducing **CS** into concrete, bricks, ceramics, flooring and pavements, polymer composites, metal alloys, etc., which

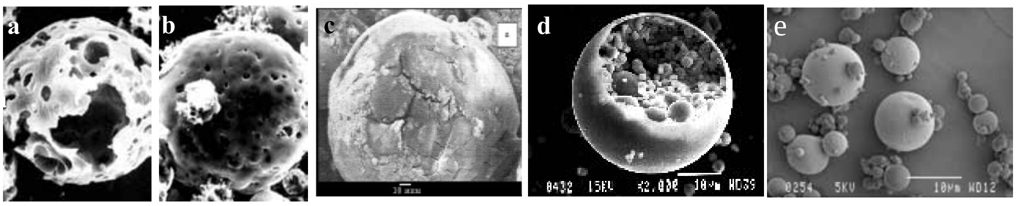

Fig. 1 Scanning electron microscopy (SEM) images of some **MS**, formed during high-temperature burning of bituminous coal (cited according to [7] and numerous publications on the Web).

---

[b] The listed areas of application are cited from the references in the Web (http://www.iccop.org). One schould distinguish thin-, and thick-walled cenospheres, thin-, and thick-wall frame particles (that are plerospheres) and various mixtures, including the non-porous particles of ash.

simultaneously have improved mechanical, thermal and sound insulation properties. The inclusion of **CS** with water-impermeable shells allows creation of various frost- and water-resistant products, **CS** have potential as filters, seals of various kinds (from seals in windows to those for wells in oil and gas production), anti-corrosion coatings, protective layers on liquid surfaces to reduce evaporation, in energy-absorbing bumpers and other car parts, in pneumatic tires, etc. Several papers explore the prospect of their use as microcontainers for storing a wide range of diverse materials - from enzymes to liquid explosives, and for encapsulation of radioactive waste, etc. At the same time, the possibility of their use as adsorbents, catalyst supports for fuel cells, photocatalysts and catalysts operating at high temperatures in aggressive environments, etc., is also investigated [16-19].

Consumer properties of the **CS** and ash are mainly determined by their chemical composition and texture, where the texture means the structure of supramolecular level. In certain literature, most attention is paid to chemical and phase composition. The research of **CS** texture is usually confined to electron-microscopic images (often the most spectacular images of defective **MS** are presented), their particle size and bulk density. Systematic analysis of the textural characteristics of **CS** and their relationship to the conditions of formation are virtually absent. This complicates the understanding of the formation mechanisms of **CS** with different characteristics, the development of strategies to monitor and optimize their properties, and the separation of **CS** with a given texture from the ash obtained at TPP using modern technologies .

The scenario of cenosphere formation during coal burning is generally accepted at present [11,12, 20-27]. It is based on the model of particles with a plastic or solid core and visco-plastic shell cover. The shell is formed from easy-to-melt (under combustion conditions) inorganic components (mainly silicates and aluminosilicates), and the core is formed of less easy-to-melt components. Gasification of the components in a closed volume of the shell leads to the formation of bubbles, which swell under the effect of increasing internal pressure. Swelling can destroy the shell or, after cooling and solidification, can result in the formation of cavities inside the **MS**. The breakthrough of gas through the shell can lead to destruction of the shell, yielding the formation of cracks or even the release of large fragments (**Fig. 1a**). In the case of a viscous-plastic state of the shell, the formation of craters is possible (**Fig. 1b**), while less plastic shells form cracks (**Fig. 1c**).

Formation of **MS** with intact shells (**Fig. 1e**) is usually explained by the decomposition of mineral components that provide a moderate amount of gaseous products (carbides, carbonates, sulfates and pyrosulfates, dehydration and dehydroxylation of clay-containing minerals, etc.) Fisher et al.[11], Raask[12], etc. Some authors point out a special role of Fe-containing compounds [11-13,16]. According to, e.g., Raask[12], at least 5% of iron oxide is necessary to form cenospheres. This idea is refuted by Ngu et al.[17], where the maximum yield of cenospheres (3.82 wt.%) is observed in ash with a minimum Fe_2O_3 content (0.54 wt.%).

More controversial is the mechanism of plerosphere formation (**Fig. 1d**). The hypothesis of their formation in a hot zone was proposed by Fisher et al.[11], where this type of **MS** was discussed for the first time. According to this hypothesis, different components in a particle melt at different moments. This is accompanied with the release of gases from $CaCO_3$ decomposition, clay dehydration, pyrolysis and burning of carbon, present on the surface or inside the ash slag particles, etc. Raask concludes[12] that "the plerospheres originate from coal particles with highly dispersed mineral matter during the combustion, and a fused silicate envelopment, inside which the carbon residue prevents coalescence of encapsulated ash particles".

A more detailed description includes the heat transfer from the shell to the core through small contact bridges, whose thermal conductivity is higher than the thermal conductivity of the gas. This intensifies local gas emission, allocation and moving of the core inside the cavity volume and its breaking into separate fragments.

An alternative mechanism of plerosphere formation from cenospheres at the stages after their escape from a hot zone was proposed elsewhere (Frandsen[25] and Shibaoka and Paulson[28]). According to this mechanism, the small particles[28] permeate inside the cenosphere cavities from the outside through the cracks and other "windows" while they are suspended in the flue gas or during and after their collection in the dust collecting equipment. Key features of this idea are: a) formation of plerospheres from cenospheres at the cooling stage, and b) presence of fractures in the shell of **MS**.

According to Yu at al.[17], the plerospheres are formed in the hot zone. The mechanisms for their formation can be based on the simultaneous involvement of several sources of gas inside one burning particle, agglomeration and coalescence of several precursor particles. Additionally, the formation of cenospheres can be incomplete (complete coalescence of bubbles under one shell does not occur) due to the release of particles from the hot zone. The probability of implementation of these mechanisms increases with the size of particles, their viscosity and the cooling rate.

At present there is no agreement in the assessment of such an important textural characteristic as the integrity of **CS** shells. The majority of publications glosses over this problem, although it is considered[9,10,16] that in typical cases, the shell of the cenospheres is perforated. This can make them suitable for a number of practical applications of cenospheres as microcontainers, but retards their usage in other applications. The situation is complicated by the fact that conventional **SEM** studies can only distinguish plerospheres and cenospheres if the shell is partially destroyed or by examination of polished blocks[15]. Independent diagnostic methods of the MS shell integrity are not developed in detail in the known literature.

In this paper, we try to eliminate the above and several other contentious issues and ambiguities. To do that we consider a systematic analysis of texture and the mechanisms of **MS** formation in detail. Simple experimental methods make it possible to distinguish between **MS** with intact and perforated shells and between plerospheres and cenospheres with intact shells. Experimental work is based on the study of hollow **MS** and fly ash, obtained during the combustion of Kuznetsk coal tar (brand DG, fraction 90-450 μm) at the Novosibirsk TPP-5. These results and the analysis of data from numerous publications permit the revision of the existing ideas about the formation and properties of hollow **MS**. As a result, we suggest a general physical-chemical model of formation of the cenospheres supramolecular structure, which can help develop better strategies to control and optimize ash cenosphere production at TPP.

2. Experimental

Samples of **MS** were separated according to the hydraulic method from fly ash collected from the last in a row of four electrostatic precipitators at the Novosibirsk TPP-5, which contains **MS** in the largest quantity (~3% wt.). The first separation step was based on the fact that **MS** float in water, and the rest of the ash sinks. The second separation step involved a 45-minute boiling in water and was applied to remove the **MS** with perforated shells and ash particles that float due to small trapped air bubbles. The **MS** that floated after such a procedure (their content was over 80%) were made a subject of the studies. These **MS** are designated here as intact **MS**, and are referred to hereinafter as **IMS**.

The studies of the internal structure of **IMS** were carried out after intensive grinding of the size fraction below 30 microns. This fraction was subjected to a third separation in water. The sunk particles were collected. These particles are called shredded **MS** (**SMS**).

The particle size distribution of **IMS** was analyzed in an ethanol suspension using a SALD-2101 (Shimadzu) instrument. The density, ρ_{He}, of **IMS** and **SMS** was measured at room temperature by helium pycnometry using an AutoPycnimeter 1320 (Micromeritics). The bulk density Δ of a layer of **MS** was measured by weighing 100 cc of a sample. To reduce the electrostatic polarization, the samples were exposed to water vapor in a desiccator. The weight of the adsorbed water vapor was taken into account during calculation. The surface area of **IMS** and **SMS** was measured from nitrogen adsorption isotherms at 77K obtained by means of an ASAP-2400 (Micromeritics) instrument. Specially manufactured large volume cells that allow the introduction of probes with a mass of 1.7 - 2.0 g made the measurements of the specific surface area reliable. However, even such large cells did not allow correct measurements of pore volume and pore volume-size distributions. The results of these measurements gave only an estimation of the total pore volume in the range below 100 nm at the level below 0.01 cc/g.

The porous structure of **IMS** was also studied by mercury porosimetry with an AutoPore 9200 (Micromeritics) instrument. These measurements showed the presence of pores mostly far larger than 15-20 microns, which are difficult to be reliably distinguished from the interparticle gaps. The volume of pores with a smaller size was found to be very small and close to ~ 0.001 cc/g. An additional estimation of pore volume with the size of less than 100 nm according to water adsorption gave a value of ~0.002 cc/g. These results allows us to believe that **IMS** have virtually no pores that are accessible from the surrounding bulk.

Detailed measurements of chemical and phase composition, as well as electron-microscopic studies were not carried out, because the fly ash and **MS** from the ashes of the same Novosibirsk TPP-5 were studied previously by means of these methods in detail in[9,10,16] and in other publications by the same authors. In the numerous measurements, the average chemical composition of main compounds in the investigated **MS** was as follows: ~ 64% SiO_2, ~ 25% Al_2O_3 and ~ 4% Fe_2O_3 (by mass), which is close to the data given by Vereshagina et al.[9] The residual content of combustible compounds in **MS** was ~ 3.0%.

3. Results

3.1 Analysis of the experimental results

The typical textural characteristics of fly ash, intact (**IMS**) and shredded (**SMS**) microspheres are presented in **Table 1**.

Table 1. Typical textural parameters of fly ash **FA**, intact (**IMS**) and shredded (**SMS**) microspheres

Sample	Diameter, D_0, μm	Specific surface area, A_0, m^2/g	Density, ρ_{He} g/cm^3.
Fly ash	29	4.9	2.23
IMS	132	1.1	0.71
SMS	35	2.6	2.44

The obtained values of the specific surface area, A_0, and density, ρ_{He}, for **FA**, **IMS**, and **SMS** are close to previously reported data [1,4,12,16]. Summarizing, A_0 and pycnometric density ρ_{He} for **IMS** have lower values compared with **FA** and **SMS**, the grinding of **IMS** is accompanied by an increase of the surface area and density. This increase can be explained by the observation that the **IMS** have a *closed porosity*. The closed pores are inaccessible for He and N_2, but open up during grinding. The value of the porosity, ε_0, is equal to the ratio of the volume of all closed pores to the volume of **IMS**, and the value of ρ_{He} for **IMS** corresponds to the apparent (or envelope) density, including the closed porosity. Let us designate this apparent density as δ to distinguish it from the true (skeletal) density, which will be designated as ρ_{He}. In turn, the ρ_{He} value for **SMS** corresponds to the true density. The values of δ and ρ are interrelated by Fenelonov and Mel' gunov, [29, 30]:

$$\delta = \rho\,(1 - \varepsilon_0) \qquad (1)$$

The closed porosity value for **IMS**, ε_0, calculated by **eq. (1)** is equal to 0.71. An analogous consideration of data presented by Vereshagin et al. [16] gave $\delta = 0.995 \pm 0.008$ g/cc, and $\rho = 2.600 \pm 0.015$ g/cc for **IMS**. The internal porosity that corresponds to these values is $\varepsilon_0 = 0.617$. A similar analysis of data from [1, 31, 32] shows that ε_0 varies in a narrow range of 0.60-0.75.

The values of true density for **SMS** are slightly higher than ρ_{He} for **FA**. This can be explained by the presence of small amounts of **IMS** in **FA** at the level of ~ 3.0 wt.%. Let us estimate the true density of **FA** according to a known equation, widely used in the studies of glass and glass-like materials (see references [33-37])

$$1/\rho_\Sigma = \Sigma X_i/\rho_i, \qquad (2)$$

where X_i is the mass content of component **i** with true density ρ_i, $\Sigma X_i = 1$. This relation was introduced by Gehlhoff and Thomas in 1926 [33] and refined in [34 - 37]. It is based on volumetric additivity.

The calculated density of **FA**, which contains 3.0% of **IMS** with apparent density $\delta = 0.71$ g/cc and true density $\rho = 2.44$ g/cc, can be estimated as $\rho = 1/(0.03/0.709 + 0.97/2.44)$, which is equal to 2.27 g/cc. This is very close to the experimentally measured values. We checked the accuracy of **eq. (1)** for the estimation of the true density of **FA** obtained from different sources [2, 38-] with variable contents of SiO_2, Al_2O_3, Fe_2O_3 and CaO. If one uses the recommended values of $\rho_{SiO2} = 2.336$ g/cc, $\rho_{Al2O3} = 2.392$ g/cc, $\rho_{Fe2O3} = 3.927$ g/cc, $\rho_{CaO} = 3.861$ g/cc, etc. by Blanco et al.[31], the deviation between the calculated and measured values of ρ_{He} does not exceed 10-15%, and decreases significantly assuming the corrections to the values of the compounds' true density proposed elsewhere Moreno et al.[32] and Gehlhoff and Thomas[33]. This confirms the applicability of **eq. (2)** for estimation of the true density of fly ash and shows a direct relationship between density and composition.

Our results were obtained for **MS** after double separation of **IMS** and **SMS**. However, they are not far from those obtained elsewhere without mentioning any additional secondary separation. This suggests that the typical **MS** obtained by burning coal in TPPs mostly have defect-free shells, impermeable to helium.

3.2 Interrelation between textural characteristics of cenospheres and plerospheres

Let us discuss the differences between the texture of cenospheres and plerospheres that allow their reliable identification. In this section we consider the problem of comparing the textural characteristics. **Fig. 2** shows the schematic structure of spherical ash particles, cenospheres, and plerospheres with the same external diameter D_0.

Below, we attempt to formulate the dependence of porosity and specific surface area of such **MS** before and after destruction of their shells.

3.2.1 Porosity. The porosity of cenospheres and plerospheres can be evaluated using their geometrical characteristics. Hollow **MS** with external diameter D_0 have a total volume of $V_0 = (\pi/6)D_0^3$ and their shell volume is expressed as:

$$V_t = (\pi/6)\, D_0^3\, [1-(1-2t/D_0)^3] = V_0\, [1-(1-2t/D_0)^3]\,. \quad (3)$$

where **t** is the thickness of the shell. The estimation of **t/D₀** according to known published electron-microscopy data usually gives $t/D_0 \leq 0.1$ [4,9,10,15,24,42]. For thin shells with $t/D_0 << 1$ **eq. (3)** can be rewritten as:

$$V_t \approx 6V_0\, (t/D_0) \quad (4)$$

Assuming that the shell takes up $(1-\varepsilon_0) = V_t/V_0$ part of the total volume of **MS**, the cenosphere closed porosity is equal to:

$$\varepsilon_0 = 1 - V_t/V_0 = 1 - 6\,(t/D_0) \quad (5)$$

In plerospheres, a part of the internal cavity is filled with small spheres. Let us designate their total volume as V_d. The degree of filling of the cavity with the internal spheres is equal to:

$$(1-\varepsilon_d) = V_d / (V_0 - V_t) \quad (6)$$

where ε_d is the porosity of the internal spheres packing. The total closed porosity of plerospheres is equal to:

$$\varepsilon_\Sigma = [V_0 - V_t - V_d] / V_0 = \varepsilon_0\, \varepsilon_d \quad (7)$$

Eq. (7) is applicable to both plerospheres and cenospheres (when ε_d = 1.0). Its substitution into **Eq. (1)** gives the apparent density δ of cenospheres and plerospheres as:

$$\delta = \rho_{He}\, (1-\varepsilon_\Sigma) \quad (1^*)$$

Thus, plerospheres generally have a lower total porosity ε_Σ, and, correspondingly, a higher δ compared with cenospheres. It is natural that if the apparent density of plerospheres δ_{pl} exceeds the water density ρ_{H2O}, they sink in water. According to **Eqs. (1*)** and **(7)**, this condition is reached at:

$$\varepsilon_t < [1 - \rho_{H2O}/\rho_{He}] / \varepsilon_0 \quad (8)$$

For example, in water at $\rho_{He} \sim 2.4$ g/cm^3 and ε_0 = 0.7, the threshold value ε_d is 0.83. This is a relatively high porosity, and thus, the major part of plerospheres sinks in water with **FA**. Moreover, the high density of plerospheres allows them to be more easily captured by electrostatic precipitators. To evaluate the presence of plerospheres in the **MS** studied in our work, we dried the sediment obtained after the second separation and tried to gather the **MS** that floated in ethanol with a density of 0.81 g/cc. After a long exposition (exceeding 1 day), only ~12% of the particles floated, however, we could not get a quantity enough for detailed studies.

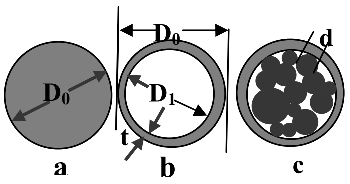

Fig. 2 A model of a spherical particle of ash (**a**), a cenosphere (**b**), and a plerosphere (**c**) of one single external diameter D_0; D_1 is the cavity diameter, **t** is the shell thickness, **d** is an average diameter of internal spheres inside the plerosphere.

3.2.2 The specific surface area. The external specific surface area, A_0, related to the mass of **IMS** with external diameter D_0 in general cases is:

$$A_0 = \xi S_0 / V_0 \delta = 6\xi / \delta D_0 \quad (9)$$

where S_0 is the *geometrical* surface area of **MS**, V_0 is the geometrical volume, ξ is the coefficient of surface roughness (for rough surfaces ξ > 1.0), and δ is equal to ρ_{He} for non-porous particles. For non-porous **MS** or **MS** with the intact shells when the internal void is inaccessible for adsorption, S_0 is the same. All three types of **MS** shown in **Fig. 2** with D_0 = Const, and ξ = Const have the same geometrical surface area S_0. But the specific surface area of a unit of mass depends on δ and thus differs for **MS** of different types.

Disruption of intact cenosphere shells by destruction or the formation of through pores, channels or cracks makes the inner surface of the **MS** accessible. In such situations, the total available specific surface area A_t of a crushed *cenosphere* shell is determined for $t/D_0 << 1$ by the equation:

$$A_t = (S_1 + S_2)/V_t \rho \approx (2/D_0 \rho)\, [1 - 2(t/D_0)] / (t/D_0) \quad (10)$$

where S_1 and S_2 are the geometrical surface areas of the external and internal surfaces of the shell with volume V_t, and ρ is the true density of this shell. The increase of the specific surface area due to shredding of cenospheres can be expressed as:

$$A_t/A_0 = 2\, [1 - 2(t/D_0)] \quad (11)$$

One can assume that according to **eq. (11)**, shredding of cenospheres should not result in more than a twofold increase of the specific surface area. Thus, if experimentally one observes a more pronounced increase of the specific surface area, this serves as an indication of the presence of plerospheres in the probe.

Access to the internal space of plerospheres should be accompanied by an additional increase of the geometrical surface area due to the surface of internal spheres. For simple estimations one can apply the following equation:

$$A_{PS} = A_d\, X + A_t\, (1 - X) \quad (12)$$

where A_t is the specific surface area of the crashed shell, determined by **eq (10)**, $A_d = 6/\rho_{1d}$ is the specific surface area of internal spheres with mean diameter of **d** and density ρ_1, **X** is the mass of the internal spheres related to the mass of a plerosphere, and (1

$-$**X**) is the mass of the shell related to the mass of the plerosphere. If $\rho = \rho_1$, the value of $\mathbf{X} = \mathbf{V_d/(V_d + V_t)}$. Expressing ε_0, ε_d, and ε_Σ through $\mathbf{V_t}$, $\mathbf{V_d}$, and $\mathbf{V_0}$ (see **eq. (5)**, one can obtain:

$$X = \varepsilon_0 \mathbf{(1-\varepsilon_d)/(1-\varepsilon_\Sigma)}. \qquad (13)$$

The substitution of **eq. (13)** in **eq. (12)** followed by a simple transformation gives:

$$\mathbf{A_{PS}/A_0 = 2[1-2(t/D_0)][(1-\varepsilon_0)/(1-\varepsilon_\Sigma)] + (D_0/d)\,\varepsilon_0\,(1-\varepsilon_d)} \qquad (14)$$

The first member in the right-hand part of eq. (14) is insignificant compared with the second member at $\mathbf{D_0/d >> 1.0}$. Thus, one can expect a significant increase of the specific surface area compared with intact shell, which is mainly determined by $\mathbf{(D_0/d)}$, ε_0, and ε_d.

According to our data, the disintegration of **CS** results in the increase of the specific surface area by a factor of 2.6/1.1 = 2.3 (see **Table 1**). This value exceeds 2 and can be explained by the presence of a small amount of plerospheres.

4. Discussion of the Mechanisms of Cenosphere and Plerosphere Formation During High-Temperature Burning of Pulverized Coal

Let us reconsider the cenosphere and plerosphere formation mechanisms and how these mechanisms are consistent with the overall scenario of pulverized coal burning and **FA** production. Pulverized coal combustion is a complex process with many interacting factors which are still not perfectly understood. The existing overall combustion models are combinations of physical-mathematical models and empirical correlations [21, 43-53].

The combustion usually starts in typically middle-size coal particles of 20 to 100 μm and includes the following characteristic stages: **a)** fast heating and de-volatilization (emission of water and volatile combustible gases) with a residence time less than 1 s, **b)** the burning of char with a residence time of no more than 1-2 s, **c)** cooling, the residence time is several seconds [48-52]. The combustion of de-volatilised gases outside the coal particle occurs during stage "**a**" , and some of the oxygen can penetrate through the flame towards the particle surface. The resultant degassed coal is usually called char. After the flame from the de-volatilised gases is extinguished, the oxygen is able to reach the particle surface and the char starts to burn (stage "**b**"). The char particle temperature is highest during burning and it may exceed the surrounding gas temperature by several hundred degrees. As a result, the particle's temperature at the burning stage may exceed 2000° C in commercial furnaces [48-50].

4.1 General description of the char burning process

Let us start with "technological" mathematical models, which are focused on the kinetics of the process, the heat and mass transfer, and the resulting **FA** dispersion during coal combustion. Calculation of the **FA** dispersion is usually based on fragmentation mechanisms, including attrition, fracturing, percolation [45,46, 54-61], or thermal stresses [62-64]. Fragmentation due to attrition corresponds to combustion in fluidized beds with a high particle concentration [65,66], This mechanism does not explain the production of numerous small fragments, whose size by orders of magnitude is lower compared with that for the parent fuel particles. During fracturing, fragmentation to only a few pieces is possible. These pieces have a size which cannot be significantly smaller than the size of the parent particles. In its turn, the percolation mechanisms of porosity generation are more universal, they are extensively used to simulate and clarify the effects of various factors on char burn-out and fragmentation [67-70].

The percolation models are frequently used for simulation of the de-volatilization and char combustion stages. In the percolation models, usually only one coal particle is considered because it is assumed that all particles show identical behavior. Usually, the coal or char structure is represented as a 3-D cubic network composed of different types of cells which are volatile matter, char or coal matter, ash and voids. An original porosity is generated by the random and uniform introduction of cells that correspond to pores in the matrix. The percolation begins with gasification of peripheral cells, which corresponds to their transformation into ash or void cells. The direction of the gasification front from periphery to center is determined by Monte Carlo procedures [67-71]. In this case the important swelling processes are not taken into account. Such processes can be accounted for when one applies Monte Carlo procedures to simulate gasification, which starts inside the particles without direct connection with their outer surface. The de-volatilization process continues until all volatile cells are depleted. Then the stage of combustion in the emptied space of pores begins. During this stage, the relation between the rates of chemical reaction of char combustion and diffusion of oxygen and reaction products is taken into account. Fragmentation takes place at a threshold porosity, defined by the theory of percolation [62,71]. For example, this threshold porosity value was determined as 0.833, corresponding to a burn-out of 25% by Arene et al.57).

The adjustment of model parameters to fit data make it possible to use all these alternative models to predict qualitatively important features of the coal and char evolution or at least to understand it. This can work well for estimation of technological parameters, but it ignores such important physicochemical mechanisms as fusion and vaporization of a significant part of inorganic components, condensation of released vapors, swell of char, appearance and disappearance of cenospheres or plerospheres, etc. Only some of the known mathematical models at least formally take into account the swelling and sintering 70,71). In other models very rapid de-volatilization and total lack of swelling are assumed by Leckner60). However, the inevitable simplification for mathematical formalization is dangerous because “Das kind mit dem bade ausschutten” [c], i.e. one can miss significant physical and chemical mechanisms that control the formation of certain types of structures.

4.2 Physico-chemical mechanisms

We believe that an adequate description of fuel particle combustion should be based on the physico-chemical factors that were ignored in the existing mathematical models. To start with, let us briefly discuss the properties of the major ash-forming compounds in coal 1-4,12), such as mineral inclusions as well as organically bound heteroatoms. The ash-forming heteroatoms can include, e.g., S, N, O, many types of metals, etc. 1-6,12). The composition and content of these heteroatoms and inclusions as well as the size of the mineral inclusions and their distribution vary significantly from one coal to another depending on coal rank, its geological location, separation method, etc. The typical mineral inclusions are alumosilicates and silicates (e.g. clays, quartz), carbonates (e.g. calcite, dolomite, siderite), sulfides (e.g. pyrite) and oxides 1-4,12-16), etc. The starting average size of such inclusions is approximately 1 μm.

The high temperature and the reducing atmosphere enhance volatilization of a portion of the inorganic ash-forming compounds. Even elements present as refractory oxides such as SiO_2, CaO and MgO with very high melting and boiling temperatures can volatilise under the reducing conditions inside the burning char. This generates such volatile forms as SiO, Ca, Mg, NaCl 53, 72-78). Typically, ash precursors, which are found as included or excluded mineral oxides in coal, are not easily volatile. These precursors are the source of coarsely dispersed ash. Whereas the ash precursors, which are found as organically-bound and as salts, are easily volatile during combustion. Such precursors are the source of finely dispersed ash. The resulting fine ash particles grow by coagulation, recondensation (Ostwald ripening79-82)) and agglomeration83,-85). Non-volatile components can melt and coalesce inside the char particles or on their surface. Some minerals do not fuse in the char during combustion and their composition remains almost unchanged throughout the combustion process, resulting in ash particles with compositions similar to that in the parent coal.

The volatilized ash compounds (especially K, Na, S, Ca, Mg, Sr, Ba, Zn, Si, chlorides, sulfates, etc.12,13,40,51-54,74-86,87)) form new fine particles by homogeneous nucleation outside the burning zone, but inside this zone they form residual ash particles inside the char particles and on the char surface by heterogeneous condensation51, 88-92). The amount of vaporized ash strongly depends on the char combustion temperature, since a higher temperature leads to more vaporization of ash materials 74,91,92). If the parent coal contains more easily volatile elements, the production of submicron particles also increases68,72). The concentration of submicron particles is affected by the furnace wall temperature, fuel/air ratio, preheat temperature and the furnace aerodynamics74, 93).

The scenario of **FA** formation based on such an approach can include four main mechanisms whose action results in the formation of a bimodal (or trimodal by Yu et al. 92)) ash particle size distribution. The fine particles (<1 μm) are produced via vaporization/condensation of easily volatile ash compounds. The large particles (>1-5 μm) are produced from fragmentation of char and excluded mineral particles [53, 94]. The extent of char fragmentation depends on the char swelling behavior 53, 95-101). If the char fragments are large and contain large mineral particles, this mineral will coalesce. The occurrence of a trimodal distribution identified by Yu et al.92) results from agglomeration of the coarse particles.

It is obvious that along with the development of modern variants of mathematical modeling, which gradually scramble out from Procrustes' bed of model restriction and are helpful for technological appreciations, fundamental research is necessary to account for possible combination mechanisms and physical simulation with minimum restrictions, assumptions, and simplifications. Such models are unavoidable at today's stage of development of math-

---

[c] Throw the babe out with the bathwater.

ematical modeling. The results of such fundamental physicochemical research can be used to develop more adequate mathematical models of solid fuel combustion.

4.3 The general scheme of supramolecular structure formation

Let us discuss the generalized physicochemical scenario of the appearance and disappearance of cenospheres as well as plerospheres during fly ash production during high-temperature coal combustion at thermal power plants. Our scenario should include all models and mechanisms considered above on the sequential characteristic stages of heating of coal, burning of char, and cooling of ash as well as the fact that the ongoing transformations strongly depend on the type, content, form and distribution of inorganic and other components in the coal. The following discussion relates to bituminous carbons (solid fuel, or **SF**) that swell during burning and can be assumed as a source for cenospheres and plerospheres.

Fig. 3 shows a generalized schematic of the formation of the supramolecular structure of the **MS** and **FA** during the high-temperature combustion of pulverized **SF**. The transfer "**a**" → "**b**" corresponds to de-volatilization at fast heating. The de-volatilization occurs from the outer surface to the center of a particle and is accompanied by a movement of a temperature front. Removing the volatile compounds should result in the formation of microporosity, but simultaneous high-temperature heating results in plasticization of the residual phase and its sintering with formation of large pores [46,47, 102-105]. The formation of porosity occurs according to the percolation mechanism and can result in fragmentation.

Fig. 3c corresponds to the starting of the char

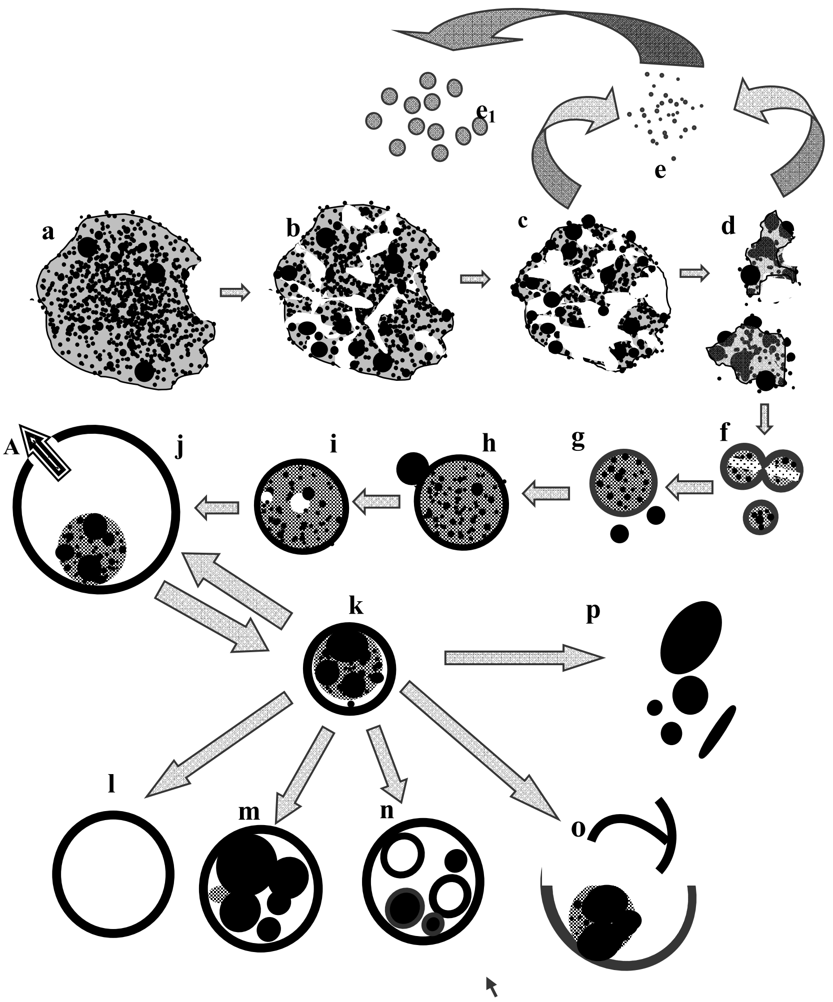

Fig. 3 Successive stages of **MS** and **FA** formation during the high-temperature combustion of pulverized solid fuel (for a description, see the text). The gray color corresponds to carbon, black to inorganic components. The arrows in **d** and **f** show the direction of the capillary forces, the arrow **f** shows the places of appearance of a concave meniscus in the contact zone between particles, the arrow **A** in **j** shows a breakthrough of gas through the shell.

burning stage inside pores and on the surface. Gas can be removed from the volume of the particles through the pores, connected to the outer surface, so the combustion reaction shifts to the diffusion regime [20,21]. In parent **SF** particles, various mineral forms are distributed randomly (**Fig. 3a**). The burning-out of char is accompanied by a concentration of mineral components on the surface, decomposition and consolidation of the chemically bound species, melting and sintering of the most fusible forms (e.g. congruent melting of metasilicate and sodium metasilicate occurs, respectively, at 1090℃ , and 875℃ , according to Bryers [14]). So the coarsely dispersed minerals, which are relatively weakly associated with carbon, can melt and coalesce. Mineral substances in bonded forms break bonds with carbon and convert to volatile products that condense according to the mechanism of homogeneous nucleation in the cooling zone (**Figs. 3e**” and **3e**$_1$) or deposit on the surface of the existing particles via heterogeneous nucleation. Nucleation via the “**e**”→“**e1**” pathway results in formation of the fine **FA** fraction, although the average particle size can increase due to Ostwald ripening.

Simultaneously, the fragmentation occurs at this stage (**Fig. 3c→Fig. 3d**). The increase in temperature results in pyrolitic breaking of a part of the bonds between the atoms of carbon. As a result, the remaining carbon fragments become labile, and a certain part of them transforms to the mobile form of pitch. The overall lability of the forming plastic *metaplast or mesophase* (by Marsh [105]) depends on the temperature and volume ratio of liquid to solid. When the latter ratio exceeds a certain threshold value, the metaplast transforms from visco-plasticity to the fluid-viscosity state [-], e.g. according to Raask [12] and Spiro [107], 50%wt. of pitch in parent SF particle is necessary to form a viscous state.

The labile metaplast at this stage consists of the products of carbon pyrolysis and labile mineral forms. Under the influence of the surface capillary forces, the metaplast modifies the surface of char particles, fills the remaining pores, and distributes evenly on the surface, forming an intact shell. Under equilibrium conditions [32, 109], such shells should have a constant curvature. This contributes to the transformation of particles of arbitrary shape into spheres (**Figs. 3d→Fig. 3f**), and provides a constant curvature and thickness of the shell. A violation of this requirement is accompanied by a spontaneous redistribution of matter in shells until their thickness and curvature becomes constant. More refractory mineral components and unburned solid carbon form the core of the corresponding hybrid particles (**Fig. 3g**) with viscoplastic shells and less plastic cores. The dynamics of the further transformation includes interrelated processes on the surface and inside such hybrid particles. The driving force behind these processes is governed mainly by the action of surface tension σ and surface curvature, while resistance to these processes is provided by viscosity η of the metaplast [62, 110].

The increase in temperature reduces the viscosity of the components forming the core, thus facilitating their gradual transition from the core to the shell. Direct contacts between particles cause the formation of a meniscus in the zones of contact and the appearance of capillary forces that bring the particles together (**Fig. 3f**). The intensity of these processes is determined by the balance of forces of surface tension and viscosity. The detailed mechanisms of such processes is considered, for example, in [111-115]. For simple estimations, one can consider the dimensionless parameter $\psi = \sigma\tau/\eta\,\mathbf{R}_0$, where σ is the surface tension of the metaplast, τ is the time, η is the viscosity of the core or shell, and $\mathbf{R}_0$ is the particle radius, or effective pathway of a transfer. Growth of ψ increases the depth of transformation. For example, a high value of ψ can lead to complete coalescence of a pair of particles in **Fig. 3f** with the formation of a single spherical particle (**Fig. 3g**), and a small value of ψ more likely corresponds to particles sintering in the contact zones with the formation of aggregates (**Fig. 3h**).

As a result, easy-to-melt mineral inclusions contribute to the growth of particle size due to sintering and coalescence, but volatile forms can deposit at contact zones accompanied by the formation of intergrown assemblies of particles, or can precipitate outside the burning zone, resulting in the formation of the small particles [31]. These effects are controlled by diffusion and kinetics, variation of “lifetime” in different zones, etc. Therefore, multiple collisions between particles and aggregates are accompanied not only by the destruction of the least stable (loose) particles according to the mechanisms of abrasion and splitting, but also the agglomeration with the formation of new aggregates, and as a result persistence and growth of the most densely packed, i.e. strong, ones.

4.4 Formation of cenospheres and plerospheres

Even more significant events occur due to the fact that the direct link of the core with the outer space is absent due to the presence of an intact shell of

metaplast at this stage. Therefore, the gas released in the cores leads to the formation of bubbles (**Fig. 3i**). The sources of this gas are the products of pyrolysis and gasification of unburnt solid fuel, decomposition of minerals as well as other volatile forms. Under equilibrium conditions, the pressure of gas in such bubbles depends on their radii **r** according to the Laplace-Young law $\Delta P = 2\sigma/r$. The difference of ΔP between bubbles with different **r** promotes the growth of large bubbles due to diffusion of gas from the bubbles of small size, and coalescence of contacting bubbles with the formation of one or several bubbles in the bulk surrounded by the shell. The pressure in the bubbles can exceed the equilibrium under real conditions of fast temperature increase. But in any case, gas release is accompanied by swelling of the hybrid particles with an increase of the external size, D0, and reduction of wall thickness **t** (the transition from **Fig. 3i** to **3j**). Such hybrid spherical particles with gas-filled cavities are the direct precursors of **MS**. To form **MS** they must withstand swelling in the hot zone, solidification during cooling, as well as survive in collisions with other particles.
Let us make estimations. Changing the relative thickness of the shell t/D_0 with swelling of microspheres is derived from equation (4) at $V_t \approx$ const in the form

$$t_i/D_{0i} = (V_0/V_{0i})\,(t_0/D_0) \qquad (15)$$

where t_0, D_0, and V_0 are the shell thickness, external diameter, and volume of an initial sphere (state 0), and t_i, D_{0i}, and V_{0i} are that for a swollen sphere (state **i**). Thus, an increase of volume is accompanied by a decrease of t_i/D_{0i}. For example, a twofold increase of volume results in a twofold decrease of t/D_0, while the external diameter increases by only 26%.

Blowing up of the shell as a result of the increase of the internal gas pressure is accompanied by an increase in stress in the shell to maximal critical values of $\sigma_{\tau,\max}$. Above this critical value the shell destructs. The theory of thin spherical shells' stability is a classic problem of the elasticity theory[116,117]. According to one of the basic equations of this theory, introduced by Laplace, in the simplest case of a thin-walled spherical shell with $(t/D_0) \rightarrow 0$, the critical gas pressure inside the cavity $P_{\max}$ is defined as

$$P_{\max} = 4\,\sigma_{\tau,\max}(t/D_0) \qquad (16)$$

where $\sigma_{\tau,\max}$, is expressed in units of pressure.

The problem of the strength of hollow microspheres of glass-like materials is intensively investigated in connection with the prospects of use of such materials for the storage of compressed hydrogen as fuel for cars[118,119], in problems of volcanology[120-130], during the studies of properties of inorganic and polymeric glassy materials[124-127], in general fracture mechanics[128-131], etc. For glass and ceramic **MS** that are considered for hydrogen storage, $\sigma_{\tau,\max} \sim 10^4$ atm[118,119]. The results of numerous studies of the strength limit of glass-like materials in various forms (microspheres, microbubbles, vesicles, etc.) at temperatures up to the temperature of vitrification T_G, give the values of $\sigma_{\tau,\max}$, in the range of 10^3 -10^5 atm[120-122]. According to Mungall et al.[120] and Romano et al.[121], the strength practically does not change if the cavity is filled with CO_2 or Xe, but may be reduced by 1-2 orders of magnitude in the presence of water vapor. The authors explain this effect with the appearance of micro-cracks in the shell due to volume changes caused by the processes of hydration-dehydration during temperature changes. It is essential that this effect is weakened when the cooling rate is high (200℃/s), which is characteristic for the conditions of a TPP, as well as with an increase of the size of **MS** at D_0> 50 microns[121]. The problem of thermal stresses in hollow spheres of glass is discussed in detail by Nowacki[129] (p.219). In general, the strength decreases with the loss of sphericity, the presence of microcracks, surface roughness and other defects that contribute to stress concentration[128,129]. These stresses decrease the strength of individual **MS** and lead to some statistical distribution of probability of their destruction[61,63,64,120,129]. Similar relationships are known for the viscoplastic or viscoelastic membranes and films at $T > T_G$ (virtrification temperature) at much smaller values of $\sigma_{\tau,\max}$[128-134].

The values of $t/D_0 = 0.06 \pm 0.04$ obtained in [15] can be considered as critical $(t/D_0)_{cr}$. Further swelling with an increase in D_0 and a corresponding decrease in **t** leads to destruction of the shell. Some spread in t/D_0 values is easily explained by, for example, variations in the values of $\sigma_{\tau,\max}$, which depends on the chemical and phase composition, plasticity, the rate of gas emission and other factors determining the mechanical, rheological and other properties of the shell[20,97,98]. It is essential that the values of t/D_0 that were obtained in by Ngu et al.[15] for intact **MS** after polishing are close to the usually observed values for shredded **MS**. Apparently in the hot zone, **MS** with $t/D_0 < (t/D_0)_{cr}$ continue to swell, and those with $t/D_0 > (t/D_0)_{cr}$ crack or transform by an oscillation mechanism, which is discussed below. As a result, only **MS** with $t/D_0 < (t/D_0)_{cr}$ can escape the hot zone and survive. The situation of $t/D_0 \ll (t/D_0)_{cr}$ is not realistic due to extremely high internal pressures in small bubbles, according to the Laplace-Young law.

This tough condition can be the cause of the small fraction of **MS** in the products of combustion in TPPs, as well as the experimentally observed narrow range of values of **t/D_0** in cenospheres and plerospheres.

In general, the destruction may occur both during the viscoplastic state in the hot zone, and during cooling to **$T < T_G$** in transition to the brittle state typical for glass-like materials. The trigger for destruction can be the growing internal pressure during a plastic stage, the external pressure, which can exceed the internal one when **MS** are cooled down, and the kinetic energy of a collision.

The variants of destruction with the formation of cracks (**Fig. 1c**) and the ejection of large fragments of shell (**Fig. 1a**) were shown earlier. The complete disintegration of **MS** into separate fragments (not shown) is also possible. All these options are typical for brittle fractures that most likely start at the stage of cooling down to **$T < T_G$**. The problem of the formation, growth and destruction of **MS** with viscoplastic or viscoelastic shells is considered, for example, by Sheng and Azevedo[21)] and Dacombe et al.[64)], who studied the formation of fly **FA** and **MS**, Yao et al.[114)] and Ribe[135)], who attempted to develop a general theory of the dynamics of thin viscous films, Mungall et al.[120,121)], who studied the cooling of volcanic lava or by van der Schaaf and Beerkens[136)] who examined the behavior of glass spheres in the molten metal.

The simplest scenario of the **MS** destruction at this stage involves breakthrough in the shell at **$t/D_0 < (t/D_0)_{cr}$** accompanied by gas emission, possible loss of part of the shell, the subsequent collapse and re-formation of an intact shell over a preserved core. In the newly formed shell, the diameter of the particle **D_0** becomes significantly smaller, and the value **t/D_0** increases to values that allow the re-formation and growth of new bubbles up to values of **$(t/D_0)_{cr}$** followed by repeated re-destruction (**Fig. 3j$\rightleftarrows$3k**). These stages of swelling and collapse of the particles can be repeated many times, until the depletion of the source of gas or the moment of transition of particles in the cooling zone[21, 64)] happens.

During such oscillations, the plastic components that form the core can move as a whole in the mesoplast of a shell or can gasify. The transport of such **MS** into the cooling zone leads to the formation of cenospheres (**Fig. 3l**), while an incomplete transition of components in the shell can be a cause of plerosphere formation (**Fig. 3m**). **Fig. 3n** shows a hypothetical schematic for plerosphere formation with hollow particles within a single shell. This can be implemented if the processes such as 3j$\rightleftarrows$3k proceed at the level of "internal" particles inside a mutual large sphere. Brittle fracture of **MS** with parameter **$t/D_0 < (t/D_0)_{cr}$** leads to the formation of fragments (**Fig. 3o**), which can sinter and transform into non-porous spheres or aggregates of **FA** (**Fig. 3p**). This allows the formation of intact particles of **FA** with a wide size distribution and various types of morphology starting from the spherical particles formed during sintering and coalescence in the hot zone, and ending with a variety of products whose transition to an equilibrium spherical form was not finished (**Fig. 3p**). According to Seames[23)] and many others, the majority of **FA** particles are spheroidal. This indicates their preferential formation and an intense sintering in the hot zone. Frequently, observed particles with a typical acute-angle shape and a size of less than 1-2 microns are clearly fragments - the products of brittle fracture in the cooling zone. One can believe that in typical situations, the formation of different forms of fly ash from bituminous coal passes through a stage of formation of the **MS**.

The case shown in **Fig. 1b** can be regarded as the consequence of an additional special type of fracture of viscoplastic shells in the hot zone. The actual conditions of the combustion of the fuel particles do not match the equilibrium. This might cause the formation of individual damaged areas in the shell with local volcano-like gas release without destroying the entire shell. The reduction of pressure to equilibrium is accompanied by a contraction of the shell and its "healing" due to the action of surface-capillary forces. This mechanism is similar to excess gas pressure discharge in wheat dough studied by Hailemariam[137)], or volcanic lava[120-123)], followed by "healing" the formed craters. This explains the presence of "craters" or their traces on the surface of **MS** as clearly observed in **Fig. 1b**. Such craters serve as emergency pressure relief valves.

The conventional ideas on the mechanism of cenosphere formation proposed by Fisher et al.[11)] and Raask[12)] attribute the main source of gas to only the mineral inclusions of types of carbonates, sulfides, sulfates, and clay minerals, the decomposition of which gives a moderate amount of gaseous products. The mechanisms "periodic shell collapse" and "pressure relief valve" (subsequently referred to as ***oscillation mechanism***) remove this restriction. Any compounds of fuel that are suitable to gas emission can be involved. Plerospheres can be formed in the hot zone as cenosphere precursors as the result of the incomplete transfer of mineral components from the core to the shell (**Figs. 3k, 3n, 3m**), and much less likely as a result of filling of the **MS** cavity with small spheres through cracks at the stage of cooling (the mechanism proposed by Goodarzi and Sanai[27]) and Shibaoka and Paulson[28])). So, the mechanisms proposed by Ngu in [15] seem to be the most probable.

4.5 Cooling stage

The cooling stage finishes the formation processes and states the molecular and supramolecular structure of the resulting materials. The formation of crystalline and amorphous solid phases sharply increases the viscosity. Simultaneously, the chemical and phase composition of the inorganic products of coal burning can significantly differ from the starting material due to the transformations that occurred and the redistribution of all mineral compounds noticed by Bryers[14]).

The cooling starts from the external surface. As a result, the temperature of the shell can be lower than that of the core, which is filled with gas in the case of cenospheres, or with solid untransformed compounds and gas in the case of plerospheres. The following events are determined by the balance between the changes of internal pressure **P** and the strength of the shell, which also changes according to the rheological properties of glass-like materials.

To illustrate these features, the typical dependence of the specific volume, ν, of a glass-like material with temperature, **T**, is shown in **Fig. 4**. The increase of **T** results in thermal expansion and increase of ν. The corresponding density, ρ, decreases. The high-temperature region (region A in **Fig. 4**) corresponds to the viscoplastic state of a melted matter. In the case of normally crystallizing compounds, a decrease of **T** to some critical $\mathbf{T}_c$ results in their crystallization (curve **I** (**AEF**)). But glass-like compounds are characterized by a high viscosity, which inhibits formation of a regular crystalline structure. Thus, curve **I** can be obtained for these compounds only during infinitely slow cooling down. More common are the curves of type **II** (**ABCD**), when transition from liquid to solid occurs within an interval of vitrification (**BC**) after some supercooling, which corresponds to an interval between $\mathbf{T}_C$ and $\mathbf{T}_1$. The vitrification temperature $\mathbf{T}_G$ (point **G** in **Fig. 4**) lies within this interval of $\Delta\mathbf{T}_G = \mathbf{T}_1 - \mathbf{T}_2$.

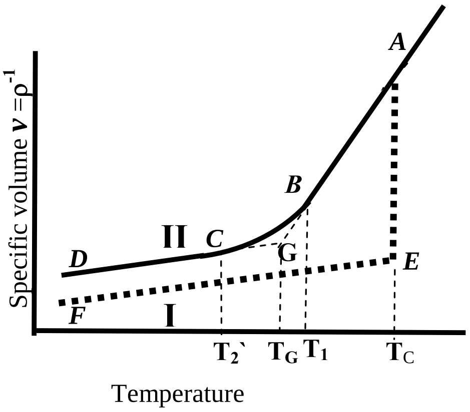

Fig. 4 Typical dependence of a specific volume ν (reciprocal to true density ρ) on temperature, **T**, for normally crystallizing (curve **I** - **AEF**), and glass-like (curve **II** - **ABCD**) compounds.

The softening temperature $\mathbf{T}_1$ corresponds to a transition from the viscous to plastic state, and the solidifying temperature $\mathbf{T}_2$ from the solid state. For many typical compositions of mineral compounds, the values of $\mathbf{T}_2 \approx 1250 \pm 250$℃, and $\mathbf{T}_1 \approx 1450 \pm 150$℃ [1-5]) apply, although in general $\mathbf{T}_2$ can vary from 480 − 500℃ for some alumosilicates to ~1500℃ (quartz) and 1700℃ (crystaballite)*4 . Usually, $\Delta\mathbf{T}_G \approx 100 - 200$℃ and, as well as $\mathbf{T}_G$, is determined by chemical composition. $\Delta\mathbf{T}_G$, and $\mathbf{T}_G$ increase with the cooling-down rate of the system.

The most essential point is that within the vitrification interval, the viscosity increases with several orders of magnitude, e.g. from $\eta \sim 10^{12}$ Pa・s (liquid melt) to 10^{16} Pa・s (solid phase), while the specific volume changes with 8÷12%[14,138]), and the rate of gas release decreases with temperature not as significantly. According to Frank-Kamenetsky[139]), with the value of carbon burning activation energy at 80-170 kJ/mol, a temperature decrease of 300÷500℃ results in only a tenfold decrease of the rate of carbon burning. Other reactions give similar estimations of the gas release rate.

The significant changes of rheological and, correspondingly, mechanical properties inhibit the action of the oscillating mechanism with shell regeneration and result in the increase of $\sigma_{\tau,\max}$ in equation (16). This increase is more considerable at $\mathbf{T} < \mathbf{T}_G$. Let us discuss possible scenarios of the events occurring during cooling down in more detail, assuming the mentioned features.

In the case of only volatile compounds, the decrease in temperature results in their supersaturation followed by rapid precipitation on the surface of neighboring particles, or nucleation of new particles. Nucleation increases the fraction of small particles with the size of 0.1 - 1.0 μm that can hardly be captured with electrostatic precipitators, and which are just as dangerous for ecology as cenospheres. These fine particles can be easily spread with the wind, penetrate into respiratory paths, etc.[2-5]. On the other hand, the larger particles can serve as distinctive collectors that can capture such volatile components and reduce their concentration. From this point of view it would be useful to develop various technologies that would facilitate the effect of deposition of volatile compounds on such "collectors".

The transformation of all forms of particles at $\mathbf{T} < \mathbf{T_2}$ to a brittle state must intensify their mechanical destruction. Cooling leads to fixation of the cavities, and the parameter $\mathbf{t/D_0}$. Microsphere shells completely lose their ability to regenerate after depressurization at $\mathbf{T} \approx \mathbf{T_2}$. The condition of maintaining the integrity of the intact shell MS can be written as

$$\mathbf{P(T)} < 4\sigma_{\tau,\max}\mathbf{(T)}\ [\mathbf{t/D_0}] \qquad (17)$$

where $\mathbf{P(T)}$ is the pressure inside the cavity, which depends on $\mathbf{T}$ and gas source, $\sigma_{\tau,\max}$ is the parameter in equation (16), which also depends on $\mathbf{T}$, as well as on other parameters. The shell is viscoplastic at $\mathbf{T} > \mathbf{T_1}$, it is plastic within $\Delta\mathbf{T_G}$, and becomes brittle at $\mathbf{T} < \mathbf{T_2}$ having high value of $\sigma_{\tau,\max}$.

The cooling of cenospheres which do not have an internal gas emission source, is accompanied by the decrease of $\mathbf{P(T)}$ (up to a 5 or 6-fold decrease). This allows fulfillment of the condition determined by **eq. (17)** when $\mathbf{T} > \mathbf{T_1}$, and moreover at $\mathbf{T} < \mathbf{T_1}$. One can explain the frequently observed brittle cracking of cenospheres to the pieces of various size with a non-uniform distribution of stresses in the shell that happens mainly at $\mathbf{T} < \mathbf{T_2}$.

The case of plerospheres, which can contain gas emission sources, is more complicated. If the gas emission at $\mathbf{T} \geq \mathbf{T_1}$ (or $\mathbf{T} \geq \mathbf{T_G}$) is not compensated by a reduction of the internal pressure due to the reduction of $\mathbf{T}$, then this **MS** is most likely doomed to be destroyed. Experimentally, one can observe only plerospheres whose shells are partially destroyed. We believe this destruction is caused by the mechanism of brittle fracture (**Fig. 1d**) at $\mathbf{T} < \mathbf{T_G}$. Plerospheres with intact shells can be observed by applying the technique of electron-microscopic analysis of thin sections[15]. But the detection of such plerospheres requires a pre-selection of **MS** with whole and broken shells, or additional measurements of the density and the accessible surface before and after crushing of the **MS**. Unfortunately, such additional studies were not carried out by Ngu[15]. Analysis of the changes in density and specific surface area in section 3.2 shows that even if plerospheres with intact shells are preserved, then their contribution is small. However, the general problem of the existence of the plerospheres with intact shells remains debatable, and also options for their efficient utilization are questionable.

5. Conclusion

Based on the presented analysis one can provide a probable sequential scheme of plerospheres, cenospheres and fly ash formation during the burning of pulverized bituminous coals with a typical composition of mineral admixtures at thermal power plants.

De-volatilization transforms the initial coal to char and shifts burning to the volume of char particles through pores. The char combustion is accompanied by the increasing concentration of all mineral forms plus the formation of volatile and condensed phases. When the burning-off degree is high, the percolation scenario proposed in mathematical models[54-70] become less probable and can be used for non-swelling forms of fossil fuel (peat, lignite, etc.) only. The formation of a supramolecular structure of the products of bituminous coal burning is governed by a joint action of burning and pyrolysis of carbonaceous material and the behavior of mineral fractions: volatility of bound forms and melting of non-volatile forms. The general schematic of the main processes is shown in

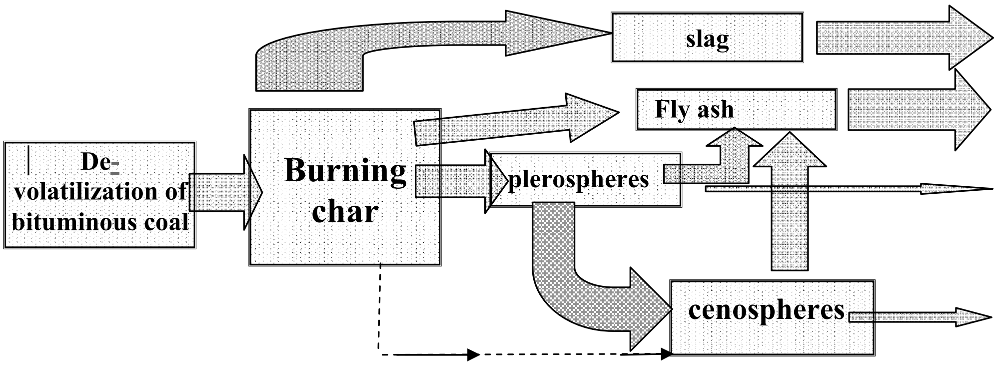

Fig. 5 The general schematic of transformation of pulverized bituminous coal during combustion in the furnaces of thermal power plants.

Fig. 5.

An intensive sintering of the products of incomplete carbon burning results in the formation of heavy residues in the form of slag (*bottom ash*) which precipitates mainly at the bottom of the furnaces. Another part of the matter is made up of slightly aggregated fine particles that are carried out by the air-gas flow and which deposits in electrostatic precipitators or ends up in the exhaust gases. The fly ash formation most likely goes through skeletal structures similar to that of plerospheres with the possible coexistence of multiple-cavity bubbles within a single particle. They are then transformed into “normal” plerospheres with one or more interior particles which can serve as the contributors of gasification. The above-discussed ***oscillation mechanism*** can start its action at this stage, resulting in the formation of microspheres or their fragmentation. The destruction of the **MS** in the hot zone or at the beginning of cooling, followed by sintering and aggregation of the resulting fragments leads to the formation of non-porous fly ash. So, fragmentation is possible during all sequential stages simultaneously with mechanical breakage due to collisions. The destruction at the cooling zone is accompanied by the formation of defective **MS** and fragments, which also partially sinter, giving a contribution to the **FA**. Preservation of many plerospheres with intact shells has a low probability. However, they can persist in the form of the largest **MS**, which successfully escaped destruction. This corresponds, for example, to data about the dependence of the content of plerospheres on their size obtained by Ngu15). So it can be assumed that the main FA precursors are the volatile mineral species and products of damage of plerospheres and cenospheres, while the main cenosphere precursors are plerospheres. Apparently, the same concept with minimal modification can describe the origin of typical swelling products of the high-temperature combustion of heavy oil, garbage, biological materials and domestic waste according to Bryers14).

The proposed scenario explains reasons for a weak dependence of the shell thickness, **t**, on the **MS** diameter **D** (**t/D** values are defined by temperature and chemical composition), and why the plerosphere size is large and their relative fraction is low compared with cenospheres. This scenario emphasizes the important role of the cooling stage for the fragmentation processes, which is usually ignored. It also includes a general picture of physico-chemical processes during the de-volatilization of coal, burning of char and cooling of fly ash based on the fundamental physico-chemical concepts, which is absent in previous well-known publications.

We hope that this analysis of the properties and genesis of the supramolecular structure of cenospheres and other products of high-temperature combustion of pulverized coal based on the mechanisms assumed here are useful from a technological point of view.

List of symbols and acronyms

CS	cenosphere
FA	fly ash
IMS	intact microsphere
MS	microsphere
PS	plerosphere
TPP	thermal power plant
SF	solid fuel
SMS	shredded microsphere
t	microsphere shell thickness
D_0	microsphere external diameter
A_0	specific surface area of intact microsphere
A_t	specific surface area of shredded microsphere
ρ_{He}	density, measured by means of helium pycnometry
ε_0	porosity of void sphere (for example, cenosphere)
ε_Σ	porosity of sphere filled with internal spheres (for example, plerosphere)
ε_d	$\varepsilon_\Sigma / \varepsilon_0$ is the porosity between internal spheres and the inside filled sphere
δ	apparent density
σ	surface tension
$\sigma_{\tau,\max}$	critical stress values
η	viscosity
P	pressure
V_0	total microsphere volume
V_t	shell volume
V_d	volume of internal spheres in plerosphere
T_G	vitrification temperature
X	mass of internal spheres related to total mass of plerosphere **(eq. 12,13)**
Xi	related mass of component **i** (2)

References

1) Kizelshteyn, J., Dubov, I.V., Shpitsgluz, A.L. and Parada, S.P. (1995): “Ash and Slag Components of TPP”, Energoatomizdat, Moscow, p.176 (in Russian).

2) Zyrynov, V. V., Zyrynov, D.V. (2009): “Fly Ash- raw material”, Maska, Moscow, p.320. (in Russian).

3) Shpirt, M.Ya., Clare, V.R. and Persikov I.Z. (1990):

"Inorganic Constituents of Solid Fuels", Chemistry, Moscow, Russia, p.382. (in Russian).

4) Sear, L.K.A. (2001): "The Properties and Use of Coal Fly Ash", Thomas Telford Ltd, London, England,p.220.

5) Drozhzhin, V.S., Piculin, I.V., Kuvaev, M.D. et al. (2005): Technical Monitoring of Microspheres from Fly Ashes of Electric Power Stations, in the Proc. of World of Coal Ash Conference, April 11 -14, Lexington, Kentucky, USA, pp.113-114.

6) Chock, D. P., Winkler, S, and Chen, C. (2000): A study of the association between daily mortality and ambient air pollutant concentration in Pittsburg, Pencylvania: J. Air Waste Manage Assoc., Vol. 50, pp.1481-1493.

7) Anderson, H. R., Bremner, S. A., Atkinson, R. W., Harrison, R. W. and Walters, S. (2001): Particulate matter and daily mortality and hospital admissions in the west midlands conurbation of the U. K. associations with fine and coarse particles, black smoke and sulfate, Occupational Environ. Med., Vol. 58, pp.504-510.

8) Heiken, G. and Wohletz, K. (1985): "Volcanic ash", University of California Press, Berkely, USA, p.201.

9) Vereshagina, T.A., Anshits, N.N., Zykova, I.D. Salanov, A.N., Tretyakov, A.A. and Anshits, A.G.: Obtaining of cenospheres from power ashes with stabilized composition and their properties, Chem. Sustain. Develop., Vol. 9, (2001), pp.379-391 (in Russian).

10) Vereshagin, S.N., Kurteeva, L.I. and Anshits, A.G. (2008): Contents of particles of various size and density in concentrates of cenospheres fly ashes from burning of coals from Kuznetsk Basin, Chem. Sustain. Develop. Vol. 16, pp.529-536 (in Russian).

11) Fisher, G. L., Chang, D.P.Y. and Brummer, M. (1976): Fly ash collected from electrostatic precipitators: Microcrystalline structures and the mystery of the spheres, Science, Vol.192, pp.553-555.

12) Raask E. (1985): "Mineral Impurities in Coal Combustion ? Behavior, Problems, and Remedial Measures", Hemisphere Publ. Corp., New York, USA.

13) Vassilev, S.V., Menendez, R., Diaz-Somoano, M . and Martinez-Tarazona, M. R. (2004): Phase-mineral and chemical composition of coal fly ash as a basis for their multicomponent utilization, Fuel, Vol.83, pp.1563-1583.

14) Bryers, R.W. (1996): Fireside slagging, fouling and high-temperature corrosion at heat transfer surface due to impurities in steam raising fuels, Prog. Energy Combust Sci., Vol.22, pp.29-120.

15) Ngu, L.-n, Wu, H. and Zhang, D.K. (2007): Characterization of ash cenospheres in fly ash from Australian power stations, Energy & Fuels, Vol.21, pp.3437-3445.

16) Vereshagin, S.N., Anshits, N.N., Salanov, A.N., Sharonova, O. M., Vereshagina, T.A. and Anshits, A.G. (2003): Microspheres of fly ash as a source for catalytic supports, adsorbents and catalysts, Chem. Sustain. Develop, Vol.11, pp.303-308.

17) Yu, D., Xu, M., Yu, Y., Lin, X, (2005): Swelling behavior of Chinese bituminous coal at different pyrolysis temperatures, Energy & Fuel, Vol.19, pp.2448-2494.

18) Koopman, M., Chawla, K.K., Ricci, W., Carlisle, K., Gladsyz, G.M., Labor, M., Jones, M.L., Kerr, K., George, M., Gouadec, G. and Tournie, A. (2009): Titania-coated glass micro-balloons and cenospheres for environmental applications, J. Mater. Sci., Vol.44, pp.1435-1341.

19) Wang, S. (2008): Application of solid ash based catalysts in heterogenic catalysis, Environ. Sci. Technol., Vol. 42, pp.7055-7063.

20) Oh, M.S., Peter, W.A. and Howard, J.B. (1989): An Experimental and Modeling Study of Softening Coal Pyrolysis, AIChE J., Vol.35, pp.775-782.

21) Sheng, C. and Azevedo, J.L.T. (2000): Modeling evolution of particles coal at combustion, Proceed. Combust. Institute, Vol.28, pp.2225-2230.

22) Matsuoka, K., Akino, H., Xu, W.C., Gupta, R.D, Wall, T.E., and Tomita, A. (2005): The Physical character of coal char formed during rapid pyrolysis at high pressure, Fuel, Vol.94, pp.63-69.

23) Seames, W.S. (2003): An initial study of the fine fragmentation fly ash particle mode generated during pulverized coal combustion, Fuel Process & Technology, Vol.81, p.109.

24) Frandsen, F.J. (2009): Ash research from palm coast, Florida to Banff, Canada: entry of biomass in modern power boiler, Energy & Fuels, Vol. 23, pp.3347-33878.

25) Sarcar, A., Rano, R, Mishra, K., K., and Mazumder, A. (2008): Characterization of cenospheres collected from ash-pond of a super thermal power plant, Energy Sources, Part A: Recovery, Utilization, and Environment Effects, Vol. 30, pp.271-283.

26) Dutta, K., Garg, A., Sangal, S., Mishra, B. K., Vankar, P., and Rohatgi P. R. (2005),:in "Energy Tends in Mineral Processing and Extractive Metallurgy, Eds. Misra, V. N., Das, S. C., and Subbaiah, T., Allied Publ., New Delhi, pp.3-7.

27) Goodarzi, F. and Sanai, H. (2009): Plerosphere and its role in reduction of the emitted fine ash particles from pulverized coal-fired power plants, Fuel, Vol. 88, pp.382-386.

28) Shibaoka, M., and Paulson, C. A. J. (1986): Genesis of char and ash plerospheres, Fuel, Vol. 65, pp.1020-1022.

29) Fenelonov, V.B. (2004): "Introduction to Physical Chemistry of the Formation of Supra-molecular Structure of Adsorbents and Catalysts", 2 ed., Novosibirsk, SB RAS, p.440. (in Russia).

30) Fenelonov, V.B. and Mel'gunov, M. S. (2006): Texturology, in "Surface and Molecular Catalysis" by ed. R. Richards, Taylor & Francis, New York, pp.257-336.

31) Blanco, F., Garsia, P., Mateos, P., and Ayala, J. (2000): Characteristics and properties of lightweight concrete manufactured with cenospheres, Cement and Concrete Research, Vol. 30, pp.1715-1722.

32) Moreno, N., Querol, X. J, Andres, M., Stanton, K., Towler, M., Nugteren,H., Janssen-Jurkovicova, M., and Jones, R. (2005): Physico-chemical characteristics of European pulverized coal combustion fly ash, Fuel,

Vol. 84, pp.1351-1363.
33) Gehlhoff, G. and Thomas, M.Z. (1926): Die physikalischen Eigenschaften der Glaser in Abhangigkeit von der Zusammensetzung, Z. Techn. Physik, Vol.7, pp.105-126.
34) Sun, K., Safford, H.W. and Silverman, A. (1940): Review of the relation of density and refractive index to the composition of glass: J. Amer. Ceram. Soc., Vol.23, pp.315-326.
35) Huggins, M.L. and Sun, K.H. (1943): Calculation of density and optical constants of a glass from its composition in weight percentage, J. Amer. Ceram. Soc., Vol.26, pp.4 -11.
36) Elliott, M.J. (1945): Glass composition and density changes, J. Amer. Ceram. Soc., Vol.28, pp.303-308.
37) Appen, A.A. and Gan, Fu-xi. (1959): Necotorye obshchie zacomernosti izmenenniya svoistv silicatnyich stekol, J. Appl. Chem. (Russ.), Vol.32, pp.983- 1206.
38) Naik, H.K., Mishra, M.K., Rao Karanam, U.M. and Deb, D. (2009): Evaluation of the role of a cationic surfactant on the flow characteristics of fly ash slurry, J. Hazard. Matter, Vol. 169, pp.1134-1140.
39) Ghosal, S. and Self, S.A. (1995): Particle size-density relation and cenosphere content of coal fly ash. Fuel, Vol.74, pp.522-529.
40) Vassilev, S.V. and Vassileva, C.G. (2007): A new approach for the classification of the coal fly ash based on their origin, composition, properties and behavior, Fuel, Vol.86, pp.1490-1512.
41) Bayat, B. (2002): Comparative study of adsorption properties of Turkish fly ash J. Hazard. Matter, Vol.95, pp.251-290.
42) Lester, E., Cloke, M. and Allen, M. (1996): Char characterization using image analysis techniques, Energy & Fuels, Vol.10, pp.696 -703.
43) Sarofim, A. F., Howard, J. B. and Padia A,S. (1977): Physical transformation of the mineral matter in pulverized coal under simulated combustion condition, Combust. Sci. Techn., Vol. 16, pp.187-204.
44) Flagan, R. C. and Friedlander, S. K. (1978): in Shaw, D. N. (ed.), Recent Developments in Aerogel Science, Wiley-Intersci., New York, pp.25-59.
45) Raask, E. (1986): Flame vitrification and sintering characteristics, ACS Symp. Ser., Vol. 301, pp.138-115.
46) Smoot, L.D. (ed.) (1993): "Fundamentals of Coal Combustion" , Elsevier Sci., New York,.
47) Smoot, L.D. and Smith, P.J. (1985): "Coal Combustion and Gasification", Plenum Press, New York, USA,.
48) Lahaye, L., Prado, G., (eds.) (1987): "Fundamentals of the Physical-Chemistry of Pulverized Coal Combustion" , Kluver Acad. Publ., Dardrecht,.
49) Lighty, J. S., Veranth, J. M., and Sarofim A.F. (2000): 2000 critical review -combustion aerosols: factors governing their size and composition and implications to human health, J. Air & Waste Manage. Assoc., Vol. 50, pp.1565-1622.
50) Bartok, W. and Sarofim, A. F. (1991): "Fossil fuel combustion, a source book," John Wiley & Sons Inc., New York, , p.866.
51) Christensen, K. A. (1995): "The Formation of Submicron Particles from the Combustion of Straw", Ph. D. Thesis, Techn. Univ. Denmark, Lyngby, Denmark,
52) Lind, T. (1999): " Ash formation in circulating fluidized bed combustion of coal and solid biomass", Ph. D. Thesis, Helsinki Univ.Technol., Espoo, Finland.
53) Wiinikka, H. (2005): "High Temperature Aerosol Formation and Emission Minimisation during Combustion of Wood Pellets", Ph. D. Thesis Lulea University Technol, Pitea, Sweden,
54) Sundback, C. A., Helbe, J. J., Boni, A. A. , Shah, N., Huffman, C. P. and Huggins, E. F. (1984): XX Intern. Symp. Combustion, The Combustion Inst., Pittsburg, pp.1495-1501.
55) Dunn-Rankin, D., and Kerstein, A. R. (1987): Numeral simulation of particle size distribution evolution during pulverized coal combustion, Combust. Flame, vol. 69, pp.193-209.
56) Srinivasachar, S., Toqan, M.A., Beer, J. M. and Ettouney, H.M. (1988): Percolation model for coal char particles combustion and fragmentation, Combust. Sci. Technol., Vol.57, pp. 55-70.
57) Arene, U., Cammarota, A., Massimilla, L., Siciliano, L. and Basu, P. (1990): Carbon attrition during the combustion of a char in a circulating fluidized bed, Combust. Sci. Technol., Vol. 73, pp.383-394.
58) Chirone, R., Massimilla, L. and Salatino, P. (1991): Comminution of carbons in fluidized bed combustion, Progr. Energy Combust. Sci., Vol. 17, pp.297-326.
59) Mitchell, R. and Akanetuk (1996): The impact of fragmentation on char conversion during pulverized coal combustion, XVI Intern. Symp. Combustion, The Combustion Inst., Pittsburg, pp.3137-3144.
60) Leckner, B. (1998): Fluidized bed combustion: mixing and pollutant limitation, Progr. Energy Combust. Sci., Vol. 24, pp.31-61.
61) N., Kurniawan, K., Griffits, T., Gralton, T. and Ray, R. (2007): Development of fragmentation models for solid fuel combustion and gasification as subroutines for inclusion in CFD codes, Fuel, Vol.86, pp.2221-2231.
62) Solomon, P.R. and Hamblen D.G. (1985): "Chemistry of Coal Conversion" (Ed. Schlosberg, R.H.), Plenum, New York, USA, pp.121-139.
63) Kerstein , A. R. and Edwards, B. F. (1987): Percolation model for simulation of char oxidation and fragmentation time-histories, Chem. Eng. Sci, Vol. 42, pp.1629-1634.
64) Dacombe, P., Pourkashanian, M., Williams. A. and Yap, L. (1999): Combustion-induced fragmentation behavior of isolated coal particles, Fuel, Vol.78, pp.1847-1857.
65) Sundback, C. A., Helbe, J. J., Boni, A. A., Shah, N., Huffman, C. P. and Huggins, E. F. (1984): XX Intern. Symp. Combustion, The Combustion Inst., Pittsburg, pp.1495-1501.
66) Liu, G., Wu, H., Gupta, R. P., Lucas, J. A., Tate, A. G. and Wall T.F (2000): Modeling the fragmentation of

non-uniform porous char particles during pulverized coal combustion, Fuel, Vol. 79, pp.627-633.

67) Salatino, P. and Massimilla, L. (1991): Modeling fragmentation by percolation in combustion of carbon, Powder. Technol., Vol. 66, pp.47-52.

68) Suzuki, A, Yamamoto, T., Aoki, H. and Miura T. (2002): Percolation model for simulation of coal combustion process, Proceed Combust. Inst., Vol. 29, pp.459.-466.

69) Kurose, R., Makino, H., Matsuda, H. and Suzuki, A. (2004): Application of percolation model to ash formation process in coal combustion, Energy& Fuel, Vol. 18, pp.1077-1086.

70) Kurose, R., Makino, H., Hashimoto, N. and Suzuki, A. (2007): Application of percolation model to particulate matter formation in pressurized coal combustion, Powder. Technol., Vol. 172, pp.50-56.

71) Sahimi, M. (1994): “Application of Percolation Theory” , Taylor & Francis, London, p.258.

72) Natusch, D. F. S., Wallace, J. R. and Evans, C. A. (1974): Science, Vol.183, pp.202-204.

73) Taylor D. D. and Flagan, R. C. (1982): The influence of combustion operation conditions on fine particles from coal combustion, Aerosol Sci. Tecnol., Vol. 1, p.103.

74) Senior, C. I., Panagiotou, T., Sarofim, A.F., Helble, J. J.: Formation of ultra-fine particulate matter from pulverized coal combustion, Preprints Symposia AChS, 45 (1), March 2000.

75) Quann, R. J. and Sarofim, A. F. (1982): Vaporization of refractory oxides during pulverized coal combustion, XIX Internat. Symposium on Combustion, The Combustion Inst., Pittsburg, pp. 1429-1440.

76) Quann, R. J., Neville, M. and Sarofim, A. F. (1990): A laboratory study of effect of coal selection on the amount and composition of combustion generated submicron particles, Combust. Sci. and Tecnol.,Vol.74, pp. 245-265.

77) Linder, E. R. and Wall, T. F. (1990): in “Mineral Matter and Ash Deposition from coal”. Eds: Bryers, R. W. and Vorres, K. S.,Unated Eng. Transtees, pp.321-331.

78) Jacob, A., Stucki, S. and Struis, R. P. W. J. (1996): Complete heavy metal removal from fly ash by heat treatment: influence of chlorides on evaporation rates, Environ. Sci. Technol., Vol. 30, pp.3275-3283.

79) Ostwald, W. (1901): “Analytisch Chemie”, 3rd ed. Enlelmann, Leipzig, Z. Phys. Chem., Vol. 37, p.385.

80) Madras, G. and McCoy, B. J. (2002): Transition from nucleation and growth to Ostwald ripening, Chem. Eng. Sci., Vol. 57, pp.3809-3818.

81) Madras, G. and McCoy, B. J. (2003): Continuous distribution theory of Ostwald ripening: comparison with the LSW approach, Chem. Eng. Sci., Vol. 58, pp.2903-2909.

82) Baldan, A. (2002): Review progress in Ostwald ripening theories and their applications to nickel base superalloys; part I; Ostwald ripening theories, J. Mater. Sci., Vol. 37, pp.2171-2202.

83) Wu, H., Bryant, G. and Wall, T. (2000): The effect of pressure on ash formation during pulverized coal combustion, Energy&Fuel, Vol.14, pp.745-750.

84) Neville, M., Quann, R. J., Haynes, B. S. and Sarofim, A. F. (1981): Vaporization and condensation of mineral matter during pulverized coal combustion, P Combust Inst., Vol 18, pp.1267-1274.

85) Helble, J., Neville and Sarofim, A. F. (1989): Factors determining the primary particles size of flame-generated inorganic aerosols, J. Colloid Interf. Sci., Vol. 128, pp.348-361.

86) Pagels, J., Strand, M., Rissler, J., Szpila, A., Gudmundson, A., Bohgard, M., Lillieblad, L., Sanati, M. and Swietlicki, E. (2003): Characteristics of aerosol particles formed during grate combustion of moist forest residue, J Aerosol. Sci., Vol. 34, pp.1043-1059.

87) Boman, C., Nordin, A, Bostrom, D. and Ohman, M. (2004): Characterization of inorganic particulate matter from residential combustion of pelletized biomass fuels, Energy & Fuels, Vol.18, pp.338-348.

88) Gupta, R. P. (2005): Coal research in Newcastle ? past, present and future, Fuel, Vol. 84, pp.1176-1188.

89) Markowski, G. R., Ensor, D. S., Hooper, R. G., and Carr, R. C. (1980): A submicron aerosol mode in flue gas from a pulverized coal utility boiler, Environ. Sci. Technol., Vol. 14, pp. 1400-1402.

90) Quann, R. J., Sarofim, A. F. (1982): Vaporization of refractory oxides during pulverized coal combustion, P. Combust. Inst., Vol. 19, pp.1429-1440.

91) Wornat M. J., Hurt, R. H., Yang, N. Y. C. and Headley, T. J. (1995): Structural and compositional transformation of biomass chars during combustion, Combust. & Fuel, Vol. 100, pp.131-143.

92) Yu, D.-X., Xu, M.-X., Yao H., Liu, X.-W., Zhou, K. (2008): Effective identification of the three particles modes generated during pulverized coal combustion, Chines. Sci. Bull., Vol. 53, pp.1593-1602.

93) Sethi, V. and Blaswas, P. (1990): Modeling of particle formation and dynamics in a flame incinerator, J. Air Waste Manage. Assoc., Vol.40, pp. 42-46.

94) Ten Brink, H. M., Smart, J. P., Vleeskens, J. M. and Williamson, J. (1994): Flame transformation and burner slagging in a 2.5 MW furnace firing pulverized coal, Fuel. Vol. 73, pp 1706-1711.

95) Liu, G., Wu, H., Gupta, R. P., Lucas, J. A., Tate, A. G. and Wall T.F. (2000): Modelling the fragmentation of non-uniform porous char particles during pressurized coal combustion, Fuel, Vol. 79, pp.627-633.

96) Helbe, J. J., Sarofim A. F. (1989): Factors determining the primary particles size of flame-generated inorganic aerosols, J Colloid Interf, Sci.,Vol. 128, pp.348-362.

97) Saastamoinen, J.J. and Richard, J.R. (1996): Simultaneous drying and pyrolysis of solid fuel particles, Combust. & Flame, Vol.106, pp.288-300.

98) Sun, Q., Li, W., Chen, H. and Li, B. (2003): The variation of structural characteristics of minerals during pyrolysis, Fuel, Vol.82, pp.669-676.

99) Yan, L., Gupta, R.P. and Wall, T.F. (2002): Ash formation from excluded minerals including consideration

of mineral-mineral associations, Fuel, Vol. 81, pp.337-344.
100) Zhao, Y., Zhang, J., Tian, C., Li, H., Shao, X. and Zheng, C. (2010): Mineralogy and chemical composition on high-calcium fly ashes and density fractions from a coat-fired power plant in china, Energy&Fuels, Vol. 24, p. 834.
101) Temeczek, J. and Palagniok, H. (2002): Kinetic of mineral matter transformation during coal combustion, Fuel, Vol.81, pp.1251-1258.
102) Van Krevelen, D. W. (1961): “Coal”, Elsevier. Amsterdam,.
103) Walker, P. L, Ausin, L. G. and Nandi, S.P. (1966): Activated diffusion of gases in molecular-sieve materials, Chemistry and Physics of Carbon, Vol. 2, pp.257-372.
104) Fitzer, E., Mueller, K. and Schaefer (1971): The chemistry of the pyrolytic conversion of organic compounds to carbon, Chemistry and Physics of Carbon”, Vol.7, pp.237-283.
105) Marsh, H. (2001): “Activated Carbon Compendium”,: Elseviern, North Shield, UK.
106) Brooks, I. D., and Taylor, G. H. (1968): The formation of some graphitizing carbons, Chemistry and Physics of Carbon, Vol. 4, pp.243-286.
107) Spiro, C. L. (1981): Space-filling models for coal: a molecular description of coal plasticity, Fuel, Vol. 60, pp.1121-1126.
108) Legin-Kolar, M., Ra?enovi?, A. and Ugarkovi?, D. (1999): Changes in structural parameters of different cokes during heat treatment to 24000C, Fuel, Vol. 78, pp.1599-1605.
109) Adamson, A. W. and Gast, A. P. (1997): “Physical Chemistry of Surfaces”, J. Wiley & Sons, Seventh ed., New York.
110) Yan. L., Gupta, R.P. and Wall, T. F. (2002): A mathematical model of ash formation during pulverized coal combustion, Fuel, Vol.81, pp. 337-345.
111) Kuczynski, G. S. (1972): Physics and chemistry of sintering, Advances in colloid and interface Sci., Vol. 3, pp. 275-330.
112) Kuczynski, G.S. (Ed.) (1975): “Sintering and Catalysis”, Plenum Press, New York, USA.
113) Geguzin Ya.E. (1984): “Physics of Sintering”, 2nd ed., Nauka, Moscow, (in Russian).
114) Yao, W., Maris, H.J., Pennington, P. and Seidel, G.M. (2005): Coalescence of viscous liquid drops, Physic Rev. E.,Vol. 17, p. 016309 (5).
115) Slesov, V.V. (2002): Gas bubbles in viscous liquids and melts. J. Colloid Interface Sci., Vol.255, pp. 274-292.
116) Landau, L.D., and Lifshitz, E.M. (1987).: “Theory of elasticity. In Course of Theoretical Physics, v.6” , 2nd ed., Pergamon, New York, USA,
117) Novozhilov, V.V. (1953): “Thin Shell Theory”, Sudostroenie, Leningrad, (in Russian); Novozhilov, V.V.: “Thin Shell Theory”, Wolters-Noordhoff, Groningen, The Netherlands (1970).
118) Duret, B. and Saudin, A. (1994): Microspheres for onboard hydrogen storage, Intern. J. Hydrogen Energy, Vol.19, pp.757-764.
119) Akunets, A.A., Basov, N.G., Bushuev, V.S., Dorogotovtsev, V.M., Gromov, A.I., Isakov, A.I., Kovylnikov, V.N., Merkul’ ev, Yu.A., Nikitenko, A.I. and Tolokonnikov, S.M. (1996): in Hydrogen Energy Progress IX. Proc.9th World Hydrogen Conf., Paris, France, (1992, June 22-25), p.149-151
120) Mungall, J.E., Bagdassarov, N.S., Romano, C. and Dingwellm, D.B.(1996): Numerical modeling of stress generation and microfracturing of vesicle walls in glassy rocks, J. Volcanolog. and Geothermal Research, vol.73, pp.33-46.
121) Romano, C., Mungall, J.E., Sharp, T. and Dingwell, D.B. (1996): Tensile strengths of hydrous vesicular glasses: An experimental study, Amer. Mineral, Vol.81, pp.1148-1154.
122) Webb, S. (1997): Silicate melts: relaxation, rheology, and the glass transition, Rev. Geophys., Vol.35, pp 191-218.
123) Hammer J. E. (2008): Experimental Studies of the kinetics and energetics of magma crystallization, Reviews in mineralogy and geochemistry, Vol.69, pp 5-59.
124) Ashby, M. F. (2006): The properties of foams and lattices, Philos. Trans. Royal Soc., A Math. Phys. Eng. Sci., Vol.364, pp.15-30
125) Murray, B.S. (2007): Stabilization of bubbles and foams, Curr. Opin in Colloid & Interf. Sci., Vol.12, pp 232-241.
126) Celarie, F., Prades, S., Bonamy, D., Ferrero, L., Bouchard, E., Guillot, C., Mariere, C. (2003): Glass breaks like metal, but at the nanometer scale. Physic Rev. Lett., Vol.90, pp. 075504 (4).
127) Guin, J-P. and Wiederhorn, S.M. (2004): Fracture of silicate glasses: ductile or brittle? Physic Rev. Lett, Vol.92, p 215502 (4 p).
128) Lawn, B.R. (1993): “Fracture of Brittle Solids”, 2nd ed., Cambridge Univers, Cambridge, England,
129) Nowacki, W. (1986): “Thermoelasticity”, Pergamon, Frankfurt, Germany.
130) Freund, L.B. (1998): “Dynamic Fracture Mechanics”, Cambridge Univer. Press, Cambridge, England.
131) Anderson, T.L. (1995): “Fracture Mechanics: Fundamentals and Application”, CRS Press, Boca Raton, USA
132) Arefmanesh, A. and Advanti, S.G. (1991): Diffusion-induced growth of a gas bubble in a viscoelastic fluids, Rheolog. Acta, Vol.30, pp. 274-283.
133) Alidibirov, M. and Dingwell, D.B. (1995): Experimental study of highly viscous magma fragmentation in explosive volcanic eruption, Per. Mineral, Vol.64, pp. 71-72.
134) Persson, B. N. J. and Brener, E. A. (2005): Crack propagation in viscoelastic solids, Physic. Rev. E, Vol.71, p. 036123 (8).
135) Ribe, N.M. (2002): A general theory for the dynamics of thin viscous sheets, J. Fluid Mechanics, Vol.457, pp. 255- 283.
136) van der Schaaf, J. and Beerkens, R. G. C. (2006): A model for foam formation, stability, and breakdown in glass-melting surfaces, J. Colloid Interface Sci., Vol.295, pp. 218-229.
137) Hailemariam, L., Okos, M. and Campanella, O. (2007): A mathematical model for the isothermal growth of bubbles in wheat dough, J. Food Eng., Vol.82, pp. 466-477.
138) Eitel, W. (1954): “The Physical Chemistry of the Silicates” , The Univers. Chicago Press, Chicago, USA, 902 p.
139) Frank-Kamenetsky, D.A. (1967): “Diffusion and Heat Transfer in Chemical Kinetics”, Nauka, Moscow, (in Russian).

Author's short biography

Fenelonov Vladimir Borisovic

Fenelonov Vladimir Borisovich - specialist in physical chemistry, professor, graduated from the Leningrad Technological Institute (LTI) in 1962, defended his PhD in 1969 at LTI. Since 1971 he works at the Boreskov Institute of Catalysis, where in 1987 he defended his dissertation for doctor of science. During the period of 1997 -2007 he was the head of the catalysts texture research laboratory at this institute, now he is the main scientific researcher. Main scientific interests are investigation of the regularities of formation of catalysts, adsorbents and other porous materials nanostructure, adsorption methods for studying of nanostructures. He is the author of more than 250 publications. His recent monographs are: Fenelonov, VB "Introduction to Physical Chemistry of the Formation of Supramolecular Structure of Adsorbents and Catalysts", 2 ed., Novosibirsk, 2004, 438 p.; VB, Fenelonov, VB and Mel'gunov, M. S. "The adsorption-capillary phenomena and the porous structure of catalysts and adsorbents (Problems and questions with answers and solutions)" , Novosibirsk, 2010, 170 p.

Mel'gunov Maxim Sergeevich

Mel'gunov Maxim Sergeevich - specialist in physical chemistry, graduated from the Novosibirsk State University in 1995, defended his PhD in 2001 at the Boreskov Institute of Catalysis. Now he is the head of the catalysts texture research laboratory at this institute. Main scientific interests are formation and characterization of porous materials and their application in adsorption science and technology. He is the author of more than 50 publications. His recent review and monograph are: Fenelonov V.B., Melgunov M.S., Texturology , In "Surface and Nanomolecular Catalysis" , Ed. R. Richards, CRC Press, 2006 pp. 257-336.; VB, Fenelonov, VB and Mel'gunov, M. S. "The adsorption-capillary phenomena and the porous structure of catalysts and adsorbents (Problems and questions with answers and solutions)" , Novosibirsk, 2010, 170 p.

Valentin Parmon

Valentin Parmon is professor and director of the Boreskov Institute of Catalysis (Novosibirsk, Russia). His expertise is as follows: catalysis and photocatalysis, chemical kinetics in condense phases, chemical radiospectroscopy, chemical methods for energy conversion, non-traditional and renewable energy sources, thermodynamics of non-equilibrium processes. As an author and a co-author, he published more than 650 scientific papers in peer-reviewed journals, 8 monographs, 33 review papers, more than 100 patents. He is a member of many professional societies such as a member of the Presidium of the Russian Academy of Sciences (RAS) and of the Presidium of the Siberian Branch of RAS; Chairman of the Russian Scientific Council on Catalysis of RAS, a Russian National representative in the European Federation of Catalytic Societies (EFCATS) and International Association of Catalysis Societies (IACS), a member of the International Advisory Board of the Institute of Surface Chemistry & Catalysis (Polish Academy of Sciences, Krakow). He is Honorary Professor of the Taiwan Technical University and of the Heiludzian Technical University (Kharbin, China). He works for many scientific journals as the editor-in-chief and editorial board. He was awarded the State Prize of the Russian Federation in Science and Technology for 2009 for the contribution to the theory and practice of catalytic methods for deep processing of hydrocarbon feedstock and utilization of renewable resources (The Decree of the President of the Russian Federation dated the 6th June 2010).

Surface Analysis of Silica Gel Particles After Mechanical Dry Coating with Magnesium Stearate[†]

Laurence Galet[1*], Yamina Ouabbas[2], Alain Chamayou[1], Philippe Grosseau[2], Michel Baron[1], Gérard Thomas[2]
Ecole des Mines d'Albi-Carmaux[1]
Ecole Nationale Supérieure des Mines de Saint Etienne[2]

Abstract

A dry coating technique has been used to change the surface properties of silica gel particles (d_{50}=55μm) by coating with different mass ratios of magnesium stearate - $MgSt_2$ (d_{50}=4.6μm): 1%, 5%, 15% and 30%. The dry coating experiments were performed using a "Hybridizer, a high-speed dry impact blending coater", manufactured by Nara Machinery (Japan). The surface morphology of the uncoated and coated silica gel particles was observed by environmental scanning electron microscopy (ESEM). The images show that a greater $MgSt_2$ coverage was observed on the surface of silica gel as the $MgSt_2$ mass ratio is increased. In addition, atomic force microscopy (AFM) analysis revealed how this coating process makes possible a discrete and uniform dispersion of the MgSt2 particles. AFM studies were carried out with a scanning probe microscope Multimode Nanoscope IIIA (Digital Instruments/Veeco Metrology Group).

Keywords: AFM phase imaging, adhesion force, dry coating, silica, magnesium stearate

1. Introduction

Dry particle coating to change the surface properties of powders is very important in many industries. Typical applications include, but are not limited, to flowability, wettability (hydrophobic/hydrophilic properties), solubility, dispersibility, flavour, shape, electrostatic, optical, electric, magnetic, etc. In dry particle coating processes, materials with relatively large particle size (host particles; 1-500 mm) are mechanically coated with fine particles (guest particles; 0.1-50 mm) in order to create new functionality or to improve their initial characteristics 1). Since the size of the guest particles are so small, van der Waals interactions are strong enough to keep them firmly attached to the host particles. Thus, either a discrete or continuous coating of guest particles can be achieved depending on a variety of operating conditions including processing time, rotation speed, weight fraction of guest to host particles and particle properties 2). **Fig. 1** below is a simple schematic illustrating the process of dry particle coating.

Over the last few years, we have performed experimental investigations of applications of the dry coating technique to study the effect of mechanical dry coating on the surface properties of powders. Our recent work is related to the modification of the flowability and the wettability properties of silica gel particles coated with different weight ratios of magnesium stearate by using a high energy impact coater Hybridizer from Nara Machinery 3) and a high shear mixer Cyclomix from Hosokawa 4). For example, the flowability of the silica gel powder was significantly decreased after treatment in the Cyclomix mixer with 15% of $MgSt_2$. Moreover, it has been found that the coating by hydrophobic $MgSt_2$ in the Cyclomix can reduce the high affinity between silica gel and water after treatment with 5% and 15% of $MgSt_2$. In those papers, it has been demonstrated that a dry particle coating technique can be used to modify the properties of silica gel powder by coating with small quantities of hydrophobic magnesium stearate in both the Hybridizer and the Cyclomix. The more uniform

---

[†] Accepted: September 23, 2010
[1] Centre RAPSODEE, UMR CNRS 2392
Campus Jarlard 81013 Albi Cedex 9, France
[2] Centre SPIN – LPMG -UMR CNRS 5148
158 Cours Fauriel 42023 Saint-Etienne Cedex 2, France
[*] Corresponding author
E-mail: laurence.galet@mines-albi.fr
TEL: +33 5 63 49 32 35 FAX: +33 5 63 49 30 25

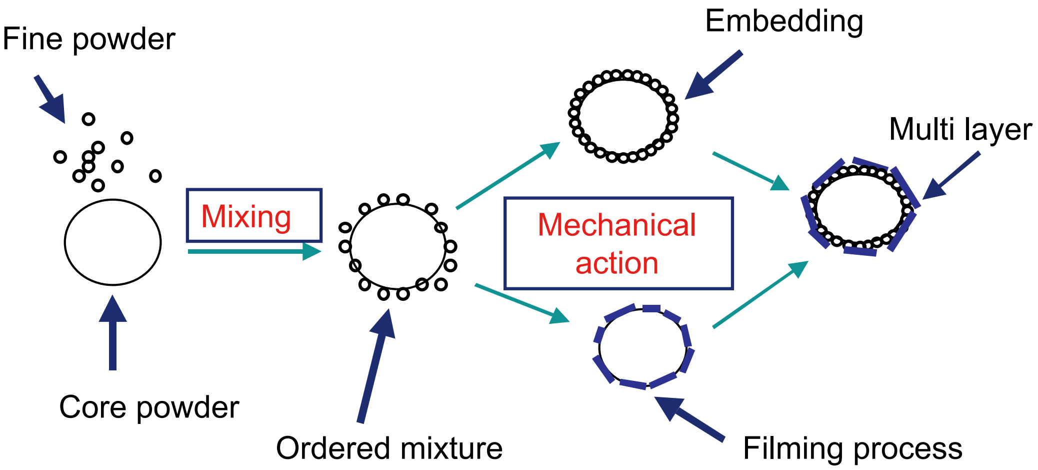

Fig. 1 Schematic principle of dry coating.

coating has been obtained after treatment in the Hybridizer device.

In this paper, we report an investigation of the surface analysis of the coated silica gel particles using atomic force microscopy in tapping mode (TM-AFM) and contact mode (CM-AFM). The TM-AFM method, based on the measurements of the oscillations of a cantilever probe in contact on the sample, has been used for several years to characterize the surface topography of particles. In particular, phase contrast images are related to characterize the attractive and repulsive probe sample interactions 5), the sample surface components 6) and the morphology of composite particles 7). The CM-AFM method consists in using a colloidal probe fixed on the cantilever to quantify the adhesion force between the particles. As an example, Kani et al report an interesting study on the silica-mica adhesion force as a function on the presence of impurities on the silica particles 8). Meincken et al. report a relationship between contact angle analysis and adhesive forces measurements by the AFM technique in a study of the surface hydrophobicity of polyurethane coatings 9). This technique has been also used to characterize the adhesion properties of pharmaceutical carriers 10). In our case, we performed AFM phase-contrast and adhesion forces measurements to characterize the surface of silica particles as a function of the magnesium stearate mass ratio (1 to 30%).

2. Experimental

2.1 Powders

Silica gel powder supplied by Merck and usually used for filling chromatography columns has been chosen as host particles for dry coating (Silica gel 60, 0.040-0.063 mm). The volume distribution of silica gel shows a population of large particles with median diameter (d_{50}) of about 55 μm. Hydrophobic magnesium stearate ($MgSt_2$) supplied by Chimiray is used as guest particles. The $MgSt_2$ is a fine, white, greasy and cohesive powder widely used in pharmaceutical formulation as a lubricant. A wider size distribution is observed for $MgSt_2$ particles. The size of $MgSt_2$ particles varies between 20 μm to less than 1 μm with a median diameter (d_{50}) of about 4.6 μm. The main properties of host and guest particles are reported in the **Table 1**.

2.2 Coating process

The hybridization system (HB, type NHS-0; Nara Machinery Co.), a high-speed dry impact blending coater, has been used to make the silica gel-$MgSt_2$ composite particles. The reactor consists in a very high-speed rotating rotor with six blades, a stator and a powder re-circulation circuit. The coating chamber

Table1 Properties of host and guest particles

Particles	Size (d_{50}) (μm) (Mastersizer 2000)	Solid density (g/cm^3) (Helium Pycnometer)	Specific surface area (SBET (m^2/g))	Pore Volume (cm^3/ g)
Silica gel	55 (D_{host})	2.07 (ρ_{host})	475	0.69
MgSt	5 (d_{guest})	1.04 (ρ_{guest})	7.7	0.02

is surrounded with a jacket in which coolant is circulated [1)]. The coating process can be summarized as follows: the powder mixture (host and guest particles) is subjected to high impaction and dispersion due to collisions with blades and the walls of the device and continuously re-circulates in the machine through the cycle tube. Particle coating is achieved due to the embedding or filming of the guest particles onto the host particles by high impaction forces and friction heat. Since the rotor of the hybridizer can rotate from 5000 to 16000 rpm, very short processing time is required to achieve coating. The operating conditions used in experiments are 4800 rpm for 5 min. The preparation of the coated particles is described in detail in previous papers 3, 4). Coating experiments have been carried out with 1%, 5%, 15% and 30% of mass fraction of guest $MgSt_2$ particles.

2.3 Particles characterization

The uncoated and coated silica gel particles were examined by environmental scanning electron microscopy (ESEM) to study the surface morphology and the covering by the $MgSt_2$ particles (XL 30 Philips). The ESEM images reveal that greater $MgSt_2$ coverage is observed on the surface of silica gel particles as the percentage of $MgSt_2$ is increased (**Fig. 2**). Additional investigations were done to analyse the surface atomic composition of the coated particles by X-ray spectroscopy confirming the presence of magnesium atoms when analysis is performed on a black spot [11)]. At 15%, the surface coverage of the $MgSt_2$ is intense but seems discrete.

Thermal analysis was used to measure the $MgSt_2$ mass fraction after treatment (TG-DSC 11 Setaram). Samples are analyzed under nitrogen gas, from 20° C to 600° C, with a ramp of 5° C/min. **Fig. 3** and **4** show the heat flow, the mass lost and the differential mass lost as a function of the temperature diagram for pure silica gel and $MgSt_2$, respectively. We observe that the silica gel particles have a main first mass loss of about 4-5% near 100° C, due to dehydration, and a second near of 2% 400-600° C, probably due to a thermal decomposition. The $MgSt_2$ has a first small mass loss near 100° C due to dehydration and a main mass loss of 85-90% between 250° C and 450 ° C due to a thermal degradation. This mass loss can be used to quantify the $MgSt_2$ in the powder mixtures.

TG-DSC experiments have been performed on silica gel-$MgSt_2$ mixtures made by manual mixing (1%, 3%, 15%, 30% and 50% mass ratios). The loss of mass obtained between 250° C and 600° C as a function of the $MgSt_2$ ratio is reported in the **Fig. 5**. This result is the mean of two measurements. The results show a very good relation between the AGT-DSC mass loss (%) as a function of the $MgSt_2$ ratio (%). The linear relation obtained with a high correlation coefficient has been used to calculate the real composition of the coated particles after processing in the reactor with a precision of less than ± 1%.

AFM measurements were made with a Multimode Nanoscope IIIA from Veeco Metrology Group. In tapping mode, the cantilever is driven to oscillate. Height, amplitude and phase images were simultaneously recorded for each sample. Beyond the standard height imaging, the phase contrast mode is quite efficient to exhibit the main surface property differences between de silica gel and $MgSt_2$.

The amplitude and the frequency of the oscillations change when the tip scans on a surface. TM-AFM images are produced by imaging the oscillating contacts of the tip with the sample surface: height and amplitude images give information on the sample surface topography and phase images give information on the atomic surface composition (interaction tip-surface). The TM-AFM measurements were performed with a MPP 11100 Silcon phosphorus doped silicium tip with a spring constant of 40 N/m. Large surface scale of surface sample has been scanned: from $250 \times 250 nm^2$ to $5 \times 5 nm^2$, for silica gel and silica gel-$MgSt_2$ coated particles (1%, 5% and 15% $MgSt_2$ mass ratio).

In contact mode AFM, the tip scans the sample in close contact with the surface. The force between the tip and the surface sample is measured as the

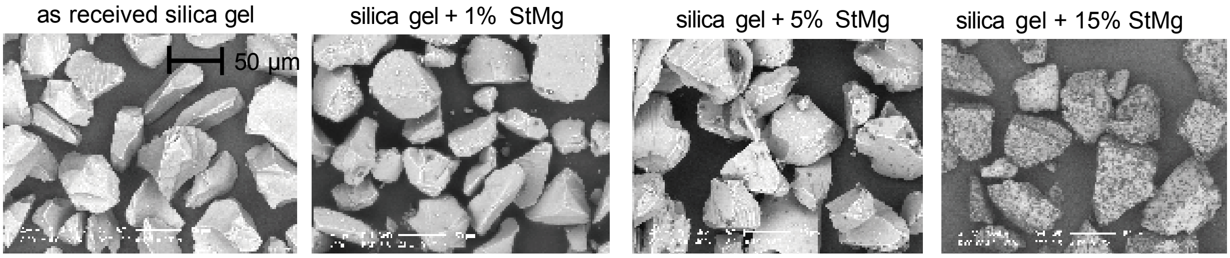
as received silica gel

silica gel + 1% StMg

silica gel + 5% StMg

silica gel + 15% StMg

Fig. 2 ESEM images of silica gel and $MgSt_2$-silica gel coated particles.

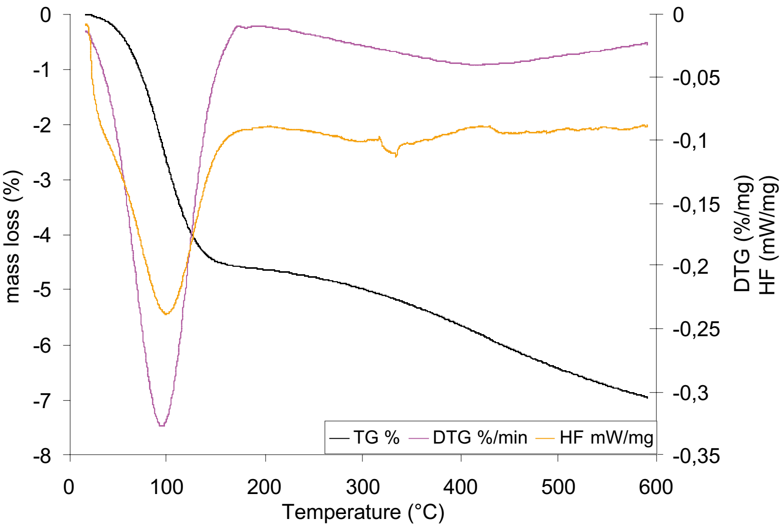

Fig. 3 TG-DSC diagrams for silica gel.

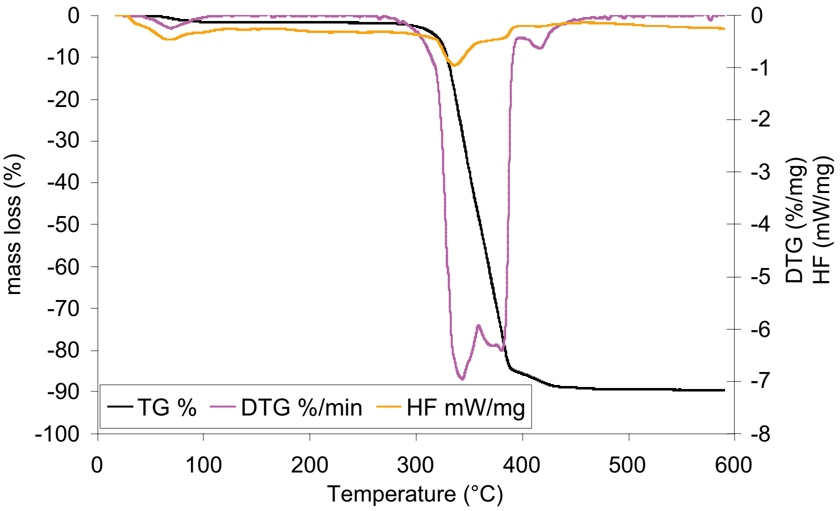

Fig. 4 TG-DSC diagrams for $MgSt_2$.

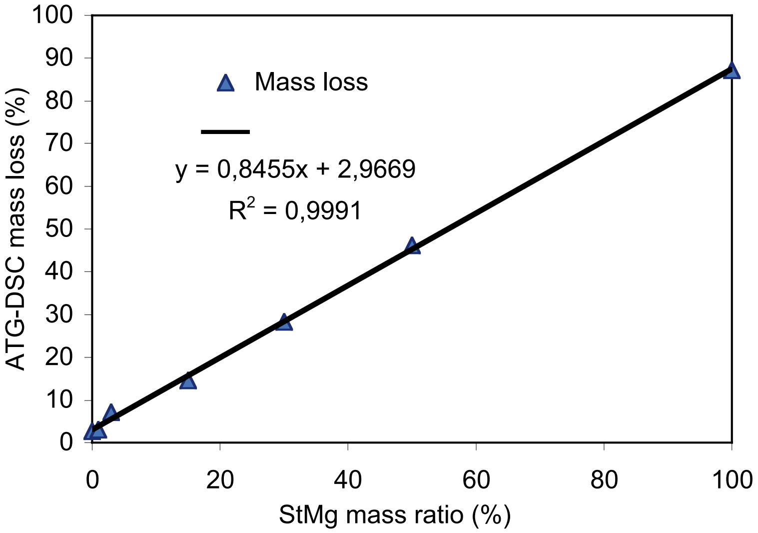

Fig. 5 Experimental relation between the TG-DSC mass loss (from 250°C to 600°C) and the mass ratio of $MgSt_2$.

distance, by maintaining a constant deflection. To examine the mechanism of interaction between silica gel and $MgSt_2$ particles, the CM-AFM measurements were performed with a NP silicon nitride tip with a spring constant of 0.32 N/m on which a $MgSt_2$ particle was glued under optical microscope. The adhesion forces were measured between the $MgSt_2$ particles attached on the end of the cantilever and the different samples of uncoated and coated particles with 1% to 30% $MgSt_2$ mass ratio. For each sample 450 force curves were obtained. The presence of the magnesium stearate particle on the tip was checked after each series of measurements.

Influence of the coating on the surface property of the silica gel particles was also studied. The sessile drop method was used to study the wettability of the different samples. We report the contact angle value of a water drop (10 ml) deposited on different particulate systems: pure silica gel, pure $MgSt_2$ and coated particles. The method performed is described in details in previous papers [3, 4].

3. Results and Discussion

The real concentration of the $MgSt_2$ after coating is calculated from the TG-DSC measurements and the calibration straight line shows in **Fig. 5**. The results are reported in the **Fig. 6**. This loss of $MgSt_2$, due to a deposit of $MgSt_2$ on the coating chamber surface, varies as a function of the introduced $MgSt_2$ mass ratio. That is from 30% for the sample containing initially 30% of $MgSt_2$ in the mixture, to 40% for the sample containing initially 5% $MgSt_2$ in the mixture.

The phase imaging TM-AFM characterisations of the samples are reported in **Fig. 7**. Concerning the $MgSt_2$, the amplitude image reveals an irregular surface topography. The phase contrast image shows various levels of phase contrast (black and white areas), which can reach 50° . The silica gel particles have a more regular surface topography, formed by spherical micro beads (about 100 to 600 nm) and a low phase contrast only due to the topography (from 0° to 10°). The analyses of the silica-$MgSt_2$ coated particles clearly reveal a modification of the surface due to the presence of the magnesium stearate, even at 1% of $MgSt_2$ introduced. With a $MgSt_2$ initial mass ratio of 15%, both the amplitude and the phase contrast images evolve into the pure $MgSt_2$ images. For the coated particles, the part of the image characterized by high phase angles can be attributed to the presence of $MgSt_2$ layers on the surface of silica gel.

The contact mode analyses bring some pertinent information about the silica gel covering by the magnesium stearate. **Fig. 8** gives an adhesion force–displacement curve for the pure products. The force measured between a particle of $MgSt_2$ fixed onto the AFM tip is about 10 nN for the pure silica gel particle. That is near 120 nN for the $MgSt_2$-$MgSt_2$, revealing a high interaction.

The adhesion force distributions for the different particulate systems are reported in the **Fig. 9**. These distributions were obtained from 450 measurements of each particulate system. This force varies proportionally to the quantity of $MgSt_2$ introduced and

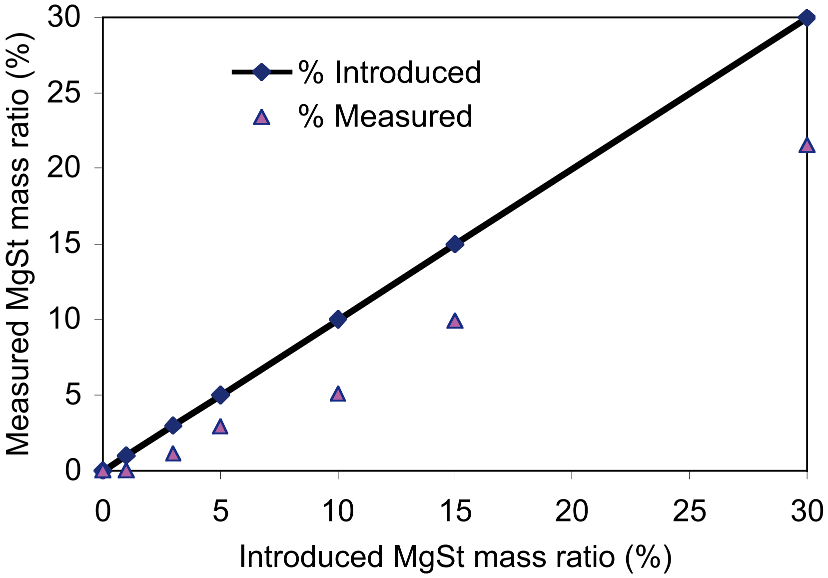

Fig. 6 Real mass fraction of $MgSt_2$ after the coating process calculates from the mass loss.

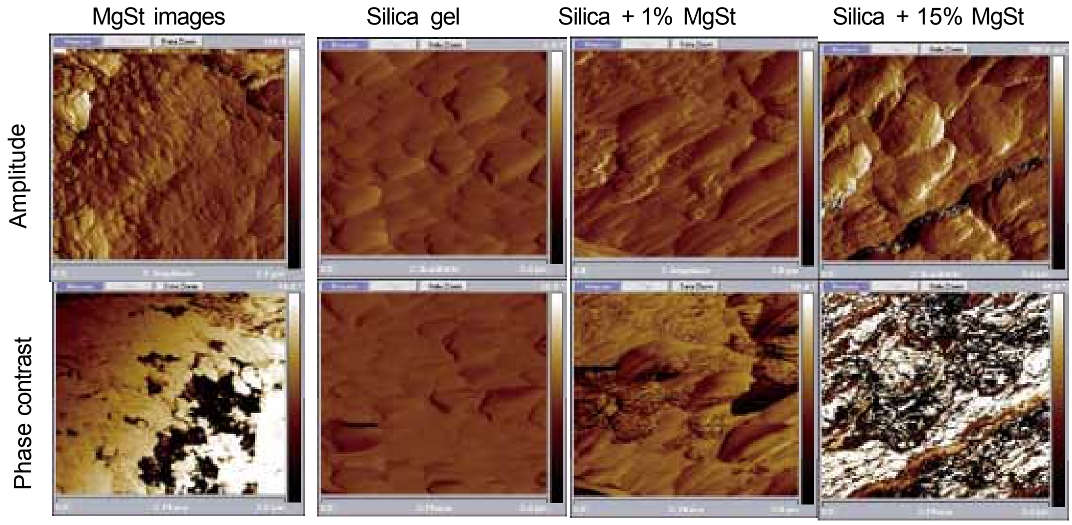

Fig. 7 TM-AFM images of $MgSt_2$, silica gel and silica coated with 1% and 15 % initial mass ratios of $MgSt_2$ (2×2 μm^2).

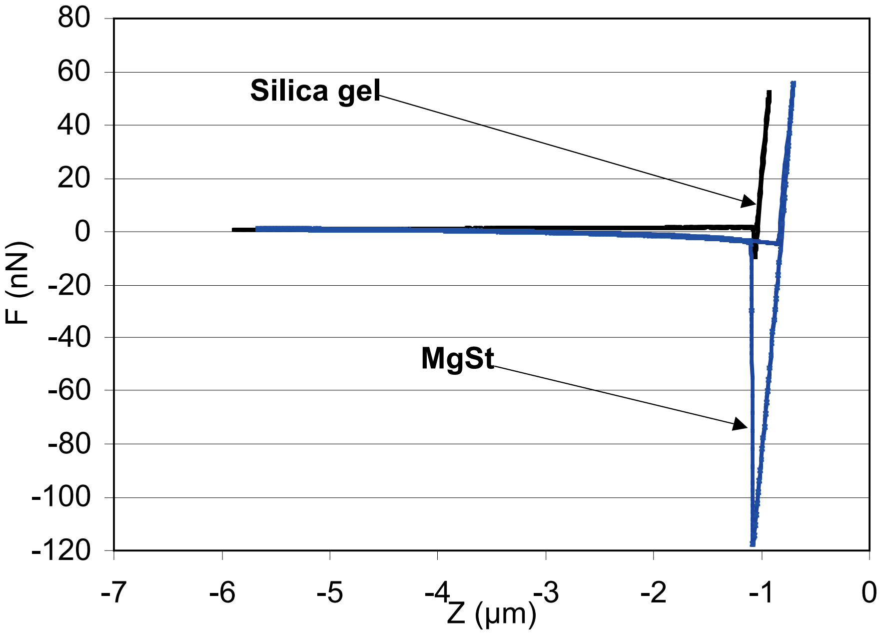

Fig. 8 Force curves F (N/m) as a function of the distance z (μm) measured with $MgSt_2$ sticked on the tip for pure silica gel and pure $MgSt_2$.

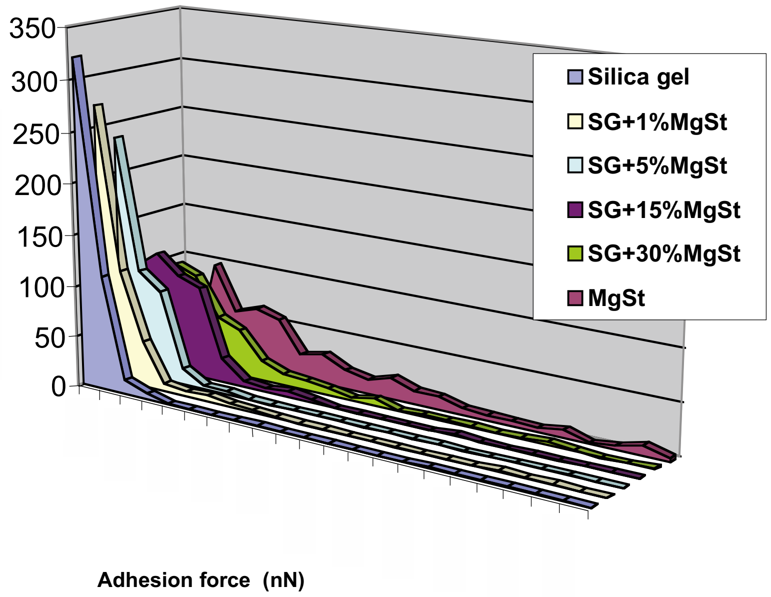

Fig. 9 CM-AFM adhesion force distribution obtained with 450 analyses for different particulate systems.

confirms the increasing presence of the MgSt$_2$ on the silica gel surface when the mass ratio increases. For the coated particles, the number of high adhesion forces increased as the mass ratio of MgSt$_2$ increases. The mean adhesion force between the MgSt$_2$ particles attached on the end of the cantilever and the MgSt$_2$ sample (68 nN) was stronger than for the silica gel sample (8 nN). The large distribution of the adhesion forces confirm the discrete deposition of the MgSt$_2$ particles onto the surface silica gel particles as observed by the ESEM images.

The mean adhesion force calculated from the 450 measurements for each system is reported in the **Table 2.** The results show an increasing of the mean value of the force as a function of the increasing of the MgSt$_2$ concentration. The mean adhesion force seems to evolve progressively to the mean value of the pure MgSt$_2$ (**Fig. 10**). This no linear evolution could be due to a random distribution of the MgSt$_2$ particles on the silica gel surface.

The affinity of water is evaluated by the behaviour of a water drop deposited on the particulate systems. The initial contact angle values are reported in **Table 3.** The **Fig. 11** shows the evolution of the contact angle as a function of the MgSt$_2$ ratio. We observe a increasing of the contact angle of the water drop as the presence of the MgSt$_2$ on the silica gel surface. This result is of course in agreement with the hydrophobicity of this compound. However, even with a low content of MgSt$_2$, the contact angle measured is significatively modified: 70° and 110° for 0.1% and 1.1% MgSt$_2$ respectively. The surface property of the silica gel particles is modified by dry coating even with a very low ratio of MgSt$_2$. This result reveal that at the water drop scale, a very few presence of MgSt$_2$ is enough to modify the hydrophilic property of the silica gel.

4. Conclusion

Dry particle coating can be used to create new generation materials with altered properties or new functionalities. This treatment creates a discrete or a continuous coating of fine particles on the surface of the large particle surface. In this study a Nara Hybridizer has been used as a dry coating device for the coating of silica gel particles with different mass ratios of MgSt$_2$ particles. ESEM observations show that MgSt$_2$ particles form a discrete coating onto the surface silica gel particles. The MgSt$_2$ surface coverage increases and the surface becomes more and more uniform as the mass ratio of MgSt$_2$ is increased. In addition to ESEM observations, AFM images and distributions curves of adhesion forces confirm the distribution of MgSt$_2$ in discrete layers onto the silica gel surface. The mean adhesion force obtained for the different particulate systems reveal a no linear evolution to the adhesion force measured for the pure MgSt$_2$. From these results, we are currently working on the development of a distribution model of MgSt$_2$ particles onto the surface of silica gel based on the adhesion force results. The sessile drop method re-

Table 2 Mean adhesion force (nN) for different particulate systems

Sample	Mean adhesion force (nN)
Pure silica gel	8
Silica gel + 2.95 % MgSt	13
Silica gel + 9.93 % MgSt	23
Silica gel + 21.51 % MgSt	35
Pure MgSt	68

Table 3 Contact angle measurements (°) for different particulate systems

Sample	Contact angle (°)
Pure silica gel	15 ± 3
0.1 %	70 ± 7
1.1 %	110 ± 5
3.0 %	112 ± 5
9.9 %	116 ± 3
Pure MgSt	125 ± 6

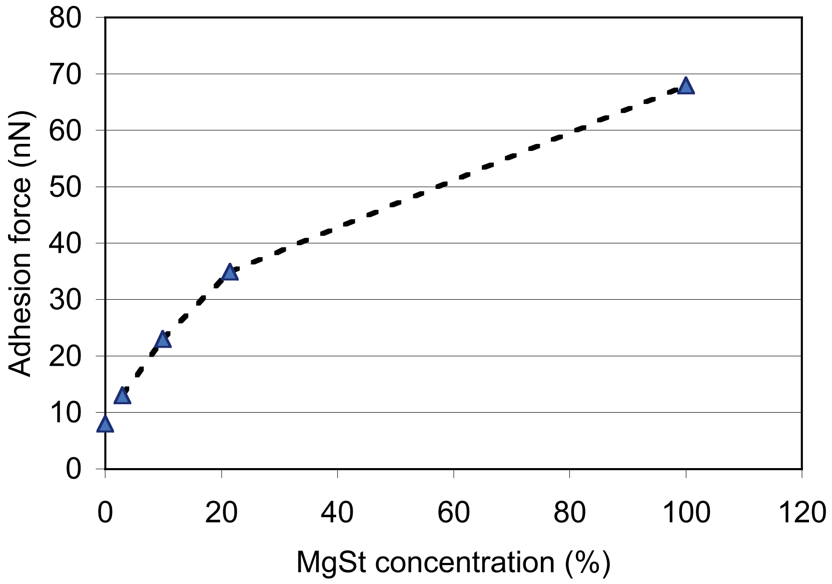

Fig. 10 Mean adhesion force (nN) as a function of the sample $MgSt_2$ concentration.

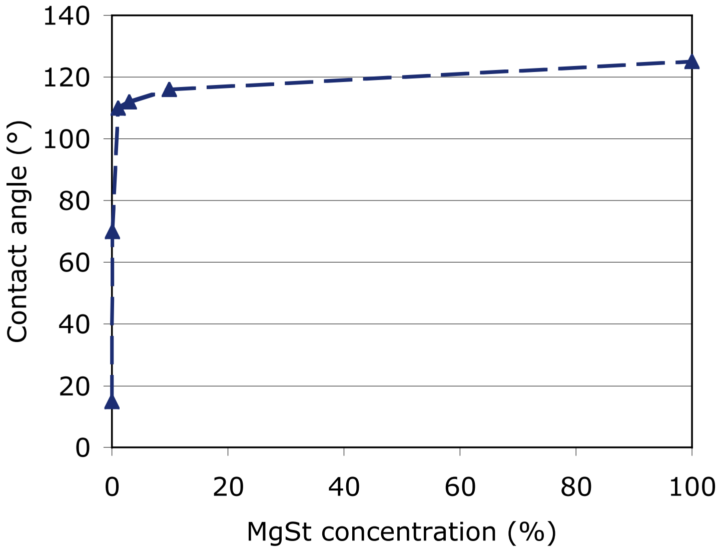

Fig. 11 Contact angle measurements (°) as a function of the sample $MgSt_2$ concentration.

veals that a discrete deposition of the $MgSt_2$ allows a real modification of the hydrophilicity of the silica gel. Less than 3% of $MgSt_2$ is enough to increase the contact angle near the value of the pure MgSt2. This additional approach confirms the efficiency of the dry coating technique to design some new composite systems with controlled end use properties.

Acknowledgements

The authors would like to acknowledge Sylvie Delconfetto for the TG-DSC measurements and Christine Rolland for the ESEM images.

Nomenclature

AFM	Atomic Force Microscopy
CM-AFM	Contact Mode Atomic Force Microscopy
ESEM	Environmental Scanning Electron Microscopy
$MgSt_2$	Magnesium Stearate
TM-AFM	Tapping Mode Atomic Force Microscopy

References

1) Yoshihara, I. and Pieper, W. (1999): Hybridization – Technology for surface modification of powders without binders, Swiss Pharma., 21, 6.
2) Pfeffer, R., Dave, R, Dongguang, N. W. and Ramlakhan, M. (2001): Synthesis of engineered particulates with tailored properties using dry particle coating, Powder Technology, 117, pp.40-67.
3) Ouabbas, Y. , Chamayou, A., Galet, L., Baron, M., Thomas, G., Grosseau, P. and Guilhot, B. (2008): Surface modification of silica particles by dry-coating: Characterization and powder ageing, Powder Technology, in press.
4) Ouabbas, Y., Dodds, J.A., Galet, L., Chamayou, A. and Baron, M. (2008): Particle-particle coating in a cyclomix impact mixer, Powder Technology, in press.
5) Chen, X., Roberts, C.J., Zhang, J., Davies, M.C. and Tendler, S.J.B. (2002): Phase contrast and attraction-repulsion transition in tapping mode atomic force microscopy, Surface Science, 519, pp. L593-598.
6) Danesh, A., Chen, X., Davies, M.C., Roberts, C.J., Sanders, G.H.W., Tendler, S.J.B. Williams, P.M. and Wilkins, M.J. (2002): Langmuir, 16, pp. 866-870.
7) Gun'Ko, V.M. et al. (2006): Composite powders with titania grafted onto modified fumed silica, Powder Technology, 164, pp. 153-167.
8) Kani, T., Tamonoki, M., Suzuki, T., Tsukada, M. and Kamiya, H. (2007): Influence on the surface-adhered nanoparticles and nanoporous structure on particle-particle interaction of silica, Powder Technology, 176, pp. 99-107.
9) Meincken, M., Klash, A., Saboa, S. and Sanderson, R.D. (2006): Influence of the viscosity and the substrate on the surface hydrophobicity of polyurethane coatings, Applied Surface Science, 253, pp. 805-809.
10) Louey, M., Mulvaney, P. and Stewart, P.J. (2001): Characterization of adhesional properties of lactose carriers using atomic force microscopy, Journal of Pharmaceutical and Biomedical analysis, 25, pp. 559-567.
11) Ouabbas, Y. (2008): Procédés mécaniques d'élaboration à sec de particules composites à propriétés d' usage contrölées – Caractérisation et stabilité d'un gel de silice, PhD Thesis, Ecole Nationale Supérieure des Mines de Saint-Etienne, N° 467GP,.

Author's short biography

Laurence Galet

Dr Laurence Galet received her Biological Engineering Ingeneer degree in 1991 and her PhD in Chemical Engineering in 1997 from the University of Technology of Compiègne.

She joined the Ecole des Mines d' Albi, France in 1998 and developped the solids-liquids interaction area. Her research interest in the Rapsodee Center-CNRS FRE 3213 are directed towards Chemical Engineering and the wettability assesement of particulates solids and their dispersion in liquid media.

She was awarded in 2009 "Chevalier" in the national "Ordre des Palmes Académiques", France.

A Novel Method of Probing the Fractional Composition of Nanosystems†

Kozlov A.S.[1]*, Petrov A.K.[1], Kulipanov G.N.[2], Aseyev V.[3]
Institute of chemical kinetics and combustion SB RAS[1],
G.I. Budker Institute of nuclear physics SB RAS[2],
University of Helsinki[3]

Abstract

The article presents a comparison of the traditional methods to investigate the fractional composition of nanosized powders, namely atomic force microscopy (AFM), scanning electron microscopy (SEM), dynamic light scatterin, (DLS) and a new one – analysis of the aerosol products of submillimeter pulse laser ablation (SLA). As has previously been proven, biological macromolecules retain activity after ablation under submillimeter wavelengths, molecules become separated in the aerosol phase and each sort of molecues forms its own fraction of the aerosol particles. We suggest that this process is made possible as the result of influence on the hydrogen and van der Waals' bonds, with the energies within the submillimeter range. Results of investigations on SiO_2 and artificial diamond clusters using the above methods in both powder and colloid states are discussed. SLA with subsequent detection of aerosol products with the help of convenient aerosol equipment is found to be simple, fast and informative, and can act as a competitor to mass spectrometry, X-ray scattering and other methods.

Keywords: THz laser ablation, nanopowders, aerosol analysis

Introduction

Laser ablation is a phenomenon thas is sure to gain broad application in science, technology [1)] and medicine [2)]. At present, the case in point is the use of the radiation with wavelengths shorter than 10μm, and this implies the destruction of a material at the molecular level. Use of the submillimeter radiation opens novel outlooks in this area. The submillimeter (terahertz) radiation is the region of the electromagnetic spectrum between the far infrared and microwave radiation. Usually this region corresponds to wavelengths from 100 to 500μm. This region has become available to researchers due to the recent development of new powerful sources of THz radiation. One of these sources is the Free Electron Laser (FEL), developed and built at the Institute of Nuclear Physics SB RAS. The radiation of this laser is pulsed wite a pulse duration of about 50 picoseconds ane a pulse period of 180 nanoseconds; the laser wavelength is tunable within the range 120 to 240 micrometers with the relative radiation line width about 10^{-3}, average power up to 400 W, and peak power up to 0.8 MW [3)].

After the soft nondestructive ablation of biological macromolecules was discovered [4,5)], the possibility arose to develop a principally new method to measure the size of nanoparticles and nanosystems of all kinds.

The phenomenon of soft nondestructive ablation involves the transport of macromolecules from a solid substrate or from solution into the aerosol phase under the action of laser radiatiof in the terahertz range; the structure and initial properties of the macromolecules aredretained. A specific feature of this radiation is small quantum energy, ~0.01 eV, which is comparable with the energy of the hydrogen and van der Waals' bonds but much less than the energy of the covalent bonds. So, the terahertz radiation is unable to dissociate molecules with a single quantum, which allowg the molecules to be transferred into the

---

[†] Accepted: September 23rd, 2010

[1] 630090, Institutskaya 3, Novosibirsk, Russia
[2] 630090, Lavrentiev prospect 11, Novosibirsk, Russia
[3] PB 55, Al Virtasen Aukio 1, FIN-00014 HY, Helsinki, Finland
[*] Corresponding author
E-mail: kozlov@kinetics.nsc.ru, TEL.: +73833332944, FAX: +73833307350

aerosol phase without destroying the primary structure. Experiments were carried out with lyophilizates and colloids of DNA, proteins and enzymes. The process of transition into the aerosol phase occurs without destruction and denaturation of molecules; all their biological properties aredpreserved. In this process, an individual fraction of macromolecules forms an individual fraction of the aerosol particles. Binary and ternary mixtures form two or three fractions of the aerosol particles, respectively [4,5]. The molecular masses of these fractions correspond to the molecular masses of the initial components. This circumstance suggests that a new universal method may be developed to determine the size of nanoparticles of any origin.

Determination of the fraction composition of nanopowders, nanocolloids and biological macromolecules is of significant interest for academic and for practical applications. Conventional methods used for this purpose are X-ray scattering, electron microscopy, and mass spectrometry; these methods are time-consuming, expensive and sometimes ambiguous. We propose to use terahertz laser ablation for the nondestructive transfer of a nanodispersed system into the gas phase, followed by its analysis using conventional aerosol instruments. In the present work, we used an automatic diffusion battery with the condensation particle counter [6] to determine the particle size distribution of ablation products within the size range 3 – 250 nm; the source of the terahertz radiation was the free electron laser (FEL) of the Siberian Center for Photochemical Research [3]. Ultrafind diamond-carbon powder and ultrafine silicon dioxide powder were used as the subject of investigation.

To demonstrate the capability of the proposed method, the results of the sample investigation obtained by means of the soft laser ablation were compared with the results obtained using conventional methods: dynamic light scattering (photon correlation spectroscopy), scanning electron and atomic force microscopy at the Department of Chemistry of the University of Helsinki.

Experimental technology and sample treatment

Commercially available ultrafind diamond-carbon and SiO_2 powders were used as the samples. The ultrafind diamond-carbon powder was obtained by detonating solid explosives at FR&PC (ALTAI) (Biysk, Russia). As reported by the manufacturer, the powder contains 40-60 mass per cent of ultrafine diamond. Particle size is 5-20 nm. The ultrafine SiO_2 powder "Tarkosil" was manufactured at the INP SB RAS by means of electron impart. According to the manufacturer's data, the average size of powder particles is 18-25 nm.

To determine the particle size distribution of the powders with conventional methods, we used the scanning electron microscope Hitachi S-4800, atomic force microscope Veeco Instrument Nanoscope V (tapping mode). Light scattering measurements were conducted using a goniometer BI-200SM, two BI-DS1 detectors, and a digital cross-correlator TurboCorr (Brookhaven Instrument Corporation). Methodological aspects of the method can be found elsewhere [7]. Time-correlation functions were analyzed with an inverse Laplace transform program CONTIN (BIC software). The mean peak value of a size distribution was a matter of choice to estimate an apparent hydrodynamic radius of scattering objects.

Intense sample preparation was carried out before the DLS and microscopic examination. The samples were transferred into a diluted solution wite a concentration of 0.01-1mg/ml, and sodium dodecyl sulfate, SDS, was added to provide colloidal stability of particles. To disintegrate the interparticle aggregates, an intense ultrasonic treatment of the solution was carried out, followed by filtration through a membrane with pore diameter 0.45μm. Measurements of the light scattering signal were carried out at the wavelength of 488 nm at angles 90° and 140° with serial dilutions of the solution under investigation. In addition, for the atomic force and scanning electron microscopy studies, the prepared solutions were additionally subjected te lyophilic drying directly on the microscopic substrates. To be sure in the absence of any significant effect the sample preparation procedure, we studied the samples at all stages of this procedure. An example of the micrograph of the prepared sample of diamond-carbon powder, obtained with the scanning electron microscope, is shown in **Fig. 1**. All the experiments were carried out at room temperature.

To study the samples by means of the submillimeter laser ablation, the sample was placed into a horizontal cell (**Fig.2**) into which an excess of filtered gaseous nitrogen was admitted, which was necessary to prevent thl ingress of aerosol from outside. Before starting the work, we always tested for the absence of aerosol in the entire air line. The power density necessary for the start of ablation was established by moving the sample along the focal axis of the sector mirror with the focal distance f=10 cm; its average value was 20 W/cm^2. No special sample preparation

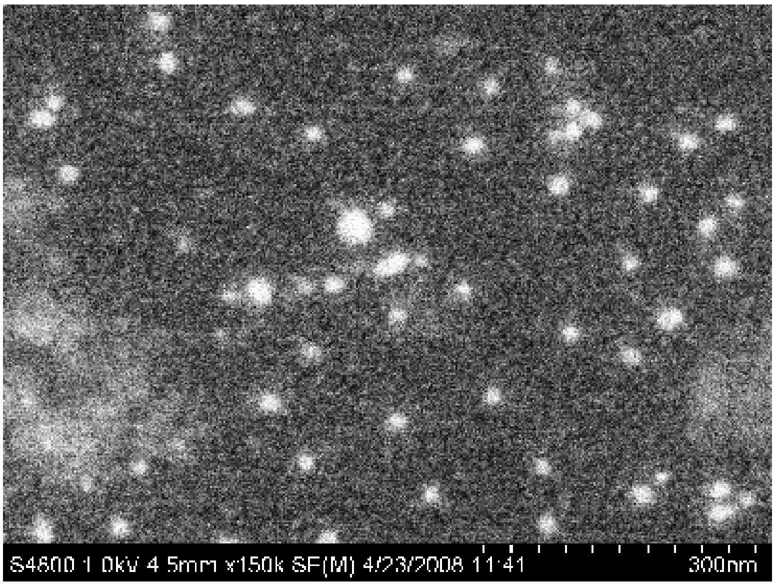

Fig. 1 An example of the micrograph of a sample of the prepared diamond-carbon powder, obtained with the scanning electron microscope.

was carried out before the ablation; the sample powders were placed on a substrate made of alumnium foil; deionized water was added (~50wt. per cent). Exposure was 3 – 10 seconds. The resultant aerosol was conveyed with nitrogen flow into a buffer reservoir of 25 liters in volume to stabilize the number concentration of the particles. The aerosol was then brought to the diffusion spectrometer of aerosols (DSA) to analyze the particle size distributione The duration of a single measurement was 4 minutes. Measurements were carried out in series of 4 measurements per series, then the size distributions were averaged over the series. Irradiation of pure substrate did not cause the formation of particles. The total number of test on each sample was over 30. The mean-root-square deviation of the average particle size did not exceed 15%.

In the present work, aerosol particles were detected by means of the diffusion spectrometer of aerosols, which is intended to measure the particle size distribution and concentration of fine aerosols of natural and anthropogenic origin. The DSA may be used to solve a broad range of problems in atmospheric chemistry and physics, in environmental monitoring and the control of industry-related emissions, and also in laboratory aerosol research. The range of measurable particle diameters is 3 to 250 nm. The range of particle concentrations measured without dilution is $< 5 \times 10^5 \mathrm{cm}^{-3}$. The flow rate of aerosol under investigation is 1 l/min.

The performance of this instrument is based on the dependence of the diffusion coefficient of nanoparticles on their size 8).

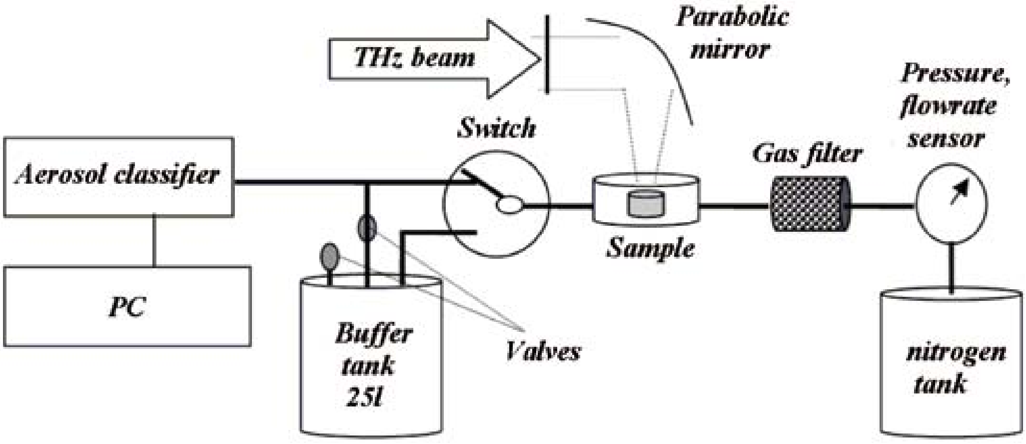

Fig. 2 Schematic of an experimental set-up.

$$D(r) = \frac{kT}{6\pi\eta r}\left(1 + \frac{Al}{r} + \frac{Bl}{r}e^{-\frac{br}{l}}\right) \qquad (1)$$

Here, k is the Boltzmann constant, T the temperature, η the gas viscosity, r the particle radius, l the free path, $A = 1.246$, $B = 0.42$, b =0.87 are constants.

This dependence is the reason why the particles of different size have different deposition rates when an aerosol flow passes through porous media; in other words, smaller particles leave the flow faster, so that the coefficient of particle passage (penetration coefficient) through such a medium contains the information about the size of particles. This circumstance is used in diffusion spectrometers of aerosols.

The basic element of the DSA is a screen-type diffusion battery. The porous medium is a packet of screens placed perpendicular to the flow. The range of particle diameters measured with the DSA is 3 to 250 nm. The scren -type battery is characterized by a simple dependence of the penetration coefficient K(r) on the particle size:

$$K(r) = \left(1 - B(D(r))^{\frac{2}{3}}\right)^{n} \qquad (2)$$

Here, n is the number of nets in the packet, B is a valug dependent on the design of the battery (the size and characteristics of the screens used in it) and on the gas flow rate through it. In the majority of cases, the second term in the bracketed expression is small, so (2) has the following form:

$$K(r) = e^{-nB(D(r))^{\frac{2}{3}}} \qquad (3)$$

In the case of a polydisperse aerosol with the density of distribution $\varphi(r)$ and concentration N, according to (3), the concentration $N(n)$ at the outlet of the diffusion battery will be

$$N(n) = N_0 \int_0^{\infty} e^{-nB(D(r))^{\frac{2}{3}}} \varphi(r)\, dr \qquad (4)$$

One can see that the problem connected wite determination of the particle size distribution and concentration with the help of DSA is reduced to measuring $N(n)$ followed by solving the integral equation [4].

So, measurement of the particle size distribution of the aerosol with the help of the diffusion battery involves consecutive counting of the concentration of aerosol particles as the aerosol flow passes through the cascades of screens (the number of cascades is 8 in our case); counting is performed with the help of the condensation counter of aerosol particles.

Diffusion batteries are a type of instruments that have made a good showing for the determination of the fractional composition of nanoaerosols during the last 50 years; they are produced by several manufacturers of research instrumentation (for example, TSI Inc., USA).

A number of natural restrictions arise when the instrument type under consideration is used. It follows from the equations presented above that only the radius of particles is taken into account during the recovery of distributions obtained with the diffusion battery, therefore, the particles whose shape differs from a sphere will be correlated, in the size distribution, with the size of a sphere having the same diffusion coefficient. Another limitation is connected with the measurement time. Indeed, the channels of the diffusion battery are scanned sequentially one after another. It is implied that both the number concentration of the aerosol and its particle size distribution remain unchanged during scanning. Special measures are taken in order to fulfill the latter condition. The total concentration of the aerosol under analysis is limited to 10^4cm^{-3}, which makes us sure that the evolution of the distribution during measurement time is insignificant. This is achieved by limiting the exposure for sample ablation and by permanent monitoring of the number concentration of the particles in the buffer vessel. Stabilization of the number concentration of the particles is achieved by using the accumulation vessels. For the flow rate of gas under analysis equal to 1 l/min, the characteristic time of concentration change in the vessel is about 30 minutes, which gives a good stabilization effect as the measurement time is 4 minutes. It should also be noted that the diffusion coefficient is independent of the density of particle material. And of course, regular tests are performed to compare the performance of our equipment with that of others and electronic microscopy [6].

Results and discussion

While studying the ablation of inorganic absorbing samples, we discovered an empirical fact that the addition of water to the sample prevents it from agglomerating.

At present, the physical mechanisms of the soft ablation remain not completely clear. One of the assumed physical mechanisms of soft ablation is the absorption of the terahertz radiation by water. Water present between the sample particles strongly absorbs the THz FEL radiation, which causes the pulsed evaporation of water and brings a part of macromolecules or clusters of the sample together with water vapor into the gas phase. The effect of water on ablation established empirically becomes more clear from this point of view.

Size distributions for the ultrafind diamond-carbon powder and ultrafine SiO_2 powder determined using different measurement procedures are shown in **Fig. 3** and **Fig. 4**. Average sizes of the major (in counted number) fraction of particles and the width of distribution are shown in the figures. For the main numeric fraction, we see a good agreement of the results obtained by means of the soft ablation with the results obtained using scanning electron and atomic force microscopy. Complexes of coarse aggregates of particles (with the mean size of 100 nm and more), obtained wite soft ablation and dynamic light scattering, are seen in the right-hand parts of the plots. One can also see a low-molecular fraction in **Fig. 4** in the left-hand part of the plot; this fraction was successfully recorded only with the help of soft ablation.

In either of the cases, only the aggregated particles were detected with dynamic light scattering in spite of our attempts te break the disaggregates by treating the sample with ultrasound and SDS. Disagreement of the DLS data with data obtained using the other methods results from a specific feature of this method. Thus, intensity of the scattered light is strongly dependent on the molar mass of the sample. Even a small-by-number fraction of large particles overcomes the signal from smaller scatterers and the small size fraction cannot be seen in the presence of a few massive aggregates.

Comparison of the results obtained using four independent methods allows us to hope that we determined the actual fractional composition of the powder sample, even in spite of the difference in the technology of sample preparation. A positive feature of submillimeter laser ablation is the actual absence of sample preparation. In this situation, only the particles of the initial substance can enter the aerosol phase. A low quantum energy of the radiation does not allow one to split the material below the threshold of chemical bonds, which was confirmed previously in the experiments with such «delicate» biological structures as enzymes and DNA [4,5].

It should be stressed additionally thae investigation of the samples by means of TEM/SEM/DLS involves time- and labor-consuming cycles of sample preparation, measurement and analysis of the results obtained, while a single determination of the fraction

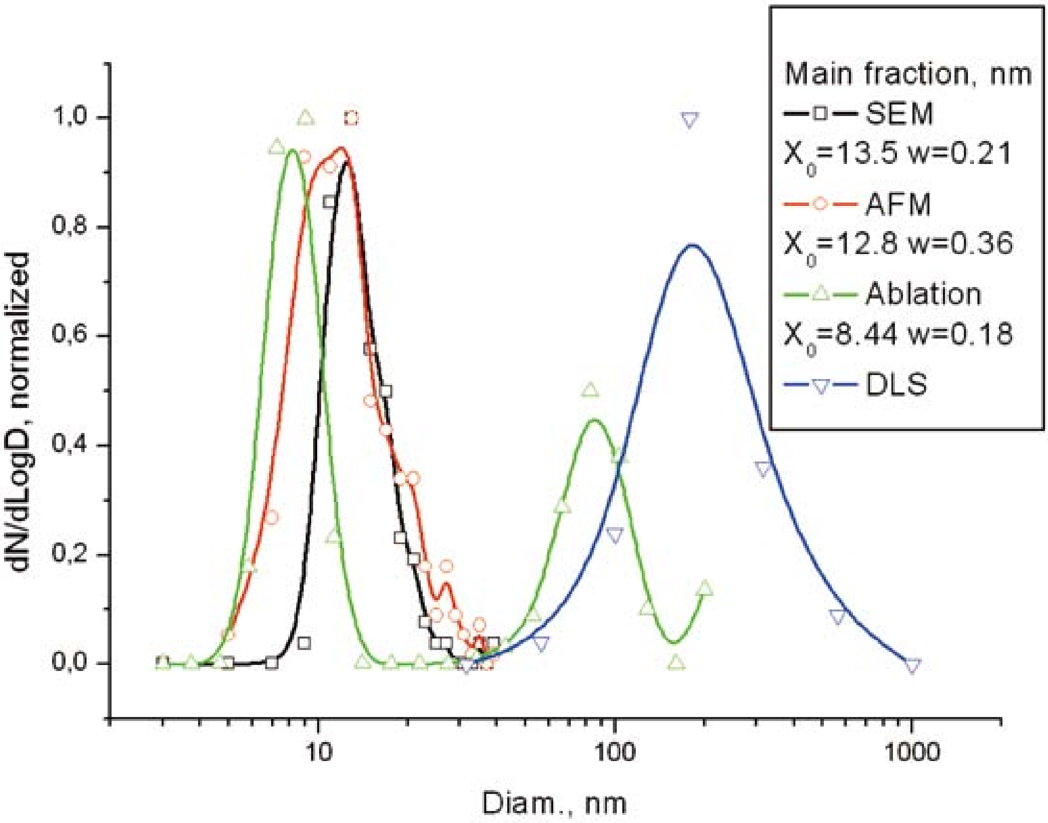

Fig. 3 Size distributions of diamond carbonaceous powder particles registered by scanning electron microscopy (SEM), atomic force microscopy (AFM), dynamic light scattering (DLS) and aerosol products of submillimeter laser ablation (Ablation).

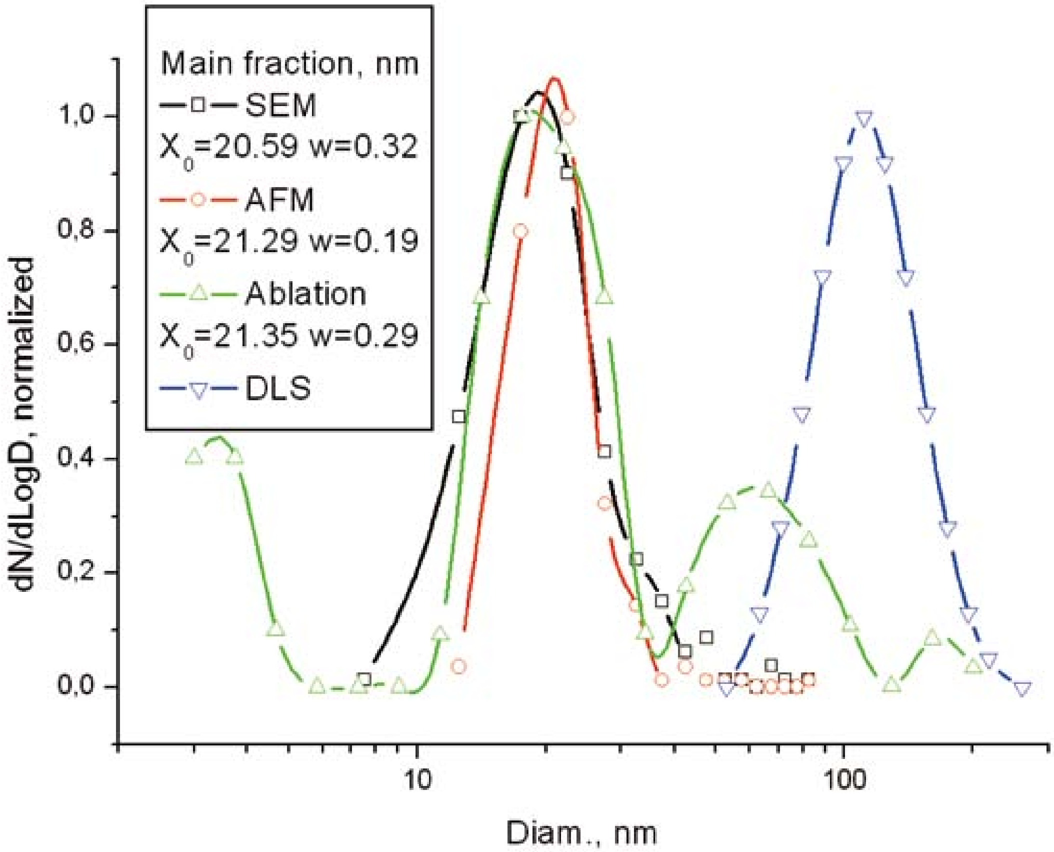

Fig. 4 Size distributions of SiO_2 powder particles registered by scanning electron microscopy (SEM), atomic force microscopy (AFM), dynamic light scattering (DLS) and aerosol products of submillimeter laser ablation (Ablation).

composition of these samples by means of analysis of the aerosol products of the submillimeter laser ablation took about 30 minutes. In addition, our method allows one not only to determine the size of particles in a mixture but also to determine the numerical concentrations of the fractions with good accuracy.

Résumé

The soft nondestructive ablation under the action of the terahertz radiation is an efficient method of transferring macromolecules and clusters from solid substrates and solutions into the aerosol phase while retaining the structural and functional features.

In comparison with conventional methods, the soft ablation method exhibits not only a good agreement of the mean particle size but also turned out to be more informative as it all of particle fractions that are non-recordable using other methods to be detected.

At present, the authors are working on mastering and optimizing the proposed method and plan to broaden the range of samples suitable for this analytical technique. We hope that our approach can become universal, that is, equally applicable in biology, chemistry of polymers, and in the investigations of organic and inorganic clusters of any origin.

Acknowledgements

The work was supported by INTAS – SB ant Grant No.: 06-1000013-8569, SB ant Grant No.: 52/20ors The authors thank the researchers from the Chemical Department of the University of Helsinki: Mikko Karesoja, Esa Puukilainen and Matti Elomaa for assistance in the investigation.

List of symbols

D	diffusion coefficient
K	penetration coefficient
k	Boltzmann constant
l	free path length of gas molecules
N	number concentration
n	number of screens
r	radius of particle
T	temperature

Greek symbols

η	gas viscosity

v density of particles distribution

φ count distribution of particles

References

1) Luk'yanchuk, B. (2002): "Laser Cleaning", World Scientific, New Jersey.
2) Vogel A., Venugopalan V. Mechanisms of pulsed laser ablation of biological tissues (2003): Chemical Reviews., Vol.103, pp.577-644.
3) Gavrilov, N.G., Knyazev, B.A., Kolobanov, E.I., Kotenkov, V.V., Kubarev, V.V., Kulipanov, G.N., Matveenko, A.N., Medvedev, L.E., Miginsky, S.V., Mironenko, L.A., Oreshkov, A.D., Ovchar, V.K., Popik, V.M., Salikova, T.V., Scheglov, M.A., Serednyakov, S.S., Shevchenko, O.A., Skrinsky, A.N., Tcheskidov, V.G., Vinokurov, N.A. Status of the Novosibirsk high-power terahertz FEL (2007): Nuclear Instruments and Methods in Physics Research A., Vol.575, pp.54-57.
4) Petrov, A.K., Kozlov, A.S., Malyshkin, S.B., Taraban, M.B., Popik, V.M., Scheglov, M.A., Goriachkovskaya, T.N., Peltek, S.E. Nondestructive transfer of complex molecular systems of various origin into aerosol phase by means of submillimeter irradiation of free electron laser (FEL) of Siberian center for photochemical research (2007): Nuclear Instruments and Methods in Physics Research A., Vol.575, pp.68–71.
5) Petrov, A.K., Kozlov, A.S., Taraban, M.B., Goryachkovskaya, T.N., Malyshkin, S.B., Popik, V.M. and Peltek, S.E. Soft ablation of biological objects caused by free-electron laser submillimeter radiation (2005): Doklady Biochemistry and Biophysics., Vol.404, pp.357-359.
6) Ankilov, A., Baklanov, A., Colhoun, M., Enderle, K.-H., Gras, J., Julanov, Yu., Kaller, D., Lindner, A., Lushnikov, A.A., Mavliev, R., McGovern, F., O'Connor, T.C., Podzimek, J., Preining, O., Reischl, G.P., Rudolf, R., Sem, G.J., Szymanski, W.W., Vrtala, A.E., Wagner, P.E., Winklmayr, W. and Zagaynov, V. Particle size dependent response of aerosol counters (2002): Atmospheric Research., Vol.62, pp.209-237.
7) Schärtl, W. (2007): "Light Scattering from Polymer Solutions and Nanoparticle Dispersions", Springer Verlag, Berlin Heidelberg, Germany.
8) Fuchs, N.A. (1964): "The Mechanics of Aerosols", Pergamon Press, Oxford, UK.

Author's short biography

Alexander S. Kozlov

Dr. Kozlov (born 1975) at the present works at the Institute of chemical kinetics and combustion as a researcher and manages the work of a userstation at the Siberian center of photochemical investigation. In 1999 he received the bachelor degree in chemical physics at the Novosibirsk state university. In 2005 he received his Ph.D. in Chemical sciences at the Institute of solid state chemistry and mechanochemistry. His Ph.D. thesis was devoted to the investigation of the various processes of nanoaerosol formation and detection in laboratory and natural conditions. He has more than 20 referred journal publication and over 20 international conference presentations.

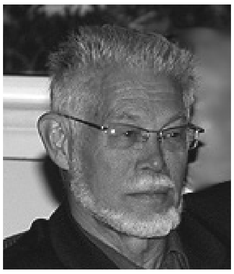

Alexander K. Petrov

Born 1938.
Education: Kemerovo University, Physics, 1961; Institute of Chemical Kinetics and Combustion Novosibirsk, Candidate Thesis, 1967; Institute of Catalysis, Novosibirsk, Doctor Thesis, 1985; Professor, 1994.
Professional: Jr. Researcher, Institute of Organic Chemistry, Novosibirsk 1963-1971; Institute of Chemical Kinetics and Combustion, Novosibirsk: 1971-1975 - Jr. Researcher; 1975-1986 - Senior Researcher; 1986-1992 - Leading Researcher; 1992-2008 - Head of Laboratory of Laser Photochemistry; 1993 -2008- Deputy Director of Institute; 1994 – Professor; 2008 - Principal Researcher.
Current Research Interest: Chemical kinetics, Laser Photochemistry, Laser isotope separation, Kinetics of vibration - excited states, Interaction of laser irradiation with matter.
He has over 150 referred publications (including 3 reviews and 2 monographs).

Professor Gennady Kulipanov

Born 1942.
Education and Career: 1958-1963 Novosibirsk State Technical University; 1963 – Budker Institute of Nuclear Physics; 1970 - Ph.D. in Physics, Budker Institute of Nuclear Physics, SB RAS; 1981 – Head of Laboratory in Budker INP SB RAS; 1991 – Deputy Director of the Budker Institute of Nuclear Physics and Director of Siberian Synchrotron Radiation Center; 1997 - Corresponding Member of Russian Academy of Sciences; 1999 – 2008 Vice-chairmen of Siberian Branch of Russian Academy of Sciences; 2002 - Academician of RAS; 2008 – Deputy Director of the Budker Institute of Nuclear Physics and Director of Siberian Synchrotron and Terahertz Radiation Center.
Research Interests: Physics of nonlinear phenomena in particle accelerators, generation and application of the synchrotron radiation (SR), free electron lasers (FEL), THz application. He is the author more than 300 publications (including 14 reviews and 1 monograph).

Vladimir O. Aseyev

Docent Dr. Aseyev (born 1968) is a senior scientist and works as a university lecturer at the Laboratory of Polymer Chemistry, University of Helsinki, Finland. He received his PhD in chemistry in 1999 at the same Laboratory and became a Doctoral Candidate in Physics and Mathematics in 2000 at the Russian Academy of Sciences, St. Petersburg, Russia. During 1999-2001, he worked at the Department of Chemical and Biochemical Engineering, University of Iowa, USA as a postdoctoral associate and then returned back to Finland. His area of interests includes physics and chemistry of water-soluble and -swellable polymers and nanoparticles.

Development of Advanced Ceramics by Powder Composite Process[†]

Junichi Tatami[1]*, Hiromi Nakano[2], Toru Wakihara[1] and Katsutoshi Komeya[1]
Graduate School of Environment and Information Sciences,
Yokohama National University[1]
Cooperative Research Facility Center,
Toyohashi University of Technology[2]

Abstract

A powder composite process was applied to develop several kinds of advanced ceramics. TiO_2 nanoparticles and Si_3N_4 particles were mixed using a powder composite process to disperse TiN nanoparticles in Si_3N_4 ceramics, which are expected to be used as novel materials for next-generation hybrid ceramic bearings. TEM observations showed that the TiO_2 nanoparticles were directly bonded to submicron Si_3N_4 particles. Si_3N_4 ceramics with uniformly-dispersed TiN nanoparticles were fabricated using the composite particles. The amount of damage caused by the Si_3N_4 ceramics with TiN nanoparticles to the mating metals in a ball-on-disk test was comparable to the damage caused by Si_3N_4 ceramics without TiN particles. Nanocomposite particles of Al_2O_3-doped ZnO prepared by a powder composite process were also used for fabricating ZnO ceramics. TEM observations revealed the uniform presence of Al_2O_3 nanoparticles on ZnO particles. A sintering body fabricated using the composite powder prepared by this powder composite process had more uniform and finer microstructures than that fabricated using a powder mixture prepared by conventional wet mixing. The ZnO ceramics prepared by the powder composite process exhibited higher electrical conductivity than those prepared by the conventional wet ball milling process. CNT-dispersed Al_2O_3 ceramics were fabricated using a powder mixture of CNT and fine Al_2O_3 powder prepared by the powder composite process. It was shown that CNTs were uniformly dispersed in the developed CNT-dispersed Al_2O_3 ceramics, and that they had high electrical conductivity and strength.

Keywords: powder composite process, silicon nitride, titanium nitride, zinc oxide, alumina, carbon nanotube

1. Introduction

Advanced ceramics are very significant materials with the potential to solve present and future environmental and energy problems. The properties of these ceramics depend, not only on the atomic bonding and crystal structure, but also on the microstructural properties such as the grain size, grain boundary, impurity, secondary phase, pores, and defects in the sintered body. In particular, the powder processing has a large influence on the latter because advanced ceramics are fabricated by shaping and sintering fine raw powders. Therefore, the advancement of ceramic powder processing techniques, including the homogeneous dispersion of raw materials, formation of a uniform green body, and analytical control of the sintering shrinkage behavior, is very important to make better ceramics. The homogeneous mixing of additives can be better achieved by using nanoparticles rather than large particles as the raw material. However, the use of the wet milling process with liquid dispersion media such as water and ethanol might lead to the reagglomeration of nanoparticles during drying. We have focused on the fabrication of advanced ceramics by using a powder composite

---

[†] Accepted: October 7rd, 2010
[1] Yokohama 240-8501, Japan
[2] 1-1Hibarigaoka, Tenpaku-cho, Toyohashi-shi, Aichi 441-8580, Japan
* Corresponding author
TEL: +81-45-339-3959, FAX: +81-45-339-3957
E-mail: tatami@ynu.ac.jp

process in which nanoparticles are mechanically mixed using only a dry mixing process, which allows us to obtain nanocomposite particles. In this process, nanoparticles are bonded to submicron particles by applying an external mechanical force, specifically a shear force[1, 2].

Many types of powder composite processes have been developed commercially[1, 2]. These nanocomposite particle processes are divided into two types: the bonding of fine particles to a core particle and the homogeneous mixing of various fine particles. The former is regarded as surface modification on the microscale and nanoscale. The powder composite process is characterized by (a) a simple dry process, (b) unlimited raw material, (c) a large amount of treatment, and (d) the easy control of the coating conditions. The particle composite behavior depends on several factors. Naito et al. reported the effects of the rotor shape, mechanical treatment conditions (rotation speed and time), and raw material particle sizes on the particle composite process[3, 4, 5, 6]. Nogi et al. also estimated the relationship between the temperature of the container and the interface of the particles[7].

Some researchers have studied the synthesis of ceramic particles and the preparation of porous ceramics using a powder composite process[8, 9, 10, 11, 12]. We also developed several kinds of dense advanced ceramics and controlled their microstructures to improve their properties[13, 14, 15]. In this paper, we will introduce the microstructure and properties of TiN-particle-dispersed Si_3N_4 ceramics, Al-doped ZnO ceramics, and CNT-dispersed Al_2O_3 ceramics fabricated by the particle composite process.

2. TiN-Nanoparticle-Dispersed Si_3N_4 Ceramics

Over 40 years have passed since Si_3N_4 ceramics were first developed. In the meantime, Si_3N_4 ceramics with high strength and fracture toughness have been developed as a result of using newly discovered SiAlONs[16, 17]; the invention of sintering aids such as Y_2O_3[18, 19]; the development of fine, pure, and highly sinterable Si_3N_4 powder[20]; the invention of a gas pressure sintering technique[21]; the advancement of the science and technology for microstructure control, etc. Si_3N_4 ceramics have been applied to automobile components such as glow plugs[22], hot chambers[23], and turbocharger rotors[24]. Around the same time, cutting tools and bearing components were also developed[25, 26, 27]. Si_3N_4 ceramic bearings were put to practical use in 1983[25]. Although the cost of Si_3N_4 ceramics was high, they were used as bearing materials in machine tools because of properties such as high strength, high toughness, high elastic modulus, high hardness, light weight, and good corrosion resistance[26, 27]. Furthermore, Si_3N_4 ceramics fabricated from Si_3N_4-Y_2O_3-Al_2O_3-TiO_2-AlN have been widely used for bearing applications. The authors have studied the sintering behavior and microstructure control of Si_3N_4-Y_2O_3-Al_2O_3-TiO_2-AlN. We found that the densification is enhanced at lower temperatures by simultaneous additions of TiO_2 and AlN to Si_3N_4-Y_2O_3-Al_2O_3[28]. It was also shown that TiN is formed by a reaction between TiO_2 and AlN or Si_3N_4, and that its size is almost the same as that of the added TiO_2[29]. Furthermore, it was clarified that the contact fatigue of Si_3N_4 ceramics is suppressed by the dispersed TiN particles[30].

Hybrid bearings composed of Si_3N_4 ceramic balls and metal rings are more popular than all-ceramic bearings because of their cost. In hybrid bearings, it is possible that hard and large TiN particles damage the mating metals in a manner analogous to the wear map concept[31]. The dispersion of TiN nanoparticles is expected to be effective in solving this problem. TiN nanoparticles can be formed from TiO_2 nanoparticles because the size of TiN should be almost the same as that of TiO_2. However, it is difficult to realize TiN nanoparticle-dispersed Si_3N_4 ceramics even if TiO_2 nanoparticles are completely dispersed in the slurry[32]. This difficulty might be because of the reagglomeration of TiO_2 nanoparticles during the drying process. We applied the powder composite process to develop TiN-nanoparticle-dispersed Si_3N_4 ceramics and lower the aggressiveness to the mating metals in a wear test.

To fabricate TiN-nanoparticle-dispersed Si_3N_4 ceramics, high-purity, fine Si_3N_4 powder (SN-E-10, Ube Co. Ltd., Japan), Y_2O_3 (RU, Shinetsu Chemical Co., Japan), Al_2O_3 (AKP-30, Sumitomo Chemical Co., Japan), AlN (F grade, Tokuyama Co., Japan), and TiO_2 (Aeroxide P 25, Nippon Aerosil Co., Ltd, Japan) were used as the raw materials. First, TiO_2 nanoparticles were dispersed in ethanol according to our previous study[32], using polyethylenimine (EPOMIN, MW1200, Nippon Shokubai Co. Ltd., Japan) by ball milling for 48 h. The Si_3N_4 powder was then mixed into the TiO_2 slurry by ball milling for 48 h, followed by the elimination of the ethanol. The pre-mixed powder was mechanically treated using a powder composer (Nobilta NOB-130, Hosokawa Micron Co., Japan) to prepare composite particles. After the powder composite process, the other sintering aids were added by ball milling in ethanol for 48 h using β-sialon balls in a silicon nitride container. After removing the ethanol, 4 wt% paraffin (melting point: 46-48℃, Junsei Chemical Co., Japan) and 2 wt% dioctyl phthalate (DOP, Wako Junyaku Co., Japan) were added as a binder and lubricant, respectively. For reference, five types of powder mixtures were also prepared using only mechanical treatment without premixing, using conventional wet ball milling with 20-, 200-, or 540-nm TiO_2 particles, and not using TiO_2 and AlN (i.e., no TiN formation in Si_3N_4 ceramics). The notations for these powder mixtures are listed in **Table 1**.

Fig. 1 shows SEM images of the powder mixtures before and after the mechanical treatment. The TiO_2 nanoparticles formed aggregates before the mechanical treatment [**Fig. 1 (a)**]. On the other hand, as shown in [**Fig. 1 (b)**], no TiO_2 nanoparticle aggregates were found in the powder mixture after the mechanical treatment, i.e., the TiO_2 nanoparticles were well dispersed. **Fig. 2** presents TEM images of the powder mixtures before and after the mechanical treatment. Although the TiO_2 nanoparticles were dispersed in ethanol by wet mixing, as reported in our previous paper 32), they reagglomerated as a result of mixing with Si_3N_4 powder and/or drying. As shown in **Fig. 2 (b)**, the mechanical treatment resulted in the uniform dispersion of the TiO_2 nanoparticles, thus suggesting that they might be strongly attached to theSi_3N_4 particles. A high-resolution TEM (HRTEM) image of a composite particle is shown in **Fig. 3**. It can be seen that a TiO_2 nanoparticle is directly bonded onto a submicron Si_3N_4 particle. At the atomic scale, the interface between the TiO_2 and Si_3N_4 was flat. Such a direct-bonded interface should be stronger than the interface of physically adsorbed particles. Si was detected in the TiO_2 particles by

Table 1 Composition and mixing process for TiN-dispersed Si_3N_4 ceramics

Notation	Composition (weight ratio)					Mixing process	Remarks
	Si_3N_4	Y_2O_3	Al_2O_3	TiO_2	AlN		
PM-N	92	5	3	5	5	Premixing +Powder composite process	TiO_2:20nm
M-N	92	5	3	5	5	Powder composite process	TiO_2:20nm
W-N	92	5	3	5	5	Conventional wet ball milling	TiO_2:20nm
W-SM	92	5	3	5	5		TiO_2:200nm
W-M	92	5	3	5	5		TiO_2:540nm
NT	92	5	3	0	0		No TiN in Si_3N_4 ceramics

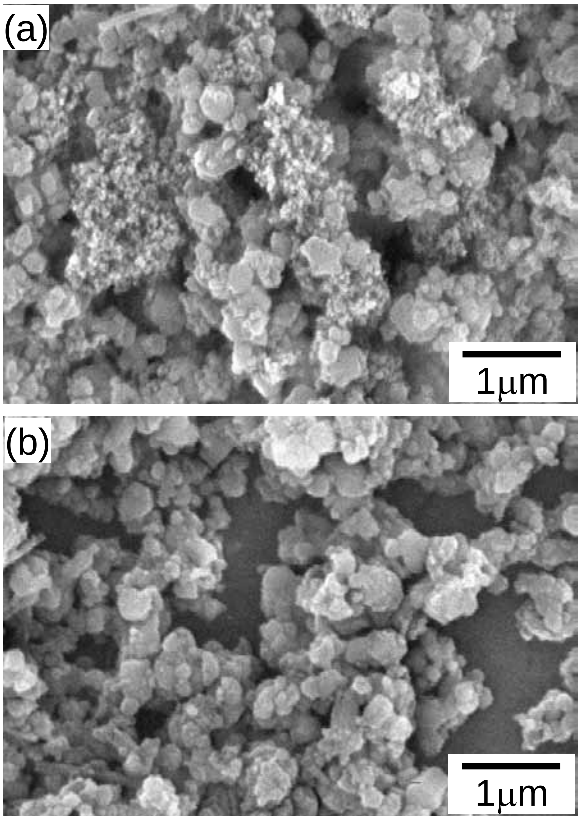

Fig. 1 SEM images of powder mixture (a) before and (b) after a powder composite process.

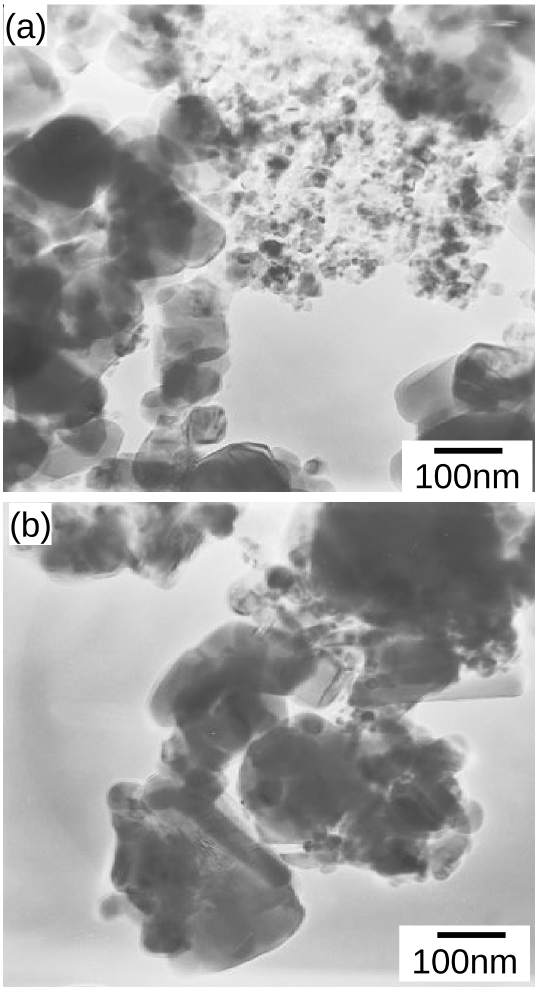

Fig. 2 TEM images of powder mixture (a) before and (b) after a powder composite process.

an EDS analysis. In addition, neck growth occurred between the TiO_2 and Si_3N_4 particles, similar to the initial stage of sintering, in spite of the mechanical treatment at ambient temperature. This phenomenon should result from the reaction between the TiO_2 and TiO_2 and/or Si_3N_4. Nogi et al. reported the relationship between the temperature of the container and the particle interface[7]. In this case, because the container temperature is 50―60℃, the interfacial temperature is expected to be around 700―800℃. On the other hand, the crystalline phase of the TiO_2 was anatase, both before and after the mechanical treatment, indicating that the temperature of the particle itself was not very high. Therefore, a mechanochemical reaction occurring just at the interface resulted in diffusion and sintering, forming the flat interface and the neck between the TiO_2 and SiO_2 layer and/or Si_3N_4 particles.

The mixed powders were sieved using a #60 nylon sieve and then molded into ϕ15×7 mm pellets by uniaxial pressing at 50 MPa followed by cold isostatic pressing at 200 MPa. After binder burnout in air at 500 ℃ for 3 h, the green bodies were fired at 1800 ℃ in 0.9 MPa N2 for 2 h using a gas pressure sintering furnace (Himulti 5000, Fujidenpa Kogyo Co., Japan). The sintered bodies were hot isostatically pressed at 1700 ℃ for 1 h under 100 MPa N2. The density of the fired samples was measured using the Archimedes method. The phase present in the samples was identified by X-ray diffraction (RINT2000, Rigaku Co., Japan). The microstructure was observed by a transmission electron microscope (TEM, JEM-3000F, JEOL, Japan) equipped with an energy-dispersive spectroscope (EDS, Voyager III, NORAN instruments). The Si_3N_4 ceramics were machined using a grinding machine (SG-45FIIH, Wasino Engineering Co., Japan) and then polished using diamond slurry. The wear property was estimated by a ball-on-disk test, which consisted of a polished Si_3N_4 disk and a steel ball bearing (SUJ-2). The testing conditions were a relative humidity of 50 ± 2% and a temperature of 22-24 ℃. The radius of the SUJ-2 ball was 3 mm. The rotation speed and radius were 10 cm s^{-1} and 3 mm, respectively. The weight was 5 N, and the running distance was 250 m. The polished and worn surfaces of the specimens were observed by scanning probe microscopy (SPM, SPA-400, Seiko Nanotechnologies, Japan).

The relative density of all of the specimens was over 98%, which was sufficiently high to measure the mechanical properties. β-Si_3N_4 and TiN were also identified as the main phases of the products in the sample, in addition to TiO_2 and AlN. **Fig. 4** shows TEM images of the TiN-dispersed Si_3N_4 ceramics. As shown in **Fig. 4 (a)**, the size of the TiN particles in the Si_3N_4 ceramics fabricated using just wet mixing was 300?500 nm. On the other hand, in the case of using composite particles prepared by premixing and

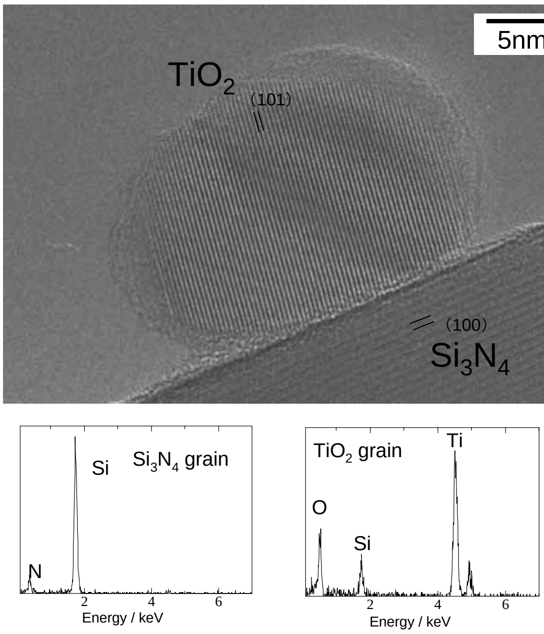

Fig. 3 High-resolution TEM image of composite particle prepared by a powder composite process.

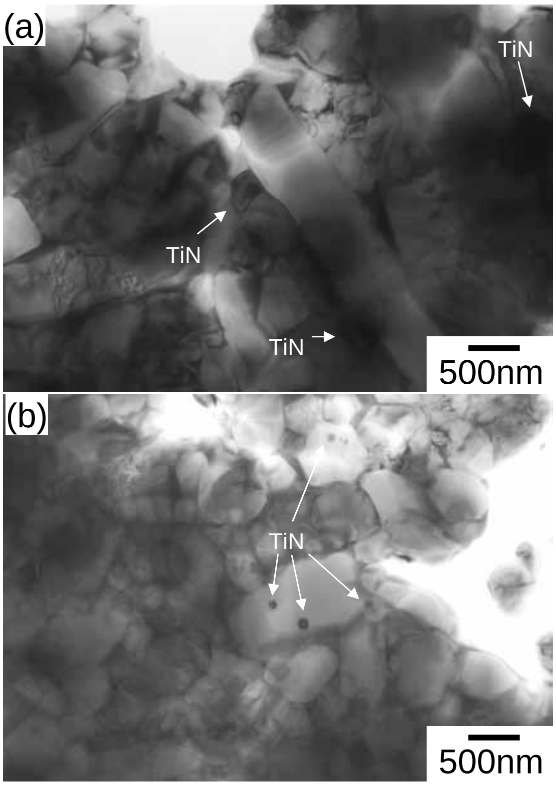

Fig. 4 TEM images of Si_3N_4 ceramics. (a) Sample W-N and (b) sample PM-N.

mechanical treatment, 20-100-nm TiN nanoparticles were found in Si_3N_4 grains and in the grain boundary (**Fig. 4 (b)**). Thus, it was shown that TiN nanoparticle-dispersed Si_3N_4 ceramics were fabricated using composite powder prepared by premixing followed by mechanical treatment.

Fig. 5 and **6** show optical micrographs of the worn surfaces of the SUJ2 balls and Si_3N_4 disks after the ball-on-disk tests. It can be observed that the areas of the SUJ2 balls worn by sample PM-N were smaller than all of the other areas, even though the wear track width of the Si_3N_4 ceramics is almost the same. The wear volume was calculated from the wear area of the ball and the worn surface profile of the Si_3N_4 disk. As listed in **Table 2**, the wear volume of the Si_3N_4 disk was independent of the Si_3N_4 ceramics, except for sample W-M. On the other hand, the wear volume of the SUJ2 ball depended on the mating Si_3N_4 ceramics, i.e., the wear volume of the ball worn by sample PM-N was not only smaller than those worn by samples M-N and W-N but was also the same as that worn by sample NT. Furthermore, the wear volumes of the steel balls worn by samples M-SM and M-M were higher than those of PM-N, thus suggesting that TiN nanoparticle dispersion should cause less damage to the mating metals.

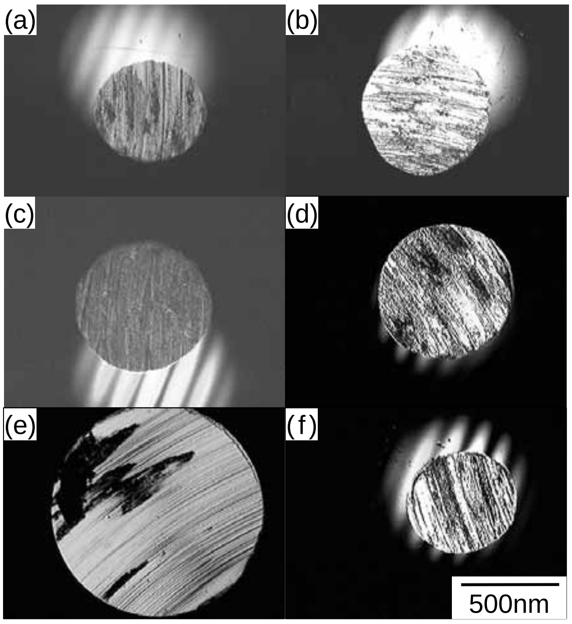

Fig. 5 Optical micrographs of worn surfaces of the steel ball after ball-on-disk test.
(a) sample PM-N, (b) M-N, (c) W-N, (d) W-SM, (e) W-M and (f) NT

Table 2 Wear volume of Si_3N_4 disk and SUJ2 ball after ball-on-disk test

Sample	Wear volume / $10^{-12}m^3$	
	Si_3N_4 disk	SUJ2 ball
PM-N	9.5	1.5
M-N	9.4	2.7
W-N	9.8	3.9
W-SM	10.9	20.7
W-M	4.4	3.5
NT	10.0	1.6

The wear behavior was evaluated by SPM observations of the worn surfaces. **Fig. 7** shows SPM images of the worn surfaces of the steel balls after the ball-on-disk tests. It was found that there were many grooves on the worn surface and that the distance between the grooves was comparable to the size of the TiN. **Fig. 8** shows the polished surface of sample W-M. Even though the surface was polished, it can be observed that a large TiN particle projects from the surface because of its high hardness. This indicates that aggressive wear was caused by hard and large TiN particles during the ball-on-disk test, similar to abrasive wear[33]. In other words, because sample PM-N had much smaller TiN particles, the abrasiveness toward the mating metallic ball was considered to be comparable to Si_3N_4 ceramics without TiN particles.

Fig. 9 shows SPM images of the worn surfaces of the TiN-dispersed Si_3N_4 ceramics. The agglomerates

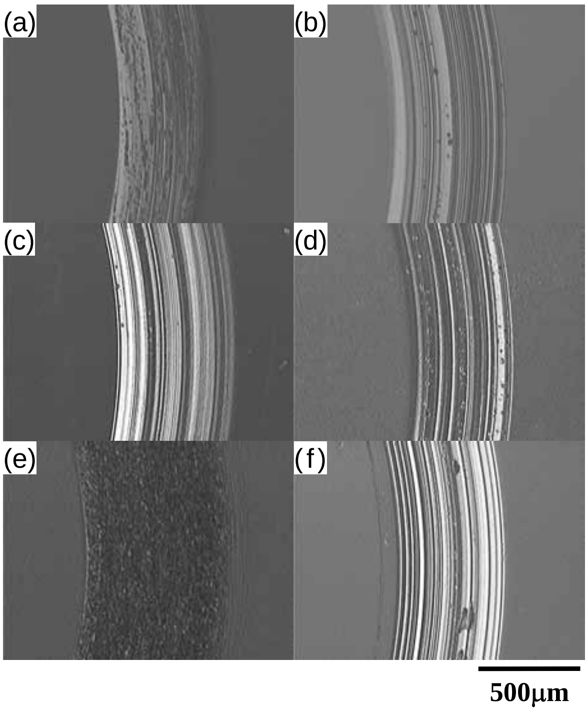

Fig. 6 Optical micrographs of worn surfaces of the Si_3N_4 disk after ball-on-disk test.
(a) sample PM-N, (b) M-N, (c) W-N, (d) W-SM, (e) W-M and (f) NT

observed on the worn surface of sample W-M might consist of metallic wear particles. Because of the adhesion of metallic particles on the worn surface of Si_3N_4 ceramics, the wear volume of sample W-M appears to be smaller than the other samples. Because the grain boundary phase is easily removed, the Si_3N_4 grain shape is emphasized. The Si_3N_4 ceramics in this study were composed of Si_3N_4 grains, TiN grains, and a grain boundary phase. It is well known that softer materials are more easily worn. Therefore, a softer grain boundary phase is considered to be preferentially worn during a ball-on-disk test. Furthermore, because the Si_3N_4 ceramics used in this study were fabricated from the same composition of sintering aids, it seems that the wear volumes of the Si_3N_4 ceramics were comparable. Thus, it was shown that TiN nanoparticle-dispersed Si_3N_4 ceramics were successfully developed using TiO_2 and Si_3N_4 composite particles prepared by pre-mixing and mechanical treatment, and that the dispersion of TiN nanoparticles lowered the aggressiveness to the mating metals in the wear test.

The developed Si_3N_4 ceramics need high mechanical properties for bearing application. ISO 26602:2009 provides a classification defining the physical and mechanical properties of silicon nitride preprocessed ball bearing materials. These materials are classified in three categories by the specification of their characteristics and microstructures. **Fig. 10** shows

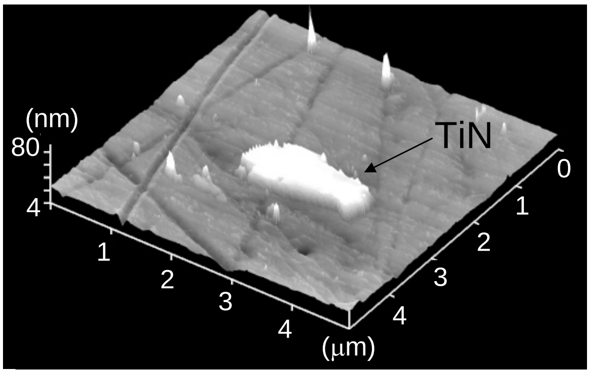

Fig. 8 SPM images of polished surface of sample W-M.

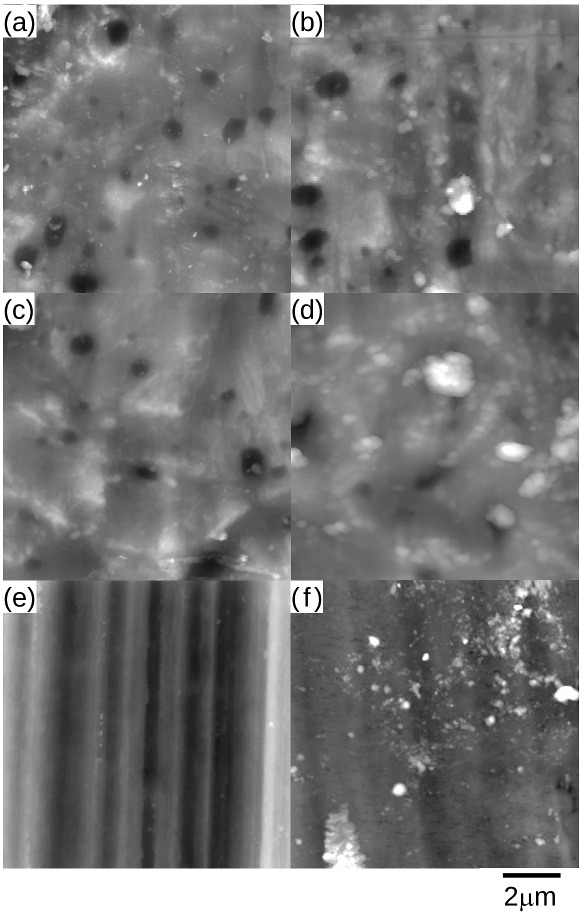

Fig. 7 SPM images of worn surface of steel ball after ball-on-disk test.
(a) sample PM-N, (b) M-N, (c) W-N, (d) W-SM, (e) W-M and (f) NT

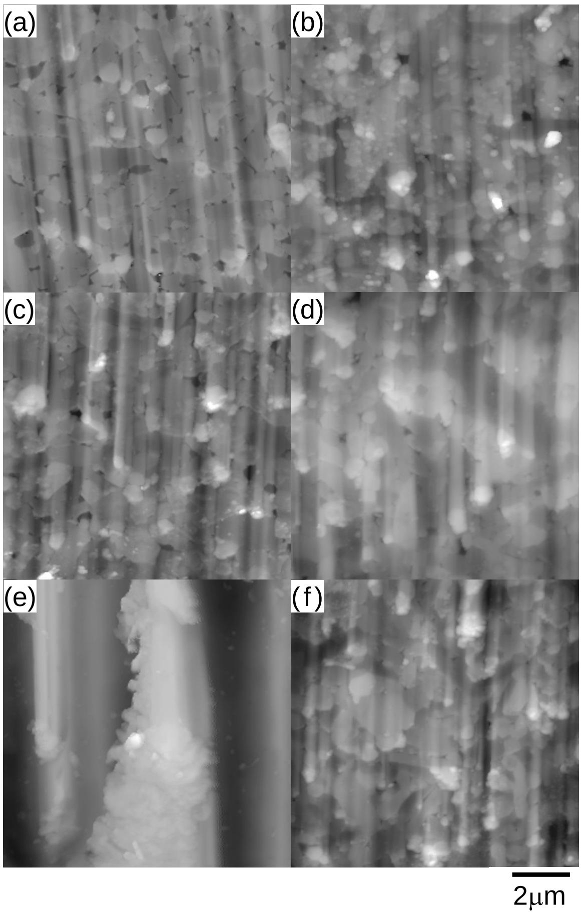

Fig. 9 SPM images of worn surface of Si3N4 disk after ball-on-disk test.
(a) sample PM-N, (b) M-N, (c) W-N, (d) W-SM, (e) W-M and (f) NT

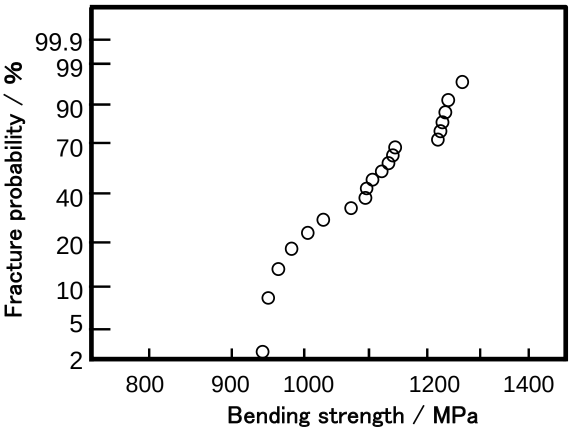

Fig. 10 Weibull plot of bending strength of sample PM-N.

the Weibull plot of the bending strength of sample PM-N. The shape factor in the Weibull plot of the bending strength was 13, and the average bending strength was 1109 MPa. The fracture toughness and Vickers hardness were 6.7 MPam$^{1/2}$ and 15.4 GPa, respectively. These are higher than the Class I values in ISO 26602 : 2009. We prepared balls using the developed material to measure the crushing strength. The crushing strength of this material was about 31.7 N, which is 1.5 times that of the conventional Si_3N_4 ceramics used for bearings. A rolling fatigue test was carried out using 3 10-mm diameter balls under a pressure of 5.9 GPa. The rolling fatigue lifetime of the developed TiN-nanoparticle-dispersed Si_3N_4 ceramics was longer than 107 cycles. Consequently, it was confirmed that the developed material has sufficient mechanical properties for use in the next generation of ceramic bearings.

3. Al-Doped ZnO Ceramics

ZnO is a typical n-type semiconductor. Numerous researchers have studied the electrical properties of ZnO ceramics for many years. Because of the advantages offered by the particular properties of ZnO ceramics, they have been used to manufacture varistors[34], sensors[35], thermoelectric transducers[36], transparent conductive films[37], light emitting diodes[38], etc. The electrical properties of ZnO ceramics are controlled by adding small amounts of additives. For example, it has been reported that Cr_2O_3, CoO, MnO, Bi_2O_3, and Pr_6O_{11} additives exhibit nonlinear electrical conductivity[39, 40]. In addition, because Al_2O_3 dissolves in ZnO, the carrier concentration can be controlled (controlled valency). Therefore, Al_2O_3-doped ZnO improves the electrical conductivity[41, 42].

Many researchers have fabricated ZnO ceramics using a solid reaction; here, a ball milling technique is normally used to mix the powder for the fabrication. The homogeneous dispersion of additives is one of the most important processes in powder processing; this process results in the production of better ZnO ceramics. This homogeneous mixing of additives can be better achieved by using nanoparticles rather than large particles as the raw material. However, the use of the wet milling process with liquid dispersion media such as water and ethanol might lead to the reagglomeration of nanoparticles during drying. Consequently, the amount of mixed material obtained might not be sufficient to take advantage of the characteristics of nanoparticles. We developed Al_2O_3-doped ZnO ceramics using nanocomposite particles composed of γ-Al_2O_3 nanoparticles and ZnO submicron particles prepared by mechanical treatment and investigated the effect of the mixing process on the electrical conductivity of ZnO ceramics.

ZnO powder (grain size: 0.2—0.6 μm, JIS 1, Hakusui Tech Co., Ltd.) and γ-Al_2O_3 powder (grain size: 7 nm, TM-300, Taimei Chemicals Co., Ltd.) were used in this study. The amounts of γ-Al_2O_3 used were 0.1, 1.0, and 3.7 mol%. These powders were premixed for 30 min by dry ball milling. This milling was carried out using Al_2O_3 balls of ϕ10 mm. The premixed powder was mechanically treated using a powder composer (Nobilta NOB-130, Hosokawa Micron Co.) working at 2000 rpm for 10 min to prepare composite powders. For reference, raw material powders of the same compositions were prepared by carrying out wet ball milling in ethanol using Al_2O_3 balls of ϕ10 mm for 24 h.

The mechanically treated powders were observed using a transmission electron microscope (TEM, JEM-3000F, JEOL Ltd.). **Fig. 11** shows the TEM images of the ZnO-Al_2O_3 powder mixture after the mechanical treatment (**Figs. 11 (a)** and **(b)**) and wet ball milling (**Figs. 11 (c)** and **(d)**). **Figs. 11 (b)** and **(d)** are enlarged TEM photographs. The angular and dark pieces of grains shown in **Figs. 11 (a)** and **(c)** represent the ZnO grains. Smaller particles can be seen on the surface of a ZnO particle in **Fig. 11 (a)**. **Fig. 11 (b)** shows that the size of the smaller particles on the ZnO particles was less than 10 nm, which was almost the same as that of the γ-Al_2O_3 used in this study. Therefore, it appears that the γ-Al_2O_3 nanoparticles were directly bonded to the ZnO particles. On the other hand, a large agglomeration of γ-Al_2O_3 was observed after wet ball milling (**Fig. 11 (c)**), and it was concluded that the γ-Al_2O_3 nanoparticles were not directly bonded to the ZnO particle

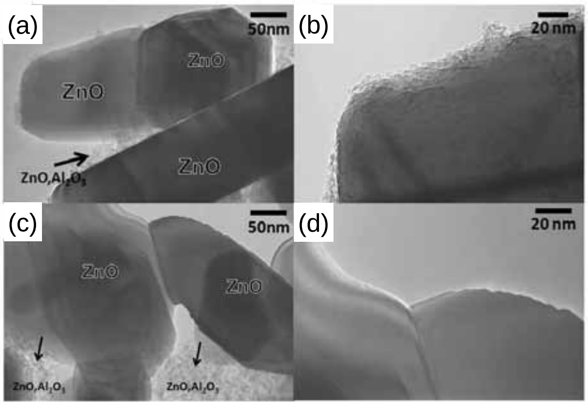

Fig. 11 TEM images of 3.7 mol% Al_2O_3-doped ZnO powder mixture (a) prepared by a powder composite process, (b) enlarged view of (a), (c) prepared by wet ball milling and (d) enlarged view of (c).

(**Fig. 11 (d)**).

Fig. 12 shows the XRD profiles of the ZnO-Al_2O_3 powder before and after the mechanical treatment, as well as the raw materials used. The characterization of the composite powder was carried out by X-ray diffraction using Cu Kα radiation. It was observed that the phases present in the composite powder consisted exclusively of ZnO and γ-Al_2O_3, which were the same as the raw materials. Therefore, we inferred that γ-Al_2O_3 bonded to the ZnO grain surface because of the mechanical treatment. In this experiment, we were also able to establish the phenomenon reported above. The estimated temperature of the particle interface[7] must be maintained below 700 ℃. It is known that the sintering shrinkage of ZnO starts at a temperature of approximately 600 ℃[43]. It should be noted that γ-Al_2O_3 is phase transformed to α-Al_2O_3 with an increase in temperature and grain growth. Therefore, the temperature of the γ-Al_2O_3 and ZnO particles themselves should be very low, but the temperature of the interface between the ZnO and γ-Al_2O_3 should be slightly higher because of the shear force.

The specific surface area was measured by the BET method using a surface area analyzer (Quantasorb, Quantachrome Instruments, USA). **Table 2** lists the specific surface area of the ZnO-Al_2O_3 powder, which was measured using the BET method after the mechanical treatment. For reference, the specific surface areas of the raw materials (ZnO and Al_2O_3) are also listed in the table. The specific surface areas of ZnO and γ-Al_2O_3 were 4.2 m^2/g and 196 m^2/g, respectively. When 3.7 mol% Al_2O_3-doped ZnO was used, the specific surface area was 12.1 m^2/g before the mechanical treatment and 10.3 m^2/g after the mechanical treatment. When 1.0 mol% and 0.1 mol% of Al_2O_3 were added, the specific surface area changed from 6.7 m^2/g to 5.5 m^2/g and from 4.6 m^2/g to 4.2 m^2/g, respectively. The above decreases in the specific surface areas were assumed to be because of the formation of a bonding area between the ZnO particles and γ-Al_2O_3 during the mechanical treatment.

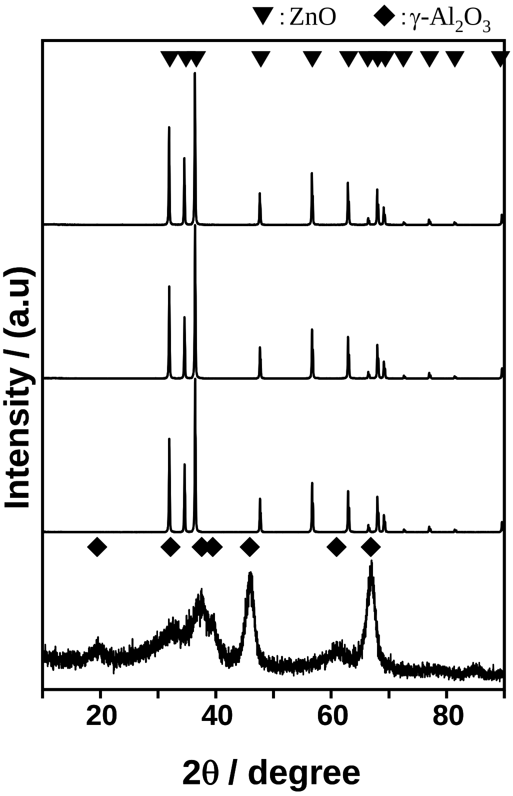

Fig. 12 XRD profiles of the raw powders and 3.7 mol% Al_2O_3-doped ZnO powder mixtures.
(a) Powder mixture before a powder composite process.
(b) Powder mixture after a powder composite process.
(c) ZnO powder.
(d) γ-Al_2O_3 powder.

The specific surface area, S_0, before the mechanical treatment was estimated as follows:

$$S_0 = S_{submicron}(1-f) + S_{nano}f \tag{1}$$

where f is the weight fraction of the nanoparticle, $S_{submicron}$ and S_{nano} are the specific surface areas of the submicron-sized particle and nanosized particle, respectively. If a cubic-shaped nanoparticle of a phase bonds to the spherical submicron particle, the total surface area should be reduced by $2L^2$. When all of the nanoparticles bonded to the submicron particles, the decrease in surface area, ΔS, per unit of weight was as follows:

$$\Delta S = \frac{2L^2}{6L^2} S_{nano} f \tag{2}$$

$$= \frac{1}{3} S_{nano} f$$

Hence, the specific surface area after bonding, S, was estimated as follows:

$$\begin{aligned} S &= S_{submicron}(1-f) + \frac{2}{3} S_{nano} f \\ &= S_{submicron} + \left(\frac{2}{3} S_{nano} - S_{submicron} \right) f \end{aligned} \qquad (3)$$

The values of the specific surface areas after the mechanical treatment, as calculated in **eq. (3)**, are also listed in **Table 3**. The calculated values of the specific surface areas were in good agreement with the experimental values. Therefore, it was concluded that the specific surface area decreased because of the bonding between the ZnO and γ-Al_2O_3 particles during the mechanical treatment and that almost all of the added γ-Al_2O_3 bonded to the ZnO particles. These results agreed well with those obtained by the TEM analysis.

In order to fabricate granules, paraffin (4 mass%, melting point: 46—48 ℃, Junsei Chemical Co., Ltd.), dioctyl phthalate (DOP, 2 mass%, Wako Pure Chemical Industries, Ltd.), and cyclohexane (S grade, Wako Pure Chemical Industries, Ltd.) were added to these mixed powders, after which the powder mixture was sieved using a 250-μm-mesh nylon sieve. The powder was then molded into cylindrical pellets by uniaxial pressing at 50 MPa followed by cold isostatic pressing at 200 MPa. After the binder was burned out in air at 500 ℃ for 3 h, the green bodies were fired at 1400 ℃ in air for 2 h.

We fabricated sintering bodies using the prepared composite powder and the powder obtained by the wet ball milling of 1.0 mol% Al_2O_3-doped ZnO. The relative densities of the sintering bodies prepared from the composite powder and the powder obtained by wet ball milling were 98.9% and 99.2%, respectively. A phase analysis using X-ray diffraction showed that the main phase was ZnO, and the secondary phase was $ZnAl_2O_4$ (**Fig. 13**).

The microstructures of the ZnO ceramics were observed using the SEM and TEM. The SEM images in **Fig. 14** show the thermally etched surfaces of 1.0 mol% Al_2O_3-doped ZnO ceramics. The dark particles represent ZnO, and the small bright particles represent ZnAl2O4. It appears that the particle size of the

Table 3 Specific surface area of the raw powders and the powder mixtures

Sample	Specific surface area (m^2/g)		
	Experimental value		Estimated value
γ-Al_2O_3	196		
ZnO	4.2		
	Powder composite process		
	Before	After	
3.7mol% Al_2O_3	12.1	10.3	9.8
3.7mol% Al_2O_3	6.7	5.5	5.8
3.7mol% Al_2O_3	4.6	4.2	4.4

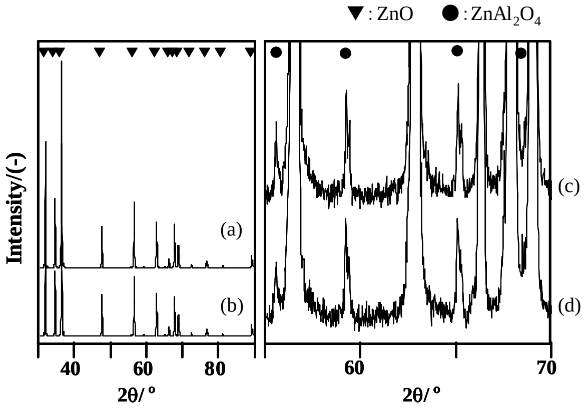

Fig. 13 XRD profiles of 1.0 mol% Al_2O_3-doped ZnO ceramics. prepared by (a, c) a powder composite process and (b, d) wet ball milling.

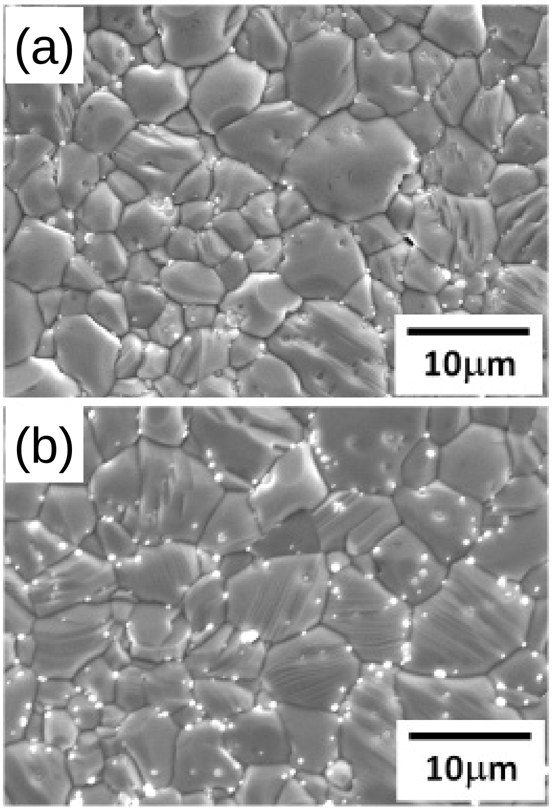

Fig. 14 SEM images of 1.0 mol% Al_2O_3-doped ZnO ceramics prepared by (a) a powder composite process and (b) wet ball milling.

ZnO prepared from the wet ball milled powder was slightly larger than that of the ZnO prepared from the mechanically treated powder. The grain size of the powder obtained after the mechanical treatment was 5.3 μm, whereas that obtained by wet ball milling was 5.6 μm. The sintered body fabricated from the mechanically treated powder had a slightly smaller and more uniform grain size than that fabricated from the powder obtained by wet ball milling. Furthermore, the particle size of the secondary $ZnAl_2O_4$ phase in the ZnO ceramics fabricated by the mechanical treatment process appeared to be considerably smaller and more uniform than that of the secondary $ZnAl_2O_4$ phase in the ZnO ceramics fabricated by the wet ball milling process. It has been reported that adding Al_2O_3 to ZnO restricted the densification and grain growth of the ZnO[44]. Therefore, the homogeneous and fine microstructure of the ZnO ceramics obtained by the mechanical treatment process can be attributed to a uniform dispersion of the nanosized γ-Al_2O_3 particles.

The electrical conductivity of the 1.0 wt% Al_2O_3-doped ZnO ceramics was measured using the four-terminal method. The electrical conductivities of the sintered bodies obtained by wet ball milling and the powder composite process were 333 S/cm and 588 S/cm, respectively. In other words, the electrical conductivity of the composite powder obtained by the powder composite process was almost twice that of the powder obtained by wet ball milling. The high electrical conductivity of the Al_2O_3-doped ZnO was attributed to the dissolution of the Al_2O_3 in the ZnO to form electrons as carriers. The grain boundary structure and impurity segregation also influenced the electrical conductivities of the ZnO ceramics. TEM images revealed that there was no difference between the sintering bodies obtained by the powder composite process and wet ball milling (**Fig. 15**). The solubility limit of Al in ZnO is 0.3 mol%, which is smaller than the amount of Al_2O_3 added. [45]. The excess amount of Al might be segregated in the grain boundary and could be present as a secondary phase ($ZnAl_2O_4$). However, there were no considerable differences in the grain boundaries and secondary phases in a comparison of the mechanical treatment and ball milling processes, except for the size of the secondary phase. This implied that the microstructure had a small effect on the difference in the electrical conductivity.

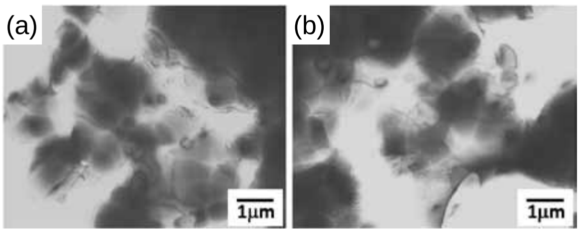

Fig. 15 TEM images of 1.0mol% Al_2O_3-doped ZnO ceramics prepared by (a) a powder composite process and (b) wet ball milling.

4. CNT-Dispersed Al_2O_3 Ceramics

Carbon nanotubes have high strength, high elastic modulus, and excellent thermal and electrical conductivities, resulting in their use as fillers for composites to improve their mechanical, electrical, and thermal properties. In our previous research, electrically-conductive CNT-dispersed Si_3N_4 ceramics were developed[46]. In the case of the CNT composite process, one of the most important problems to be solved is the uniform dispersion of CNTs. Here, we tried to prepare a powder mixture of CNTs and Al_2O_3 using the powder composite process and then fabricate CNT-dispersed Al_2O_3 ceramics using the nanocomposite particles.

The raw materials were multiwall carbon nanotubes and an alumina powder (Taimei Chemical, TM-DAR, 0.2 μm). 2 wt% (4 vol%) of the carbon nanotubes were mixed with alumina using a powder composer (Nobiruta, Hosokawa Micron Co., Japan). **Fig. 16 (a)** shows the CNT-Al_2O_3 powder mixture prepared by the powder composite process. It was found that granules composed of CNTs and Al_2O_3 particles were formed, and there were no agglomer-

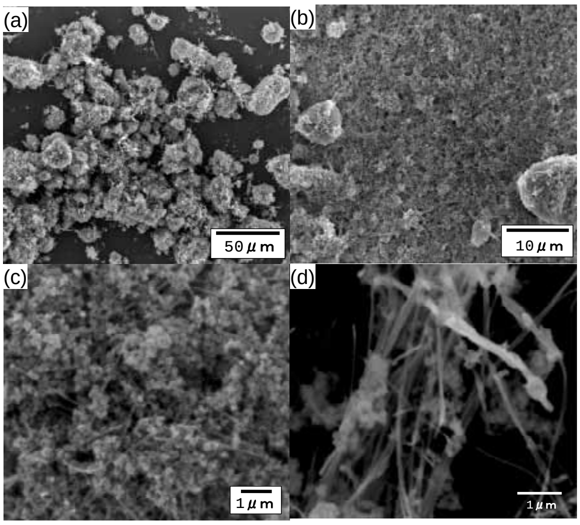

Fig. 16 TSEM images of powder mixture of CNTs and Al_2O_3 using a powder mixture prepared by a powder composite process.
(a) As-recieved powder.
(b) After ultrasonification in ethanol.
(c) and (d) Enlarged view of (b)

ates of CNTs. **Figs. 16 (b)** and **(c)** are SEM photographs of the powder mixture shown in **Fig. 16 (a)** after ultrasonification. The granules were easily pulverized by ultrasonic irradiation, and the CNTs were homogeneously dispersed in the Al_2O_3 powder. This indicated that the CNTs and Al_2O_3 were uniformly mixed by the particle composite process. **Fig. 16 (d)** is an enlarged view of the CNT-Al_2O_3 powder mixture. Fine Al_2O_3 particles were fixed on the CNTs. This phenomenon is similar to that seen with the SiO_2 nanoparticle-SiO_2 fiber prepared by a powder composite process, as reported by Naito et al.[9]

The powder mixture was fired at 1750℃ for 1 h in an Ar atmosphere using a hot pressing technique. The applied pressure was 30 MPa. A 20 × 20 × 5 mm ceramic plate was obtained. After cutting the sample into 3 × 4 × 20 mm pieces, the relative density, bending strength, and electrical conductivity were evaluated. The microstructure was observed by SEM. **Fig. 17** shows the microstructure of the CNT-Al_2O_3 composite fabricated by hot pressing. There were no large pores in the sintered body in spite of the inhibition of the densification by the CNTs. The bulk density of this sample was 3.82 g/cm^3, and the relative density was 92%. The grain size of the Al_2O_3 in this composite was about 2 μm, which is much smaller than that of pure Al_2O_3 ceramics hot-pressed under the same conditions (**Fig. 17 (b)**). The inhibition of grain growth resulted in the lowering of grain boundary migration because of the dispersed CNTs. In the enlarged photograph (**Fig. 17 (c)**), many projecting CNTs and small holes can be observed in the sintered body. These is evidence of the bridging or pullout of CNTs, which is similar to fiber reinforced ceramics.

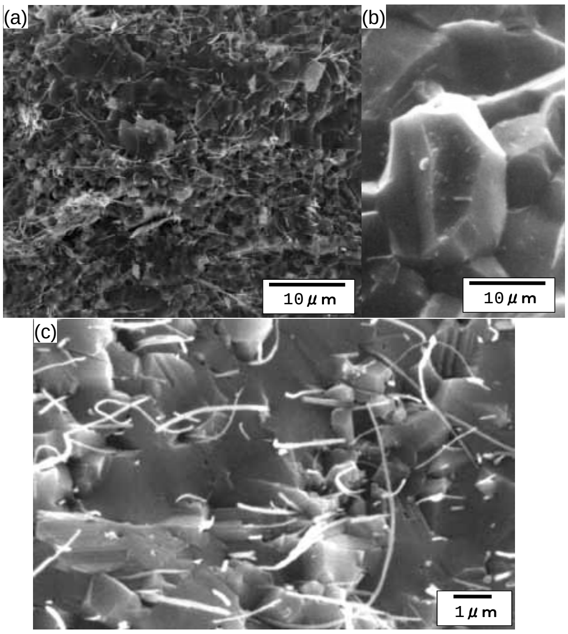

Fig. 17 SEM images of fracture surfaces of (a) CNT-dispersed Al_2O_3 ceramics fired at 1700℃ by hot pressing (b) Al_2O_3 ceramics without CNTs fired at 1700℃ by hot pressing and (c) enlarged view of (a).

The bending strength and electrical conductivity of the CNT-Al_2O_3 composites using nanocomposite particles are listed in **Table 3**. The bending strength of the CNT-Al_2O_3 composites was 423 MPa, which is higher than that of pure Al_2O_3 ceramics sintered by hot-pressing at the same temperature. This strengthening should be caused by the limitation of the grain growth and the reinforcement by the bridging and pullout of CNTs. The electrical conductivity of the developed CNT-Al_2O_3 composites was 448 S/m. This value was almost the same as the 12 wt% CNT-dispersed Si_3N_4 ceramics[43]. The achievement of such a high electrical conductivity by the addition of only 2 wt% CNTs is attributed to the homogeneous dispersion of the CNTs by the powder composite process, which formed numerous electrically conductive paths in the ceramics. Consequently, CNT-dispersed Al_2O_3 ceramics with high strength and high electrical conductivity were developed using nanocomposite particles prepared by the powder composite process.

5. Conclusions

A particle composite process was applied to develop several kinds of advanced ceramics. TiO_2 nanoparticles and Si_3N_4 particles were mixed using this powder composite process to disperse TiN nanoparticles in Si_3N_4 ceramics, which are expected to be used as novel materials for next-generation hybrid ceramic bearings. TEM observations showed that the TiO_2 nanoparticles were directly bonded to submicron Si_3N_4 particles. Si_3N_4 ceramics in which TiN nanopar-

Table 4 Density, bending strength and electrical conductivity of CNT-dispersed Al_2O_3 ceramics

CNT content	2wt%
Bulk density	3.82 gcm^{-3}
Relative density	97.8 %
Bending strength (3-point bending test)	423 MPa
Electrical conductivity (DC 4 terminal method)	448 S/m (=0.22 Ω cm)

ticles were uniformly dispersed were fabricated using the composite particles. The amount of damage caused by the Si_3N_4 ceramics with TiN nanoparticles to the mating metals in a ball-on-disk test was comparable to the damage caused by the Si_3N_4 ceramics without TiN particles. Nanocomposite particles of Al_2O_3-doped ZnO prepared by the powder composite process were also used to fabricate ZnO ceramics. TEM observations revealed that Al_2O_3 nanoparticles were uniformly present on ZnO particles. The sintering body fabricated using the composite powder prepared by this powder composite process had more uniform and finer microstructures than that fabricated using the powder mixture prepared by conventional wet mixing. The ZnO ceramics prepared by the powder composite process exhibited higher electrical conductivity than those prepared by the conventional wet ball milling process. CNT-dispersed Al_2O_3 ceramics were fabricated using a powder mixture of CNTs and a fine Al_2O_3 powder prepared by the powder composite process. It was shown that the CNTs were uniformly dispersed in the developed CNT-dispersed Al_2O_3 ceramics, and they had a high electrical conductivity and strength.

References

1) Naito, M., Kondo, A. and Yokoyama, T. (1993): Applications of Comminution Techniques for the Surface Modification of Powder Materials, ISIJ International, No. 33, pp. 915?924.
2) Hosokawa, M., Nogi, K., Naito, M. and Yokoyama, T. (2007): “Nanoparticle Technology Handbook,” Elsevier, Oxford, UK.
3) Naito, M., Hotta, T., Asahi, S. and Tanimoto, T. (1998): Deposition of Fine Particles on Surface of Core Particles by High-Speed Elliptical Rotor-Type Mixer, Kagaku Kogaku Ronbunshu, No. 24, pp. 52-56.
4) Naito, M., Hotta, T., Asahi, S., Tanimoto, T. and Endoh, S. (1998): Effect of Processing Conditions on Particle Composite Process by a High-Speed Elliptical-Rotor-Type Mixer, Kagaku Kogaku Ronbunshu, No. 24, pp. 99-103.
5) Naito, M., Hotta, T., Tanimoto, T., Endoh, S. and Nogi, K. (2000): Effect of Fine Particle Size on Particle Composite Process by a High-Speed Elliptical-Rotor-Type Mixer, Kagaku Kogaku Ronbunshu, No. 26, pp. 62-67.
6) Hotta, T., Naito, M. Szeplvolgyi, J., Endoh, S. and Nogi, K. (2001): Effect of Rotor Shape on Particle Composite Process by a High-Speed Elliptical-Rotor-Type Mixer, Kagaku Kogaku Ronbunshu, No. 27, pp. 141-143.
7) Nogi, K., Naito, M., Kondo, A., Nakahira, A., Niihara K. and Yokoyama T. (1996): New Method for Elucidation of Temperature at the Interface Between Particles under Mechanical Stirring, J. Japan Soc. of Powder and Powder Metallurgy, No. 43, pp. 396-401.
8) Fukui, T., Murata, K., Ohara, S., Abe, H., Naito, M. and Nogi, K. (2004): Morphology control of Ni?YSZ cermet anode for lower temperature operation of SOFCs, J. Powder Sources, No. 125, pp. 17-21.
9) Naito, M. Abe, H., Kondo, A., Yokoyama T. and Huang, C. C. (2009): Smart Powder Processing for Advanced Materials, Kona Powder and Particle Journal No.27, pp. 130-143.
10) Abe, H., Abe, I., Sato, K. and Naito, M. (2005): Dry Powder Processing of Fibrous Fumed Silica Compacts for Thermal Insulation, J. Am. Ceram. Soc., 88, pp.1359-1361.
11) Sato, K., Chaichanawong, J., Abe, H. and Naito, M. (2006): Mechanochemical synthesis of $LaMnO_3$ fine powder assisted with water vapor, Material Letters, 60, pp.1399-1402.
12) Tatami, J., Kodama, E., Watanabe, H., Nakano, H., Wakihara, T., Komeya, K., Meguro, T. and Azushima, A. (2008): Fabrication and wear properties of TiN nanoparticle-dispersed Si3N4 ceramics, J. Ceram. Soc. Japan, No. 116, pp.749-754.
13) Tasaki, S., Tatami, J., Nakano, H., Wakihara, T., Komeya, K. and Meguro, T. (2010): Fabrication of ZnO ceramics using ZnO/Al_2O_3 nanocomposite particles prepared by mechanical treatment, J. Ceram. Soc. Japan, No. 118, pp. 118-121.
14) Hiratsuka, D., Junichi T., Wakihara, T., Katsutoshi, K. and Meguro, T. (2009): Fabrication of AlN ceramics using AlN and nano-Y_2O_3 composite particles prepared by mechanical treatment, Key Engineering Materials, No. 403, pp. 245-248
15) Kodama, E., Tatami, J., Wakihara, T., Meguro, T., Komeya, K. and Nakano, H. (2009): Fabrication and mechanical properties of TiN nanoparticle-dispersed Si3N4 ceramics from Si3N4-nano TiO_2 composite particles obtained by mechanical treatment, Key Engineering Materials, No. 403, pp. 221-224.
16) Oyama, Y. and Kamigaito, S. (1971): Solid Solubility of Some Oxides in Si3N4, Jpn. J. Appl. Phys., No. 10, pp. 1637.
17) Jack, K. H. and Wilson, W. I. (1972): Ceramics Based on the Si-Al-O-N and Related Systems, Nature Physics Science. No. 238, pp. 28-29.
18) Tsuge, A., Nishida, K. and Komatsu, M. (1975): Effect of Crystallizing the Grain-Boundary Glass Phase on the High Temperature Strength of Hot-Pressed Si3N4, J. Am. Ceram. Soc., No. 58, pp. 323-326.
19) Komeya, K. (1984): Development of Nitrogen Ceramics, Am. Ceram. Soc., Bull., No. 63, pp. 1158-1159.
20) Yamada, T. and Kotoku, Y. (1989): Jpn. Chem. Ind. Assoc. Mon., No. 42, pp. 8.
21) Mitomo, M. (1976): Pressure Sintering of Si3N4, J. Mater. Sci., No. 11, pp. 1103-1107.
22) Kawamura, H. and Yamamoto, S. (1983): Improvement of Diesel Engine Startability by Ceramic Glow Plug Start System, SAE Paper, No. 830580.

23) Kamiya, S., Murachi, M., Kawamoto, H., Kato, S., Kawakami, S. and Suzuki, Y. (1985): Silicon Nitride Swirl Chambers for High Power Charged Diesel Engines, SAE, No. 850523.

24) Hattori, H., Tajima, Y., Yabuta, K., Matsuo, Y., Kawamura, M. and Watanabe, T. (1986): Gas Pressure Sintered Silicon Nitride Ceramics for Turbocharger Application, Proc. 2nd International Symposium bon Ceramic Materials and Components for Engines, pp. 165 (1986).

25) Komeya, K. and Kotani, H. (1986): Development of Ceramic Antifriction Bearing, JSAE Rev., No. 7, pp. 72-79.

26) Takebayashi, H., Tanimoto, K. and Hattori, T. (1998): Performance of Hybrid Ceramic Bearing at High Speed Condition (Part 1), J. Gas Turbine Soc. Japan, No. 26, pp. 55-60.

27) Takebayashi, H., Tanimoto, K. and Hattori, T. (1998): Performance of Hybrid Ceramic Bearing at High Speed Condition (Prat 2), J. Gas Turbine Soc. Japan, No. 26, pp. 61-66.

28) Tatami, J., Toyama, M., Noguchi, K., Komeya, K., Meguro, T. and Komatsu, M. (2003): Effect of TiO2 and AlN Additions on the Sintering Behavior of the Si3N4-Y_2O_3-Al_2O_3 System, Ceramic Transactions, No. 247, pp. 83-86.

29) Yano, T., Tatami, J., Komeya, K. and Meguro T. (2001): Microstructural Observation of Silicon Nitride Ceramics Sintered with Addition of Titania, J. Ceram. Soc. Japan, No. 109, pp. 396-400.

30) Tatami, J., Chen, I. W., Yamamoto, Y., Komastu, M., Komeya, K., Kim, D. K., Wakihara, T., Meguro, T. (2006): Fracture Resistance and Contact Damage of TiN Particle Reinforced Si_3N_4 Ceramics, J. Ceram. Soc. Japan, No. 114, pp. 1049-1053.

31) Adachi, K., Kato, K. and Chen, N. (1997): Wear Map of Ceramics, Wear, No. 203, pp. 291-301.

32) Zheng, S., Gao, L., Watanabe, H., Tatami, J., Wakihara, T., Komeya, K. and Meguro, T. (2007): Improving the Microstructure of Si_3N_4-TiN Composites Using Various PEIs to Disperse Raw TiO_2 Powder, Ceramics International, No. 33, pp. 355-359.

33) Gahlin, R. and Jacobson, S. (1999): The particle size effect in abrasion studied by controlled abrasive surfaces, Wear, No. 224, pp. 118-125.

34) Ogasawara, T., Tanaka, R., Sugawara, K. and Sugawara, T. (2000): Effect of the Additives on the Nonlinear Coefficient of ZnO Varistor, J. Ceram. Soc. Japan, No. 108, pp. 565-570.

35) Xu, J., Pan, Q., Shun, Y. and Tian, Z. (2000): Sens. Actuators B, 66, 277-279 (2000).

36) Ohtaki, M., Tsubota, T., Eguchi, K. and Arai, H. (1996): High-temperature thermoelectric properties of (Zn1-xAlx)O, J. Appl. Phys., No.79, pp. 1816-1818.

37) Nakamura, M., Ikuta, K., Aoki, T., Suzuki, A., Matsushita, T. and Okuda, M. (2008): Ultra Thin Al-doped Transparent Conducting Zinc Oxide Films Fabricated by Pulsed Laser Deposition Method, J. Vac. Soc. Jpn., No. 51 pp. 323-325.

38) Tsukazaki, A., Kubota, M., Ohtomo, A., Onuma, T., Ohtani, K., Ohno, H., Chichibu, S. F. and Kawasaki, M. (2005): Blue Light-Emitting Diode Based on ZnO, Jpn. J. Appl. Phys., No. 44, pp. L643-L645.

39) Matsuoka, M. (1971): Nonohmic Properties of Zinc Oxide Ceramics, Jpn. J. Appl. Phys., No. 10, pp.736-746.

40) Mukae K., Tsuda K. and Nagasawa I. (1977): Nonohmic properties of ZnO-rare earth metal oxide-Co_3O_4 ceramics, Jpn J. Appl. Phys., No. 16, pp.1361-1368.

41) Tanaka, M., Tsubone, T. and Yanagida, H. (1974): Electrical Conductivity of Sintered Bodies of ZnO Doped with Al_2O_3, Yogyo Kyokaishi, No. 82, pp. 271-277.

42) Kaga, H., Kinemuchi, Y., Yilmaz, H., Watari, K., Nakano, H., Nakano, H., Tanaka, S., Makiya, A., Kato, Z. and Uematsu, K. (2007): Orientation dependence of transport property and microstructural characterization of Al-doped ZnO ceramics, Acta Mater., No. 55, pp. 4753-4757.

43) Ewsuk, K. G., Ellerby, D. T. and DiAntonio, C. B. (2006): Analysis of Nanocrystalline and Microcrystalline ZnO Sintering Using Master Sintering Curves, J. Am. Ceram. Soc., No. 89, pp. 2003-2009.

44) Han, J., Mantas, P. Q. and Senos, A. M. R. (2001): Densification and Grain Growth of Al-doped ZnO, J. Mater. Res., No. 16, pp. 459-468.

45) Shirouzu, K., Ohkusa, T., Hotta, M., Enomoto, N. and Hojo, J. (2007): Distribution and Solubility Limit of Al in Al_2O_3-Doped ZnO Sintered Body, J. Ceram. Soc. Japan, No. 115, pp. 254-258.

46) Tatami, J., Katashima, T., Komeya, K., Meguro, T., Wakihara, T. (2005): Electrically Conductive CNT-Dispersed Silicon Nitride Ceramics, J. Am. Ceram. Soc., No. 88, pp. 2899-2893.

Author's short biography

Junichi Tatami

Dr. Junichi Tatami received B.S., M.S., and Ph.D. degrees in inorganic materials from Tokyo Institute of Technology , Japan in 1992, 1994 and 1997, respectively. He was a research fellow of Japan Society for Promotion of Science in Tokyo Institute of Technology in 1997. He joined Yokohama National University as a research associate in 1997. He was promoted to be an associate professor in 2002. His current interest is the development of high performance and more reliable fine ceramics by advanced powder processing.

Hiromi Nakano

Dr. Hiromi Nakano received B.S., M.S., and Dr. (Eng.) from Toyohashi University of Technology, Japan in 1981, 1983 and 2000, respectively. She joined Murata Manufacturing Co., Ltd. in 1983. She transferred to Ryukoku University in 1989. She transferred to Toyohashi University of Technology as an associate professor in 2009. Her current interest is characterization of the materials using a transmission electron microscope to control of the material properties and the design of new materials.

Toru Wakihara

Dr Toru Wakihara received his Engineering degree from the University of Tokyo, School of Engineering in 1999. He completed his Graduate thesis in 2001 in the Department of Chemical System Engineering, Graduate School of Engineering, University of Tokyo. He completed his doctoral thesis in the same department in 2004. In 2004, Dr Wakihara took up a post as Research Associate in the Graduate School of Environment and Information Sciences at Yokohama National University where the main topics of his research were on Nitride, Oxynitride, Carbide and Ceramic Processing and also zeolites. In 2007, he was appointed as Assistant Professor at Yokohama National University.

Katsutoshi Komeya

Dr. Katsutoshi Komeya received B.S. degree in electrochemistry from Yokohama National University(YNU), Japan in 1962, and Ph.D. degree in inorganic materials from Tokyo Institute of Technology, Japan in 1977. After he spent in Toshiba R & D Center, Japan, for 27 years, he moved to YNU. He was promoted to be an associate professor in 2002, a professor in 1992 and an emeritus professor in 2004. His current interest is the high performance non-oxide ceramics, especially Si3N4 and AlN. After retirement of YNU in 2004, he is continuing to study the above nitrides in YNU. He is a fellow of American Ceramic Society.

Information Articles

The 44th Symposium on Powder Technology

The 44th Symposium on Powder Technology was held on September 6th, 2010 at Tokyo Garden Palace Hotel under the sponsorship of the Hosokawa Powder Technology Foundation and with the support of Hosokawa Micron Corporation. The symposium was very successful as usual with the attendance of 134 including 23 academic people. The symposium subject was “New Materials Produced by Nanoparticle Handling Technology”.

• Opening Address	Prof. Hiroaki Masuda (Kyoto Univ.)
Session 1 Chairperson: Prof. Jusuke Hidaka (Doshisha Univ.)	
• Fabrication of Highly Structural Controlled Ceramics by Advanced Colloidal Processing	Yoshio Sakka (National Institute for Materials Science)
• Development of nano-particle composite technique for low Pt-loading PEFCs	Hirokazu Munakata (Tokyo Metropolitan University)
Session 2 Chairperson: Prof. Ko Higashitani (Kyoto Univ.)	
• Viscoelastic designs of Nanoparticle dispersion and their applications for functional fluids	Hiroya Abe, Akira Kondo, Shinya Yamanaka, Makio Naito (Osaka University)
• The effect of slurry control on structure and characteristic of electronic ceramics	Ichiro Nakamura (Murata Manufacturing Co.,Ltd.)
Session 3 Chairperson: Prof. Makio Naito (Osaka Univ.)	
• Development of high performance materials for cosmetics with nano-structure control technology	Koji Mine (Kao Corporation)
• Development of dispersion and compounding processes of nanoparticles and their applications to advanced fire-fighter uniform	Toyokazu Yokoyama (Hosokawa Micron Corp.)
• Closing Address	Yoshio Hosokawa (Hosokawa Micron Corporation)

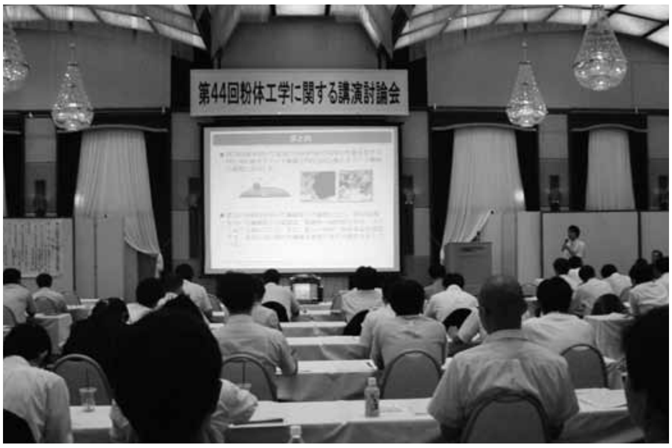

GENERAL INFORMATION

HISTORY OF THE JOURNAL

In the history of KONA Powder and Particle Journal, two organizations have been playing an important role. The one is the Council of Powder Technology, Japan (CPT) and the other is the Hosokawa Powder Technology Foundation (Hosokawa Foundation). The CPT was established in 1969 by Hosokawa Micron Corporation as a non-profit organization to enhance the activities of research and development on powder science and technology. The Hosokawa Foundation was established in 1991 as a public-service corporation approved by the Ministry of Education, Culture, Sport, Science and Technology of Japan. The issues from No.1 (1983) to No.12 (1994) of KONA were published by CPT and the issues from No.13 (1995) by the Hosokawa Foundation.

The aim of KONA in the early days was to introduce excellent Japanese papers to the world and thus KONA consisted of papers recommended by some Japanese academic societies and translated from Japanese to English. From the issue of No.8, the CPT changed its editorial policy to internationalize the KONA and to incorporate papers by authors throughout the world in addition to translated papers. In response to this change, three editorial blocks have been organized in the world; Asian-Oceania, American and European. The policy and system have not changed even after the Hosokawa Foundation has taken over from the CPT. From the issue of No.27(2009), publication of translated papers has been terminated and only original papers have been published. The CPT is active still today and collaborates with the Hosokawa Foundation.

AIMS AND SCOPE

KONA publishes papers in a broad field of powder science and technology, ranging from fundamental principles to practical applications. The papers descriping technological experiences and critical reviews of existing knowledge in special areas are also welcome.

The submitted papers are published only when they are judged by the Editor to contribute to the progress of powder science and technology, and approved by any of the three Editorial Committees. The paper submitted to the Editorial Secretariat should not have been previously published except .

CATEGORY OF PAPERS

- Invited papers
  Original research and review papers invited by the KONA Editorial Committees.
- Contributed papers
  Original research and review papers submitted to the KONA Editorial Committees, and refereed by the Editors.

SUBMISSON OF PAPERS

Papers should be sent to each KONA Editorial Secretariat.

- Asia/Oceania E'ditorial Secretariat
  Mr. T. Kawamura
  Hosokawa Powder Technology Foundation
  Shodai-Tajika,1-9, Hirakata, 573-1132 Japan
- Europe/Africa E'ditorial Secretariat
  Dr. J. Stein or Mrs. P. Krubeck
  Hosokawa Micron
  Division of Hosokawa Alpine AG.
  Welserstr. 9-11, 51149 Koeln, GERMANY
- Americas Editorial Secretariat
  Dr. C.C. Huang
  Hosokawa Micron Powder Systems
  10 Chatham Road, Summit NJ 07901 USA

Publication in KONA Powder and Particle Journal is free of charge.

PUBLICATION SCHEDULE

KONA is published annually. The publication date is December 25th.

SUBSCRIPTION

KONA Powder and Particle Journal is distributed free of charge to senior researchers at universities and laboratories as well as to institutions and libraries in the field throughout the world. The publisher is always glad to consider the addition of names of those who want to obtain this journal regularly to the mailing list. Distribution of KONA is made by each Secretariat.

Free electronic publication of KONA Powder and Particle Journal is available in
http://www.kona.or.jp

INSTRUCTIONS TO AUTHORS

(1) Manuscript format

- Electric files should be submitted to the Editorial Secretariat by online. Authors' short biography and photograph should be attached to the final version.
- The structure of manuscripts should follow the following order; title, authors, affiliations, abstract, keywords, main text, (acknowledgement), (appendix), (nomenclature), references. The items with parentheses are not mandatory. The text should be in single-column format. Figures and tables can be imported into the main text. If figures and table are collated in a separate section at the end of the article, indicate their approximate locations directly in the text. If symbols are defined in a nomenclature section, symbols and units should be listed in alphabetical order with their definition and dimensions in SI units If symbols are not defined in a nomenclature section, they should be defined in the text.
- Full postal addresses must be given for all the authors. Indicate the corresponding author by the mark“*” after the name. Telephone and fax numbers and e-mail address should be provided for the corresponding author.
- Abstract should not exceed 200 words.
- The appropriate number of keywords is 5 or 6.
- Symbols and units should be listed in alphabetical order with their definition and dimensions in SI units.
- Concerning references, either the numbering system or the alphabetical system should be adopted. In the numbering system, references should be numbered in sequence starting at the beginning of the paper. References should be given in the following form:
  1) Carslaw, H. C. and Jaeger, J. C.(1960): “Conduction of Heat in Solids” , 2nd ed., Clarendon Press, Oxford, England.
  2) Howell, P. A. (1963):US Patent, 3, 334,603
  3) Jia, R. (1990): “Surface Properties of Coal and Their Role in Fine Coal Processing,” Ph.D. Dissertation, University of California at Berkeley.
  4) Zhang, N. and Rosato, A. D. (2006): Experiments and Simulations on Vibration Induced Densification of Bulk Solids, KONA Powder and Particle Journal, No.24, pp.93-103.

  In the alphabetical system, all publications cited in the text should be presented in alphabetical order of the authors. In the text make references by name and year, e.g. Zhang and Rosato (2006). Reference to papers with more than 3 authors should show the name of the first author followed by “et al.”

(2) Reprint

- The authors shall receive 50 free reprints. Additional reprints will be furnished when ordered with return of galley proof.

(3) Copyright and permission

- Original papers submitted for publication become immediately the property of the Hosokawa Powder Technology Foundation and remain so unless withdrawn by the author prior to acceptance for publication or unless released by the Editor. The original papers in KONA should not be reproduced nor published in any form without the written permission of the Hosokawa Foundation. Authors are responsible for obtaining permission from the copyright holder to reproduce any figures and photos for which copyright exists.

HOSOKAWA MICRON

Hosokawa Micron Ltd. is a member of the Hosokawa Micron Group, responding to global needs through an emphasis on materials science and engineering. The Group is an international provider of equipment and Technology for powder and particle processing, product recovery, plastics processing and confectionery products. The Group maintains facilities for research, engineering, manufacturing, and service in each of the world's major industrial markets.

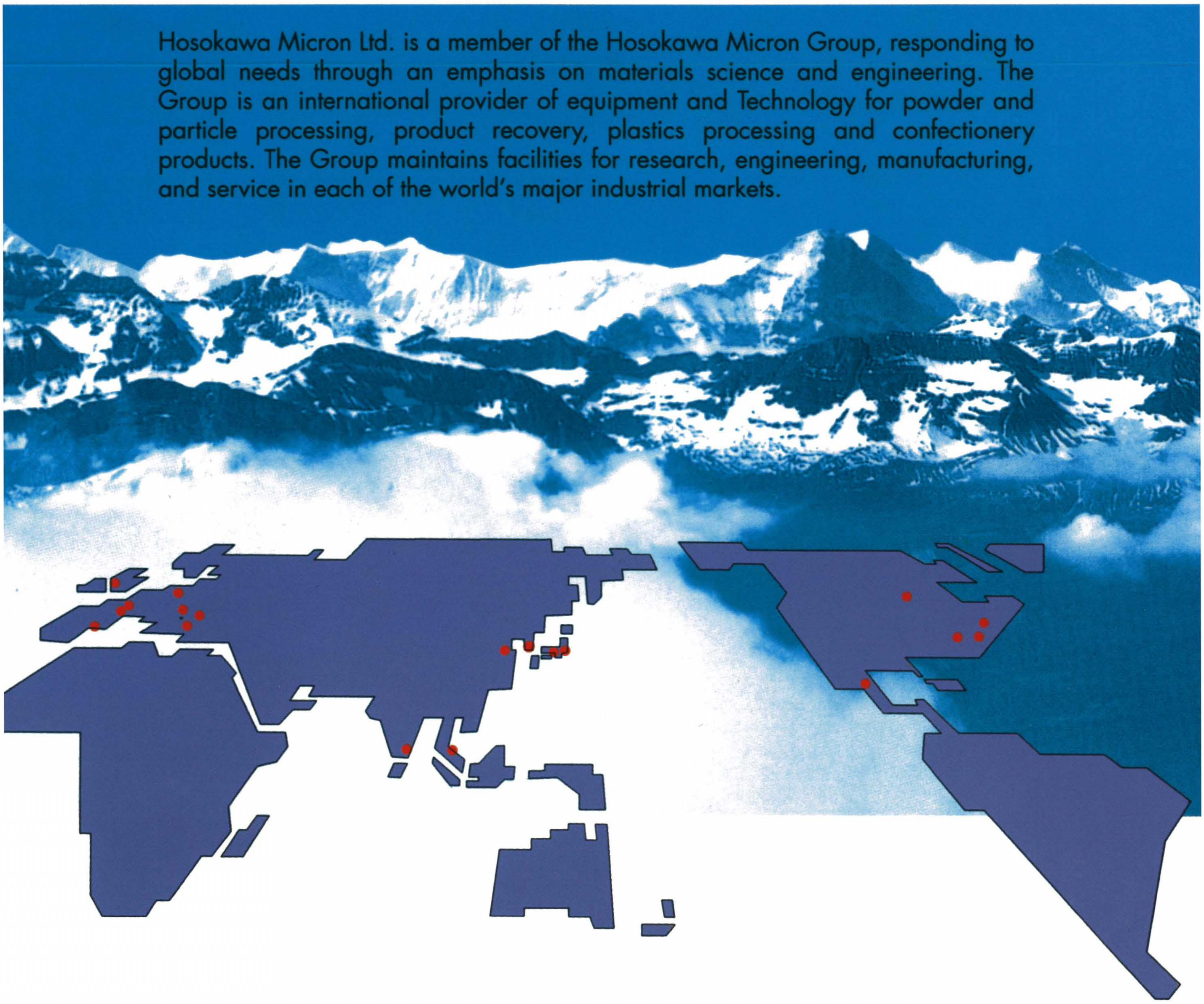

Process Technologies for Tomorrow

HOSOKAWA MICRON

Headquarter Locations;
HOSOKAWA MICRON CORPORATION
http://www.hosokawamicron.co.jp